europhysics
conference
abstracts

17th EPS Conference on

Controlled Fusion and Plasma Heating

Amsterdam, 25-29 June 1990

Editors: G. Briffod, Adri Nijsen-Vis, F.C. Schüller

Contributed Papers
Part I

Published by: European Physical Society

...es Editor: Prof. K. Bethge, Frankfurt/M.

...aging Editor: G. Thomas, Geneva

VOLUME 14 B Part I

XVII FUSION AMSTERDAM 1990

Het HUIS RYNHUIZEN

Max-Planck-Institut für Plasmaphysik
5005 4198
25. JAN. 1991
Bibliothek

17th
FUSION
AMSTERDAM
1990

A

17th European Conference on

Controlled Fusion and Plasma Heating

Amsterdam, 25-29 June 1990

Editors: G. Briffod, Adri Nijsen-Vis, F.C. Schüller

Contributed Papers
Part I

0053-91

EUROPHYSICS CONFERENCE ABSTRACTS is published by the
European Physical Society, © 1990
Reproduction rights reserved

This volume is published under the copyright of the European Physical Society. We want to inform the authors that the transfer of the copyright to EPS should not prevent an author to publish an article in a journal quoting the original first publication or to use the same abstract for another conference. This copyright is just to protect EPS against using the same material in similar publications.

PREFACE

The 17th European Conference on Controlled Fusion and Plasma Heating was held in Amsterdam, the Netherlands, from the 25th to the 29th of June 1990 by the Plasma Physics Division of the European Physical Society (EPS).

The Conference has been organized by the FOM-Instituut voor Plasmafysica Rijnhuizen, which is part of the Foundation for Fundamental Research on Matter (Stichting Fundamenteel Onderzoek der Materie). FOM is supported by the Dutch Research Organization NWO and Euratom.

The Conference has been sponsored by the Koninklijke Nederlandse Academie van Wetenschappen (KNAW) and by the Foundation Physica.

The programme, format and schedule of the Conference are determined by the International Programme Committee appointed by the Plasma Physics Division of the EPS.

The programme included 18 invited lectures; from the contributed papers 24 were selected for oral presentation and 470 for poster presentation.

This 4-volume publication is published in the Europhysics Conference Abstract Series and contains all accepted contributed papers received in due time by the organizers. The 4-page extended abstracts were reproduced photographically using the manuscripts submitted by the authors. The invited papers will be published in a special issue of the journal "Plasma Physics and Controlled Fusion" and sent free of charge to each registered participant.

The editors would like to acknowledge the skillful and dedicated support given by Laura van Veenendaal - van Uden, Rosa Tenge - Tjon A Tham and Cora de Bruijne in preparing the manuscripts for reproduction in these four volumes.

May 1990

The Editors

INTERNATIONAL PROGRAMME COMMITTEE

G. Briffod, Chairman, CEN, Grenoble, France
K. Appert, CRPP, Lausanne, Switzerland
R. Balescu, Université Libre de Bruxelles, Belgium
F. De Marco, Euratom-ENEA, Frascati, Italy
C. Gormezano, JET Joint Undertaking, Abingdon, United Kingdom
L. Laurent, Association Euratom-CEN, St. Paul-lez-Durance, France
S. Ortolani, Association Euratom-CNR, Padova, Italy
D.D. Ryutov, Academy of Sciences, Novosibirsk, USSR
F.C. Schüller, FOM-Rijnhuizen, Nieuwegein, The Netherlands
S.E. Segre, Euratom-ENEA, Frascati, Italy
P.E. Stott, JET Joint Undertaking, Abingdon, United Kingdom
H. Wobig, Max-Planck-Institut für Plasmaphysik, Garching bei München, FRG

LOCAL ORGANIZING COMMITTEE

M.J. van der Wiel, Chairman, FOM-Rijnhuizen, Nieuwegein
F.C. Schüller, Vice-Chairman, FOM-Rijnhuizen, Nieuwegein
A. Nijsen-Vis, Scientific Secretary, FOM-Rijnhuizen, Nieuwegein
J.T. van den Hout, Treasurer, FOM-Rijnhuizen, Nieuwegein
A.J.H. Donné, FOM-Rijnhuizen, Nieuwegein
N.J. Lopes Cardozo, FOM-Rijnhuizen, Nieuwegein
J. Rem, FOM-Rijnhuizen, Nieuwegein
H. Hopman, FOM-AMOLF, Amsterdam
D.C. Schram, Technical University, Eindhoven

CONTENTS

Part I	- A	TOKAMAKS	
		A1 Tokamaks, General	I-1 – I-101
		A2 Scaling Laws	I-102 – I-149
		A3 Determination of Transport Coefficients	I-150 – I-198
		A4 Fluctuations	I-199 – I-214
		A5 Results Pellet Injection	I-215 – I-246
		A6 H-Mode	I-247 – I-302
		A7 MHD Phenomena	I-303 – I-414
		A8 Vertical Instabilities	I-415 – I-430
Part II	- B	STELLARATORS	
		B1 Experiments	II-431 – II-487
		B2 Theory	II-488 – II-532
	- C	ALTERNATIVE MAGNETIC CONFINEMENT SCHEMES	
		C1 Reversed Field Pinches	II-533 – II-588
		C2 Other Magnetic Confinement Schemes	II-589 – II-666
	- D	MAGNETIC CONFINEMENT THEORY AND MODELLING	
		D1 Magnetic Confinement Theory	II-667 – II-776
		D2 Modelling	II-777 – II-860
		D3 General Theory	II-861 – II-973
Part III	- E	HEATING BY NEUTRAL BEAM INJECTION	III-974 – III-986
	- F	RF HEATING	
		F1 Ion Cyclotron Resonance Heating	III-987 – III-1071
		F2 Electron Cyclotron Resonance Heating	III-1072 – III-1136
		F3 Lower Hybrid Heating	III-1137 – III-1189
	- G	CURRENT DRIVE AND PROFILE CONTROL	
		G1 Electron Cyclotron Current Drive	III-1190 – III-1238
		G2 Lower Hybrid Current Drive	III-1239 – III-1294
		G3 Others	III-1295 – III-1340
	- H	IMPURITY AND EDGE PHYSICS	III-1341 – III-1483
PART IV	- I	DIAGNOSTICS	
		I1 Results	IV-1484 – IV-1611
		I2 Technique/New Method	IV-1612 – IV-1724
	- J	BASIC COLLISIONLESS PLASMA PHYSICS	IV-1725 – IV-1851
	- K	INERTIAL CONFINEMENT FUSION	IV-1852 – IV-1883

PAPER IDENTIFICATION

All contributed papers are listed with their title and responsible author. In those cases where no author was underlined the first author mentioned was taken. The day of the poster presentation of each paper, followed by the number of the poster board, is given under the title in the list of contributed papers. The four poster sessions will be held on:

Monday afternoon indicated as Mo,
Tuesday afternoon indicated as Tu,
Thursday afternoon indicated as Th,
Friday afternoon indicated as Fr.

The poster boards are numbered from 1 to 130. From the 494 contributed papers, 24 were selected for oral presentation. The authors of those orally presented papers were requested to give also a poster presentation. Most of them confirmed that they were prepared to do so.

TITLE LIST OF CONTRIBUTED PAPERS

A. TOKAMAKS

D-D neutron production from JET plasmas.
First author: G. Sadler et al.
Mo 1 A 1 I-1

Peaked profiles in low q high current limiter plasmas in JET.
First author: P.J. Lomas et al.
Mo 2 A 2 I-5

The fusion performance of JET limiter plasmas using Be coated graphite and solid Be surfaces.
First author: T.T.C. Jones et al.
Mo 3 A 3 I-9

The role of various loss channels in the ion energy balance in T-10.
First author: E.L. Berezovskij et al.
Mo 4 A 4 I-13

First experiments and numerical simulation of a plasma column compression in high field tokamak.
First author: E.A. Azizov et al.
Mo 5 A 5 I-14

A study of poloidal and toroidal rotation in the TJ-1 ohmically heated tokamak.
First author: B.G. Zurro et al.
Mo 6 A 6 I-18

Runaway electron fluctuations studies in TJ-I.
First author: L. Rodríguez et al.
Mo 7 A 7 I-22

Particle and impurity confinement in helium discharges in the Texas Experimental Tokamak (TEXT).
First author: W.L. Rowan et al.
Mo 8 A 8 I-26

The first Mexican small tokamak.
First author: L. Meléndez-Lugo et al.
Mo 9 A 9 I-30

The confinement improvement modes in JIPP T-11U.
First author: Y. Hamada et al.
Mo 10 A 10 I-34

Measurements of fluctuations and space potential profiles in the Texas Experimental Tokamak (TEXT).
First author: P.M. Schoch et al.
Mo 11 A 11 I-38

Test of ITG-mode marginal stability in TFTR.
First author: M.C. Zarnstorff et al.
Mo 12 **A12*** I-42

Perturbative transport studies of neutral beam heated TFTR plasmas using carbon pellet injection.
First author: R.A. Hulse et al.
Mo 13 A 13 I-46

Measurements of radial profiles of transport parameters of HE^2 on TFTR.
First author: E.J. Synakowski et al.
Mo 14 A 14 I-50

T_e profile invariance under transient conditions on ASDEX.
First author: H.D. Murmann et al.
Tu 1 A 15 I-54

The isotope dependence of confinement in ASDEX: Part 2.
First author: F. Wagner et al.
Tu 2 A 16 I-58

Demixing of impurities and hydrogen as deduced from Z_{eff} profiles in the boronized ASDEX.
First author: K.H. Steuer et al.
Tu 3 A 17 I-62

Confinement studies in sawtooth-free ohmic discharges.
First author: U. Stroth et al.
Tu 4 A 18 I-66

Modifications of density profile and particle transport in ASDEX during lower hybrid heating and current drive.
First author: O. Gehre et al.
Tu 5 A 19 I-70

Particle transport studies on TCA using the dynamic response of the effective mass.
First author: Th. Dudok de Wit et al.
Tu 6 A 21 I-74

Transition to high density discharges through hard gas puffing.
First author: Z.A. Pietrzyk et al.
Tu 7 A 22 I-78

Current penetration measurements in TUMAN-3 by active charge exchange diagnostics.
First author: V.I. Afanasiev et al.
Tu 8 A 23 I-82

* This paper will also be presented orally on Friday 29 June at 9.40 hrs.

Ohmic discharges in TORE SUPRA - Marfes and detached plasmas.
First author: J.C. Vallet et al.
Tu 9 A 24 I-86

Toroidal plasma rotation in JET.
First author: H.P.L. de Esch et al.
Tu 10 A 25 I-90

ELM-free H-mode with CO- and CTR-neutral injection in ASDEX.
First author: F. Ryter et al.
Tu 11 **A26*** I-94

A regime showing anomalous triton burnup in JET.
First author: S. Conroy et al.
Tu 12 A 27 I-98

Scaling from JET to CIT and ITER-like devices using dimensionless parameters.
First author: J. Sheffield
Mo 15 A 28 I-102

Extrapolation of the high performance JET plasmas to D-T operation.
First author: J.G. Cordey et al.
Mo 16 A 29 I-106

Global H-mode scalings based on JET and ASDEX data.
First author: O. Kardaun et al.
Mo 17 A 30 I-110

Transport studies in high recycling neutral beam heated discharges on TFTR.
First author: D.W. Johnson et al.
Mo 18 A 31 I-114

Energy confinement scaling laws for FT ohmic plasma.
First author: G. Bracco et al.
Mo 19 A 32 I-118

Profile consistency coupled with MHD equilibrium extended to non stationary plasma conditions.
First author: M. Roccella et al.
Mo 20 A 33 I-122

Scaling dimensionally similar tokamak discharges to ignition.
First author: R.E. Waltz et al.
Mo 21 A 34 I-126

Transport code simulations of IGNITOR..
First author: M.F. Turner et al.
Mo 22 A 35 I-130

* This paper will also be presented orally on Tuesday 26 June at 14.30 hrs.

A physics perspective on CIT.
First author: R.J. Goldston et al.
Mo 23 A 36 I-134

Burn threshold for fusion plasmas with helium accumulation.
First author: B.D. Fried et al.
Mo 24 A 37 I-138

Heating profile and sawtooth effects on energy confinement in elongated tokamak plasmas.
First author: J.D. Callen et al.
Mo 25 A 38 I-142

The scaling of confinement with major radius in TFTR.
First author: L.R. Grisham et al.
Mo 26 A 39 I-146

Coupling of plasma particle diffusion and heat flow in TEXT.
First author: D.L. Brower et al.
Th 1 A 40 I-150

Sawtooth heat pulse propagation and electron heat conductivity in HL-1.
First author: Gancheng GUO et al.
Th 2 A 41 I-154

Evidence of coupling of thermal and particle transport from heat and density pulse measurements at JET.
First author: G.M.D. Hogeweij et al.
Th 3 A 42 I-158

Determination of local transport coefficients by heat flux analysis and comparisons with theoretical models.
First author: B. Balet et al.
Th 4 A 43 I-162

Dynamic response of plasma energy and broad-band magnetic fluctuations to additional heating in JET.
First author: C. Nardone et al.
Th 5 A 44 I-166

Analysis of heat pulse propagation in plasmas using Fourier methods.
First author: A. Jacchia et al.
Th 6 A 45 I-170

Particle and thermal transport in TEXT from perturbation experiments.
First author: K.W. Gentle et al.
Th 7 A 46 I-174

Investigation of coupled energy and particle transport.
First author: M. Cox et al.
Th 8 A 47 I-178

Is the ion confinement improving in ASDEX H-mode discharges?
First author: O. Gruber et al.
Th 9 A 48 I-182

Momentum transport studies on ASDEX.
First author: A. Kallenbach et al.
Th 10 A 49 I-183

Dynamic response analysis as a tool for investigating transport mechanisms.
First author: Th. Dudok de Wit et al.
Th 11 A 50 I-187

Heat and density pulse propagation in ASDEX.
First author: L. Giannone et al.
Th 12 A 51 I-151

Study of the electron heat pulse propagation from ECRH on T-10.
First author: A.A. Bagdasarov et al.
Th 13 A 52 I-195

Dimensionality analysis of chaotic density fluctuations in tokamak.
First author: F.C. Schüller et al.
Fr 1 A 53 I-199

Density fluctuation measurements via reflectometry on DIII-D during L- and H-mode operation.
First author: E.J. Doyle et al.
Fr 2 A 54 I-203

Investigation of density fluctuations in the ASDEX tokamak via collective laser scattering.
First author: E. Holzhauer et al.
Fr 3 A 55 I-207

Fluctuations and transport in DITE.
First author: G. Vayakis et al.
Fr 4 A 56 I-211

Online density feedback on ASDEX for pellet-refuelled discharges.
First author: R. Loch et al.
Fr 5 A 57 I-215

Simultaneous evolution of temperature and density perturbations following pellet injection in JET.
First author: J.R. Martin-Solis et al.
Fr 6 A 58 I-219

Impurity behavior in pellet-fuelled plasma of JT-60.
First author: T. Sugie et al.
Fr 7 A 59 I-223

Fast cooling phenomena with ice pellet injection in JIPP T-IIU tokamak.
First author: K.N. Sato et al.
Fr 8 A 60 I-227

The pellet trajectory toroidal deflection in T-10.
First author: A.A. Bagdasarov et al.
Fr 9 A 61 I-231

Scaling of experimentally determined pellet penetration depths on ASDEX.
First author: R. Loch et al.
Fr 10 A 62 I-235

Repetitive pellet injection combined with ion cyclotron resonance heating in ASDEX.
First author: J.-M. Noterdaeme et al.
Fr 11 **A63*** I-239

Evolution of pellet clouds and cloud structures in magnetically confined plasmas.
First author: L.L. Lengyel et al.
Fr 12 A 64 I-243

Transport of impurities during H-mode pulses in JET.
First author: L. Lauro Taroni et al.
Tu 13 A 65 I-247

Particle and heat deposition in the X-point region at JET.
First author: D.P. O'Brien et al.
Tu 14 **A66**** I-251

ICRH produced H-modes in the JET tokamak.
First author: V.P. Bhatnagar et al.
Tu 15 **A67***** I-255

The compatibility of the JET H-mode with other regimes of improved performance.
First author: A. Tanga et al.
Tu 16 A 68 I-259

Radiation asymmetries and H-modes.
First author: N. Gottardi et al.
Tu 17 A 69 I-263

Electric field profile of plasmas with improved confinement in JFT-2M tokamak.
First author: K. Ida et al.
Tu 18 A 70 I-267

* This paper will also be presented orally on Tuesday 26 June at 14.10 hrs.
** This paper will also be presented orally on Tuesday 26 June at 13.30 hrs.
*** This paper will also be presented orally on Tuesday 26 June at 13.50 hrs.

Comparison of thermal and angular momentum transport in neutral beam-heated hot-ion H- and L-mode discharges in DIII-D.
First author: K.H. Burrell et al.
Tu 19 A 71 I-271

The effects of carbonization on the confinement properties of the DIII-D H-mode.
First author: D.P. Schissel et al.
Tu 20 A 72 I-275

Physics of the L to H transition in DIII-D.
First author: H. Matsumoto et al.
Tu 21 A 73 I-279

Transport properties of high β_{pol} PBX-M plasmas.
First author: B. LeBlanc et al.
Tu 22 A 74 I-283

H-mode behaviour induced by edge polarization in TEXTOR.
First author: R.R. Weynants et al.
Tu 23 A 75 I-287

ELMS as triggered and as triggering relaxation phenomena in ASDEX.
First author: O. Klüber et al.
Tu 24 A 76 I-291

Long-pulse heating in ASDEX L- and H-mode discharges.
First author: O. Vollmer et al.
Tu 25 A 77 I-295

Ohmic H-mode in "TUMAN-3" tokamak.
First author: S.V. Lebedev et al.
Tu 26 A 78 I-299

Runaway electron production during major disruptions in TORE SUPRA.
First author: G. Martin et al.
Th 14 A 79 I-303

Runaway relaxation oscillation on HL-1 tokamak.
First author: Xuantong DING et al.
Th 15 A 80 I-307

Energy loss in a major disruption and MHD instabilities at low q in the HL-1 tokamak.
First author: Qingdi GAO
Th 16 A 81 I-311

MHD-Perturbations in T-10.
First author: P.V. Savrukhin et al.
Th 17 A 82 I-315

Sawtooth modulated density fluctuations in the central plasma region of NBI-heated discharges in TEXTOR.
First author: M. Jadoul et al.

Th 18 A 83 I-319

High-beta regimes in JET.
First author: P. Smeulders et al.

Th 19 **A 84*** I-323

Sawtooth stabilisation by fast ions: comparison between theory and experiments.
First author: F. Porcelli et al.

Th 20 A 85 I-327

JET neutron emission profiles and fast ion redistribution from sawteeth.
First author: F.B. Marcus et al.

Th 21 **A 86**** I-331

The detailed topology of the m=1 instability in the JET sawtooth collapse.
First author: S.W. Wolfe et al.

Th 22 A 87 I-335

Density limits in JET with beryllium.
First author: C.G. Lowry et al.

Th 23 A 88 I-339

Faraday rotation measurements on JET, and the change in the safety factor profile during a sawtooth collapse.
First author: J. O'Rourke et al.

Th 24 A 89 I-343

Sawtooth triggered disruptions at the density limit on DITE.
First author: G.M. Fishpool et al.

Th 25 A 90 I-347

Electromagnetic interactions between plasmas and vacuum vessel during disruptions in the Hitachi tokamak HT-2.
First author: M. Abe et al.

Th 26 A 91 I-351

Asymmetric effects of an l -1 external helical coil on the sawtooth amplitude on Tokoloshe tokamak.
First author: D.E. Roberts et al.

Th 27 A 92 I-355

* This paper will also be presented orally on Friday 29 June at 9.00 hrs.
** This paper will also be presented orally on Friday 29 June at 9.20 hrs.

Measurement of ohmic tokamak momentum confinement times from controlled locking and unlocking of tearing modes.
First author: D.E. Roberts et al.
Fr 13 A 93 I-359

The characteristics of low-q discharges on HT-6B tokamak.
First author: Guoxiang LI et al.
Fr 14 A 94 I-363

Profiles and MHD activities in PBX-M tokamak.
First author: H. Takahashi et al.
Fr 15 A 95 I-367

The beta limit in the DIII-D tokamak.
First author: J.R. Ferron et al.
Fr 16 A 96 I-371

MHD characteristics and edge plasma stability during periods of ELM activity in PBX-M.
First author: S.M. Kaye et al.
Fr 17 A 97 I-375

Resonant magnetic perturbations and disruption studies on COMPASS-C.
First author: A.W. Morris et al.
Fr 18 A 98 I-379

Stabilisation of sawtooth oscillations by trapped energetic particles in TEXTOR.
First author: J. Ongena et al.
Fr 19 A 99 I-383

Production of high poloidal beta equilibria limited by an inboard separatrix in TFTR.
First author: S.A. Sabbagh et al.
Fr 20 A 100 I-387

Soft-X-ray tomography of sawteeth and m=1 modes on ASDEX.
First author: R. Büchse et al.
Fr 21 A 101 I-391

Density limit in ASDEX under clean plasma conditions.
First author: A. Stäbler et al.
Fr 22 A 102 I-395

Theoretical analysis of high-beta JET shots.
First author: T.C. Hender et al.
Fr 23 A 103 I-399

Analysis of the energy heat quench during a disruption in TEXTOR.
First author: K.H. Finken et al.
Fr 24 A 104 I-403

Enhanced turbulence during the energy quench of disruptions.
First author: G.J.J. Remkes et al.
Fr 25 A 105 I-407

High density mode in "TUMAN-3" tokamak.
First author: L.G. Askinasi et al.
Fr 26 A 106 I-411

Nonlinear vertical displacement instability of elongated plasma in tokamak and its stabilization.
First author: Guoyang YU et al.
Th 28 A 107 I-415

Vertical instabilities in JET.
First author: P. Noll et al.
Th 29 A 108 I-419

Scaling of poloidal currents during rapid vertical displacement events.
First author: G.W. Pacher et al.
Th 30 A 109 I-423

Experiments at high elongations in DIII-D.
First author: E.A. Lazarus et al.
Th 31 A 110 I-427

B. STELLARATORS

Electron cyclotron radiation (ECR) asymmetry measurements at 2 ω_{He} in the L-2 stellarator.
First author: D.K. Akulina
Th 55 B 1 II-431

Confinement studies of ECRH plasmas in a toroidal heliac.
First author: G.D. Conway et al.
Th 56 B 2 II-435

Measurements of the fast ion distribution during neutral beam injection and ion cyclotron heating in ATF.
First author: M.R. Wade et al.
Th 57 B 3 II-439

Bootstrap current studies in the Advanced Toroidal Facility.
First author: M. Murakami et al.
Th 58 **B 4*** II-443

Impurity transport in ATF and the effect of controlled impurity injection.
First author: L.D. Horton et al.
Th 59 B 5 II-447

Transport study on ECH- and NBI- heated plasmas in the low-aspect-ratio helical system CHS.
First author: H. Iguchi et al.
Th 60 B 6 II-451

Cleanup and improvement of operational performance of ATF by chromium and titanium gettering.
First author: R.C. Isler et al.
Th 61 B 7 II-455

Confinement and stability on Heliotron E plasma.
First author: K. Kondo et al.
Th 62 B 8 II-459

Efficiency of electron-cyclotron plasma heating in the L-2 stellarator.
First author: Eh.D. Andryukhina et al.
Fr 49 B 9 II-463

Ray tracing during ECRH by X-wave on the second harmonic of ω_{ce} in L-2 stellarator.
First author: K.M. Likin et al.
Fr 50 B 10 II-467

Particle transport and recycling studies on the W VII-AS stellarator.
First author: F. Sardei et al.
Fr 51 B 11 II-471

* This paper will also be presented orally on Tuesday 26 June at 14.50 hrs.

H_α-spectroscopy on WVII-AS.
First author: A. Dodhy et al.
Fr 52 B 12 II-475

Results from X-ray measurements on the Wendelstein W7-AS stellarator.
First author: A. Weller et al.
Fr 53 B 13 II-479

First results with neutral injection into W VII-AS stellarator.
First author: W. Ott et al.
Fr 54 B 14 II-483

Statistical analysis of electron heat conduction on W7-AS.
First author: G. Kühner et al.
Fr 48 B 15 II-484

Two-ion ICRH heating in the flexible heliac TJ-II.
First author: J.F. Miramar Blázquez
Th 63 B 16 II-488

Influence of TJ-II flexibility upon ECRH.
First author: F. Castejón et al.
Th 64 B 17 II-489

Ideal interchange stability boundaries for stellarator configurations.
First author: L. García
Th 65 B 18 II-493

Self-stabilization of ideal modes in a heliac.
First author: C. Alejaldre et al.
Th 66 **B 19*** II-497

Determination of Boozer magnetic coordinates.
First author: A. López Fraguas et al.
Th 67 B 20 II-501

Bootstrap currents in heliac TJ-II configurations.
First author: A. Rodríguez Yunta et al.
Th 68 B 21 II-505

Equilibrium and stability of high ι TJ-II configurations.
First author: A. López Fraguas et al.
Fr 55 B 22 II-509

A general theory of LMFP neoclassical transport in stellarators.
First author: C.D. Beidler
Fr 56 B 23 II-513

* This paper will also be presented orally on Tuesday 26 June at 15.10 hrs.

On the edge structure of the W VII-AS stellarator.
First author: F. Rau et al.
Fr 57 B 24 II-517

Physics studies for the H-1 heliac.
First author: B.D. Blackwell et al.
Fr 58 B 25 II-521

Study of plasma equilibrium currents in an 1=3 torsatron.
First author: V.N. Kalyuzhnyj et al.
Fr 59 B 26 II-525

Impurity flux reversal in 1=2 torsatrons using RF heating.
First author: D.L. Grekov et al.
Fr 60 B 27 II-529

C. ALTERNATIVE MAGNETIC CONFINEMENT SCHEMES

Ion temperature measurements on the ETA-BETA II RFP.
First author: L. Carraro et al.
Tu 53 C 1* II-533

Carbon emission measurements on the RFP ETA-BETA II.
First author: M.E. Puiatti et al.
Tu 54 C 2 II-537

Shell gap modification and limiter insertion in the REPUTE-1 RFP.
First author: S. Shinohara et al.
Tu 55 C 3 II-541

Observations of high energy electrons in TPE-1RM15 reversed field pinch.
First author: Y. Yagi et al.
Tu 56 C 4 II-545

Coherent soft X-ray oscillations and magnetic flux regeneration in the REPUTE-1 RFP.
First author: Y. Shimazu et al.
Tu 57 C 5 II-549

Impurity ion temperature and rotational velocity observations in the HBTX1C RFP.
First author: R.A. Bamford et al.
Tu 58 C 6 II-553

Ion heating and confinement in the HBTX1C Reversed Field Pinch.
First author: P.G. Carolan et al.
Tu 59 C 7** II-557

Ion power loss in the HBTX1C Reversed Field Pinch.
First author: K.J. Gibson et al.
Th 69 C 8 II-561

RFP plasma resistance following laser ablation of carbon.
First author: B. Alper et al.
Th 70 C 9 II-565

Particle confinement in the HBTX1C Reversed Field Pinch.
First author: M.J. Walsh et al.
Th 71 C 10 II-569

High current density toroidal pinch discharges with weak toroidal fields.
First author: J.R. Drake et al.
Th 72 C 11 II-573

* This paper will also be presented orally on Thursday 28 June at 13.30 hrs.
** This paper will also be presented orally on Thursday 28 June at 13.50 hrs.

Relaxation, reconnection and the MHD dynamo.
First author: D.A. Kitson et al.
Th 73 C 12 II-577

Magnetic and electrostatic fluctuation measurements on the ZT-40M reversed field pinch.
First author: K.F. Schoenberg et al.
Th 74 C 13 II-581

Finite element analysis of helically symmetric equilibria.
First author: T. Honma et al.
Th 75 C 14 II-585

MHD stability of a plasma with anisotropic component in the rippled magnetic field.
First author: V.V. Arsenin
Tu 60 C 15 II-589

Hot electron plasmas instabilities in open traps OGRA-4 and OGRA-4K.
First author: M.I. Belavin et al.
Tu 61 C 16 II-593

Self organization of wave coupling at SK/CG-1 machine and conceptual design of SK/CG-2.
First author: S. Sinman et al.
Tu 62 C 17 II-597

FRC: TC-I machine results.
First author: M. Machida et al.
Tu 63 C 18 II-601

Study of an FRC with n=1 external perturbations.
First author: B.A. Nelson et al.
Tu 64 C 19 II-605

Optimization of pulse plasma production in Z-pinch systems.
First author: L.I. Rudakov et al.
Tu 65 C 20 II 609

Extrap L-1 experimental stability.
First author: J. Scheffel et al.
Tu 66 C 21 II-610

Dense plasma heating in a mirror trap during injection of 100 kJ microsecond electron beam.
First author: A.V. Burdakov et al.
Th 76 C 22 II-614

On possibility of creating MHD-stable plasma distribution in axisymmetric paraxial mirror.
First author: S.V. Kuz'min et al.
Th 77 C 23 II-618

Magnetic and Langmuir probe measurements in the SPHEX spheromak.
First author: D.A. Kitson et al.
Th 78 C 24 II-622

Magnetic field configuration of FBX-II spherical torus.
First author: M. Irie et al.
Th 79 C 25 II-626

Correlation between magnetic tearing and X-ray emission in coaxial discharges.
First author: H.M. Soliman et al.
Th 80 C 26 II-630

Specific operational modes of high-current pinch discharges.
First author: M. Sadowski et al.
Th 81 C 27 II-634

Field-reversed configurations: a search for a viable reactor option.
First author: M. Heindler et al.
Th 82 C 28 II-638

Self-similar dynamics of fiber initiated high-density Z-pinch.
First author: M.A. Liberman et al.
Fr 61 C 29 II-639

Improved understanding of current drive and confinement in spheromaks.
First author: R.M. Mayo et al.
Fr 62 C 30 II-643

Diffusion-driven currents in a Z-pinch.
First author: B. Lehnert
Fr 63 C 31 II-647

Passage of powerful current pulses through plasma layer.
First author: L.E. Aranchuk et al.
Fr 64 C 32 II-651

New spectroscopic results from EXTRAP-T1 plasma.
First author: J.H. Brzozowski et al.
Fr 65 C 33 II-655

Compression, heating and fusion in dynamic pinches stabilized by an axial magnetic field.
First author: M.A. Liberman et al.
Fr 66 C 34 II-659

The dense Z-pinch project at Imperial College.
First author: M.G. Haines et al.
Fr 67 C 35 II-663

D. MAGNETIC CONFINEMENT THEORY AND MODELLING

Turbulent drift of electrons across a magnetic field: the effect of an average electric field.
First author: M.B. Isichenko et al.
Tu 98 D 1 II-667

Anomal diffusion in plasmas across the magnetic field in approaching of strong turbulence.
First author: A.B. Arutiunov et al.
Tu 99 D 2 II-671

Average magnetic surfaces in TBR-1 tokamak.
First author: S.J. de Camargo et al.
Tu 100 D 3 II-675

Suppressing effect of electrostatic waves on drift wave instability.
First author: Yongxiang YIN
Tu 101 D 4 II-679

Drift dissipative instabilities in a two electron temperature plasma.
First author: M. Bose et al.
Tu 102 D 5 II-684

Effects of ripple losses on fusion alpha particle distributions.
First author: G. Kamelander
Tu 103 D 6 II-685

Stationary spectra of short-wave low-frequency fluctuations in a finite-beta plasma.
First author: P.P. Sosenko et al.
Tu 104 D 7 II-686

The effect of magnetic field perturbations on the numerically derived diffusion coefficient for the fast alpha particles.
First author: E. Bittoni et al.
Tu 105 D 8 II-687

On diffusion of magnetic field lines.
First author: D.F. Düchs et al.
Tu 106 D 9 II-691

Toroidal ion temperature gradient driven weak turbulence.
First author: N. Mattor et al.
Tu 107 **D 10*** II-695

On self-consistent distribution function of high-energy alpha particles in axisymmetric tokamak.
First author: V.A. Yavorskij et al.
Tu 108 D 11 II-699

* This paper will also be presented orally on Thursday 28 June at 14.10 hrs.

Magnetic island self-sustainment by finite Larmor radius effect.
First author: M. Hugon et al.
Tu 109 D 12 II-703

The long wavelength limit of the ion-temperature gradient mode in tokamak plasmas.
First author: F. Romanelli et al.
Tu 110 D 13 II-707

Solitary vortex solution of nonlinear η_i-mode equations.
First author: F. Romanelli et al.
Tu 111 D 14 II-711

Neoclassical transport calculations for "linear" MHD equilibria.
First author: H. Werthmann et al.
Tu 112 D 15 II-715

Diffusion of ions in presence of nearly overlapping magnetic islands.
First author: J.T. Mendonça et al.
Th 93 D 16 II-719

Toroidal η_i-mode turbulence with collisional trapped electron effects.
First author: A. Jarmén et al.
Th 94 D 17 II-723

The anomalous resistivity in the neutral sheet of the magnetotail.
Guilding center theory in the reversed magnetic geometry.
First author: Jian-lin MU et al.
Th 95 D 18 II-727

Specific edge effects on turbulence behaviour.
First author: L. Laurent et al.
Th 96 D 19 II-728

Ripple induced stochastic diffusion of trapped particles in tokamak reactors.
First author: J-P. Roubin et al.
Th 97 D 20 II-732

Microtearing modes.
First author: X. Garbet et al.
Th 98 D 21 II-736

Modelling of improved confinements in tokamaks.
First author: S.I. Itoh et al.
Th 99 D 22 II-740

The effect of the radial electric field on the L-H mode transition.
First author: M. Tendler et al.
Th 100 D 23 II-744

A fast method for simulating α-particle orbits in tokamaks.
First author: W.D. D'haeseleer
Th 101 D 24 II-748

The neoclassical effects on resistive MHD modes in general toroidal geometry.
First author: Duk-in Choi et al.
Th 102 D 25 II-752

Low frequency electrostatic instabilities in a toroidal plasma with a hot ion beam.
First author: M. Liljeström
Th 103 D 26 II-756

Radiation-induced η_e-modes.
First author: P.K. Shukla et al.
Th 104 D 27 II-760

Ionization and charge exchange effects on dissipative drift modes in an edge tokamak plasma.
First author: D.K. Morozov et al.
Th 105 D 28 II-764

Equilibrium beta limit and alpha-particle containment in stellarators as a function of their aspect ratio.
First author: F. Alladio et al.
Th 106 D 29 II-765

Collisionless two-fluid theory of toroidal η_i stability.
First author: J.P. Mondt et al.
Th 107 D 30 II-769

Modelling of transport in stochastic magnetic field regions.
First author: M.A. Hellberg et al.
Th 108 D 31 II-773

Simplified models for radiational losses calculation in a tokamak plasma.
First author: A.B. Arutiunov et al.
Tu 113 D 32 II-777

Physical accuracy estimate of global energy confinement scaling laws for tokamaks.
First author: A.N. Chudnovskij et al.
Tu 114 D 33 II-781

Transport model of canonic profiles for ion and electron temperatures in tokamaks.
First author: Yu.N. Dnestrovskij et al.
Tu 115 D 34 II-785

Plasma periphery influence on plasma core confinement under auxiliary heating.
First author: S.I. Krasheninnikov et al.
Tu 116 D 35 II-789

Current density and energy transport in high temperature plasmas.
First author: B. Coppi et al.
Tu 117 D 36 II-793

Unified physical scaling laws for tokamak confinement.
First author: J.P. Christiansen et al.
Tu 118 D 37 II-797

Assessment of transport models on the basis of JET ohmic and L-mode discharges.
First author: Ch. Sack et al.

Tu 119 D 38 II-801

A quantitative assessment of ∇T_i-driven turbulence theory based on JET experimental data.
First author: F. Tibone et al.

Tu 120 D 39 II-805

Transport of scrape-off layer plasma in toroidal helical system.
First author: K. Itoh et al.

Tu 121 D 40 II-809

Sensitivity of ignition conditions to plasma parameters for a compact tokamak.
First author: G. Cenacchi et al.

Tu 122 D 41 II-813

Studies of burn control for ITER/NET.
First author: H. Persson et al.

Tu 123 D 42 II-817

On tearing mode stabilization by local current density perturbations.
First author: E. Westerhof

Fr 97 **D 43*** II-821

Implementation of scaling laws in 1-1/2-d transport codes and applications to the ignition spherical torus.
First author: A. Nicolai et al.

Fr 98 D 44 II-825

Simulation of density profile peaking and energy and particle transport in the IOC regime.
First author: G. Becker

Fr 99 D 45 II-829

Unified χ_e scaling for the ohmic, L and intermediate regimes of ASDEX.
First author: G. Becker

Fr 100 D 46 II-833

Changes in the density profile due to the m=2 tearing mode in ASDEX.
First author: M.E. Manso et al.

Fr 101 D 47 II-837

Determination of off-diagonal transport coefficients from particle and power balance analysis.
First author: O. Gruber et al.

Fr 102 **D 48**** II-841

* This paper will also be presented orally on Thursday 28 June at 14.50 hrs.
** This paper will also be presented orally on Thursday 28 June at 15.10 hrs.

Thermal bifurcation and stability of an edge diverted plasma.
First author: H. Capes et al.
Fr 103 D 49 II-845

On bootstrap current enhancement by anomalous electron-electron collisions.
First author: A. Nocentini
Fr 104 D 50 II-849

Direct derivation of neoclassical viscosity coefficients in tokamaks.
First author: J.D. Callen et al.
Fr 105 D 51 II-853

Tokamak density profiles associated with vanishing entropy production.
First author: E. Minardi
Fr 106 D 52 II-857

Discrete Alfvén waves in cylindrical plasma: arbitrary beta and magnetic twist.
First author: H. Shigueoka et al.
Th 109 D 53 II-861

Three wave interactions in dissipative systems.
First author: J. Teichmann et al.
Th 110 D 54 II-864

Stationary states with incompressible mass flow in ideal MHD.
First author: U. Gebhardt et al.
Th 111 D 55 II-868

Determination of the plasma current density profile in a tokamak from magnetic and polarimetric measurements.
First author: J. Blum et al.
Th 112 **D 56*** II-872

New evaluation of the fusion cross-sections.
First author: H.-S. Bosch et al.
Th 113 D 57 II-873

The relaxation in two temperature plasma.
First author: I.F. Potapenko et al.
Th 114 D 58 II-877

A multiple timescale derivative expansion method applied to the Fokker-Planck equation for the description of plasma relaxation and turbulent transport.
First author: J.W. Edenstrasser
Th 115 D 59 II-881

Equilibria and dynamics of a fusion reactor plasma.
First author: H. Wilhelmsson
Th 116 D 60 II-885

* This paper will also be presented orally on Thursday 28 June at 14.30 hrs.

Numerical simulation of the internal kink m = 1 in tokamak.
First author: H. Baty et al.
Th 117 D 61 II-889

Thermal plasma core instability.
First author: A.B. Arutiunov et al.
Th 118 D 62 II-893

Numerical simulation of the tearing-mode in tokamak with non-circular cross section. New approach to study nonlinear evolution of resistive helical modes.
First author: Yu.N. Dnestrovskij et al.
Th 119 D 63 II-894

Stabilisation of drift-tearing modes at the breakdown of the constant-ψ approximation.
First author: F. Porcelli et al.
Th 120 D 64 II-898

On the existence of a Benard-like convective instability in the sawtooth evolution.
First author: F. Spineanu et al.
Th 121 D 65 II-902

Global, resistive stability analysis in axisymmetric systems.
First author: A. Bondeson et al.
Th 122 D 66 II-906

Alpha-particle driven MHD instabilities in ignited tokamaks.
First author: C.Z. Cheng
Th 123 D 67 II-910

To the question of adiabatic R-compression in tokamak.
First author: N.N. Gorelenkov et al.
Th 124 D 68 II-914

Magnetic field structure at the onset of sawtooth relaxations.
First author: J.T. Mendonça et al.
Fr 107 D 69 II-918

The m = 1 internal kink mode in a rotating tokamak plasma with anisotropic pressure.
First author: H.J. de Blank
Fr 108 D 70 II-919

Interaction of resonant magnetic perturbations with rotating plasmas.
First author: T.C. Hender et al.
Fr 109 D 71 II-923

The effect of the plasma shape on the accessibility of the second stability regime.
First author: Oh Jin KWON et al.
Fr 110 D 72 II-927

Global ideal MHD stability of 3D plasmas with pseudo-vacuum treatment for free-boundary modes.
First author: U. Schwenn et al.
Fr 111 D 73 II-931

Transition between resistive kink and Kadomtsev reconnection.
First author: K. Lerbinger et al.
Fr 112 D 74 II-935

Tearing mode stabilization by energetic trapped ions.
First author: D. Edery et al.
Fr 113 D 75 II-938

Asymptotic theory of the non-linearly saturated m = 1 mode in tokamaks with q(0) < 1.
First author: A. Thyagaraja et al.
Fr 114 D 76 II-942

Large gyroradius m = 1 Alfvén modes and energetic particles.
First author: T.J. Schep et al.
Fr 115 D 77 II-946

Tearing modes in high-S plasmas.
First author: A. Voge
Fr 116 D 78 II-950

Influence of triangularity and profiles on ideal-MHD beta limits for NET.
First author: C.G. Schultz et al.
Fr 117 D 79 II-954

Influence of an X-point and its poloidal location on the ideal MHD stability of a quasi-circular tokamak.
First author: A. Roy et al.
Fr 118 D 80 II-958

Simulation of MHD activity during density limit disruptions in JET.
First author: R. Parker et al.
Fr 119 D 81 II-962

Effect of sheared toroidal plasma flows on equilibrium and stability of tokamaks.
First author: A. Sen et al.
Fr 120 D 82 II-966

Alpha containment, heating, and stability in the IGNITEX experiment.
First author: R. Carrera et al.
Fr 121 D 83 II-970

E. HEATING BY NEUTRAL BEAM INJECTION

A one dimensional volume ion source model.
First author: D.J. Mynors
Mo 72 E 1 III-974

Surface effects in D^- ion sources for neutral beam injection.
First author: R.M.A. Heeren et al.
Mo 73 E 2 III-978

Present status of the design of a DC low-pressure, high-yield D^- source.
First author: W.B. Kunkel et al.
Mo 74 E 3 III-979

Cascade arc hydrogen source for plasma neutralizers.
First author: D.C. Schram et al.
Mo 75 E 4 III-983

F. RF HEATING

Trapped and passing ion transport in ICRH tokamak plasmas.
First author: M.V. Osipenko et al.
Mo 44 F 1 III-987

Automic FMS mode tracking during ICRH in TO-2 tokamak.
First author: I.A. Kovan et al.
Mo 45 F 2 III-991

Studies of mode conversion physics for waves in the ion cyclotron range of frequences.
First author: G.J. Morales et al.
Mo 46 F 3 III-995

Ballistic-wave analysis of gyroresonant heating.
First author: A.N. Kaufman et al.
Mo 47 F 4 III-999

Edge absorption of fast wave due to Alfvén resonance and wave nonlinearity in ICRH.
First author: J.A. Heikkinen et al.
Mo 48 F 5 III-1003

D-He^3 fusion yield in higher harmonic ICRF heated plasma.
First author: M. Yamagiwa et al.
Mo 49 F 6 III-1007

Theoretical analysis of higher harmonic ICRF heating in JT-60.
First author: K. Hamamatsu et al.
Mo 50 F 7 III-1011

^{3}He-D fusion studies and α-particle simulations using MeV ions created by ICRH in the JET tokamak.
First author: D.F.H. Start et al.
Mo 51 **F 8*** III-1015

Fast ion orbit effects in high power ICRH modulation experiments in the JET tokamak.
First author: D.F.H. Start et al.
Mo 52 F 9 III-1019

Analysis of ICRF coupling and heating in CIT and JET.
First author: J.E. Scharer et al.
Mo 53 F 10 III-1023

Studies on the distribution function of minority ions under ICRF wave heating.
First author: Duk-in Choi et al.
Mo 54 F 11 III-1027

* This paper will also be presented orally on Monday 25 June at 13.45 hrs.

Parasitic coupling of the fringing fields of an ion-Bernstein wave antenna.
First author: S.C. Chiu et al.
Tu 42 F 12 III-1031

Mode coupling between I.C.R.F. waves propagating outside the $\underline{B}$-$\nabla\underline{B}$ plane.
First author: B.M. Harvey et al.
Tu 43 F 13 III-1035

An analysis of ridged waveguide for plasma heating by using integral equation method.
First author: T. Honma et al.
Tu 44 F 14 III-1039

Study of the neutron yield behaviour in ICRH and NBI heated discharges on TEXTOR.
First author: G.Van Wassenhove et al.
Tu 45 F 15 III-1040

Eigenfunctions of the anisotropic quasilinear Fokker-Planck equation.
First author: D. Lebeau et al.
Tu 46 F 16 III-1044

ICRF heating up to the 4.5 MW level on TFTR.
First author: J.E. Stevens et al.
Tu 47 **F 17*** III-1048

ICRF hydrogen minority heating in the boronized ASDEX tokamak.
First author: F. Ryter et al.
Tu 48 F 18 III-1052

Induction of parallel electric fields at the plasma edge during ICRF heating.
First author: M. Brambilla et al.
Tu 49 F 19 III-1056

Ion-cyclotron absorption of fast magnetosonic waves by cold minority ions in an open trap.
First author: V.E. Moyseenko et al.
Tu 50 F 20 III-1060

RF plasma heating in the gas-dynamics mirror trap.
First author: I.F. Potapenko et al.
Tu 51 F 21 III-1064

Experimental study of strong nonlinear wave phenomena during ICRH on TEXTOR.
First author: R.Van Nieuwenhove et al.
Tu 52 F 22 III-1068

Some features of ECRH in inhomogeneous magnetic fields.
First author: V.A. Zhil'tsov et al.
Mo 55 F 23 III-1072

* This paper will also be presented orally on Monday 25 June at 14.05 hrs.

Observation of "H"-like phenomena at the beginning phase of ECR-heating on T-10.
First author: A.V. Sushkov et al.
Mo 56 F 24 III-1076

Reasons for averaged electron-density limitation - Experimental study in T-10 and simulation.
First author: V.V. Alikaev et al.
Mo 57 F 25 III-1080

Optimization of break-down and of initial stage of discharge with ECH in T-10.
First author: V.V. Alikaev et al.
Mo 58 F 26 III-1084

Nonlinear heating by a spatially localized electron cyclotron wave.
First author: D. Farina et al.
Mo 59 F 27 III-1088

Power absorption and energy confinement during LH injection in ASDEX.
First author: R. Bartiromo et al.
Mo 60 F 28 III-1092

Scattering and localizability of ECH power in CIT.
First author: G.R. Smith
Mo 61 F 29 III-1096

Combined electron cyclotron ray tracing and transport code studies in the Compact Ignition Tokamak.
First author: M. Porkolab et al.
Mo 62 F 30 III-1100

Stochastic electron energy diffusion in electron cyclotron heating.
First author: R. Pozzoli et al.
Mo 63 F 31 III-1104

Calculated power deposition profiles during ECRH on the FTU tokamak.
First author: S. Cirant et al.
Th 47 F 32 III-1108

Microwave breakdown of the neutral gas around the EC resonance in high power transmission lines for ECRH.
First author: L. Argenti et al.
Th 48 F 33 III-1112

Ray tracing study of the second electron cyclotron harmonic wave absorption and current drive.
First author: S. Pešić et al.
Th 49 F 34 III-1116

High power mode-purity measurements on the 60 GHz transmission line for ECRH on RTP.

First author: A.G.A. Verhoeven et al.

Th 50 F 35 III-1117

ECRH sustained breakdown plasmas in RTP.
First author: R.W. Polman et al.

Th 51 F 36 III-1121

The electron temperature behaviour study in FT-I tokamak plasma heated by the ordinary and extraordinary ECRH waves.
First author: M.Yu. Kantor et al.

Th 52 F 37 III-1125

Electron-cyclotron heating in NET using the ordinary mode at down-shifted frequency.
First author: G. Giruzzi et al.

Th 53 F 38 III-1129

Recent electron cyclotron heating results on TEXT.
First author: B. Richards et al.

Th 54 F 39 III-1133

RF Alfvén wave heating of a high-beta plasma column.
First author: F.L. Ribe et al.

Mo 64 F 40 III-1137

Generation of fast magnetosonic waves in a mirror trap.
First author: A.G. Elfimov et al.

Mo 65 F 41 III-1141

Nonlinear transformation of Alfvén waves in a hot plasma.
First author: V.P. Minenko et al.

Mo 66 F 42 III-1145

Experimental studies of kenetic Alfvén waves on CT-6B tokamak.
First author: Daming ZHANG et al.

Mo 67 F 43 III-1149

Electron absorption of fast magnetosonic waves by TTMP in JET.
First author: F. Rimini et al.

Mo 68 F 44 III-1150

Ion Bernstein wave experiments and preliminary observations of Alfvén wave resonance in tokamak KT-5B.
First author: W. LIU et al.

Mo 69 F 45 III-1154

Edge-plasma heating via parasitic-torsional-mode excitation by Faraday-shielded ion-Bernstein-wave antennas.
First author: S. Puri

Mo 70 F 46 III-1158

Propagation absorption and particle dynamics of ion-Bernstein wave in tokamaks.
First author: A. Cardinali et al.
Mo 71 F 47 III-1159

Modelling of the interaction of energetic ions with lower hybrid waves on JET.
First author: E. Barbato
Fr 41 F 48 III-1163

Probe measurements of lower-hybrid wavenumber spectra in the ASDEX edge plasma.
First author: M. Krämer et al.
Fr 42 F 49 III-1167

Transition from electron- to ion-interaction of LH-waves in ASDEX.
First author: H.-U. Fahrbach et al.
Fr 43 F 50 III-1171

Alfvén wave heating in ASDEX.
First author: G.G. Borg et al.
Fr 44 F 51 III-1175

An experimental study of Alfvén wave heating using electrostatically shielded antennas in TCA.
First author: G.G. Borg et al.
Fr 45 F 52 III-1179

Acceleration of beam ions in simultaneous injection of NB and LH wave on JT-60.
First author: M. Nemoto et al.
Fr 46 F 53 III-1183

Stochastic heating of charged particles by two modes of plasma oscillations.
First author: V.S. Krivitaky et al.
Fr 47 F 54 III-1187

G. CURRENT DRIVE AND PROFILE CONTROL

On the filling of the "spectral gap" by particles in the process of a driven current generation.
First author: S.I. Popel et al.
Mo 76 G 1 III-1190

The effect of the induced RF current density profile during lower-hybrid current drive on the evolution of the q profile and sawteeth stabilization.
First author: M. Shoucri et al.
Mo 77 G 2 III-1191

The 3.7 GHz lower hybrid current drive system for the tokamak de Varennes.
First author: A. Hubbard et al.
Mo 78 G 3 III-1195

Effect of quasi-linear distortions on the LH-wave current drive in a reactor-tokamak.
First author: V.S Belikov et al.
Mo 79 G 4 III-1199

Parametric decay instabilities studies in ASDEX.
First author: V. Pericoli Ridolfini et al.
Mo 80 G 5 III-1203

Quasilinear theory for spatially delimited wave patterns.
First author: E. Canobbio et al.
Mo 81 G 6 III-1207

Parametric study on lower hybrid current drive efficiency for next step devices.
First author: H. Takase et al.
Tu 67 G 7 III-1211

Combined operation of pellet injection and lower hybrid current drive on ASDEX.
First author: F.X. Söldner et al.
Tu 68 G 8 III-1215

Transport effects on current drive efficiency and localisation.
First author: M. Cox et al.
Tu 69 G 9 III-1219

M=2 mode limit on lower hybrid current drive in ASDEX.
First author: H. Zohm et al.
Tu 70 G 10 III-1223

Evaporation rate of an hydrogen pellet in presence of fast electrons.
First author: B. Pégourié et al.
Tu 71 G 11 III-1227

Lower hybrid wave experiments in TORE SUPRA.
First author: M. Goniche et al.
Tu 72 G 12 III-1231

Modelling of plasma current ramp-up by lower hybrid waves: comparison with experiments and application to NET.
First author: J.G. Wégrowe et al.
Tu 73 G 13 III-1235

Numerical studies of an electron cyclotron current drive efficiency and the role of trapped particles.
First author: Yu.N. Dnestrovskij et al.
Mo 82 G 14 III-1239

Impact of source power spectrum on ECRH current drive efficiency.
First author: A.G. Shishkin et al.
Mo 83 G 15 III-1243

Electron cyclotron current drive and tearing mode stabilization in ITER.
First author: L.K. Kuznetsova et al.
Mo 84 G 16 III-1247

Three-dimensional Fokker-Planck analysis on RF current drive in tokamaks.
First author: A. Fukuyama et al.
Mo 85 G 17 III-1251

Linear evaluation of current drive in TJ-II.
First author: F. Castejón et al.
Mo 86 G 18 III-1255

Electron cyclotron current drive experiments on DIII-D.
First author: R.A. James et al.
Mo 87 G 19 III-1259

Investigation of electron cyclotron emission in the ASDEX tokamak during lower hybrid current drive and heating.
First author: K. Wira et al.
Mo 88 G 20 III-1263

Electron cyclotron current drive for $\omega < \omega_c$.
First author: A.C. Riviere et al.
Tu 74 G 21 III-1267

Current drive experiments at the electron cyclotron frequency.
First author: V. Erckmann et al.
Tu 75 **G 22*** III-1271

Non-inductive currents in W VII-AS: experimental results and theoretical modelling.
First author: U. Gasparino et al.
Tu 76 G 23 III-1275

Current drive by electron-cyclotron and fast waves in DIII-D.
First author: G. Giruzzi et al.
Tu 77 G 24 III-1279

* This paper will also be presented orally on Monday 25 June at 14.25 hrs.

Lower hybrid current drive in DITE.
First author: B. Lloyd et al.
Tu 78 **G 25*** III-1283

Coupling of the 2 x 24 waveguide grill at 2.45 GHz in ASDEX.
First author: F. Leuterer et al.
Tu 79 G 26 III-1287

Lower hybrid current drive efficiency at 2.45 GHz in ASDEX.
First author: F. Leuterer et al.
Tu 80 G 27 III-1291

Simulation of fast waves current drive by multi-loop antennae in ITER.
First author: V.L. Vdovin et al.
Mo 89 G 28 III-1295

A 1-2/2 D Eulerian Vlasov code for the numerical simulation of beat current drive in a magnetized plasma.
First author: M. Shoucri et al.
Mo 90 G 29 III-1299

High frequency current drive by nonlinear wave-wave interactions.
First author: S.J. Karttunen et al.
Mo 91 G 30 III-1303

Possibility of ion current drive by RF helicity injection.
First author: K. Hamamatsu et al.
Mo 92 G 31 III-1307

Development of fast-wave ICRF current drive systems at ORNL.
First author: R.H. Goulding et al.
Mo 93 G 32 III-1311

Current drive via Landau damping of kinetic Alfvén wave in toroidal geometry.
First author: A.G. Elfimov et al.
Mo 94 G 33 III-1315

RF current drive by a standing Alfvén wave in the R-O device as a possible effect of RF helicity injection.
First author: A.G. Kirov et al.
Mo 95 G 34 III-1319

Profile control with lower hybrid waves on ASDEX.
First author: F.X. Söldner et al.
Tu 81 **G 35**** III-1323

Tearing mode stabilization by local current density profiling in tokamak.
First author: M.P. Gryaznevich et al.
Tu 82 G 36 III-1327

* This paper will also be presented orally on Monday 25 June at 14.45 hrs.
** This paper will also be presented orally on Monday 25 June at 15.05 hrs.

Surface wave antenna for excitation of travelling fast magnetosonic or ion Bernstein waves in plasma.
First author: A.V. Longinov et al.
Tu 83 G 37 III-1331

Hard X-ray emission during 2.45 GHz LH experiments on ASDEX.
First author: A.A. Tuccillo et al.
Tu 84 G 38 III-1335

Neutral beam current drive with balanced injection.
First author: D. Eckhartt
Tu 85 G 39 III-1336

Absorption characteristics of 200 MHz fast wave in JFT-2M tokamak.
First author: Y. Uesugi et al.
Tu 86 G 40 III-1340

H. IMPURITY AND EDGE PHYSICS

Special phenomena of edge density fluctuations in HL-1 tokamak.
First author: Qingwei YANG et al.
Mo 96 H 1 III-1341

Influence of neutral injection inhomogeneity on tokamak edge plasma.
First author: M.Z. Tokar'
Mo 97 H 2 III-1345

Influence of the helical resonant fields on the plasma edge of TBR-1 tokamak.
First author: I.L. Caldas et al.
Mo 98 H 3 III-1349

Edge fluctuation studies in ATF.
First author: C. Hidalgo et al.
Mo 99 H 4 III-1353

Effect of limiter composition on Z_{eff} and recycling in JET.
First author: J.P. Coad et al.
Mo 100 **H 5*** III-1357

Charge exchange spectroscopy measurements of light impurity behaviour in the JET beryllium phase.
First author: H. Weisen et al.
Mo 101 H 6 III-1361

Retention of gaseous (Ar, He) impurities in the JET X-point configuration.
First author: G. Janeschitz et al.
Mo 102 H 7 III-1365

Modelling impurity control in the JET pumped divertor.
First author: R. Simonini et al.
Mo 103 H 8 III-1369

Scrape-off layer parameters at JET during density limit discharges.
First author: S. Clement et al.
Mo 104 H 9 III-1373

Temperatures and densities in the JET plasma boundary deduced from deuterium and beryllium spectra.
First author: M.F. Stamp et al.
Mo 105 H 10 III-1377

Formation of detached plasmas during high power discharges in JET.
First author: G.M. McCracken et al.
Mo 106 H 11 III-1381

* This paper will also be presented orally on Friday 29 June at 11.00 hrs.

An investigation into high ion temperatures in the JET plasma boundary.
First author: S.K. Erents et al.
Mo 107 H 12 III-1385

Edge plasma behaviour in the FT tokamak.
First author: V. Pericoli Ridolfini
Mo 108 **H 13*** III-1389

Scrape-off layer based model for the disruptive tokamak density limit and implications for next-generation tokamaks.
First author: K. Borrass
Mo 109 H 14 III-1393

Simulation of edge plasma and divertor conditions in NET/ITER.
First author: H.D. Pacher et al.
Mo 110 H 15 III-1397

Collector probe measurements of impurity fluxes in TEXTOR with molybdenum and graphite limiters.
First author: M. Rubel et al.
Mo 111 H 16 III-1401

Electron excitation coefficients for the continuous spectrum of deuterium.
First author: B.M. Jelenković et al.
Mo 112 H 17 III-1405

3d-Monte Carlo modelling of the neutral gas transport in pump limiters.
First author: A. Nicolai
Mo 113 H 18 III-1409

Radiation from impurities in JET limiter plasmas during the C and Be phases.
First author: K.D. Lawson et al.
Mo 114 H 19 III-1413

Modelling of carbon in the TFTR edge plasma.
First author: B.J. Braams et al.
Fr 68 H 20 III-1417

First-wall behavior in TFTR.
First author: C.S. Pitcher et al.
Fr 69 H 21 III-1419

Multi-species impurity accumulation phenomena in ASDEX.
First author: G. Fussmann et al.
Fr 70 H 22 III-1423

Power flow and electric current asymmetries in the ASDEX SOL.
First author: N. Tsois et al.
Fr 71 H 23 III-1427

* This paper will also be presented orally on Friday 29 June at 11.20 hrs.

Determination of impurity transport coefficients by sinusoidal modulated gas puffing.
First author: K. Krieger et al.
Fr 72 H 24 III-1431

Impurity transport and production in lower hybrid discharges in ASDEX.
First author: R. De Angelis
Fr 73 H 25 III-1435

Plasma edge behavior on the way to and at the density limit.
First author: K. McCormick et al.
Fr 74 H 26 III-1439

Thermoelectric currents in the scrape-off layer.
First author: R. Chodura
Fr 75 H 27 III-1443

Influence of plasma-neutral interactions on ALT-II pump limiter performance during NI heating at TEXTOR.
First author: R.A. Moyer et al.
Fr 76 H 28 III-1447

An analytical model for neutral and charged particles in closed pump limiter.
First author: M.Z. Tokar'
Fr 77 H 29 III-1448

Ergodized edge experiments in JFT-2M tokamak.
First author: T. Shoji et al.
Fr 78 H 30 III-1452

Edge turbulence and its possible suppression by velocity shear in TEXT.
First author: Ch.P. Ritz et al.
Fr 79 H 31 III-1456

A comparison of fluctuations and transport in the scrape-off layer of a limiter [TEXT] and divertor tokamak [ASDEX].
First author: R.D. Bengtson et al.
Fr 80 H 32 III-1460

Structure of density fluctuations in the edge plasma of ASDEX.
First author: A. Rudyj et al.
Fr 81 H 33 III-1464

Evaluation of neutral gas flux measurements in the ASDEX-divertor with respect to divertor-geometry and recycling.
First author: D. Meisel et al.
Fr 82 H 34 III-1468

A study of impurity transport in the TEXTOR plasma boundary.
First author: S.J. Fielding et al.
Fr 83 H 35 III-1472

Effects of boronisation on the plasma parameters in TCA.
First author: B. Joye et al.
Fr 84 H 36 III-1476

Pump limiter influence on the helium discharge parameters in TUMAN-3 tokamak.
First author: V.I. Afanasiev et al.
Fr 85 H 37 III-1480

I. DIAGNOSTICS

Tokamak T-10 soft X-ray imaging diagnostic.
First author: P.V. Savrukhin et al.
Mo 27 I 1 IV-1484

Measurement of neutral deuterium fluxes on T-10 periphery.
First author: E.L. Berezovskij et al.
Mo 28 I 2 IV-1488

Density fluctuation measurements on ATF using a two-frequency reflectometer.
First author: E. Anabitarte et al.
Mo 29 I 3 IV-1492

Measurements of deuteron density profiles in JET.
First author: W. Mandl et al.
Mo 30 I 4 IV-1496

First measurements of electron density profiles on JET with a multichannel reflectometer.
First author: R. Prentice et al.
Mo 31 **I 5*** IV-1500

A method for the determination of the total internal magnetic field in JET.
First author: L. Porte et al.
Mo 32 I 6 IV-1504

Current profile measurement using neutral He beam in JT-60 tokamak.
First author: H. Takeuchi et al.
Mo 33 I 7 IV-1508

Real time profiling of total radiation in the TJ-1 tokamak by a fluorescent detector.
First author: B.G. Zurro et al.
Mo 34 I 8 IV-1512

Ion temperature determination from neutron rate measurements during deuterium injection.
First author: B. Wolle et al.
Mo 35 I 9 IV-1516

Absolute determination of high neutron yields for ASDEX.
First author: R. Bätzner et al.
Mo 36 I 10 IV-1520

Plasma diagnostics in infrared and far-infrared range for Heliotron E.
First author: K. Kondo et al.
Mo 37 I 11 IV-1524

* This paper will also be presented orally on Friday 29 June at 10.00 hrs.

Neutral beam probe diagnostic at TEXTOR.
First author: E.P. Barbian et al.
Mo 38 I 12 IV-1528

Visible bremsstrahlung measurements on TEXTOR for the determination of Z_{eff} under different discharge and heating conditions.
First author: J. Ongena et al.
Mo 39 I 13 IV-1532

Electron density propagation on magnetic surface in T-10 during pellet injection.
First author: N.L. Vasin et al.
Mo 40 I 14 IV-1536

Measurements of ion cyclotron emission and ICRF-driven waves in TFTR.
First author: G.J. Greene et al.
Mo 41 I 15 IV-1540

Density fluctuation measurements from microwave scattering on TFTR.
First author: R. Nazikian et al.
Mo 42 I 16 IV-1544

Influence of neutron scattering on measured TFTR neutron profiles.
First author: J.D. Strachan et al.
Mo 43 I 17 IV-1548

Edge density X-mode reflectometry of RF-heated plasmas on ASDEX.
First author: R. Schubert et al.
Th 32 I 18 IV-1552

Measurement of poloidal rotation on ASDEX.
First author: J.V. Hofmann et al.
Th 33 I 19 IV-1556

Localized density measurements on ASDEX using microwave reflectometry.
First author: M.E. Manso et al.
Th 34 I 20 IV-1560

Tangential soft X-ray/VUV tomography on COMPASS-C.
First author: R.D. Durst et al.
Th 35 I 21 IV-1564

A new probe to determine the Mach number of plasma flow in a magnetized plasma.
First author: K. Höthker et al.
Th 36 I 22 IV-1568

Reflectometry observations of density fluctuations in Wendelstein VII-AS stellarator.
First author: J. Sanchez et al.
Th 37 I 24 IV-1572

On density and temperature fluctuations observed by ECE diagnostics in Wendelstein VII-AS stellarator.
First author: H.J. Hartfuss et al.
Th 38 I 25 IV-1576

Fast scanning fiber-multiplexer used for plasma-edge visible spectroscopy on TORE SUPRA.
First author: W.R. Hess et al.
Th 39 I 26 IV-1580

Fusion profile measurement on TORE SUPRA.
First author: G. Martin et al.
Th 40 I 27 IV-1584

First density fluctuations observations by CO_2 scattering in TORE SUPRA.
First author: C. Laviron et al.
Th 41 I 28 IV-1588

Turbulence studies in TJ-1 tokamak by microwave reflectometry.
First author: J. Sanchez et al.
Th 42 I 29 IV-1592

X-mode broadband reflectometric density profile measurements on DIII-D.
First author: E.J. Doyle et al.
Th 43 I 30 IV-1596

Strongly non-maxwellian electron velocity distributions observed with Thomson scattering at the TORTUR tokamak.
First author: C.J. Barth et al.
Th 44 I 31 IV-1600

Microturbulence studies on DIII-D via far infrared heterodyne scattering.
First author: R. Philipona et al.
Th 45 I 32 IV-1604

Ion temperature measurements at JET.
First author: H.W. Morsi et al.
Th 46 I 33 IV-1608

A simple and sensitive instrument for plasma electron temperature determination.
First author: Yu.V. Gott et al.
Tu 27 I 34 IV-1612

Determination of poloidal fields by the pecularities of elliptically polarised probe wave in tokamak.
First author: Yu.N. Dnestrovskij et al.
Tu 28 I 35 IV-1616

Space-time tomography problem for plasma diagnostic.
First author: Yu.N. Dnestrovskij et al.
Tu 29 I 36 IV-1620

Electron and ion tagging diagnostic for high temperature plasmas.
First author: F. Skiff et al.
Tu 30 I 37 IV-1624

Transient internal probe diagnostic.
First author: E.J. Leenstra et al.
Tu 31 I 38 IV-1628

On the possibility of laser diagnostics of anisotropically superheated electrons in magnetic fusion systems.
First author: A.B. Kukushkin
Tu 32 I 39 IV-1632

Collective scattering spectra with anisotropic distributions of fast ions and alpha particles.
First author: U. Tartari et al.
Tu 33 I 40 IV-1636

Feasibility study of bulk ion temperature measurement on JET by means of a collective scattering of a gyrotron radiation.
First author: F. Orsitto
Tu 34 I 41 IV-1640

On the possibilities of spectroscopic measurements of various electric fields and related plasma parameters for tokamak conditions.
First author: E. Oks
Tu 35 I 42 IV-1644

Modelling of non-thermal electron cyclotron emission during ECRH.
First author: V. Tribaldos et al.
Tu 36 I 43 IV-1648

Physics studies of compact ignition plasmas using neutron measurements.
First author: G. Gorini et al.
Tu 37 I 44 IV-1652

The multi-channel interferometer/polarimeter for the RTP tokamak.
First author: A.C.A.P.van Lammeren et al.
Tu 38 I 45 IV-1656

Application of function parametrization to the analysis of polarimetry and interferometry data at TEXTOR.
First author: B.Ph.van Milligen et al.
Tu 39 I 46 IV-1660

Feasibility of alpha particle diagnostics for the active phase of JET, using Charge Exchange Recombination Spectroscopy.
First author: G.J. Frieling et al.
Tu 40 I 47 IV-1664

Polarization rotation and ion Thomson scattering.
First author: D.A. Boyd
Tu 41 I 48 IV-1668

A possible electric field measurement by a molecular hydrogen beam.
First author: W. Herrmann
Fr 27 I 49 IV-1672

The limitations of measurements of the local wavenumber.
First author: A. Carlson et al.
Fr 28 I 50 IV-1676

Ion temperature measurements in the TCA tokamak by collective Thomson scattering.
First author: M. Siegrist et al.
Fr 29 I 51 IV-1680

Thomson scattering diagnostics development in FT-I tokamak for the electron temperature temporal variation measurements.
First author: M.Yu. Kantor et al.
Fr 30 I 52 IV-1684

In-beam study of $^{9}Be(\alpha\, n_1\, \gamma)^{12}C$ reaction, promising as fast alpha-particle diagnostics in tokamak plasmas.
First author: V.G. Kiptilyj et al.
Fr 31 I 53 IV-1688

A high resolution LIDAR-Thomson scattering system for JET.
First author: H. Fajemirokun et al.
Fr 32 I 54 IV-1692

Localization of fluctuation measurement by wave scattering close to a cut off layer.
First author: X.L. Zou et al.
Fr 33 I 55 IV-1693

Polarization of hard X rays, a contribution to the measurement of the non-thermal electron distribution function (L.H.C.D.).
First author: M. Hesse et al.
Fr 34 I 56 IV-1697

The Thomson scattering systems of TORE SUPRA. First results.
First author: J. Lasalle et al.
Fr 35 I 57 IV-1701

Differential electron-cyclotron wave transmission for investigation of a lower-hybrid fast tail in the reactor regime.
First author: R.L. Meyer et al.
Fr 36 I 58 IV-1705

Diagnostic potentialities of electron cyclotron waves in L.H. current drive experiments.
First author: G. Ramponi et al.
Fr 37 I 59 IV-1709

Feasibility of diagnostic of JET LHCD plasmas by means of X-ray crystal spectroscopy.
First author: F. Bombarda et al.
Fr 38 I 60 IV-1713

The JET time of flight neutral particle analyser.
First author: G. Bracco et al.
Fr 39 I 61 IV-1717

Project of magnetic fluctuation measurement by cross polarization scattering in the TORE SUPRA tokamak.
First author: M. Paume et al.

Fr 40 I 62 IV-1721

J. BASIC COLLISIONLESS PLASMA PHYSICS

To the theory of Jupiter's decametric S-emission.
First author: A.G. Boyev et al.
Mo 115 J 1 IV-1725

On a gas-dynamic description of scattering of a rapid electron cloud in a plasma.
First author: V.N. Mel'nik
Mo 116 J 2 IV-1729

Nonequilibrium spectra forming for relativistic electrons interacting with MHD-turbulence.
First author: A.E. Kochanov
Mo 117 J 3 IV-1733

Resonant absorption of MHD bulk waves via surface modes.
First author: V.K. Okretic et al.
Mo 118 J 4 IV-1737

Nonlinear transparency of underdense plasma layer under the effect of intense circularly-polarized electromagnetic wave.
First author: V.V. Demchenko
Mo 119 J 5 IV-1741

Formation and equilibrium of an electron plasma in a small aspect ratio torus.
First author: Puravi Zaveri et al.
Mo 120 J 6 IV-1745

Formation of vortices in a toroidal plasma.
First author: A.K. Singh et al.
Mo 121 J 7 IV-1749

Arbitrary-amplitude electron-acoustic solitons in a two electron component plasma.
First author: R.L. Mace et al.
Mo 122 J 8 IV-1750

The obliquely propagating electron-acoustic instability
First author: M.A. Hellberg et al.
Mo 123 J 9 IV-1754

Generation of extraordinary mode radiation by an electrostatic pump in a two electron temperature plasma.
First author: S. Guha et al.
Mo 124 J 10 IV-1758

Propagation of electromagnetic waves in a modulated density plasma.
First author: M. Lontano et al.
Mo 125 **J 11*** IV-1762

* This paper will also be presented orally on Monday 25 June at 16.00 hrs.

Laser wakefield acceleration in an external magnetic field.
First author: P.K. Shukla
Mo 126 J 12 IV-1766

Radiative energy transport in thermonuclear plasmas.
First author: S. Puri
Tu 87 J 13 IV-1770

Nonlinear excitation of P-polarized surface wave in anisotropic plasma layer.
First author: Sh.M. Khalil et al.
Tu 88 J 14 IV-1774

Non-linear coupling of drift modes in a quadrupole.
First author: J.A. Elliott et al.
Tu 89 J 15 IV-1778

A two-dimensional collisionless model of the single-ended Q-machine.
First author: S. Kuhn et al.
Tu 90 J 16 IV-1782

Ion-acoustic eigenmodes in a collisionless bounded plasma.
First author: S. Kuhn et al.
Tu 91 J 17 IV-1786

Plasma heating by a strong multimode laser field.
First author: R. Daniele et al.
Tu 92 J 18 IV-1790

Turbulence and fluctuation induced transport in a double plasma device.
First author: M.J. Alport et al.
Tu 93 J 19 IV-1794

Resonant four-wave mixing and phase conjugation in an unmagnetized plasma.
First author: N.C. Luhmann, Jr. et al.
Tu 94 J 20 IV-1798

Kinetic vortices in magnetized plasmas.
First author: A.G. Sitenko et al.
Tu 95 J 21 IV-1802

Electron-cyclotron waves in non-maxwellian, relativistic plasmas.
First author: F. Moser et al.
Tu 96 J 22 IV-1803

Ion cyclotron wave excitation by double resonance parametric coupling.
First author: A. Fasoli et al.
Tu 97 J 23 IV-1807

Ion wave excitation for the study of wave-induced transport.
First author: T.N. Good et al.
Fr 86 J 24 IV-1811

The sheath formation near an electron absorbing boundary.
First author: N. Jelić et al.
Fr 87 J 25 IV-1815

Kinetic description of nonequilibrium plasma fluctuations.
First author: O.D. Kocherga
Fr 88 J 26 IV-1819

On the role of anomalous resistivity in a dynamics of plasma switching.
First author: A.S. Kingsep et al.
Fr 89 J 27 IV-1820

Kinetic theory on Alfvén solitions in collisional plasmas.
First author: Chuan-Hong PAN et al.
Fr 90 J 28 IV-1824

Ion-acoustic rarefactive soliton in two-electron temperature plasma.
First author: V.K. Sayal et al.
Fr 91 J 29 IV-1828

Relativistic dispersion functions for anisotropic plasmas.
First author: M. Bornatici
Fr 92 J 30 IV-1832

Boundary Larmor radius effects.
First author: Jin LI et al.
Fr 93 J 31 IV-1836

Numerical solution of the Vlasov-Maxwell system in the heavy-ion fusion problems.
First author: O.V. Batishchev et al.
Fr 94 J 32 IV-1840

Nonstationary self-action of electromagnetic wave beams in the beat accelerator.
First author: L.A. Abramyan et al.
Fr 95 J 33 IV-1844

Self-interaction of the magnetohydrodynamic surface waves at the plasma-metal boundary.
First author: N.A. Azarenkov et al.
Fr 96 J 34 IV-1848

K. INERTIAL CONFINEMENT FUSION

Detection of SRS produced electron plasma waves by the use of enhanced Thomson scattering.
First author: E.J. Leenstra
Th 83 K 1 IV-1852

Measurements of mass ablation rate and ablation pressure in planar layered targets.
First author: F. Dahmani et al.
Th 84 K 2 IV-1856

Heavy-ion driver design for indirect-drive implosion experiments.
First author: R.C. Arnold et al.
Th 85 K 3 IV-1860

Nova Program at LLNL.
First author: D. Correll et al.
Th 86 K 4 IV-1861

Study of instabilities in long scalelength plasmas with and without laser beam smoothing techniques.
First author: O. Willi et al.
Th 87 K 5 IV-1864

Hydrodynamic behavior of the plasma ablation in laser-irradiated planar targets.
First author: D.P. Singh et al.
Th 88 K 6 IV-1867

Experimental studies on the mechanism of Mach wave generation.
First author: V. Palleschi et al.
Th 89 K 7 IV-1871

Evaluating KrF lasers for ICF applications.
First author: D.C. Cartwright et al.
Th 90 K 8 IV-1875

Second harmonic: a versatile diagnostic for laser interaction with underdense plasmas.
First author: D. Giulietti et al.
Th 91 K 9 IV-1876

Excitation of sound by electromagnetic pulse in a dense semi-infinite non-isothermal collisional plasma.
First author: V.I. Muratov et al.
Th 92 K 10 IV-1880

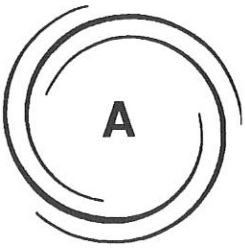

TOKAMAKS

A1 TOKAMAKS, GENERAL

D-D NEUTRON PRODUCTION FROM JET PLASMAS

G.Sadler, J.M.Adams, S.Attenberger, B.Balet, J.G.Cordey, O.N.Jarvis, T.T.C.Jones, P.Kupschus, B.Laundy, P.J.Lomas, M.J.Loughlin, F.B.Marcus, M.Olsson, P.M.Stubberfield, D.F.H.Start, A.Tanga, P.R.Thomas, B.Tubbing, P.van Belle

JET Joint Undertaking, Abingdon, Oxfordshire, OX14 3EA, England

Abstract: The D-D neutron yield obtained from JET plasmas during the 1989 operating period under conditions of intense auxiliary heating (NBI and ICRH) has been compared with results obtained during the 1988 campaign. The maximum neutron emission strength has been more than doubled from 1.45 10^{16} n/s to 3.45 10^{16}n/s. A substantial increase of the yield with applied RF power due to RF-acceleration of deuterons has been observed in many cases during combined heating.

Introduction: A systematic approach to the optimisation of the D-D fusion reactivity from JET plasmas by using combined NBI and RF heating was started in 1988 and first results are described in ref [1]. Since then several changes to the JET machine have been made, those of relevance for the present investigation being: a) the introduction of beryllium, first by evaporation and then later in the form of a belt-limiter made out of Be tiles and b) the conversion of part of the NBI injection system from 80 keV D° to 140 keV D°. As in the pre-Be phase [1], a range of plasma geometries were assessed: plasmas resting on the belt limiter and on the inner wall, and plasmas with a double-null X-point magnetic configuration.

Comparison with previous results:

a) **Inner wall limited discharges:** The scaling of neutron yield with additional heating power shows the same behaviour as observed previously, with the maximum neutron yield being limited by the dilution of the fuel ions by the sudden increase of carbon impurities when the carbon bloom threshold is exceeded. However, because of the gettering action of Be, yields comparable to the record yields of 1988 (1.4 10^{16} n/s) could be obtained regularly without having to condition the wall with a lengthy sequence of He discharges.

b) Belt Limiter discharges: Discharges resting on the belt limiter showed a distinct improvement, both during the Be evaporation phase (Carbon limiter) as well as during the Be limiter phase. With NBI only, record yields of 1.7 10^{16}n/s (exceeding all 1988 values) could be achieved. Best previous limiter discharges reached 8.4 10^{15} n/s, as can be seen from fig. 1 where the maximum neutron yield reached is shown as a function of NBI power for a large set of the 1988 and 1989 limiter discharges. The main reason for this enhancement is shown to come from the improved density control due to the gettering action of Be [2]. Following the introduction of Be, no difference is apparent between discharges limited on the inner wall and discharges in contact with the belt limiter. However, discharges resting on the belt limiter have the advantage that RF power can be coupled to them with relative ease. As demonstrated in fig. 1, this leads very often to a significant enhancement of the neutron yield. The highest yield discharge (2.2 10^{16} n/s) was obtained during a series of similar beam heated discharges and the addition of 9 MW of RF power led to

a doubling of the yield.

c) Double-Null X-point configuration: By far the highest neutron yield discharges were obtained in the double-null X-point configuration, with most of them developing an H-mode. The record neutron yields were generated by NBI only discharges. The improvement here was mainly attributable to the spreading of the heat load on the X-point tiles by sweeping of the X-point, thus delaying the influx of impurity ions and allowing the thermal component of the neutron emission to build up. This component reached 50% of the total for the highest yield discharge. A clear scaling of neutron yield with applied NBI power could not be established due to the variable time delay and the strong build-up of the thermal component before the maximum emissivity was reached.

140 keV vs 80 keV beam comparison: The slowing-down averaged reactivity of a 140 keV deuteron, which is typically four times that of an 80 keV deuteron, shows the importance of the conversion of 6 out of the 16 installed PINIS from 80 keV to 140 keV injection energy. The effect of the higher injection energy could be demonstrated by the substitution of 80 keV beams by 140 keV beams half-way through the heating pulse. From the resulting sudden increase of the neutron yield, a typical quality factor of 1.75 for the generation of beam induced neutrons per unit power by 140 keV beams as compared to 80 keV beams was deduced. This is in excellent agreement with the expected increase as only 60% of the particles are injected at full energy. Neutron energy spectra obtained before and after the changeover confirm this observation; after the changeover, the component corresponding to low energy deuterons accounts only for 5-10% of the total beam induced neutrons. The high energy beams also have a better penetration, leading to a higher concentration of beam particles in the centre of the plasma thus enhancing the neutron yield by better fueling and increased beam-beam reactions during hot ion mode plasmas.

RF-driven tail reactivity: When applying ICRF heating at the H minority fundamental frequency to D^0-beam heated deuterium plasmas, a large enhancement of the fusion yield (theoretically up to a factor of 10) is expected by formation of a strong tail above the injection energy via second harmonic coupling to the deuterons. As already mentioned above, many cases with large RF enhancements in neutron yield have been observed, including the highest neutron yield limiter discharge, for which the neutron yield is more than double the yield obtained with NBI heating alone at equal NBI power. In order to assess the number of neutrons due to the RF induced high energy tail, use was made of the TRANSP code to calculate the thermal and beam induced components of the neutron yield using the measured background plasma parameters as input parameters. Preliminary runs for this particular discharge show that a minimum of 40% of the total neutron yield cannot be accounted for if the RF is assumed to produce only changes in the background plasma. The highest such value observed in the pre-Be phase was 25% [1]. A 30 % short-fall has also been found in a final TRANSP run for a different discharge. The presence of fast deuterons with energies in the MeV range in RF heated plasmas has been clearly established by the observation of γ-lines from the $^9Be(d,n)^{10}B$ and $^9Be(d,p)^{10}Be$ reactions [3]. Moreover, there is a correlation between the stored fast particle energy, measured with the diamagnetic loop and enhanced neutron production. Definitive proof of the presence of a significant number of deuterons with energies well above the NBI injection energy was obtained for the first time from neutron energy spectra, which showed a distinct tail. The most pronounced example found so far (discharge 20725) is shown in fig.2, where the measured neutron spectrum is compared to

that of a NBI-only heated case. A preliminary assessment based on unfolding the spectrum using precalculated shapes for the various components (thermal, beam induced and RF driven) indicates that, in this case, at least 60% of the neutrons were caused by RF accelerated deuterons. The same analysis applied to discharge 20934 (fig.3) gives a deuterium tail temperature of 60-75 keV that accounts for 30-40 % of the total neutron yield. A possible explanation for this increased deuterium tail formation as opposed to previous observations is the absence of H in these discharges due to a combination of pellet fueling and Be gettering.

Be neutrons: The interaction of fast RF-driven protons and deuterons with Be impurity ions can lead to the generation of neutrons via $^{9}Be(p,n)^{9}B$ and $^{9}Be(d,n)^{10}B$ reactions. For high power RF-only heated discharges, these neutrons can constitute a significant fraction of the total neutron yield. The effect is particularly pronounced during long sawtooth-free periods, when the fast ion population can build up without being redistributed by sawtooth crashes. The $^{9}Be(d,n)^{10}B$ cross-section peaks at around 1 MeV, where it reaches a value of 350 mbarns in contrast to the $D(d,n)^{3}He$ cross section, which reaches a maximum of only 110 mbarns at around 3.5 MeV. At 450 keV they are equal (62 mbarns). Assuming a two temperature Maxwellian distribution function for the fast RF-driven minority, the ratio of d-d neutrons to d-Be neutrons as a function of tail temperature has been calculated to be 3.7 at 100 keV and 0.32 at 1 MeV with a cross-over point at around 200 keV. Before the introduction of Beryllium into JET the measured neutron spectra were Gaussian with a width reflecting the doppler broadening of the Maxwellian distributed ions. However, for a number of recent discharges heavily distorted spectra were observed with a broad flat distribution underlying the d-d peak. On several occasions, spectra were obtained for which the 2.5 MeV peak was absent altogether. A systematic study showed that this distortion is correlated with the length of sawtooth free periods and the Be concentration as obtained from visible spectroscopy measurements, although there are exceptions. The distortion is also found to be correlated with the γ-ray intensity from reactions of fast deuterons with Be.

Summary and conclusion: Significant improvements in the D-D neutron emission have been achieved. Neutron yields comparable to those obtained in inner wall limited discharges are now regularly produced in belt limiter hot ion mode discharges due to the improved density control from the gettering action of Be. Highest values have been achieved in double-null X-point discharges developing H-modes due to the delay in the impurity influx from tile heating by X-point sweeping and, simultaneously alternating the load between upper and lower X-point. Combined H minority ICRF and NBI heating leads to enhanced neutron yields by RF acceleration of deuterons. Enhancements exceeding 60% have been observed in contrast to the pre-Be phase, where a maximum of 25% was found. The efficiency of the RF in accelerating deuterons is so high that, in high power RF-only discharges, the neutron yield from reactions of these fast deuterons with Be impurities ions can significantly contribute to the total yield.

References: 1) J.M.Adams et al, 'D-D Fusion Reactivity Studies in High Temperature Plasmas', 1990, JET preprint JET P(90) 10.
2) T T Jones et al., this conference
3) G Sadler et al., IAEA technical commitee meeting, Kiev 1989, JET-P(89) 77

Fig 1 Peak Neutron Yield vs Neutral Beam Power

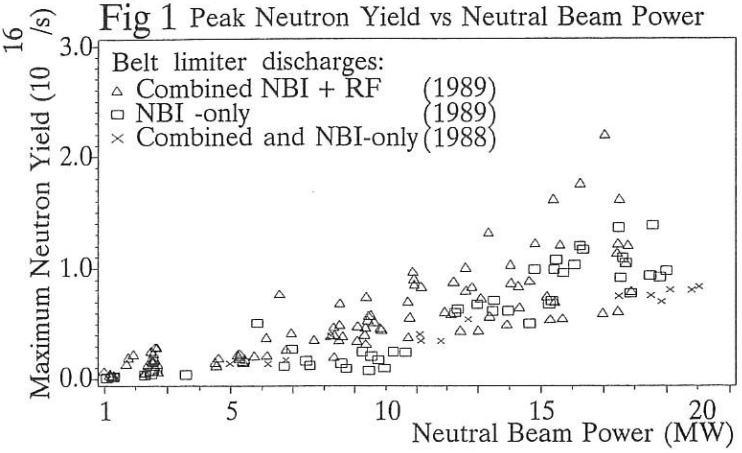

Fig 2 Neutron Energy Spectra for shot 20725 and 20932

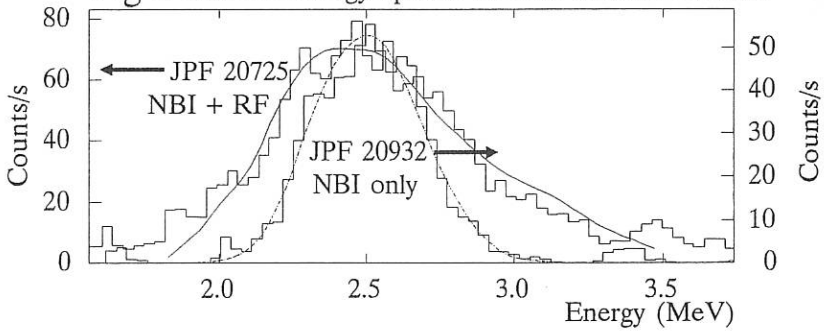

Fig 3 Neutron Energy Spectrum for shot 20934

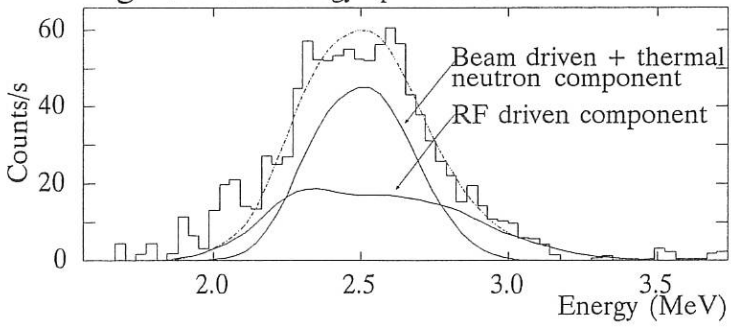

PEAKED PROFILES IN LOW q HIGH CURRENT LIMITER PLASMAS IN JET

S. Attenberger, B. Balet, D. J. Campbell, J. P. Christiansen, G. A. Cottrell, A. Edwards, T. T. C. Jones, P. Kupschus, P. J. Lomas, P. Nielsen, J. O'Rourke, D. Pasini, R. Prentice, G. Sadler, G. Schmidt#, P. Stubberfield, A. Taroni, F. Tibone, H. Weisen.

JET Joint Undertaking, Abingdon, Oxon, OX14 3EA, UK
 # PPPL, Princeton, New Jersey, USA.

1. Introduction.

JET plasma pulses characterised by a safety factor $q_\psi \sim 3$, e.g. plasma currents of 5-7MA, normally feature broad profiles of current, density and temperature. Such pulses are relevant for reactor studies but their fusion performance can be reduced by sawteeth which affect a large region. Experiments have already demonstrated that application of high power ion cyclotron heating (ICRH) during the current rise phase can result in long sawtooth free periods [1].

In section 2, three types of new experiment are described using a fast (1MA/s) current rise at constant q_ψ, ICRH and pellet injection, with the Carbon belt limiter conditioned by Beryllium evaporation. Section 3 briefly explains the current penetration during the current rise phase. The electron heating with ICRH is discussed in section 4, and the effects of the various plasma density profiles are described in section 5.

2.Experimental Results.

The *first* type of experiment has ICRH early in the current rise, from $\sim 2.5MA$, after the first sawteeth appear. Sawteeth are then suppressed for periods lasting several confinement times and well into the 5MA flat top despite the radius of the $q_\psi = 1$ surface growing to 0.5m. The axial electron temperature quickly reaches steady values $T_{e0} \lesssim 12keV$ with strongly peaked profiles at low axial densities $n_{e0} \sim 2.5 \times 10^{19} m^{-3}$. Figs 1 and 2 show LIDAR n_e and T_e profiles taken 1.5s after the start of ICRH for such a pulse (#20371).

In the *second* type of experiment pellet injection prior to the ICRH transiently produces a high axial density and a highly peaked density profile provided that the pellets penetrate deeply (inside $q_\psi = 1$). However variations in the pellet penetration depth produce a wide variety of density

profiles. Usually sawteeth are absent and polarimeter data shows $q_{\psi 0} > 1$ in these cases. Figs 1 and 2 also show n_e and T_e profiles for such a case, again taken 1.5s after the start of ICRH (#20370).

In the *third* type of experiment pellets are injected at intervals throughout the current rise to build up a peaked density profile with $n_{e0} \lesssim 2.3 \times 10^{20} m^{-3}$ and $q_{\psi 0} > 1$ by the time 5MA is reached. The ICRH is then switched on following the last pellet. With only 6MW of ICRH an enhanced neutron feature was produced, similar to ref [2] but now at 5MA, and 1.5 sec after the start of the ICRH a vestigial peaked profile with $n_{e0} \sim 6 \times 10^{19} m^{-3}$ remained, as shown in fig 1 (#20388). T_{e0} was much lower than in the previous experiment but T_{i0} was $\sim T_{e0} \sim 5keV$. The global confinement was improved by $\sim 30\%$ compared with gas fuelled plasmas, and high values of $n_{D0}\tau_E T_{i0}$ in the range 3 to 4 $\times 10^{20} m^{-3} s\, keV$ were produced transiently ($\lesssim 0.7s$).

In both second and third types of experiment the density decays during the ICRH but the density profile shape can remain peaked. In contrast to the first type of experiment, these experiments with ICRH following pellet injection often show MHD activity in the core of the discharge which might explain the decay of the central density. The electron temperature profiles are broader in the flat top heating case than in the current rise case as shown in fig 2. These new experiments demonstrate that a wide variety of n_e and T_e profiles can be established at low q_ψ without sawteeth and that $T_{e0} \sim 10keV$ can be reached with the density constant, decreasing or increasing with time.

3.The Current Rise Phase.

The initial current rise phase up to $\sim 2.5MA$ can show MHD instabilities before the first sawteeth appear, and during this time the plasma resistivity is anomalous. The magnetic field diffusion during the subsequent 1MA/s rise from 2.5 to 5MA has been studied using the TRANSP code [3] for an Ohmic pulse (#20360). The time evolution of the surface voltage and the q profiles from polarimetry can be completely described by neoclassical resistivity calculated from measured profiles of T_e and Z_{eff}. As the current approaches 5MA the q_ψ profile becomes shallow with $q_\psi \lesssim 1$ out to half radius and this shape is then maintained during the flat top.

4.Electron Heating.

A general feature of the experiments is a fairly sudden change in the electron heating rate observed from an initial $10keV/s$ to a low value $\lesssim 1keV/s$ which persists for the remainder of the sawtooth free period. The gradient ∇T_e can reach 20-30 $keVm^{-1}$. Previous experiments [1] showed a

linear rise of T_e with increasing ICRH power per particle P_{RF}/n_{e0}. The recent experiments (without pellets) cover a wider range of P_{RF}/n_{e0} and suggest there is a saturation of T_e or ∇T_e as shown in fig 3 (note that sawtoothing and sawtooth free cases are distinguished by open and solid symbols respectively). This saturation may be due to thermal transport or possibly an effect of a different ICRH deposition profile. In such plasmas, the fast ion slowing down time is long and the some fast ions have high energies $\gtrsim 1 MeV$ where orbit effects might be important [4]. Analysis of the fast ion stored energy and comparison with theoretical prediction suggest that orbit effects are small in these high current discharges. Also, the highly peaked T_e profile suggests that the deposition profile is still peaked.

5.Pellets + ICRH.

For the wide range of density profiles in the second and third types of experiment, the saturation of T_e with P_{RF}/n_{e0} is less marked as shown in fig 4. However the data does not extend to such high values of P_{RF}/n_{e0}. Comparing figs 3 and 4 it can be seen that $T_e \sim 10keV$ can be reached with P_{RF}/n_{e0} ranging from 1 to 4.5 despite the variations in density profile and time evolution. Further transport analyses of these results will be presented in order to determine the mechanism for the saturation.

6.Conclusions.

The experiments described in this paper have demonstrated that the deleterious effects of sawteeth in low q_ψ JET discharges can be eliminated for a wide range of density profiles. The current penetration remains neoclassical despite the high temperatures and current ramp rate. A saturation in T_e sets in at values $P_{RF}/n_{e0} \sim 2$ whereas ion heating experiments [5] show a linear rise of T_i with increasing NBI power per particle P_{NB}/n_{e0} up to 20keV and $P_{NB}/n_{e0} \sim 6$. Further experiments are required to resolve this difference.

[1] M.Bures et al, Plasma Physics and Controlled Fusion **31** (1989) p1843 and JET-P(89)03 p77.
[2] G.L.Schmidt and the JET Team, Plasma Physics and Controlled Nuclear Fusion Research, Proceedings 12th IAEA Conference, Nice, Vol **1** (1988) p215.
[3] R.J.Goldston et al, J. Comp. Phys. Vol **43** (1981) p61.
[4] D.F.H.Start et al, this conference.
[5] T.T.C.Jones et al, this conference.

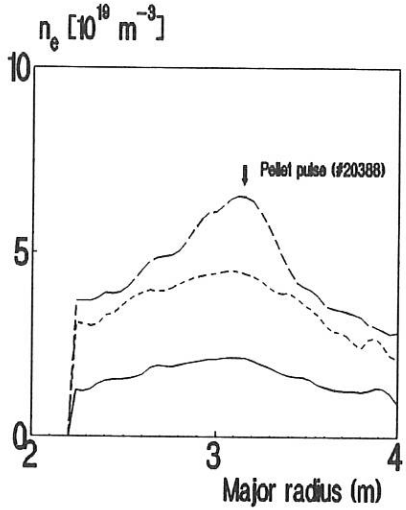

FIG. 1. Density profiles for current rise ICRH #20371 full curve, pellets + curr. rise ICRH #20370 dotted curve, pellets+FT ICRH #20388 dashed curve.

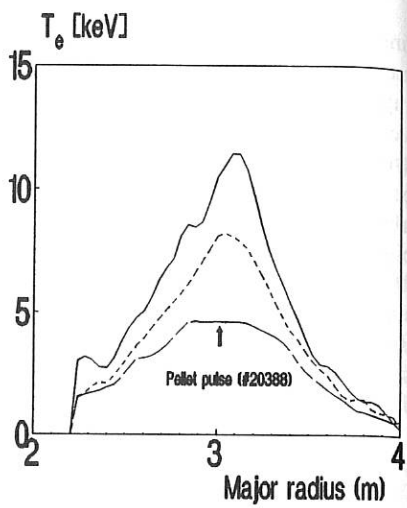

FIG. 2. Temperature profiles for the same three pulses shown in Figure 1.

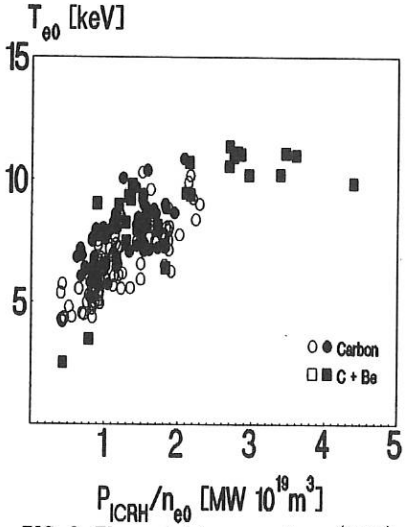

FIG. 3. The axial temperature (ECE) in current rise ICRH experiments vs power – density ratio.

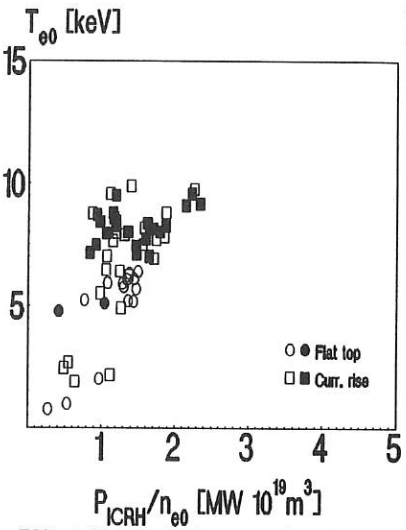

FIG. 4. The axial temperature in curr. rise ICRH experiments with pellet inj. before ICRH vs power to density ratio.

THE FUSION PERFORMANCE OF JET LIMITER PLASMAS USING BE COATED GRAPHITE AND SOLID BE SURFACES

T T C Jones, P J Lomas, S Attenberger, J P Christiansen, G A Cottrell, R Gianella, L de Kock, P Kupschus, G McCracken, C G Lowry, P Nielsen, D Pasini, R Prentice, G Sadler, M F Stamp, D D R Summers, M von Hellerman and H Weisen

JET Joint Undertaking, Abingdon, Oxfordshire OX14 3EA, UK

Introduction. A major part of the recent JET experimental programme has been devoted to optimising the performance of materially limited plasmas. This paper describes results of experiments designed to maximise the fusion yield, measured in terms of DD reaction rate R_{DD}, corresponding Q_{DD}, and fusion product $n_D(0)T_i(0)\tau_E$. The data therefore refer to low density, hot-ion plasmas with predominantly NB heating using mixed 80kV and 140kV D^0 beams, and also combined NB plus H-minority ICRH. The most important aspect of the experiments concerns the relative performance of bare graphite, Be coated graphite, and solid Be limiter surfaces in respect of density control and impurity influxes. These factors largely determine the attainable fusion yield and the maximum duration of the high-yield phase of the discharge. The NB driven fusion yield and $n_D(0)T_i(0)$ product are expected to increase if the density profile can be made more peaked. Profile peaking from the effect of NB fuelling has been demonstrated for bare graphite and Be coated graphite limiters. With solid Be limiters a new scenario has been developed in which the target plasma density profile was controlled using pellet injection. Using this technique $R_{DD} = 4.2\times10^{16}s^{-1}$ was obtained,the highest ever value for a JET limiter plasma, using 17MW NBI combined with 9MW ICRH. There is also evidence for a substantial contribution to R_{DD} arising from synergetic effects /1/ in this case.

Review of high fusion yield results with bare graphite surfaces. During 1989, JET operation prior to the introduction of Be took place at a time when the machine was not particularly well conditioned immediately following the restart of plasma operation. Therefore the 1988 data /2/ provide a more representative baseline for bare graphite plasma facing surfaces. In summary, the most effective density control ($P_{tot}/<n_e> \lesssim 16\times10^{-19}MWm^3$) was obtained for plasmas in contact with the graphite protection tiles of the vessel inner wall following intensive conditioning by He tokamak discharges. The high T_i regime ($T_i(0)>20keV$) was readily entered and $n_D/n_e \sim 0.5$ was obtained at the highest P_{tot}/n_e. Density profile peaking from NB fuelling was observed, and $Q_{DD} \lesssim 8\times10^{-4}$ achieved. A severe limitation to performance was the carbon bloom emanating from excessively heated tile edges, which invariably occurred after $\lesssim$ 1s at full NB power. For the belt-limiter, insufficient density control was available to access

the hot-ion mode even following He conditioning. At moderate P_{tot}/n_e, $Q_{DD} \lesssim 5\times10^{-4}$ and $n_D/n_e \sim 0.4 - 0.8$ were obtained, depending on conditioning. The above results refer to 3MA discharges; at 5MA, no experiments with inner-wall plasmas and high power heating have been attempted, but for belt-limiter plasmas the accessible range of P_{tot}/n_e was much reduced.

Results with Be coated graphite surfaces. Be was first introduced into JET in the form of evaporated films 10-50 nm in thickness. Density control comparable to the best 1988 inner-wall data was obtained in both inner-wall and belt-limiter configurations with no further vessel conditioning. The favourable density control properties deteriorated only partially over successive discharges between overnight evaporations. $n_D/n_e \sim 0.6$ was obtained at the highest values of P_{tot}/n_e in both configurations, representing a slight improvement for the inner-wall data.

The fusion performance of inner-wall plasmas was equivalent to the best 1988 data, but despite an attempt at realigning the tiles during the preceeding shutdown the carbon bloom problem remained. Fig.1a illustrates an inner-wall discharge early in a sequence following Be evaporation. The density remained steady even in the presence of 18 MW NBI until the onset of the C bloom. Z_{eff} initially fell and the density profile became peaked due to NB fuelling; a peaking factor $n_e(0)/n_e \sim 3$ was attained at the maximum of $R_{DD,}$ in line with predictions based on the relative core (NBI) and edge (recycling) fuelling rates /3/. According to PENCIL code predictions of the beam-plasma reaction rate, the fall in R_{DD} is due, in roughly equal measure, to simultaneous broadening of the electron density profile and falling fuel concentration following the C influx, with n_D/n_e actually approaching zero before the end of the heating pulse.

The improved hydrogenic pumping by the belt-limiter after Be evaporation ($P_{tot}/\langle n_e \rangle \lesssim 14\times10^{-19}$MWm^3) led to an increase in Q_{DD} to 6.5×10^{-4}. Fig.1b illustrates the behaviour of a hot-ion belt-limiter plasma; the density control was not quite so effective as in the inner-wall case as indicated by the rising density during NBI but a peaked density profile nevertheless developed. The fall in R_{DD} is again attributable both to density profile broadening and C limiter influxes, but the latter appeared to be of a more benign nature than the inner-wall blooms, the plasma tending towards a new steady-state with reduced yet non-zero n_D/n_e. A few low density 5MA belt-limiter discharges with NBI heating were were also performed, which achieved central ion temperatures $T_i(0) > 14$keV, and fusion product $n_D(0)T_i(0)\tau_E \sim 1.9\times10^{20}$m^{-3}.keV.s This latter parameter compares with $\sim 1.5\times10^{20}$m^{-3}.keV.s obtained in both belt-limiter and inner-wall configurations at 3MA. Q_{DD} was however less ($\lesssim 5\times10^{-4}$) in the 5MA case.

Results with solid Be belt-limiter. Following installation of solid Be belt-limiter tiles the accessible range of $P_{tot}/\langle n_e \rangle$ was extended to 20×10^{-19}MWm^3 at 3MA whilst $n_D/n_e \sim 0.6$ was maintained. At moderate values of P_{tot}/n_e , n_d/n_e was improved to better than $\sim$ 0.8. For plasma equilibria well matched to the belts, Be influxes were generally

observed after $\lesssim$ 1s of high power heating. This led to termination of the high yield phase in a similar manner to the graphite belt case. Until the end of the ~2.5s heating pulses of these experiments, Be light intensity levels and n_D/n_e subsequently remained at roughly steady but degraded levels compared with the pre-influx phase of the discharge.

Despite low particle recycling, it was not possible to obtain a peaked density profile by NB fuelling alone, and Q_{DD} did not exceed 7.7×10^{-4} for gas fuelled target plasmas. One possible explanation is a stronger influence of sawteeth due to reduced toroidal field in these experiments (2.4T c/f 3.1T). Also, effects due to differing ionisation profiles from incoming Be and hydrocarbon species may play a role. In order to recover favourable peaked density profiles several 4mm pellets were injected during the OH phase. Heating was subsequently applied as the density profile relaxed. It was not possible to sustain the profile shape by NB fuelling, as illustrated in Fig. 2 which is based on single LIDAR profiles taken over several discharges to build up the time evolution. While the profile was still centrally peaked, a transient phase of substantially enhanced R_{DD} was observed for both NB and combined heating. With combined heating, there is evidence for 2nd harmonic acceleration of the beam deuterons from neutron spectra /1/ and indirectly from magnetic measurements of the pressure anisotropy.

Best fusion product values similar to the Be coated graphite limiter results were obtained, in the discharges with pellet fuelled target plasmas which also gave the highest R_{DD} and $Q_{DD}(\sim9\times10^{-4})$.

Summary of high fusion yield results. Fig.3 summarises data for all three surface states for 3MA belt-limiter discharges and shows that the ratio $P_{NB}/n_e(0)$ is a good predictor for Q_{DD} , as expected when beam-plasma reactions dominate, thus illustrating the importance of effective density control. The scatter is attributable to variations in plasma purity and profile shape, differing mixes of 80keV and 140keV beams, and to varying amounts of ICRH which, whilst increasing R_{DD}, generally depress Q_{DD}. A particular feature of the pellet fuelled target plasma is that addition of up to 9MW ICRH produced no degradation in Q_{DD} and led to the record R_{DD} for a JET limiter plasma. Although no differences in global confinement due to Be have been observed, the equivalent Q_{DT} (thermonuclear) as deduced from $n_D(0)T_i(0)\tau_E$ for belt-limiter plasmas is substantially improved mainly from the stronger pumping capability with Be evaporation and Be tiles.

References

/1/ G Sadler et al, this conference.

/2/ C G Lowry et al, 16th Conference on Controlled Fusion and Plasma Physics, 1989. Europhys. Conf. Abstracts Vol. 13B, Part 1, p87

/3/ T T C Jones et al, Bull. Am. Phys. Soc. Vol.34 No.9 p2054 and JET-P(89)80

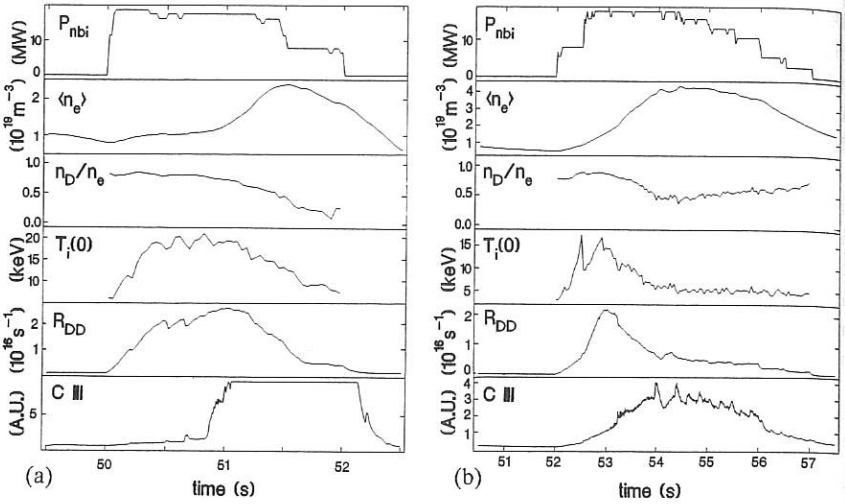

Fig.1 Plasma parameters during the heating phase of low density discharges after Be evaporation: (a) Inner-wall plasma (JET pulse #19693) and (b) Belt-limiter plasma (#19689). $T_i(0)$ and n_D/n_e are from carbon CX recombination spectroscopy.

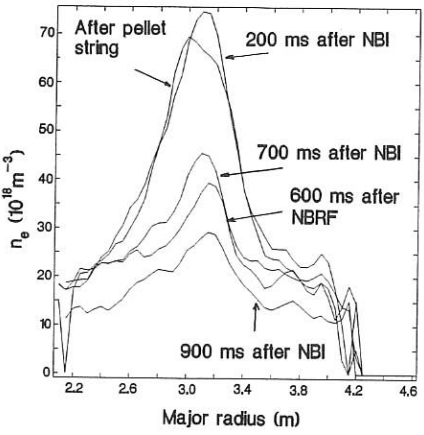

Fig.2 Density profile evolution reconstructed using LIDAR data from several discharges with solid Be limiters. In each case heating was applied to pellet fuelled target plasmas with roughly similar peaked density profiles.

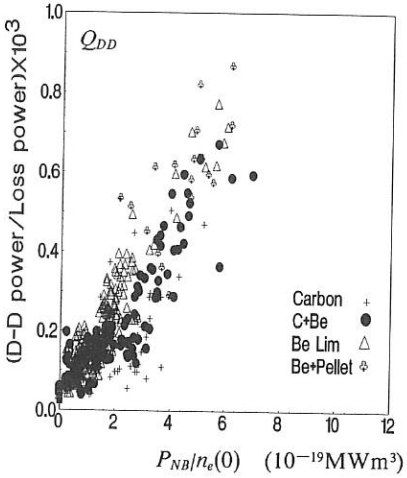

Fig.3 Plot of Q_{DD} vs. $P_{NB}/n_e(0)$ for 3MA discharges in contact with the belt-limiters in all three surface states, showing also the effect of pellet-peaked target profiles for solid Be tile data.

THE ROLE OF VARIOUS LOSS CHANNELS IN THE ION ENERGY BALANCE IN T - 10

E.L.Berezovskij, A.A.Medvedev, A.Yu.Pigarov
I.V.Kurchatov Institute of Atomic Energy, 123182 Moscow, USSR

The ion energy balance study on T-10 performed recently under Ohmic and microwave plasma heating has shown that one needs to introduce the anomalous ion heat conduction coefficient, noticeably different from the neoclassical one in comparison between the real ion energy losses and the data from the neoclassical transport theory, and to the central zone. This increase in the peripheral anomaly turns out to be dependent on the atomic flux from the vacuum chamber walls.

The results of the studies in spatial distributions of atomic fluxes along both major and minor torus circumferences are given in the paper. On the basis of these results the calculations allowing one to determine the role of ion energy losses through the channels of convection and charge exchange under various operating conditions of the facility have been done and thus the role of the losses determined by heat conduction is singled out in the total ion energy balance.

FIRST EXPERIMENTS AND NUMERICAL SIMULATION OF A PLASMA COLUMN COMPRESSION IN HIGH FIELD TOKAMAK

E.A.Azizov, G.G.Gladush, V.N.Dokuka, V.E.Lukash, S.V.Mirnov, R.R.Khairutdinov

I.V.Kurchatov Institute of Atomic Energy, Moscow, USSR

In a high magnetic field tokamak TSP [1] experiments were being conducted to study plasma properties at the 1-st stage of a tokamak cycle preceeding the plasma column compression along minor radius. Toroidal field B_T was created by two generators TKD-200; B_T=2T at R=1 m. Plasma current range of 100-200 kA was inverstigated with the safety factor $q \sim 3$. Plasma parameters were close to those obtained in other tokamaks with the same dimensions and energetics. Experimental data analisis shows, that there exist x - point near inner surface of the column (R=70-5 cm), i.e. the configuration is the same one of Japanes tokamak DIVA.

Numerical simulation. An air inductor placed outside the central opening of the torus is used in the TSP to excite plasma current. This inductor produced a sufficiently high poloidal magnetic field in the region of the plasma column, which can significantly affect the shape and dimensions of the plasma column cross-section at the initial stage of current input. The inductor can also have similar effect on the column at a plasma current close to the limit, imposed by the facility energetics. In this case while compressed on major radius the column experiences an attraction from the main inductor coil, which under certain conditions can lead to a violation of the quasisteady character of the compression process and column ejection onto the inner wall of the vacuum vessel.

Model. To calculate the process of current input to TSP and plasma column compression on major radius 1-1/2D evolutional code DINA [2] was used. An MHD equilibrium is described in a two-dimensional approximation and transport processes and magnetic field diffusion in a one-dimensional one taking into account a specific shape of magnetic surfaces. In the equation for plasma density beside the diffusion flux a term simulating plasma transport by convection was taken into account. Electron thermoconductivity was chosen in accordance with the Merezhkin-Mukhovatov scaling (T-11). The calculation for currents induced on the vessel walls due to the plasma column movement was done including a vacuum vessel inductance.

Analitical model. Plasma compression on the major radius is produced by increasing the current in the compression coil I_c. Due to an elongated shape of the vacuum chamber the plasma can be compressed by 2.5 times. Preservation of the toroidal and poloidal fluxes yields the plasma current I_p:

$$I_p=I_p^o/R[\ln(8R_o/a_o)-2][\ln(8\sqrt{RR_o}/a_o)-2]^{-1}+0.5c(I_i^o\int_o^{R_o}b_i(R)RdR-$$

$$-I_i(R)\int_o^R b_i(R)RdR)R^{-1}[\ln(8\sqrt{RR_o}/a_o)-2]^{-1}+0.25R^{-1}cb_c[I_c^{(o)}R_o^2-$$

$$-I_cR^2][\ln(8\sqrt{RR_o}/a_o)-2]^{-1} \qquad (1)$$

The compression coil current necessary to maintain the column in the point R can be found from the balance of the forces of the column compression and expansion.

$$I_c=-b_i(R)I_i/b_c-I_p(b_cRo)^{-1}[\ln(8\sqrt{RR_o}/a_o)-1.25]-$$

$$-2\pi cn_okT_oa_o^2(R_o/R)^{7/3}(I_pRb_c)^{-1} \qquad (2)$$

At obtaining (2) it was assumed that the plasma density and temperature increase according to the adiabatic law. In the expression (1-2) I_i - the current in the inductor coils, $b_i(R)$, b_c - the coupling coefficients ($b_i(R)=B_i(R)/I_i$, $b_c=B_c/I_c$, B_i, B_c - the magnetic field of the inductor and the compression coil). The initial values of parameters are marked with the index "o". It can be seen from (1,2), that during the column compression a plasma current rise can slow down. This effect is due to decreasing of the external poloidal magnetic field flux at the plasma edge, which leads to generating inversed emf and opposite sign current. As to the behavior of compression coil current with decreasing R, it is determined by competing of the first and the rest terms (2). As seen from (2), the second and the third terms are negative and decrease with decreasing R, and the first term is positive and increases with decreasing R, ($b_i(R)$ increases with decreasing R). From Fig.1 it is seen, that at $\beta_j^o=0.5$ and $|I_i|>25$ kA I_c - non monotonous function of R: i.e., at the monotonous compression coil current increasing (by module) there occurs a moment, when the column spontaneously jumps into a state with smaller radius R. With increasing the initial β_j^o such a jump is observed at larger values of the inductor current. Thus at $\beta_j^o=1$ the spontaneous compression can occur at $|I_i|>35$ kA. The plasma current in some range of R can even decrease with decreasing R at large I_i (Fig.1). To reduce the influence of the reversed emf it would be possible during compression to increase the current in the inductor in such a way that a negative emf could not be generated (i.e. the second term in (1) should be kept equal to zero). However, the calculations showed that no significant plasma current rise can be achieved in this case (see the curves 3',5' Fig.1), while the solution disappears, which corresponds to a stable compressed state (curve 5 Fig.1).

Fig.1 shows, that at one value of the compression current three steady states of the plasma column can exist at different values of the plasma current. This confirms a possibility of

simultaneous existance of two plasma columnein the tokamak, whioh correspond to stable solutions with $\partial I_c/\partial R>0$.The MHD-equilibrium calculations of two columnes attracting each other showed that such equilibrium to be possible (see Fig.2). The curves differ by the ration of initial currents in the columnes. At such approach the idea of two columnes in the tokamak remains open. Two columnes can develop, for example, at breakdown. At this stage two regions with a zero-poloidal field develop in the chamber where the most favourable conditions for gas breakdown arise.

The process of "spontaneous" compression of the plasma column can be approximatily described by adding a force from currents induced in the vessel to equation (2). Substituting the vessel by two plates [3], obtain

$$V_o^{-1}dR/dt=[I_c^o-I_c(R)]I_p^{-1}(R),\ V_o=c^3db_c(4\pi\sigma\delta)^{-1}$$

where 2d - the distance between the plates, σ, δ - the conductivity and thickness of the vacuum vessel wall. For the TSP conditions at the compression current $I_c^o=-40$ kA the "jump" time is 6 ms at $\beta_j^o=1$.

1-1/2D model. 1-1/2D calculations considering the plasma resistivity are on the whole consistent with the results obtained for a "o"-dimensional model of ideal plasma. One can select the scenario of compression in such a way,that the compression velocity is constant. For example, at $\beta_j^o=1$, $I_p^o=500$ kA, $I_i=-30$ kA the compression occurs in a quasi-stationary way at a rate of $6\cdot10^3$ cm/s (Fig.3). At a fixed compression coil current the plasma column does not stop, the velocity sharply slows down. This effect is dueto a resistive decay of plasma current I_p.The picture substantially changes if the compression takes place at a larger current in the inductor coil ($I_i=-34$kA) In this case, if the compression current is fixed on the unstable part of the curve $I_c(R)$,the situation is quite different. The movement of the column is sharply accelerated and the rate of the plasma temperature rise is increased. The violation of the quasi-stationary compression takes place. The calculations showed that in spite of the energetic time (~14 ms) being close to the compression time (~10 ms) ions are being heated adiabatically. Due to generation of a reverse emf on the inner part of the plasma column the skinning current is negative (Fig.4). For this reason the Troyon factor at the stage of compression can exceed 4. These calculations also showed that a divertor configuration with zero field on the horizontal axis is being formed during the compression stage and zero field point moves inwards in front of the plasma column.

References.

1.E.A.Azizov, E.P.Velikhov, B.B.Kadomsev, V.D.Pismenny, V.A.Chujnov,V.A.Glukhikh et al. XII Int.Conf.on Plasma Phys.and Controlied Nucl.Fusion Reseach, Nice, France, 1988.
2.E.A.Azizov et al. Preprint 3-251, IVTAN, Moscow, 1988.
3.V.E.Zhogolev, S.V.Putvinskij, "Nuclear Fusion", 1982, 22, 947.

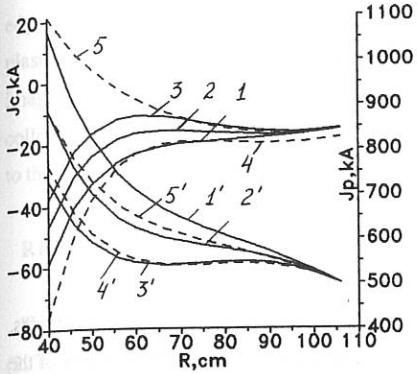

Fig.1 Plasma column position vs compression coil current. 1-I_i=-20kA,β_j^o=.5,2-I_i=-25kA 3-I_i=-30kA; 4-I_i=-35kA,β_j^o=1; 5-I_i(0)=-30kA. 1'-5'-plasma current vs large column radius, a_o=20 cm.

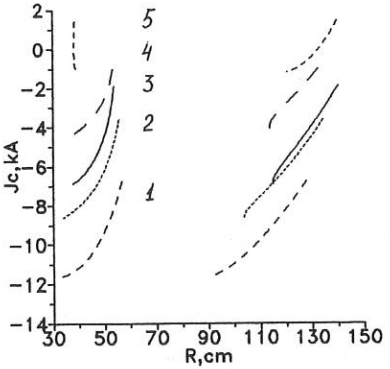

Fig.2 Plasma colunmes positions vs compression coil current for different initial plasma currents in inner column:1-I_{p1}=100kA; 2-I_{p1}=200kA;3-I_{p1}=250kA;4-I_{p1}=300kA; 5-I_{p1}=400kA; initial total current 500kA, a_o=15 cm.

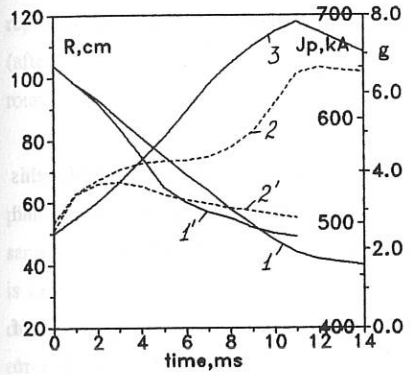

Fig.3 Plasma column position (1-I_i=-30kA,1'-I_i=-34kA), plasma current (2-I_i=-30kA, 2'-I_i=-34kA).Troyon factor g (3-I_i=-30kA) vs time.

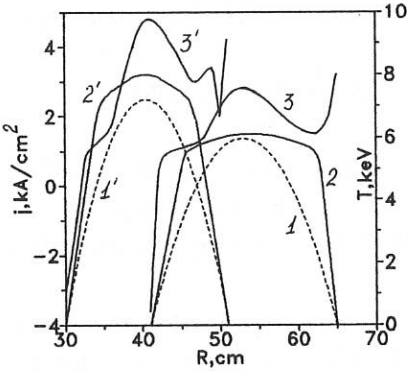

Fig.4 Radial profiles of plasma parameters 1,1'-T_e,2,2'-T_i,3,3'-j. (1,2,3) at t=9ms and (1',2',3') at t=13 ms, I_i=-30kA.

A STUDY OF POLOIDAL AND TOROIDAL ROTATION IN THE TJ-I OHMICALLY HEATED TOKAMAK

B. Zurro and TJ-I Team

Asociación EURATOM/CIEMAT para Fusión. E-28040 Madrid. Spain

INTRODUCTION

Plasma rotation is of paramount interest for understanding confinement in magnetic devices. The magnitude and direction of poloidal rotation are interrelated with the diffusion fluxes of the bulk component and of the plasma impurities. For this purpose poloidal rotation velocity profiles have been measured as a function of density, in order to establish some empirical correlation between particle transport and rotation, when the tokamak operational space is covered. Preliminary measurements of toroidal rotation velocity have been performed for estimating how important is its contribution to the observed poloidal flow. Measurements of plasma rotation in ohmically heated tokamak can be found in (1) and the references therein, but systematic studies as a function of radius, density and other parameters are not available.

EXPERIMENTAL SET-UP

TJ-I is an ohmically heated tokamak (R_0 = 30 cm, a = 10 cm) and was operated for this experiment with toroidal fields ranging from 0.8 to 1.5 T and a plasma current between 35 and 45 kA. The chord averaged electron density was varied between 0.5 and $3x10^{13}$ cm^{-3}.

Rotation measurements have been performed in the TJ-I tokamak by measuring the shift of well known and isolated ionic lines with spatial resolution. For this purpose a 1 m monochromator with an intensified multichannel detector mounted in its focal plane was used. A linear dispersion of 2.6 Å/mm is typical in third order, and a thermal drift of 0.1 pixel per 0.1 ºC must be corrected during a sequence. The line of sight can be scanned by a shot to shot technique. A set of 20 good reproducible discharges are needed to obtain a rotation profile

from different ions with ionization potential ranging from 40 to 390 eV. Fortunately for these measurements, it is possible to observe emission from highly ionized impurities at the plasma edge, supposedly due to charge exchange of deconfined ions of higher charge which reach the plasma periphery with high temperature. For poloidal rotation measurements the input slit is imaged onto the plasma edge and rotated 90º; for toroidal rotation measurements the light collected along different chords almost tangential to the major torus circumference, is relayed to the input slit by means of a lens and a quartz fibre bundle.

RESULTS

The TJ-I plasma poloidal rotation profiles have been measured using the following lines: CV (2271 Å), OV (2781 Å), OVI (5290 Å), CIII (2296 Å); first ion peaks at plasma center, whereas these oxygen ions peak at a radius between 2-6 cm and the last one at the plasma edge. To construct a rotation profile with these ions, it is necessary to expose three different spectral ranges using the optical multichannel intensified detector. The OV is measured in third order and the others in first due to the presence of interferences lines when trying to work in higher orders. The rotation velocity is determined by scanning the line of sight of the spectrometer across the plasma cross section on a shot to shot basis during a series of well reproducible discharges. Changes in the location of the line center measured at half intensity (after been corrected for thermal drift) are attributed to Doppler shifts. A method to deduce rotation from line integrated data was explained before (2).

Fig. 1a shows a typical shift profile for CV as well as its line integrated emission profile; a pixel unit in this figure is equivalent to 0.2 Å. In Fig. 1b the angular poloidal velocity of the same ion along with that of a peripheral one (CIII) is plotted versus line averaged density, as it is varied between 0.5 to 2.6×10^{13} cm^{-3}; positive velocities correspond to electron diamagnetic drift direction. It is worth to notice that central and intermediate ions rotates in TJ-I in the electron diamagnetic direction with a velocity which diminishes as the density increases. However, an edge ion like CIII rotates in the opposite direction at low densities, see Fig. 1b, and in the electron diamagnetic direction between 1.5 to 2.6×10^{13} cm^{-3}. Intermediate ions like OVI and OV, which data are not included in Fig. 1, behave similarly to CV with plasma density but rotate with lower angular velocities.

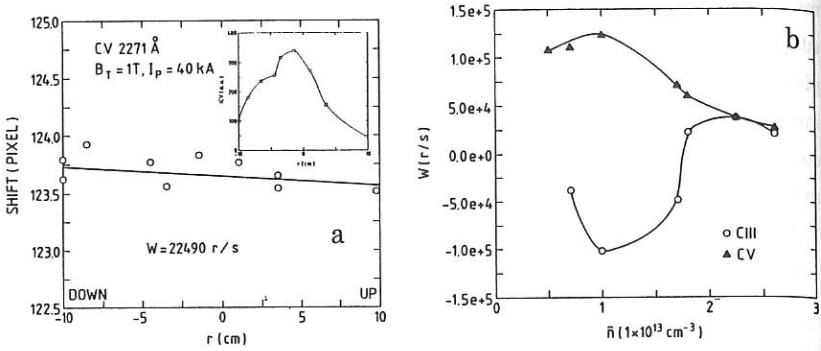

Fig. 1. a) Typical shift and line averaged emission profiles for CV; b) Dependence of angular poloidal rotation with line averaged density for central (CV) and edge ions (CIII).

This inversion of the rotation is clearly evident in OV shift profiles and other ions which emission peak at medium plasma radius. In TJ-I plasmas we can detect emission from CV, OV and CIII along peripheral plasma chords, but the inversion or reduction in poloidal rotation is markedly more evident in the two last ions. We provisionally ascribe this effect to the fact that since CV ions at the edge have thermal temperatures in the same range than central ones, the viscosity and other effects which damp the rotation should be less effective for it than for the colder particles. In Fig. 3, an angular poloidal velocity profile, obtained from data shift profiles from three different ions, is shown.

In order to elucidate the meaning of the measured velocity, v_θ, we must consider the basic mechanisms driving it. From the radial component of the flux-surface averaged ion momentum equation, we can put $v_\theta = v_E + v_D + B_\theta/B_T\, v_T$, where the meaning of these terms is the conventional one (3). To estimate the importance of the last term, the poloidal projection of the toroidal flow, we have measured the ionic toroidal velocity by using the OVI line at 5290 Å, well transmitted by a fiber guide. The raw profile so obtained is depicted in Fig. 4, where pronounced deeps are evident around the position of the q=2 rational surface; islands could be the cause of this observed rotation damping as has been theoretically suggested. The plasma in TJ-I rotates in the counter current direction. Although the absolute values of toroidal

estimated from these data are in the same range as poloidal rotation velocities, when entered in previous equation its contribution to the poloidal rotation is less than 10%. A pixel in this figure is equivalent to 0.2 Å. A more detailed analysis of rotationprofiles at three different plasma densities will be presented. Similarly, the dependence of plasma rotation with toroidal field, which according to first measurements seems to rise with it, will be presented at the conference.

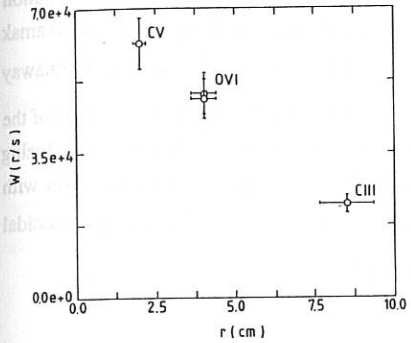

Fig. 3. Plot of poloidal rotation as a function of radius for $\bar{n}$=1.8x10^{13} cm^{-3}.

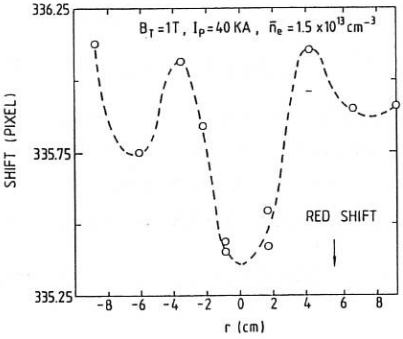

Fig. 4. Toroidal rotation profile showing damping supposedly due to magnetic islands.

In conclusion, TJ-I plasmas exhibit sheared angular rotation profiles, whereas at high densities the entire plasma rotates in the electron diamagnetic drift direction, at densities below 1.5x10^{13} cm^{-3} the cold peripheral ions rotates in the opposite direction. The toroidal rotation seems to have a modest contribution to the poloidal flow, being the ExB term the dominant drive of poloidal plasma rotation, at least at low densities.

REFERENCES

(1) R. D. Benjamin et al., Phys. Rev. **41A**, 1034 (1990).

(2) B. Zurro, Proc. 16th Europ. Conf. Contr. Fusion Plas. Phys. (Venice), **IV**, 1445 (1989).

(3) V. I. Bugarya et al., Nuclear Fusion **25**, 1707 (1985).

RUNAWAY ELECTRON FLUCTUATIONS STUDIES IN TJ-I

L. Rodríguez R., J. A. Vega
Asociación Euratom-Ciemat para Fusión
28040 MADRID-SPAIN

Introduction

The runaway electron characteristics (energy, confinement time, distribution function, and intensity spectra) have been studied for ohmic discharges in TJ-I tokamak (R_0=0.3 m, a=0.1 m, B_T < 1.5 T, I_p < 60 kA) by using a simple 2-D model for runaway dynamics [1]. In the present work, this model has been used to study time evolution of the runaway electrons along a TJ-I discharge under different plasma conditions by analyzing fluctuations on the total hard-X-ray flux signal. Frequency spectra and correlation with n_e fluctuations, either at the edge of the plasma, or n_e inside the plasma, and poloidal magnetic field fluctuations B_ϑ have been analyzed.

Experimental set-up

The experimental setup used consists of, on the one hand, by a data acquisition system that allows to record in a same TJ-I discharge, different X-ray spectra, coming from a Si(Li) detector and two NaI(Tl), one of them "viewing" the plasma column tangentially and the second one, perpendicularly, with seven 4 ms time-windows that correspond to the rise, plateau and sloping down of the discharge. In addition, a third NaI(Tl) detector working in current mode for hard-X-ray total flux fluctuations, a Langmuir probe measuring density fluctuations [2], a microwave reflectometer working in the band 30-55 GHz to obtain n_e fluctuations with radial resolution [3], and a magnetic pick-up coil to study B_ϑ fluctuations are used.

As to photon spectra, data acquisition was accomplished by using four channel camac modules (LC6210) described in [4]. Fluctuation signal data acquisition used identical modules, which were digitized at a 1 MHz sampling rate. Conventional FFT was used for data analysis.

Experimental results

Discharges with hard-X-ray fluctuations have been observed in low toroidal field conditions (0.9 T) and low density: 0.8 x10^{13} cm^{-3} at maximum current intensity, and falling down at puffing gas cut-off. Loop voltage is 3 V at I_p maximum (figure 1).

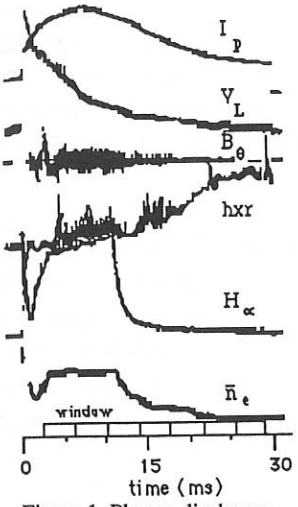

Figure 1. Plasma discharge.

1-X rays spectra.

Pulse height amplitude spectra have been measured with fluctuations and accumulated in 9 repetitive discharges in seven time windows beginning 2 ms after discharge start-up. Electron temperature obtained from Si(Li) detector and the inverse value of hard-X-ray spectra slope (expressed in keV) are shown in figure 2. Hard X-ray data are obtained from "tangential" detector since perpendicular one does not provide a good statistical result. The value of

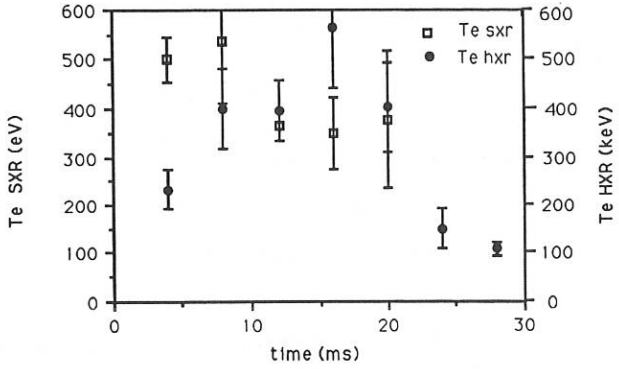

Figure 2. Electron temperature from SXR and inverse HXR spectra slopes.

the inferred runaway confinement time are shown in figure 3. The evolution of electron temperature corresponds to a normal discharge with the highest temperature at current maximum, and the values higher than normal ones can be related with the no perpendicular viewing chord of the detector. The runaway regime at the end of the discharge can explain the absence of low energy photons in this detector. Runaway confinement time is higher than in discharges without fluctuations, but this can be explained by the low electrons density. After fluctuations there is a loss of runaway electrons with a higher confinement time.

2-Fluctuations

Fluctuation frequency spectra are shown in figure 4 for the second time window, where the HXR flux presents fluctuations in the time signal and no disruption was observed. Reflectometer frequency is chosen at 35 GHz (r = 6 cm). Langmuir probe and reflectometer both present a high level of fluctuations. MHD signal has two zones of high activity, one around 50 kHz and a second one around 100 kHz, that does not appear without HXR fluctuations. V_L frequency spectra is also peaked around 50 kHz.

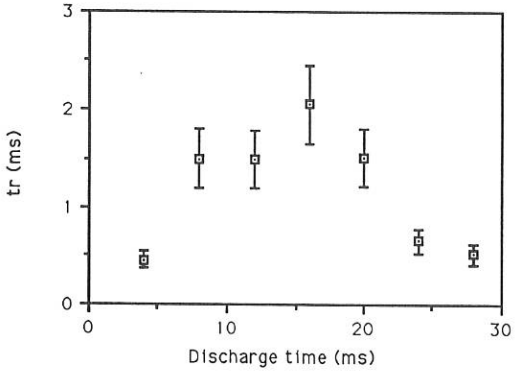

Figure 3. Runaway confinement time.

Frequency spectra obtained from HXR present a dominant frequency around 5 kHz.

From these measurements, it is seen that low frequency fluctuations are related with MHD activity and high frequency ones decrease like density spectra (in the border and inside) with an exponential shape, suggesting that high density fluctuations in HXR

flux are induced by density fluctuations. Runaway confinement times are in agreement with previous measurements from total particle flux [2] and spectroscopy [5].

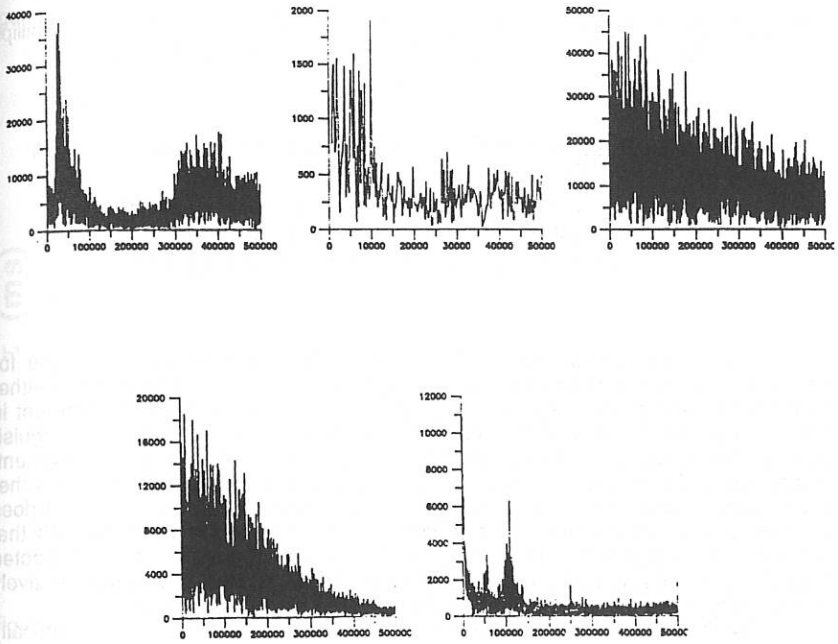

Figure 5. Frequency spectra from a)V_L, b) HXR, c) Langmuir probe, d) reflectometer, e) MHD. On x-axis frequency is in Hz and on y-axis amplitude is in arbitrary units.

1-L. Rodríguez R., L. Vázquez, A.P. Navarro. 16th Conf. on Contr. and Plasma Physics, vol 13B, I, 311.1989.

2-C. Hidalgo et al. To be published in Nuclear Fusion, vol. 30.

3-E. Anabitarte et al. J.Phys. D, 21, 1384-1390, 1988.

4-J.Vega. 8 th Topical Conf. on High Temperature Diagnostics. Hyannis-Massachusetts. May 1990

5-B.Zurro et al. Plasma Phys. and Controlled Fusion. 30, 1767, 1988.

PARTICLE AND IMPURITY CONFINEMENT IN HELIUM DISCHARGES IN THE TEXAS EXPERIMENTAL TOKAMAK (TEXT)*

W. L. Rowan, A. G. Meigs, M. E. Austin,† J. Y. Chen,§ R. L. Hickok,‡ P. E. Phillips, B. Richards, Ch. P. Ritz, P. M. Schoch,‡ X. Z. Yang,# Z. M. Zhang§

The Fusion Research Center, The University of Texas, Austin, TX USA
†Auburn University, Auburn, AL USA
§Institute of Plasma Physics, Academia Sinica, Heifei, PRC
‡Rensselaer Polytechnic Institute, Troy, NY
#Institute of Physics, Academia Sinica, Beijing, PRC

In the Texas Experimental Tokamak (TEXT), the confinement time for particles and impurities is significantly longer in a helium plasma than in either hydrogen or deuterium plasmas. In a general sense, a study of confinement in helium plasmas is warranted simply to identify the features which distinguish helium from hydrogen plasmas and thus perhaps learn more about confinement. In particular, the focused goals of this experiment were 1) to determine whether electrostatic turbulence contributes significantly to edge transport in He as it does in H [1] and 2) to contrast the behavior of impurities in He plasmas with that observed in H plasmas. In addition to the transport results, an unexpected diagnostic result was that He and H plasmas are qualitatively and quantitatively distinct in both the toroidal plasma rotation and the plasma potential.

For these experiments, the plasmas generated in TEXT were Ohmically heated. The major radius was 1 m, and the minor radius was limited to 0.26 m by a full aperture, poloidal titanium carbide coated graphite limiter. Typically, the data was taken during a 300 ms interval in which the macroscopic quantities such as I_p and $\bar{n}_e$ were constant.

The particle flux, Γ, was derived from measurements of the particle source, S, via the continuity equation

$$\nabla \cdot \Gamma = S.$$

The local particle source was inferred from spectroscopic measurements of the rate of ionization of the fueling gas.[1] For both H and He, the particle confinement measurements refer to confinement of the fully stripped ion. The particle confinement time, τ_p, is used here as a convenient tool for comparison of the discharges and is defined as

$$\tau_p = \frac{\int n_i(r) dV}{\Gamma A_p}$$

where A_p is the surface area of the plasma.

In figure 1, there is a comparison of two particle confinement time density scaling studies, one for He and one for H. For both, I_p=200 kA, B_ϕ=2.5T, and $q(\rho=1)$=4. Clearly, particle confinement time is longer in helium, but it is also interesting that the confinement scales differently in H and He. Specifically, the low density increase in confinement apparent in the hydrogen results (see also figure 2) is not evident in helium.

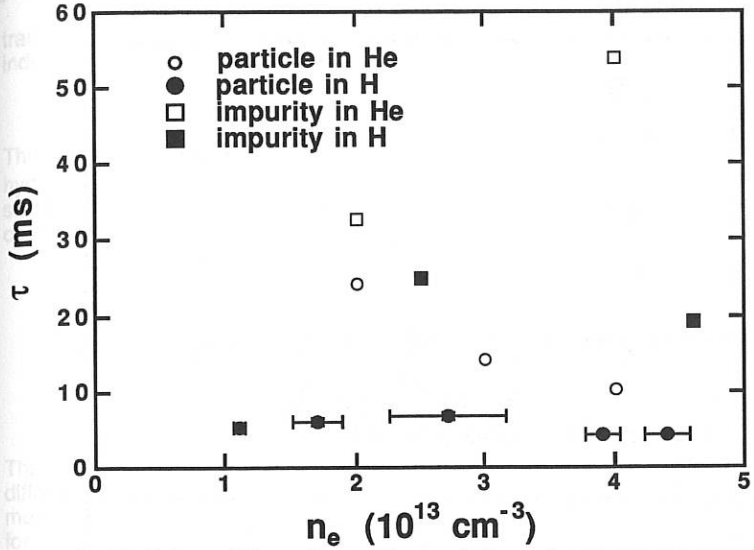

Figure 1. Particle and impurity confinement times for H and He plasmas with I_p=200 kA, and B_ϕ=2.5T.

As shown in figure 2, the density scalings in H and D are self-similar. Although the confinement time for D is larger than that for H, the principal features of the density scaling are the same, an increase in τ_p with $\overline{n}_e$ at low density and a decrease at higher $\overline{n}_e$. The scaling for He is not self-similar with those for H and D. The H and D results suggest that there is an isotopic dependence in the transport. When the He results are also considered, the transport mechanism appears more complex perhaps even suggesting a dependence on ion mass.

One component of the total particle flux, Γ, is that due to electrostatic turbulence, $\Gamma(\tilde{E}\times B)$. In figure 3, that component is compared with the total flux which was derived from the spectroscopic measurements as described earlier. The magnitudes of the two sets of values have fairly large uncertainties and agreement can be claimed only to about 50%. In the figure, $\Gamma(\tilde{E}\times B)$ is normalized

to Γ at $\bar{n}_e = 4\times10^{19}m^{-3}$ to demonstrate that the total flux and this turbulent component scale in the same way. This result coupled with a previous similar result in H [1] suggests that electrostatic turbulence is a major driving mechanism for particle transport. While the phenomenological conclusion of the previous paragraph may indeed be correct, it should be modified so that the electrostatic turbulence is acknowledged as a major contributor to transport and, if there is an isotopic dependence or an ion mass dependence, then these must be acting through the turbulence.

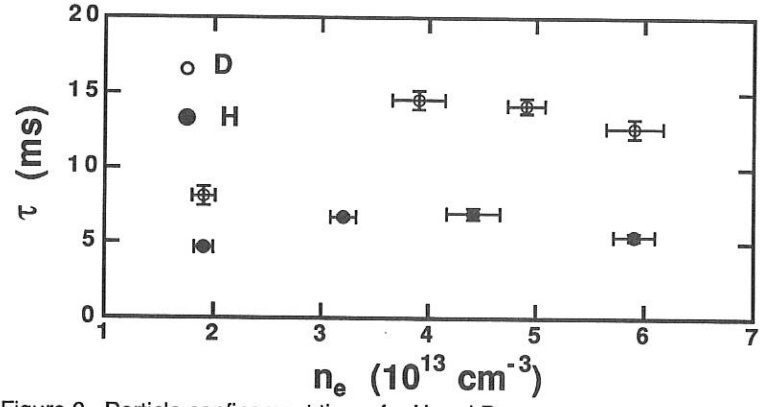

Figure 2. Particle confinement times for H and D.

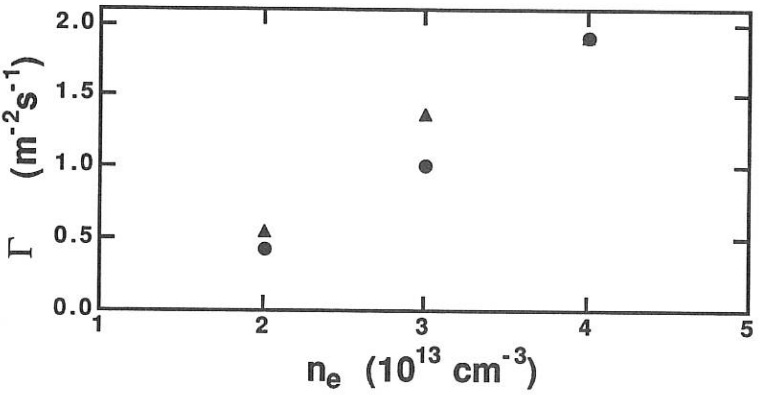

Figure 3. Particle flux at the plasma boundary for He plasmas. Total particle flux is represented by (●). The particle flux inferred from electrostatic turbulence measurements is represented by (▲).

The impurity transport information is derived from the temporal evolution of a short pulse of scandium which was injected into the plasma by laser ablation. The confinement time for the highest ionization stage is shown in figure 1 for the same plasma conditions as for the particle confinement results described earlier. Clearly, the central impurity confinement time is much longer in He than in H. From comparisons of the transient response of the lower stages of ionization of Sc which appear at the plasma edge with the behavior of the higher stages near the center, it follows that impurities are more peaked in the He case.

The impurity transport in the H and He cases was simulated using the FRC transport code CHAPO.[2] In the simulation, the impurity flux is assumed to be independent of charge state and to consist of diffusive and convective terms,

$$\Gamma = -D\frac{\partial n_z}{\partial r} + V n_z \frac{r}{a}$$

The case simulated is for I_p=200kA, B_ϕ=2.8T, and $\bar{n}_e = 2.5\times10^{19}$ m^{-3}. The hydrogen and the helium cases are alike to the extent that they can both be simulated with this model, but as might be expected they differ in the transport coefficients. The simulation results are summarized in table 1.

Table 1. Impurity transport coefficients in helium and hydrogen plasmas.

Plasma Ion	$D\left(\frac{m^2}{s}\right)$	$V\left(\frac{m}{s}\right)$
H	1.0	-5.0
He	1.3	-15.0

The diffusion coefficient is essentially the same for the two cases. The major difference is in the convective velocity, V. The larger inward convection leads to a more strongly peaked impurity profile and to a longer confinement time. At least for these discharge conditions, impurity transport in He is characterized by a stronger inward convection than in H.

Plasma rotation and plasma potential were both measured during these experiments, the former using Doppler shift of ambient impurity spectra and the latter using a heavy ion beam probe. A striking result was a reversal of the toroidal rotation direction when the fuel gas was changed from H to He. This was promptly traced to a reduction in the inward-directed electric field. If the neoclassical velocity is naively used as a comparison, then the rotation in H is much smaller than expected while the rotation in He is of the order of the expectation.

REFERENCES

1. ROWAN, W. L., KLEPPER, C. C., RITZ, C. P., et al., Nucl. Fusion 27 (1987) 1105.
2. WILEY, J. C., CHAPO, A One-Dimensional Transport Code, FRC Report 328, The University of Texas Fusion Research Center, Austin (1988).

THE FIRST MEXICAN SMALL TOKAMAK

L. Meléndez-Lugo*, R. López-Callejas, E. Chávez-Alarcón, R. Valencia-Alvarado, S. Barocio-Delgado, S. Colunga-Sánchez.

Instituto Nacional de Investigaciones Nucleares, Laboratorio de Física de Plasmas, Apartado Postal 18-1027, Col. Escandón, México 11801, D.F., México.
* Also Instituto Politécnico Nacional, Sección de Graduados ESIME, Unidad Profesional Zacatenco, Col. Lindavista, México 07360, D.F., México.

Abstract

We describe the design, construction and partial operation of a small Tokamak facility (NOVILLO Tokamak) intended for research purposes, with the following main characteristics: R=0.23 m, a_p = 0.06 m, $I_{max} \simeq 12$ kA, $B_T \simeq 4.7$ kG, $T_e \simeq 150$ eV, $T_i \simeq 50$ eV, $\tau_E \simeq 5$ msec, $q \simeq 3$.

The predominant design conditions were: stray field due to the hourglass shaped ohmic heating transformer $\simeq 10$ G, toroidal magnetic field ripple less than 1% at R = 0.23 m, vertical equilibrium magnetic field $B \simeq 150$-315 G with appropiate decay index $n_o \simeq 0.5$, and multiple access ports covering a total area of 617.78 cm^2 for diagnostic purposes.

The vacuum system provides a base pressure of 4×10^{-8} mbar. According to a residual gas analyzer, 80% of the base pressure is reported as being due to water.

Furtherly, a general description of the design and construction of the power sources and data adquisition system is also included.

The tokamak operation in the discharge cleaning regime was obtained with a 10 kW 17 kHz oscillator for 50-100 msec, at a pulse rate of 2 pps and a gas (H_2) working pressure between 1.5 - 4.7×10^{-4} mbar.

1. Structural and Magnetic Specifications /1/.

NOVILLO small tokamak has been conceived as a first step facility focoused on experimental research and future scaling. Four 316/L stainless steel 90° Bends are assembled by O-ringed insulating flanges to provide a 0.0032 m wall thick toroidal vacuum chamber with a 0.23 m major and 0.06 m minor radii, allowing a total port covered area of 617.78 cm^2 whose base vacuum pressure, under 4.0×10^{-8} mbar, is reached by a TPU/500 Balzers turbomolecular pump.

A central hourglass shaped bobbin acts as an 1.2 mH ohmic heating transformer (OHT) fed by a double fast-slow (C_f=0.44 mf/V_f=12 kV, C_s=4500 mf/V_s=1700 V) capacitor bank while a 12 module toroidal coil run on a 62 uf/20kV bank is perfoming B_T=0.47 T, I_T=1500 A, R_T=0.32 Ω and a ripple $\leq$ 1% at the major radius, Fig. 1.

In consequence, a maximun current I_p=12 kA and temperatures $T_i \simeq 50$ eV $T_e \simeq 150$ eV are attainable implying a B_p=0.04 T β=0.997 and $\tau_E \simeq 5$ msec.

Spurious OHT field inside the chamber is to be counterbalanced by a 210 G vertical field supplied also by a fast-slow field with V_F = 1700 V, C_F = 0.736 mf, V_S = 250 V, C_S = 45 mf leading to a decaying index $n_o \simeq 0.5$.

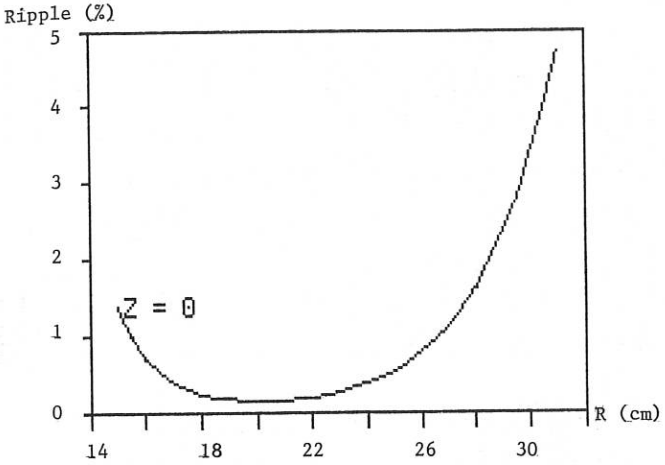

Fig. 1. Toroidal field ripple versus major radius R.

2. Present periphereal systems

Six capacitor banks in the ranks 62.5-45000 uf, 0.25-18 kV, 147-26010 J, 180-6031 A, 1.43-9.0 mH including 1.17-15 msec for current rise-time, supply the magnetic systems by means of a charge circuit. Endowed - with a GL-7703 General Electric ignitron it manages a voltage up to 20 kV and currents $\simeq$ 2 c/sec. A 120 sec recovery time is required by consecutive shoots of the capacitor system and a TTL technology time control unit - synchronise the 6 banks.

Once an IBM compatible PC-AT system is available, a 32 channel prototype circuit for acquisition data system (ADS) will be in operation (Fig. 2).

3. Development of cleaning discharges /2/.

Residual gas analysis at the base pressure exhibits an 80 % water - vapour and 20 % hydrogen, oxigen and carbon spectrum. Water contents can be further diminished up to 20 % by an adequate baking process. When used as a leak detector, the spectrometre indicates partial pressures at the -- components 28, 14, 32 and 16 attributable to atmospheric air. Comparative measurements are carried out with argon as a test gas.

So, in order to accomplish an efficient vacuum surface conditioning, a discharge cleaning plasma has been produced by means of low temperature

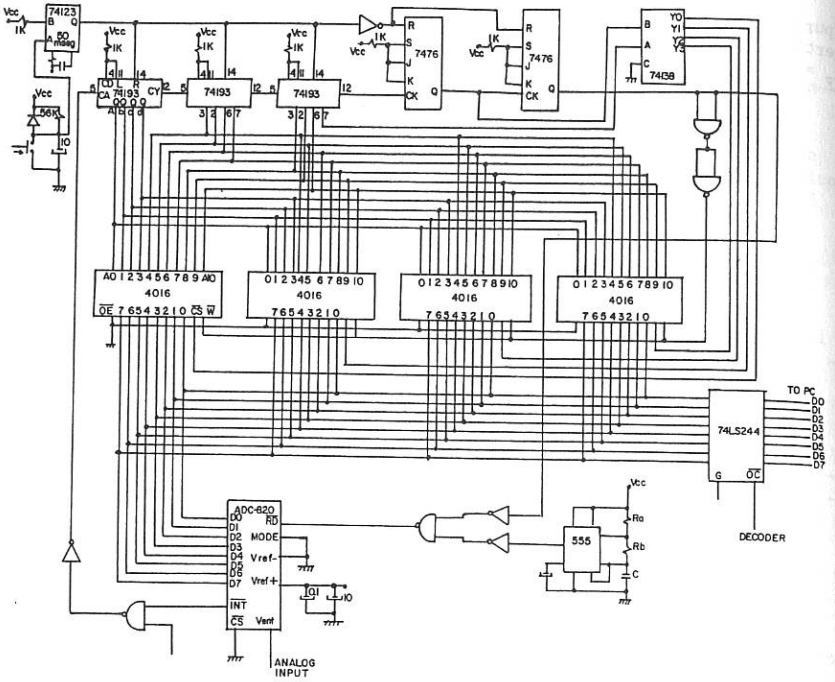

Fig.2. The prototype circuit for the acquisition data system

Hydrogen discharges sustained for several hours per day at a 2 pps pulse - rate, and a working pressure between 1.5 and 4.7×10^{-4} torr.

To this purpose, 17.5 kHz AF fields drive about 10 kW into the discharge thanks to a AF power oscillator. Being specifically designed and assembled, it consists of a T8W7/8000 water cooled triode, plate power supply tank circuit and grid pulser as shown in figure 3, enabling 0-50 msec AF - pulses amounting 10 kV peak to peak voltage and a 70 A rms current.

The discharge cleaning mode has been successfully performed by a 2 Hz repetitive operation of the toroidal field in a 600 G regime on a 5 msec 180 A pulse cheme simultaneous to the oscillator discharge (Fig. 4).

We wish to acknowledge the assistance of the IAEA (project MEX/1/015) in the activities above reported.

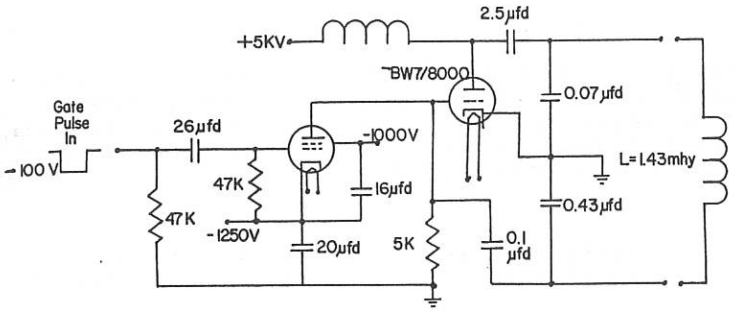

Fig. 3. AF oscilator (the coil is the OHT).

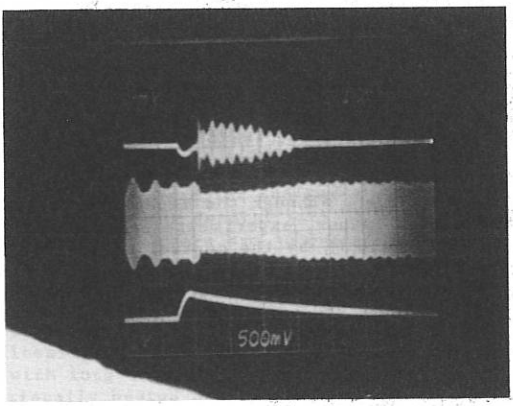

Fig. 4. Osciloscope discharge cleaning plasma current (top),oscilator OHT current (center) and toroidal magnetic field (botton).

References

/1/ Miyamoto K., "Plasma Physics for Nuclear Fusion", MIT Press, 1980.
/2/ J. Ramos S. et al., Rev Mex Fis Vol 29 No. 4, 1983, pag. 557-592

THE CONFINEMENT IMPROVEMENT MODES IN JIPP T-11U

Y. Hamada, A. Ando, K. Kawahata, K. Ida, M. Masai, M. Sakamoto, K. N. Sato, K. Toi, R. Akiyama, K. Adati, S. Hidekuma, S. Hirokura, O. Kaneko, H. Ikegami, A. Karita, Y. Kawasumi, R. Kumazawa, T. Kuroda, K. Narihara, Y. Ogawa, K. Ohkubo, Y. Oka, T. Ozaki, M. Sasao, K. Sato, T. Seki, F. Shimpo, S. Tanahashi, Y. Taniguchi, and T. Tsuzuki, T. Watari

National Institute for Fusion Science, Nagoya 464-01, Japan
1) Department of Applied Physics, Chubu University, Kasugai 487, japan

ABSTRACT

The various confinement improvement modes different from H-mode, are found in JIPPT-11U. They are characterized by the steep density gradient. The study of the turbulence in these modes is also performed.

INTRODUCTION

An important task of tokamak research is to develope the method of the confinement improvement and to understand its physics. Recently experimental results on TFTR and ASDEX showed that the optimizations of the fueling and the wall condition are one of the ways to the confinement improvement different from H-mode , although the mechanism is not well understood [1,2]. In the present paper, experimental results on the improved confinement of JIPP T-11U[3], by the control of the fueling such as gas puffing and NBI, are reported. In addition the preliminary results on the study of the density turbulence in those improved confinement mode is presented.

GAS PUFFING

The effects of variation of the strong gas puffing on the ohmic plasmas are shown in fig. 1. After the gas puffing rate is reduced, the loop voltage drops and diamagnetism and the neutron yield are observed to increase, while the average plasma density is kept nearly constant. The peaking factor of the plasma density $n_e(0)/\langle n_e(r)\rangle$, keeps on increasing to about the value of 3.0 after the decrease of gas-puffing. The ECE temperature in fig. 1 decreases in the last phase, while the electron temperature measured by the PHA analysis of the soft x-ray does not decrease. The decrease in the ECE signal is attributed to the cyclotron cutoff of the ECE emission[4] and supports the fact that plasma keeps on peaking on the improved phase. This is the first observation of IOC (Improved Ohmic Confinement) mode[2] i.e. the switching of SOC(Saturated Ohmic Confinement) to LOC(Linear Ohmic Confinement) in limiter discharges. After the reduction of gas-puffing the joule-input decreases due to the decrease of the loop voltage and the radiation measured by the bolemeter arrays decreases roughly in proportional to the decrease of joule heating.

These facts mean that the effect of radiation in IOC is not significant.

Counter NBI

Comparison of plasma behaviours with co- and counter-injected neutal beams of 300 kW net power is shown in fig. 2. The counter-injected plasma is characterized by higher impurity and higher plasma density, in accordance with a better particle confinement[5,6,7]. In addition, the counter NBI plasma has much higher peak ion temperature and toroidal rotational velocity as shown in fig.2. The central ion temperature and toroidal rotation velocity increase as the peaking factor increases during the pulse width of counter-NBI. In case of co-injected plasmas, the peaking factor, ion temperature and rotation speed stay constant at the latter half of the pulse. These facts indicate the close connection between the radial inwards flow and the improvement of ion energy and momentum confinement in conunter-injected plasmas. The improved confinement can be also obtained by pellet injection. The degree of the improvement is larger when the density profile of the pellet-injected plasma is more peaky.

TURBULENCE STUDY

In order to study the improvement mechanism, the FIR heterodyne scattering of HCN laser light of 100mW was performed on the limiter-IOC mode with counter injection of neutral beam. The area of the observation by the FIR scattering is chosen to be in upper half of the plasma so that directions of the propagation of turbulence along electron and ion diamagnetic drift can be distinguished[3]. The typical scattering signals are shown in fig. 3, where the limiter IOC plasma is almost the same with the case of fig. 1. When the IOC mode was set by the decrease of gas-puffing, the integrated scattered signals of turbulences with the propagation vectors along electron diamagnetic drift and ion diamagnetic drift, both show the decrease, while the plasma density is kept almost constant. But at the time NBI is introduced, there are no change in the scattered signals. The wavelength of the turbulences shown in this figure have the waves of 10 cm^{-1} and corresponds to the wavelength of the maximum growth rate in drift wave instability. This may suggest that the confinement of the NBI heated plasma is not determined by the drift-wave turbulence while the ohmic plasma confinemnt is limited by the drift-wave turbulences. The magnetic turbulence with long wavelength may be the candidates for the confinement of the additionally heated plasmas, since the magnetic turbulence with long wavelenth will not be effectively detected by FIR laser scattering. Further study will be performed with the introduction of HIBP and reflectometry for the study of the plasma turbulence in the various confinement mode.

REFERENCE

[1] R.J. Hawryluk et al., in Plasma Physics and Controlled Nuclear Fusion Research (Proc. 11th IAEA Conf. Kyoto, 1986) Vol.1 51(1987).
[2] F.X. Soldner et al., Phys. Rev. Lett. 61 1105(1988).
[3] K. Kawahata, et al., in Plasma Physics and Controlled Nuclear Fusion Research (Proc. 12th IAEA Conf. Nice, 1988) Vol.1 287(1989).
[4] D.J. Campbell and A. Eberhagen, Plasma Physics and Controlled Fusion Vol.26 689(1984).
[5] S. Yamamoto, et al., in Plasma Physics and Controlled Nuclear Fusion

Research (Proc. 9th IAEA Conf. Baltimore,1982) Vol.1 73(1983).
[6] M. Murakami et al., in Plasma Physics and Controlled Nuclear Fusion Research (Proc. 10th IAEA Conf. London,1984) Vol.1 87(1985).
[7] O. Gehre et al., Phys. Rev. Lett. 60 1502(1988).

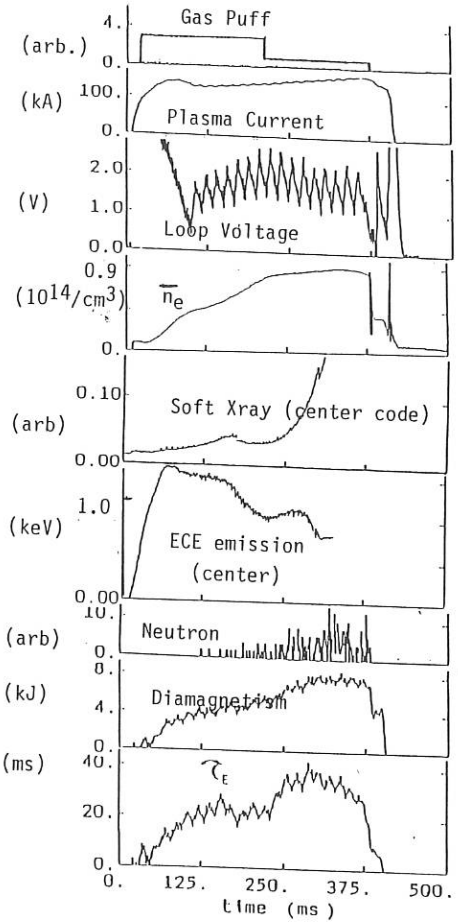

Fig. 1. Characteristics of the limiter IOC mode

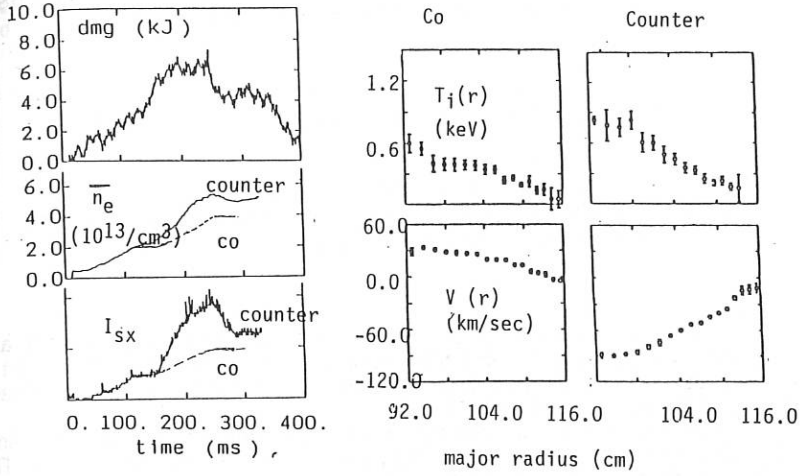

Fig. 2. Characteristics of the co and counter injected plasma. Plasma current is about 200 kA and NBI net power is 300 kW.

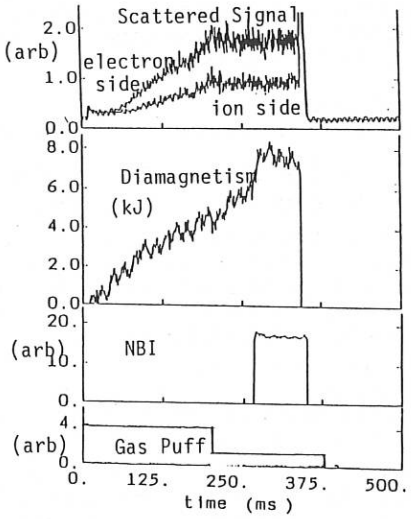

Fig. 4. FIR scattered wave and plasma behaviours. The experimental condition is the same with case of Fig. 1 with counter-injected NB of 300 kW.

MEASUREMENTS OF FLUCTUATIONS AND SPACE POTENTIAL PROFILES IN THE TEXAS EXPERIMENTAL TOKAMAK (TEXT)*

P. M. Schoch, R. L. Hickok, A. J. Wootton,† and X. Z. Yang#

Rensselaer Polytechnic Institute, Troy, NY
†The Fusion Research Center, The University of Texas, Austin, TX USA
#Institute of Physics, Academia Sinica, Beijing, PRC

A Heavy Ion Beam Probe (HIBP) has been used to measure density and space potential fluctuations, and the space potential profile in TEXT. Part A presents the fluctuation data with emphasis on poloidal variations. Space potential profiles are discussed in Part B.

TEXT is a non-divertor tokamak with a major radius of R=1m and a minor radius of a=0.26m The results presented are for ohmic heated discharges. The HIBP on TEXT consists of injecting singly charged thallium ions into the plasma with ion energies up to 540kev.[1] Doubly charged ions, produced dominantly be electron impact ionization, are detected using an electrostatic energy analyzer. The change in ion energy is a measure of the space potential, and normalized variations of the detected current are a measure of density fluctuations. The density and potential fluctuations are simultaneously measured at up to three spatial locations, this allow evaluation of the phase angle and coherence between the fluctuations, as well as estimates of wave numbers.

PART A: Poloidal variation of fluctuations

Figure 1 shows contour plots of density fluctuation data taken during a 2.8T, 200kA helium discharge with a line average density $\bar{n}_e = 2*10^{19}$ m^{-3}. The vertical axis is normalized radius in flux coordinates, $\rho \sim r/a$. The horizontal axis is poloidal angle θ where $\theta = 0$ is the outside midplane of the plasma, and $\theta = 90$ is the top. This plot shows the outer portion of the circular plasma mapped onto a rectangular grid: flux surfaces would be represented by horizontal lines.

The density fluctuation levels ($\tilde{n}/n$) are large at the plasma surface and decrease towards the plasma interior. The fluctuation level is not constant on a flux surface, but actually varies by 30% at the ρ=0.9 surface. The plasma space potential fluctuations also show a poloidal variation, as does the phase angle between density and potential fluctuations, (not shown.) The combined effect of all these variations is that the particle flux due to electrostatic fluctuations would vary by nearly 100% over this poloidal range, (at $\rho = 0.9$ and assuming that there are no poloidal variations in average wavenumbers and electron density.) The poloidal variation would be consistant with a m=4 mode, possibly a stationary island chain. The radial location of $\rho = 0.9$ coincides with the $q = 4$ flux surface for this discharge. This is not the first measurement of poloidal asymmetries for ohmic

heated plasmas in TEXT [2]; however, it is the first measurement with potential and phase angle information.

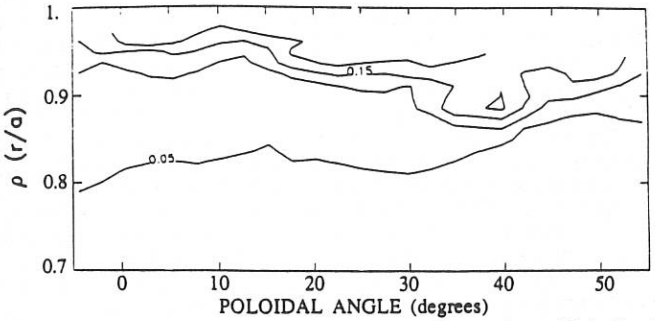

Fig. 1 Contours of constant relative density fluctuations ($\tilde{n}/n$). Contour levels are, from bottom to top, $\tilde{n}/n$ = 0.05, 0.10, 0.15, and 0.20.

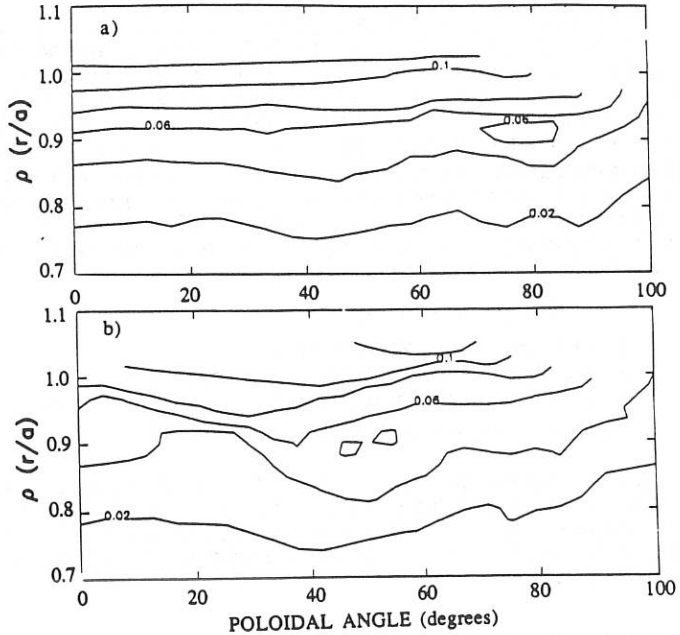

Fig. 2 Contours of constant relative density fluctuations ($\tilde{n}/n$). Fig. 2a is for the discharge before the resonant helical perturbation is applied. Fig. 2b is for during the perturbation. Contour lines from bottom to top are for $\tilde{n}/n$ = 0.02, 0.04, 0.06, 0.08, 0.10, 0.12.

Figure 2 shows density fluctuations of a 2T, 190kA, hydrogen discharge with $\bar{n}_e = 2*10^{19}$ m^{-3}. Figure 2a shows the contours of density fluctuations for this discharge. There is a high degree of poloidal symmetry, the variation seen may be due to finite sample volume effects of the HIBP. Figure 2b shows contours of density fluctuations for the same discharge after a resonant helical magnetic perturbation has been applied. The resonant fields are produced using discrete poloidal coils placed around and outside the vacuum vessel.[3] For this discharge the dominant toroidal mode number n=2, with multiple poloidal mode numbers around m~7. There is a strong correlation between the island chains produced by the magnetic perturbation and the changes in the fluctuation levels. When the current in the perturbing coils was reversed, the changes in fluctuation levels moved poloidally to match the changes in the island chains. The similarity between Figs. 1 and 2b leads to the speculation that the poloidal variation in Fig. 1 could be driven by external magnetic field errors which produce stationary magnetic islands. There is no other evidence on TEXT to support this speculation. Work on DIII-D and other machines would indicate that such islands might exist [4,5].

PART B: potential profiles

The HIBP has measured space potential profiles for TEXT discharges during Ohmic Heating, strong MHD activity, ECH, and with applied resonant helical magnetic perturbations. Due to space limitations and for continuity with part A, profiles will be presented for before and during the applied resonant helical perturbation, as shown in Fig. 3. The radial electric field is negative, (inward pointing) for the nonperturbed discharge for all radii inside of the limiter. This changes during the applied field to a positive value for $\rho > 0.85$. Figure 4 shows the dependance of the potential profile on the magnitude of the perturbation. The region of positive electric field increases with increases in the perturbation.

Analysis shows that the radial electric field in the absence of the magnetic perturbation is consistent with the ion momentum balance:

$$E_r = \frac{1}{e n_i}\frac{\partial P_i}{\partial_r} + \langle V_{\phi i} B_\theta \rangle - \langle V_{\theta i} B_\phi \rangle$$

n_i and P_i are the ion density and pressure,
B_θ and B_ϕ are the poloidal and toroidal magnetic field,
$V_{\theta i}$ and $V_{\phi i}$ are the poloidal and toroidal plasma rotation velocity, and
$V_{\theta i}$ is taken as the neoclassical value and $V_\phi \approx 0$.

During the magnetic perturbation there is an edge region of stochastic magnetic field. In this region, particles can reach the limiter along field lines. Electrons would leave the plasma more rapidly, giving rise to a positive ambipolar electric field which adjusts the electron flow rate to equal the ion rate.[6] The radial electric field can be expressed as:

$$E_r = -\frac{T_e}{e} \times \frac{\partial}{\partial_r}[\ln (nT^{\frac{1}{2}})]$$

This is consistent with the measured electric field and the edge density and temperature profiles in TEXT during the magnetic perturbation. Increases in the

magnitude of the perturbation cause increases in the region of stochastic fields, this is qualitatively consistent with the measured potential profiles.

The measurements of potential profiles in TEXT are consistent with those calculated from radial ion momentum balance using experimental values of the density, ion temperature and neoclassical plasma poloidal rotation velocity. When the magnetic flux surfaces are distorted enough to cause island overlap,(as by applying a magnetic perturbation), the potential profiles are consistent with estimates from stochastic field theory. This latter statement indicates that intrinsic magnetic fluctuations may not be large enough to drive stochastic regions in TEXT, because the electric field is everywhere negative.

REFERENCES

1. P. M. Schoch, et. al., Rev. Sci. Instrum. 57 (1986) 1825.
2. D. L. Brower, et. al., Nuclear Fusion, Vol. 27, No.12 (1987).
3. A. J. Wootton, et. al., Proc. 11th Int. Conf., Kyoto, IAEA, 1 (1987) 181.
4. R. J. LaHaye, et. al., 2nd Transport Task Force Transport Meeting, Hilton Head, S.C. (1990).
5. Personal communication with T. Evans, G.A. (1990).
6. R. W. Harvey, et. al., Phy. Rev. Lett., Vol 47, No.2 (1981).

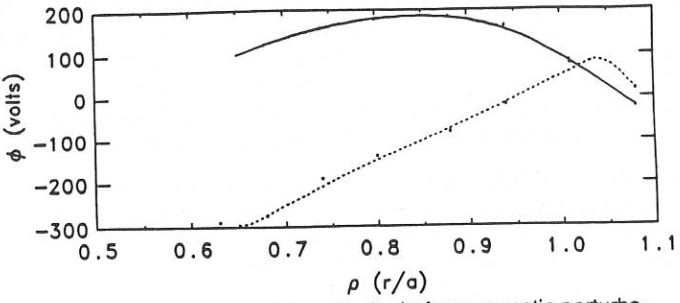

Fig. 3 Plasma space potential profile for before magnetic perturbation (dashed line) and during perturbation (solid line). Magnitude of current in perturbing coil is I_h = 4kA.

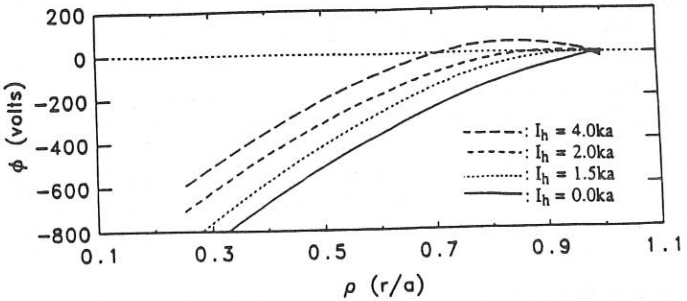

Fig. 4 Potential profile for different levels of magnetic perturbation. I_h is magnitude of current in coil.

TEST OF ITG-MODE MARGINAL STABILITY IN TFTR.

M.C. Zarnstorff, N.L. Bretz, P.C. Efthimion, B. Grek, K. Hill, D. Johnson, D. Mansfield, D. McCune, D.K. Owens, H. Park, A. Ramsey, G.L. Schmidt, B. Stratton, E. Synakowski, and G. Taylor.

Plasma Physics Laboratory, Princeton University, Princeton NJ 08543 USA.

Previous studies of steady state transport in supershots[1] have shown that the ion and electron thermal diffusivities, χ_i and χ_e, are much larger than neoclassical predictions, and are reduced for plasmas with peaked density profiles. In addition, it was found that the ion temperature and density profile shapes were correlated such that the plasma was close to the theoretical [2,3] marginal stability for ion temperature gradient driven turbulence (ITGDT) [4]. Similar results were obtained for related plasmas with unidirectional injection[5]. Since theoretically predicted transport[6] is larger than observed, ITGDT transport should be able to enforce near marginal stability. Due to the large values of T_i/T_e, $2-3$ for supershots, the flat-density expressions for a critical $L_{T_i} \equiv \partial_r \log T_i$ threshold for ITG-mode stability were found to be appropriate.

To test and confirm the ITGDT marginal stability of these plasma, the peaked density profiles of supershots have been transiently broadened, using either a helium gas puff or a deuterium pellet. If marginal stability to ITGDT is controlling the transport in these plasmas, the ion thermal transport should adjust during the perturbation to attempt to keep the plasma near the stability boundary.

The target plasmas discussed here are supershots with $I_P = 1$ MA, $B_T = 4.8$ T, $R = 2.45$ m, and 14 MW of balanced co- and counter-tangential ~ 100 keV deuterium neutral beam injection. This produced a plasma with $n_e(0) \approx 5 \times 10^{19}$ m^{-3}, $n_e(0)/\langle n_e \rangle \sim 2.3$, $T_e(0) \approx 8$ keV, $T_i(0) \approx 25$ keV, and $\tau_E/\tau_E^L \approx 2.7$, where τ_E^L is the confinement time from L-mode scaling[7]. The density profile was perturbed by injecting either 2.5 Torr-liters of He in a 16 msec pulse (see Fig. 1a) or by injecting a deuterium pellet (Fig. 1b). The gas pulse perturbed the outer half of the plasma, while the pellet size could be chosen to produce perturbations at various radii. The perturbed $n_e(r,t)$ is measured by a ten-channel infrared interferometer array, with a time resolution of 0.5 msec, and Thomson scattering. The $T_i(r,t)$ response is measured by charge-exchange recombination spectroscopy of the C VI 5292 Å line, with a time resolution of 10 msec.

The consequences of the different perturbations are the same: the plasma is driven far from the theoretical ITG stability boundary during the perturbation (Fig. 2). The density profile is locally broadened ($L_{n_e} \equiv \partial_r \log n_e$ increased by a factor ~ 8), but the T_i profile becomes slightly steeper (L_{T_i} dropped), as seen in Fig. 2. In contrast,

the theoretically predicted[3] critical-L_{T_i} for ITG-mode linear instability is predicted to increase during the perturbation, making the plasma more unstable. The increase in the critical L_{T_i} is due to T_i/T_e dropping during the perturbation, and due to the increase in L_n. While changes in the Z_{eff} profile have not yet been included in the analysis, they are expected to increase the critical L_{T_i} further (i.e. indicating the plasma is more unstable). Similar results are obtained using other expression[2] for the critical L_{T_i}.

The thermal energy transport in these plasmas has been analyzed by the $1\frac{1}{2}$-D time-dependent code TRANSP [8] using the experimentally measured temperature and density profiles. $T_e(r,t)$ is measured by ECE spectroscopy and Thomson scattering. The ion depletion is calculated using tangential visible-bremsstrahlung measurements for Z_{eff} and x-ray spectroscopic measurements of metallic concentrations. Edge hydrogenic-neutral influx is inferred [9] from the measurements of an array of absolutely calibrated H_α detectors. The beam-ion slowing down distribution is simulated as a separate species not subject to anomalous transport, consistent with experimental observations at low power [10]. The beam ions are treated as joining the background thermal ion species when their energy falls below $\frac{3}{2}T_i$. Electron-ion energy exchange is assumed to be classical.

The transport analysis indicates that the ion heat flux q_i remains approximately constant throughout the perturbations, as seen in Fig. 3. The increase in ion heat flux after the pellet perturbation appears to be consistent with the density increase, in that the inferred $\chi_i \equiv q_i/n_i\nabla T_i$, Fig. 4, is not changed. The theoretically predicted χ_i for fully turbulent ITGDT[6] is a factor of 3 to > 30 times larger than the observed values (varying with minor radius). In addition, microwave scattering during the perturbations shows the emergence of a broad spectral feature rotating in electron-drift direction, but no apparent structure rotating in the ion-drift direction (as would be expected for ITGDT).

Thus, even though the ITGDT stability threshold is strongly violated by the perturbations and the ITGDT transport is predicted to be strong enough to dominate the observed transport, we find that the ion thermal transport is unaffected by the perturbation. We conclude from this experiment that the anomalous ion thermal transport in supershots is not controlled by ITGDT marginal stability, as presently understood. As a consequence, the observed [1,4] parametric dependencies of χ_i and χ_e in the supershot regime (both *decrease* with *increasing* T_i, T_e, or β_P) may need to be reexamined.

We are grateful for the support of the TFTR group and for discussions with H. Biglari, P. Diamond, T.S. Hahm, and G.W. Hammett. This work was supported by the US DOE, contract number DE-AC02-76-CHO-3073.

[1] ZARNSTORFF, M. C. et al., in *Plasma Physics and Controlled Nuclear Fusion Research 1988*, volume 1, p. 183, IAEA, Vienna, 1989.
[2] ROMANELLI, F., Phys. Fluids B **1** (1990) 1018.
[3] HAHM, T. S. and TANG, W. M., Phys. Fluids B **1** (1990) 1185.

[4] ZARNSTORFF, M. C. et al., in *Proc. 16th European Conf. on Contr. Fus. and Pl. Heating*, volume 1, p. 35, EPS, 1989.
[5] SCOTT, S. et al., Phys. Rev. Lett. **64** (1989) 531.
[6] BIGLARI, H., DIAMOND, P. H., and ROSENBLUTH, M. N., Phys. Fluids B 1 (1990) 109.
[7] GOLDSTON, R. J., Plasma Phys. **26** (1984) 87.
[8] HAWRYLUK, R. J., in COPPI, B. et al., editors, *Physics of Plasmas Close to Thermonuclear Conditions*, volume 1, p. 19, CEC, Brussels, 1980.
[9] HEIFETZ, D. H. et al., J. Vac. Sci. Technol. A **6** (1988) 2564.
[10] RADEZTSKY, R. H. et al., in *Proc. 15th European Conf. on Contr. Fus. and Pl. Heating*, volume 1, p. 79, EPS, 1988.

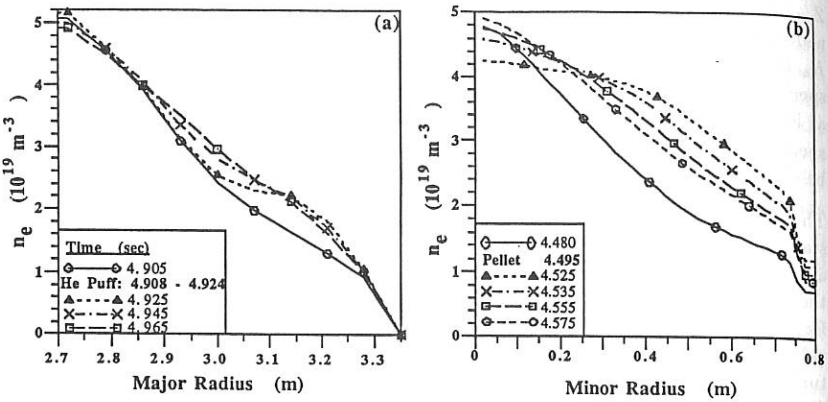

Fig. 1. Measured density profiles before and after (a) He gas puff perturbation and (b) pellet perturbation.

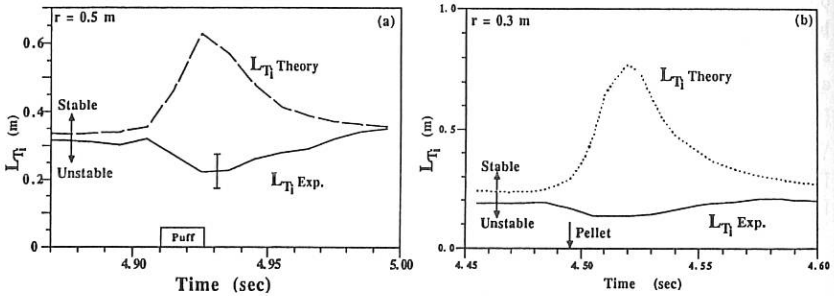

Fig. 2. Time evolution of measured L_{T_i} and predicted marginally stable L_{T_i} [3] for (a) He gas puff perturbation and (b) pellet perturbation.

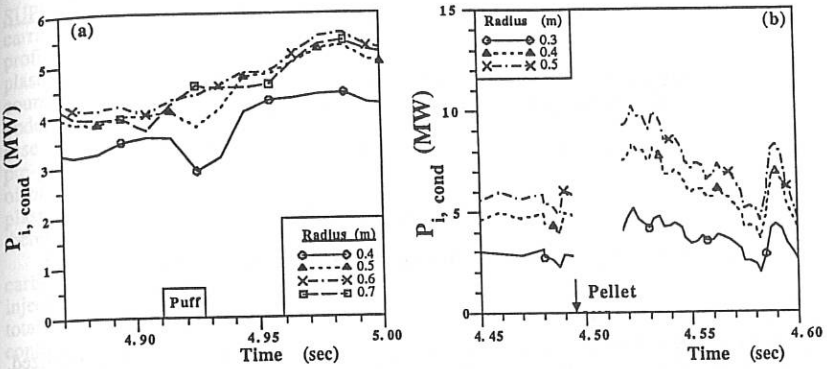

Fig. 3. Time evolution of ion heat flux q_i, calculated from the ion power balance equation, for (a) He gas puff perturbation and (b) pellet perturbation.

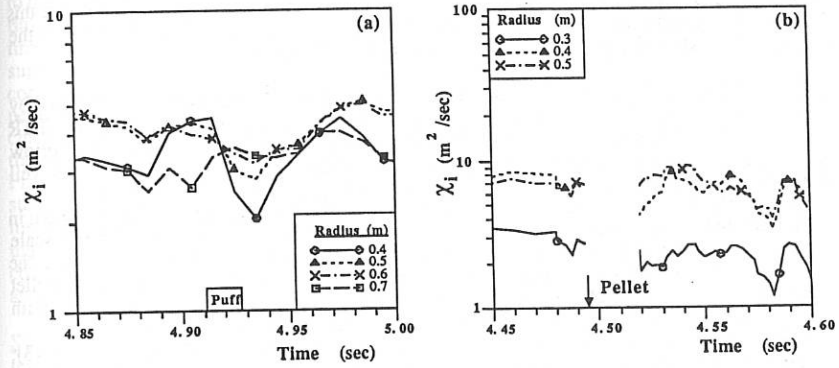

Fig. 4. Time evolution of $\chi_i \equiv q_i/n_i\nabla T_i$ for (a) He gas puff perturbation and (b) pellet perturbation.

PERTURBATIVE TRANSPORT STUDIES OF NEUTRAL BEAM HEATED TFTR PLASMAS USING CARBON PELLET INJECTION

R.A. Hulse, A. Cavallo, D. Johnson, H. Park, A.T. Ramsey, G.L. Schmidt, B.C. Stratton, E.J. Synakowski, G. Taylor

Princeton University, Princeton, NJ 08543 USA

J. Terry, B. Howell, E. Marmar

Massachussetts Institute of Technology, Cambridge, MA 02139 USA

INTRODUCTION - Carbon pellets have been successfully used to produce well localized, moderate-sized density and temperature perturbations deep in the confinement region ($r/a \sim 0.5$) of high-power neutral beam heated TFTR plasmas. These experiments have been carried out specifically to extend the potential of pellet injection as an approach to detailed heat and particle transport studies, with the ultimate objective of identifying significant dependencies in the transport matrix based on analysis of the plasma response to such perturbations of the various thermodynamic driving terms. The use of carbon pellets allows one to achieve the deepest penetration of high-temperature plasmas for a given perturbation size, relative to other perturbation techniques such as gas puffing[1,2], laser ablation[2], and deuterium[3,4,5] or lithium[6] pellet injection. The initial results reported here serve to both establish the basic viability of this approach, and, in addition, show several transport effects of immediate physics interest in the response of L-mode and supershot plasmas to the pellet perturbations.

L-MODE EXPERIMENTS - Fig. (1) shows the electron density profile evolution produced by carbon pellet injection into the steady-state neutral beam heated phase of an L-mode TFTR plasma with I_p = 1.4 MA and P_b = 11 MW of balanced neutral beam power. The hollow electron density profile immediately following the pellet deposition at t = 3.425 s peaks well into the plasma, as desired, subsequently filling in smoothly until a sawtooth at t = 3.5 s.

The pellet perturbation is also clearly seen in the electron temperature profiles, as shown in Fig. (2) for this same plasma. Of particular interest is the existence of a fast time scale component to the electron temperature profile relaxation following the pellet. As shown in the figure, this profile relaxation to a significantly reduced gradient similar to that of the pre-pellet plasma occurs on a time scale on the order of the 4 ms resolution of this measurement, with $T_e(r)$ simultaneously decreasing at smaller minor radii while increasing at larger radii.

Other aspects of the response of this plasma to the perturbation are shown in Fig. (3), together with the behavior of a reference no-pellet shot (shown as dashed). In Fig. 3(a), the perturbation to the total electron density is seen to be roughly $\Delta N/N \sim 30\%$, with a smooth decay indicating a 1/e particle confinement time scale of approximately $\tau_p \sim 80$ ms. The pellet contribution to the plasma Z_{eff} as measured by visible bremsstrahlung also decays in a similar fashion, indicating similar transport and confinement of the carbon ions as for the electrons.

The plasma total stored energy, measured magnetically, is shown in Fig. 3(b), and is seen to be unperturbed by the pellet (the slight variation after t ~ 3.8s is due to a drop in beam power). The electron stored energy (determined from the electron density and temperature profiles) exhibits a small, transient increase within this constant total stored energy, recovering on the time scale of the electron density and Z_{eff} decay. This behavior reflects a transient shift in energy partition between the electron, thermal ion, and fast ion channels, presumably directly attributable to this increase in density and Z_{eff} during this time. The energy confinement time in Figure 3(c) does not show any significant response to the pellet perturbation, reflecting the unperturbed behavior of the plasma total stored energy.

SUPERSHOT EXPERIMENTS - Carbon pellet injection into supershot plasmas has also been carried out, successfully yielding similar deep r/a ~ 0.5 penetration, hollow electron density profiles, and relaxation behavior qualitatively similar to that shown in Fig. (1) for the L-mode plasma. Details of the perturbation amplitude, transport time scales, and profile shapes, of course, differ, as will be discussed. Supershot electron temperature profiles are also seen to undergo a fast time scale post-pellet relaxation similar to that shown in Fig. (2) for the L-mode case. This recovery of both L-mode and supershot electron temperature profiles towards their pre-perturbation gradients on time scales of $\tau << 10$ms is suggestive as it relates to the issue of profile consistency and possible marginal stability criteria[7]. However, some supershot plasmas exhibit strong MHD activity for several milliseconds after the pellet deposition, thereby obscuring this and other fast time scale post-pellet transport behavior.

Fig. (4) shows the response of an $I_p = 1.0$ MA, $P_b = 14$MW (balanced) supershot to carbon pellet injection, to be compared with the Fig. (3) data for the L-mode case. Pellet injection occurs at t = 4.519 s, as the stored energy reaches its maximum. Perturbation of the total electron density (Fig. 4a) is in this case $\Delta N/N \sim 70\%$, with a 1/e point indicating a particle confinement time scale of $\tau_p \sim 45$ms. As with the L-mode case, visible bremmstrahlung Z_{eff} measurements indicate similar particle confinement for the carbon ions.

In Fig. 4(b), we see that, in sharp contrast to the L-mode case, the plasma total stored energy shows a dramatic response to the pellet perturbation, dropping for ~ 150ms after the pellet, and recovering only slowly to the original supershot level by the end of the beam heating phase. Within this dropping total stored energy, the electron stored energy component shows a similar but more marked transient rise than for the L-mode case, again presumably attributable to a similar transient change in the electron-ion coupling and fast ion slowing down in this now even more ion energy dominated plasma. This decrease of the total stored energy in response to the pellet perturbation translates into a corresponding marked drop in the energy confinement time, as seen in Fig. 4(c). In a series of other pellet injections into supershots, similar overall time behavior has been seen for perturbations produced both early in the ramp-up phase of the supershot, as well as later into the evolved supershot phase as shown here. No simple correlation is seen between recovery of the profile peakedness factor $n_e(0)/\langle n_e \rangle$ following the pellet perturbation and the long time scale recovery of the energy confinement time. Detailed characterization of this drop in energy confinement in terms of changes in the associated transport coefficients is still under study, but three features of the effect are separately notable. First, there is the apparent absence of this effect in the L-mode case. Second, the loss of total stored energy occurs on a transport time scale, not more rapidly as might be associated with the instantaneous violation of some marginal stability condition[4]. Finally, there is the observation that the recovery of the energy confinement time occurs only slowly on a time scale long compared with decay of the density perturbation, as indicated by the electron and Z_{eff} decays, as well as slowly relative to the $\tau \sim 100$ms energy relaxation and fast ion slowing down times.

SUMMARY - Carbon pellet injection has been successfully employed as a perturbation technique in neutral beam heated TFTR plasmas. Several effects of transport physics interest are evident in the plasma response to these perturbations, and further detailed analysis of the energy and particle transport fluxes and associated local transport coefficients is in progress.

ACKNOWLEDGEMENT - This work was supported by USDOE # DE-AC02-76-CHO-3073.

1) E. Synakowski et.al., this conference
2) P.C. Efthimion et.al. Proceedings of the 12th IAEA Conference on Plasma Physics and Controlled Nuclear Fusion Research (1988), paper IAEA-CN-50/A-V-4, p. 307-321
3) A.D. Cheetham et.al., *ibid*, IAEA-CN-50/A-VII-14, p 483-493
4) M. Zarnstorff et.al., this conference
5) R.A. Hulse et.al., Proceedings of the IAEA Technical Committee Meeting on Pellet Injection and Toroidal Confinement (1988), IAEA-TECDOC-534, p. 99-105
6) E.S. Marmar et.al., *ibid*, p.181-187
7) E.D. Fredrickson et.al., Nuclear Fusion 27, p. 1897-1904 (1987)

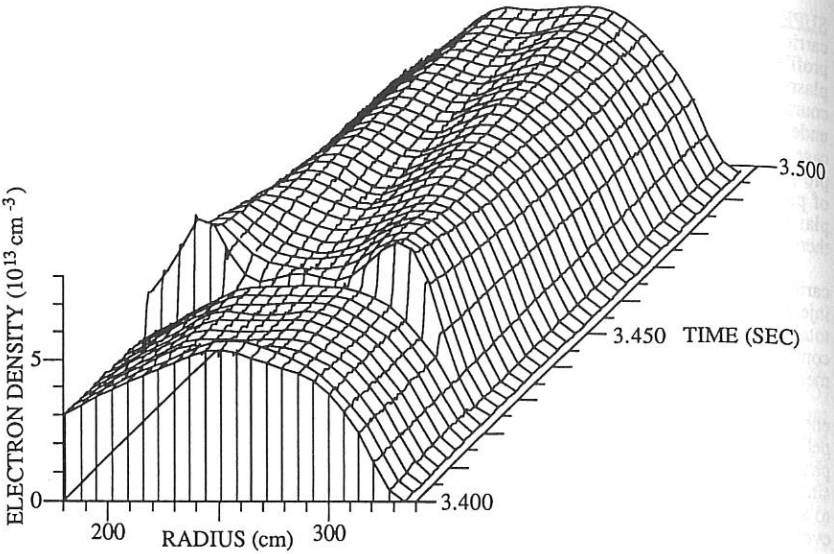

Fig. 1 Electron density profile evolution following carbon pellet injection into I_p= 1.4MA, P_b= 11MW L-mode plasma 40774

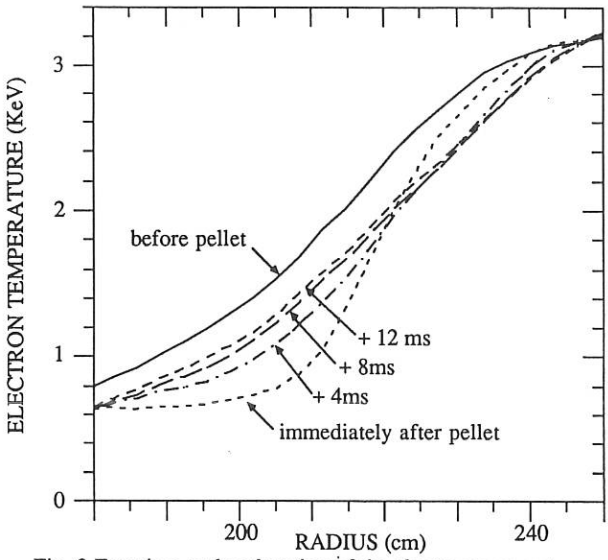

Fig. 2 Fast time scale relaxation of the electron temperature profile following carbon pellet injection in L-mode plasma 40774

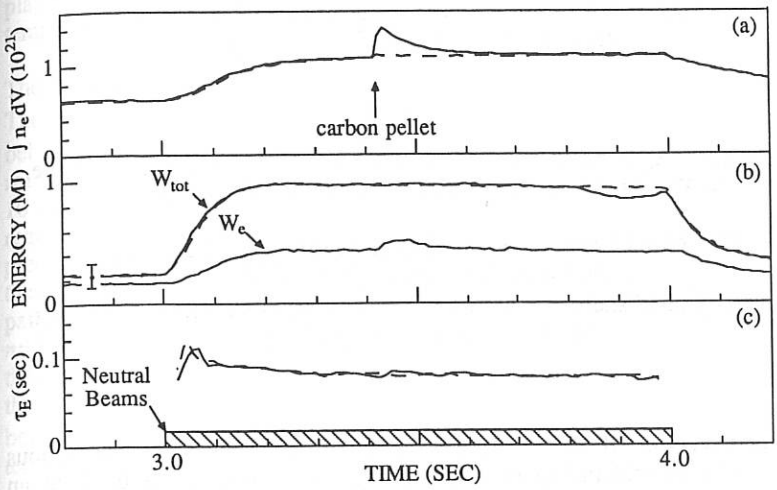

Fig. 3 (a) Total electrons, (b) total stored energy and electron stored energy, and (c) energy confinement time for L-mode plasma 40774 with carbon pellet injection at 3.425 s (dashed no-pellet shot 40772).

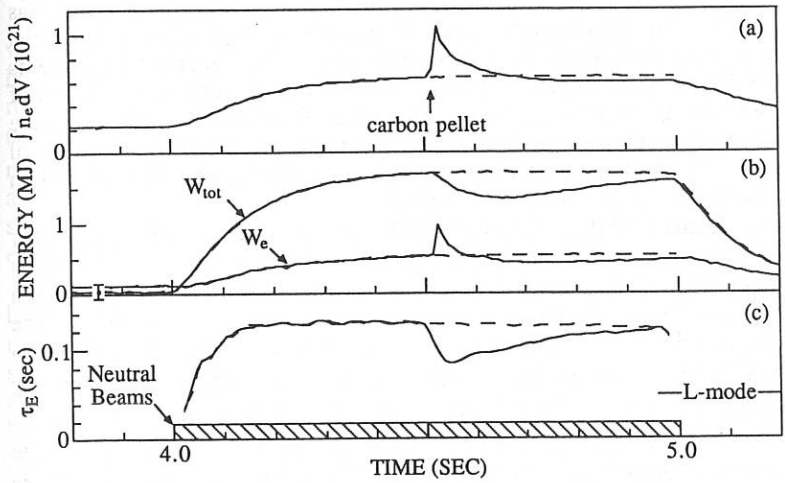

Fig. 4 (a) Total electrons, (b) total stored energy and electron stored energy, and (c) energy confinement time for supershot plasma 43160 with carbon pellet injection at 4.519 s (dashed no-pellet shot 43159).

MEASUREMENTS OF RADIAL PROFILES OF TRANSPORT PARAMETERS OF HE^{2+} ON TFTR

E. J. Synakowski, B. C. Stratton, P. C. Efthimion, R. J. Fonck,[a] R. A. Hulse, D. W. Johnson, D. K. Mansfield, H. Park, and S. D. Scott

Princeton Plasma Physics Laboratory, Princeton University
Princeton, New Jersey USA 08543
[a] University of Wisconsin at Madison, Department of Nuclear Engineering, Madison, Wisconsin USA 53706

The behavior of helium in a tokamak plasma will be of tremendous importance in the cost and operations of future fusion devices. In this light, an understanding of helium transport is essential. In this paper we describe the first measurements of spatial structure of transport coefficients of He^{2+} in a tokamak plasma. Charge exchange recombination spectroscopy (CHERS) [1] has been used to measure the time evolutions of $n_{He2+}(r)$ following a helium puff on TFTR. The temporal behavior of the He^{2+} density at several spatial points has been modelled with the impurity transport code MIST [2], allowing the spatial structure of transport coefficients to be adduced. The transport coefficients have indeed been found to have large spatial variations, increasing by a factor of several between r/a = 0.35 and the plasma edge. Diffusivities and convective velocities in this region are at least 100 times those predicted by neoclassical theory. Inside the inversion radius, transport rates are reduced, but are still an order of magnitude above neoclassical values.

The plasmas for this experiment had a major radius of 2.45 m, a minor radius of 0.80 m, a plasma current of 1.4 MA, a toroidal field of 4 T, and a discharge duration of 6 seconds. These plasmas were neutral-beam heated with 7 MW of co-directed deuterium injection from 3.5 to 4.5 seconds. The targetplasma had a deuterium prefill only. The peaking parameter $n_e(0)/\langle n_e \rangle$ was typical of most low-density L-mode discharges on TFTR, while the energy confinement time was modestly higher than the L-mode value ($\tau_E = 1.3\tau_{EL\text{-}mode}$). Central ion temperatures were 9-10 keV during the beam flattop, and the central electron temperatures were ~5 keV. The central Z_{eff} was 4.0. These discharges possessed ~150-200 ms sawteeth and had an inversion radius of r/a =0.30-0.35. A 16 ms helium puff was introduced at 4.2 s, well into the equilibrium phase of the neutral beam pulse. The line-averaged density of the plasma increased by 2-3% as a result of the puff; the perturbation in electron temperature was somewhat less.

plasma increased by 2-3% as a result of the puff; the perturbation in electron temperature was somewhat less.

The CHERS spectrometer was used to view a coinjecting heating beam. The neutral beam-CHERS sightline intersection radii are separated by ~10 cm. The He^{2+} density evolution after the puff was measured by following the time behavior of the n=4-3 4686 Å line of He^{1+}, induced by charge exchange recombination with beam neutrals. Time resolution for these measurements was 10 ms, and the data was averaged together from fourteen discharges without regard to sawtooth phase. The helium profiles were inferred by calculating the predicted line brightnesses including the effects of neutral beam attenuation and the drifting ion plume [1]. Beam attenuation was calculated using the mean free path treatment of Boley *et al* [3], and reaction rate coefficients for inducing the n=4-3 transition by charge exchange with beam neutrals was calculated from theoretical UDWA calculations [4]. The reaction rate coefficient for exciting this transition by charge exchange from the n=2 level of beam neutrals [5] has been calculated using the CTMC code of Olson [6]. With central ion temperatures of ~10 keV, charge exchange from thermal halos is negligible [7].

The time evolution of the densities was modelled by solving the impurity continuity equation using the impurity transport code MIST. It is assumed that the helium flux can be expressed as

$$\Gamma_{He} = -D(r)\nabla n_{He} + V(r)n_{He}$$

where D is the helium diffusivity and V is the convective velocity. The neutral helium source has been programmed into MIST by assuming that the energy of recycled neutral helium is 0.1 eV, typical of the temperature of a carbon tile on the bumper limiter. The time behavior of the He^{2+} source was deduced from measurements of the n=2-1 304 Å He^{1+} line by a VUV spectrometer viewing along a radial chord at the bumper limiter. Use of this measurement of the source eliminates the need for any assumptions regarding helium recycling efficiency.

In the modelling, D and V are constrained such that $D/V = L_{He}$, the helium scale length in equilibrium . It is found that no spatially constant D will reproduce the data satisfactorily. The range of D and V that best fit the data is shown in figure 1. Of note is that the best-fit D(r) varies by over an order of magnitude across the plasma, with the largest variations found near the plasma boundary and for r/a < 0.35. The nonviability of D=constant is illustrated in figures 2 and 3. Figure 2 shows the measured local He^{2+} density at (a) r = 65 cm and (b) r = 39 cm. Also shown in this figure are MIST modelling results using D(r) and V(r) of figure 1 (solid line) and $D = 1.2 \times 10^5$ cm^2s^{-1} (again with $D/V = L_{He}$; dashed line). The results for the two cases are indistinguishable at r = 65 cm. Diffusivities on the order of 10^5 cm^2s^{-1} are required there. However, D =

constant cannot reproduce the data successfully at r = 39 cm while maintaining agreement at r = 65 cm (figure 2(b)). Agreement with the data at all radii is

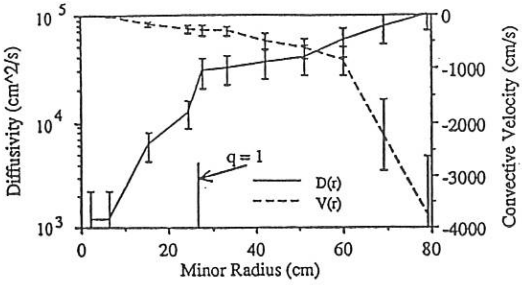

Fig. 1 - D(r) and V(r) for He^{2+}. Error bars indicate estimated range of acceptable transport coefficients, including statistical errors and those due to uncertainties in He^{2+} profile shape.

found only if large spatial variations in D as shown in figure 1 are used. Errors in the inferred transport coefficients were estimated by propagating a ± 20% uncertainty in the beam stopping cross sections through the profile shape calculations as well as including estimates of the uncertainty of the best fits. Measured and modelled profiles after the puff are shown in Figure 3. Figure 3a

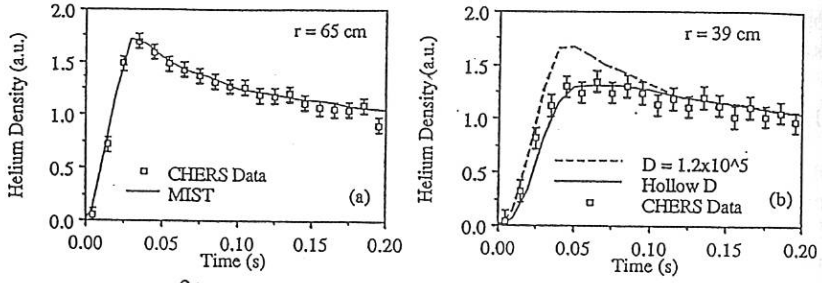

Fig. 2 - Measured He^{2+} density and modelling results for the transport coefficients in figure 2 and for D = $1.2x10^5$ cm^2s^{-1} (with D/V constrained as discussed in the text). (a). r = 65 cm. Modelling results for the two cases are indistinguishable. (b). r = 39 cm. The predicted evolutions differ.

shows the profiles inferred from CHERS measurements. To note is the short time scales (~50 ms) required for the profile at r/a > 0.5 to reach its final scale length. However, the time scale required to reach the final scale length for r/a < 0.5 is typically ~100 ms, suggestive of slower transport there. Figure 3b shows the modelled profile shapes from MIST using the transport coefficients of figure 2. Excellent reproduction of the measured profiles is achieved. However, the profiles obtained using the constant D required to match the data at r = 65 cm do not reproduce the measured time evolutions (figure 3c); transport is found to be much too rapid in the interior. More modest values of constant D also fail to reproduce the profile evolutions observed.

Finally, thermal transport coefficients have been calculated using the steady-state transport code SNAP. Interestingly, it is found that $D(r) \sim \chi_i(r) \sim \chi_\phi(r) > \chi_e(r)$ (figure 4). The implications of ratios of the impurity fluxes to the heat and momentum fluxes on the viability of proposed transport mechanisms is being explored.

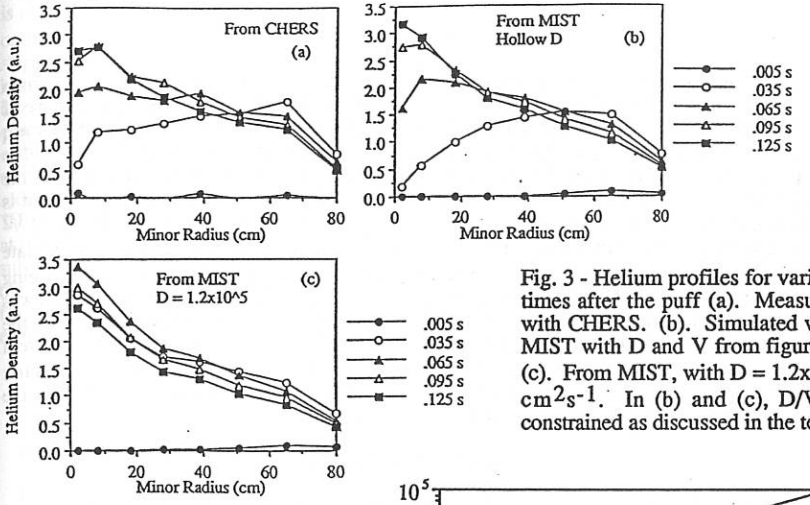

Fig. 3 - Helium profiles for various times after the puff (a). Measured with CHERS. (b). Simulated with MIST with D and V from figure 2. (c). From MIST, with $D = 1.2 \times 10^5$ $cm^2 s^{-1}$. In (b) and (c), D/V is constrained as discussed in the text.

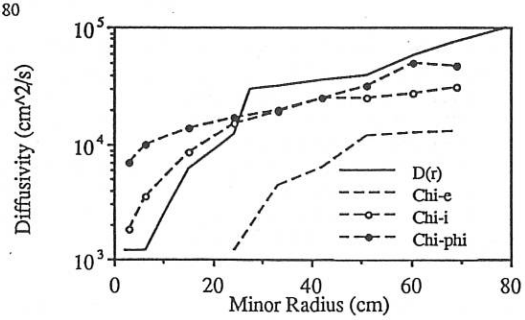

Fig. 4 - Helium diffusivity D(r) and χ_e, χ_i, and χ_ϕ as calculated with SNAP.

This research was conducted under DOE grant No. DE-AC02-76-CHO-3703.

[1] R. J. Fonck, D. S. Darrow, and K. P. Jaehnig, Phys. Rev. A **29**, 3288 (1984).

[2] R. A. Hulse, Nucl. Technol. Fusion **3**, 259 (1983).

[3] C. D. Boley, R. K. Janev, and D. E. Post, Phys. Rev. Lett. **52**, 534 (1984).

[4] H. Ryufuku, Japan Atomic Energy Research Institute Report JAERI-82-031, 1982 (unpublished).

[5] R. C. Isler and R. E. Olson, Phys. Rev. A **37**, 3399 (1988).

[6] R. E. Olson and A. Salop, Phys. Rev. A **16**, 531 (1977).

[7] B. C. Stratton *et al.*, accepted for publication in Nuclear Fusion

T_e Profile Invariance under Transient Conditions on ASDEX.

H. Murmann, H. Zohm , ASDEX - and NI Team
Max Planck Institut für Plasmaphysik,
D-8046 Garching, FRG, Euratom Association

Introduction

The resilience of the electron temperature profile in a tokamak plasma is a well known phenomenon , but not at all understood. On ASDEX it was found that the normalized shape of the electron profile can be represented as a fairly straight line with constant slope outside the q = 1 surface; the different T_e profile shapes at various q_a values are only due to changes within the q = 1 suface /1/; a similar behaviour has also been found on other machines /2/. As the safety factor seems to be the only clear parameter to influence the temperature profile, it is often argued that the current density profile is actually invariant and the stiff coupling $j \sim T^{3/2}$ causes the T_e profile consistency. This early analysis was carried out under steady state conditions, and is now extended to transient ASDEX plasmas with the plasma current being stepped up and down within the same discharge. The conductivity of the plasma column was calculated radially and time resolved including neoclassical trapped particle effects using the measurements of $T_e(r,t)$ and $n_e(r,t)$ with the 60 Hz Nd:YAG laser scattering system. Current profiles were then calculated with a diffusion code starting with a radially constant electric field from a steady state discharge and the electric field at the plasma edge derived from the measured loop voltage around the torus as boundary condition.

Experimental results

Fig. 1 shows a neutral beam heated discharge with a plasma current I_p of 0.42 MA being stepped down within 0.15 sec to 0.28 MA and up again within the same discharge. In fig.2 the development of the current distribution j(r,t) is displayed separately for the two cases when the current is ramped down and up. The beam heating power was 2 MW and basically constant during the ramp phases. In the first case the loop voltage becomes negative, which is reflected in a negative current density at the plasma edge at the beginning of the current change at t = 1.35 sec. When I_p has reached its minimum value at t = 1.5 sec the current density also takes its maximum negative value at the plasma boundary. Within the next ~200 ms the current disturbance diffuses towards the hot centre until it reaches another equilibrium at about t = 1.7 sec.

The development of temperature profiles during this transient phase is quite different as shown in fig.3. Normalized at about half radius the profiles exhibit the usual invariance with changes only inside the q = 1 suface as a consequence of the changing plasma current. These profile changes, however, do not follow the external q_a - value but rather the amplitude of the current density at the core. The temperature profile is certainly not coupled rigidly to the current density as in a stationary state, but the profiles do have the tendency to show a slight deformation at the edge in the same way as j(r) after a disturbance of the total current.

During the current decrease the electron temperature profile remains unchanged. The decrease of $T_e(0)$ doesn´t begin before j(0) begins to drop at t ~1.5 sec., which is the time when the current disturbance has reached the plasma centre during its diffusion process. This phenomenon is also reflected by the integrated thermal energy content of the electrons as shown in fig 3a. It also begins to decrease at t = 1.5 sec., when I_p is already down at 0.28 MA. Thus the energy confinement time stays constant while the current is being ramped

down and the relation $\tau_E \sim I_p$ does certainly not hold in this transient phase. This is also demonstrated in an overshooting of the poloidal beta as shown in fig.4b. τ_E remains at the high value corresponding to the initial current typical 2 - 3 energy confinment times before it rapidly decreases.

The observed delay of the change of the electron energy against the plasma current change is much less, when I_p is ramped up again (s. fig.1c and 4). This can be understood if one considers the difference in the j(r,t) profiles in the two cases of a negative or positive current step in fig.1. In the first case with $dI / dt < 0$, the power deposition, mostly neutral beam heating, remains unchanged in the centre until the diffusion process has come to an end and the plasma center is affected. The ohmic power is also deposited mainly in the centre as the current density at the boundary is negligible. Thus the energy transport from the centre to the edge is not very much affected and the temperature profiles and gradients remain unaltered until the confinement properties of the inner confinement zone is changed owing to the reduced current density j(0) .
When dI / dt is positive, on the other hand, there is an instantaneous rise of the current density at the edge with a localized additional ohmic heating of the electrons at the boundary and a subsequent instantaneous hampering of the heat outflow from the plasma centre. In this case the total energy rises with much less delay against the plasma current, which is also seen in fig. 4. This delay time disappeares in the case of pure ohmic heating. In our opinion this effect indicates the important influence of edge gradients to the global confinement.

Conclusions

- The invariance of the electron temperature profile prevails also during a transient plasma phase, when the total plasma current is strongly varied;
- the dominant parameter is not q_a, but more the central current density which influences the profile at the $q = 1$ surface;
- the current density is certainly not an invariant quantity when the plasma is not stationary;
- τ_E is no longer a linear function af I_p , when $dI / dt \neq 0$;
- profile gradients at the plasma boundary play a decisive role for the global confinement behaviour;
- the mechanism which governs profile invariance is not simply dominated by q_a or other local parameters .

References

/1/ Murmann, H. , Wagner, F., e.a., in Controlled Fusion and Plasma Heating , Proc. 13th Europ. Conference , Schliersee 1, (1986), 216

/2/ Fredrickson, K. M., e.a., Nuclear Fusion, 27, 11 (1987)

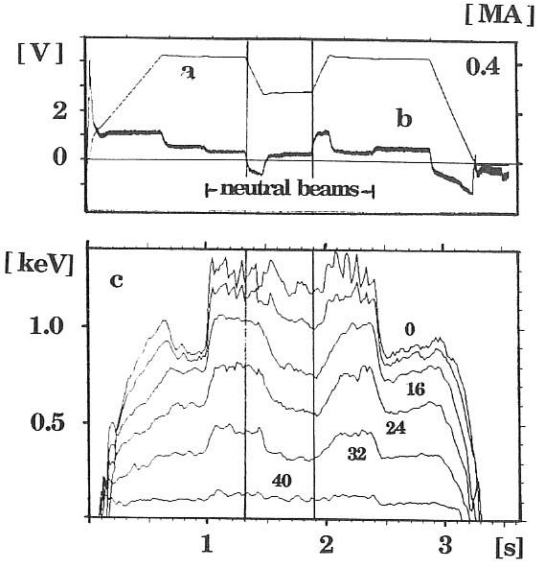

fig. 1 shot 30691
a) plama current
b) loop voltage
c) electron temperatures at different plasma radii versus time measured with the Nd:YAG laser system ; r = 0,8,16,24,32,40 cm ; neutral beam heating from 1 sec - 2.4 sec, P = 2 MW

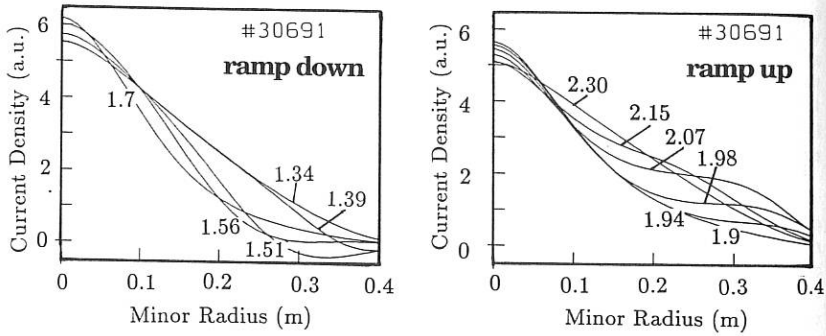

fig 2. shot 30691: current densities j(r,t) calculated from a diffusion code at different times t[s] given as parameter in the curves. The plasma onductivity $\sigma(r,t)$ was calculated from the measured electron temperatures und densities and Z_{eff}. The plasma current was ramped down and up again (0.42 MA / 0.28 MA) during the discharge.

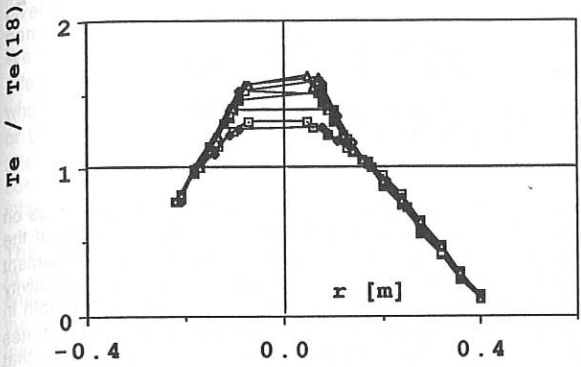

fig.3. shot 30691: Electron temperature profiles normalized at r = 18 cm (the influence region of the q = 1 surface) within the time interval 1.3 sec ≤ t ≤ 2.2 sec, covering the current ramping phase 0.42 MA / 0.28 MA. The normalized profiles are invariant for r ≥ 18 cm also in the transient phase.

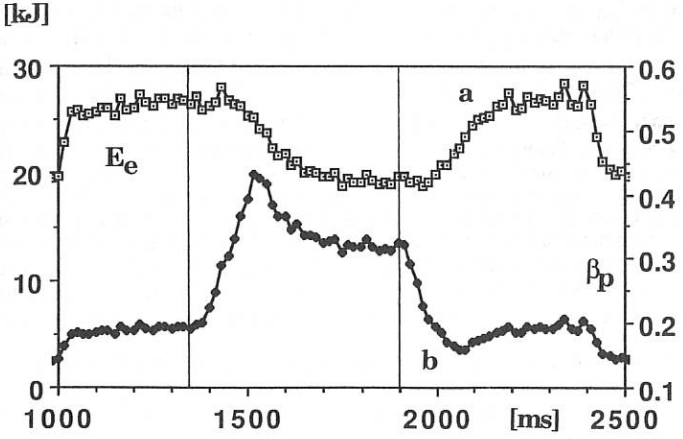

fig. 4. shot 30691:total integrated electron thermal energy (a) and the poloidal beta of the electrons as measured with the Nd:YAG system, versus time. the change of the total energy is delayed against the onset of the current change by about 200 ms during ramping down. When thre current is ramped up again the delay is much shorter. This is also manifested in the overshoot of β_p function vs time.

THE ISOTOPE DEPENDENCE OF CONFINEMENT IN ASDEX: PART 2

F. Wagner, M. Bessenrodt-Weberpals, L. Giannone,
A. Kallenbach, K. McCormick, F.X. Söldner, U. Stroth

Max-Planck-Institut für Plasmaphysik, Garching, FRG
Euratom Association

Abstract

In this paper we continue our report on the study of the dependence of plasma parameters on the ion mass A_i. Both under ohmic and beam heating conditions a strong sensitivity of the central electron temperature, the electron and total energy content , the energy confinement time, and sawtooth repetition time are observed. The previously observed strong sensitivity of the edge density on A_i is a secondary effect. The observation of an A_i dependence both in lower hybrid heated discharges but also in the momentum confinement with NI demonstrates that the ion mass affects both electron and ion transport. Transport analysis indicates that the effective heat diffusivity is lower in deuterium for all radii.

Introduction

The ion mass is a substantial and robust scaling parameter of the confinement time in all regimes of Asdex /1/. Deuterium plasmas show the better confinement. This is not in agreement with theoretical expectation. Previously it has been noted that deuterium has the better confinement both in predominantly electron or ion transport dominated plasmas and that both energy and particle transport are affected /2/. A strong sensitivity of the central electron temperature T_{eo} and as a consequence of the electron and of the total energy content, E_e and E_o, and the power input P_{oh} was observed under ohmic conditions. The A_i variation of both E_o and P_{oh} gives rise to the strong dependence of τ_E on A_i { $\tau_E \propto A_i^{0.5}$ in the ohmic saturated regime, SOC }. Other parameters which vary strongly with A_i in the SOC regime are the edge density $n_e(a)$ { $\propto A_i^{-0.8}$ } and the sawtooth repetition time τ_{SZ} { $\propto A_i^{0.54}$ }.
Because of the difficulty of theory to understand the underlying mechanisms, a careful study is necessary to rule out the possibility that the isotope effect does not enter heat and particle transport directly but is actually the result of a secondary process e.g. different onset conditions for turbulence. As deuterium discharges display generally more peaked density profiles, η_i or η_e driven turbulence might be a possibility for such a secondary causality. Hydrogen or deuterium pellets fuelling target plasmas of the same isotopic mass lead to discharges with n_e-profiles which are peaked sufficiently for η_i or η_e turbulence to be stabilized. Nevertheless, pellet refuelled deuterium plasmas show the better energy confinement.
Though the improvement of τ_E with A_i is a welcome development with regard to DT operation, the isotope effect has also a negative aspect linked to the stronger scaling of the particle confinement time τ_p with A_i { $\propto A_i^1$ } and the different MHD activity: At the same plasma density, the divertor gas and plasma densities are lower in deuterium and, as a consequence, the divertor impurity retention efficiency must be lower. Together with the higher impurity sputtering, the more pronounced impurity accumulation tendency and the less effective sawtooth-cleaning of the plasma core, deuterium discharges are more susceptible for developing impurity problems.

A_i dependence in the discharge breakdown phase

The isotope effect can be noted shortly after breakdown of the discharge. The gas consumption and the H_α radiation differ notably after about 100 ms after breakdown; deviation in β_{pol}, the loop voltage and the electron temperature can be detected after about 200 ms. Such, the

isotope effect is present in a phase where the plasma current profile is not steady state, the divertor configuration is not well established, and the electron distribution may still be non-Maxwellian.
We have further studied whether the method of plasma build-up introduces the isotope effect. Two identical low-density helium discharges ($\bar{n}_e = 1.5 \times 10^{13}$ cm^{-3}) are compared where in the plateau phase the density was ramped up to $\bar{n}_e = 4.5 \times 10^{13}$ cm^{-3} by either H_2 or D_2 gas puffing. The isotope effect was still present in the two high-density phases. With this study we rule out another secondary effect viz. that the appreciably larger gas consumption in the initial discharge phase of hydrogen forces the plasma boundary to interact with a large amount of gas throughout the pulse which might cause some degradation.

The isotope effect in lower hybrid heated discharges
In order to study the isotope effect under conditions of strong electron heating and of an energy content basically determined by electrons, lower hybrid (2.45 GHz) was applied in the range $.63 \leq P_{LH}$ (MW)≤ 1.1 and $1.4 \leq \bar{n}_e$ (10^{13} cm^{-3}) ≤ 4.3. For the lower power T_{eo} increased typically by 50 %. Both in the ohmic target plasma as with LH, the central electron temperature was larger in D^+ than H^+. In the density range from 2 to 3×10^{13} cm^{-3}, when neither extreme non-Maxwellian electron distribution nor different ion coupling of the wave at the edge play a significant role a similar scaling of T_{eo} { $T_{eo} \propto A_i^{0.24}$ } like in the ohmic LOC regime is observed. The presence of the isotope effect under LH conditions indicates that the ion mass enters directly the electron heat transport as already indicated by the dependence of T_{eo} and E_e on A_i in the OH LOC regime /2/.
The study of the sawtooth propagation, however, did not yield any direct evidence for an A_i dependence in χ_e^{SZ}. Under OH conditions at $\bar{n}_e = 2 \times 10^{13}$ cm^{-3}, $\chi_e^{SZ} \approx$ 3-5 m^2/s is observed both for H^+ and D^+ which is a factor of 3-4 above the value from transport analysis. No isotope dependence in χ_e^{SZ} can be resolved.

The isotope effect in momentum confinement
As the parameter dependence of A_i is noted also in ohmic discharges at high density (close to the density limit) where the dominance of ion transport is expected, we have separately studied ion transport via momentum confinement in L-mode discharges with NI/3/. A strong isotope dependence of the momentum confinement time { $\tau_\Phi \propto A_i^{1\pm0.02}$ } or the momentum diffusivity averaged over the gradient region { $\chi_\Phi \propto A_i^{-0.87\pm0.02}$ } is observed. The analysis is based on 33 discharges. The results clearly show that A_i affects ion transport characteristics.

Comparison of OH discharges with carbonized or boronized walls
In our previous report we have studied the isotope effect under carbonized wall conditions. Now we will supplement these studies with results from boronized walls. The plasma parameters are varied in the following ranges: $200\text{kA} \leq I_p \leq 450\text{kA}$, $1.8\text{T} \leq B_t \leq 2.8\text{T}$, 2.5×10^{13} cm$^{-3} \leq n_e \leq 5.5 \times 10^{13}$cm^{-3}. The results from the regression analysis are shown in Table1. The comparison with the results in the SOC regime from the carbonized wall series / 2 / shows the reproducibility of the regression exponents. With respect to the A_i dependence (analyzed in the form of a power law, exponents given in brackets), we again observe a strong dependence of T_{eo} (C: 0.36; B: 0.33), E_e (C: 0.27; B: 0.36), E_o (C: 0.28; B: 0.47), P_{oh} (C: -0.22; B: -0.18), τ_E (C: 0.50; B: 0.65) and τ_{SZ} (C: 0.54; B: 0.44). Much weaker, however, is the isotope dependence of the edge density. With carbonized walls, $n_e(a) \propto A_i^{-0.81}$ and with boronized walls $n_e(a) \propto A_i^{-0.29}$ is observed.

Comparison of NI and OH discharges with boronized walls

We have extended the ohmic parameter study of A_i to NI heated discharges with fixed NI power of 1.6MW. The ohmic power input can be neglected at this auxiliary heating level. The results of the regression analysis are shown in Table 2. A strong A_i dependence is observed in the following parameters: T_{eo} (NI: 0.25; OH: 0.33), E_e (NI: 0.24; OH: 0.36), E_o (NI: 0.44; OH: 0.47), τ_E (NI: 0.34; OH: 0.65) and τ_{SZ} (NI: 0.46; OH: 0.44). The A_i scaling of τ_E is weaker but all parameters which show a clear isotope scaling under OH conditions display it also with strong auxiliary heating. The scaling of the edge density $n_e(a)$, however, further diminishes to $n_e(a) \propto A_i^{-0.17}$.

In a separate study /4/ we could demonstrate the dependence of the edge density on the power flux within the SOL and describe it by a simple 1D-model. The application of these considerations clearly explains the strong A_i scaling of $n_e(a)$ in the carbonized case by the sensitivity of the impurity radiation from the plasma on A_i ($P_{RAD} \propto A_i^{0.3}$). In deuterium, the actual power flux in the SOL is low on account of high impurity radiation and the edge density is low. With boronization the impurity radiation is strongly reduced, the power flux into the SOL is high even for D^+ and therefore the isotope dependence of $n_e(a)$ is reduced. This trend continues to auxiliary heated discharges.

Results from transport analysis

We have tried to study the radial range where the heat diffusivity is affected by the choice of the isotope mass. This study is guided by the conventional wisdom that different transport mechanisms may prevail in various radial zones: the core of the plasma is governed by sawteeth, the insulation zone by electrostatic and the edge zone by resistive turbulence. In order to have sufficient accuracy for this study, we have done a series of high density ($n_e = 7.2\times10^{13}$ cm^{-3}) discharges so that we could do a single fluid analysis which does not discriminate between electron and ion transport. The heat diffusivities for hydrogen and deuterium are plotted in Fig. 1. The central part of the discharge is additionally treated with a sawtooth model with various assumptions of sawtooth amplitude and radius of q=1 surface around the measured quantities. Figure 1 indicated that sawteeth contribute to the core transport in particular in hydrogen (shorter τ_{SZ}). Furthermore, it is shown that $\chi_e^{D^+}$ is lower than $\chi_e^{H^+}$ for all radii irrespective of the expected transport mechanisms in the various radial zones.

Summary

We have increased the evidence that the ion mass affects both electron and ion transport. The most sensitive parameters which respond to A_i are the electron temperature, the electron and total energy content, the confinement time and the sawtooth repetition time. These dependences apply generally. The A_i dependence of the edge density is understood as a consequence of different radiation levels in H^+ and D^+ giving rise to differences in the SOL power fluxes. Heat diffusivity is lower for D^+ over the whole cross-section. Still no theoretical explanation can be given. The consideration of those parameters which are known to depend on A_i (like the electron-ion coupling time τ_{ei}, the Alfven-velocity, the sound velocity or the ion-ion collision time) does not give clear hints.

References

/1/ H.D. Murmann, et al. Proc. 15th Europ. Conf., Dubrovnik, Part1, p3.
/2/ F. Wagner, et al. Proc. 16th Europ. Conf., Venice, Part1, p195.
/3/ A. Kallenbach, et al. Proc. 17th Europ. Conf., Amsterdam, to be published.
/4/ M. Bessenrodt-Weberpals, et al. PSI Conf. 1990, to be published.

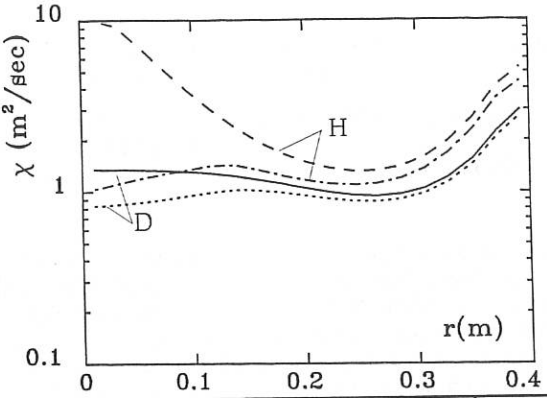

Figure 1.
Radial variation of the single-fluid heat diffusivity for H^+ and D^+ series at n_e=7.2 $\times 10^{13}$ cm^{-3}, 420 kA, 2.2T. The plasma core is analyzed with and w/o a separate sawtooth model.

	const.	Ip		Bt		ne		Ai
Poh	5.62E-04	1.13	0.02	-0.35	0.03	0.26	0.02	-0.18
Eo	1.55E-02	1.19	0.04	-0.32	0.07	0.44	0.05	0.47
Ee	1.32E+02	1.17	0.01	0.00	0.00	0.44	0.02	0.36
τE	3.80E+01	0.00	0.00	0.00	0.00	0.21	0.05	0.65
Teo	1.35E+02	0.29	0.02	0.72	0.03	-0.50	0.03	0.33
<Te>	2.34E+00	0.96	0.02	0.00	0.00	-0.55	0.03	0.29
Teo/<Te>	5.75E+01	-0.66	0.03	0.68	0.05	0.00	0.00	0.05
neo	2.57E+00	-0.13	0.01	0.18	0.02	0.91	0.02	0.08
<ne>	1.91E-01	0.27	0.03	0.00	0.00	0.98	0.04	-0.12
neo/<ne>	1.12E+01	-0.40	0.03	0.28	0.05	0.08	0.04	0.17
Tio	3.55E+02	0.17	0.04	0.35	0.06	-0.42	0.04	0.00
tSZ	1.20E+02	-0.48	0.09	0.00	0.00	0.27	0.11	0.44
Eo	2.40E-01	0.87	0.02	-0.14	0.04	0.14	0.02	0.44
Ee	5.25E-02	0.88	0.02	0.09	0.03	0.52	0.02	0.24
τE	1.10E+00	0.55	0.03	-0.14	0.04	0.09	0.03	0.34
Teo	2.63E+02	0.27	0.03	0.55	0.05	-0.46	0.04	0.25
<Te>	6.61E+00	0.83	0.02	0.11	0.03	-0.49	0.02	0.13
Teo/<Te>	3.98E+01	-0.56	0.03	0.44	0.05	0.00	0.00	0.12
neo	1.45E+00	0.00	0.00	0.09	0.02	0.90	0.01	0.07
<ne>	5.13E-01	0.08	0.02	-0.06	0.02	1.11	0.02	-0.15
neo/<ne>	2.82E+00	-0.11	0.02	0.14	0.03	-0.21	0.02	0.22
tSZ	1.10E+01	0.15	0.07	0.23	0.11	-0.39	0.07	0.46

Table:
Exponents of the regression analysis in the form const $\times I_p^{\alpha} \times B_t^{\beta}$... . The column following the power gives the standard error; R is the regression coefficient. Table 1a: results for the ohmic, 1b for the NI phase (1.6 MW). Units: ms, kA, T, 10^{13} cm^{-3}, kJ, eV.

DEMIXING OF IMPURITIES AND HYDROGEN AS DEDUCED FROM Z_{eff} PROFILES IN THE BORONIZED ASDEX

K.-H. Steuer, H. Röhr, W. Engelhardt, G. Fussmann, A. Kallenbach, B. Kurzan, H.D. Murmann and ASDEX, NI Team
Max-Planck-Inst.f.Plasmaphysik, D-8046 Garching, FRG, EURATOM Association

Substantial progress towards fusion has been made in the confinement, stability and heating of tokamak plasmas. The transport behaviour of magnetically confined plasmas, however, is still an unsolved problem. The transport mechanisms of hydrogen and of impurities are known to be different, leading to phenomena such as impurity accumulation on axis, especially in good confinement regimes, and more generally to demixing of the various species. Besides energy losses from impurity radiation, one has to be concerned about dilution of the fuel-ion density, and about effects that impurities may have on the main ion and electron transport. To understand the transport behaviour of the different plasma species, one needs their spatial density profiles. The evolution of the electron density profiles is well known, the impurity profiles may be inferred from spectroscopic measurements, but usually the proton density profiles are less well documented. From reliable Z_{eff} measurements it is possible to infer the proton density profile using a typical species mix derived from spectroscopic data and assuming quasi-neutrality. It is covenient to represent the various impurities by a characteristic impurity ion with a density n_z and a fictive charge Z ($Z = \Sigma n_i Z_i^2 / \Sigma n_i Z_i$; $i \geq 2$). A typical value for Z is 7, indicating that light impurities are dominating. Comparing the different profiles, we find characteristic differences in the electron, proton and impurity transport behaviour.

Z_{eff} diagnostics

The detection system of the ASDEX Nd: YAG laser scattering device is used to measure the bremsstrahlung along 16 chords in 3 different broad wavelength bands between 820 nm and 1060 nm with a spatial resolution of 4 cm. Line radiation is negligible in these bands, as verified by spectroscopic measurements. Using in addition the simultaneously measured n_e and T_e profiles, we obtain radial Z_{eff} profiles. The statistical errors are mainly caused by the density measurement and vary in the range between 10% on axis and 30% in the plasma edge.

Carbon and oxygen density profiles and their Z_{eff} contributions are absolutely measured by charge exchange recombination spectroscopy (CXRS) during beam injection. This method allows an independent cross-check for low-Z impurity density profiles.

Experimental results

1) Plasma parameter improvements with boronization

Boronization of ASDEX results in significantly improved plasma conditions. The decrease of Z_{eff} on axis due to boronization may be seen in fig. 1 for ohmic discharges. As a consequence of the reduction of metal and light impurities (Fe, Cu, O) Zeff is strongly reduced for all electron densities and reaches values close to 1 at densities $\bar{n}_e \geq 3 \cdot 10^{13}$ cm^{-3}.

The increase of Z_{eff} normally observed during auxiliar heating is also markedly reduced as shown in fig. 2 for LH-heating.

2) Transport behaviour in the central plasma region

The average radial flux Γ of the various plasma species is frequently described by the same empirical formula (1) leading to the same profile shape for all particles :

$$\Gamma = -D\frac{\partial n}{\partial r} + v_o\frac{r}{a}n \qquad (1)$$

In boronized discharges we find, however, that this expression cannot be used simultaneously for all species with the same coefficients, because the observed profiles of protons, electrons and impurities are different. For the central plasma, where the particle sources are negligible in stationary cases the fluxes vanish and from the density profiles in figs. 3-6 we can determine the ratio of D/v_o which is a characteristic decay length of the profiles. Assuming constant coefficients D and v_o we determine their ratio by comparing the profiles at r = 0 and r = 25 cm (table 1).

table 1	$n_e(0)$ (10^{13} cm^{-3})	$Z_{eff}(0)$	D/v_o (cm) electrons	D/v_o (cm) deuterons	D/v_o (cm) impurity (Z=7)
OH (fig. 3)	1.8	2.7	27	40	14
OH	3.5	1.8	19	25	7
OH (fig. 4)	5.0	1.4	22	28	7
H-mode	6.0	2.7	22	40	11
Ctr.-inj.	7.0	3.3	12	36	4.5

2.1 OH plasmas

In ohmic discharges at low densities (fig. 3) we see that the deuteron profiles tend to flatten in contrast to the neoclassical prediction of an increased Ware pinch at low collision frequency. The impurities are peaked by a factor 3-4 as compared to the deuterons (table 1). This is characteristic of boronized discharges and was not observed before. It may be due to the reduction of metallic impurities which, in non-boronized cases, expel the lighter impurities from the central region.

The electron peaking is stronger than that of the deuterons and cannot be ascribed to sources by ionization of impurities. It is clearly a transport phenomenon indicating that the transport coefficients are different for electrons, protons and impurities. They also depend in different ways on the plasma parameters.

2.2 Auxiliary heated plasmas

In the ELM-free H-mode (co-injection) the electron profiles in the bulk plasma are very similar to the comparable ohmic case but the Z_{eff} values are higher. The impurity peaking is somewhat reduced and the deuteron profiles are broader (fig. 5).

During counter injection there is a strong accumulation of impurities. The central concentrations are: B (1%), C (1.5%), O (1.5%), and Cu (0.2%) resulting in a fictive impurity charge of Z=8.5. In the accumulation case the difference between electron and deuteron transport is

particularly pronounced. The deuteron profiles become slightly flatter than those in comparable ohmic discharges. Strong peaking of electrons in the central region is observed, which is again not explainable by internal ionization sources. It must be due to a change of the ratio D/v_0 for the electrons, but we cannot decide from the measurements whether D is decreasing or v_0 is increasing.

In contrast to previous observations we now find an accumulation of light impurities which dominate Z_{eff}. The accumulation of light impurities was possibly prevented by the accumulation of metallic impurities in non-boronized conditions. A further hint for the evidence of this finding is provided by CXRS, which shows an even stronger peaking of oxygen (Z = 8) as compared to carbon (Z = 6) during the accumulation phase . A discussion of multispecies accumulation phenomena in the framework of neoclassical theory is being presented at this conference /2/.

3) Observations in the plasma edge

There is a general tendency in all discharges for Z_{eff} to increase towards the plasma edge (see figs. 3-6). From a simple diffusive model like (1) with the same transport coefficients for all species this is to be expected, since the penetration depth of neutral hydrogen is much longer than that of neutral impurities. A closer look at the profiles shows, however, that the profiles of the impurity ion has a positive gradient towards the plasma edge, which cannot be explained by the source distribution. Charge exchange recombination spectroscopy confirms these profiles. The transport behaviour of hydrogen and impurities must be different. An outward drift velocity of the impurities is formally required to describe the observation. This demixing effect may even be stronger than evident from the figures as we have assumed Z = 7 for the characteristic ion which may be too high in the boundary region where impurities are usually in a lower ionization stage. This strange transport behaviour is possibly explained by neoclassical temperature screening which in particular during the H-mode with its very steep temperature gradients at the boundary results in flat Zeff profiles in the centre and in a Z_{eff} increase towards the edge /2/.

Ref.: /1/ H. Röhr, K.-H. Steuer, Rev. Sci. Instrum. 59 (8), 1875 (1988).
/2/ G. Fussmann et al. , this conference.

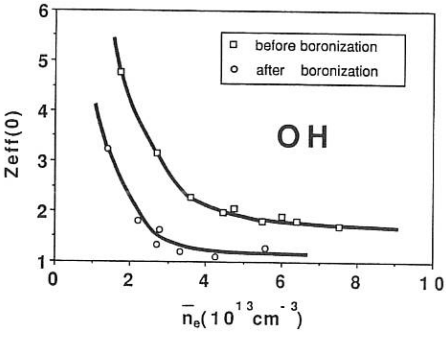

Fig. 1 Density dependence of Z_{eff} before and after boronization

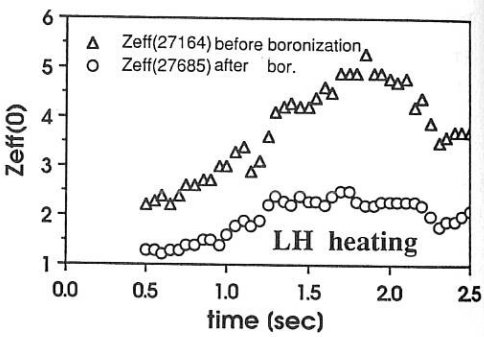

Fig. 2 Improvement of Zeff due to boronization in LH heated plasmas

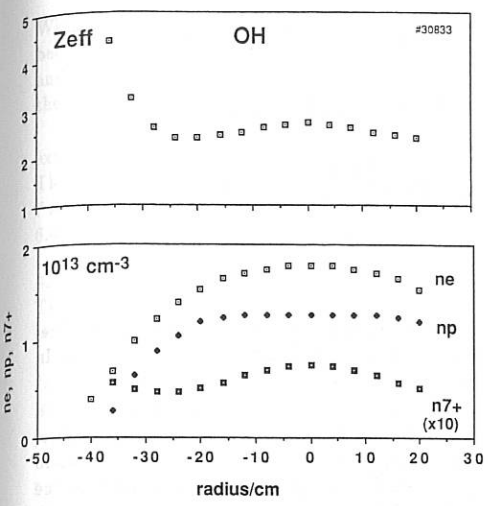

Fig. 3 Zeff-, electron-, deuteron- and impurity ion density profiles for OH plasma at low density

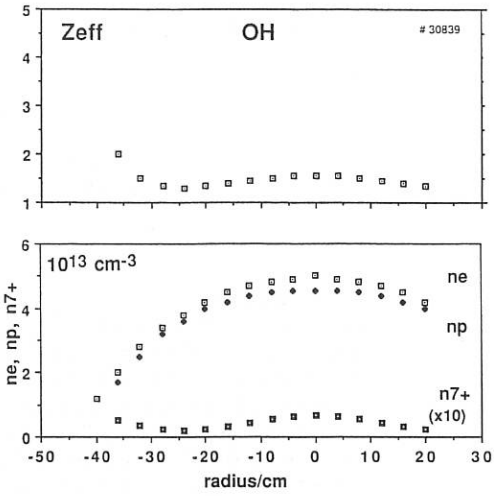

Fig. 4 Zeff-, electron-, deuteron- and impurity ion density profiles for OH plasma at high density

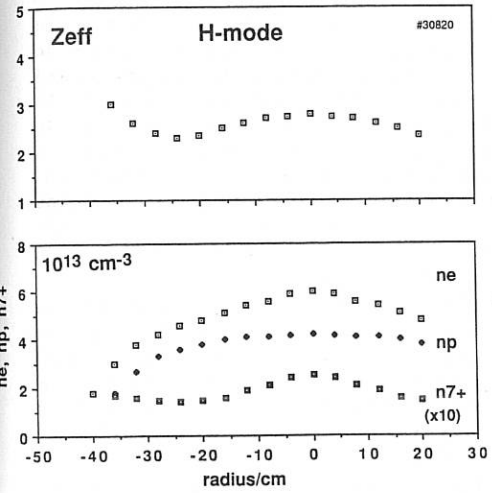

Fig. 5 Profiles of Zeff, electrons, deuterons and impurity ions in the H-mode (t=1.2s)

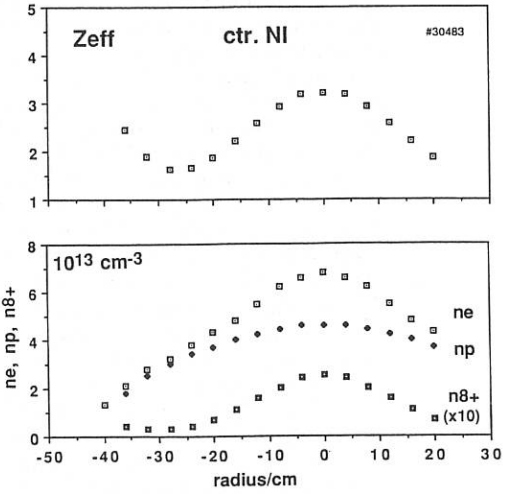

Fig. 6 Profiles of Zeff, electrons, deuterons and impurity ions for ctr. injection (t=1.38s)

CONFINEMENT STUDIES OF SAWTOOTH-FREE OHMIC DISCHARGES

U. Stroth, R. Büchse, W. Herrmann and K. Krieger

Max-Planck-Institut für Plasmaphysik,
EURATOM-IPP Association D-8046 Garching, FRG

1. Introduction

Fusion reactor studies are based on H-mode plasmas because of the improved energy confinement and, being realized in the divertor configuration, the possibility of impurity control. In H-mode plasmas impurities are controlled in the edge by ELMs.

The problem of impurity accumulation rules out another family of discharges with improved energy confinement time (τ_E). This family is characterized by centrally peaked density profiles and its members at ASDEX are the IOC regime [1], pellet [2] and counter neutral beam injection discharges [3]. In all cases impurity accumulation can lead to a limitation of the τ_E improvement or to disruptions of the plasma. In this contribution we present sawtooth free discharges, another member of the peaked density family. They achieve stationarity with a saturation in the impurity accumulation. Because sawtooth activities are absent in these stationary discharges, they are an ideal opportunity to study the transport properties of a peaked density plasma.

2. Properties of Sawtooth-Free Discharges

The systematic investigation of sawtooth-free discharges has become possible after boronization of the ASDEX vacuum vessel. They appear in a transition stage from freshly boronized to unboronized conditions. This gives reason to the assumption that sawtooth-free plasmas need a specific impurity mixture to develop. Only under these conditions sawtooth-free phases can be reached as soon as the external gas flux to the plasma is reduced in order to establish a density plateau at low line averaged densities. As an example, in Fig. 1 we compare a sawtooth-free discharge to a sawtoothing one. The bifurcation appears at 0.5 s. A small gaspuff broadens one discharge. This can be seen at the density peaking factor (central to volume averaged electron density, $Q_N = n_e(0)/\bar{n}_e^V$). The sawteeth develop then as usual. When the plateau density is reached, the external gas flux is reduced. This leads to a strong peaking of the other discharge while the already sawtoothing one does not change its density profile.

The peaking of the density profile leads to impurity accumulation which is saturated, as it can be seen from the soft X-ray signal, when the neutral beam starts injecting at 1 s. The then enhanced impurity production leads to a further accumultation which drops when the density profile starts to flatten. The flattening of the density profile can be due to an enhanced gas flux that is needed to compensate the deteriorated L-mode particle confinement. The sawteeth set in after the the density profile has flattend. The signals of the sawooth-free discharges are similar to those of O-type plasmas at Doublett III [4].

At low densities parameter studies of Deuterium discharges led to the following results: Q_N does not depend on the edge safty factor q_a and is between 2.1 and 2.3. It is well separated from values of sawtoothing discharges which are 1.5 at low q_a and 1.8 at q_a=4.3. Q_N is the same in sawtooth-free D and He discharges. The peaking of the radial electron temperature (T_e) profile depends in the same way on q_a, independently whether the discharges are sawtoothing or not.

With decreasing q_a the temperature profile flattens. In the sawtoothing discharges this occurs because of a expanding q=1 surface and a consequent enhancement of the sawtooth transport and in the sawtooth-free discharges because of a central impurity accumulation at higher rates the lower q_a.

At high densities sawtooth-free discharges are difficult to achieve because of the higher external gas flux needed. We observed sawtooth-free discharges during a density limit program. They remained sawtooth-free up to the density limit at the high line averaged density of $7 \times 10^{19} m^{-3}$ at $I = 320kA$ and $B_{tor} = 2.17T$. This has to be compared with a density limit of $6.4 \times 10^{19} m^{-3}$ in the sawtoothing case

3. Stabilization of Sawtooth-Activities

Two mechanisms can in principle stabilize sawteeth: the vanishing of the q=1 surface with a central q value above 1 or a stabilization by profile effects in the presence of a q=1 surface.

In counter injection discharges we observe the first mechanism. The moderately peaked density profiles invoke impurity accumulation in the plasma centre. This leads to an increasing Z_{eff} and, because of high radiative losses, decreasing central T_e. Consequently the current profile broadens and the central q value rises above 1.

A different mechanism can stabilize sawteeth in ohmic discharges. This is demonstrated in Fig. 2. The upper part shows line averaged density ($\bar{n}_e$) and soft X-ray intensity, integrated along a chord of 4 cm minor radius, of a sawtooth-free discharge that remained stable for 3 s. During the first density plateau at $\bar{n}_e = 2.2 \times 10^{19} m^{-3}$ a strong m=1 mode reveals the presence of a q=1 surface. This is in accordance with neoclassical current density calculations which are shown in the lower left part of the figure. The calculation gives a q=1 surface at $r \cong 9$ cm in accordance with the data from the soft X-ray camera array, where the m=1 activity vanishes between 7.5 and 10 cm. At 1 s the density is ramped up to a second plateau at $3.5 \times 10^{19} m^{-3}$. This broadens the T_e profile and consequently the current profile. The central q value increases obove 1. This is again in accordance with the soft X-ray data, which shows that the m=1 mode vanishes. The calculations were performed using measured radial Z_{eff} profiles. In agreement with soft X-ray data they show that sawteeth can be stabilized even in the presence of a q=1 surface. This has also been reported for ICRH plasmas at JET [5].

Also the sawtooth-free discharge of Fig. 1 has a central q value below 1. Since the T_e profiles of the discharges in Fig. 1 are almost the same, it can be deduced that the steep density gradient in the centre stabilizes the sawteeth. Also during neutral beam heating, at 1.3 s, the density profile first flattens and then, 70 ms later, sawteeth set in.

4. Transport Studies

For the improvement of τ_E found in discharges with peaked density profiles two mechanisms are held to be responsible [6,7]. A common feature is the reduction of the sawtooth activity which accounts for an improvement in the plasma centre but this only gives a small contribution to the global improvement. The main effect is speculatively attributed to the flattening of the ion temperature gradient in the confinement zone, leading to a suppression of the η_i mode there and to ion energy transport on the neoclassical level.

These arguments also hold for the IOC regime where the linear dependence of τ_E on density is recovered towards higher densities. The loss of the density dependence in the SOC regime can therefore be attributed to the anomalous transport mechanisms described above. At low densities IOC and SOC have the same τ_E (called LOC). This is already a hint, that the anomalous transport mechanisms responsible for the SOC regime are not as active in this domain. Therefore it is not surprising that the global τ_E of sawtooth-free discharges are

found at the upper margin of the values for the LOC and IOC regimes. That the ion energy transport is on the neoclassical level can be seen from Fig. 3. The ion temperature (T_i) from our active beam neutral particle analyser coincide with the band for T_i predicted from neoclassical transport using values for Z_{eff} between 1 and 2. Also the impurity accumulation can be explained with a neoclassical inwards drift ($V_{inv} = 3m/s$ at the edge and 0 in the centre) and a constant diffusion coefficient with neoclassical and anomalous contributions of the same order ($D_{ano} \cong D_{neo} \cong 1200m^2/s$). In Fig. 4 we analyzed three sawtooth-free discharges at different toroidal field (B_{tor}) and otherwise identical plasma parameters. Since T_e is almost identical, the soft X-ray intensities are a measure of the impurity concentration. With the same transport coefficients the average trends of accumulation and saturation are well reproduced. The B_{tor} dependence of the neoclassical transport coefficients together with a small anomalous contribution to the diffusion coefficient explain 50% of the difference in the soft X-ray emission and 50% are due to minor changes in the central electron temperatur.

Finally we performed transport calculations for the discharge of Fig. 1 with an early sawtooth-free and a late sawtoothing phase. We use neoclassical transport for the ion channel, in the first phase because of the results in Fig. 3 and in the second because neither T_e nor the diamagnetic β_{pol} do change.

The results are shown in Fig. 5. In the upper part the enhanced radiative losses in the centre of the sawtooth-free discharge can be seen. The minor differences in the electron-ion exchange term are due to different Z_{eff} and density profiles. It is surprizing that the reduction of sawtooth energy transport does not lead to higher T_e values but to enhanced radiation by almost the same amount as the sawtooth transport is reduced. As a result one finds a strong reduction of the thermal electron diffusivity, χ_e, as shown in the lower part of the Figure. In the χ_e of the sawtoothing discharge the contribution from the sawteeth is contained. An estimate from a simpel sawtooth model, however, shows that the reduction in χ_e can not be explained by the vanishing sawteeth alone and χ_e must be further reduces together with the amount of energy to be transported in order to leave T_e unchanged.

References

[1] SÖLDNER, F. X., MÜLLER, E. R., WAGNER, F., et al., Phys. Rev. Lett. **61** (1988) 1105.

[2] GRUBER, O., KAUFMANN, M., LACKNER, K., et al., Comparison of confinement in hydrogen versus deuterium in multi-pellet fuelled OH discharges, in *Proc. of the* 15^{th} *Europ. Conf. on Controlled Fusion and Plasma Heating, Dubrovnik*, pages 27–30, 1988.

[3] GEHRE, O., GRUBER, O., MURMANN, H. D., et al., Phys. Rev. Lett. **60** (1988) 1502.

[4] JAHNS, G. L., EJIMA, S., GROEBNER, R. J., et al., Nucl. Fusion **22** (1982) 1049.

[5] BHATNAGAR, V. P., CORDEY, J. G., JACQUINOT, J., et al., Plasma Phys. Controlled Fusion **31** (1989) 333.

[6] GRUBER, O., WAGNER, F., KAUFMANN, M., , et al., Influence of density profile shape on plasma transport in ASDEX, in *Proc. of the* 15^{th} *Europ. Conf. on Controlled Fusion and Plasma Heating, Dubrovnik*, pages 23–26, 1988.

[7] STROTH, U., FAHRBACH, H.-U., HERRMANN, W., et al., Nucl. Fusion **29** (1989) 761.

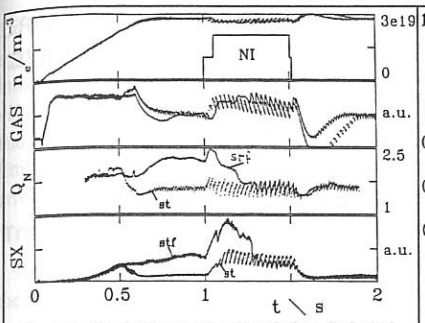

Figure 1: Comparison of sawtooth-free (stf) and sawtoothing (st) discharges. Density, external gas flux, density peaking and soft X-ray intensity.

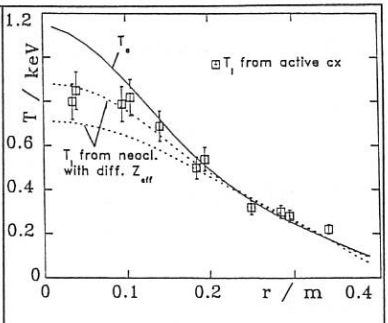

Figure 3: Electron and ion temperatures at 0.8 s of discharge in Fig. 2 (see text).

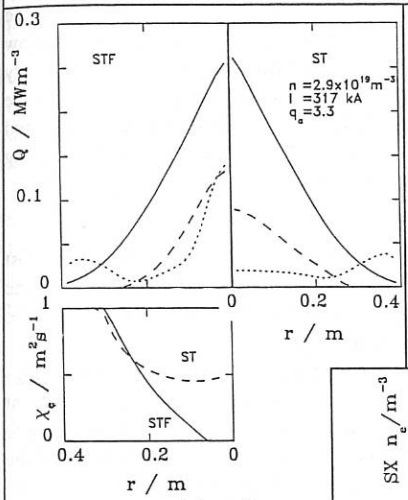

Figure 5: Top: power balance for a sawtooth-free (stf, left) and a sawtoothing (st, right) phases of the discharge out of Fig.1. Ohmic (full), radiation (dotted) and electron-ion exchange (dashed) contributions are plotted. Bottom: resulting electron heat diffusivities.

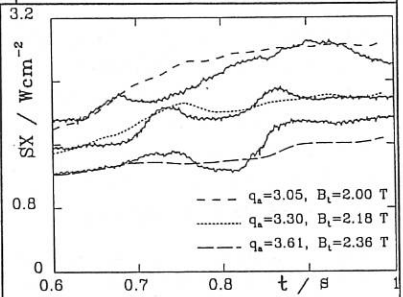

Figure 4: Measured and calculated soft X-ray intensities of three discharges at different B_{tor}, I=317kA and n_e=2.9x10^{19}m^{-3}.

Figure 2: Sawtooth-free ohmic discharge at q_a=4.2 and I=250kA. Top: density and soft X-ray intensity. Bottom: neoclassical current density calculations.

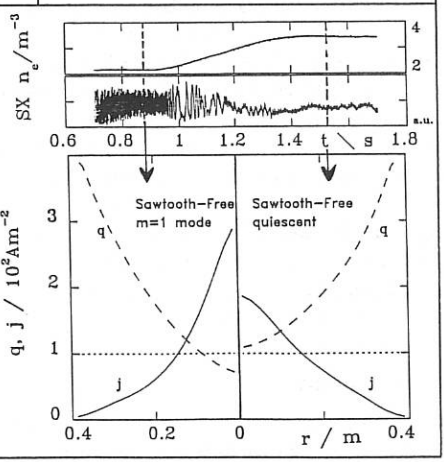

MODIFICATIONS OF DENSITY PROFILE AND PARTICLE TRANSPORT IN ASDEX DURING LOWER HYBRID HEATING AND CURRENT DRIVE.

O.Gehre, K.W.Gentle*, ASDEX- and LH-Team

Max-Planck-Inst.f. Plasmaphysik, D-8046 Garching, FRG, EURATOM-Association
*University of Texas,Austin,USA

Introduction

The behaviour of the electron density profile in ASDEX, measured by HCN-laser interferometry during lower hybrid power (2.45 GHz) injection into ohmic target plasmas was studied for operation with symmetric $N_{//}$ spectra and LH current drive cases. For the same parameters oscillating gas-puff experiments were performed. These experiments allow evaluation of both the particle diffusion and inward convection from the propagation of density perturbations, induced in the different interferometer channels. An improved version of the particle transport code, described in /1/, was used for the analysis. The discharges included average densities of $n_e = 1.2 - 2.6 \cdot 10^{13}$ cm^{-3}, the launched LH power (~1 MW) allowing full RF current drive only at the lower densities in this range.

Modification of density profiles

With a grill phasing of 0 0 π π, corresponding to a symmetric spectrum at low $N_{//}$, almost no modification of the density profile is found. Only for the highest LH powers does the sawtooth period slightly increase at low densities and the profiles show weak broadening. No influence on sawteeth and profile shape is seen at the higher densities.

More dramatic changes of the density profile are encountered for non-symmetric settings of the grill phase with $N_{//}$ around two (75°, 90°), which are typical for optimum current drive. In this case stabilization of sawteeth already was possible at moderate LH powers due to modification of the current profile. In ohmic discharges this would lead to peaking of the density profile, because the central transport effect of sawteeth is switched off. In contrast, current drive at the low densities results in a continuous profile broadening with increasing LH power. For conditions close to full current drive (i.e. $E \sim 0$) the profiles show a flat centre or may even become hollow (Fig.1). Strong central electron heating is seen in these cases, leading to axial values of T_e above 5 keV, if the m=1 mode, remaining in the plasma after stabilization of sawteeth, becomes stable at LH powers close to full current drive /2/.

At the higher densities, where only partial current drive was possible, sawteeth can be still stabilized with increased LH power, but now the familiar central peaking of the density distribution occurs (Fig.2).

Transport analysis

The evaluation of transport coefficients is based on a transport code, which allows an independent description of diffusion D and convection V in a model, delivering typical values for the inner and outer part of the plasma and a linear transition region /3/. For V an additional

1/r dependence is imposed, to maintain V=0 on axis. Small density perturbations about equilibrium, induced by sinusoidal modulation of the gas valve, are analyzed at different radial interferometer positions.The measured amplitude and phase pattern is compared to calculated values, gained from a solution of the particle conservation equation, including both diffusion and convection and a realistic source term. The numbers for D and V are fixed by a non-linear fitting procedure, for which the transition radii have to be choosen appropriate for minimum error.

Transport results

For low density and injection of symmetric LH spectra , as compared to the ohmic phase, the transport analysis shows a slight decrease of both diffusion and inward convection in the central plasma region, while a moderate increase of D and decrease of V is found in the gradient zone (Figs. 3 and 4).The resulting decrease of the density gradients in this region is consistent with the measured profile modifications. No changes are seen for symmetric spectra, if the density is increased above $2 \cdot 10^{13}$ cm^{-3} .

For cases close to full current drive at a density of ~$1.3 \cdot 10^{13}$ cm^{-3} a central diffusion is inferred,which is reduced by a factor of up to five, while the convective drift term in the inner part of the plasma decreases and may reverse its sign, as compared to the ohmic case.In the outer region both D and V are slightly reduced, the convective term keeping its inward direction. These changes in transport are demonstrated in figs. 5 and 6.

For partial current drive at densities above $2 \cdot 10^{13}$ cm^{-3} the central D is only moderately reduced and V stays nearly unchanged at very low values, while both parameters show an increase above ohmic levels at larger radii (Figs. 7 and 8). These transport modifications could explain the above-mentioned profile changes for current drive at different densities.

Summary and conclusion

In conclusion, the analysis indicates only a small effect of lower hybrid power on particle transport in the target gas for symmetric spectra. In contrast, there are clear modifications for the current drive case. At low densities and conditions close to full LH-current drive, transport seems to be governed by changes initiated by current drive, while the sawtooth term dominates at the higher densities, where only partial current drive was possible.

References

/1/ K.W. Gentle, B. Richards, et al., Plasma Physics and Controlled Fusion 29, 1077 (1987)

/2/ F. X. Söldner, R. Bartiromo, et al., this conference

/3/ O. Gehre, G. Fußmann, K. W. Gentle, et al., Proc.of the 16th European Conference on Controlled Fusion and Plasma Physics, Venice (1989), Vol. 1, p. 167

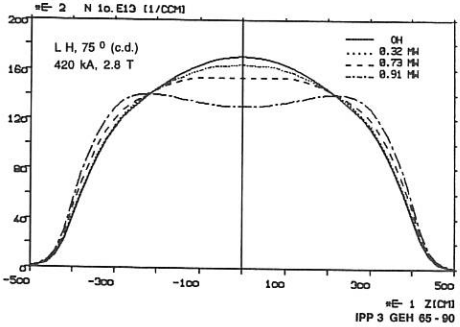

Fig. 1: Development of the electron density profile with increasing LH power for current drive at an average density of ~ $1.3 \cdot 10^{13}$ cm^{-3} (Sawteeth are stabilized above ~.5 MW)

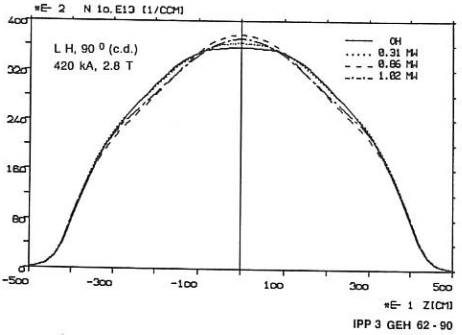

Fig. 2: As in fig.1, but shown for current drive at a density of ~ $2.6 \cdot 10^{13}$ cm^{-3} (Sawteeth are stabilized above ~.7 MW)

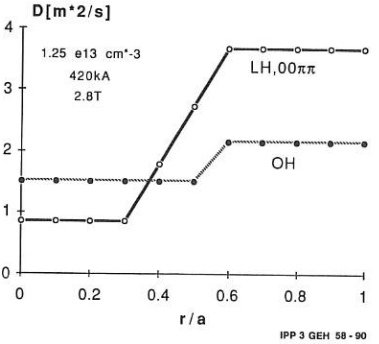

Fig. 3: Modification of the radial profile of diffusion, shown for LH with a symmetric spectrum (0 0 π π) into an ohmic plasma of ~$1.3 \cdot 10^{13}$ cm^{-3} density.

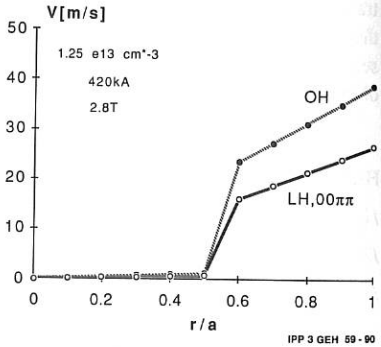

Fig. 4: Modification of the radial profile of convection, shown for the same case as in fig. 3.

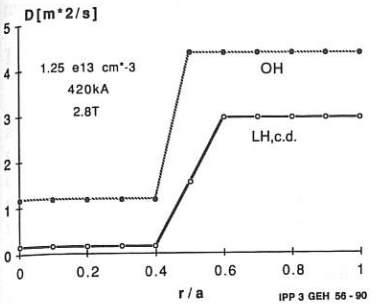

Fig. 5: Radial profile of diffusion,shown for the case of full current drive, as compared to the ohmic phase, at a density of $\sim 1.3 \cdot 10^{13}$ cm^{-3}.

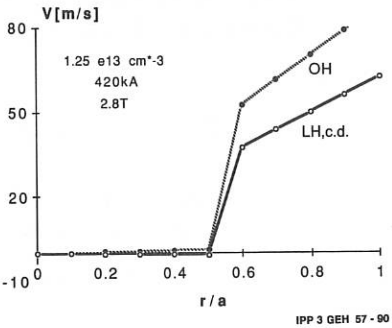

Fig. 6: Radial profile of convection, shown for the same parameters as in fig. 5. In the central plasma region the convective drift term becomes outward directed during current drive.

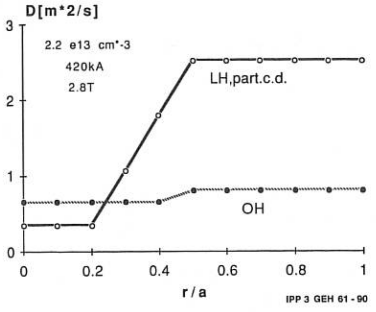

Fig. 7: Radial profile of diffusion during the ohmic phase and with partial LH current drive, at a density of $\sim 2.2 \cdot 10^{13}$ cm^{-3}.

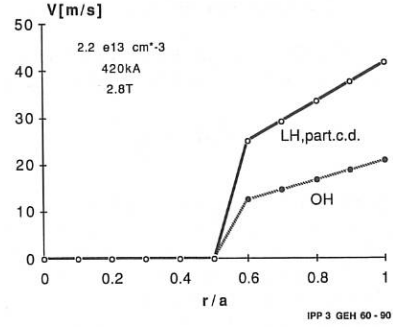

Fig. 8: Radial profile of convection, shown for the same conditions as in fig. 7.(The lower ohmic values of D and V, as compared to figs. 5/6, are due to a strong density dependence of transport over the linear range /3/)

PARTICLE TRANSPORT STUDIES ON TCA USING THE DYNAMIC RESPONSE OF THE EFFECTIVE MASS

Th. Dudok de Wit, B.P. Duval, B. Joye, J.B. Lister

Centre de Recherches en Physique des Plasmas
Association Euratom-Confédération Suisse
Ecole polytechnique Fédérale de Lausanne
CH-1015 Lausanne, Switzerland

I) Introduction

Particle tagging in a tokamak provides an attractive method for studying transport mechanisms. The injection of test particles at the plasma edge and the subsequent measurement of their concentration at the centre can be used to quantify the underlying transport mechanisms. This was done on the TCA tokamak by injecting hydrogen into a deuterium discharge, and simultaneously measuring the temporal evolution of the central effective mass and the edge ionisation rate.

II) Measurement of the effective mass

For different species of ions with mass A_i and density n_i, the effective mass can be defined as the number of nucleons per free electron :

$$A_{eff} = \sum_k \frac{n_i}{n_e} A_k \qquad (2.1)$$

Typical values are 1 for hydrogen only, 2 for deuterium and close to 2 for most fully stripped impurities. Hence for clean plasmas, a real-time measurement of A_{eff} provides a measurement of the ratio of hydrogenic species.

The effective mass at the plasma centre is measured by frequency tracking a global Alfvén wave during the plasma current flat-top (R=0.61 m, a=0.18 m, $I_p \leq 170$ kA, B_ϕ=1.51 T, $\bar{n}_e \leq 10^{20}$ m^{-3}). The diagnostic, described in [1], gives A_{eff} in real-time with an accuracy of 3% and a temporal resolution < 0.2 ms. Numerical simulations show that the measured mass is heavily weighted by the centre of the plasma [2].

The hydrogen and deuterium recycling rates at the plasma edge are inferred from the intensity of the H_β and D_β lines as measured by a visible spectrometer. The spectrum is repetitively integrated and acquired every 2-3 ms. This limits the temporal resolution of the diagnostic.

The ratio of the intensities of the lines yields a measurement of the incremental effective mass, which we define as :

$$R_A = 1\frac{I_H}{I_H+I_D} + 2\frac{I_D}{I_H+I_D} \qquad (2.2)$$

Since the impurity concentration was always small, and the analysis is based on

changes of R_A, impurities can be neglected and R_A is proportional to the effective mass at the plasma edge.

III) Dynamic response analysis

The diagnostics described both provide a well-localised measurement and allow a simultaneous monitoring of the mass change at the plasma edge and at the centre. In this experiment we puff hydrogen into deuterium plasmas and measure the subsequent change in R_A and A_{eff}, fig. 1. For relatively small density increases ($\Delta n_e/n_e \lesssim 30\%$) the measured mass changes are proportional to the local density of the injected gas. We therefore conclude that the dynamic response of the central effective mass to the edge incremental mass is governed by the particle transport of the injected species.

Several methods allow us to study the dynamic response of A_{eff} to R_A. In order to retain the maximum amount of information, we extract the transfer function by performing a system identification analysis :

$$H(\omega) = \frac{A_{eff}}{R_A} \tag{3.1}$$

This transfer function is most easily expressed by its gain $|H(\omega)|$ and its phase $\angle H(\omega)$. These are given over a continuous frequency range ($0 < f < 1/2\tau$, τ is the temporal resolution) and determine the underlying particle transport mechanisms. Next, we compare this experimental transfer function with the one obtained from a particle transport model.

IV) Particle transport model

We assume that the transport of the injected gas can be described by a simple model which includes spatially uniform diffusion coefficient and convective velocity [3] :

$$\frac{\partial n_k}{\partial t} = \frac{1}{r}\frac{\partial}{\partial r}\left(rD\frac{\partial n_k}{\partial r}\right) + \frac{1}{r}\frac{\partial}{\partial r}\left(r^2 v\frac{n_k}{a}\right) + S(r) \tag{4.1}$$

The effect of the injected gas is analysed as a time-dependent perturbation of its density :

$$n_k(r,t) = \bar{n}_k(r) + \tilde{n}_k(r)e^{-j\omega t} \tag{4.2}$$

The homogeneous solution of equation 4.1 is a confluent hypergeometric function :

$$\tilde{n}_k(r) = \tilde{n}_{ko}\, M\left(-\frac{j\omega a}{2v}, 1, \frac{vr^2}{2aD}\right) e^{-\frac{vr^2}{2aD}} \tag{4.3}$$

so that the transfer function becomes :

$$H(\omega) = \frac{\tilde{n}_k(r=0)}{\tilde{n}_k(r=a)} = \Big/ M\left(-\frac{j\omega a}{2v}, 1, \frac{va}{2D}\right) e^{-\frac{va}{2D}} \tag{4.4}$$

which for the range of v and D values considered here can be approximated by a Bessel function :

$$H(\omega) \approx e^{\frac{va}{4D}} \Big/ J_o\left(\sqrt{\frac{va}{D} + \frac{j\omega a^2}{D}}\right) \qquad (4.5)$$

This simple model adequately reproduces the measured transfer function, fig. 2. A non-linear optimisation routine is further used to estimate v and D by minimising the phase and gain differences between the measured and the calculated transfer function. The frequency dependence of the amplitude and the phase is dominated by the value of the diffusion coefficient, whereas the convective velocity mostly determines the average amplitude. Due to the good parameter sensitivity of the diffusion coefficient, the highest accuracy is achieved for D. Its statistical measurement error is typically 10%. The value of v however is more difficult to extract, since it is very sensitive to the absolute calibration of the diagnostics; in general, the accuracy is 0.8 ms^{-1}.

V) Experimental Results

The dynamic response measurements were made for two different conditions which have important implications on the validity of the measured particle transport.

1) First results, in an unconditioned tokamak, indicated that a negligible fraction of the injected hydrogen was absorbed by the vessel wall. Since we could assume particle conservation, the mass measurement could be used to determine the hydrogen transport coefficients. Measurements at q_a=3.1, $\bar{n}_e$= 3–5·10^{19} m^{-3} gave the following results :

$$D = 0.58 \pm 0.04 \ m^2s^{-1}$$
$$v = 0.57 \pm 0.83 \ ms^{-1}$$

For comparison, results obtained under similar conditions from particle balance equations and laser ablated impurity injection [4] gave :

$$D_{pb} = 0.70 \pm 0.20 \ m^2s^{-1}$$
$$D_{abl} = 0.73 \pm 0.10 \ m^2s^{-1} \quad \text{respectively.}$$

We note that $D_{pb} > D$, which implies that the central mass change is due to a diffusion of the injected gas as well as the plasma working gas, as one would expect.

2) Other experiments were performed in a tokamak in which a film of boron carbide had been deposited. This film appeared to significantly enhance the working gas absorption by the vessel, accompanied by a partial release during subsequent discharges [5]. Under these conditions, particle conservation was no longer satisfied. The edge incremental mass was no longer measured by the H_β and D_β line intensities which were more influenced by local edge recycling. The absence of this measurement prohibited our analysis.

VI) Conclusion

The dynamic response of the effective mass provides an attractive method of studying transport of an isotope of the working gas injected into a plasma. Provided the absorption at the tokamak vessel wall is sufficiently small, the method can be used to separately estimate the diffusive and the convective transport coefficients. The measured values are consistent with those obtained from global particle balance equations.

References

1) Alikaev V., A. Bagdasarov A., Berezovskii E. et al., Plasma Physics and Contr. Fusion **29** (1987)1286.
2) Lebeau D., Koch R. et al., proc. 16th EPS conference, Venice 1989, vol III, 1061.
3) Gentle K.W., Richards B, Waelbroeck F, Plasma Physics and Contr. Fusion **29** (1987) 1077.
4) Joye B., Lister J.B., Moret J.-M. et al., Plasma Physics and Contr. Fusion **30** (1988) 743.
5) TFR group, Nuclear Fusion **26** (1986) 849.

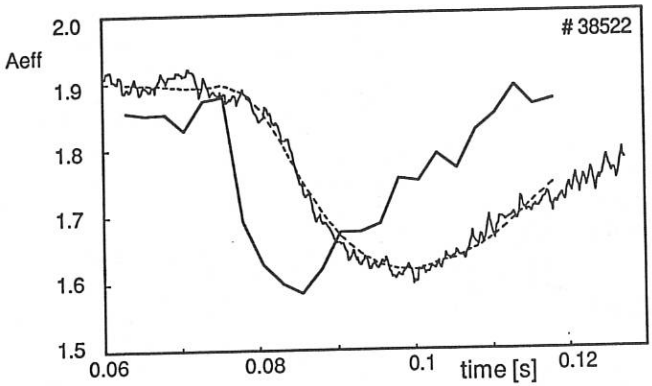

Figure 1
Temporal evolution of the effective mass during hydrogen injection in a deuterium plasma, showing : R_A measured at the edge (bold line), Aeff measured at the centre (plain), Aeff as simulated from R_A (dashed) with the transfer function shown in fig. 2.

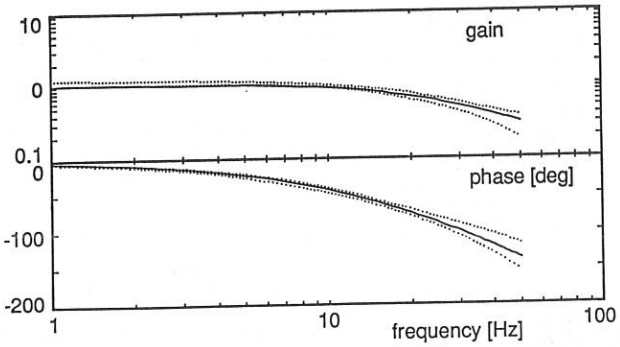

Figure 2
Bode diagrams of the transfer function as extracted from fig. 1, showing : the gain $|H(\omega)|$ and the phase $\angle H(\omega)$ with their measurement error (dotted line), the gain and the phase as calculated from the best fit for D and v (plain line).

Transition to High Density Discharges through Hard Gas Puffing

Ch.Nieswand, Z.A. Pietrzyk, A. Pochelon, R. Behn, A. Knight.

Centre de Recherches en Physique des Plasmas
Association Euratom-Confédération Suisse
Ecole Polytechnique Fédérale de Lausanne
21 av. des Bains, CH-1007 Lausanne Switzerland

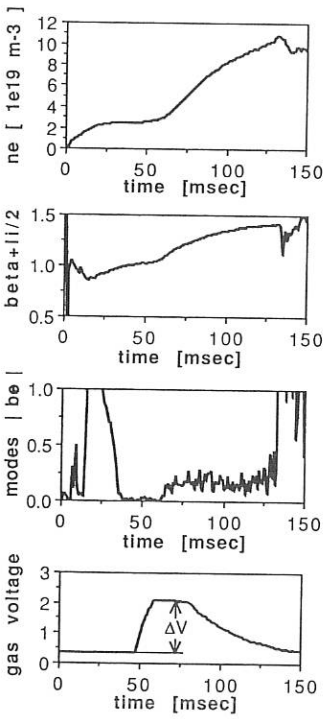

Fig. 1. Time evolution of line density, $b_{p+li/2}$, mode activity and gas valve voltage.

For certain experiments, and to improve plasma performance, high values of plasma density are required. The density limit for quasi stationary discharges (QSD), with soft gas puffing, is approximately $5 \cdot 10^{19}$ m^{-3} in the TCA tokamak. We have observed, however, that higher line average densities, above 10^{20} m^{-3}, can be obtained by hard gas puffing. When this hard puffing is followed by a gentle decrease of the gas flux, reproducible discharges without disruption can be obtained. In these discharges the density limit achieved $\bar{n}_e R/B_t = 3.9 \cdot 10^{19}$ $m^{-2}T^{-1}$ (for $q_a = 3.2$), was similar to that found in a similar sized machine[1] and to that observed in JET[2]. The Troyon β_{tor} limit[3], which for TCA at $q_a = 3.2$, is 1.3%, was closely approached at the end of these discharges near the density limit. All of the data to be presented were obtained on TCA with boronized walls at constant plasma current and with $q_a = 3.2 \pm 0.1$, although it is believed that the main features do not depend on the treatment of the walls.

A Thomson scattering system was used to measure the electron temperature and density at ten radial points and a single time in the discharge. Other standard TCA diagnostics were also used. Figure 1 shows the typical time dependence of the gas valve voltage,

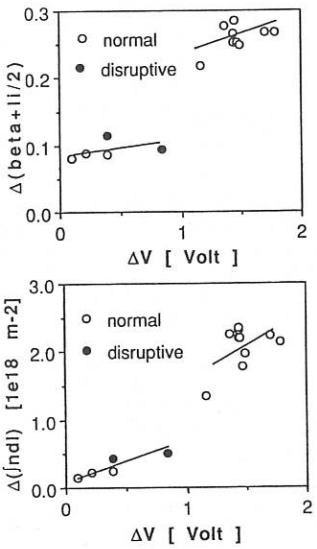

Fig. 2. Change in line density and $b_p+l_i/2$, as a function of gas step voltage.

together with the electron density, $\beta_p+l_i/2$ and the level of mode activity. In these hard puffing discharges the plasma density and $\beta_p+l_i/2$ responded in a highly non-linear fashion to the gas input. Figure 2 shows the change in density and $\beta_p+l_i/2$, defined as the difference between their values at the beginning of the hard puff and 40 ms later, as a function of the height of the gas valve voltage pulse. For low gas valve voltages, the plasma density increased until the typical QSD density limit was reached, whereupon large mode activity generally led to a disruption. As the voltage was increased further, there came a point when the plasma gas acceptance suddenly increased and the plasma attained a much higher density. By this hard puff method, strong mode activity and disruptions at the QSD density limit could be avoided. A similar discontinuity in the behaviour of $\beta_p+l_i/2$ was also observed. The hard puff produced only a moderate increase in mode activity and an increase in the plasma resistance at later times. These observations are indicative of a transition to a different discharge regime.

The response of other plasma parameters to the hard puff is shown in Figs. 1 and 3. In general, the plasma started to react to the puff after a delay of about 5 ms. At this time the parameters $\beta_p+l_i/2$, T_e, n_e and T_i (not shown in these figures) started to increase. In addition, the density profile flattened ($n_e(0)/\langle n_e\rangle$ decreased) and the temperature profile peaked. Initially the electron temperature increased for about 20-25 ms which is 3 to 9 times longer than the energy confinement time τ_E = 4-7 ms at this time. Within experimental error the increase in $\beta_p+l_i/2$ can be attributed solely to the increase in β_p, however the fact that the temperature peaking ($T_e(0)/\langle T_e\rangle$) increased suggests that l_i may also have increased. During the initial phase the sawtooth period increased linearly with the density (Fig. 4), in approximate agreement with the TFR sawtooth scaling.[4] The change in mode activity (Fig. 1) is a further indication of a change of the current profile during this initial phase.

After the initial phase the electron temperature and the peaking of the electron temperature started to decrease. The electron density began to peak at about 50 ms after the start of the puff, when the gas valve voltage was reduced, but it was always flatter than at the beginning of the discharge. $\beta_p + l_i/2$ increased continuously and β_p and β_{tor} were almost linear functions of the density up to the hard puff density limit. Measurements of the pressure profile showed that the radius of the maximum value of $|dp/dr|$ moved out for the first 50 ms of the puff. During the initial phase the sawtooth period increased linearly until the QSD density limit was reached. Thereafter it remained constant and only started to increase again near the density limit for these hard puff discharges (see Fig. 4).

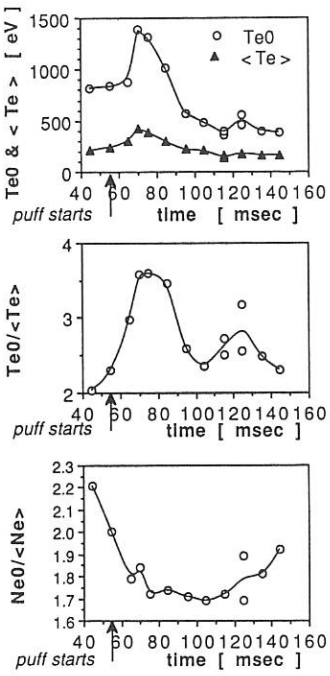

Fig. 3. Measurements of central temperature, volume averaged temperature and temperature and density peaking factors as a function of time.

A possible explanation of the plasma behaviour at the beginning of the puff is that a large amount of cold gas reduced the temperature at the plasma edge. (This was not measured as the last exterior Thomson scattering channel was not reliable at these low densities.) As the total current remains constant, the current density on axis would increase, which would result in stronger heating near the axis and a corresponding increase in the electron temperature. It is also possible, however, that a dense cold gas blanket reduces the losses and increases the energy confinement. The ion temperature (measured by charge exchange and collective Thomson scattering[5]) increased. This is to be expected since both the electron temperature and density increased, which favours transfer of power to the ions. However, the ion temperature did not decrease at later times. The strong influx of gas at the plasma edge made the density and dp/dr profiles broader. This broadening is known to increase MHD stability against kinks.[6] Detailed numerical simulations would be needed to determine if this is why higher densities can be obtained with hard puffing. The

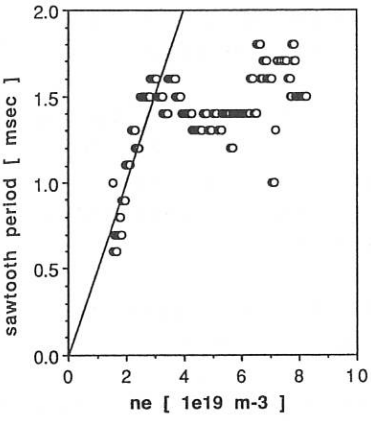

Fig. 4. Sawtooth period as a function of line averaged density for a hard puff discharge.

almost constant sawtooth period above the stationary density limit (QSDL), departing from the linear increase below the QSDL, suggests a strong modification of the current density profile. The peaking of the density profile at later times suggests that these hard puffing discharges might be similar to the IOC discharges in ASDEX.[7] However, the kinetic energy confinement time saturates at high density, as in the SOC regime.[7] Also, the ratio τ_E/n_e increased for a short time after puffing but then decreased during the later reduction of the gas valve voltage. The peaking of the density did not produce an increase in τ_E, as would be expected in an IOC discharge. The density peaking, $n_e(0)/\langle n_e \rangle$, is lower in the hard puff discharges than in QSDs near the QSD density limit. We conclude that these hard puffing discharges are not IOC discharges. Nevertheless, the method of hard puffing reported here allows plasmas to be created which are close to the Murakami density limit and the Troyon β limit.

The authors acknowledge stimulating discussions with Dr. A. Bondeson and Prof. F. Troyon, as well as the experimental support of the TCA group. This work was supported by the Swiss National Science Foundation.

References

1. M. Greenwald , et al., MIT report PFC/JA-86-22 (1988)
2. C. G. Lowry and JET team, APS Plasma Physics Meeting, Anaheim, USA (1989). (Also JET report JET-P(89)80)
3. F. Troyon, et al., Plasma Phys. and Contr. Fusion **26**, 209 (1984).
4. C. W. Simm, Ph.D. Thesis, Lausanne report LRP 334/87 (1987)
5. M. S. Siegrist, et al., this conference.
6. G. Schultz, et al., Lausanne report LRP 396/90 (1990)
7. F. X. Söldner, et al., 16th European Conference on Controlled Fusion and Plasma Physics, Venice, part I, 187 (1989)

CURRENT PENETRATION MEASUREMENTS IN TUMAN-3 BY ACTIVE CHARGE EXCHANGE DIAGNOSTICS

V.I.Afanasjev, F.V.Chernyshev, V.E.Golant, E.R.Its, A.B.Izvozchikov, V.G.Kiptilyj, A.I.Kislyakov, A.V.Khudoleev, A.A.Korotkov, S.Ya.Petrov, V.V.Rogdestvensky, N.V.Sakharov, K.G.Shahovets, S.P.Yaroshevich

A.F.Ioffe Physical-Technical Institute Academy of Sciences, USSR

A technique for measuring the poloidal magnetic field in a tokamak based on using of a molecular beam was suggested in [1]. In this method the molecular hydrogen beam is injected into a plasma and escaping hydrogen atoms formed by the following ionization of H_2^o and dissociation of molecular ions H_2^+ are detected. Recently its potentialities have been analyzed for ASDEX tokamak [2]. The first measurements were made on the TUMAN-3 tokamak [3].

On TUMAN-3 the measurements of the poloidal magnetic field B_φ were made with a set-up for active charge exchange diagnostics: an injector of the atomic beam DINA-4A mounted on a vertical port and a five-channel atomic analyzer mounted on a horizontal port in the equatorial plane. The beam energy was about 10 keV, duration of beam pulse was 10^{-4} s, beam dimension in the poloidal direction was 2 cm, fraction of H_0^2 of the beam was very small (about 1%) but enough for measurements.

Due to geometry conditions the measurements were carried out only near the plasma axis ($r < 5$ cm). B_φ was measured as a function of the radius in the main torus plane, position of plasma current was determined and the current density, $j(r)$, near the axis of the discharge was calculated from these data. Ohmically heated helium discharges in the toroidal magnetic field $B_\theta = 5.2$ kG, with mean plasma density $\bar{n}_e = 1 \cdot 10^{13}$ cm^{-3}, Zeff = 3 were investigated. The TUMAN-3 device dimensions are: major radius $R_k = 55$ cm, minor radius $a = 23$ cm. Measurements were made in steady state period of the

discharge for two values of the plasma current I_p = 40 kA and I_p = 70 kA (regimes Ia and Ib) and for the initial period of the discharge for different current ramps: "slow" (~ 4 MA/s, regime II) and "fast" (~ 12 MA/s, regime III). For regimes II and III the different technique of the preionization was used: only electron cyclotron radiation (EC) or (EC + UV) radiation. In the latter case the breakdown voltage was lower.

Results of B_φ measurements for regimes Ia and Ib are presented in Fig.1 as a function of the radius.("+" - for B_φ up, "-" - for B_φ down)It is seen that the current density which correlates with a slope of the $B_\varphi(R)$ dependence is the same for both regimes (~ 53 $\pm$ 5 A/cm^2) but the discharge axis moves inside at 2 cm with increasing plasma current from 40 kA to 70 kA. Both these effects can be explained by broadening of the current density distribution and by decreasing of the internal inductance.

Fig.2 shows the discharge oscillograms for regime II and III: plasma current I_p, soft and hard X-ray emissions and signal of the X-ray spectrometer for $E_\gamma \simeq 1$ MeV (N_γ). Fig.3 presents the results of the measurements (circles, triangles and crosses) together with computer simulated current distributions for regimes II and III (solid curves). For the simulation computer code developed in [4] was used. Model for calculation of the time evolution of the current distribution is based on the neoclassically conductivity, the experimentally observed time evolution of the mean plasma density and plasma current as well as time evolution of B_θ were taken into account in simulating the j(r). From comparison of the experimental and simulated results one can conclude that in the case of the fast current ramp (regime III) current penetration is determined by classical skin effect for both types of the preionization (EC - open triangles, EC + UV - full triangles). For regime III current penetration depends on the type of the preionization and, respectively, of the breakdown voltage. For the lower breakdown voltage (EC + UV preionization, full circles) the plasma current density j(r) near the discharge axis is rather close to j(r) determined by the classical skin effect. In the

case of the high breakdown voltage (EC preionization, open circles) current penetration time is much higher. At the 10 ms of the discharge there are piratically no the current in the center plasma and it becomes measurable at the 20th ms. The time evolution of the γ-ray flux with $E_\gamma \simeq 1$ MeV (Fig. 2) shows that in this regime there is a beam of the accelerated electrons in the plasma up till 17th ms of the discharge. Conditions of the generation of such beam in TUMAN-3 plasma are discussed in [5]. These results shows that the beam has a hollow shape and it screens, for instance [6], the central discharge part from the current penetration.

The authors would like to express their gratitude to P.N.Yushmanov for his help in the calculations of the current density distribution.

1. F.C.Jobes. 2nd Topical Conf. on High-Temperature Plasma Diagnostics. Santa Fe, 1978. Report LA-7160-C, p.101
2. W.Herrmann. 16th Europ. Conf. on Contr. Fusion and Plasma Heating. Venice, 1989, v.13B, Part IV, p.1541
3. V.I.Afanasjev, F.V.Chernyshev, A.I.Kislyakov et al. Preprint 1406, Ioffe Physical-Technical Institute, 1989 & PISMA V GETF, 50, 1989, 453-457 (in Russian)
4. G.V.Pereverzev, P.N.Yushmanov. Preprint IAE-4545/15, Kurchatov Institute of Atomic Energy, 1987 (in Russian)
5. S.E.Bender, G.N.Deshko, A.B.Izvozchikov et al. 15th Europ. Conf. on Contr. Fusion and Plasma Heating, Dubrovnik,1988, p.I, 71-74.
   N.I.Vinogradov, A.B.Izvozchikov, K.G.Shahovets et. al. Preprint 1177, Ioffe Physical-Technical Institute, 1987. (in Russian)
6. H.Knoepfel, D.A.Spong, S.J.Zweben. Phys. Fluids, 1977, v.20, p.511

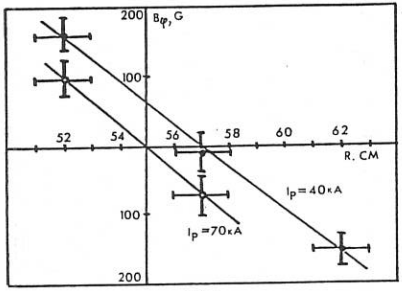

FIG.1

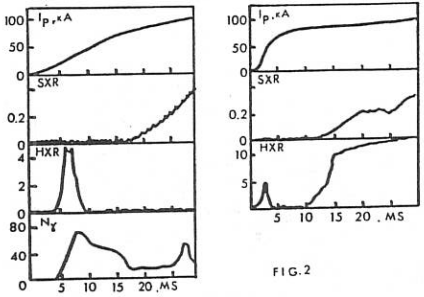

FIG. 2

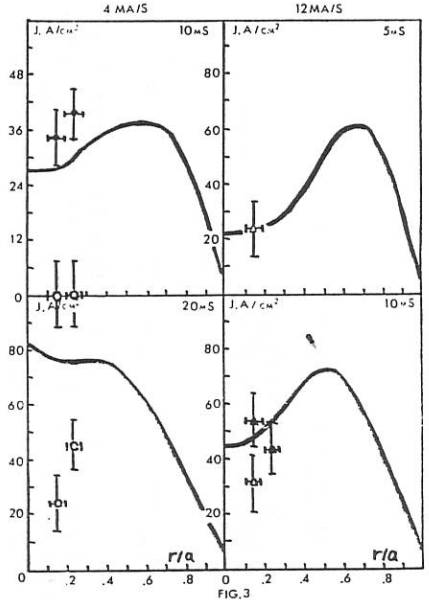

FIG. 3

OHMIC DISCHARGES IN TORE SUPRA - MARFES AND DETACHED PLASMAS

J.C. VALLET and TORE SUPRA TEAM

Association Euratom-CEA sur la fusion
CEN Cadarache 13108 Saint-Paul-lez-Durance

1 / TORE SUPRA PLASMA CHARACTERISTICS

TORE SUPRA current recently reached 1.9MA exceeding the 1.7MA design value. Experiments are usually carried out with D.C. 4 Tesla toroidal field. Discharges are either leaning on the graphite inner first wall or limited by movable pump limiters located outboard and at the bottom of the vacuum chamber. The plasma major radius can be changed, typically from 2.25m to 2.45m, the maximum minor radius is .8m for either situation. Density is controlled by preprogrammed of feedback gas puffing and by pellet fuelling. Both deuterium and helium have been used. the volume average density was varied from $1.10^{19}m^{-3}$ to $4.10^{19}m^{-3}$.

A 1.MA D_2 typical discharge with density $2.10^{19}m^{-3}$ has ion and electron central energy of 1.8keV and 2.2keV respectively. Energy lifetime from diamagnetic measurements is .18s in accordance with integration of local energy content.

2 / RADIATIVE PHENOMENA.

a) experiments

In this section, we investigate particular plasma conditions which lead to Marfes and Detached Plasmas in ohmically heated He and D_2 discharges limited by the inner wall (major radius $R_0 \approx 2.31m$, minor radius $a \approx .75m$). Marfes and Detached Plasmas are studied with various space and time resolved diagnostics: Bolometers [1] (16 vertical chords), I.R.interferometers (5 vertical chords), E.C.E Michelson giving Te profiles along the major radius, Soft Xrays (43 vertical chords), and $H\alpha$ signal (18 vertical chords). The line integrated data are inverted using the equilibria identified by the IDENTC magnetic code. Plasma parameters are $2. \leq B_T \leq 4.T$, $.3 \leq Ip \leq 1.8MA$, $1. \leq n_e \leq 4.10^{19}m^{-3}$, $Te_0 \leq 2.5keV$. For this study the key parameter is the M.q product, M is the Murakami parameter and q the safety factor - $M.q \approx 1.6\rho$ with $\rho = \pi a^2 n_e / Ip$ as defined in [2]. The maximum M.q value corresponds to the density limit.

On Tore Supra the ratio of the total radiated power to the ohmic power is found to grow linearly with M.q. The slope for He is approximately one third of the slope for D_2 (fig.2).

The following phenomena: Attached Plasma, Marfe, Detached plasma, have characteristic signatures on radiation profiles (fig 1 raw profiles). They are

sequentially observed when the M.q product is risen. The inverse sequence may be observed when M.q is decreased. For a given gas and a given impurity content the thresholds for transitions from Attached Plasmas to Marfes and from Marfes to Detached Plasmas ,like the density limit itself, correspond to particular M.q values.

b) Attached plasmas

Attached plasmas are characterized by a strong poloidal asymmetry in the non inverted radiated power profiles, with a maximum located in front of the inner wall, due to gas recycling. The ratio of the radiated power in the asymmetrical part of the profile to the total radiated power (P_{asy}/P_{rad}) is also found to grow linearly with M.q (fig 3), the slope is the same for He and D_2,.

For very clean He discharges , the ratio P_{asy}/P_{rad} reached 60% for M.q≈15($10^{19}m^2T^{-1}$), and 35% for M.q≈8.5 in D_2. When M.q is risen above these thresholds, plasmas enter in the poloidally moving Marfes region [3], and the profile asymmetry begins to decrease.

c) Marfes

Marfes are initialized in the equatorial plane, on the high field side, and then move up (in the ion drift direction) on a time scale of several seconds even during steady state plasma operation. The poloidal extension of the Marfe is about 30° and the line integrated density perturbation is about $10^{18}m^{-2}$ as observed when the Marfe crosses the I.R. interferometer inner chord. When M.q reaches 16. or 17. for He, or 9. for D_2 the bolometer profile asymmetry reaches a very low level plasma gets detached.

d)Detached plasmas

Plasma detachment phases are monitored by the reduction of the Hα signal [4] integrated along a line of sight which intercepts the inner wall in the equatorial plane, i.e. where the plasma-wall interaction is maximum. Usually for attached plasma this signal is roughly proportional to the plasma current, this relationship disappears when the plasma detaches (fig 4). Detached plasmas are produced during dynamical phases i.e. gas puffing or current decay [5].Common features for Detached Plasmas are: the radiated power approximately equals the ohmic power , radiation are coming from a very poloidally symmetric shell localized at the plasma edge, the plasma radius become much smaller than the radius defined by the main limiter (inner wall), all profiles ,electron density, electron temperature, soft Xrays, contract in the radial direction, the hot plasma core is surrounded with a cold and tenuous plasma.

On Tore Supra plasma detachments may also be observed during the initial rise of the plasma current. In this case temperature profiles are found very peaked all along the fast current ramp up (fig.5b). This temperature profile evolution have to be correlated with anomalous current diffusivity effect [6]. Detached plasma phases are often terminated by a series of minor disruptions corresponding to the density limit effect. Density limit is encountered for M.q≈25 in He and M.q≈10. in D_2. One effect of the first minor disruption is to re-attached the plasma to the main limiter, in a time scale less than 10 ms. The minor disruptions are accompanied by inward motions of the plasma column. On figure 4 the plasma current oscillations at the end of the discharge are due to

these minor disruptions,the delay between the plasma current and the $H\alpha$ signal is given by the integration time (32ms) on $H\alpha$.

e)profiles evolution

This sequence of events is for example observed on the He discharge 2246. This discharge is not in the cleanest He discharge series, so that the transitions expressed in M.q are:

$$A.P. \leq 5.5 \leq Marfe \leq 7 \leq D.P. \leq 12 \approx D.L.$$

Figure 1 and figure 4 show that plasma evolves from detached in the current rise (T1=.24s) to Attached Plasma (T2=1.96s) ,goes to Marfe regime (T3=2.5s) and then back to detached phase during current decay (T4=2.97s). Figure 5a shows the evolution of the radiating shell obtained by Abel inversion at T2 and T4. At T2 only the outer half profile is inverted . At T4 both ohmic and radiated power are equal to 800kW , the maximum emissivity is 85 kW/m^3 at $r/a \approx .5$,and 0. for $r/a \geq .7$. Fig 5.b gives the electron temperature profiles on the equatorial plane for T1,T2 and T4 . At T1 the profile is nearly triangular with Te < 50eV at $r/a \approx .5$. At T4, the temperature on axis is still 1.2keV,and is well below 50eV for $r/a \geq .5$. The temperature profile at T4 presents a large Shafranov shift ,which agrees with the high internal inductance ($li \approx 2.8$) given by IDENTC with $\beta pol \approx 0.1$. Figure 5.c gives the electron density profiles at T2 and T4. On the current flat top $q_a \approx 7$ and $q_0 \approx 1.05$, at T4 $q_a \approx 12.5$ and q_0 drops below 1. 0, IDENTC localizes the q=3 surface at $r/a \approx .5$. Figure 6. shows soft xrays profiles evolution from attached to detached plasma for D_2 shot 2340.

3 / CONCLUSIONS

1) The ratio of radiated power to ohmic power is found to grow linearly with M.q
2) Attached plasma, Marfe, Detached plasma are sequentially observed when M.q is risen.
3) Detached plasma with an effective radius as small as .7 time the limiter radius was observed on TORE SUPRA.

References :

[1] C. ANDELFINGER, F. MAST, G. SCHRAMM, J.C. VALLET, W. WEBER
15th symp. on Fusion Technology,Utrecht September 13-17 1988

[2] B. LIPSCHULTZ
Journal of Nuclear Material 145-147 (1987) p. 15-25

[3] F.P. BOODY, C.E. BUSH, S.S. MEDLEY, H .K. PARK, J.F. SCHIVELL
Journal of Nuclear Material 145-147 (1987) p. 196-200

[4] U. SAMM AND R.R WEYNANTS
16th European conf.on controlled fusion and plasma physics, Venice March 13-17 1989

[5] J.F.SCHIVELL, C.E. BUSH, D.K. MANSFIELD, S.S MEDLEY, H.K. PARK
Fusion Technology, vol. 15, July 1989 p. 152

[6]D.J. CAMPBELL, E. LAZZARO,M.F.F.NAVE, J.P.CHRISTIANSEN,J.G. CORDEY
F .C. SCHULLER ,P.R. THOMAS Nuclear Fusion , vol. 28,No.6 (1988)

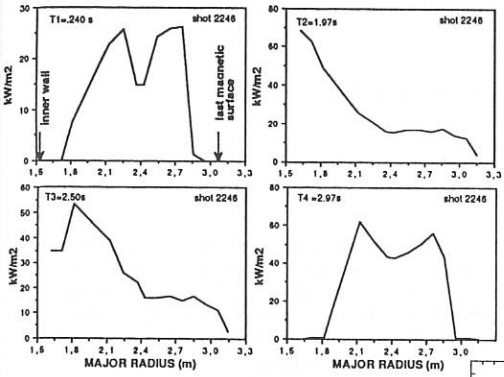

Fig.1 (four raw bolometer profiles)

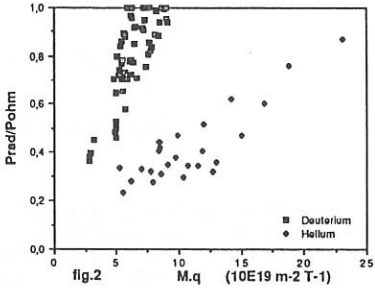

fig.2

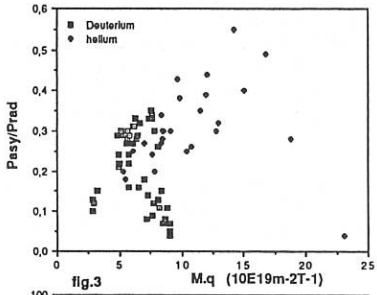

fig.3

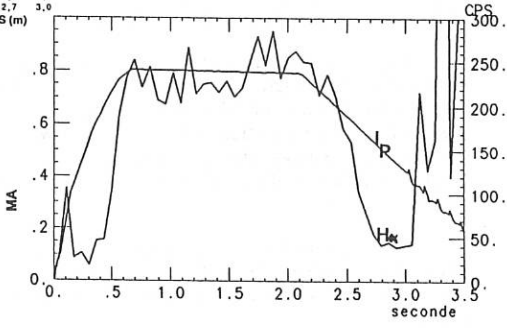

fig.4

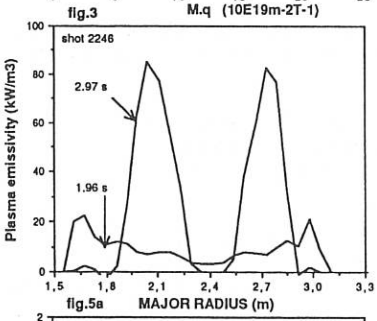

fig.5a

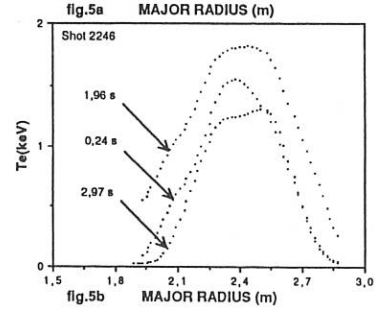

fig.5b

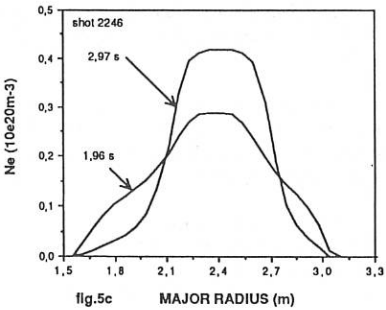

fig.5c

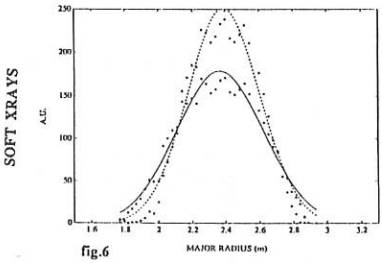

fig.6

TOROIDAL PLASMA ROTATION IN JET

H P L de Esch, D Stork and H Weisen

JET Joint Undertaking, Abingdon, Oxon OX14 3EA, UK

A database has been constructed which contains data on toroidal plasma rotation, collected from nearly 200 JET pulses where near 'steady-state' (ie., the beams had been on for at least 0.6 seconds and $d\omega/dt \sim 0$) rotation conditions exist. Neutral Beam Injection (NBI) heated discharges without ICRH heating or strong MHD modes exhibit a rotation velocity which strongly correlates with the ion temperature, indicating that the mechanism for NBI heating is also responsible for rotation and that ion thermal energy and momentum losses are also quite similar.

Figure 1 gives the central angular frequency as a function of the central ion temperature. It is readily seen that neutral beam only heated plasmas (open symbols) have a rotation velocity proportional to their ion temperature. $d\omega/dT_i$ is 6.2 krad/(s keV). Similar graphs have been obtained in other positions of the plasma with $d\omega/dT_i$ between 6 and 8 krad/(s keV). Distinguishing between the open symbols in Fig.1 suggests that H-mode plasmas rotate slightly faster than plasmas which are materially limited, with X-point plasmas in L-mode somewhere in between.

Application of RF (black diamonds in Fig.1) slows the plasma down. This is not an artifact of extra RF ion heating without the momentum input which the beams provide, but a real slowing down. As soon as the RF switches on the rotation decreases. This confirms data described earlier in [1].

MHD modes slow the plasma down even more. Locked modes bring the plasma completely to a halt. The influence of MHD and locked modes on plasma rotation is described in more detail in [2].

The results given in Fig.1 are independent, at least to first order, of the main plasma parameters (I_p, B_ϕ, n_e, Z_{eff}, T_e, q and of the nature of the limiter surfaces (carbon, beryllium or berylliated carbon). Plasmas have been observed in which n_e or Z_{eff} changed strongly, whereas the other parameters, including rotation, remained constant.

The fact that the rotation frequency is proportional to the ion temperature (with an offset for H-modes and X-points) enables us to compare the momentum and ion thermal transport coefficients directly with great accuracy. In steady-state ($\partial/\partial t = 0$) and in the absence of convection (heat pulse propagation measurements suggest this is true for $r/a<0.9$) the momentum and ion heat diffusivities χ_ϕ and χ_i are given by:

$$\frac{1}{r}\frac{d}{dr}\left(rmn\chi_\phi \frac{d\omega R}{dr}\right) = \frac{2\left(P_{nbi}(r) + P_{nbe}(r)\right)}{V_b}\frac{R_t}{R}(1\text{-}\ldots) \qquad (1)$$

$$\frac{1}{r}\frac{d}{dr}\left(rn\chi_i \frac{dkT_i}{dr}\right) = -P_{nbi}(1\text{-}\ldots) + P_{ie} + \frac{\omega R}{r}\frac{d}{dr}\left(rmn\,\chi_\phi \frac{d\omega R}{dr}\right) \qquad (2)$$

in which m is the plasma ion mass, n the density, ω the angular frequency, R the major radius, R_t the beam tangency radius (R_t/R~0.5 at JET), V_b the beam particle velocity, P_{nbi} the beam power to the ions, P_{nbe} the beam power to the electrons and P_{ie} the power from the ions to the electrons. The missing terms in the brackets correspond to small corrections for the reduction in heating and momentum input which arise from charge exchange losses and the effects of the relative motion of the rotating plasma on the deposition by the beams.

By setting $\omega = \alpha T_i + b$ and $\chi_\phi = ß\chi_i$ (α, ß and b constant) we can eliminate the d/dr() terms in (1) and (2) and obtain:

$$\beta = \chi_\phi / \chi_i = \frac{2 R_t}{\alpha\, m R^2 V_b} \left(1+\frac{P_{nbe}}{P_{nbi}}\right) / \left(1+\frac{P_{ie}}{P_{nbi}}\right) \qquad (3)$$

The missing terms of eqs.(1) and (2) cancel in first order. Taking them into account in eq.(3) gives a few percent difference.

Equation (3) is derived for a pure plasma (whether deuterium, pure carbon or pure beryllium). In JET there is usually one main impurity: carbon (in the carbon limiter phase) or beryllium (in the beryllium limiter phase). Labelling deuterium with D and the impurity with Z (Z=6 for carbon and Z=4 for beryllium) we define the effective diffusivities:

$$<\chi_\phi> = \frac{m_D n_D \chi_\phi^D + m_Z n_Z \chi_\phi^Z}{m_D n_D + m_Z n_Z} \text{ and } <\chi_i> = \frac{n_D \chi_i^D + n_Z \chi_i^Z}{n_P + n_Z} \qquad (4)$$

noting that $m_Z \simeq Z\, m_D$; $n_Z/n_e = (Z_{eff}-1)/(Z(Z-1))$ $n_D/n_e = (Z-Z_{eff})/(Z-1)$ we obtain:

$$\frac{<\chi_\phi>}{<\chi_i>} = \frac{Z+1-Zeff}{Z} \frac{n_D\chi_\phi^Z + Zn_Z\chi_\phi^Z}{n_D\chi_i^D + n_Z\chi_i^Z} \equiv \frac{Z+1-Z_{eff}}{Z}\beta_D \qquad (5)$$

Plotting $ß_D = Z/Z+1-Z_{eff} * <\chi_\phi>/<\chi_i>$ against T_i yields the picture given in Fig.2. The data in Fig.2 has been measured over a full range of plasmas, ie., from almost pure deuterium to almost pure beryllium or carbon and many intermediate mixtures. Only data points accurate to within 20% have been included in Fig.2. This means that $ß_D = 1.0 +/- 0.3$ for all JET plasmas without RF or strong MHD and $T_i > 4$ keV. This translates into:

$$\chi_\phi^Z = \frac{(1 \pm 0.3)}{Z} \chi_i^Z \qquad (6)$$

This simply reflects the fact that rotation is no different for a pure carbon (beryllium) plasma as for a pure deuterium plasma. The result given in formula (6) agrees with the prediction of η_i theory for deuterium, which claims $\chi_\phi = \chi_i$. No predictions about non hydrogen isotopes can be made with η_i theory in its present state.

Momentum diffusivities have been directly compared with the values given by η_i theory [3,4]. N Mattor points out that the formulae given in refs.[3,4] are superceded by [5] (and cautions that this and other predictions from η_i theory must be regarded tentative conclusions based on idealised models and not as the single prediction from η_i theory):

$$\chi_\phi = 0.037 \frac{L_s^2}{L_n^3} \frac{(m)^{1/2}}{(eB)^2} \frac{T_e^3}{(T_i+T_e)^{3/2}} (\eta_i - 1.2)^3, \quad \eta_i = \frac{L_n}{L_{T_i}} \qquad (7)$$

The errors on the value of χ_ϕ given in this expression corresponds even in the best cases to approximately 100%, even when discounting the errors in the numerical constants. The correct order of magnitude is obtained by using [7], except for plasmas with flat density profiles (notably H-modes), where χ_ϕ is calculated an order of magnitude too high. Figure 3 gives the prediction from η_i theory for a number of selected pulses where the density profile is well determined. Reciprocal diffusivities have been plotted. The pulses with a very flat density profile (γ=0.0; black diamonds) do not agree with η_i theory, the pulses with more peaked profiles do, within the rather large error bars (open symbols).

Our results contradict the gyroviscous theory [6] which gives an explicit formula for the rotation velocity. The expression given in [6] was modified in the following way to reflect the situation at JET. To account for a situation with deuterium and one dominant impurity species, we rederived the expression from the gyroviscous coefficients given for any species Z. This leads to the replacement of Z_{eff} by $Z/(Z+1-Z_{eff})$. As the angle of tangency of the beams had not been taken into account we added a factor R_t/R~0.5. This reflects the fact that perpendicular beams (R_t=0) would cause no plasma rotation. The gyroviscous theoretical expression thus reads:

$$\omega(r) = \frac{2\left(P_{nbi}(r)+P_{nbe}(r)\right) R\, e\, B}{m_D\, T_i(r)\, n_e(r)} \left(\frac{2m_b}{E_b}\right)^{0.5} \frac{Z}{Z+1-Z_{eff}} \frac{R_t}{R} \qquad (8)$$

and this was compared with the data from Fig.1 without MHD.

The comparison is given in Fig.4. The errors in the calculated values are around 50%. The gyroviscous rotation velocities are an order of magnitude too low (ie. the gyroviscous stress prediction is an order of magnitude too high), except for a few cases which have a low T_i and a high Z_{eff} due to carbon bloom phenomena. This disagreement should not be a surprise as the scaling $1/T_i$ is obviously wrong when Fig.1 is compared.

CONCLUSIONS

NBI heated plasmas without RF or strong MHD modes show a rotation velocity which increases linearly with the ion temperature and shows little dependence on other parameters.

This leads to the momentum diffusivity χ_ϕ being equal to $(1 \pm 0.3)/Z$ times the ion heat diffusivity χ_i. This agrees for deuterium with η_i theory, which predicts $\chi_\phi=\chi_i$. The order of magnitude of χ_ϕ agrees with η_i predictions, except for flat density profiles, where the prediction is an order of magnitude too high. The present data invalidate the gyroviscous rotation theory, which predicts the rotation velocity an order of magnitude too low in nearly all cases.

REFERENCES

[1] D Stork et al., contrib. paper 14th European Conf. on Contr. Fus. and Plasma Phys., Madrid (1986). Europhysics Conf. Abstracts, Vol 11D, I, pp.306-309.
[2] J A Snipes et al., Nucl. Fusion 30(1990)205.
[3] N Mattor, P H Diamond, Phys. Fluids 31(1988)1180.
[4] N Mattor, P H Diamond, Phys. Fluids B1(1989)1993.
[5] N Mattor, Culham Report CLM-P872 (1989) and private communication.
[6] W M Stacey, C M Ryu, M A Malik, Nucl. Fusion 26(1986)293.

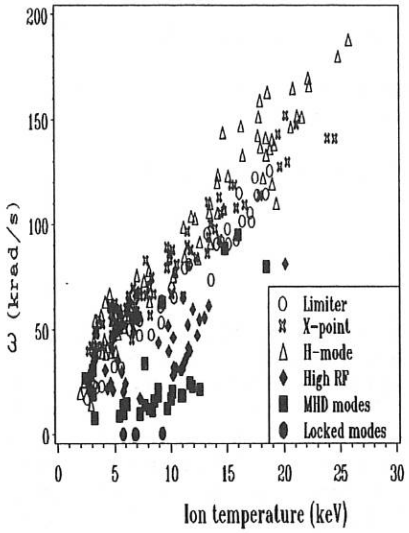

Fig. 1: Rotation frequency versus ion temperature. The effect of RF heating and MHD activity.

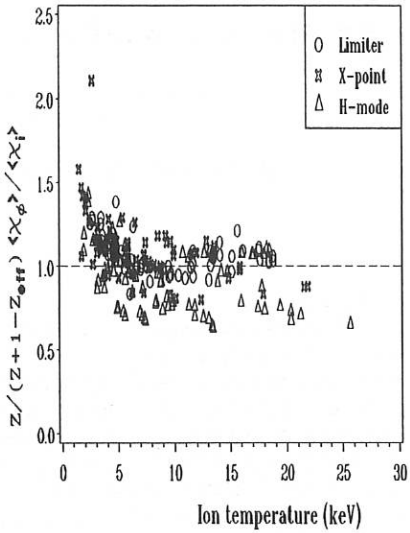

Fig. 2: Ratio of momentum and ion heat diffusivities. Data with RF or strong MHD have been excluded.

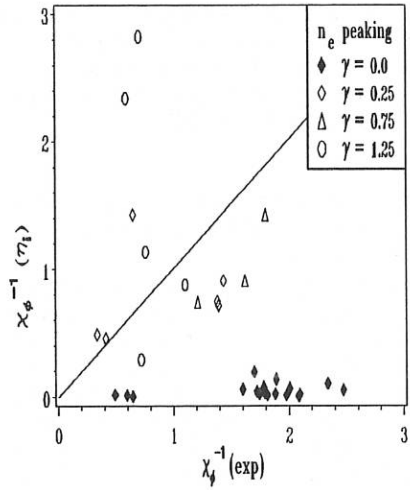

Fig. 3: Reciprocal of momentum diffusivities. Comparison of η_i theory with experiment.

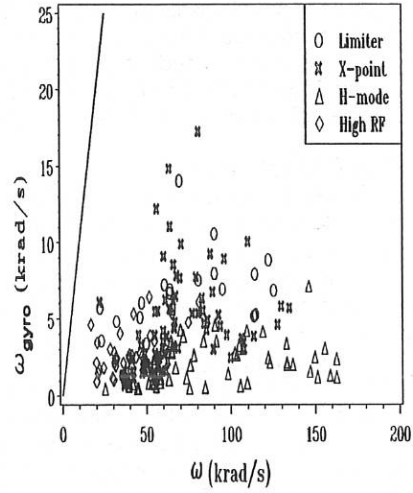

Fig. 4: Gyroviscous rotation prediction versus experiment. Data with RF or strong MHD have been excluded.

Max-Planck-Institut für Plasmaphysik
8046 Garching bei München

ELM-FREE H-MODE WITH CO- AND CTR-NEUTRAL INJECTION IN ASDEX

F. Ryter, O. Gruber, O. Vollmer, F. Wagner,
ASDEX-Team, NI-Team

Max-Planck-Institut für Plasmaphysik, Euratom-Association
D 8046 Garching

1. Introduction

Since the discovery of the H-mode, the divertor of ASDEX has often been modified. In the first configuration till the hardening [1] in 1986, the conductance of the by-pass between the divertor and the main chamber was low and the power threshold to obtain the H-mode was around 1 MW. Under these conditions the H-mode was discovered and extensively studied [2]. After the hardening this conductance was about 3 times larger and the power threshold was considerably higher (1.8 MW). During summer 1989 the conductance has been reduced again to the level of the first version by closing the by-passes and the power threshold is back to 1 MW. The plasma profiles evolve differently after the onset of the H-phase when the divertor is open or closed. For the open divertor a density pedestal develops after the transition while for the closed divertors the density increase at the edge is moderate and the electron temperature increase is larger. It is also observed that, on the average, the improvement factor of the H-confinement compared to the Goldston scaling [3] is about 1.4 for the open configuration and 1.8 for the closed ones. This paper presents confinement studies performed since the divertor has been closed again and particularly the scaling of H-discharges with only few Edge Localised Modes (ELMs). Long ELM-regulated stationary H-phases were studied separately and are presented in a companion paper [4].

2. Experimental conditions:

Most of the discharges analysed here were performed under boronised conditions. With boronisation Z_{eff} is close to unity during the ohmic phase and the iron influx from the wall during injection is strongly reduced.

We obtained ELM-free discharges over a large range of plasma currents 280 kA $\leq$ Ip $\leq$ 460 kA and magnetic fields 1.5 T $\leq$ Bt $\leq$ 2.6 T. We had hydrogen or deuterium neutral injection into deuterium plasmas. The injection power was 2.4 MW for hydrogen injection and 2.7 MW for deuterium injection, except for few discharges in which we performed a power scan. The key parameter for obtaining discharges with few ELMs is the plasma position possibly due to the stabilising effect of the vessel wall. This is illustrated in Fig. 1 and Fig. 2 which show an optimum of the ELM-free duration for the horizontal position around Rp = 1.68 m and for the vertical position around z = 1.5 cm. The longer ELM-free H-phases were obtained at low current and magnetic field and lasted between 150 ms and 190 ms.

The discharges studied here are not stationary: after the L-H transition the

plasma energy, the density and the radiation increase rapidly. The quiescent phase is terminated by sequences of ELMs, causing a rapid drop in plasma energy and density, and finally either by a disruption or a back-transition into the L-mode. These discharges have no sawteeth during the H-phase. Although not stationary, these discharges allow scaling studies of the H-confinement without strong perturbation of the ELMs.

3. Confinement:

3.a) co-NI

Among the discharges, we selected the ones having an ELM-free phase lasting longer than 50 ms (typical confinement time) or having only few single ELMs over a longer period and therefore a strong energy increase. Fig. 3 shows the confinement time normalised to the Goldston scaling for the corresponding parameters versus plasma current for these discharges and for some L-discharges. The improvement of confinement in the H-mode decreases with plasma current. To compare the intrinsic confinement during L- and H-phases, the confinement time of the H-phase is corrected for the radiated power in the central region. This is necessary because of the strong central radiation during the quiescent H-phase due to impurity accumulation, essentially copper originating from the divertor neutralisation plates. The correction is made in the form $\tau_E^{cor} = \tau_E(1- \int P_{rad} / \int P_{heat})^{-1}$. The integrals are calculated in the central region for $r/a \leq 0.5$. This is justified by TRANPS analysis which showed that the radiation corrected local confinement time is nearly constant over the main part of the plasma cross section. The results with correction are also reported in Fig. 3. It seems that the degradation with plasma current is stronger for the corrected confinement. In fact, the radiation power in the central region is somewhat higher for the low values of the plasma current. This related to the longer duration of the quiescent phases obtained at low current. Fig. 4 shows the confinement time versus plasma current with and without radiation correction. Without radiation correction the confinement time increases linearly with Ip ($\tau_E \approx$ 0.17 Ip) except for the highest Ip values. It must be noted here that the density is very similar for low and high current and therefore the beam deposition profile is the same. The radiation corrected values introduce a clear variation of the quality factor τ_E/Ip with Ip. Its dependence versus q_a of great importance for a reactor study, is given in Fig. 5. A clear maximum of the quality factor is obtained around $q_a = 3$ both for corrected and uncorrected confinement times. Many of the results for $q_a < 3$ were obtained for currents lower than 420 kA indicating that q_a is possibly the key parameter for τ_E/Ip and not Ip.

In the recent conditions we made a power scan between 1.2 and 2.2 MW for totally ELM-free discharges to study the power dependence of τ_E. Fig. 6 shows a power dependence which is comparable with the L-mode scaling and a stronger decrease with power when the confinement time is corrected for radiation. For the radiated corrected points the heating power is $P_{tot} - P_{rad}(0 \leq r/a \leq 0.5)$. This results confirm earlier findings [5].

3.b) Ctr-NI:

As already observed before, the H-mode power threshold is 20% lower for counter neutral injection (Bt and Ip reversed) than for co-NI. We obtained 50 ms long absolutely ELM-free H phases with ctr-NI. The plasma energy decreases before the occurrence of ELMs due to the rapid increase of the central radiation and perhaps also due to the more off-axis power deposition of the beams. It follows that the confinement time normalised to the L-mode scaling is not as good as that obtained with co-NI as can be inferred from the data points in Fig. 3.

4. Beta limit.

Extensive beta limit studies during the H-mode were performed previously in ASDEX [6]. The limit manifested itself during a discharge by a smooth saturation of the plasma energy followed by a slow decrease, seldom by a disruption. Previously the beta limit was reached at 2.8 Ip/aBt. Beta is derived from the diamagnetic measurements. For the discharges presented here the maximum values of beta normalised to Ip/aBt are reported versus q_a in Fig. 5 which shows that now the Troyon factor is slightly larger than before. It must be noted that the maximum is now reached as beta is still increasing with time and it is limited by the occurrence of ELMs. This does not mean that the ELMs are the results of the beta limit because we also observe ELMs far from the limit, for instance at low power. We suppose that a better stabilisation of the ELMs would allow even higher beta values. We attribute this to the boronisation which reduces Z_{eff} and the central radiation. As a consequence, the current profile may be more peaked than before and gives rise to better stability of ballooning modes at similar pressure profiles.

Conclusion

With its new closed divertor configuration ASDEX is able to produce ELM-free H-discharges over a large range of machine parameters. It seems that the improvement of the H-confinement decrease with plasma current and that the quality factor has a maximum around q_a=3. Thanks to the boronisation the plasmas are cleaner than previously and higher beta values could be reached.

Acknowledgment

We wish to thank the operation teams of the ASDEX, and NI groups.
We are particular grateful to our colleagues who performed the boronisation.

References

[1] H. Niedermeyer et al., Plasma Physics and Contr. Fusion, 30, 11, (1988)
[2] The H-mode of ASDEX, Report IPP III/151, (1989)
[3] R. J. Goldston Plasma Physics and Contr. Fus. Vol. 26 (1984) 87
[4] O. Vollmer et al. Long-pulse heating in Asdex L- and H-mode discharges, this conference.
[5] F. Wagner at al. 15th EPS Conf. Europhysics Abstracts, Vol. 1 p. 207 (1988)
[6] O. Gruber et al. 11th IAEA Conf. Kyoto 1986 Vol.1 p. 357 (1987)

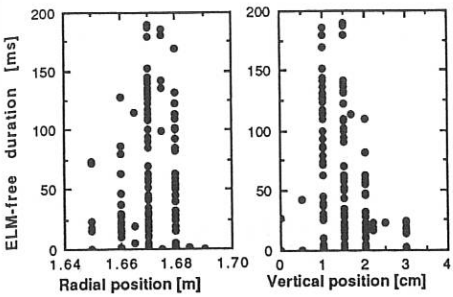

Fig.1 and 2: Influence of the plasma position on the ELM-free phase duration.

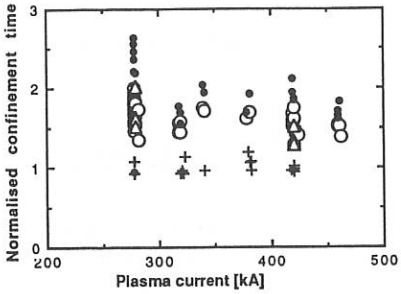

Fig. 3 Confinement time normalised to the Goldston scaling. crosses: L-mode; circles: co-NI without radiation correction and closed circles with correction; triangles: ctr-NI with correction.

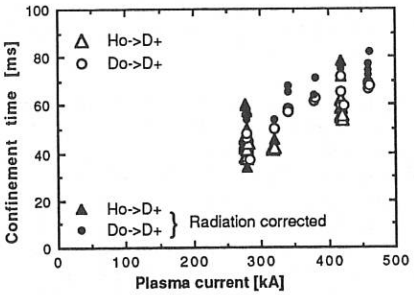

Fig. 4 Confinement time versus plasma current for co-NI discharges.

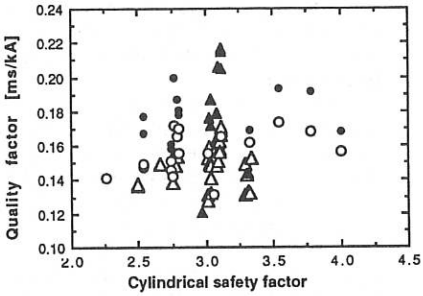

Fig. 5 Quality factor τ_E/I_p versus cylindrical safety factor. Same symbols as in Fig. 4

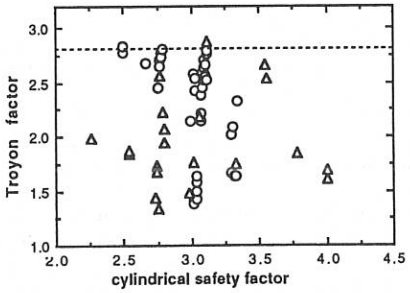

Fig. 6 Troyon factor Beta/(Ip/aBt) versus safety factor.The line indicates the earlier results. Same symbols as in Fig. 4

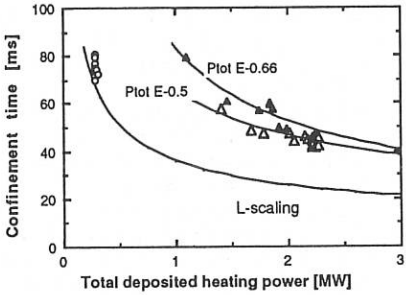

Fig.7 Power dependence of the confinement time for ELM-free discharges: Ho->D+, 280 kA,1.73T

A REGIME SHOWING ANOMALOUS TRITON BURNUP IN JET

S. Conroy, O.N. Jarvis, M. Pillon*, G. Sadler

JET Joint Undertaking, Abingdon, OX14 3EA, England
*Associazione EURATOM-ENEA, CRE Frascati, Italy

Abstract

Measurements of triton burnup made at JET in 1989 are in good agreement with a simple classical model of the triton slowing down, for the majority of discharges. For discharges with a long slowing down time (greater than 2 seconds), a much reduced burnup has been observed, suggesting that the tritons undergo diffusion with a diffusion constant of 0.10 $m^2 s^{-1}$. Also, the experimental 14 MeV neutron yield is 30% lower than expected for Beryllium limiter discharges.

Introduction

D-D fusion reactions produce nearly equal quantities of 2.45 MeV neutrons and 1.01 MeV tritons. The tritons are well confined in the JET plasma with a slowing down time of up to several seconds. Approximately 1% of the tritons undergo a D-T reaction, emitting 14 MeV neutrons. The 14 MeV neutron signal is delayed relative to the 2.45 MeV neutron signal, as the peak D-T fusion reactivity occurs at a triton energy of 180 keV. By observing both the 2.45 MeV and 14 MeV neutron signals, information on the thermalisation and confinement properties of tritons may be deduced. The information is of direct relevance to α particle heating. Previous publications have shown the behaviour of tritons in JET to be classical, within experimental errors [1].

Neutron detection and detector calibration

The 2.5 MeV neutron emission is measured with 3 pairs of fission chambers [2]. These are calibrated using activation techniques to an accuracy of better than $\pm$10%. The time-integrated 14 MeV neutron flux at a point just outside the vacuum vessel is measured through the induced activation of copper foils [3]. As copper is inconvenient to use on a shot-to-shot basis, a second activation reaction, $^{28}Si(n,p)^{28}Al$, is also used. ^{28}Al decays with a half-life of 2.24 minutes, emitting a 1.778 MeV γ ray. The short half-life and easily distinguishable γ ray make this an ideal material for automatic monitoring of the 14 MeV neutron yield per discharge. Time-resolved 14 MeV neutron emission rates are measured using (n,p) and (n,α) reactions in a 450mm^3 silicon diode positioned outside the vacuum vessel. The charged reaction products slow down in the diode, generating an output pulse-height spectrum proportional to the energy deposited. By counting only pulses corresponding to an energy of greater than 8 MeV deposited in the diode, a signal proportional to the 14 MeV neutron emission rate is obtained. The time resolved 14 MeV neutron detector was upgraded for 1989 by adding two Faraday shields around the diode to provide electrical shielding and introducing a water cooling system in order to stabilise the detector temperature.

The calibration of the 14 MeV neutron detectors is derived by use of neutron transport codes to relate the flux at the activation system irradiation ends to the total neutron emission from the plasma [4]. The copper activation has a better known cross-section than the silicon activation and hence is used to give the primary calibration. The silicon activation and silicon diode systems are both cross calibrated with the the copper activation, with an estimated error of $\pm 10\%$.

Data analysis

This is performed by comparing the experimental 14 MeV neutron emission rate with a simple classical model of the triton burnup. The simplest model consists of some 12,000 groups of tritons, the size of the group proportional to the 2.45 MeV neutron emissivity at the time and place of production. These groups are then allowed to slow down in the plasma using the classical test particle formulation of the energy loss rate. The time resolved neutron emission rate due to the triton group slowing down is calculated and summed over all the groups. It has been upgraded in order to allow the modelling of triton diffusion and loss of confinement effects. Diffusion is simulated by releasing 1,200,000 triton groups and allowing them to scatter randomly as they slow down, the amount of scatter dependent upon the diffusion coefficient. Comparisons with analytic solutions of the diffusion equation in cylindrical geometry are in good agreement with this technique. Loss of confinement is simulated by reducing the size of each group of tritons as they slow down, an exponential decrease of the form $e^{-t/\tau}$ being used. It is noted that the results from the loss of confinement model can be made to agree well with those from the diffusion model by a suitable choice of τ. This is of importance as the diffusion model is too slow for normal use.

Results

Figure 1 shows the absolute 2.45 MeV and 14 MeV neutron emission rates observed from a 4 MA X-point plasma with deuterium neutral beam heating and a primary plasma impurity of Carbon. The absolute calculated 14 MeV neutron emission rate is also shown and is in good agreement with the experimental data. The calculation uses purely classical triton slowing down and a 2.0 s confinement time, the origin of which is discussed later. This is in contrast to previously published results where a factor of 1.15-1.20 had to be applied to the energy loss rate of the tritons in order to obtain good agreement. The majority of discharges observed during the last experimental campaign had slowing down times less than 0.75 seconds and for these the confinement loss term has a minor effect ($< 20\%$).

Figure 2 shows the time integrated calculated 14 MeV neutron yield plotted against the measured 14 MeV neutron yields. The data points correspond to integrations over entire shots and have been selected by the following criteria; $I_p \geq 3$MA, $P_{NBI} > P_{RF}$, and $Z_{EFF} < Z_i$ where Z_i is the atomic number of the primary plasma impurity. The plasma current limitation restricts the discharges to those with a prompt loss fraction of less than 5%, necessary because the analysis code does not include this effect. P_{NBI} must be greater than P_{RF} in order to ensure that the bulk of the neutrons detected by the fission chambers are from D-D reactions. The Z_{eff} limitation is to limit the error on the calculated deuterium density estimation to $\pm 20\%$. The figure shows two well defined lines. The upper line corresponds to plasmas with beryllium as the primary impurity, whereas the lower corresponds to carbon.

The figure suggests that the model overestimates the 14 MeV neutron emission rate by 50% during Be impurity plasmas and underestimates by 10% during C impurity plasmas. The slowing down observed during each discharge appears to be well modelled, indicating the problem lies in the absolute calibration of the detector or the deuterium density profile used. As some of the C impurity plasmas occurred after the bulk of the Be impurity plasmas, it seems unlikely that the source of the discrepancy between C and Be impurity plasmas lies with variations in the absolute calibration of the 14 MeV neutron detector. A systematic error of $\pm 20\%$ could be attributed to the calculation of the axial deuterium density but cannot resolve the Be : C discrepancy. The most likely explanation lies in the use of line integrated visible bremsstrahlung measurements with assumed flat Z_{eff} profiles. Charge-exchange measurements indicate that the impurity profiles are peaked on axis for Be plasmas and flat, if not hollow, for C plasmas.

The confinement loss time of 2.0 s described earlier has been obtained from observation of a number of discharges where the triton slowing down time exceeded 2 seconds. These discharges had high electron temperatures (6-8 keV) and low electron densities ($\approx 10^{19} m^{-3}$) for an extended period. Figure 3 shows the measured 2.45 MeV and 14 MeV neutron emission rates and the calculated 14 MeV neutron emission rates for two conditions. All the calculated 14 MeV neutron emission rates have been divided by 1.5 as the discharge had Beryllium as the primary impurity. The purely classical calculation overestimates the 14 MeV neutron emission rate considerably in the later parts of the discharge, but not the earlier parts. This suggests that some process is occurring whereby the tritons are lost or transported to regions of the plasma where they cannot react. This has been simulated by using a diffusive transport term, D. Figure 3 also shows the calculated 14 MeV neutron emission rate with $D = 0.10 \pm 0.05$ $m^2 s^{-1}$. The diffusion can be modelled by a triton confinement loss time of 2.0 seconds and this factor has been incorporated into the rest of the calculations. It must be stressed that the results are of a preliminary nature and are dependent upon the accuracy of the data from a number of diagnostics. More work will need to be undertaken to confirm this result.

Conclusions

The time evolution of 14 MeV neutron emission indicates that for the majority of experimental regimes, a classical model of the energy loss rate of fast ions is a good approximation. Particle transport effects become more pronounced as the slowing down times increase, consistent with a triton diffusion coefficient of 0.10 ± 0.05 $m^2 s^{-1}$. Other interpretations of these observations may be possible. Hence, further work is required to make more definite statements. There also appears to be a systematic overestimation of the deuterium density by the 14 MeV neutron production simulation code when Beryllium is the primary plasma impurity, but not for Carbon.

References

[1] S. Conroy, O. N. Jarvis, G. Sadler, G. B. Huxtable, Nuc Fus **28** (1988) 2127

[2] O N Jarvis et al, 'Further calibrations of the time-resolved neutron yield monitor', JET IR(85)06

[3] P Batistoni et al, Proc. 15th European Conference on Controlled Fusion and Plasma Physics, Dubrovnik 1988, vol 12B part I (1988) 135 et loc cit

[4] M Pillon et al, 'Calibration of neutron yield activation measurements at JET using MCNP and FURNACE neutron transport codes', JET P(88)10

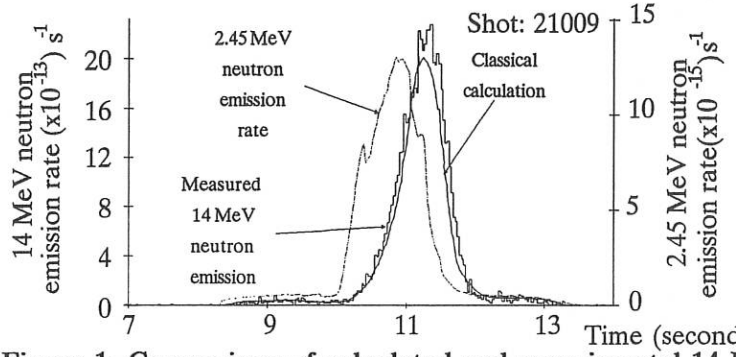

Figure 1: Comparison of calculated and experimental 14 MeV neutron emission rates for a carbon impurity plasma.

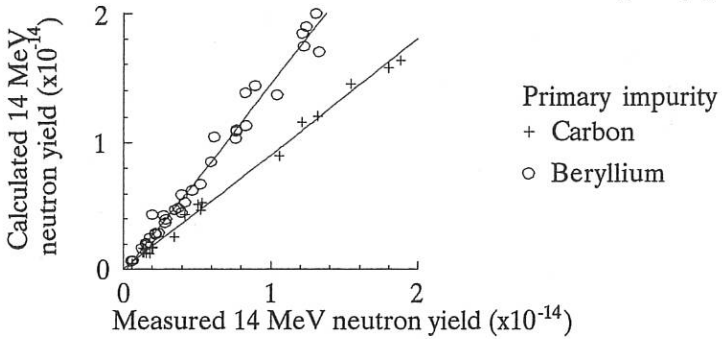

Figure 2: Calculated and measured 14 MeV neutron yields

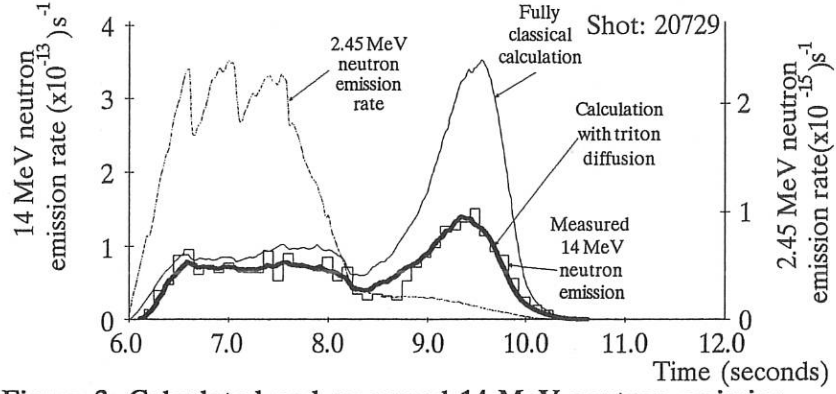

Figure 3: Calculated and measured 14 MeV neutron emission rates with and without the triton diffusion model

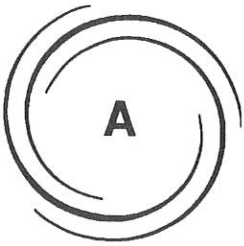

TOKAMAKS

A2 SCALING LAWS

A2

SCALING FROM JET TO CIT AND ITER-LIKE DEVICES USING DIMENSIONLESS PARAMETERS*

J. Sheffield

Fusion Energy Division, Oak Ridge National Laboratory, Oak Ridge, TN 37831, U.S.A.

1. DIMENSIONLESS SCALING FOR PLASMAS

A concern with the approach of empirical scaling [1] to predict the performance of future experiments is the lack of a theoretical basis for the prediction. A complementary approach, using dimensionless analysis to scale between experiments, was proposed by Bickerton and London [2], Kadomtsev [3], and Bickerton [4].

Since JET does not have identically the same dimensionless shape parameters, aspect ratio R/a, and ellipticity $\kappa = b/a$ as the present CIT and ITER, the scaling is made to the similar devices CIT′ and ITER′, operating at reduced field and current; 5.7 T and 6.5 MA for CIT′ and 1.5 T and 4.9 MA for ITER′. It is then argued that raising the field and current at constant q will improve the performance to a degree for which fairly close bounds can be deduced.

The dimensionless parameters for a fusion plasma are R/a, κ, δ, q, ν_*, ρ/a, β, A_i, Z_{eff}, n_e/n_i, T_e/T_i, ϕ/T, V/v_t, v_t/c, N_D, and λ_n/a [3], To make our analysis correct, the source terms for particles, momentum, and power input must also scale appropriately to maintain similar solutions for the governing equations [5]. In particular, the normalized power density $p/\eta j^2 =$ constant.

In practice, as pointed out by Kadomtsev, not all of the dimensionless parameters need be held constant or be specified. In typical tokamak conditions the number of particles in a Debye sphere N_D is not important, ϕ/T, V/v_t, n_e/n_i, and T_e/T_i are invariant if the other parameters are invariant, and v_t/c maybe neglected. For pellet fueling, the fueling by slow neutrals at the plasma edge will be small and λ_n/a may be neglected.

The physics scaling of alpha particle effects in burning plasmas is treated by Bickerton [4]. It is beyond the scope of this analysis.

Thus, the key dimensionless plasma parameters, assuming that R/a, κ, δ, q, A_i, and Z_{eff} are held constant, are the collisionality $\nu_* \propto (qRn)/T^2 = k_1$; normalized gyroradius $\rho/a \propto (A_i^{1/2}T^{1/2})/(aB) = k_2$; beta $\beta \propto (nT)/B^2 = k_3$; and the normalized power density $p/(\eta j^2) \propto (T^{3/2}P)/(B^2R) = k_4$; where P is the total power delivered to the plasma. If we now scale from one device to another, changing the field B, at constant R/a, A_i, and q; $a_2/a_1 = (B_1/B_2)^{0.8}$ then $T_2/T_1 = (B_2/B_1)^{0.4}$, $n_2/n_1 = (B_2/B_1)^{1.6}$, $P_2/P_1 = (B_2/B_1)^{0.6}$. The energy confinement time $\tau \propto (a^3nT)/P$ or $\tau_2/\tau_1 = B_1/B_2$. The confinement parameter scales as $[(nT\tau)_2]/[(nT\tau)_1] = B_2/B_1$. The current $I \propto aB$ or $I_2/I_1 = (B_2/B_1)^{0.2}$. The number of particles in a Debye sphere $N_D \propto T^{3/2}/n^{1/2}$ or

*Research sponsored by the Office of Fusion Energy, U.S. Department of Energy, under contract DE-AC05-84OR21400 with Martin Marietta Energy Systems, Inc.

$N_{D_2}/N_{D_1} = (B_1/B_2)^{0.2}$. The normalized neutral mean free path $\lambda_n/a \propto T^{1/2}/naA_i^{1/2}$ or $(\lambda_n/a)_2/(\lambda_n/a)_1 = (B_1/B_2)^{0.6}$.

2. JET PLASMA PERFORMANCE AT MAXIMUM PARAMETERS

JET performance is modelled well by the power scaling law developed by the ITER team [1], which has the virtue that it scales very nearly correctly with the dimensionless parameters. For the L-mode of operation,

$$\tau_E^{\mathrm{ITER}} = 0.048 A_i^{0.5} I^{0.85} B^{0.2} \langle n_{20} \rangle^{0.1} a^{0.3} R^{1.2} \kappa^{0.5} P^{-0.5} \ \text{(s)}$$

(with I in MA, B in T, the electron density $\langle n_{20} \rangle$ in particles $\times 10^{20}$ m^{-3}, R and a in m, and P in MW). Recent results from JET [6] operating in the H-mode at $B = 2.8$ T, $I = 4.0$ MA, $R = 3.1$ m, $\langle T \rangle = 5.5$ keV, and $\langle Z_{\mathrm{eff}} \rangle = 1.8$, with beryllium gettering, neutral beams, and ion cyclotron heating (ICH), are encouraging. The data may be used to benchmark H-mode performance. Using these parameters and comparing the result to the measured confinement time yields an H-mode factor of 2.55. For the purpose of assessing CIT′ and ITER′ performance, we estimate the performance of JET operated at full power and high density using the multiplier 2.55; see Table I.

Direct projections from JET to make the plasma volume of the new device CIT′ similar to CIT may be accomplished by setting $B_2/B_1 = 1.74$ (see Table I).

Approximately, if the projected plasma in Table I had been D-T, and ignoring any gain because $T_i/T_e > 1$, we would have for the fusion power $P_F \simeq 0.16 \kappa a^2 R \langle n_{20} T \rangle^2$ (MW), so $P_F \simeq 79$ MW with $P_\alpha \simeq 16$ MW. Therefore $Q = 79/(56 - 16) = 2$, at the low B, I values given.

3. SCALING CIT′ TO FULL PERFORMANCE USING THEORETICAL SCALE-UP

Now that the CIT′ performance has been obtained at approximately half the field and current, it is interesting to speculate on how the plasma performance will change when the field and current are raised at constant q and total power. As B and I are raised, the energy confinement time should improve and the temperature should rise at constant power. In order to keep the dimensionless parameters roughly constant, one may choose to increase the density. To minimize the difference in the projections of a variety of theoretical models I choose to set $n_3/n_2 = (B_3/B_2)^{0.9}$ (i.e. the dimensionless parameters will **not** be held constant).

A number of theoretical models are used for the thermal diffusivity χ. They are summarized by Ross [7]. As expected, each scales correctly with field,

$$\chi \propto \frac{a^2}{\tau} \quad \text{or} \quad \frac{\chi_2}{\chi_1} = \frac{t_1}{t_2} = \frac{n_1 T_1}{n_2 T_2} = \left(\frac{B_1}{B_2}\right)^{0.6} \quad \text{at constant power}$$

For everything fixed (including the profiles), except n, T, and B, the Perkins dissipative trapped electron (DTE) model has

$$\chi_a \propto \frac{T^{7/2}}{nB^2 L_n^2} \quad \text{or} \quad \frac{\chi_2}{\chi_1} = \left(\frac{B_2}{B_1}\right)^{1.4} \left(\frac{B_1}{B_2}\right)^{1.6} \left(\frac{B_1}{B_2}\right)^{2} \left(\frac{B_2}{B_1}\right)^{1.6} = \left(\frac{B_1}{B_2}\right)^{0.6}$$

The other models [7] to be used are the Perkins collisionless trapped electron model, the Diamond DTE model, the Diamond collisionless drift wave-1 model, the Horton ion temperature gradient model, the Garcia rippling model, and the Carreras resistive ballooning model. Setting $n_3/n_2 = (B_3/B_2)^{0.9}$, as discussed above with B_3 set at 10 T, yields for T_3/T_2 values varying from 1.27 to 1.44. Even in the worst case the plasma would ignite, see Table I.

4. SCALING FROM JET AND CIT TO ITER′

A similar scaling from JET to ITER′, see Table I, shows that the gulf (in terms of dimensionless parameters between experience in expected operating regimes which can be benchmarked on existing equipment and the operating regime of ITER) is substantially greater than the gap between existing devices and CIT.

By scaling with constant dimensionless parameters from JET one may identify the performance of a CIT-like device (CIT′) and an ITER-like device (ITER′) operating at reduced field and current. In fact, other devices, such as DIII-D and Alcator C-Mod, may be used to project the performance for CIT′ for a range of fields and currents (at constant q). Similarly, CIT′ may be added to the contributors in projecting ITER′ performance. The parameters of these devices are given in Table II for $q_{0.95} = 3.1$. Note that their aspect ratios and ellipticities are not identical. A reduced minor radius was used for DIII-D to make the aspect ratio more like those of CIT and ITER. The scaled parameters for ITER′ are given in Table III.

ACKNOWLEDGEMENTS

Discussions with P. Rebut (JET) on the proper scaling for power and with R. Bickerton (U. Texas) on the history of dimensionless scaling analysis were very helpful in the preparation of this paper.

This research was sponsored by the Office of Fusion Energy, U.S. Department of Energy, under contract DE-AC05-84OR21400 with Martin Marietta Energy Systems, Inc.

REFERENCES

[1] TAKIZUKA, T., MUKHOVATOV, V., Summary Report, ITER Confinement Workshop, ITER-TN-PH-9-2, Garching, FRG (1989) (to be published in *Nuclear Fusion*).
[2] BICKERTON, R.J., LONDON, H., *Proc. Phys. Soc.* **72** (1958) 116.
[3] KADOMTSEV, B.B., *Sov. J. Plasma Phys.* **1** (1975) 295.
[4] BICKERTON, R.J., Comments *Plasma Phys. Controlled Fusion* **13** (1989) 29.
[5] SHEFFIELD, J., submitted to *Nuclear Fusion*, ORNL/P-90/0979 1990.
[6] KEILHACKER, M., JET TEAM, *Bull. Am. Phys. Soc.* **34** (1989) 1912.
[7] ROSS, D.W., DIAMOND, P.H., DRAKE, D.F., et al., Thermal and Particle Transport in Tokamaks: Theoretical Models for Ignition Studies, Rep. FRCR-295 (DOE/ET-53193-7), University of Texas, Austin (1987).

TABLE I. SCALINGS FOR CIT′ AND ITER′

		CIT′		ITER′	
Parameters	JET	Scaled from JET	Scaled from theoretical models	Scaled from JET, $I = 6.0$ MA	Scaled from CIT′
R (m)	3.1	2.0	2.0	6.0	6.0
a (m)	1.1	0.7	0.7	2.13	2.13
κ	1.85	1.85	1.85	1.85	1.85
B (T)	3.3	5.74	10.0	1.45	2.53
I (MA)	5.8	6.48	11.3	4.90	8.60
q_ψ	3.6	3.6	3.6	3.6	3.6
P (MW)	40	56	56	24	24
A_i	2.5	2.5	2.5	2.5	2.5
$\nu_*/(\nu_*)_{\rm JET}$	1	1	1.02	1	1.02
$(\rho/a)/(\rho/a)_{\rm JET}$	1	1	0.64	1	0.64
$\beta/\beta_{\rm JET}$	1	1	0.69	1	0.69
$(P/\eta j^2)/(P/\eta j^2)_{\rm JET}$	1	1	0.47	1	0.47
$\langle n_{20}\rangle$	1.0	2.4	4.0	0.27	0.44
$\langle T\rangle$ (keV)	5.4	6.8	8.6	3.9	5.0
τ (s)	0.94	0.54	1.1	2.1	4.3
$Q_{\rm equivalent}$	0.9	2.0	∞	0.4	2.5

TABLE II. PARAMETERS OF PRESENT EXPERIMENTS ($q_{0.95} = 3.1$)

	DIII-D	C-Mod	JET
R (m)	1.67	0.67	3.1
a (m)	0.62	0.21	1.1
κ	1.85	1.80	1.85
B (T)	2.1	9.0	3.3
I (MA)	2.4	3.0	6.6

TABLE III. PARAMETERS FOR ITER′ ($q_{0.95} = 3.1$) SCALED FROM VARIOUS BASIC EXPERIMENTS

	Scaling experiment				
	DIII-D	C-Mod	JET	CIT′	ITER′
R (m)	6.0	6.0	6.0	6.0	6.0
a (m)	2.23	1.88	2.13	2.10	2.13
κ	1.85	1.80	1.85	1.85	1.85
B (T)	0.42	0.58	1.45	2.53	5.00
I (MA)	1.74	1.73	5.60	9.73	19.3

EXTRAPOLATION OF THE HIGH PERFORMANCE JET PLASMAS TO D-T OPERATION

by B. Balet, J.G. Cordey and P.M. Stubberfield

JET Joint Undertaking, Abingdon, Oxon, OX14 3EA, U.K.

Abstract D-T simulations of JET high performance plasmas are completed using the TRANSP code with differing injection configurations and particle transport models. Thermonuclear yields exceeding 10 MWatts are obtained with several scenarios, the best one being the injection of 140 keV D beams into a tritium background plasma. This scenario is sensitive to the particle transport model but injecting mixed deuterium (140 KeV) and tritium (160 keV) into a D-T background plasma is found to give a reasonably high yield (>9MW) and is not so dependent on the transport model.

I Description of high performance pulses

During 1989 several H- mode plasmas were obtained in which the D-D fusion yield exceeded 6×10^{16} reactions per second [1]. The improved performance was obtained by the combined use of Beryllium as a limiter material (which gettered the oxygen) and X-point sweeping to distribute the heat load over the tiles in the X-point region.

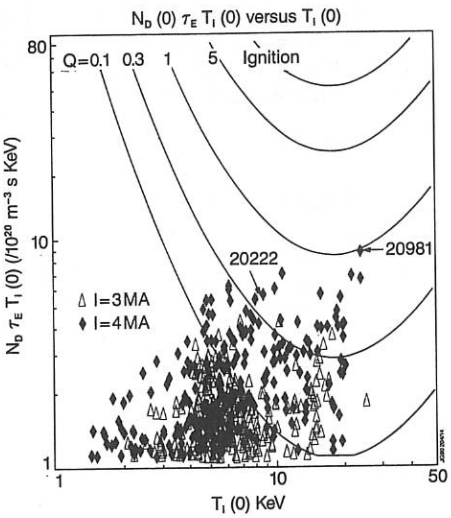

In this paper the D-T performance of two of these pulses is examined, one is a hot-ion pulse (#20981) with $T_i >> T_e$ (22 keV and 8 KeV respectively) and the other is a pellet fuelled pulse (#20222) which is in thermal equilibrium with $T_i = T_e$ (~8 keV). In the simulations differing beam configurations are used, the objective being to assess the best configuration for the D-T phase of operation of JET. The two pulses were selected using the standard $n\tau_\varepsilon$ T_i versus T_i plots, shown in figure 1. Here the Q curves are for parabolic profiles of density and temperature raised to the power $^1/_2$ and $^3/_2$ respectively. Several other types of profiles have been tried including ones closer to the measured profiles but it is found that the Q curves are actually very insensitive to the precise form of the profiles. The density and temperature profiles for the two shots under

consideration are shown in Fig. 2 at the time of peak neutron yield, the other parameters of these pulses are listed in Table 1.

Table I

Pulse No.	I (MA)	B (T)	P (MW)	$\dot{W}$ (MW)	τ_ε (S)	$n_d T_i \tau_\varepsilon$ (X 10^{20})
20981	4	2.8	17	8	1.1	8
20222	4	2.8	16	8	1.25	5.6

The time behaviour of the two pulses was first simulated by the $1^1/_2$-D TRANSP [2] code for the actual conditions of 140/80 keV D injection into a D background. The TRANSP code uses the measured profiles of density, temperature and Z_{eff} as well as many other quantities. A good check on the consistency of this data is shown by the comparison in Fig. 3 of the predicted and measured neutron yield for the hot ion pulse #20981. The agreement is very good for both pulses, and this along with other checks indicates that the input data used by the code is fully consistent. The origin of the neutrons in the simulation of #20981 is also shown in Fig. 3, the yield is dominated by neutrons from fast-thermal reactions until the ion temperature reaches its peak value at t=11.4s. The drop in the yield from t=11.4 secs onwards is due to the strong carbon influx (Carbon Bloom).

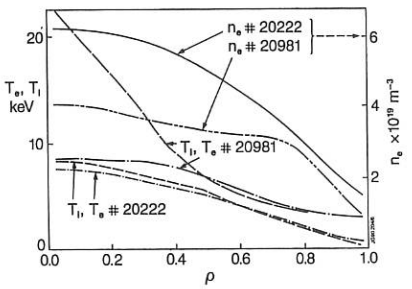

Fig 2. Ion and electron temperature and the electron density profiles versus the normalised radius ρ for the two pulses.

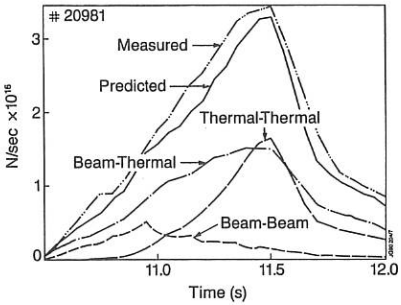

Fig 3. Measured and predicted D-D neutron yield versus time for pulse 20981, the three components are also shown.

II D-T Simulations The D-T simulations are completed by rerunning the code with the same measured profiles and replacing the background deuterium plasma by a tritium one or by changing the injected gas to tritium.

The first scenario had both boxes injecting 140 keV deuterons into an initially tritium background plasma. The result is shown in Fig. 4 for both the hot ion and thermal equilibrium pulses. The hot ion pulse achieves a power output of ~12MW whilst the pulse in equilibrium reaches 8MW. The main reason for the higher value of the yield in the hot ion case is the higher ion temperature which improves both the thermal-thermal and the beam-thermal emission. The beam-thermal yield is also higher in #20981 due to the higher electron temperature in the region where the fast ions are deposited.

In the above simulations the density of the thermal plasma is assumed to evolve in such a manner that the tritium and deuterium density profiles are identical as is shown in Fig. 5 (model A). The reason for the larger concentration of tritium is due to the initial gas fill being tritium and the only source of deuterium being from the injected beam.

The simulations were then repeated with a more pessimistic assumption concerning the particle transport, (model B) in which the flux Γ is assumed to be proportional to $V_0\, n_{D,T}$ where V_0 is the same for both species. In this case the deuterium and tritium profiles are very different (Fig. 5) with the deuterium strongly peaked in the central region and replacing the tritium. This incomplete mixing of the D and T leads to a much reduced thermonuclear yield see table II. Although as yet there are no detailed measurements of the mixing of hydrogenic species it is likely that model B may be more appropriate than model A.

Table II

#20981

Beam		Target	Particle transport model	Fusion Power (MW) thermal -thermal	beam -thermal	beam -beam	Total fusion power (MW)	Q
D140	→	T	A	3	8.7	-	11.7	0.85
Co			B	2	5	-	7	0.5
D140, T160	→	D-T	A	3.5	5.8	0.3	9.6	0.75
Co Co			B	3.4	5.5	0.3	9.2	0.72
D140, T160	→	D-T	A	3.5	6.0	0.3	9.8	0.76
Co Counter								

#20222

D140	→	T	A	1.4	6.0	-	7.4	0.55
Co			B	1.4	5.2	-	6.6	0.5
D140, T160	→	D-T	A	1.4	3.7	0.1	5.2	0.41
Co Counter			B	1.4	4.0	0.1	5.5	0.43

$$Q = P_{th\text{-}th}/(P\text{-}\dot{W}) + (P_{b\text{-}th} + P_{b\text{-}b})/P$$

One obvious technique to improve the D-T mixture is to inject tritium with one box and deuterium with the other into a 50:50 D-T mixture. It is found that in this case with both particle transport models, the mixture remains

approximately 50:50 across the profile and the power output is still greater than 9 MW.

To check whether the beam-beam yield could be enhanced by reversing the direction of injection of one box this case was also simulated. Table II shows that this did not improve the beam-beam contribution presumably because the relative velocity of the counterstreaming D-T ions was well beyond the peak in the D-T cross section.

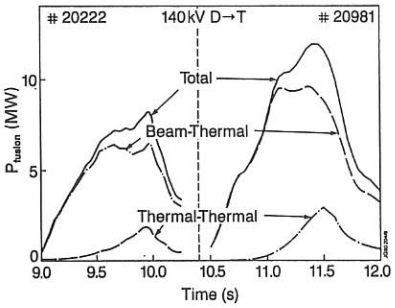

Fig 4. Predicted fusion power versus time for the hot ion pulse #20981 and the pulse in thermal equilibrium #20222 for 140 keV deuterium injection into a tritium background.

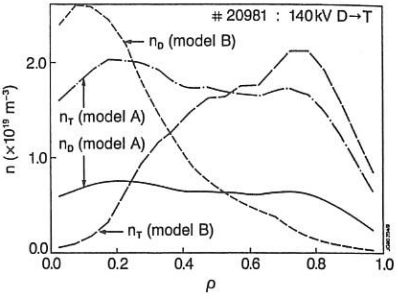

Fig 5. Thermalised deuterium and tritium density profiles for the two transport models A & B.

Summary Simulations assuming the same conditions as have recently been achieved in JET D-D plasmas show that with a D-T plasma, fusion power yields of the order of 10 MW and Q greater than 0.7 can be achieved with a variety of beam-plasma scenarios.

References

[1] Keilhacker, M., Overview of JET Results using a Beryllium First-Wall APS 1989.

[2] Goldston, R.J., et al., J. Comput. Phys. 43 (1981) 61.

Acknowledgements

The authors wish to acknowledge the work of their colleagues in the JET team in obtaining these high performance pulses. The pellet injection results were obtained during work performed under a collaboration agreement between the JET Joint Undertaking and the U.S. Department of Energy (USDOE).

GLOBAL H-MODE SCALINGS BASED ON JET AND ASDEX DATA

O. Kardaun°, K. Thomsen, J. Cordey, F. Wagner°, et al., the JET and ASDEX Teams

JET Joint Undertaking, Abingdon, Oxon OX14 3EA, UK
°Max-Planck-Institut für Plasmaphysik, 8046 Garching, BRD

In this paper we present a discussion of the global confinement time scaling for NBI heated, ELMy H-mode shots, using a combined dataset from JET and ASDEX.

Only co-injected, NBI heated shots with a sufficiently long and constant P_{NBI} and not close to the beta limit have been selected. To avoid transients influencing the regression, only one timepoint per shot was analysed (where W_{dia} is maximal, while $\dot{W}_{dia}/P_{tot} < 0.3$). The JET dataset consists of 53 ELMy H-mode shots, D into D^+. It is part of the 1986-1988 dataset, discussed in [1], extended with shots from 1989, which were partly performed with Beryllium wall conditioning. The ASDEX dataset consists of 170 ELMy H-mode shots, H into D^+, from two major operating periods: (1) 110 shots before the introduction of the ICRH antenna, and (2) 60 shots after the introduction of the antenna and before the hardening of the vessel.

The essential characteristics of the two datasets are summarized in the first part of the Table, which gives the geometrical mean values and standard deviations, as well as the correlations, for variables that are deemed to be important for the confinement time scaling. (The Table is entirely based on a logarithmic scale, since a simple power-law expression leads to a linear model on that scale.) The upper part of the Table contains all the essential information for making a simple power law regression (without the effects of DN/SN and wall conditioning).

A full empirical scaling is as follows:

$$\tau_{dia} = c(q_{cyl})(A/Z)^{1/2}(B_t I_p)^{.33\pm.03}(P_{tot} - \dot{W}_{dia})^{-.34\pm.03} L^{2.0\pm.07} \langle n_e \rangle^{.24\pm.03} \qquad (1)$$

where

$$c(q_{cyl}) = \begin{cases} e^{1.0\pm.08} q_{cyl}^{.17(\pm.08)} & \text{for } q_{cyl} < 2.9 \\ e^{1.4\pm.08} q_{cyl}^{-.65(\pm.07)} & \text{for } q_{cyl} > 2.9 \end{cases}$$

and $L = (2\pi^2 Rab)^{1/3}$ is the cubic root of the volume of the vessel (JET: 2.96m, 1.25m, 2.12m, ASDEX: 1.65m, 0.4m, 0.4m). In Eq. (1), τ_{dia} is expressed in sec., and the other dimensional variables in 'ITER' units, (5 T, 22 MA, 100 MW, 10^{20} m^{-3}) and (6.0m, 2.2m, 4.4m). Neglecting triangularity, the transitions from (I_p,B_t,Vol) to (q_{cyl},$B_t I_p$,Vol) and ($I_p/(\pi ab)$,$B_t/(2\pi R)$,Vol), see Fig. 1^a and 1^b, are on log. scale simple linear transformations, whose effects on the regression and the Table are easily assessed. We feel free to switch from one to the other, equivalent, representation. Initial differences stemming from the operating period at ASDEX cease to be significant in the above scaling. The regression is based on the assumption that τ_{dia} scales as $(A/Z)^{1/2}$, with $A/Z = 2$ for JET and $\simeq 1.5$ for ASDEX. This may influence the exponent 2.0 for L. (For an arbitrary isotope exponent $\alpha_{A/Z}$, one has $2.0 - 0.27(\alpha_{A/Z} - 0.5)$.) Simultaneously with Eq. (1), the following multiplicative constants have been fitted: SN: for JET: 18%(±4%) better than DN, but for

ASDEX: SN 12%(±2%) worse than DN; Beryllium evaporation (JET)/ no carbonisation (ASDEX): 14%(±3%) better than carbonisation. The errors denote one standard deviation (from ordinary linear least squares). The estimate of the residual (relative) error in τ_{dia} is 9%, which can be viewed on the residual plot (Fig. 2). It is instructive to compare this scaling with the separate scalings of the two tokamaks, see the lower part of the Table. The two-regime regression line was used as a variation to a quadratic term in $\ln(q_{cyl})$. Within the data range, the differences are minor. The change in q_{cyl} dependence for $q_{cyl} < 2.9$ and $q_{cyl} > 2.9$ appears to be mainly due to ASDEX. The conclusion is that there seems to be a definite difference in the q_{cyl} dependence in JET and ASDEX, which adds to the uncertainty in the extrapolation to $q_{cyl} = 1.8$ for ITER. Furthermore, the statistical condition of the combined dataset is somewhat impaired by the quite strong correlation between I_p and L. Some improvement could be possibly be gained by an extended q_{cyl} scan in ASDEX, and with some low I_p shots at JET.

As argued in [2] and elsewhere, it can be useful to write the scaling relationship as a leading term (with dimension time) multiplied with a function F of dimensionless variables. Different theories give different leading terms and a different number of dimensionless variables on which the confinement time is supposed to depend. If the function F is of a power-law type, it can be shown that on logarithmic scale this corresponds to a linear transformation followed by a linear restriction on the coefficients. As the regression problem is invariant under linear transformations, the restriction can be translated into a linear restriction on the coefficients of the dimensional variables [2]. Without restrictions, we have for the coefficients of

$$(q_{cyl}, I_p B_t, P, < n >, L, \Delta_{DN,asd}, \Delta_{DN,jet}, \Delta_{wall})$$

$$(-.31, .41, -.35, .22, 1.8, .11, -.16, .11), \qquad \text{with rmse : } 10.03\%.$$

The dimension restriction (which is e.g. common to both long and short wavelength turbulence theory [2]) reads $4\alpha_L - 8\alpha_n - 3\alpha_P - 6\alpha_{BI} = 5$. It gives

$$(-.34, .35, -.36, .21, 1.9, .11, -.19, .11), \qquad \text{with rmse : } 9.94\%.$$

The regression errors are similar as in the Table (between 2 and 5%). The largest deviations (for $I_p B_t$, L, and $\Delta_{DN,jet}$) are at least consistent with the observed collinearities in the variables. The dimension restriction is rather well satisfied by the data. Fig. 3 compares the empirical scaling with some published scalings for (mainly) L-mode [3], with an adjusted constant. As judged by (essentially) the χ^2_4 statistic ($F_{4,217} \simeq \chi^2_4/4$), within the error bars, these scalings do not fit the data very well.

The 'predictions' for $\tau_{dia}(s)$ in ITER ($A/Z = 2.5$) are 4.8(±.8) and 4.6(±.8), respectively. The unrestricted formula with 2 regimes for q_{cyl} gives 4.3(±.8). The indicated uncertainty (2 std dev) is not to be construed as the final uncertainty in the prediction for ITER. It is only the estimated prediction error under the assumption that the type of scaling used is essentially correct and that the main variables influencing the regression have been included. Aspect ratio and elongation scaling as well as profile effects and further wall conditioning aspects may change the picture.

[1] EPS XVI, Venice 1989, p. 253-257, [2] Christiansen et al., submitted to Nuclear Fusion, [3] Engelmann, Mukhovatov, et al. NAU/ITER-TN-PH-8-7.

Table JET-ASDEX global H-mode database

	units	av.	std	(min,max)	correlations (on logarithmic scale)

ASDEX (ELMy, H into D^+, NBI only, 170 shots, one point per shot ($\dot{W}_{dia} = 0$)

					I_p	B_t	P_c	$\langle n_e \rangle$	τ_{dia}
τ_{dia}	ms	49	8	(26,69)	1				.71
I_p	MA	0.33	0.06	(0.17,0.45)	**.48**	1			.28
B_t	T	2.2	0.15	(1.5,2.6)	**.30**	.10	1		-.11
P_c	MW	2.4	0.55	(1.4,3.4)	**.53**	.19	.14	1	.53
$\langle n_e \rangle$	$10^{20}/m^3$	.35	0.07	(0.15,0.5)					
Δ_{wall}		-6%		(-1,0)	half-axes 95% ellipse:				
Δ_{DN}		62%		(0,1)	0.73, 0.57, 0.37, 0.17				

JET (ELMy, D into D^+, NBI only, 53 shots, one point per shot (W_{dia} maximal)

					I_p	B_t	P_c	$\langle n_e \rangle$	τ_{dia}
τ_{dia}	ms	670	180	(415,1120)	1				.52
I_p	MA	3.3	0.78	(2.1,5.1)	**.59**	1			.47
B_t	T	2.4	0.69	(1.1,3.5)	**.32**	.27	1		-.22
P_c	MW	8.0	3.0	(4.0,14.6)	**.41**	.20	**.45**	1	.50
$\langle n_e \rangle$	$10^{20}/m^3$	.32	0.18	(0.09,0.6)					
Δ_{wall}		-72%		(-1,0)	half-axes 95% ellipse:				
Δ_{DN}		30%		(0,1)	1.5, 0.86, 0.76, 0.43				

combined (ELMy, NBI only, 223 shots, one point per shot)

					I_p	B_t	P_c	$\langle n_e \rangle$	L	τ_{dia}
τ_{dia}	ms	91	192	(26,1120)	1					.990
I_p	MA	.577	1.0	(0.17,5.1)	**.39**	1				.362
B_t	T	2.24	0.34	(1.1,3.5)	**.92**	**.36**	1			.884
P_c	MW	3.23	2.4	(1.4,14.6)	-.05	.14	.007	1		-.049
$\langle n_e \rangle$	$10^{20}/m^3$	0.34	0.11	(0.09,0.6)	**.984**	**.31**	**.91**	-.13	1	.986
L	m	2.60	2.6	(1.73,5.37)						
Δ_{wall}		-22%		(-1,0)	half-axes 95% ellipse:					
Δ_{DN}		50%		(0,1)	4.1, 0.93, 0.66, 0.44, 0.20					

Simple scaling relations (power law exponents)

	$q_{cyl,<3}$	$q_{cyl,>3}$	$B_t I_p$	P_c	$\langle n_e \rangle$	Δ_{wall}	Δ_{DN}	rmse
τ_{dia} (ASDEX)	0.15 (.20)	−.64 (.08)	.41 (.05)	−.30 (.04)	.15 (.04)	.13 (.03)	.13 (.02)	8%
τ_{dia} (JET)	.10 (.11)	.13 (.24)	.33 (.05)	−.54 (.06)	.34 (.04)	.20 (.05)	−.16 (.05)	10%

$\Delta_{DN} = 1$ for DN and 0 for SN
$\Delta_{wall} = -1$ for carbonisation, $\Delta_{wall} = 0$ for no carbonisation (ASDEX),
$\Delta_{wall} = 0$ for C tiles + C limiters and Be evaporation, or C tiles and Be limiters (JET)

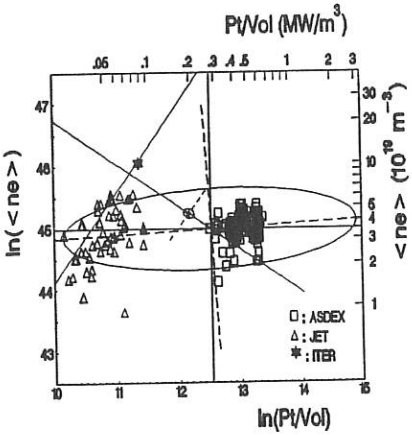

FIG. 1.a Geometry of JET–ASDEX ELMy H–mode confinement scaling. A 2D projection from regression of τ_E on Ip,Bt,Pt,<ne> and volume. The small ellipse shows a 95% confidence region for the regression parameters. Explanation is continued in Fig. 1.b.

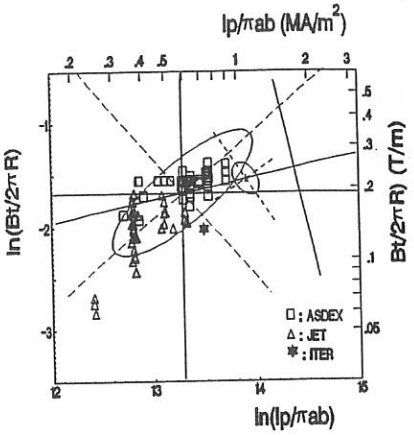

FIG. 1.b Geometry of JET–ASDEX ELMy H–mode confinement scaling. The solid line through the small ellipse shows the direction in which τ_E varies most. The perpendicular line corresponds to a constant τ_E which is equal to 2 times the value at the center of gravity.

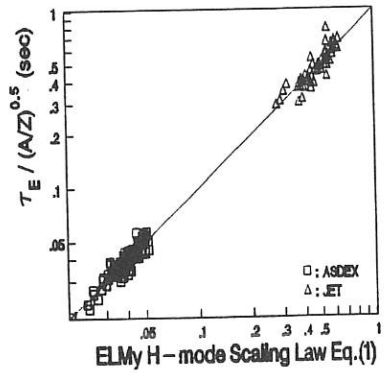

FIG. 2. Residual plot of JET–ASDEX ELMy H–mode confinement scaling.

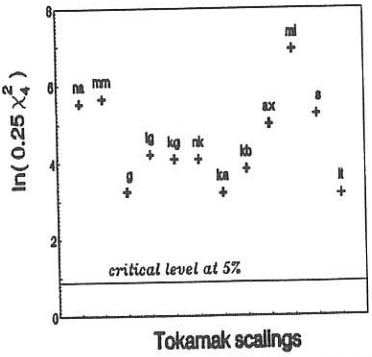

FIG. 3. Distance between empirical power–law fit and published power–law scalings which are listed below.

na : *Neo–Aleator*	ka : *Kaye All*
mm: *Merezkin–Mukhovatov*	kb : *Kaye Big*
g : *Goldston*	ax : *Old ASDEX H–mode*
lg : *Lackner–Gottardi*	ml : *Mirnov*
kg : *Kaye–Goldston*	s : *Shimomura*
nk : *Neo–Kaye*	it : *ITER 89*

TRANSPORT STUDIES IN HIGH RECYCLING NEUTRAL BEAM HEATED DISCHARGES ON TFTR*

D.W. Johnson, S.D. Scott, C.W. Barnes, M. Bell, M. Bitter, C. E. Bush, E. Fredrickson, B. Grek, K.W. Hill, H. Hsuan, D.K. Mansfield, H. Park, A. T. Ramsey, B.C. Stratton, E.J. Synakowski, G. Taylor, E.H. Towner, R.M.Weiland, M. Zarnstorff

Princeton University Plasma Physics Laboratory
Princeton, New Jersey 08543 USA

Introduction - Historically, the study of local transport in L-mode discharges has had mixed success because of the difficulty of making sufficiently precise measurements of the ion temperature profile $T_i(R)$ in this regime. Recently, the more routine availability of this data on TFTR has led us to renew the study. Systematic uncertainties in the $T_i(R)$ measurements still leave unresolved some of the details of the variations of the thermal diffusivities χ_i and χ_e, but it is nonetheless possible to observe a correlation of the local transport properties with global parameters in these discharges. Over much of the minor radius, we find a comparable relative reduction in both χ_i and χ_e with plasma current and an increase of both with injected power. Also, we obtain a global scaling for the thermal stored energy.

Experimental Conditions and Analysis - When the TFTR carbon inner belt limiter is loaded with deuterium gas, the recycling coefficient is high (R~1.0)[1], and L-mode global confinement scaling is observed.[2] As distinct from the supershot regime, which results when the limiter is conditioned to pump deuterium and minimize recycling (R~0.6)[1], L-mode discharges are characterized by broader density profiles, $n_{e0}/\langle n_e \rangle$ = 1.4 - 1.8 (1.8-3.0 for supershots), lower global energy confinement τ_E/τ_E^{Lmode} = 0.9 - 1.3 (2.5-3.0), and lower ion temperatures T_{i0}/T_{e0} = 1.0 - 1.5 (2.0-4.0). The plasmas studied here had R,a = 2.58,0.93 m, I_p = 0.9 - 2.1 MA, B_T = 2.5 - 4.6 T, P_{inj} = 0 - 20 MW, and $n_e(10^{19}cm^{-3})$ = 2.0 - 6.5. Deuterium neutral beam injection (E_{inj} ~ 100 keV) was used with deuterium target plasmas. Peak temperatures ranged from T_{e0} = 2 - 6 keV and T_{i0} = 2 - 9 keV. Since the density is correlated with I_p and P_{inj}, to minimize the n_e variation for the single parameter scans, gas puffing was used prior to the onset of the 0.7 - 1.0 s heating pulse to control the density near the end of injection.

The 1-D transport code SNAP was used to determine the local transport coefficients by solving the power and momentum balance based on measured profiles in the steady-state phase near the end of the heating pulse. Inputs to the code include $T_i(R)$ and $v_\phi(R)$ measured by charge exchange recombination spectroscopy (CHERS [3]) of CVI, and x-ray crystal spectroscopy [4] of FeXXV. $T_e(R)$ was measured by ECE radiometry and Thomson scattering, and $n_e(R)$ by a ten channel infared interferometer and Thomson scattering. Z_{eff} was determined by visible bremsstahlung emission and assumed to be flat across the profile. Neutral influx was determined from a 5 channel H_α monitor. Convection (taken to be $3/2\Gamma T$) is not significant in the power balance of these discharges; however electron-ion coupling (assumed to be classical) is a critical

term, and uncertainties in this term as well as the radiated power often dominate the power balance outside r/a ~ 0.7.

Scaling of the Thermal Stored Energy - For 120 discharges spanning the parameter ranges indicated above, regression fits for the scaling of the total stored energy from magnetic measurements result in:

$$W^{M}_{TOTAL}(\text{regression}) = 0.21\, I_p^{0.99\,(7)} P_{TOT}^{0.55(3)} n_e^{-0.12(7)} \qquad (1)$$

similar to earlier results.[2] ($P_{TOT}=P_{inj}+P_{OH}$) At high P_{inj}, even in high recycling conditions, the unthermalized beam ions contain a significant fraction of the total stored energy (W_{BEAM}/W_{TOTAL} = .20 - .45 for these discharges) and W_{BEAM} scales differently than W_{TOTAL}. Using the 50 shots for which we have more detailed profiles of $T_i(R)$, one obtains a tight fit to $W_{BEAM}(\text{regression}) = 0.036\, P_{inj}^{0.94} T_{e0}^{0.97} n_e^{-1.04}$ for the calculated energy stored in beam ions. One can then determine the scaling of the thermal stored energy ($W_{THERMAL}=W^{M}_{TOTAL} - W_{BEAM}(\text{regression})$) for the full dataset :

$$W_{THERMAL}(\text{regression}) = 0.14\, I_p^{1.23\,(7)} P_{TOT}^{0.29(3)}\, n_e^{0.48(7)}. \qquad (2)$$

This result indicates a substantially stronger I_p and n_e dependence and weaker P_{TOT} dependence than the traditional L-mode scaling. The scaling expressions in (1) and (2) are significantly different. As has been pointed out previously [5], this is one reason that care should be taken in applying global scaling results.

Ion Temperature Measurements - Figure 1 shows measured profiles for a discharge with parameters I_p = 1.2 MA, P_{inj} = 9.2 MW, B_T = 3.8 T, and $n_e = 3.1\times10^{19}$ m^{-3}. The discrete points show the $T_i(R)$ values from the CVI 5292Å line and the FeXXV 1.85Å line (the instrumental width for each is ~1.0 kev). Repeated comparisons of CHERS $T_i(R)$ profiles using the CVI 5292Å line and the CVI 3435Å line on successive discharges indicate a temperature independent offset, with the 3435Å determination typically ~.3 kev higher at the large major radius edge, increasing to ~.9 kev higher near the center of the discharge. The systematic differences in the $T_i(R)$ profile determinations are not understood. The fact that there are more mechanisms which make a line broader rather than narrower, and the existence of a charge-exchange-excited, small satellite feature on the long wavelength side of the 3435Å line (as also observed on ASDEX[6]), give us more confidence in the 5292Å determination, which we use in the analysis below. The error bars for the CHERS data are best estimates of systematic uncertainties, and are several times the statistical errors in the data. A full uncertainty analysis continues. To check the sensitivity to this choice of $T_i(R)$ profile, we will later point out changes to conclusions which result when a profile consisting of the high value of the error bars in the 5292Å determination is used.

Calculated $T_i(R)$ profiles using different χ_i models are shown for comparison in figure 1. Note that $\chi_i=(2\text{-}4)\chi_e$ gives reasonable agreement for this discharge, consistent with previous results in high recycling conditions.[7,8] As shown in fig. 2, the model $\chi_i = 0.5\chi_e$ consistently overestimates the measured T_i from both diagnostics.

Single parameter scans and global scaling - Although the ultimate goal of this transport study is to determine the dependence of local transport coefficients on local variables, these variables are difficult to control. Since the thermal stored energy scales strongly with I_p and P_{inj}, a step in understanding local transport is made by investigating the correlation of χ_i and χ_e with these global quantities. To this end, scans in I_p and P_{inj} were performed and care was taken to hold constant other parameters, particularly density.

Figure 3a shows the change in the calculated $\chi_i(r)$ and $\chi_e(r)$ for a plasma current scan. As I_p was changed from 1.2 MA to 2.1 MA with other quantities held constant, T_{e0} increased from 3.5 to 6.2 keV and T_{i0} rose from 3.3 to 7.5 keV. Transport analysis was done near the peak in the T_e sawtooth amplitude. (ΔT_e^{ST} = 0.2 keV at 1.2 MA, 1.5 keV at 2.1 MA, sawtooth period ~$2\tau_E$) The scale lengths L_{Te} and L_{Ti} (where L_x=d(lnX)/d(lnR)) were unchanged. The density profile was more peaked in the high current case ($n_e(0)/<n_e>$=1.9 vs 1.5) and the scale length L_{ne} decreased by a factor of 4 over r/a ~ 0.2 - 0.7. In this and other scans described below, the power balance outside r/a=0.7 is problematic, because radiated power and electron-ion coupling become large and uncertain in this region. Note that both χ_i and χ_e were reduced as I_p increased.

The injection power was varied from 9.2 to 17.0 MW with other machine parameters held constant, and figure 3b shows the effect on the thermal diffusivities. In this case the peak temperature variations were T_{e0} = 3.4 - 3.7 keV and T_{i0} = 3.0 - 3.7 keV, and the profile shapes of T_e, T_i and n_e showed no significant variation. χ_i and χ_e both increased by similar relative amounts.

Figures 4a and 4b show the variation of χ_i and χ_e (r/a = .45) with I_p (at constant P_{inj}) and with P_{inj} (at constant I_p) for less constrained datasets assuming the 5292Å determination of $T_i(R)$. As shown by the solid lines, both χ_i and χ_e show similar relative variations - both decreasing with plasma current and increasing with heating power. It is interesting to compare these results with those obtained previously in the supershot regime, where χ_i and χ_e inferred from a similar analysis show variations of less than a factor of 2 over similar ranges in I_p and P_{inj} [9].

If the higher choice for the $T_i(R)$ profile as discussed above is used, the magnitudes of $\chi_i(r)$ and $\chi_e(r)$ are more similar (χ_i/χ_e~2 rather than ~4). However, the trends displayed in figures 3-4 are not significantly changed. The dashed lines in fig. 4a and 4b show the trends in the scaling of $\chi_i(r)$ and $\chi_e(r)$ with this treatment, and further uncertainty analysis is ongoing.

*This research was conducted with DOE grant No. DE-AC02-76-CHO-3703

References

[1] H. F. Dylla, *et al.*, Controll. Fusion and Plas. Phys. **11D**, 698 (Madrid,1987).
[2] M.G. Bell, *et al.*, Plasma Phys. Controll. Fusion **28**, 1439 (1986)
[3] R.J. Fonck, *et al.*, Phys. Rev. A **29**, 3288 (1984)
[4] M. Bitter, *et al.*, Rev. Sci. Instrum. **57**, 2145 (1986)
[5] M. Sugihara, *et al.*, Nuclear Fusion **26**, 1547 (1986)
[6] P. Carolan, *et al.*, Phys. Rev. A **35**, 3454 (1987)
[7] S. Scott, *et al.*, Phys. Rev. Lett. **64**, 531 (1990)
[8] S. Scott, *et al.*, (submitted for publication in Phys. Fluids B)
[9] M. Zarnstorff, *et al.*, IAEA-CN-50/A-3-3, 191, (Nice, 1988)

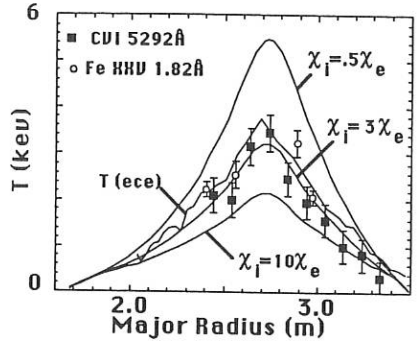

Fig.1 Comparison of measured T_i profiles with those calculated with the models $\chi_i = n\chi_e$ Also shown is the measured T_e profile.

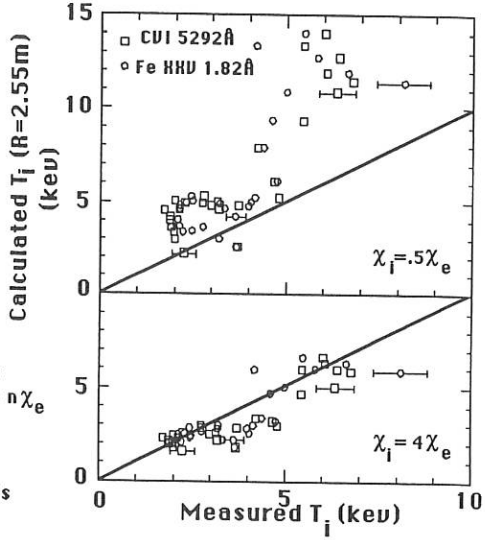

Fig. 2 (right) Comparison of T_i (R=2.55m), measured vs calculated with two χ_i models

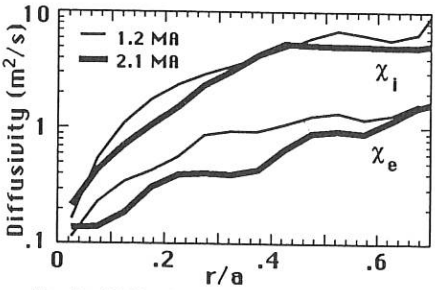

Fig. 3a Diffusivity profiles for plasmas with P_{inj}=13.2MW, $\bar{n}_e = 3.1 \pm .1 \times 10^{19} m^{-3}$

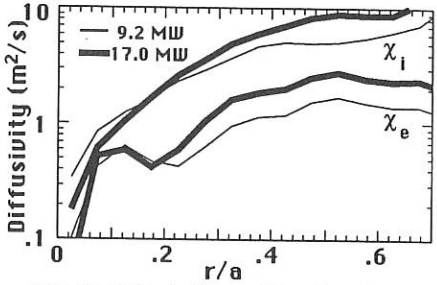

Fig. 3b Diffusivity profiles for plasmas with I_p=1.2MA, $\bar{n}_e = 3.2 \pm .2 \times 10^{19} m^{-3}$

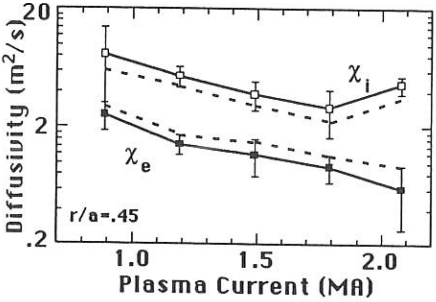

Fig. 4a Correlation of diffusivities with I_p for P_{inj}=12±1 MW

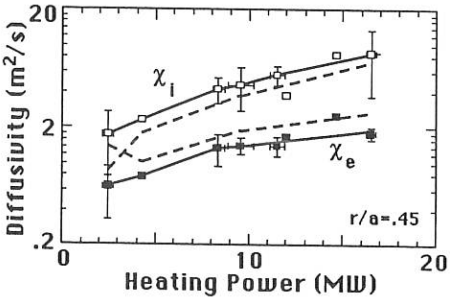

Fig. 4b Correlation of diffusivities with P_{inj} for I_p=1.2MA

ENERGY CONFINEMENT SCALING LAWS FOR FT OHMIC PLASMA

G.Bracco, P.Buratti, F.Orsitto, D.Santi

Associazione EURATOM-ENEA sulla Fusione
Centro Ricerche Energia Frascati
C.P. 65 , 00044 Frascati (Roma) ITALY.

A database on energy confinement in FT has been prepared including ohmic plasma results for magnetic field in the range 2.5 to 10 T, line averaged density from 1. to 30 10^{19} m-3, q values from 2.5 to 6.5 and for deuterium, hydrogen and helium working gases. The database refers to plasma pulses of 1988 and 1989 operation. This paper considers only deuterium discharges which form the bulk of plasma pulses. Plasma major radius is 0.83 m and minor radius is 0.20 m.

The global confinement time has been evaluated from kinetic data. The electron temperature profile is measured by a single pulse Thomson Scattering system at seven radial position. Electron density is measured by a single channel HCN interferometer, which provides the line averaged density. The density profile is then assumed parabolic: but this assumption does not affects significantly the evaluation of the global confinement. Information on ion temperature is provided by measured neutron yield and by charge exchange analysis. The ion temperature profile has been computed by the solution of the ion power balance making use of the neoclassical thermoconductivity and the results agreed within the experimental error bars with the measured data. It can be noted that at high density (> 1.10^{20} m-3) even the results with a neoclassical multiplier factor of three still agreed with experimental data. The ion temperature from the neoclassical power balance has been used in the global confinement time computation. The Z effective is deduced from the experimental plasma resistivity using neoclassical corrections.

The resulting global confinement time has been compared with several standard scaling laws and the results are shown in fig.1,2,3,4,5 where points are selected for different magnetic field values according to the code shown in table 1.

The comparison fig.1 with the neo-Alcator scaling law in its TFTR expression [1] shows that FT data are 20% lower than the scaling but very near to the PLT ones. At high scaling parameter values a saturation is found which corresponds to density greater than 10^{20} m-3.

The Goldston scaling [2] is shown in fig.2 where the global confinement is given by the combination of the ohmic and the auxiliary heating scalings using the ohmic power as the total power. This scaling underestimates the FT confinement by a 40%.

The Rebut-Lallia scaling [3] is shown in fig.3. This scaling overestimates the confinement of about 25% and the data suggest that the magnetic field dependence is too strong.

The Lackner-Gottardi scaling [4] is shown in fig.4 and it

provides the best fit to FT global confinement.

The collisionless electron trapped mode scaling [5] in fig.5 reproduces the average values but with a large dispersion.

1) Efthimion at al.(1984). Proc.10th Int.Conf.on Plasma and Controlled Nuclear Fusion Research, (IAEA,London)CN-44/A-I-2
2) R.J.Golston, Plasma Physics and Controlled Fusion, 26,87(1984)
3) Rebut,P.H.,Lallia,P.P. and Watkins,M.L.(1988).Plasma Physics and Controlled Nuclear Fusion Research (IAEA,Nice)CN-50/D-4-1
4) K.Lackner,N.Gottardi JET-P(88)77
5) F.Romanelli, Plasma physics and Controlled Fusion, 31,1535(1989)

Tab.1:
Magnetic Field (T)

○	2.0	3.0
△	3.0	5.0
+	5.0	6.5
◇	6.5	7.5
⊠	7.5	8.5
¤	8.5	10.

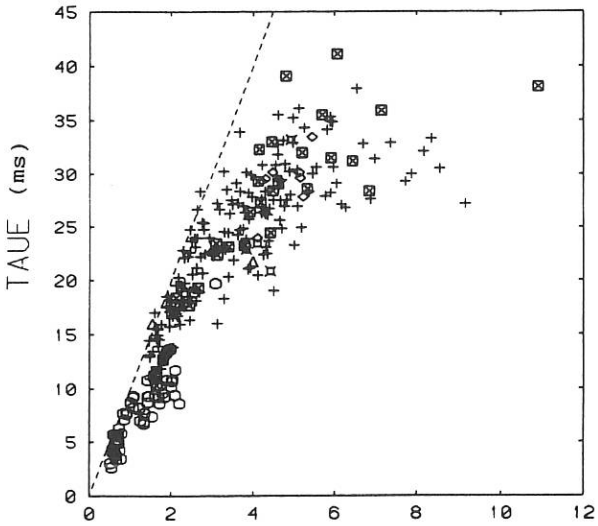

fig.1 TFTR Neo-Alcator scaling

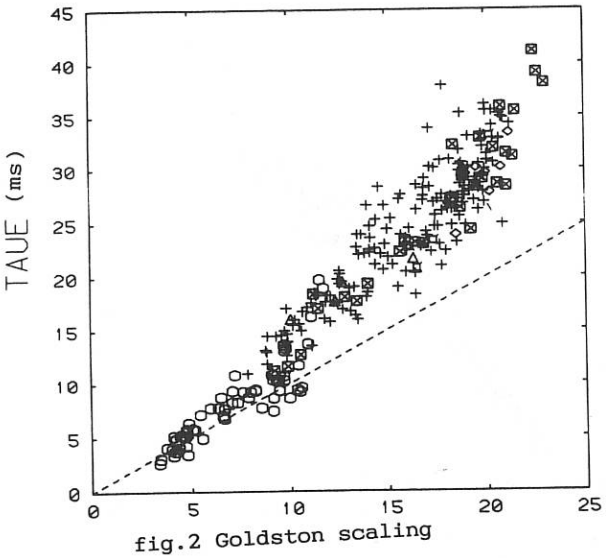

fig.2 Goldston scaling

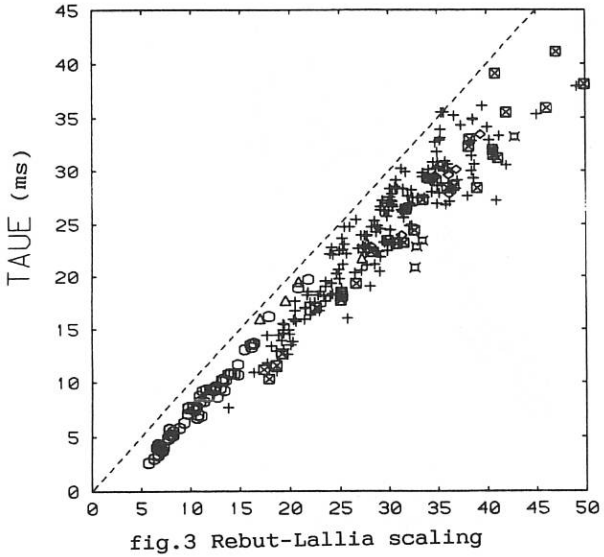

fig.3 Rebut-Lallia scaling

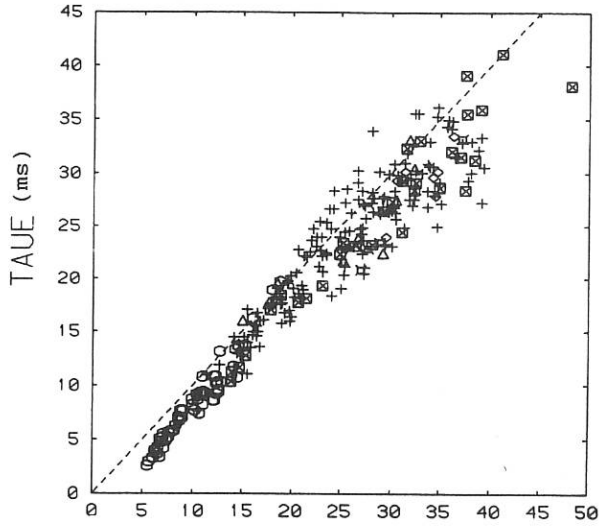

fig.4 Lackner-Gottardi scaling

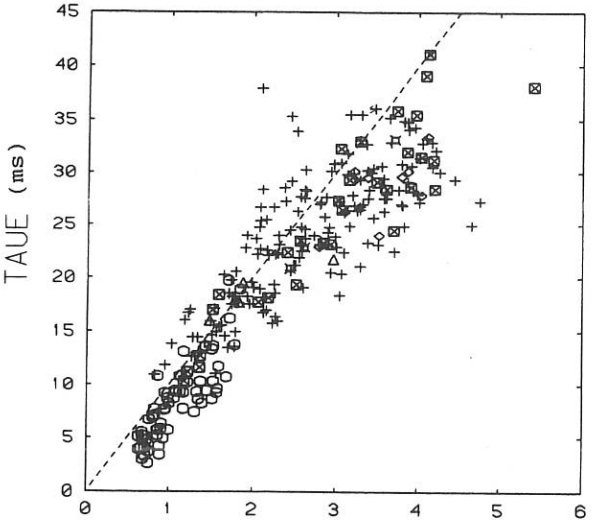

fig.5 Collisionless trapped electron scaling

PROFILE CONSISTENCY COUPLED WITH MHD EQUILIBRIUM EXTENDED TO NON STATIONARY PLASMA CONDITIONS

P. Micozzi, M. Roccella

Associazione EURATOM–ENEA sulla Fusione
Centro Ricerche Energia Frascati
C.P. 65 – 00044 Frascati, Rome, Italy

INTRODUCTION

A profile consistency based on the parallel component of the ohmic law coupled with MHD equilibrium has been used to obtain electronic temperature profiles, both for stationary and non stationary tokamak plasmas. The ohmic law contains a resistive neoclassical term and one term that accounts for the bootstrap current contribution. A numerical code has been developed to solve the problem where the equilibrium is solved using the toroidal multipole method [1]. For stationary plasmas we have obtained temperature profiles close to the experimental data for a lot of machines very different in size, elongation, plasma current, toroidal field and density (JET, TFTR, Asdex, Alcator–A, Alcator–C and FT). Only some examples of the obtained fits are given in this report. The main feature of the model is the capability to provide a parametrization of the ohmic law also in non stationary cases. In agreement with some experimental evidences the model foresees a strong peaking of the temperature profile in non stationary plasmas only when the central value of q is decreasing in time. An upper limit for the duration of the monster–like pulses can be also estimated by the model.

PLASMA MODEL

The approximation $T_e = T_i$ has been assumed. The density profiles are given a–priori to simulate euristically the different experimental situations (pellet or gas puffing injection).

Due to the presence of the sawtooth inside $q = 1$ region, the ohmic law must be retained only outside this region if the inductive terms during the sawtooth are disregarded. We used this criterius for the ordinary sawteeth activity, for which the periods are commonly much lower than the characteristic energy diffusion times and assume that the temperature be flat inside this region. This assumption can result somewhat pessimistic for the more compact machines [2]. In presence of the sawteeth stabilization (giant sawtooth, monster–like pulse or after the pellet injection) the contribution of the inductive term to the plasma current has been taken into account (see next). The current density profile is determined giving the position (the value ψ_1, of the poloidal flux ψ) corresponding to the $q = 1$ surface. To find this position we start from the consideration [3] that for given current and density profile the temperature consistent with the neoclassical resistivity may present a relative maximum outside the plasma axis. If the ohmic law should be

maintained beyond this limit it would produce an hollow temperature profile that is not physically significant. Since to justify that the ohmic law is not satisfied we must assume that some unknown term contributes to the current (as e.g. the inductive term during the sawteeth), the hypothesis that the point of the maximum in temperature be internal to the $q = 1$ surface seemed us justified. This assumption poses a lower limit to the peaking of the current density in the region before the $q = 1$ surface: i.e. the peaking for which $q = 1$ at the surface where the electronic temperature attains its maximum. Since the size of the $q = 1$ region increases with the assumed peaking of the current outside this region, the average temperature peaking factor $T(0)/\langle T\rangle$ and the fusionistic performances of a machine, for a given plasma thermal content, are not sensibly affected by this assumption. The choice of the minimum size for the $q = 1$ region has been found the more appropriate for the most of the experimental well behaved stationary discharges that have been examinated, and it has been commonly adopted in these cases. This rule have been also found in qualitative agreement with the euristic assumption of $r_1 = a/q_a$ where r_1, a are the $q = 1$ surface and the plasma minor radii. It has been assumed [4] the following form of the parallel component of the generalized ohmic law

$$\langle J_{\|}^{\mathrm{tot}} B\rangle = \langle J_{\|}^{E} B\rangle + \langle J_{\|}^{b} B\rangle \tag{1}$$

where the suffixes E, b stand for the contributions to the total current due to the electric field and to the bootstrap current respectively (the brackets denotes surface averages). The bootstrap term is taken from reference [4], the first term reads

$$\langle J_{\|}^{E} B\rangle = \sigma_{nc}\langle E_{\|} B\rangle = \sigma_{nc}[\langle E_{\phi} B_{\phi}\rangle + \langle E_p B_p\rangle] \ ,$$

where σ_{nc} is the neoclassical conductivity. Writing more explicitly all the inductive contributions during non stationary conditions

$$\langle J_{\|}^{E} B\rangle = \frac{\sigma_{nc}}{V'}(-q\dot{\psi}_a - q_0\dot{\psi}_0 + \dot{x})$$

where the label a indicates the plasma boundary, $V' = dV/d\psi$ is the ψ derivative of the volume V enclosed by the flux surfaces ψ and $\dot{x}$ is formally defined by

$$\dot{x} = \int_{\psi_0}^{\psi} \left(\frac{\partial q}{\partial t}\right)_{\tilde{\psi}} \mathrm{d}\tilde{\psi} = A\dot{\psi}_0 + B\dot{p} + c\dot{q}_a + D\dot{q}_0 \ . \tag{2}$$

The last equality (A, B, C, D being known functions of ψ depending on the particular MHD equilibrium solution) is obtained using a behaviour of q vs. ψ of the form

$$q = \begin{cases} (q_a - q_0)(1 - \psi/\psi_1)^p + q_0 & \psi \le \psi_1 \\ q_0 & \psi \ge \psi_1 \end{cases}$$

where p is a parameter to be found to fit the real behaviour of q from the equilibrium.

Let be $H = \langle J_{\|}^{\mathrm{tot}} B\rangle$ obtained from the equilibrium and $b = \langle J_{\|}^{b} B\rangle$. Taking the ratio of eq. (1) at the generic ψ and at ψ_1 we obtain

$$T = T_1 \left\{ \frac{q_0(H - b)\Gamma V'}{\Gamma_1[V_1'(H_1 - b_1)q + \sigma_{nc1}(\dot{\psi}_0 q_0(q - q_0) + \dot{x}q_0 - \dot{x}_1 q)]} \right\}^{2/3} \tag{3}$$

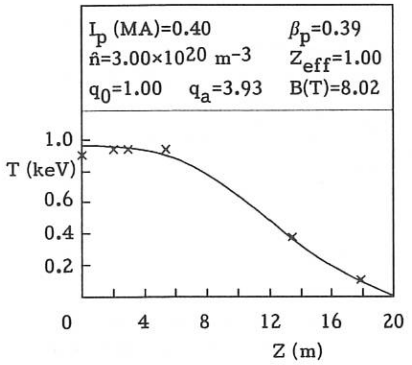

Fig. 1 – Our model (full line) and the experimental data for a compact devices (FT) [7] (stationary conditions).

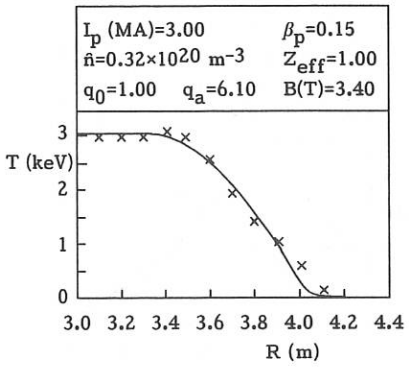

Fig. 2 – Our model (full line) and the experimental data for a large tokamaks (JET [5]) (stationary conditions).

where the suffix 1 denotes the quantities at ψ_1 and Γ is the neoclassical correction factor to the Spitzer resistivity.

This equation set the formal relation between temperature and current density, both in stationary and non stationary conditions, that has been used to determine the temperature profiles. The second term in the denominator of eq. (3) is due to non stationariety. This term can account for the very different temperature profiles observed during plasma current rise and during sawteeth stabilization. It turns out that the first three terms of the eq. (2) don't affect appreciably the temperature profile, that indeed, as it has been experimentally observed, can be dramatically changed only when the value q_0 of q on axis is lowering in time ($\dot{q}_0 < 0$). It must be remarked that, no matter of how low is the value of q that can be reached during sawtooth stabilization, the temperature peaking maintains as long as $\dot{q}_0$ has a negative high enough value.

COMPARISON WITH EXPERIMENTAL TEMPERATURE PROFILES

The model has been checked with some examples of experimental temperature profiles in various tokamaks (Asdex, JET, TFTR, Alcator–A, Alcator–C, FT). The obtained fits are all within the experimental uncertainty both for small and large tokamaks. Some of the fits obtained in the stationary cases are shown in figs 1 to 2.

The theory seems to account for the less extended central flat region commonly observed in the colder and denser plasmas of the compact tokamaks (fig. 1). When characteristic times of the order of the magnetic diffusion time are used a complete peaking of the temperature profile is commonly obtained.

Figs 3 (giant–sawtooth [5]) and 4 (monster–like pulse [6]) show the fits obtained for two JET pulses during the sawtooth stabilization.

In these examples, during the stabilization times (about 0.2 s for the giant

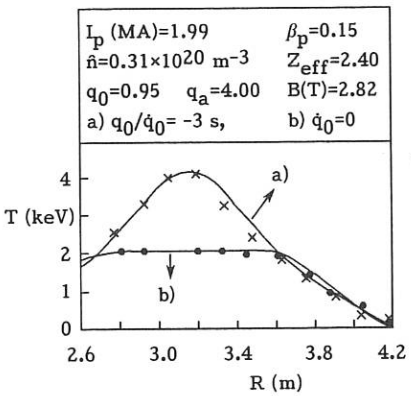

Fig. 3 – Giant sawtooth at the JET. Comparison with the experimental data: a) during giant rise $\dot{q}_0 < 0$; b) after the sawtooth crash $\dot{q}_0 \cong 0$.

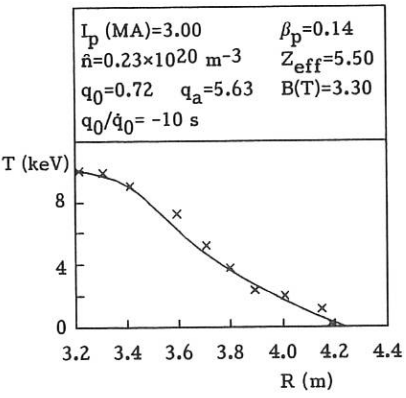

Fig. 4 – Monster sawtooth at the JET. Comparison with the experimental data during monster rise $\dot{q}_0 < 0$.

and 3 s for the monster), q_0 is made to decrease from 1 to the expected values at the end of these times ($q_0 \approx .95$ for the giant and $q_0 \approx .7$ for the monster). If we assume that during stabilization the size of the hollow region of the temperature must drop to zero and that the minimum value of q_0 on the axis that can be achieved is about 0.7 (monster pulse), we can argue the maximum time needed by the monster sawtooth before the crash.

It can be deduced that the maximum duration of hypothetic monster–like pulses in FTU, IGNITOR, JET and JIT should be of the order of 0.3s, 1s, 3s and of several tens of seconds respectively. All the examples considered, except for FTU, being of comparable βp.

REFERENCES

[1] Alladio F., Crisanti F., Nucl. Fus. **26** (1986) 1143.

[2] Alladio F., Vlad G., Phys. Fluids 31 (1988) 602.

[3] Giannella R., Roccella M., ENEA Report RT/Fus/88/28 1988.

[4] Kim Y.B, Callen J.D., Hamnen H., JET Report R(88) 02 January 1988.

[5] Rebut P.H., Brusati M., Plasma Phis. and Controlled Fusion 28 (1986) 113.

[6] JET shot n. 16065, R. Giannella, *Private Communication.*

[7] FT shot n. 18884, G. Bracco, *Private Communication.*

SCALING DIMENSIONALLY SIMILAR TOKAMAK DISCHARGES TO IGNITION*

R.E. WALTZ, J.C. DEBOO, and M.N. ROSENBLUTH,†

General Atomics
San Diego, California 92186-9784, U.S.A.

The tokamak operates in a variety of confinement regimes suggesting there may be several transport mechanisms in combination. The detailed parametric dependence of each is likely to be very complicated. However, it can be argued that all plasma diffusion mechanisms can be divided into the extremes of gyro-Bohm (gB) or Bohm (B) types depending on their scaling with ion gyroradius ρ_s relative to the minor radius a: $\rho_s a$ [$\rho_s = c_s/\Omega_i$, $c_s = \sqrt{T/m_i}$, $\Omega_i = eB/m_i c$]. These correspond to turbulent (or classical) diffusion processes with short or long step sizes scaled to ρ_s or a, respectively. The local diffusivities and confinement times can be written as $D_{gB} = (c_s/a)\rho_s^2 F_{gB}$ or $D_B = c_s \rho_s F_B$ and $\tau_{gB} = B^{-1}(\rho_s/a)^{-3}\bar{F}_{gB}$ or $\tau_B = B^{-1}(\rho_s/a)^{-2}\bar{F}_B$, respectively. The form factors (F) are possibly complicated functions of the dimensionless parameters associated with geometry (safety factor q, aspect ratio R/a, elongation b/a), atomic and profile parameters (A, Z_{eff}, L/a where L is any plasma or heating gradient length), and the plasma parameters collisionality ($\hat{\nu} \propto \nu a/c_s$) and β (or $\hat{\beta} = \beta/\beta_{crit}$ where $\beta_{crit} \propto a/Rq$). [Dependence on the Debye length λ_D/a is not considered.] Discharges with all these dimensionless parameters including ρ_s/a the same would have $\tau \propto B^{-1}$ [1–3] and could be called dimensionally identical in their transport properties. It is well known that isolating the dependence on the dimensionless variables [ρ_s/a, $\hat{\nu}$, $\hat{\beta}$, ...] imposes a single constraint [2] on the scaling of τ with respect to machine variables [B, a, P, n, ...]. In this paper, we observe that while dimensionally identical discharges cannot be scaled to ignition, existing and proposed ignition regime tokamak discharges can have all these dimensionless parameters the same except ρ_s/a. We shall call such discharges "dimensionally similar" and focus on the scalings with respect to ρ_s/a.

If either the gyro-Bohm or Bohm type scaling dominates (or at least an suitable admixture remains constant with the similarity variables fixed), then we have a powerful method for size (a) and field (B) scaling existing discharges to ignition. For dimensionally similar discharges it is easy to show that $\tau_{gB} \propto Ba^{5/2}$, $[n(0)T(0)\tau]_{gB} \propto B^3 a^{5/2} \propto I^3 a^{1/2}$ with $P_{gB} \propto Ba^{1/2}$ and $\tau_B \propto B^{1/3}a^{5/3}$, $[n(0)T(0)\tau]_B \propto B^{7/3}a^{5/3} \propto I^{7/3}a^{-2/3}$ with $P_B \propto B^{5/3}a^{4/3}$. In addition, $n \propto B^{4/3}a^{-1/3}$, $T \propto B^{2/3}a^{1/3}$, and $\rho_s/a \propto B^{-2/3}a^{-5/6}$. {It is clear from the latter that dimensionally identical discharges have (B^4a^5) constant with $n(0)T(0)\tau \propto B$ in addition to $\tau \propto B^{-1}$ [3]}. The most severe limitation to dimensionally similar scaling is imposed by the operating density limit which is most likely a radiation collapse limit $n_{limit} \propto (B/Rq)(P/P_{OH})^{1/2}$ (see Ref. 4). Thus, $n/n_{limit} \propto B^{1/3}a^{2/3}(P/P_{OH})^{1/2}$ with

*This is a report of work sponsored by the U.S. Department of Energy under Contract No. DE-AC03-89ER51114.

†Also at University of California at San Diego, San Diego, California

$(P/P_{OH})_{gB} \propto 1$ whereas $(P/P_{OH})_B \propto B^{2/3}a^{1/6}$. This limit is most restrictive in scaling to larger size rather than larger field.

The method is most clearly illustrated with a B field scaling of DIII–D to a "CIT-like" device. Bremsstrahlung power losses (P_{br}) scale as $n^2T^{1/2}a^3$ and we can assume fusion alpha power gains (P_α) scale as $n^2T^3a^3$ in the ignition regime $\langle T\rangle \sim 3$ to 10 keV [see Ref. 4 for formulas]. We need only solve the ignition power balance $P_0 x_B^{\delta_B} x_a^{\delta_a} = P_{\alpha 0} x_B^{14/3} x_a^{10/3} - P_{br0} x_B^3 x_a^{5/2}$ for $x_B = B_1/B_0$ and/or $x_a = a_1/a_0$ given the power loss P_0 with P_{br0} and $P_{\alpha 0}$ evaluated for a given experimental discharge with a_0, B_0, average density $\langle n\rangle_0$, and average temperature $\langle T\rangle_0$. $\delta_B = 1(5/3)$ and $\delta_a = 1/2(4/3)$ for gyroBohm (Bohm). x_B and x_a are the numerical increases in field and/or size to obtain ignition. Clearly, these will be derived from discharges with largest $\hat{\beta}$, lowest q, and otherwise best $n(0)T(0)\tau$. Figure 1 shows a field scaling x_B ($x_a = 1$) for some DIII–D H–modes with $0.4 < \hat{\beta} < 0.6$, $3 < q_{MHD} < 4$ ($q_{ellipse} = 2.2$ to 3.0), $B = 2.1$ T, $a \sim 62$ cm, $2.7 < R/a < 2.8$, $1.8 < b/a < 2.1$ versus gross collisionality $\hat{\nu} \equiv \bar{n}_{13}^3 a^5(m)R^2(m)(b/a)^2/W^2$ (MJ). Parabolic $(1 - r^2/a^2)^\alpha$ profiles were used with $\alpha_n = 0.5$, $\alpha_T = 3/2\cdot(q_{ellipse} - 1) \sim 1$ and $T_i = T_e$. These are preliminary conservative assumptions intended to illustrate the method rather than a final optimal result. The method can be improved with $T_i \neq T_e$ and actual profiles. Clearly there is a crucial difference between gyroBohm and Bohm scaling.

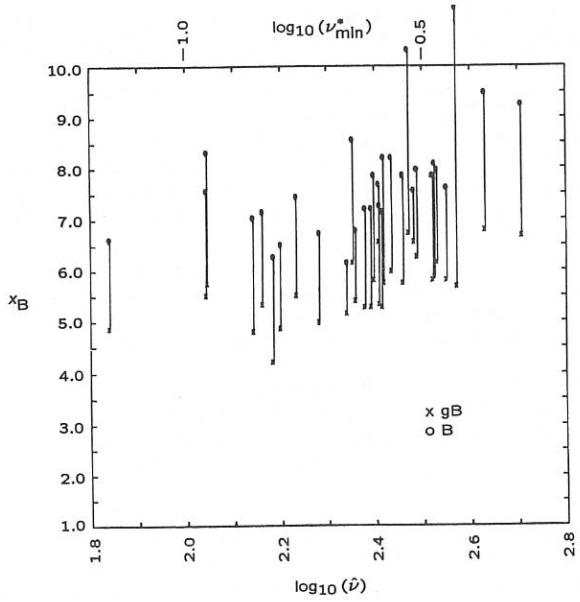

FIG. 1. B field scaling of DIII–D H–mode discharges to ignition.

There is, however, at least a modern theoretical predisposition toward the shortwave or gyroBohm type scaling. The collisional or neoclassical diffusion losses are of the gyroBohm type. All the electrostatic drift wave modeling formula used for fitting and ignition projections assume

All the electrostatic drift wave modeling formula used for fitting and ignition projections assume wavelengths and mixing lengths scaled to ρ_s (*e.g.*, Ref. 4). In the present context, these may be seen as interpretation formulas for $\bar{F}_{gB}$. However, the gyroBohm type scaling is not limited to $E \times B$ drift wave transport. It includes formulas for magnetic transport from micro-tearing modes (similar to $E \times B$ collisional drift wave scaling), electromagnetic transport at very short (c/ω_{pe}) scales {*e.g.*, Ohkawa type models $D \propto v_{eth}/Rq \cdot (c/\omega_{pe})^2 \propto (c_s/a)\rho_s^2 \cdot [1/\beta \cdot a/Rq \cdot (m_e/m_i)^{1/2}]$} and magnetic diffusion of the Carreras-Diamond-Rechester-Rosenbluth type {*e.g.*, $D \propto (c_s/a)\rho_s^2 \cdot [\hat{\nu}\beta^{1/2}\hat{\beta}^{3/2}(m_i/m_e)^{1/2}]$}. There are fewer Bohm examples. Apart from the likelihood that Bohm scaling obtains in a sharp boundary layer where $1/L \propto 1/\rho_s$, there is a recent suggestion from numerical simulation of resistive MHD turbulence [5] that dominant wave numbers scale to $m = n \cdot q$ with lowest n. This leads to a mixed but nearly Bohm scaling $D \propto c_s\rho_s(\rho_s/a)^{1/3}$.

Unfortunately, the experimental distinction between gyroBohm and Bohm types scaling is not entirely clear. Apart from the dependence on $\hat{\nu}$ and $\hat{\beta}$, $\tau_{gB} \propto B^{4/5}a^3n^{3/5}P^{-3/5}$ and $\tau_B \propto B^{1/3}a^{5/2}n^{1/2}P^{-1/2}$ at fixed q, R/a, and b/a. This can be compared to Goldston L–mode scaling $\tau_L \propto Ba^{2.4}n^{+0}P^{-0.5}$. Christiansen, Cordey, and Thomsen [6] have statistically analyzed JET L– and H–mode discharges in terms of τ_{gB} and τ_B. Replacing B with B_θ and $\hat{\beta}$ with $\hat{\beta}_\theta$ to describe the experimental q dependence, they found that gyroBohm scaling fit best with F_{gB} $(= \bar{F}_{gB}^{-5/2}) \propto \hat{\nu}^{0.4}\hat{\beta}_\theta^{0.4 \text{ to } -0.4}$. A large intermachine data base can be analyzed under the single constraint as

$$\tau \propto B^{-1}(\rho_s/a)^{\alpha_1}\hat{\nu}^{\alpha_2}\hat{\beta}^{\alpha_3}q^{\alpha_4}(R/a)^{\alpha_5}(b/a)^{\alpha_6} \quad , \tag{1}$$

which then determines

$$\tau \propto B^{\beta_0}a^{\beta_1}P^{\beta_2}n^{\beta_3}q^{\beta_4}(R/a)^{\beta_5}(b/a)^{\beta_6} \quad . \tag{2}$$

Bickerton [7] recently found for a large L–mode data base $\beta_0 = 1.08$, $\beta_1 = 2.31$, $\beta_2 = -0.579$, $\beta_3 = 0.069$, $\beta_4 = 1.0$, $\beta_5 = 0.01$, $\beta_6 = 0.212$. This is equivalent to $\alpha_1 = -1.58$, $\alpha_2 = -0.214$, $\alpha_3 = -0.985$, $\alpha_4 = -1.35$, $\alpha_5 = -0.270$, $\alpha_6 = 2.13$. From $\alpha_1 = -1.58$, a scaling less favorable than Bohm ($\alpha_1 = -2$) is indicated.

Statistical regression of raw confinement time suffers three problems: how to weigh discharges particularly in inter-machine comparisons, co-variance of some machine variables, and perhaps most important, how to correct for atomic effects such as fast ion storage and beam penetration. For fast ion storage we can correct experimental τ_E by $[1 - \tau_E/\tau_s \cdot G_e/2]$ where τ_s is the volume average slowing time down and G_e ($\sim 1/2$) is a function of beam voltage. The correction for beam penetration can be handled by normalizing the discharge confinement times from each machine to the penetration at $2\bar{n}_s$. $\bar{n}_s$ is the density at two mean free paths along the path giving 13% shinethrough. The confinement time renormalization appears to be insensitive to the profile and temperature dependence of the assumed diffusion. Table I shows a constrained analysis of an L–mode data base weighted by reportage. It is clear that these corrections to the confinement time induce a more favorable density scaling and change the ρ_s/a scaling away from Bohm to gyroBohm ($\alpha_1 = -2.07$ to $\alpha_1 = -3.15$). Perhaps corollary to this is the observation that low density ohmic neoalcator scaling in dimensionally consistent form [8] $\tau_{OH} \propto na^{5/4}R^2(P/P_{OH})^\gamma$ has $\tau_{OH} \propto B^{-1}(\rho_s/a)^{(-3.5 \text{ to } 4.2)}$... for $\gamma = 0$ to -0.8. In this case, no atomic corrections are needed.

The single constraint of plasma physics offers the possibility that B scaling in any single machine (at fixed R/a, b/a) can determine the ρ_s/a scaling and thus the universal size scaling (for any given regime). For example, in the L–mode, variation of the machine variables B, P,

TABLE I
L-MODE FITS OF CONFINEMENT TIME, EQS. (1) AND (2)

	β_0	α_1 β_1	α_2 β_2	α_3 β_3	α_4 β_4	α_5 β_5	α_6 β_6	RMS FIT FACTOR
RAW		−2.07	−0.378	0.0514	−1.04	−0.327	1.92	1.43
	0.790	1.94	−0.187	−0.078	−0.804	−0.368	1.75	
	(1.04)	(2.46)	(−0.624)	(0.197)	(−0.859)	(−0.142)	(0.147)	(1.22)
FAST ION & PENETRATION CORRECTIONS		−3.15	−0.175	0.374	−1.67	0.721	2.67	1.56
	0.757	2.99	−0.460	0.568	−0.701	1.05	1.85	
	(1.01)	(3.69)	(−0.772)	(1.23)	(−0.633)	(1.59)	(1.80)	(1.34)

( ) = unconstrained
Kaye 85: 108 (ISX-B), 215 (DITE), 227 (DIII), 4 (TFTR), 32 (ASDEX), 42 (PDX), 70 (PLT), 73 (TFTR)
Kaye 88: 16 (DIII-D), 401 (JET), 70 (JFT-2), 276 (JT- 60), 189 (TFTR)

n, I allows α_1, α_2, α_3, α_4 to be determined. The constraint allows five variables β_0, β_2, β_3, β_4, and in particular the size scaling β_1 to be determined. This is illustrated in Table II for JET L-modes.

TABLE II
SINGLE MACHINE SIZE SCALING

	β_0	α_1 β_1	α_2 β_2	α_3 β_3	α_4 β_4	RMS FIT FACTOR
UNCORRECTED JET-L	1.30	−2.68 2.58	−0.435 −0.447	−0.337 0.020	−1.50 −1.02	1.15
CORRECTED JET-L	1.30	−3.78 3.19	−0.402 −0.498	0.0974 0.345	−2.01 −1.01	1.16

Experiments on DIII-D are in progress to determine the gyroradius scaling by a 0.7 to 2.1 T B scan at a particular fixed $\hat{\nu}$, $\hat{\beta}$, q (the density and power will vary appropriately over the scan). These experiments are expected to distinguish $\tau_{gB} \propto B$ from $\tau_B \propto B^{1/3}$. We expect, however, that detailed examination of the local diffusion (rather than simply the uncorrected global τ_E) will be required for a definite conclusion.

References

[1] B.B. Kadomtsev, J. Plasma Phys. **1** (1975) 295.
[2] J.W. Connor and J.B. Taylor, Nucl. Fusion **19** (1977) 1047.
[3] J. Sheffield, Oak Ridge National Laboratory Report ORNL/P-90/0979 (March 1990).
[4] R.E. Waltz, R.R. Dominguez, and F.W. Perkins, Nucl. Fusion **29** (1989) 351.
[5] B.A. Carreras and P.H. Diamond, Phys. Fluids B **1** (1989) 1011.
[6] J.P. Christiansen, J.G. Cordey, K. Thomsen (private communication, March 1990).
[7] R. Bickerton, Transport Task Force Workshop, Hilton Head, South Carolina, February 1990.
[8] W.W. Pfeiffer, R.E. Waltz, Nucl. Fusion **19** (1979) 51.

TRANSPORT CODE SIMULATIONS OF IGNITOR

M F Turner, J W Connor, M Cox, R Fitzpatrick, R J Hastie, T C Hender, G P Maddison, D C Robinson and T N Todd

Culham Laboratory, Abingdon, Oxfordshire, OX14 3DB, England
(Euratom/UKAEA Fusion Association)

1 Introduction

IGNITOR is a high magnetic field (B_T = 11 T, I = 10MA, with possible brief excursion to B_T = 13T, I = 12MA), compact (a = 0.45m, b = 0.78m, R = 1.2m), Ohmically heated device intended to attain ignition transiently during a 2-4s current flat top [1]. The purpose of this paper is to contribute to assessing whether, or under what conditions, ignition in D-T is possible. Because of uncertainties in energy confinement, sawtooth behaviour and MHD stability, this requires that a range of possibilities be explored. At the lowest level a wide ranging survey of the consequences of present empirical confinement time scalings and other assumptions (eg $Z_{\rm eff}$, profile shape) is carried out using a $\frac{1}{2}$D code (ie a zero dimensional code which accounts for profile factors). This is followed by a 1D time-dependent energy transport analysis, with a preset constant thermal conductivity, which can make rapid parameter scans (eg to investigate the effects of sawteeth and profile assumptions on the discharge evolution). A $1\frac{1}{2}$D code, which follows the evolution of the magnetic configuration in a shaped tokamak, in large aspect ratio ordering, is used to complement the simplified 1D study. This code employs transport coefficients and sawtooth models based on theoretical considerations. Finally, our results are summarised and discussed.

2 $\frac{1}{2}$D (POPCON) Ignition Studies

This study computes the powers associated with neoclassical Ohmic heating, P_{OH}, α-heating, P_α, bremsstrahlung, P_B, and synchrotron radiation, P_S, allowing for plasma para- and dia-magnetism, and the combined transport and line radiation loss P_L implicity represented by a number of empirical scalings for energy confinement time $\tau_E^{(2)}$ (Kaye-Goldston, Kaye (old), Goldston, Mereshkin-Mukhovatov, Neo-Alcator with optional power degradation (obtained by convolving neo-Alcator scaling with the OH power-temperature degeneracy factor to a chosen power), Shimomura-Odijima, Rebut-Lallia, Kay-big, Todd[3], Gottardi- Lackner[4]). In computing these powers allowance is made for profiles of $n, T, \eta_{NC}, <\sigma v>$ and B (based on profiles of the form $n = n_o(1-r^2/a^2)^{\gamma_n}$ etc), plasma shape, impurity dilution effects and $Z_{\rm eff}$. These powers can be used to assess whether ignition (ie $P_\alpha > P_{\rm LOSS}$, where $P_{\rm LOSS} = P_B + P_S + P_L$) occurs and whether or not it is achieved within the discharge pulse duration t_p, ie if $t_{\rm ch} < t_p$, where $t_{\rm ch}$ is the characteristic heating time $W_{\rm TOT}/(P_{\rm OH} + P_\alpha - P_{\rm LOSS})$.

These quantities have been calculated for IGNITOR conditions between 10MA, 11T and 12MA, 13T with $Z_{\rm eff}$ = 1 to 1.5, γ_n = 1 to 3, and γ_T = 1 to 2 for the various

confinement scalings. Net **P**ower **o**utput **con**tours are evaluated in the $\bar{n}, T_{io}$ plane, spanning typically $0.5 \rightarrow 12\times10^{20}m^{-3}$ and $3 \rightarrow 30$keV with a spot check at a prescribed point. Typical results from these spot checks are shown in Table 1 along with comments referring to the full POPCON plots.

The general conclusion is that global ignition is possible provided the energy confinement time exceeds about 0.45s and the density profile is significantly peaked. Core ignition (ie within 25% to 30% of the minor radius) is also checked in this analysis (assuming global and central confinement times are equal) and appears to be more readily attainable. The number of scaling laws allowing ignition for the same profile assumptions increases as the performance is increased from 10MA, 11T to 12MA,13T.

3 1-D Ignition Studies

This model solves time dependent radial electron and ion transport equations in cylindrical geometry. Density profiles of the form $n = n_o(1-r^2/a^2)^{\gamma_n}$ and equilibrium current profiles of the form $J = J_o(1-r^2/a^2)^{\nu}$, with J_o determined by the central q value (allowing for paramagnetic enhancements appropriate to IGNITOR geometry) and ν given by matching the total current I, are specified and are independent of time. Electron heating arises as a competition between neoclassical ohmic- and α-power and losses due to bremsstrahlung radiation, equipartition to the ions and transport. Ion heating depends on the balance of α-power and equipartition against transport losses. α-particles resulting from a 50-50DT mixture are assumed to deposit their energy instantaneously at their birth radius, and a spatially constant Z_{eff} arising from a single impurity ($Z_i = 6$) is assumed. Sawteeth are represented by an empirical model using a prescribed mixing radius r_m and preset sawtooth period τ_s. The thermal diffusivities K_e and K_i are increased greatly within r_m for a short time each sawtooth period, during which 50% of the α-power is prescribed to be promptly lost and density is optionally either unaffected or flattened over r_m. For simplicity an Intor like-form $K_e = K_i = K$ (preset constant) are used (which reproduces a JET Ohmic discharge reasonably well) allowing rapid parameter sensitivity scans.

IGNITOR simulation scans are made about the reference case $B_T = 11$T, $I = 10$MA, $n_o = 1.5 \times 10^{21}m^{-3}, \gamma_n = 3, Z_{\text{eff}} = 1.5$, which requires a value of K corresponding to $\tau_E > 0.38s$ to ignite without sawteeth. (Note that Neo-Alcator scaling gives 0.45s). Sawteeth of repetition period 100ms increase the required τ_E by $\geq 50\%$. Thus $\tau_E = 0.4s$ fails to ignite with $\tau_s = 100$ms, although the core ($r < a/3$) reaches a fusion parameter of $Q \sim 5$. Power degradation, modelled as $K \propto \sqrt{(P_{\text{OH}} + P_\alpha)/P_{\text{OH}}}$, has been studied and indicates that ignition can just be achieved with $\tau_E = 0.65$s (at $t = 2$s). Varying the peak density shows a weak optimum at $n_o \sim 1.2 \times 10^{21}$ (Fig 1). Finally a scan of I (with B_T (T) = I (MA) + 1) shows increasing the machine performance is strongly favourable (Fig 2).

4 $1\frac{1}{2}$D Ignition Studies

This code follows the evolution of the q-profile, toroidal field and the shape of the flux surfaces using an analytic expansion in the inverse aspect ratio and plasma shape[5]. The modelling includes finite slowing down time and orbit effects in P_α, neoclassical and paramagnetic effects in P_{OH}, Chang-Hinton neo-classical and toroidal-η_i-mode anomalous ion losses, bremsstrahlung and line radiation losses. The electron losses are based on a generic form for the thermal diffusivity χ_e which is a sum of $\chi_1 = C_1 T_e^{1/2} r^2/nR^3$ due to collisionless skin depth turbulence and $\chi_2 = C_2 T_e^{3/2} q/B^2 R$ due to collisionless

drift wave turbulence[6] (the choice of the geometrical factors being guided by theory and experiment). The sawtooth model is similar to that used in the 1D model but supplemented by a large anomalous resistivity which is triggered at each sawtooth collapse when q_o falls below $q_c \sim 0.7$; this rapidly returns q_o at each cycle to typical experimental values. Two cases for electron transport are considered. Since the approach to ignition is essentially an Ohmic phase, the form χ_1, benchmarked against JET ohmic cases, is first used; secondly, to simulate degradation, a sum of χ_1 and χ_2 is used, coefficients being benchmarked against T-10 with central ECRH[7] which may well mimic α-power effects. Results summarized in Table 2 are broadly in agreement with the 1D simulations.

5 Conclusion

It appears from the $\frac{1}{2}$D calculations (Table 1) that global ignition during the discharge pulse of IGNITOR at the standard performance (B_T = 11T, I = 10MA) is possible provided that the profiles are rather peaked. The 1D and $1\frac{1}{2}$D codes, which can study sawtooth effects, indicate the importance of sawtooth stabilisation for ignition (as shown in Table 2). However optimisation of the current rise scenario, not explored here, could significantly improve the ignition prospects. At the enhanced performance (B_T = 13T, I = 12MA) ignition is much more probable (Fig 2).

TABLE 1

Typical Results of $\frac{1}{2}$D POPCON Analyses for IGNITOR
($q_0 = 0.7, Z_{\rm eff} = 1.5, Z_i = 6, \mathcal{R}_{\rm synch} = 0.5, \gamma_T = 1.5$, check point $\bar{n}_{20} = 7, T_{io} = 10.5$keV)

Scaling Law	I MA	B T	γ_n	P_{OH} MW	P_α MW	P_{tr} MW	P_B MW	P_S MW	$\tau_{E(tr)}$ secs	$\tau_{E(LOSS)}$ secs	Comments
Neo-Alcator (no degradation)	10	11	3	8.2	20.1	15.3	5.2	0.6	0.67	0.48	Ignites trivially for $\bar{n}_{20} \geq 4$
Neo Alcator (with $P_{TOT}^{-0.5}$)	10	11	3	8.2	20.1	19.5	5.2	0.6	0.52	0.40	Ignites easily for $\bar{n}_{20} \geq 6$
Kaye-Big ($P_{AUX} = P_{TOT}$)	10	11	3	8.2	20.1	28.3	5.2	0.6	0.36	0.30	Fails strongly
Kaye-Big ($P_{AUX} = P_{TOT} - P_{OH}$)	10	11	3	8.2	20.1	19.1	5.2	0.6	0.53	0.41	Barely ignites, near $\bar{n}_{20} \approx 7$
Goldston ($P_{AUX} = P_{TOT} - P_{OH}$)	10	11	3	8.2	20.1	61.6	5.2	0.6	0.16	0.15	Fails very strongly
Rebut-Lallia	10	11	3	8.2	20.1	22.1	5.2	0.6	0.46	0.36	Ignites easily for $\bar{n}_{20} \geq 9$
Todd (Saulx-les-Chartreux)	10	11	3	8.2	20.1	47.8	5.2	0.6	0.21	0.19	Fails very strongly
Lackner-Gottardi	10	11	3	8.2	20.1	35.4	5.2	0.6	0.29	0.25	Fails strongly
Lackner-Gottardi	12	13	3	11.9	20.1	25.0	5.2	0.93	0.41	0.33	Ignites only for $\bar{n}_{20} \geq 11$
Lackner-Gottardi	12	13	1.5	11.9	17.0	30.8	5.3	1.1	0.36	0.30	Fails strongly

TABLE 2

$1\frac{1}{2}$D Ignitor Modelling Results
using JET and T-10 Benchmarking

	$n_{eo} = 1.5 \times 10^{21} m^{-3} < n_e >= 0.55 \times 10^{21} Z_{eff} = 1.2$			
	JET Benchmark			T-10 Benchmark
q_o	0.4	0.7	0.8	0.3
$\tau_s s$	∞	∞	200	∞
τ_E (2.8s)	0.8	0.7	0.48	0.3
t_{ign} s	1.5	2.7	∞	∞
T_{io} keV	8.5	8.5	3.0	4.5
P_α MW	15	17	1.7	2.1
P_{OH} MW	8	8	15	18.5
β_p	0.22	0.25	0.13	0.12

References

1. B Coppi, Vuoto XVIII, 153 (1988)
2. ITER Concept Definition V2 Ch3 (IAEA/ITER/D5/3)
3. T N Todd, European Tokamak Workshop, Saulx-les Chartreux
4. K Lackner & N Gottardi JET Report JET P(88) 77
5. R Fitzpatrick, C G Gimblett, R J Hastie & T J Martin, to be submitted to Plasma Physics and Controlled Fusion
6. J W Connor, Plasma Physics and Controlled Fusion **30** 619 (1988)
7. V V Alikaev et al, in Plasma Physics and Controlled Nuclear Fusion Research, Proc of the 10th Int Conf, London (IAEA, Vienna, 1985) Vol 1 p419

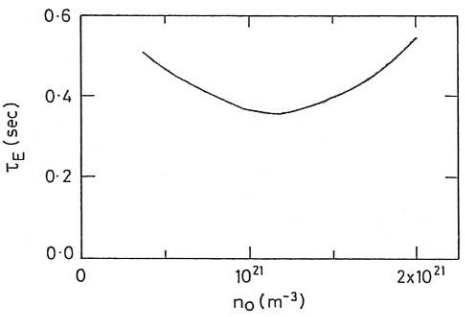

Figure 1 τ_E required for ignition in 2.8 sec as a function of density n_o

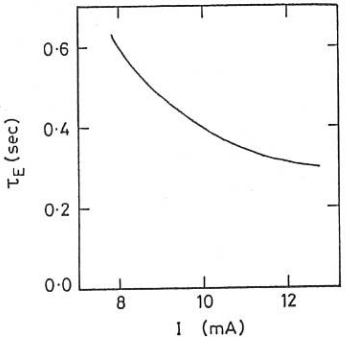

Figure 2 τ_E required for ignition in 2.8 sec as a function of plasma current I.

A PHYSICS PERSPECTIVE ON CIT

R.J. Goldston[1], G. Bateman[1], M. G. Bell[1], R. Bickerton[2], E. A. Chaniotakis[3], D. R. Cohn[3], P. L. Colestock[1], D. N. Hill[4], W. A. Houlberg[5], S. C. Jardin[1], S. S. Medley[1], G. H. Neilson[5], W. A. Peebles[6], F. W. Perkins[1], N. Pomphrey[1], M. Porkolab[3], J. A. Schmidt[1], D. J. Sigmar[3], R. D. Stambaugh[7], D. P. Stotler[1], M. Ulrickson[1], R. E. Waltz[7], K. M. Young[1]

Introduction

The mission of the CIT device is to study the physics of self-heated fusion plasmas, and to demonstrate the production of substantial amounts of fusion power. In order to achieve this mission with maximum confidence, and minimum cost, CIT is designed as a high-field, compact, copper-alloy-magnet device of modest pulse length. The most appropriate dimensionless parameters to measure extrapolation in confinement physics are $\omega_c\tau_E$ and $nT\tau_E/B$. CIT is projected to stand midway between JET and the ITER interim conceptual design in these parameters, and so represents a *relatively* modest step. Nonetheless, because for dimensionlessly similar devices ($aB^{4/5}$ = const.[1]) $nT\tau_E$ is proportional to B, we project CIT to have about the same $nT\tau_E$ as ITER, ~10x that of JET. Our projections for confinement, impurity levels, and profile shapes indicate that CIT should attain Q ~ 25, with 20 MW of heating power (P_{fus} = 500 MW), corresponding to β = 3% (=2I/aB). Even given pessimistic assumptions, CIT should achieve its basic mission to determine the confinement physics, operational limits, and α-particle dynamics of self-heated fusion plasmas with α power greater than auxiliary heating power, while producing more than 100 MW of fusion power. In reaching these conditions CIT will also explore heating, fueling, and plasma handling techniques necessary to produce self-heated fusion plasmas, at surface power densities appropriate for economic DT fusion reactors.

Dimensionless Scaling Analysis

Kadomtsev[1] has shown that under rather general assumptions a class of dimensionlessly similar devices is characterized by $I_p \propto B^{1/5}$, $a \propto B^{-4/5}$, $n_e \propto B^{8/5}$, $P \propto B^{3/5}$, $\tau_E \propto B^{-1}$, $nT\tau_E \propto B$. The usefulness of this approach for projecting the performance of future devices has been stressed by Rebut, Lackner, and Sheffield. We have tested Kadomtsev's analysis by performing linear regression on the Kaye-ITER[2] L-mode database in the following form:

1. Princeton University, Princeton N.J.
2. University of Texas, Austin TX
3. Massachusetts Institute of Technology, Cambridge MA
4. Lawrence Livermore National Laboratory, Livermore CA
5. Oak Ridge National Laboratory, Oak Ridge TN
6. University of California, Los Angeles CA
7. General Atomics Corp., San Diego CA

$$\ln(B^{\gamma}\tau_E) = \nu_1 + \nu_2\ln(aB^{4/5}) + \nu_3\ln(n_eB^{-8/5}) + \nu_4\ln(PB^{-3/5}) + \nu_5\ln(q) + \nu_6\ln(R/a) + \nu_7\ln(\kappa) + \nu_8\ln(A_i) \quad \text{(eq. 1)}$$

with the exponent of B, γ, taken as variable. Since the intrinsic measurement error in this database probably approaches 10%, it is remarkable that the fit optimizes with 12.6% R.M.S. error at γ=0.934, close to the theoretical value of 1.0. The fit error rises parabolically to ~16% for $|\gamma - 1| = 1$.

Examination of existing ohmic heating results reveals that PLT and Alcator C density-scan data are extremely close to dimensionless similarity in all respects except for aspect ratio (3.3 vs. 3.9). The confinement measurements from these two devices, plotted on appropriate axes (fig. 1), show remarkable agreement in magnitude and in variation with normalized density, supporting the extension of the Kadomtsev dimensionless-similarity analysis to high-field tokamaks.

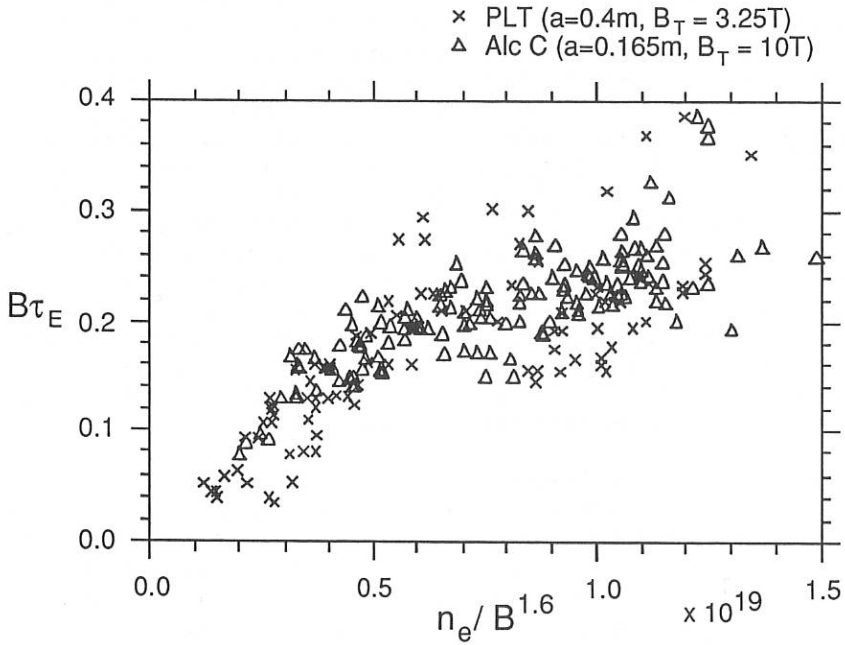

Fig. 1. PLT and Alcator C[3] data plotted on Kadomtsev axes (all units SI).

Kadomtsev's analysis has been tested previously by noting the closeness of various OH and L-mode scaling relations to meeting the constraint of equation (1) with γ=1. Indeed an L-mode scaling relation derived by linear regression on the Kaye-ITER database, constrained via equation (1) with γ=1, differs from a free regression fit in its prediction for CIT parameters by only 10%. The Kadomtsev similarity per-

spective, then, can be used to understand the advantages of attaining high $nT\tau_E$ by working at high magnetic field. Since $nT\tau_E$ is maximized for a class of dimensionlessly similar devices by operating at high B and small size, the distance in dimensionless parameters (e.g. ν_*, ρ_i/a, $\omega_c\tau_E$, $nT\tau_E/B$) which must be traversed from present devices to a device which achieves the $nT\tau_E$ required for high gain is minimized at high B. Thus the physics risk with respect to confinement extrapolation is minimized. Since for fixed magnet technology, cost scales much more strongly with size than with field strength (up to the appropriate stess limits), the cost/performance ratio is also minimized by operating in this regime. The appropriate pulse length for a compact high-field DT tokamak is $5 - 10\tau_E$, where helium ash build-up can be observed but active pumping is not required. The limit to this high-field, reduced-size approach is set by 1) the need to test reactor-like plasma-handling techniques (flexible divertors, high elongation), 2) the need to maintain adequate access for diagnostics and for intense auxiliary heating (in order to ensure the ability to perform α-particle physics studies at relevant temperatures and β's even if confinement is relatively poor), and 3) the need to limit surface power density at the β required to study the relevant α physics.

Performance Projections

It is important to project for CIT not only the expected performance, but also the range of uncertainty of performance, in order to assess the degree of confidence in achieving CIT's mission. The main CIT parameters are: R=2.14m, a=0.66, κ_{95}=2, B_T=10T, I_p=11MA. We take as baseline parameters for performance projection: τ_E^{Hmode} = 1.85x ITER89-P L-mode scaling, Z_{eff} = 1.65 due to carbon and helium, square-root-parabolic density profiles, and trapezoidal temperature profiles, flat from r = 0 to a/q_{95}.

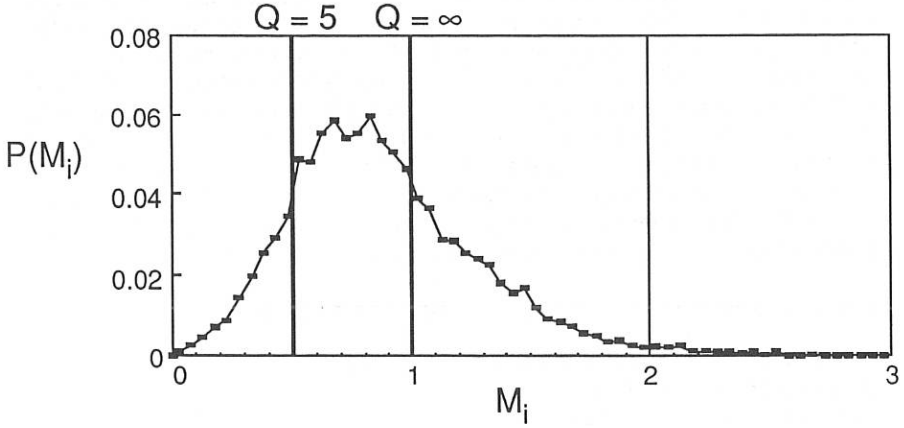

Fig. 2. Relative probability distribution of ignition margin, $M_i = P_\alpha/P_{loss}$. $Q = 5M_i/(M_i - 1)$. (Bin width, $\Delta M_i = 0.05$, 5000 samples.)

For the ranges of uncertainty of the most important variables, we take a Gaussian distribution of confinement time with 1σ width +/- 25%, a Gaussian distribution of density profile exponent, α_n, with 1σ width +/- 0.5 and a lower cut-off at 0, and a Gaussian distribution of Z_{eff} with 1σ width +/- 0.35 and a lower cut-off at 1.2. The helium ash concentration is taken to be 3% of the electron density for $\tau_E \geq 1.85$x ITER89-P (corresponding to 1.5GJ of fusion energy production, with 100% helium ash accumulation), falling linearly to 0.5% for 1.4x ITER89-P. We use a Monte Carlo sampling technique[4] to evaluate the distribution of expected performance (fig. 2), and find that a moderate level of optimism leads to ignition even at reduced field and current, while moderate pessimism leads to Q ~ 5. The median projected performance is found to be Q ~ 25, corresponding to 500 MW of fusion power with 20 MW of auxiliary heating.

The CIT Physics Program

The CIT physics program will be a natural continuation of tokamak confinement research into the high $nT\tau_E$, α-dominated DT regime. Full understanding of the physics behavior in this regime will ultimately be required to optimize a tokamak reactor. Profile and fluctuation diagnostics will be provided in order to make contact with results from previous experiments, and new diagnostic techniques for understanding transport will be implemented as appropriate. Diagnosis of edge plasma behavior in the H-mode (scrape-off widths, parallel and perpendicular transport, fluctuations, and impurity behavior) will be especially important to understand and optimize divertor operation at reactor-like surface power densities. Diagnostics will be provided on CIT to measure the distribution of contained α particles, the loss of α particles due to α-driven instabilities, and the mode properties of α-driven instabilities. The clearest test of α heating efficiency requires operation at $Q \geq 5$, where the α power begins to dominate over the auxiliary heating power. At Q = 5 the "offset-linear" or "incremental confinement time" paradigm[5] provides a useful basis for comparing 40 MW of α + RF heating in a DT plasma to a baseline case of 20 MW of RF heating in a non-reacting plasma. In the range Q = 5 to ignition, CIT can study the initial α-driven thermal excursion for a period of $5 - 10\tau_E$. With adequate feedback bandwidth, 0-D calculations indicate that very high Q's can be stably controlled via modulation of the RF heating power, but 1 1/2-D calculations suggest that profile evolution (in effect excursions from a given fixed-profile <nT> vs. <n> plane) will be most important in affecting burn dynamics.

This work supported by U.S. DOE contract DE-AC02-76-CHO-3073

[1] B.B. Kadomtsev, Soviet Journal of Plasma Physics **1** (1975) 295.

[2] S. Kaye, private communication

[3] S. Wolfe, private communication

[4] S. Ho, J. Perkins, Nuclear Fusion **29** (1989) 81.

[5] M. Bell et al., Plasma Physics and Controlled Fusion **28** (1986) 1329.

Burn Threshold for Fusion Plasmas with Helium Accumulation*

B.D. Fried, G.J.Morales, and R.J.Taylor

Institute for Plasma and Fusion Research
University of California, Los Angeles, CA 90024-0205

The ignition and burn criteria for fusion plasmas are re-evaluated, taking into account the ratio of α particle confinement time τ_α to energy confinement time τ. Due to helium ash build-up, the burn threshold is raised substantially compared to the usual ignition criterion. No steady state burn is possible when $\tau_\alpha/\tau > 15$, and even small concentrations of impurities can substantially reduce this upper limit, resulting in stringent requirements on radial transport, recycling and pumping of helium ash. H-mode plasmas, which may exhibit high values of τ_α, are undesirable for steady state burning, since large τ_α implies low fueling rate and hence low fusion power yield.

The classic requirement for fusion power generation is that the Lawson parameter $n\tau$ exceed $2x10^{20}$ sec/m^3 at a plasma temperature T $\sim$ 10 keV. The condition $n\tau T > 2x10^{21}$ sec keV m^{-3}, or, equivalently, $\beta B^2\tau > 1.6$ Tesla^{2}sec, is a way of approximately taking into account the temperature dependance. However, these simplified criteria ignore the thermalized helium population, which can dilute the D-T fuel and increase the energy loss due to bremsstrahlung radiation. We examine here the effects of this helium "ash" accumulation, which could be of importance in predicting the performance of ignition experiments such as ITER and CIT. Both of these devices appear to lie below the simplified ignition thresholds if they operate in L-mode, so some increase in $\beta B^2\tau$ is required. Since B fields are already near the stress limits of present materials and β has been pushed to (and is restricted by) the MHD (Troyon) limit, it will be necessary to raise τ, for example by operating in H-mode, which increases τ by a factor of two or more. However, the particle confinement time also increases, and, in fact, by a much larger factor, so the ratio $\gamma \equiv \tau_\alpha/\tau$ of effective α particle containment time to central energy confinement time can increase appreciably during a transition from L-mode to H-mode.

Using a highly simplified, phenomenological model, we find that γ is a crucial parameter for steady steady burn. Our model assumes that the electron density n is feedback controlled, and hence can be treated as a constant; that the central energy confinement time τ determined by

plasma processes other than bremsstrahlung and synchrotron radiation is also a constant; and that all species can be represented by a common temperature T. Conservation of energy and α particles then leads to two coupled differential equations for T and the relative helium ion concentration $\alpha \equiv n_{He}/n$ Dividing both equations by n^2 and measuring n and T in units of $10^{20}m^{-3}$ and keV, respectively, we obtain the scaled equations

$$n^{-1}3(1 - \alpha/2)(d/dt + 1/\tau)T = h + (1 - 2\alpha)^2 F E_\alpha - (1 + 2\alpha)b \ , \qquad (1)$$

and

$$n^{-1}(d/dt + 1/\gamma\tau)\alpha = (1 - 2\alpha)^2 F \ , \qquad (2)$$

where $\alpha \equiv n_{He}/n$ is the relative He concentration; $h = p_{ext}/n^2$, p_{ext} being the external heating power density; $b = 0.334T^{1/2}$ is the bremsstrahlung coefficient; $F(T) = 322T^{-0.8}[1+(T/30)^{1.3}]^{-1}\exp\{-22T^{-3.6}\}$ gives the fusion reaction rate[1]; and $E_\alpha = 3500$ keV.

The stationary solutions of these equations are obtained by setting the time derivatives and h equal to zero. Eliminating $n\tau$ gives a cubic equation for α as a function of T, and $n\tau$ can then be determined from Eq. (2). The results for the case h = 0, corresponding to a burning plasma, are shown in Fig. 1, where α and the resultant $n\tau = \alpha/\gamma F(1-2\alpha)^2$ and fusion power $p_f = n_D n_T \langle\sigma v\rangle_f E_f = [2.29x10^{-5}(1-2\alpha)^2 n^2 F]Mw/m^3$ are plotted as functions of T for various values of γ. [E_f = 17.5Mev is the total fusion energy.] For situations where the bremsstrahlung is relatively unimportant (b very small), Eqs. (1) and (2) , with h = 0, give $\alpha = (3\gamma T/E_\alpha)/(1 + 3\gamma T/2E_\alpha)$, leading to the (nearly straight) plots of α vs. T which are shown (dotted) in the lower portion of Fig. 1b for γ = 1, 3 and 5. In the opposite limit, where bremsstrahlung is more important than other energy loss mechanisms (convection, diffusion, etc.) i.e., when the left side of (4) can be neglected, α satisfies a quadratic equation whose physically relevant solution is shown as the uppermost, dotted curve, labelled bremsstrahlung limit, in Fig. 1b. In Fig. 1a, each point on a given γ contour represents a possible steady state fusion burn. For that same γ value, points inside the contour correspond to uncontrolled burning, while points outside are below the threshold for burning. The asterisks on the curves in Fig.1 represent a "comfortable" operating point, with γ = 5, T = 20 keV, α = 9% and $n\tau = 2.5 \times 10^{20}$sec/m^3, yielding a fusion power of 2 $Mw/m^3/(n_{20})^2$. Note that **no steady state D-T burn is possible unless $\gamma < 15$.** If terms representing additional impurities are added to the left side of (1) and to the bremsstrahlung term on the right, a similar analysis shows that small impurity concentrations significantly reduce this upper limit,. Contamination with 3% of oxygen or 6% of beryllium, for example, cuts it in half.

The minimum values of $n\tau T$ and $\beta B^2\tau$ required for burning are shown in Fig. 2. Even for $\gamma = 5$ in a pure plasma, a $\beta B^2\tau$ value of 3.2 is required, i.e. a factor of 6 higher than has been achieved on JET ($\beta = 8\%$, $\tau = 0.5$ sec., $B = 3.5T$) and a factor 16 greater than TFTR ($\beta = 4\%$, $\tau = 0.2$sec., $B = 5T$). Since the prospects for substantially increasing either β or B are not promising at this time, it is essential to find methods of increasing τ and to do this without increasing γ, which would raise the required $n\tau T$ even more. (For example, as illustrated in Fig. 2, transition from L-mode operation, with $\gamma = 1$ and $n\tau T$ half the ignition threshold, to H-mode could double τ, but if γ increases by a factor of 10, as experiments seem to indicate[2,3], the plasma would remain well below the burning threshold.)

Our simple model can also be used to examine ignition transients, as might be experienced in a short pulse device like CIT. We fix $n\tau$ and the power input, h, and solve the coupled equations (1) and 2) for T and α as functions of time. Figures 3a and 3b show the results for $n\tau = 2.5 \times 10^{20}$sec/m^3 and $p_{ext} = 0.1$ Mw/m^3 at $n = 10^{20}$m^{-3} (corresponding to $h = 6.25$) for $T < 20$ keV; the input power is turned off when $T > 20$ keV. Only cases with γ below 5 are ignited indefinitely; for larger γ there is only a fusion "afterglow" for a time of order 5τ.

We conclude that to achieve ignition and sustained burning, it will be essential to increase τ and, at the same time, keep γ as low as possible, i.e. limit τ_α. Given the large cost of even an experimental D-T machine, the alternative option of building a long pulse **hydrogen** tokamak large enough to guarantee the achievement of fusion burn conditions is quite attractive. By injecting helium to simulate α particle generation, such a device could be used to examine a number of fusion plasma questions and to explore methods for decreasing the α particle confinement time (i.e., reducing γ).

* *This work was supported by the U.S. Department of Energy*

REFERENCES

1) The expression for F uses an empirical fit to the experimental data cited in the NRL Plasma Formulary (1987), p. 45, for the fusion reaction rate $<\sigma v>$.

2) P.H. Rebut and P.P. Lallia, Fusion Engineering and Design 11 (1989) 1-21. Also A. Gondhalekar, et al. 15th Euro. Conf. on Cont. Fus. and Plasma Phys., Dubrovnic 1988, Vol. 12b, part 1, p. 151.

3) R.J. Taylor, et al., Phys. Rev. Lett. 63, 2365 (1989).

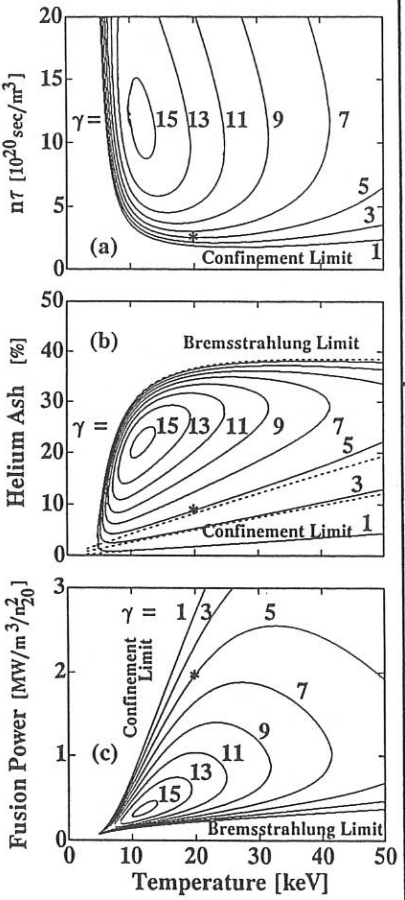

Fig. 1. Steady state contours of $n\tau$; the alpha particle concentration α; and the fusion power density as functions of temperature for several values of the ratio $\gamma \equiv \tau_\alpha/\tau$ of alpha particle removal time to energy confinement time.

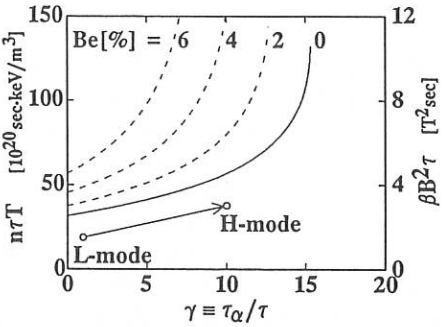

Fig. 2. Minimum $n\tau T$ required for steady state burn vs. γ

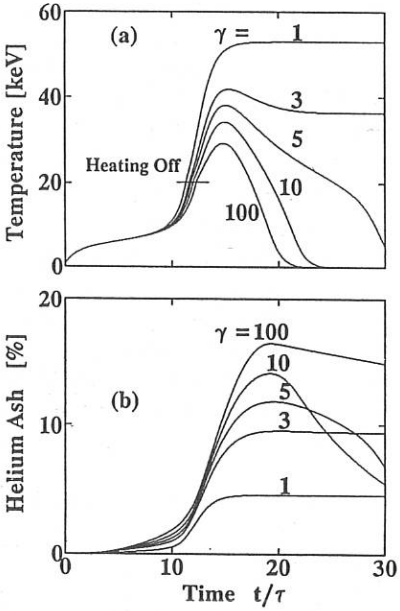

Fig. 3. Temperature rise and helium ash accumulation for $n\tau = 2.5 \times 10^{20} sec/m^3$ and $p_{ext} = 0.1 Mw/m^3/(n_{20})^2$. The heating is turned off when T reaches 20 keV.

HEATING PROFILE AND SAWTOOTH EFFECTS ON ENERGY CONFINEMENT IN ELONGATED TOKAMAK PLASMAS*

J.D. Callen and Z. Chang
University of Wisconsin, Madison, WI 53706-1687 U.S.A.
A.G. Kellman and D.P. Schissel
General Atomics, San Diego, CA 92138-5608 U.S.A.

1. Introduction

There is at present no completely satisfactory model of anomalous transport in plasmas. However, there are a number of indications that a simple local transport model[1,2] can be used to describe changes in the global energy confinement caused by variations in the heating profile, sawteeth, and their combination in auxiliary heated tokamak plasmas. In this work we use the local transport model to further investigate the various effects related to energy confinement degradation.

2. Theoretical Model

The time averaged (over the sawtooth repetition time) global energy confinement time for a tokamak can be written, according to the local transport model,[2,3] as

$$\tau_E = \tau_\chi \eta_Q f_s + \tau_{ped}, \qquad (1)$$

where η_Q is the heating effectiveness, $0 \le \eta_Q \le 1$. $\eta_Q = 1$ when the heating profile $Q(\rho)$ is centrally peaked [$Q \propto \delta(\rho)$]; $\eta_Q = 0$ when $Q(\rho)$ is edge localized [$Q \propto \delta(\rho - 1)$]. f_s is the time-averaged sawtooth degradation effect[2]:

$$f_s = (1 - L)(1 - S)\, g(t_R/\tau_E) + [1 - g(t_R/\tau_E)] \qquad (2)$$

where L is the transport volume degradation contribution (L = 0 for mixing radius $\rho_m = 0$), S is the sawtooth effect related to the heating profile [$S \le 0$; the equality holds for $Q \propto \delta(\rho)$], and $g(x) = (1 - e^{-x})/x$ represents the time average of the sawtooth effects. τ_{ped} is the temperature pedestal confinement time -- it will be neglected in this work. τ_χ in Eq. (1) is the ideal energy confinement time [without sawteeth ($f_s = 1$), for no pedestal effect ($W_{ped} = 0$) and with a centralized heating profile ($\eta_Q = 1$)].

In order to obtain the analytic expressions for the confinement degradation study, we adopt a cylindrical geometry and use the model profiles: density $n(\rho)$=constant (a discussion of density profile effects can be found in Ref. [2]), thermal diffusivity $\chi(\rho)=\chi_0/(1-\alpha\rho^2)$ and heating profile $Q(\rho)=Q_0(1-\rho^2)^\gamma$ (Fig. 1), where α and γ are constant parameters.

η_Q effect. Using these profiles we obtain

$$\eta_Q = \left(\frac{1-\alpha}{1-\alpha/2}\right)\left(\frac{\gamma+1}{\gamma+2}\right) + \left(\frac{\alpha}{2-\alpha}\right)\left(\frac{\gamma+1}{\gamma+3}\right) \qquad (3)$$

For a peaked $Q(\rho)$ (i.e., $\gamma >> 1$), η_Q approaches unity independent of the $\chi(\rho)$ profile, while when $Q(\rho)$ is flat (i.e., $\gamma=0$), η_Q equals 1/2 for $\alpha=0$ [flat $\chi(\rho)$] and 1/3 for $\alpha=1$ [$\chi(\rho)$ increasing strongly toward the edge]. Therefore, the radially increasing $\chi(\rho)$ enhances the η_Q degradation effect. This property holds true regardless whether sawteeth are present or not.

η_Q and sawtooth effects. In the sawtooth degradation factor f_s [Eq. (2)], L is independent of the heating profile, but S is closely related to $Q(\rho)$. Fig. 2 shows that, in fact, broad heating profiles (small γ) reduce the sawtooth degradation effect significantly. An interesting special case is that where the heating profile is localized outside the mixing radius (e.g., in the ECH heating case[4]). Then, the S term nearly cancels the L term, so that $f_s \simeq 1$[3]. Both the sawtooth and heating profile effects are shown in Fig. 3. We can see that for a given ρ_m (< 0.6) the rapid change of τ_E with varying $Q(\rho)$ occurs in the region $0 < \gamma < 5$. When ρ_m is very large ($\gtrsim 0.6$), the dependence of τ_E on $Q(\rho)$ is relatively small, which indicates that the approach of changing $Q(\rho)$ alone becomes inefficient for high current (low q) sawtoothing discharges. This phenomenon was observed previously in a "thought experiment" derived from DIII-D data[3].

Sawtooth repetition time effect. One way of suppressing the sawtooth effect is to extend their repetition time (t_R)[4]. Fig. 4 shows τ_E as a function of t_R/τ_E. We find that since the slope depends on the heating profile, {e.g., $\partial\tau_E/\partial(t_R/\tau_E) \propto \eta_Q[1-(1-L)(1-S)]$ for $t_R < \tau_E$}, when $Q(\rho)$ is flat, the improvement of τ_E (for large ρ_m) by extending t_R is very weak, while when $Q(\rho)$ is peaked, this t_R extension approach is quite efficient. In other words, extending the sawtooth period t_R should be combined with centrally peaking the heating profile [if the $Q(\rho)$ was flat] in order to obtain the largest increase in τ_E.

$\chi(\rho)$ effect. Since a flatter $\chi(\rho)$ profile also gives larger f_s,[2] both heating profile and sawtooth effects can be reduced by improving the plasma edge transport (see Fig. 5).

Elongation effect. The physical picture discussed above for a cylindrical tokamak is also suitable for elongated plasmas. The geometric effect is included in the model through the factors $dV(\rho)/d\rho$ and $\langle|\nabla\rho|^2\rangle$[1]. Preliminary analysis using DIII-D low-q H-mode data shows that when the current profile, q_{95}, $\chi(\rho)$ and sawtooth activity are kept the same, the elongation (κ up to 2) causes $\lesssim 3\%$ variations in the confinement time.

Summary of DIII-D data analysis results[3]. DIII-D low-q NBI heated H-mode data have been analyzed using this model. The results show that the saturation and fall off of τ_E as current increases observed in two different elongation (κ=1.75 and 2.05) experiments[5] can be basically explained by taking into account both the neutral beam heating profile and sawtooth effects. For the high current discharges, peaking the heating profile centrally alone can improve the τ_E by up to 20%. Suppression of sawteeth alone give a maximum of a 15% improvement. The combination of these two approaches can however improve τ_E by up to 60%.

3. Conclusions

Detailed theoretical analysis of the various effects related to the tokamak global energy confinement time in the presence of sawteeth shows that the heating profile plays an important role in the τ_E degradation analysis. It enters in the heating effectiveness factor η_Q as well as in the sawtooth degradation factor f_s. A reasonably centrally peaked $Q(\rho)$ can make sawteeth suppression schemes very efficient. On the other hand, increasing the sawtooth period can also increase the efficiency for achieving better confinement by peaking $Q(\rho)$. These results should be applicable to all tokamaks, especially for the strongly auxiliary heated tokamaks like DIII-D, TFTR, JET, CIT and ITER. The elongation effect *alone* appears to be small in the τ_E degradation analysis. However, there are some experimental indications that the $\chi(\rho)$ profile may change with elongation (from $\alpha \sim 1$ for circular discharges toward $\alpha \sim 0$ for $\kappa \gtrsim 2$), and this could cause more significant but indirect elongation effects on τ_E.

References

[1] J.D. Callen, J.P. Christiansen, J.G. Cordey, P.R. Thomas, K. Thomsen, Nuclear Fusion **27**, 1857 (1987).
[2] Z. Chang and J.D. Callen, Nuclear Fusion **30**, 219 (1990).
[3] Z. Chang, J.D. Callen, D.P. Schissel, A.G. Kellman, J.C. DeBoo and R.T. Snider, "Sawtooth Induced Global Energy Confinement Degradation In DIII-D", TTF Transport Meeting, Hilton Head SC, Feb 1990.
[4] R.T. Snider, *et al*, Phys. Fluids **B 1**, 404 (1989).
[5] K.H. Burrell *et al*, Plasma Physics and Controlled Fusion **31**, 1649 (1989).

* Research supported by the U.S. DOE under grants DE-FG02-86ER53218 and DE-FG02-87ER52140 (UW) and contract DE-AC03-89ER51114 (GA).

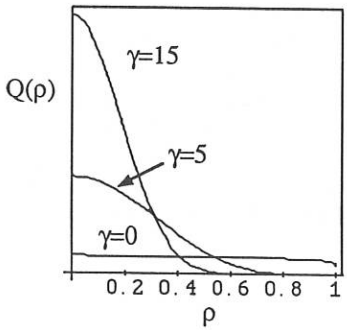

Fig. 1. Model heating profiles Q(ρ) for constant heating power.

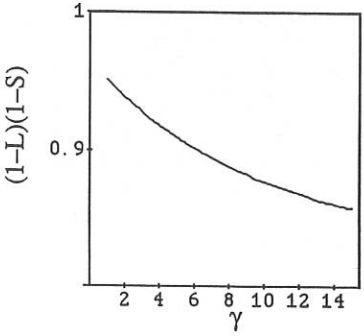

Fig. 2. Heating profile effect on the sawtooth flattening factor. α=0.5, ρ_m=0.4.

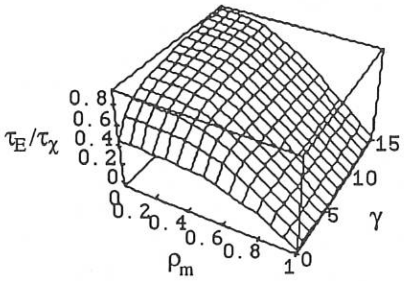

Fig. 3. Dependence of τ_E on both the sawtooth mixing radius and heating profile. t_R=0, α=0.5.

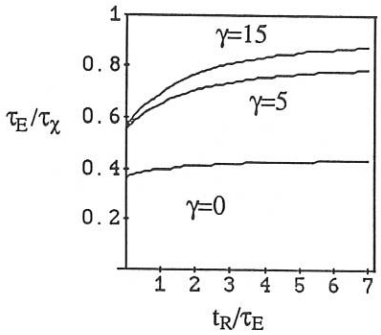

Fig. 4. Sawteeth repetition time effect for different heating profiles. ρ_m=0.6, α =0.5.

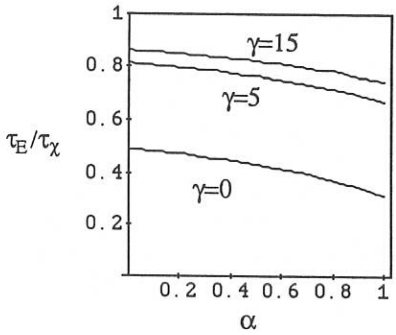

Fig. 5. Effective thermal diffusivity profile effect on τ_E. ρ_m=0.4, t_R/τ_E=0.5.

THE SCALING OF CONFINEMENT WITH MAJOR RADIUS IN TFTR

L. R. Grisham, S.D. Scott, R.J. Goldston, Cris W. Barnes, M.G. Bell, R. Bell, N.L. Bretz, C.E. Bush, A. Cavallo, B. Grek, G.H. Hammett, K.W. Hill, A. Janos, F. Jobes, D. Johnson, D.K. Mansfield, D. Mueller, J.A. Murphy, Y. Nagayama, H.K. Park, A.T. Ramsey, J. Schivell, B. Stratton, E.J. Synakowski, G. Taylor, H.H. Towner, R.M. Wieland, and M.C. Zarnstorff

Plasma Physics Laboratory, Princeton University
Princeton, New Jersey USA 08543

Introduction

Plasma-size scans have been performed in the TFTR tokamak to investigate the effect of aspect ratio and major radius on energy confinement in high-recycling L-mode plasmas heated by neutral beam injection. The plasma size was varied by more than a factor of two (a = 0.4→0.9 m, R = 2.08→3.2 m), while the aspect ratio varied from 2.8 - 8.0. The first size scan directly determined the dependence of τ_E on aspect ratio (or, equivalently, major radius) by comparing pairs of discharges with the same minor radius, beam power, plasma current and q_{cyl}, but different major radius and B_T. The second size scan also held q_{cyl} constant, but kept I_p proportional to a/R and $P_b \propto Ra$, to determine whether there is an advantage in τ_E or $\langle nT \rangle \tau_E$ to be gained from increasing either I_p or R/a at the expense of the other. This part of the experiment was motivated by observations that cost estimates for proposed high-performance tokamaks (CIT, ITER) are an increasing function of $I_p \times R/a$, and that heat flux to the divertor plate ($q_{flux} \propto P_b/Ra$) represents an important technical constraint.

Major Radius Scaling Experiment

TFTR is equipped with a carbon-tile toroidal belt limiter on the inner wall at R = 1.65 m and with two carbon-carbon composite poloidal-ring limiters on the outer wall at R = 3.60 m. The first plasma size scan compared pairs of plasmas with the same minor radius, plasma current, and beam power formed on the inner or outer limiters (see Fig. 1 & Table I). The toroidal field for all discharges was adjusted to maintain $q_{cyl} = 3.0 - 3.2$, with the exception of the R/a = 3.2/0.40 plasmas which had $q_{cyl} = 2.5$. The beam power for each pair was set at the maximum power handling capability of the outer limiter; this ensured that all plasmas were dominated by auxiliary power ($P_b/P_{OH} \geq 10$). Gas puffing was employed to maintain high density ($\bar{n}_e \sim 5 \times 10^{19}$ m^{-3}) for all plasmas except the smallest ones on the inner wall (a = 0.43 m), for which $\bar{n}_e = 3.2 \times 10^{19}$ m^{-3}. These densities were high enough to suppress the calculated beam contribution to diamagnetic stored energy to values typical of L-mode (20 - 33%), but low enough to allow good beam penetration, with beam power peaking factors $h(0)$ in the range 1.4 - 3.2. First-orbit beam losses were calculated to be only a few percent of the beam power, with a maximum of 7% for the inner wall 0.43 m plasmas, and beam shine-thru was typically $\leq$ 1% of P_b. Fokker-Planck calculations show that expected fast ion power losses due to ripple were

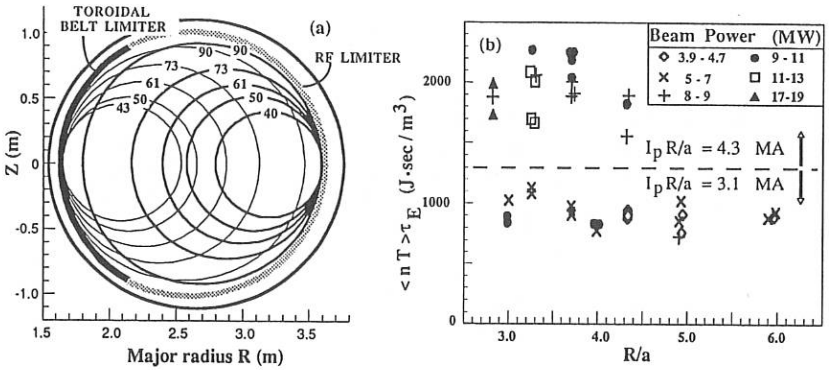

Figure 1: (a) Location of plasmas inside the TFTR vacuum vessel in these size-scaling experiments. (b) Measured $\langle nT\rangle\tau_E$ in scans at constant I_pR/a.

$\leq 15\%$ even for small plasmas on the outer limiter (where the edge peak-to-average ripple reaches $\sim 2\%$) because the tangentially-injected ions suffer little pitch-angle scattering until their energy drops to $E_{\rm crit}$. Two other standard L-mode plasma characteristics were less well reproduced. First, the loss of beam power by charge-exchange was calculated to reach 40% in the small $a = 0.40$ m plasmas (5-30% for $a \geq 0.50$ m) and thus represents a major uncertainty in the deduced size scaling. Second, the plasma density and Z_{eff} in discharges on the outer limiter rose continuously throughout the short ($\sim$ 250 ms) beam heating pulse allowed by limiter surface heating constraints, although τ_E reached equilibrium within one energy confinement time ($\sim$ 50 – 80 ms).

Table I summarizes the dependence of total stored energy (as measured by magnetic diagnostics) with major radius for three pairs of plasmas with significantly different major radius. Expressed in power-law form, the observed size scaling is $W_{\rm tot}^{\rm dia} \propto R^{1.6-1.7}$. Plasmas at small R have an anisotropic beam ion population ($P_\parallel/P_\perp \geq 1.0$) because the angle of beam injection ($R_{\rm tan}$ = 1.74-2.23 m) becomes more tangential for smaller major radius plasmas. This explains why the major radius scaling of total stored energy deduced from equilibrium magnetics (which are sensitive to $P_\parallel$) is weaker than from the diamagnetic measurements. The thermal stored energy is itself estimated by subtracting from W_{tot} the total beam energy calculated by a 1-D Fokker-Planck code using the measured T_e and n_e profiles. Kinetic measurements of W_{tot} based on measurements of $T_e(R)$ by Thomson scattering and ECE, $n_e(R)$ by Thomson scattering and multichannel interferometry, $T_i(R)$ by charge-exchange recombination spectroscopy, and Z_{eff} by visible bremsstrahlung (assumed independent of radius) typically agree with the diamagnetic measurements within 10-15% except for the 40 cm plasmas on the outer limiter. Estimates of the scaling of thermal stored energy with major radius typically yield $W_{th} \propto R^{\geq 1.5}$.

Constant I_pR/a Scan

The range of aspect ratio was increased by the addition of 0.70 and 0.90 m plasmas on both the inner and outer limiters for studies of plasma performance scaling at

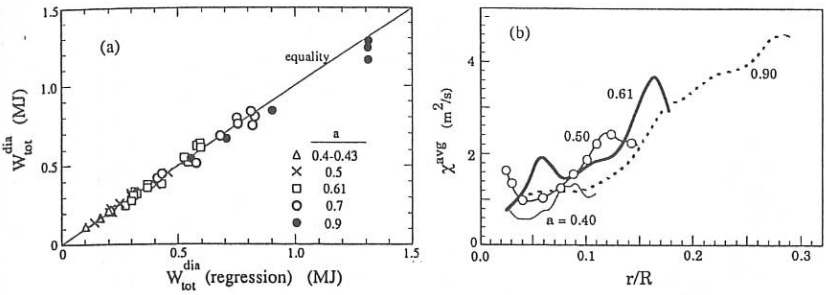

Figure 2: (a) The regression formula $W_{tot}^{dia} = 0.045 I_p^{1.11} P_b^{0.48} R^{1.62} a^{0.06}$ accurately represents the measured diamagnetic stored energy. (b) χ^{avg} as a function of local inverse aspect ratio for plasmas formed on the outer limiter.

constant I_pR/a (= 3.1 MA and 4.3 MA). Figure 1b illustrates the variation of $\langle nT\rangle\tau_E$ with aspect ratio, including data taken in scans at constant P_b/Ra (corresponding to constant power flux to a hypothetical divertor configuration) and data at other beam powers, 4 - 10 MW for I_pR/a = 3.1 MA and 8.5 - 18 MW for I_pR/a = 4.3 MA. The $\langle nT\rangle\tau_E$ values were derived from diamagnetic measurements of total stored energy ($\langle nT\rangle\tau_E \equiv \tau_E{}^{dia} W_{tot}^{dia}$/Volume). The basic result is that $\langle nT\rangle\tau_E$ is, at most, a weak function of aspect ratio for a fixed value of I_pR/a. Barring significant corrections to the calculated beam charge-exchange losses, this suggests that ignition tokamak designs extrapolated from L-mode scaling can resolve the trade-off between I_p and R/a on the basis of engineering considerations rather than plasma confinement. Comparing the two scans at I_pR/a = 3.1 MA and 4.3 MA, we observe that $\langle nT\rangle\tau_E$ increases roughly as $(I_pR/a)^{2.4\pm0.1}$. Notice that there is no observed dependence of $\langle nT\rangle\tau_E$ on beam power, consistent with standard L-mode scaling for which $\tau_E \propto P_b^{-0.5}$.

Power-law regressions were applied to the entire dataset of plasma size scans, including also an equal number of discharges from large-plasma L-mode scans (a = 0.8 − 0.9 m, I_p = 0.9 - 2.1 MA, P_b = 6 - 20 MW; see [1]). The data were constrained only by the requirements of near-balanced injection with $P_b \geq 2$ MW and $P_{\|}/P_{\perp} \leq 1.3$. The regressions yield excellent fits (statistical $R^2 \geq 0.98$) to total stored energy, $W_{tot}^{dia} = 0.045 I_p^{1.11} P_b^{0.48} R^{1.62} a^{0.06}$ and $W_{tot}^{eq} = 0.066 I_p^{1.09} P_b^{0.45} R^{1.36} a^{0.10}$ in units MJ, MA, MW and meters. Figure 2a shows the measured size-scan data plotted as a function of the diamagnetic energy regression. There is little correlation between R and a in the dataset (correlation coefficient = -0.1), but strong correlations among P_b, I_p, and a (correlation coefficients $\sim$ 0.8). The effects of toroidal field and plasma density on the confinement scaling are currently under analysis. B_T correlates with plasma size through the imposed constraint that q_{cyl} be constant, while plasma density has been found to affect the scaling of thermal stored energy in L-mode plasmas [1]. Notice that the variation of W_{tot} with major radius found by regression is similar to that obtained from the inner/outer limiter comparisons described earlier.

Profiles of Thermal Diffusivity

To examine the importance of toroidicity to heat transport in these plasmas where

a	(m)	0.40-0.43		0.50		0.61	
R	(m)	2.08	3.20	2.15	3.10	2.26	2.99
R/a		5.2	8.2	4.3	6.2	3.7	4.4
I_p	(MA)	0.40	0.40	0.50	0.50	0.63	0.63
P_b	(MW)	4.5	4.4	6.5	6.3	8.6	8.5
$\bar{n}_e$	10^{19} m^{-3}	3.4	5.4	5.6	5.1	4.7	5.6
Z_{eff}		1.5	3.3	1.2	3.6	1.4	2.4
$T_e(0)$	(keV)	2.2	2.0	1.7	2.0	1.6	1.6
$P_\parallel/P_\perp$		1.86	1.02	1.30	1.02	1.16	1.00
W_{tot}^{dia}	(kJ)	114	224	170	314	247	383
$W_{beam}^{dia}/W_{tot}^{dia}$		0.25	0.26	0.15	0.26	0.18	0.18
m $[W_{tot}^{dia} \propto R^m]$		1.59		1.72		1.59	
m $[W_{th}^{dia} \propto R^m]$		1.56		1.34		1.60	
W_{tot}^{eq}	(kJ)	163	227	197	318	268	383
$W_{beam}^{eq}/W_{tot}^{eq}$		0.53	0.28	0.32	0.28	0.38	0.20
m $[W_{tot}^{eq} \propto R^m]$		(0.79)		1.35		1.30	
m $[W_{th}^{eq} \propto R^m]$		1.78		1.51		2.20	

Table 1: Plasma parameters for major radius scans at constant a, I_p, P_B, and q_ψ. $T_e(R)$ measured by Thomson scattering; $P_\parallel/P_\perp$ from diamagnetic and equilibrium magnetics.

the ion-electron heat exchange is large, we consider an average thermal diffusivity defined as $\chi^{avg} \equiv P_{flux}/(n_e\nabla T_e + n_i\nabla T_i)$, where P_{flux} is the total heat flux (convection, conduction, radiation) flowing through a flux surface. Figure 2b illustrates χ^{avg} as a function of local inverse aspect ratio (r/R) for discharges of varying minor radius formed on the outer limiter. For the discharges shown, the beam power ranges from 4.4 to 8 MW and the plasma current is correlated with a (increasing from 0.40 MA to 1.52 MA in the largest plasmas), while q_{cyl} remains constant at 3.0 - 3.2 (except $q_{cyl} = 2.54$ at $R/a = 3.2/0.4$). The radiated power fraction in these discharges is 25 - 30%, and the combination of convection and radiation becomes the dominant term in the power balance outside $r/a \geq 0.7$. The salient feature of Fig. 2b is that χ^{avg} seems to depend upon the local r/R, indicating that high-aspect-ratio plasmas resemble the central cores of larger minor radius plasmas at lower aspect ratio and suggesting that toroidicity plays an important role in governing transport.

Conclusion

We find that the diamagnetic stored energy scales as $R^{1.6-1.7}$ with an estimated experimental uncertainty of approximately ± 0.2 in the exponent, while the minor radius dependence appears to be relatively weak. Plasma fusion performance as measured by $\langle nT\rangle\tau_E$ is insensitive to aspect ratio for a fixed value of I_pR/a, which may allow greater flexibility in tokamak designs based on L-mode scaling. Local heat transport appears to depend strongly on the local inverse aspect ratio, which is consistent with the weak a scaling of W_{tot}.

This work was supported by U.S. DOE contract DE-AC02-76-CHO-3073.

[1] D.W. Johnson *et al.*, these proceedings.

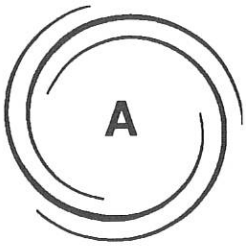

TOKAMAKS

A3 DETERMINATION OF TRANSPORT COEFFICIENTS

COUPLING OF PLASMA PARTICLE DIFFUSION AND HEAT FLOW IN TEXT

D.L. Brower[a], C.X. Yu[a], S.K. Kim[b], K.W. Wenzel[c], M.E. Austin[d], M.S. Foster, R.F. Gandy[d], W.L. Li[a], N.C. Luhmann, Jr.[a], S.C. McCool, M. Nagatsu[a], W.A. Peebles[a], Ch. P. Ritz, B.A. Smith

Fusion Research Center, University of Texas, Austin, Texas 78712 USA

[a]Institute of Plasma and Fusion Research, University of California, Los Angeles, California
[b]FOM-Instituut voor Plasmafysica, Nieuwegein, The Netherlands
[c]Plasma Fusion Center, Massachusetts Institute of Technology, Cambridge, Massachusetts
[d]Auburn University, Auburn, Alabama

Detailed measurements of heat and particle transport are made on the TEXT tokamak by analyzing the dynamics of the post-crash sawtooth perturbation. Comparison of the density and temperature perturbation amplitudes, temporal and radial evolution, and scalings are made. The radial dependence of the perturbation amplitudes are similar although the density change ($\Delta n_e/n_e \leq 0.06$) is generally less than, but of same order as, the temperature change ($\Delta T_e/T_e \leq 0.15$). The sawtooth density and temparature perturbations are measured to be in phase ($\Delta\Phi<5^o$) and highly correlated (>95%). Both the density and temperature perturbations are observed to be transported out through the confinement zone at the same rate and exhibit comparable scalings with variation of plasma parameters. These results provide direct evidence for the theoretically predicted coupling of plasma diffusion and heat flow[1] and may also explain why perturbative measurements of χ_e are typically larger than equilibrium measurements by factors of 2 to 4 on TEXT.

The effects of the sawtooth perturbation on the electron density, electron temperature and soft x-ray emission are shown in Fig. 1, for the plasma center and three radial locations spaced from just outside the mixing radius to the edge. Data were obtained by averaging over approximately 50 cycles ($\tau_{st} \simeq 3$ ms) during steady-state operation of the same Ohmic discharge. The inversion radii, as determined from each measurement, are the same with $r_{inv} \simeq 6.5$ cm. On axis, the temperature change is 12% while the density perturbation is 5%. At the mixing radius $\Delta T_e/T_e \simeq 8\%$, approximately 5 times larger than $\Delta n_e/n_e$. After the sawtooth crash, the electron temperature profile flattens to the inversion radius while the density profile broadens but remains centrally peaked.[9] From Fig. 1, it is important to note that the waveforms for density, temperature and soft x-rays are essentially the same at each radial position. The radial dependence of the width and time-to-peak (t_p) for the perturbation maximum are similar. By themselves, these results strongly suggest that heat and particle transport occur at the same rate, thereby implying coupling.

The soft x-ray emission per unit volume associated with photons with energies above the cutoff ($\simeq$1 keV for TEXT) can be roughly approximated[4] in the form $Cn_e^2 r_e^{\alpha}$, where C reflects the impurity contribution. For the data in Fig. 1, the exponent α ranges from approximately 2 (r=10 cm) to 10 (r=21 cm). Consequently, the change in the soft x-ray intensity at the mixing radius ($r \simeq 10$ cm) due to ΔT_e is 5 times greater than that due to Δn_e. The change in the soft x-ray signal, at the edge ($r \simeq 21$ cm), due to ΔT_e is 25 times larger than Δn_e. At each radial position, the temperature

perturbation is by far the major contributor to the soft x-ray signal for the low Z_{eff} (≤ 2) TEXT plasmas. Hence, for the remainder of this paper, fluctuations in the soft x-ray signal will be treated as being dominated by changes in the electron temperature, and not changes in the electron density.

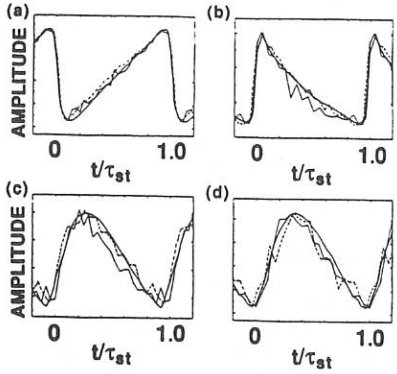

Figure 1. Normalized time histories of sawtooth perturbation for electron density (fine line), electron temperature (dashed line), and soft x-rays (bold line), at four radial locations: (a) r = 0, (b) r = 11 cm, (c) r = 17 cm, and (d) r = 22 cm. Discharge conditions are I_p = 300 kA, B_T = 2.8 T, and $\bar{n}_e \simeq 3 \times 10^{13}$ cm^{-3} in a hydrogen plasma.

The interrelation between the sawtooth density and temperature perturbations can also be explored by examining the radial dependences of various parameters. For instance, a comparison of the time-to-peak (t_p) for the perturbation maximum is shown in Fig. 2(a). The values for heat and particles are indistinguishable over the range investigated and linear for $100 \leq r^2 \leq 350$ cm^2, which corresponds to the confinement zone in TEXT. In addition, the radial dependence of the perturbation maximum exhibits a r^{-4} fall-off as shown in Fig. 2(b). The spatial dependence of the sawtooth phase shift[10], referenced to a central chord [see Fig. 2(c)], shows a linearly decreasing phase, Φ, outside the inversion radius. At each position, the measured phase delays are the same within experimental error. These points are computed at the first harmonic of the sawtooth frequency with similar results being obtained for higher order harmonics. By computing directly the phase difference between density and temperature, one finds that outside the inversion radius, phase differences are typically less than 5°, even at the edge. Correlation of the density and temperature signals is greater than 95%. The relations shown in Fig. 2 are consistent with a diffusive transport model.[2,3] This result, along with the high correlation and small phase difference between the density and temperature sawteeth, strongly supports the notion that the two are indeed coupled.

To further investigate the relationship between heat and particle transport after the sawtooth crash, the scaling behavior of $\Delta(r^2)/\Delta t_p$ for density and temperature perturbations is examined. Dependences on q_a and $\bar{n}_{eo}$ are most clearly obtained by performing a regression analysis yielding $(\Delta(r^2)/\Delta t_p) \propto q_a^{-[2.2\pm.2]} \bar{n}_{eo}^{-[0.2\pm.1]}$. Scaling trends are the same for particles and heat with each being much more dependent upon q_a than $\bar{n}_{eo}$. By varying the working gas through use of hydrogen, deuterium and helium, one finds that $\Delta(r^2)/\Delta t_p \propto [Z/M_i]^{0.5}$ is measured for both particles and heat, where Z is the ion charge and M_i is the ion mass. Similar relations are observed for the parameter $[\Delta\Phi/\Delta r]^{-2}$. This again suggests that particle and heat transport resulting from the sawtooth crash may be coupled. The strong q_a scaling may reflect a radial dependence since the region over which the slope is measured moves closer to the limiter, where heat transport is known to be larger, as q_a decreases. For purposes of this study, it is only

important to note that the scaling is the same for density and temperature perturbations.

Simple estimates of the heat and particle transport using the sawtooth perturbation can be made by employing standard analysis techniques where the relations $\Delta(r^2)/\Delta t_p$ or $[\Delta\Phi/\Delta r]^{-2}$ are proportional to χ_e or D_e.[2,3] As a specific example using the data in Fig. 2, the radial variation of t_p gives $D_e \simeq 1.5$ m^2/s, whereas, $\chi_e \simeq 2.25$ m^2/s making $\chi_e/D_e = 1.5$. These values for χ_e and D_e represent a spatial average over the region investigated. However, since the step size (Δr) and step time (Δt) for the density and temperature sawteeth are identical, the transport rate ($\Delta r^2/\Delta t$) for heat and particles must be the same, i.e. $\chi_e/D_e = 1$. Correct treatment of the coupled equations must force the solution giving equal rates of heat and particle transport in order to reach agreement with the experimental results. The value computed for χ_e is roughly three times the equilibrium estimate of the electron thermal diffusivity. Differences between χ_e and D_e obtained by using these simple models serve to point out their limitations. The degree to which the measured coupling can account for the discrepancy between perturbative and equilibrium estimates of thermal transport remains to be determined.

Increased electrostatic fluctuations during the sawtooth cycle have also been proposed, in addition to coupled heat and particle transport, as a possible explanation for the observed discrepancy between perturbative and equilibrium measurements of the electron thermal transport. Along with the compelling evidence for coupled heat flow and particle diffusion on TEXT, a clear correlation also exists between density fluctuations and the sawtooth collapse as shown in Fig. 3(a). A prompt burst of microturbulence activity occurs simultaneously with the sawtooth relaxation (crash duration $\simeq$ 30 μsec) at which time the density fluctuation level can more than double. Enhanced turbulence has been observed to last the entire time necessary for the perturbed pulse to pass(t_p). Changes in n are maximum inside the mixing radius. Modifications to the frequency spectra during the sawtooth cycle are broadband as seen in Figs. 3(b-e). Langmuir probe measurements in the scrape-off-layer plasma of TEXT have measured a doubling of the fluctuation-induced particle flux on the time scale of t_p.[4]

In addition, changes in both the particle and heat transport are observed as precursors of up to 100 msec before high-density limit disruptions. Increases in D_e and χ_e of $\simeq$50% are measured (see Fig. 4). Associated with the confinement degradation are significant increases in the microturbulence levels (see Fig. 4). The high-density ion mode, previously associated with an active ion-pressure-gradient-driven instability, is greatly enhanced ($\geq$100%) while the electron drift-wave type turbulence remains essentially unchanged. This instability may drive the deterioration in particle and energy confinement which then leads to the high-density limit disruption.[5]

This work is supported by the U.S. Department of Energy under contract nos. DE-FG03-86ER-53225 and DE-AC05-78ET-53043.

1. M. Hossain et al., Phys. Rev. Lett. 58,487(1987).
2. S.K. Kim, D.L. Brower, W.A. Peebles, N.C. Luhmann, Jr., Phys. Rev. Lett. 60,577(1988).
3. E.Fredrikson et al., Nuclear Fusion 26,849(1986).
4. T.L. Rhodes, Ph.D. Dissertation, University of Texas at Austin, 1989.
5. M. Greenwald et al., Nuclear Fusion 28,2199(1988).

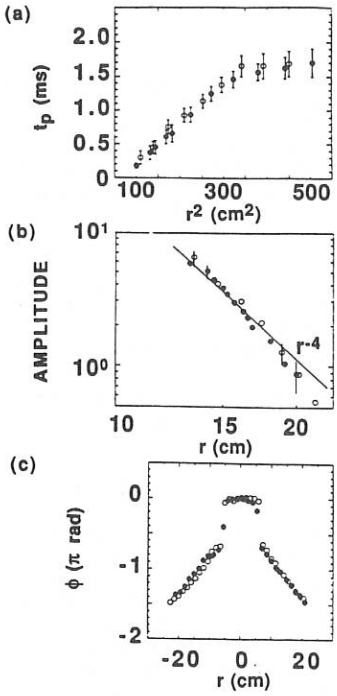

Figure 2. Radial dependence of (a) time-to-peak, t_p, (b) normalized perturbation amplitude, and (c) phase with respect to central chord. Solid circles refer to the density perturbation and open circles refer to the soft x-ray ($\propto T_e$) perturbation. Discharge conditions are I_p = 200 kA, B_T = 2 T, and $\bar{n}_e \simeq 3 \times 10^{13}$ cm^{-3} in a hydrogen plasma.

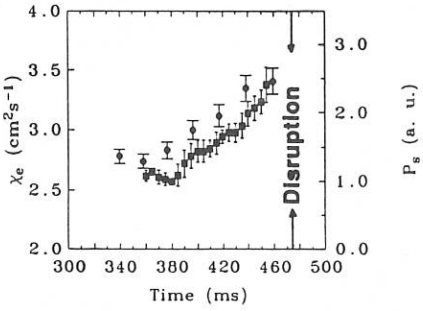

Figure 4. Time dependence of χ_e (circles) and $P_s \propto \tilde{n}^2$ (squares) for a disrupting discharge.

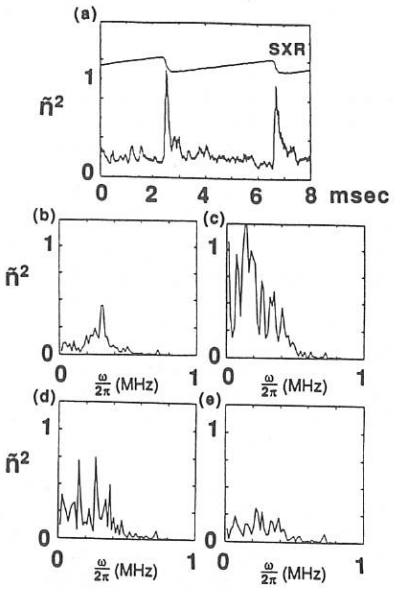

Figure 3. (a) Temporal variation of square of electron density fluctuations (arbitrary units), measured via far-infrared laser scattering, for poloidal wave vector k_Θ = 12 cm^{-1}. Scattering volume was positioned above the midplane at the major radius. (b-e) Changes in the broadband density fluctuation frequency spectra. Fourier transforms are taken over windows of width ±100 μs about t_o= (b) 6.3, (c) 6.7, (d) 7.1, and (e) 7.7 ms.

SAWTOOTH HEAT PULSE PROPAGATION AND ELECTRON HEAT CONDUCTIVITY IN HL-1

GUO Gancheng, ZHONG Yunze, DONG Jiafu,
GAO Qingdi, FU Bingzhong, HOU Junmei,
RUAN Libo, XU Guangbi, ZHENG Yongzhen

Southwestern Institute of Physics,
Leshan, Sichuan, China

1. INTRODUCTION

The propagation of heat pulse induced by sawteeth was studied in hydrogen and helium plasma for a wide range of plasma parameters. The propagation time of heat pulse is quadratic in the radius. The electron heat conductivity $\chi_e(r)$ in the outer confinement region of the plasma was deduced from the propagation time of the heat pulse on the high and low field sides of the plasma column. It is concluded that the value of $\chi_e(r)$ outside the mixing radius is related to the sawtooth inversion radius, the electron density and the sawtooth period. A comparison of χ_e determined by heat pulse propagation with those obtained from power balance have been made.

2. HEAT PULSE PROPAGATION ANALYSIS

The equation which governs the electron temperature perturbation $\tilde{T}e(r,t)$ caused by sawteeth can be written .

$$\frac{3}{2} n_e \frac{\partial \tilde{T}_e(r,t)}{\partial t} = \frac{1}{r} \frac{\partial}{\partial r} \left(r n_e \chi_e \frac{\partial}{\partial r} \tilde{T}_e(r,t) \right) \tag{1}$$

where χ_e is the electron heat conductivity.
with the initial condition $\tilde{T}e(r,0) = Te(r,0) - Te_0(r)$.

For a constant Ne and χ_e ,

$$\tilde{T}_e(r,t) = \frac{a^2}{2t} e^{-a^2 r^2/4t} \int_0^{r_0} r' dr' \, \tilde{T}_e(r',0) e^{-a^2 r'^2/4t} I_0\left(\frac{a^2 r r'}{2t}\right) \tag{2}$$

where $a = 3/(2\chi_e)$, I_0 is zero order Bessel function.

If $\tilde{T}e(r,0)$ is expressed by the sum of two δ-function, i.e., $\tilde{T}e(r,0) = T_1 \delta(r - r_1) + T_2 \delta(r - r_2)$,one located at r_1 near the axis, and the other located at the edge of the mixing region which is at $r_2 = \sqrt{2}\, r_1$,Eq.(2) can be written as follow

$$\tilde{T}_e(r,t) \approx \frac{a^2}{2t} A e^{-a^2 r^2/4t} \left[e^{-a^2 r_1^2/4t} I_0\left(\frac{a^2 r r_1}{2t}\right) - e^{-a^2 r_2^2/4t} I_0\left(\frac{a^2 r r_2}{2t}\right) \right] \tag{3}$$

where $A=r_1 T_- = -r_2 T_+$.

For typical parameters of sawtoothing discharge in HL-1, Eq(3) can be simplified to

$$t_p = \frac{3(r-\sqrt{2}\,r_s)^2}{4\chi_e} \qquad (4)$$

where tp is the time at which $\tilde{T}e(r)$ reaches its maximum. So the electron heat conductivity χ_e can be deduced from the approximate formula above.

With a modified initial and boundary condition Eq(1) was numerically solved. The numerical result shows that the slope of the $tp \sim r^2$ curve depends on the value of r_s/a, e.g. $\Delta tp/\Delta r$ is about $1/5\chi_e$ ——$1/9\chi_e$ (as $r_s/a =$ 1/6——1/3) for $\sqrt{2}r_s < r < 0.7a$. The results of the propagation of heat pulse in the outer confinement region of plasma depend on the inversion radius r_s have been confirmed by experiment data in HL-1.

3.EXPERIMENT RESULTS AND DISCUSSION

The heat pulse propagation was measured by the soft X-ray imaging system in HL-1. Fig.1 is soft X-ray signals from the chords on the low and high field sides, which show the propagation feature of the heat pulse induced by the sawtooth crash. The variety of propagation speed of the heat pulse which occur before the soft X-ray sawteeth disappear, can be seen in Fig.1(b). As is shown in Fig.2, the propagation time tp of the heat pulse is quadratic in the radius for $r > \sqrt{2}\,r_s$, which demonstrates the diffusive characteristic of a heat pulse in plasma. A deviation from the quadratic relation is observed at $r \approx 13$cm (material limiter radius is 18cm), showing the effect of the plasma edge on the pulse propagation. In general, the inversion radius of sawtooth is small (line average inversion radius is 3-4cm) in the HL-1 discharges, a good situation for the measurement of heat conductivity exist.But when both the shift of plasma column and r_s increase, only two chords are available for measuring the heat pulse propagation.

Fig.3 shows χ_e-values for different line average electron densities. A strong increase of χ_e with radius is found, since the electron density decreases with radius, high χ_e-values can be expected as radius becomes larger. The evolution of χ_e profile for a sawtoothing discharge is shown in Fig.4. Large χ_e values was obtained as shown (circle dots) in plot during the ramping phase of the plasma current, simultaneously with the small inversion radius and lower electron density. A higher electron density however gave a lower χ_e value and exhibited a slower χ_e increase with radius.

An dependence of heat conductivity χ_e on sawtooth period is shown in Fig.5, it indicates that the χ_e value is sensitive to τ_s .

In Fig.6, inversion sawteeth from five chords on the high field side are shown. The heat pulse at different radius reach maximum at nearly the same time, but in the region $r > 8$ cm the propagation of heat pulse becomes normal. This phenomenon is similar to that observed in TFTR [2]. In the HL-1 discharges the very fast propagation of heat pulse is related to large outward shift of the plasma column. The rapid heat transport may be the result of the sawtooth crash mechnism itself.

The χ_e values found based on the propagation of heat pulse are about two to four times those obtained from power balance [3].

ACKNOWLEDGEMENT

The authors would like to thank computer group for data acquisition and to thank all scientists and technicians for their support to this work. The soft X-ray measurement were partially supported by International Atomic Energy Agency Contract No. 4550/R1/RB.

REFERENCE

[1]Soler,M., Callen,J.D., Nucl. Fusion 19 (1979) 703

[2]K.M.McGuire, Plasma Physics and Controlled Fusion 30 11(1988)1391

[3]Ruan Libo, The primary analysis of the electron heat conduction in the central plasma hot core of HL-1 Tokamak, to be published.

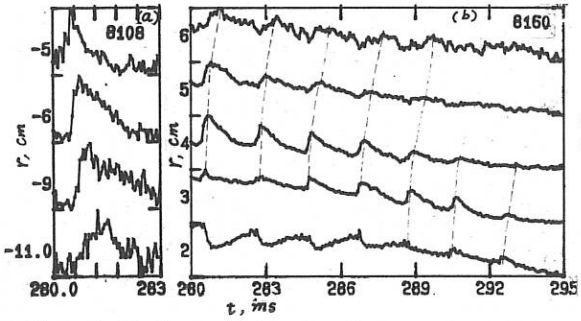

FIG.1 Soft X-ray signals from selected chords, illustrating the propagation of the heat pulse.

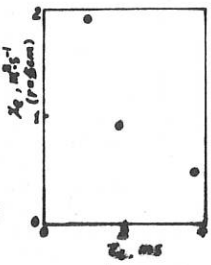

FIG.5 χ_e versus sawtooth period

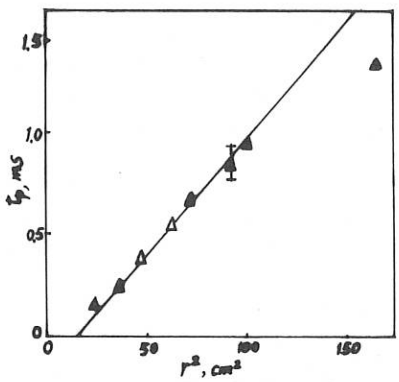

FIG.2 Arrival time of heat pulse peak on high (full dots) and low (open dots) field side versus r^2.

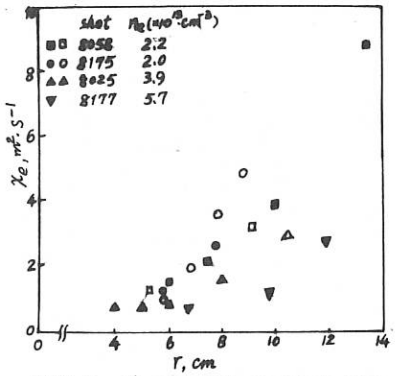

FIG.3 χ_e versus radius for different line average electron densities.

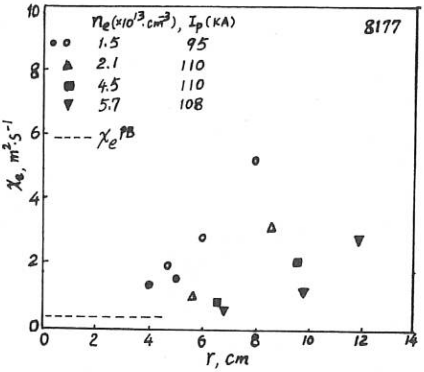

FIG.4 Evolution of χ_e-profile for a sawtoothing discharge.

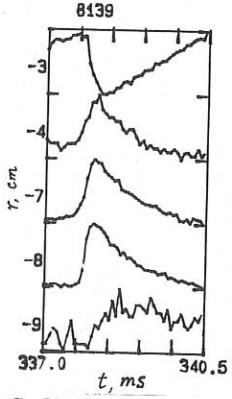

FIG.6 Soft X-ray sawteeth from selected chords, showing the rapid heat transport.

EVIDENCE OF COUPLING OF THERMAL AND PARTICLE TRANSPORT FROM HEAT AND DENSITY PULSE MEASUREMENTS AT JET.

G.M.D.Hogeweij*, J.O'Rourke, A.C.C.Sips* and J.C.M.de Haas*,$

JET Joint Undertaking, Abingdon, Oxfordshire OX14 3EA, U.K.
* FOM Instituut voor Plasmafysica "Rijnhuizen", The Netherlands
$ Present Address: General Atomics, PO Box 85608, San Diego, CA 92138

INTRODUCTION

The evolution of electron temperature and density perturbations can be used to determine transport coefficients. At JET, the electron thermal conductivity and particle diffusivity have been determined following the profile evolutions after the injection of small pellets and the sawtooth collapse [1,2].

In this paper, an integrated analysis of heat and density pulses following a sawtooth collapse is presented. The data is obtained by simultaneous measurements of the electron temperature using ECE and electron density, using reflectometry. The analysis uses the complete time evolution after the collapse and takes into account a) coupling between heat and particle transport, b) the effects of the inward propagating density pulse due to a change of recycling at the edge when the heat pulse reaches the limiter and c) the observed enhanced damping of the heat pulse, mainly due to electron–ion energy exchange.

MEASUREMENT OF HEAT AND DENSITY PULSES

A 12 channel ECE polychromator measures the evolution of the electron temperature after a sawtooth collapse. Its spatial resolution allows us to observe the perturbation on the electron temperature at 4–6 radial positions up to 30 cm outside the mixing radius. Similarly a 12 channel o–mode reflectometer monitors the evolution of the electron density. Typically 4–7 channels of the reflectometer are located outside the mixing radius, depending on the magnitude and shape of the electron density profile.

The measurements show clearly that an outward propagating heat pulse arrives at the limiter before the outward propagating density pulse and produces an inward propagating density pulse through a change in the edge recycling.

In addition, we observe a temporary decrease of the local electron density when the heat pulse passes (Fig.1). This effect can not be attributed to a horizontal displacement of the plasma column, because it is also observed on channels of the far infra–red interferometer which are situated inboard of the magnetic axis. A (radially symmetric) readjustment of the equilibrium due to the change in the pressure profile induced by the sawtooth can also be excluded: a solution of the pressure balance equation

$$\frac{d}{dr}\,\delta p = -\frac{d}{dr}\,\delta\left(\frac{B_\phi^2}{2\mu_0}\right)$$

for the discharges analyzed here leads to displacements of the flux surfaces (at the radii at which the measurements are made) of less than 0.1 mm.

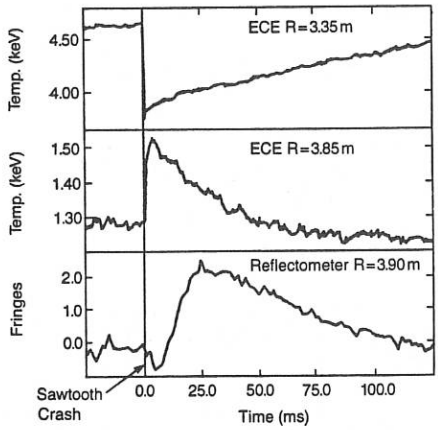

Fig.1:
Simultaneously measured evolutions of the temperature and density at approximately the same location in the plasma. For comparison also the central temperature is shown. Note the dip in the density which occurs at the same time the temperature reaches its maximum.

ANALYSIS TECHNIQUE

Starting from the equations describing the energy balance and particle balance and using the following equations for the fluxes

$$-\Gamma = D\,\nabla n + n\,V$$
$$-q = n\,\chi\,\nabla T + n\,T\,U$$

with particle and heat pinches V and U, a linearized set of coupled equations can be derived for the perturbations:

$$\dot{z} = A\,\nabla^2 z + B\,\nabla z + C\,z + S$$

with

$$z = \begin{bmatrix} n_{pert} \\ T_{pert} \end{bmatrix}, \qquad S = \begin{bmatrix} S_{pert} \\ Q_{pert} \end{bmatrix}$$

where n_{pert} and T_{pert} are the normalized perturbations of the electron density and temperature, and S_{pert} and Q_{pert} the perturbed particle and heat sources.

A is a linearized diffusion matrix. A_{11} and A_{22} correspond to D_{dp} and $2\chi_{hp}/3$ in the absence of coupling, while the off–diagonal terms A_{12} and A_{21} represent the influence of coupling. B and C are linearized pinch and damping matrices.

Simulations of the heat and density pulses are obtained by treating the problem as an initial value problem where T_{pert} and n_{pert} vanish at the plasma edge. In a least squares search numerical predictions are matched to the measurements by varying all elements of A to include the effects of coupling. Based on previous heat and density pulse analysis [2,3], also the particle pinch term B_{11} and the heat pulse damping term C_{22} are taken into account. The other elements of B and C are set to zero, so enhanced damping on the density pulse and a linearized heat pinch are not included. The perturbed edge particle source term S_{pert} is matched to D–alpha measurements; the perturbed heat source term Q_{pert} is set to zero.

RESULTS

Simultaneous measurements of heat and density pulses have been made in 3 MA limiter bounded plasmas at 3 T with up to 10 MW of ICRF heating. Table 1 gives an overview of the elements of the linearized diffusion matrix for 5 pulses. The error bars quoted in table 1 have been computed by varying the parameter until the quadratic sum of the deviations between data and simulation doubles for one of the channels. An example of measured data and the best numerical fit is given in Fig.2.

Table 1:
Overview of the linearized diffusion coefficients for 5 pulses with a plasma current of 3 MA and toroidal field of 3 Tesla. $\langle n_e \rangle$ is given in units of 10^{19}.

Pulse	A_{11} (m^2/s)	A_{22} (m^2/s)	A_{12} (m^2/s)	A_{21} (m^2/s)	P_{rf} (MW)	Z_{eff}	$T_{e,av}$ (keV)	$n_{e,av}$ (m^{-3})
19596	0.40 ± 0.08	4.0 ± 1.2	-0.65 ± 0.12	0.2 ± 0.5	3.9	2.1	1.9	2.0
19611	0.30 ± 0.10	2.1 ± 0.3	0.00 ± 0.25	0.0 ± 0.4	0.5	1.7	0.9	2.5
19614	0.29 ± 0.11	4.4 ± 1.8	-0.7 ± 0.7	0.1 ± 0.5	8.1	2.3	1.9	3.0
19617	0.28 ± 0.10	3.9 ± 1.0	-0.6 ± 0.3	0.1 ± 0.5	7.8	2.4	1.9	2.9
19619	0.30 ± 0.08	2.4 ± 0.6	-0.5 ± 0.4	0.15 ± 0.3	5.7	2.3	1.9	2.7

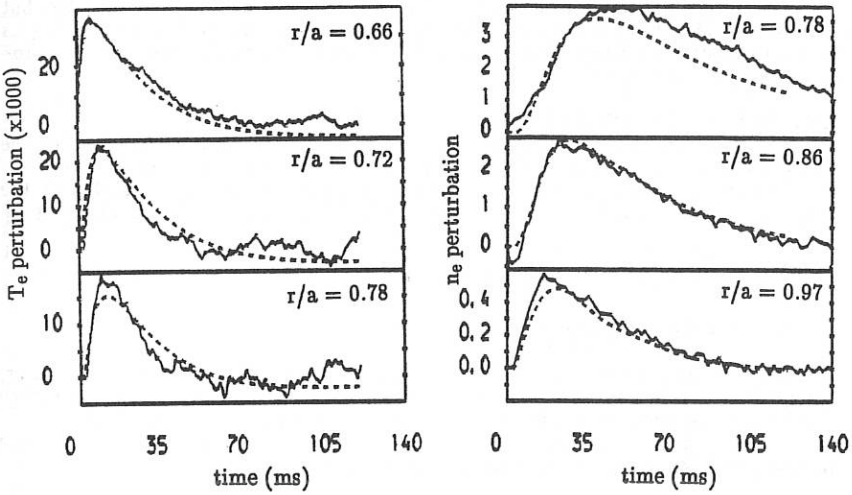

Fig.2:
Measurements of the ECE polychromator and the reflectometer at various radial positions for pulse 19614 (full line), compared with the best numerical fits (dashed line). The electron temperature is normalized to the central electron temperature. The density changes are represented by phase changes (fringes) of the reflectometer.

A clear indication for the coupling between energy and particle transport is the non–zero value of A_{12} needed to simulate the initial decrease in the local density. This effect is illustrated in Fig.3.

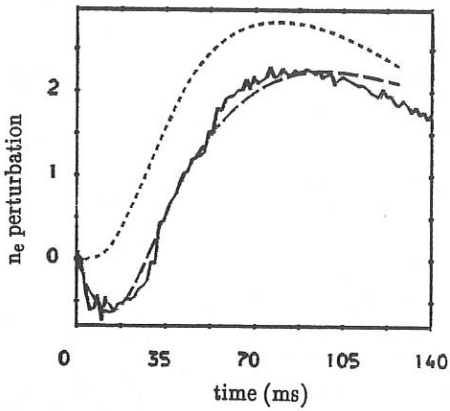

Fig.3:
Measured density evolution of pulse 19596 at $r/a = 0.66$ compared with numerical simulations including coupling (dashed line) and without coupling (dotted line). Note that the initial decrease of the local density is only simulated when coupling is included.

The inward particle convection term B_{11} is large, order 4–10 m/s at the edge, but decreases rapidly further inwards. The electron temperature damping term C_{22} is needed to model the decay of the heat pulse amplitude correctly, and can be represented as $1/\tau_d$, with $\tau_d \simeq 15$–40 ms.

DISCUSSION AND CONCLUSIONS

The previously reported large ratio of χ_{hp} / D_{dp} of ~ 10 [1,2,3] is confirmed by the current analysis and the results obtained for A_{22} agree with previous scaling of χ_{hp} [3].

The off–diagonal terms in A represent the dependence of the particle flux on the temperature gradient and the dependence of the heat flux on the density gradient as [4]

$$A_{12} = \frac{\partial D}{\partial \nabla T}\frac{T_0}{n_0}\nabla n + \frac{\partial V}{\partial \nabla T}T_0$$

$$A_{21} = \frac{2}{3}A_{11} + \frac{2}{3}\frac{\partial \chi}{\partial \nabla n}\frac{n_0}{T_0}\nabla T + \frac{\partial U}{\partial \nabla n}n_0$$

Thus $A_{12} < 0$ implies the existence of a temperature–gradient driven particle pinch or, equivalently, a diffusion coefficient which is a decreasing function of ∇T. The large error bars on A_{21} preclude a definite statement on the existence of a heat pinch.

In conclusion, a method has been developed to assess the heat and particle diffusivity and the effects of coupling in a consistent way.

REFERENCES

[1] Cheetham A. et al, 12th International Conference on Plasma Physics Controlled Nuclear Fusion Research, Nice, October 1988, IAEA–CN–50/I–2–2.
[2] Sips A.C.C. et al., 16th European Conference on Controlled Fusion and Plasma Physics, Venice, March 1989. Vol 13B, Part I, p.99.
[3] Lopes Cardozo N.J. and de Haas J.C.M., Nucl. Fusion.30 (1990) p.521
[4] Gentle K.W., Phys Fluids 31 (1988) p.1105

DETERMINATION OF LOCAL TRANSPORT COEFFICIENTS BY HEAT FLUX ANALYSIS AND COMPARISONS WITH THEORETICAL MODELS

B. Balet, D. Bartlett, J.G. Cordey, C. Gowers, G.W. Hammett*, M. v. Hellerman, J. O'Rourke, P. Morgan, P. Nielsen, G. Sadler, P.M. Stubberfield, H. Weisen.

JET Joint Undertaking, Abingdon, Oxon, OX14 JEA, U.K.
*Princeton Plasma Physics Laboratory, Princeton, New Jersey, U.S.A.

Five very different JET pulses have been analysed using the $1^1/_2$ - D transport code TRANSP [1]: a) a high performance hot ion H-mode, b) a monster sawtooth shot, c) a pellet fuelled ICRH discharge, d) an ICRH heated H-mode discharge, e) a standard L-mode discharge. The main characteristics of these pulses are shown in Table I.

TABLE I	I_p (MA)	B_t (T)	P_{NBI} (MW)	P_{RF} (MW)	$n_e(o)$ (m^{-3}) x 10^{19}	$T_e(o)$ (keV)	$T_i(o)$ (keV)
Hot ion H-mode	4.0	2.8	17.	-	4.76	8.82	22.33
Monster Sawtooth	3.0	3.0	2.6	8.9	4.46	8.8	6.13
Pellet + ICRH	3.1	3.2	5.2	12.5	6.47	11.81	8.94
ICRH H-mode	3.1	2.8	-	6.3	5.4	4.71	4.7
L-mode	3.1	3.0	17.8	-	3.44	6.92	11.26

The measured profiles of temperature, density, Z_{eff} as well as many other quantities are input data to TRANSP. Checks on the consistency of the data are made by comparing the predicted and measured values of diamagnetic energy, surface voltage, total neutron yield, neutron emission profiles etc. The transport coefficients X's and D_e are defined by:

$$Q_{i,e} = - \chi_{i,e}\, n_{i,e} \nabla T_{i,e} + 5/2\, \Gamma_{i,e}\, T_{i,e};\quad M = - \chi_\varphi\, n_i m_i \nabla U_\varphi + m_i \Gamma_i U_\varphi;\quad D_e = \frac{-\Gamma_e}{\nabla n_e}$$

where $\Gamma_{i,e}$ is the particle flux, $Q_{i,e}$ is the total heat flux and M is the angular momentum flux.

Transport in the hot ion H-mode plasma: The high power flow into the ion channel leads to an ion temperature profile which substantially exceeds the electron temperature for $\rho = r/a \leq 0.5$. The ion power balance is between NBI and ion heat conduction; the equipartition energy is the second largest loss channel. In the electron power balance, the equipartition energy is twice the direct input power from NBI, the electron heat conduction is the main loss and is comparable to the ion conduction.

Transport in the monster sawtooth shot: The ICRH heating occurs within $\rho \leq 1/4$ and with up to 80% of the input power heating the electrons; this gives rise to an electron temperature larger than that of the ion for $\rho < 0.5$. The electron power balance is between ICRH and electron heat conduction. In the ion power balance, ICRH, NBI and equipartition energy contribute equally. Ion heat conduction is the main loss and is ~ 20% lower than the electron heat conduction.

Transport in the pellet fuelled ICRH discharge: A high and peaked density profile is established by injection of a 4 mm diameter deuterium pellet prior to the onset of auxiliary heating. The ICRH heating occurs within $\rho \leq 1/2$ with 60% heating the electrons. The ion power balance is between ICRH, the equipartition energy (~20% of the total input power at half radius) and the ion heat conduction. The electron power balance is between ICRH, and electron heat conduction which is half the ion heat conduction.

An error analysis has been completed for these 3 shots and the results for the transport coefficients are shown in Fig. 1 and summarised in Table II. In all cases χ_i is much larger than its neoclassical value. D_e is close to 0.0 for the hot ion H-mode and increases with radius for the monster sawtooth and the pellet + ICRH (from 0.05 to 0.6 m^2/s). These results are in agreement with heat and particle pulse analysis [2].

TABLE II	χ_e/χ_i $\rho < 0.4$	χ_e/χ_i $\rho > 0.4$	χ_φ/χ_e	D_e/χ_e $\rho < 0.4$	D_e/χ_e $\rho > 0.4$
Hot ion H-mode	≥ 1.75	0.3 - 1.8	0.5 - 2	0.0	0.0
Monster sawtooth	1.5 - 10	0.1 - 1	0.5 - 2	0.02 - 0.04	0.05 - 0.4
Pellet + ICRH	1/3 - 1	0.1 - 1	-	0.1 - 0.2	0.1 - 0.4

Due to the absence of T_i profile data, a similar study was not possible for the ICRH H-mode. However, a good simulation was obtained with $\chi_i = \chi_e$.

Due to the large errors in the separation of χ_i and χ_e, a comparison of these different shots is only possible by plotting χ_{eff} = (total conduction)/($n_e \nabla T_e + n_i \nabla T_i$) (see Fig. 2). A good confinement in the centre is obtained with peaked T_i profile (hot ion H-mode and pellet + ICRH); the two H-modes show good confinement in the outer region whereas the monster sawtooth and pellet + ICRH discharges have confinement characteristics of an L-mode.

Comparison with theory: Two theoretical models are considered: the ion temperature gradient model [3] and the Rebut-Lallia critical temperature gradient model [4]. Results are shown in Fig. 3. The anomalous χ_i predicted by the η_i - mode theory is much too high in the centre of the plasma in all cases and too low in the outer region for the pellet + ICRH and the monster sawtooth discharges. These results are in agreement with quantitative predictions done with representative L-mode plasmas in JET [5]. The Rebut-Lallia model is good

for the monster sawtooth and the hot ion H-mode but fails in the pellet + ICRH case, this may be due to uncertainties in the q profile.

Conclusion: A detailed study of the local confinement properties of different regimes of JET plasmas has been made and transport coefficients have been evaluated with their error bars. The η_i-mode theory fails to reproduce the anomalous transport whereas the Rebut-Lallia critical temperature gradient gives reasonable agreement except in the pellet fuelled shot.

Acknowledgements:

The pellet injection results were obtained during work performed under a collaboration agreement between the JET Joint Undertaking and the U.S. Department of Energy (USDOE). The ICRH deposition profiles were provided by V. Bhatnagar and L.-G. Eriksson.

References:

[1] Goldston R.J., et al. (1981) J. Comput. Phys. 43, 61.
[2] Cheetham A.D., et al., 12th Conf. on Plas. Phys. and Contr. Nucl. Fus. Res., Nice (1988) I-2-2.
[3] Hamaguchi S., et al. Fluctuation Spectrum and Transport from Ion Temperature Gradient Driven Modes in Sheared Magnetic Fields. DOE/ET - 53088-388. IFSR #383.
[4] P.H. Rebut, et al., Proc. 12th IAEA Conference, Nice, 1988, paper IAEA-CN-50/D-4-1. with modifications as in JET Report-R(89) 16,184.
[5] Tibone F., et al., a quantative assessment of ∇T_i - driven turbulence theory based on JET experimental data, submitted to this conference.

Figure captions:

Fig. 1: χ_e, χ_i, χ_i neoclassical, χ_φ ρ_{or} a) hot ion H-mode. b) Monster sawtooth. c) Pellet + ICRH versus $\rho \equiv r/a$.

Fig. 2: χ_{eff} versus ρ for 5 different shots.

Fig. 3: χ_i of TRANSP, η_i model and Rebut-Lallia model for a) Hot ion H-mode. b) Monster sawtooth c) Pellet + ICRH versus major radius R.

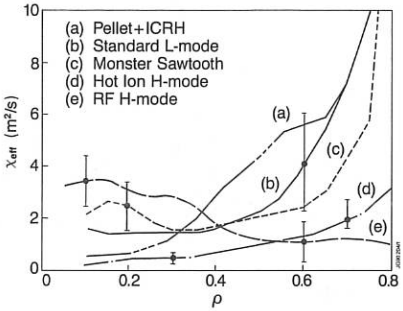

Fig. 2.

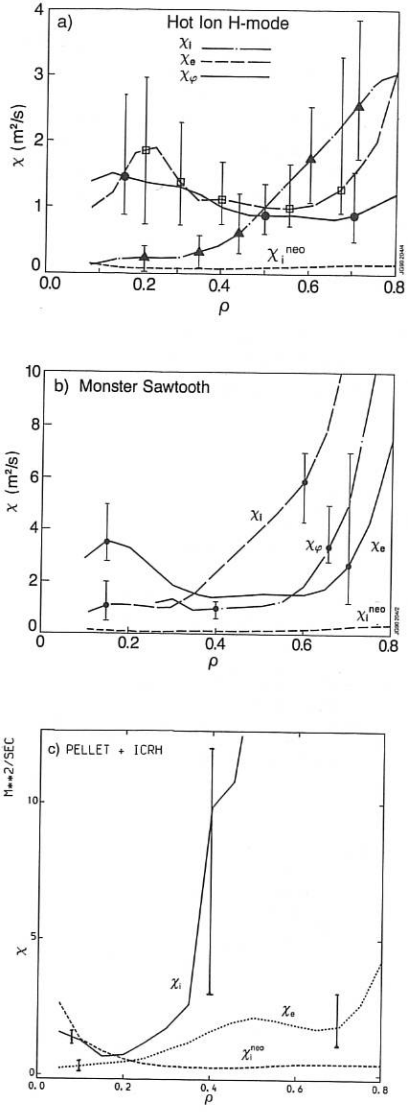
a) Hot Ion H-mode
χ_i
χ_e
χ_φ
χ_i^{neo}
χ (m²/s)
ρ
b) Monster Sawtooth
χ_i
χ_φ
χ_e
χ_i^{neo}
χ (m²/s)
ρ
c) PELLET + ICRH
M**2/SEC
χ_i
χ_e
χ_i^{neo}
ρ

Fig.1

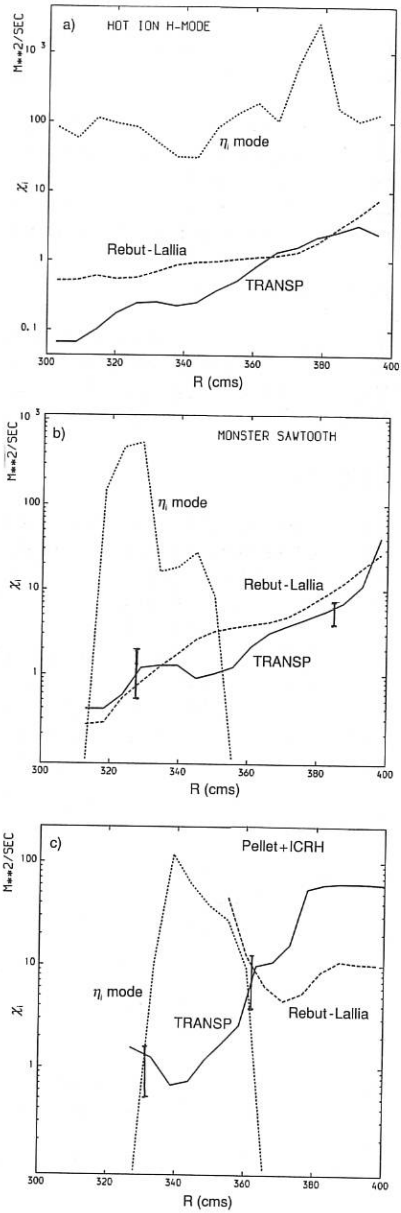
a) HOT ION H-MODE
M**2/SEC
χ_i
η_i mode
Rebut-Lallia
TRANSP
R (cms)
b) MONSTER SAWTOOTH
M**2/SEC
χ_i
η_i mode
Rebut-Lallia
TRANSP
R (cms)
c) Pellet+ICRH
M**2/SEC
χ_i
η_i mode
TRANSP
Rebut-Lallia
R (cms)

Fig.3

DYNAMIC RESPONSE OF PLASMA ENERGY AND BROAD-BAND MAGNETIC FLUCTUATIONS TO ADDITIONAL HEATING IN JET

C Nardone, F De Luca*, P M Hansen,
A Jacchia+, P Mantica+, K Thomsen

JET, Joint Undertaking, Abingdon, Oxon OX14 3EA, U K
* Università degli Studi di Milano, Milano, Italy.
+ Istituto Fisica del Plasma, Assoc. EURATOM -ENEA/CNR,Milano, Italy.

1. INTRODUCTION The discrepancy between the transport coefficients inferred from analyses of the steady-state power balance and of the evolution of temperature profile perturbations, and the observation that the heat flux may not be simply proportional to the local product $n\nabla T$, have led to conclude [1,2] that the energy confinement in JET is determined either by an effective thermal conductivity which is itself a function of ∇T, or by an energy balance containing a term formally equivalent to a "heat pinch". The former interpretation was less favoured by comparisons with the results of heat pulse propagation studies [1], but could not be definitely excluded. The latter has found its most successful embodiment to date in the "critical temperature gradient" model by Rebut and Lallia [3].

From the point of view of global parameters in steady-state, a similar picture was inferred from the observed relationship between plasma energy content W and input power P, leading either to a Goldston-like power law ($W \sim P^{1/2}$) or to an offset linear ($W \sim W_o + \tau_{Einc}P$) representation for the energy content. Both scalings provide good fits to the JET data [4]. Within the framework of an offset linear model, while the energy replacement time τ_E degrades with input power, the actual plasma transport properties are best characterized by a constant "incremental" time $\tau_{Einc} = dW/dP$. According to [3], τ_{Einc} will reflect the form of the local anomalous thermal conductivity induced by ergodization of the magnetic field lines.

In this paper we show (par.2) that τ_{Einc} can be considered as an effective timescale for the global energy time evolution in response to variations in the input power. The time evolution of the edge measured magnetic fluctuations in the same discharges has been modelled with another timescale, different in principle from the energy one, that has been found very well correlated with it (par.3).

2. ENERGY TRANSPORT We have modelled the time evolution of the energy response ΔW to variations ΔP in the input power using the equation

$$\frac{d\Delta W(t)}{dt} + \frac{\Delta W(t)}{\tau_{Edyn}} = \Delta P(t) \qquad (1)$$

where τ_{Edyn} is the "dynamic" energy confinement time. We considered both NB and ICR heated discharges, restricting the analysis to limiter configuration and to power levels lower than 12 MW.

The value of τ_{Edyn} has been deduced from a best-fit of the experimental W(t) using two different methods. First, we used as input for (1) a simple P(t) waveform (a step for the NBI cases, a linear or a parabolic ramp for the ICRH shots), in order to exploit the analytical solution of the equation. Second, for a reduced number of shots we solved numerically (1) using the experimental P(t). Fig.1 shows an example of such a fit, where also the W(t) corresponding to the extremes of a typical error bar ($\pm 10\%$) for τ_{Edyn} have been plotted. The following three points can be made as results of the analysis.

- In almost all shots the energy time evolution can be reproduced accurately by eq (1), i.e. only one time constant is required to model W(t). As a consequence, very good agreement is found between τ_{Edyn} and τ_{Einc}, while τ_E approaches the same value for increasing power.

- The dynamic confinement time is found to be the same both for the rise and fall phases of the energy evolution, and it does not show any dependence on power and density.

- By looking at cases of multiple NBI steps and combined NBI and ICRH, it has been checked that τ_{Edyn} does not depend on the initial power level or on the type of auxiliary heating.

The values of τ_E, τ_{Edyn} *and* $\tau_{Einc} \simeq \Delta W/\Delta P$ for the shots analysed are plotted in fig.2 as a function of power. We notice that the linear trajectory of W(t) as a function of $(P - W)$ (fig.3) is an independent observation that supports, from the point of view of a single-shot time evolution, the view that offset linear scaling laws for the energy replacement time are more appropriate than power laws. This is also confirmed by the fact that the same time constant is found both for the rise and the fall phase.

3. MAGNETIC FLUCTUATIONS Transport models based on magnetic turbulence, such as the Rebut-Lallia model [3], are compatible with the previous observations. Furthermore, earlier analyses of the steady-state levels of magnetic fluctuations have shown a correlation with the global confinement [5]. Therefore the extension of the analysis to the dynamic behaviour of the fluctuations can bring further evidence on the link between transport and magnetic turbulence.

The time evolution of the rms level of the poloidal magnetic field fluctuations $|\tilde{B}_\theta|$ in the frequency range 40 ± 8 kHz measured by one pick-up coil on the equatorial plane has been empirically investigated by using the same eq (1). The frequency range chosen allows investigation of broad-band turbulent activity, which is generally expected to be due to a superposition of high m,n modes resonant in the plasma peripheral region, avoiding contributions to the signal from coherent low m,n MHD modes. Fig.1c shows a typical fit to determine τ_{fl}, the dynamic response time of the magnetic fluctuations, the error bars being larger ($\pm$ 40%) than in the energy case because of the higher noise level on $|B_\theta|$. The contribution to the signal variation due to the change in Shafranov shift has been verified to be negligible at the power levels considered and does not affect the

determination of τ_{fl}. Also, the fluctuations can be represented as evolving with a single time constant during the transient phase of the heating, and fig.4 shows that this time constant is very well correlated with τ_{Edyn}.

4. CONCLUSIONS The analysis of the dynamic response of the plasma energy to the power input variations suggests that the plasma energy evolution may be determined by an effective energy timescale (τ_{Edyn}) that does not depend on power. This appears to be an independent confirmation of previous results of local and global transport studies [1,2]. The correlation between the saturated magnetic fluctuation level and τ_E^{-1} [5] would accordingly have to be reinterpreted: since fluctuations do increase during the heated phases and follow τ_{Edyn}, their variation should be seen more as a consequence of the change of plasma parameters than as a driving force for the effective transport mechanism. However, further analysis is required before drawing such a conclusion, since one must not ignore that the measured fluctuations do not come from the plasma core and that also saturation phenomena could be invoked to justify the experimental evidence.

ACKNOWLEDGMENTS We are glad to acknowledge helpful discussions with F Tibone, A Tanga, P Thomas and A Taroni.

REFERENCES

[1] B Tubbing et al, *Nucl Fusion*, **27** (1987) 1843.
[2] J D Callen et al, *Nucl Fusion*, **27** (1987) 1857.
[3] P H Rebut et al, IAEA-CN-50/D-IV-1, Nice 1988.
[4] J G Cordey et al, IAEA-CN-47/A-II-3, Kyoto 1986.
[5] M Malacarne, P A Duperrex, *Nucl Fusion*, **27** (1987) 2113.

FIGURE CAPTIONS

Fig.1 *Time evolution of plasma energy W for a 5 MA, 3 T, 2 MW ICR heated shot.*
a. total power input P_{tot} (MW)
b. MHD equilibrium measured W in MJ (broken line) and fitted W (middle continuous line) with $\tau_{Edyn} = 0.37 \pm 0.04$ s. The outer lines refer to the error bar for τ_{Edyn}.
c. same as b. for $|\tilde{B}_\theta|$(40kHz), with $\tau_{fl} = 0.37 \pm 0.15$ s.

Fig.2 *τ_E, τ_{Einc} and τ_{Edyn} (s) vs P_{tot} (MW) for a 3 MA subset of the discharges considered. τ_E is calculated twice for every shot, immediately before the additional heating, and when the plasma energy has been saturated. The broken line corresponds to the average τ_{Edyn} of the subset.*

Fig.3 *Plasma energy W (MJ) vs (P_{tot} less dW/dt) (MW) for a 3 MA, 3 T, high density shot, combined heating (10 MW NBI + 10 MW ICRH). The inset shows the time traces of P_{NBI}, P_{ICRH}, P_{tot} and W.*

Fig.4 *τ_{fl} vs τ_{Edyn} (s) for the set of 35 discharges considered. A typical error bar is shown.*

fig.1

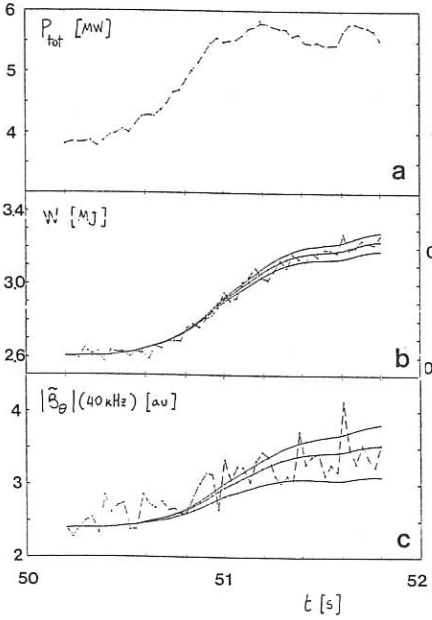

fig.2

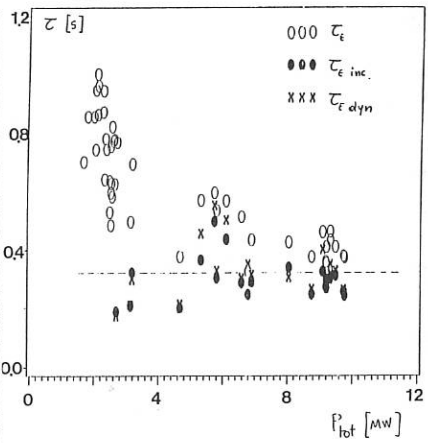

fig.3

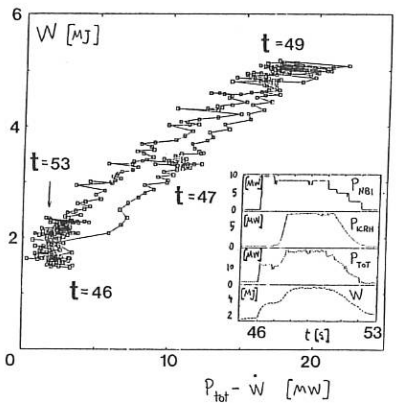

fig.4

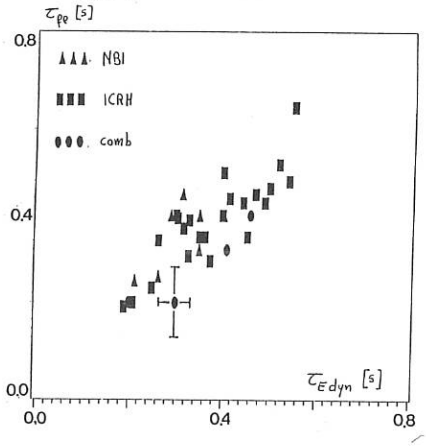

ANALYSIS OF HEAT PULSE PROPAGATION IN PLASMAS USING FOURIER METHODS

A.Bruschi, F.De Luca, G.Gorini, A.Jacchia, N.Lopes Cardozo*, P.Mantica

Istituto di Fisica del Plasma, Associazione EURATOM- ENEA-CNR, via Bassini 15, 20133 Milano, Italy
**FOM Instituut voor Plasmafysica 'Rijnhuizen', Associatie EURATOM-FOM, postbus 1207 3530 BE Nieuwegein, The Netherlands*

Introduction

The heat pulse following the sawtooth collapse of a toroidal plasma has usually been studied using the Initial Value (I.V.) method. This method determines the electron thermal diffusivity, χ_e, by fitting the predictions of a diffusive model starting from an initial perturbation (assumed to mimic the sawtooth crash) to the electron temperature perturbation, $\tilde{T}_e$, measured at different radii. Under reasonable simplifying assumptions, the heat diffusion equation can be solved analytically [1], and simple formulae are obtained to determine χ_e from the time delay of the maximum of $\tilde{T}_e$ at different radii. Alternatively, the $\tilde{T}_e$ waveforms can be Fourier analyzed in time [2]. This approach is independent of the initial perturbation, and makes use of the complete $\tilde{T}_e$ waveforms to determine the phase differences of their harmonic components, $\tilde{T}_{e\omega}$, at different radii. Due to the non-sinusoidal shape of the perturbation, the propagation can be studied at different frequencies. Clearly, the I.V. and Fourier methods should give consistent results if the measured heat pulses can be described accurately with a simple diffusion equation.

Including a damping term in the Fourier method

As has been shown in [3 to 5], the perturbed source terms in the heat balance can seriously affect the heat pulse, and this can be modelled by adding a damping term to the diffusion equation. In slab geometry one has $T_{et}=(2/3)\chi_e T_{exx}-T_e/\tau$, where τ denotes the damping time-constant and the subscripts t and x denote differentiation with respect to time and x, the spatial coordinate. The diffusivity χ_e can be expressed as $\chi_e=(3/4)\, v_\phi/\alpha$ (eqn.1), where $v_\phi=\omega/\phi_x$ denotes the phase velocity and $\alpha=\tilde{T}_{e\omega x}/\tilde{T}_{e\omega}$ the inverse dacay length of

the amplitude of a harmonic component with frequency ω. For cylindrical geometry small corrections to this formula must be applied. From a Fourier analysis of $\tilde{T}_e$ at various radii, the phase velocity and the decay length are readily determined. Eqn.(1) is the analog of the formula for χ_e using the I.V. method, derived in ref [5].

Application to simulated and measured heat pulses.

As a test case for the Fourier method we use data from JET pulse #7960, published in [4]. This concerns $\tilde{T}_e$ at 12 radii, measured with ECE grating spectrometer. In Fig.1 the heat pulses are shown at three radii. The analysis in [4], using the I.V. method, yields χ^{HP}=1.8 m^2/s.

We have used a cylindrical diffusion code to simulate the heat pulses, applying the same correction as in ref. [4] for the effect of the Shafranov shift and of the elongation of the plasma (for shot 7960 χ/χ_{cyl}~1.8). As expected, the simulated pulses match the measurements fairly well as far as the peak time and amplitude are concerned.

To test the Fourier method we applied it to both the experimental and simulated heat pulses. The application to experimental data requires considerable attention because i) the sawtooth repetition rate is often not constant and ii) the slow decay of the heat pulse can be affected by spurious phenomena [6]. Concerning i) we find that it is better to analyze the single heat pulse (if necessary obtained by phase-locked averaging of many sawtooth cycles). To suppress the effect of distortions in the tail of the heat pulse, we remove as much from the tail as is possible without introducing artifacts in the analysis. Whether artifacts are introduced is checked by analyzing the simulated heat pulse and giving it the exact same treatment as the measured heat pulse. The truncation induces a mismatch of the initial and final value of the waveform. We remove this mismatch by adding to the data record a number of zeros before and a constant prolongation after the truncated pulse, and removing the resulting linear offset [7]. Furthermore, a Tuckey lag window with cut-off point at 0.3-0.5 of the record length is used in the calculation of the power and cross-phase spectra. We explored the frequency range up to 50 Hz, in which the cross-coherence values for the experimental signals are still significantly above the expected statistical error (Fig.2).

The effect of the tail truncation is shown in Fig.3. Without truncation the amplitude and, especially, the phase of $\tilde{T}_e$ show wild variations as a function of frequency. Truncation at t=30 ms is found to remove the large oscillations. The same truncation, when applied to the simulated heat pulses, introduced a systematic error not larger than ±15% in the determination of χ_e. As a practical rule, we find that this systematic error is small provided the maxima of the heat pulses are well within the truncated data records.

Despite the fact that the maxima of the experimental heat pulses are fitted fairly well by the simulated pulses, we find that their cross-phase spectra are significantly different (Fig.4). Consequently, the values for χ_e determined from the Fourier spectra are also different from the χHP derived by means of the I.V. method (Fig.5). This discrepancy can be attributed to the rise phase of the heat pulse, the delay between pairs of experimental heat pulses being significantly shorter than the corresponding delay between simulated curves. Very interesting is the apparent dependence of χ_e on the frequency ω. This is larger than the ±15% uncertainty in the analysis, but further evidence is required before we can draw hard conclusions from this result. Ref.[2] finds no such dependence in the analysis of heat pulses in TFTR. Here we just point out that a diffusive model based on a single χ_e value would inevitably give a flat χ_e versus ω dependence. On the other hand, the observed frequency dependence can be reproduced if we assume that the observed heat pulse is the superposition of two diffusive pulses propagating with different velocities. Such a superposition could arise from the presence of off-diagonal terms in the transport matrix. The existence of this type of coupling has already been shown in studies of simultaneous heat and density pulses in JET [8].

References

[1] M.Soler, J.D. Callen, Nucl.Fus. **19** (1979) 703.
[2] E.D.Fredrickson et al., Nucl.Fus. **26** (1986) 849.
[3] W.J.Goedheer, Nucl.Fus. **26** (1986) 1043.
[4] B.J.D.Tubbing, N.J.Lopes Cardozo, M.J. Van der Wiel, Nucl.Fus. **27** (1987) 1843.
[5] N.J. Lopes Cardozo, B.J.D.Tubbing, F.Tibone, A.Taroni, Nucl.Fus. **28** (1988) 1173.
[6] K.S.Riedel et al., Nucl.Fus. **28** (1988) 1509.
[7] NAG Fortran Library Manual, Mark.12, Vol.6.
[8] G.M.D Hogeweij et al., this conference

Acknowledgement

The authors acknowledge the cooperation of JET, in particular the electron temperature group, who made available the ECE data used in the analysis.

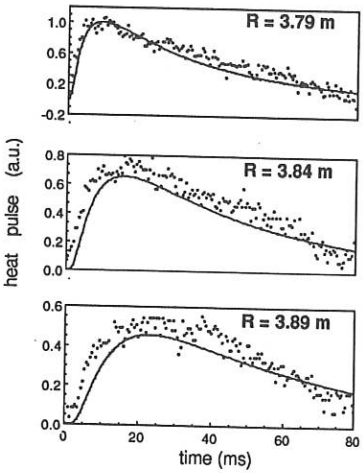

Fig.1 Experimental (dots) and simulated with χ_e= 1.8 m^2/s (line) heat pulses at three selected radial positions for the JET shot #7960. The data are normalized to the maximum of the heat pulse at R=3.79 m.

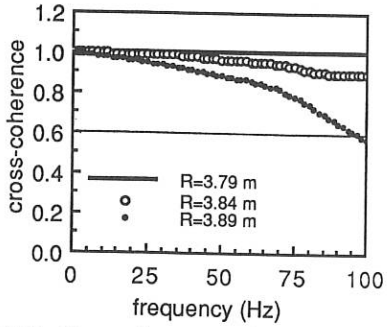

Fig.2 Cross-coherence vs frequency for the three experimental channels using as reference the radial position R=3.79 m and data truncation at t=30 ms. The expected statistical error level (~0.6) is also plotted.

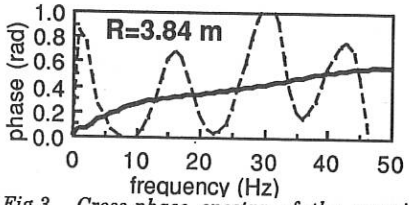

Fig.3 Cross-phase spectra of the experimental heat pulse between the radial positions R=3.84 m and R=3.79 m. The dashed line represents the spectrum obtained without any data manipulation. The continuus line represents the spectrum obtained with a truncation of the data at t=30 ms.

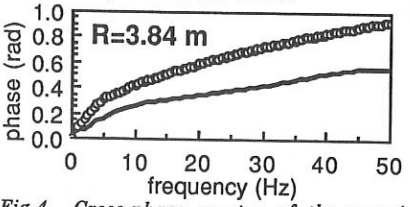

Fig.4 Cross-phase spectra of the experimental heat pulse (thin line) and of the simulated heat pulse with χ_e= 1.8 m^2/s (thick line). The cross-phase is calculated for the radial position R=3.84 m, taking the pulse at R=3.79 m as reference.

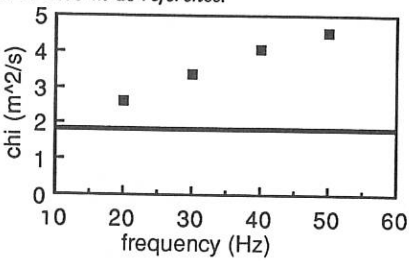

Fig.5 Frequency dependence of the value χ_e determined from the Fourier analysis of the experimental heat pulse data. The line is the χ_e = 1.8 m^2/s value determined by the I.V. method.

PARTICLE AND THERMAL TRANSPORT IN TEXT FROM PERTURBATION EXPERIMENTS*

K.W. Gentle, M.E. Austin†, D.L. Brower‡, G. Castle, G. Cima§, R. Gandy†, W.L. Li‡, N.C. Luhmann‡, S.C. McCool, D.M. Patterson, W.A. Peebles‡, P.E. Phillips, B. Richards, W.L. Rowan, P.M. Schoch◊, B.A.Smith, D.C. Sing, A.J. Wootton, C.X. Yu‡

Fusion Research Center, The University of Texas at Austin , USA

Density variations induced by modulation of the gas feed and temperature variations induced by modulation of ECRH power constitute linear perturbations, the analysis of which provide a measure of particle and thermal transport. In addition to the direct inferences of transport coefficients, such experiments can examine the linearity of the processes and through cross-coupling, provide evidence of off-diagonal terms in the transport matrix. Furthermore, the response of the (electrostatic) turbulence to the perturbations can be an indication of the causes of the turbulence.

Particle Transport. Diffusion coefficients and convective velocities have been obtained with radial resolution for a wide range of ohmic hydrogen discharges. The response to sinusoidal density modulation from seven radial interferometer chords may be accurately described by a model with a value D(0) in the central third of the plasma, an independent value D_e in the outer third, and a linear transition in between. A similar form was used for convective velocity, but with a factor of (r/a). Typical results for the coefficients as a function of density [$10^{19}m^{-3}$] are illustrated (up to the density limit) for a number of discharges at I_p=300kA and B_T=2.8T; the solid triangles are D_e and the bars D(0)[m^2/s]. The decrease of D with rising density is a uniform pattern in the data. Similarly, the central D is smaller than the outer value, although they converge at the density limit. (The radial variation of D is qualitatively that of a local inverse density dependence, but such a model is not quantitatively adequate.)

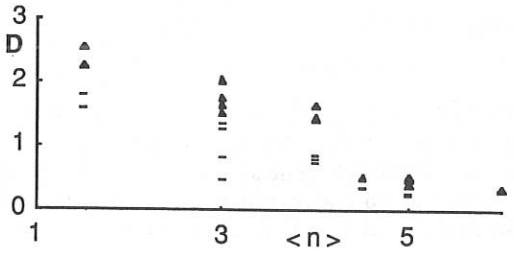

The inward convective velocity in the outer half of the plasma, V_e[m/s], is always strong, although it does decrease as the density limit is approached. The neoclassical pinch velocity, without reduction for collisionality, is less than 2 m/s for these conditions. The convective velocity in the core (not shown, but compare S in core below), is smaller, often even negative (outward), and shows no clear functional dependence. The density dependence illustrated is robust, appearing in all data. No similarly robust scalings with q, I_p, or B_T have been seen. Particle transport seems linear and independent of the frequency of modulation. Density perturbations from 2% to 15% have been imposed without systematic changes in the coefficients inferred. This argues against marginal stability models or highly nonlinear dependences on the density gradient, etc.

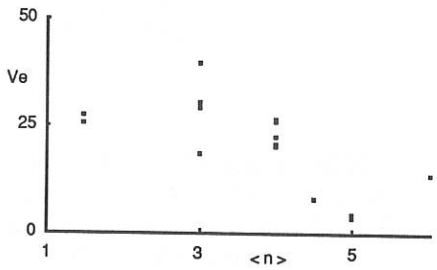

These transport coefficients describe a linear perturbation about equilibrium and are not necessarily those which describe the equilibrium itself;[1] differences arise if D or V depend upon the density, temperature, etc. or their gradients. The equilibrium D_o and V_o cannot be independently determined, but their ratio determines the profile shape. The equilibrium shape may be fitted with a dimensionless ratio $S_{eq}=aV_o/D_o$ (limiter radius a=0.26 m) having central and outer values as above; these may be compared with the ratio of the transport coefficients measured from perturbations. For the outer portion of the plasma, $S=aV_e/D_e$ is consistently larger, by factors ranging from 0.9 to 3, than the value characteristic of the equilibrium profile, as illustrated with data from a broad range of discharges. Since most plausible effects would cause $D_e \geq D_o$, these results require that $V_e \geq V_o$. This can be interpreted as a strong constraint on possible forms of D. If for example $D \propto n^{\alpha}(\frac{\partial n}{\partial r})^{\beta}T^{\gamma}(\frac{\partial T}{\partial r})^{\delta}$ is assumed, $\beta \sim 0$ is necessary, $\alpha<0$ is acceptable, and $\gamma \cong -\delta$. As a consequence, none of the usual drift wave models would be admissible. The corresponding results for the core are more varied, as shown. Although central convection for equilibrium is always inward, the perturbation can give either sign, and the value is generally less than the equilibrium value. This must reflect a combination of complex processes,

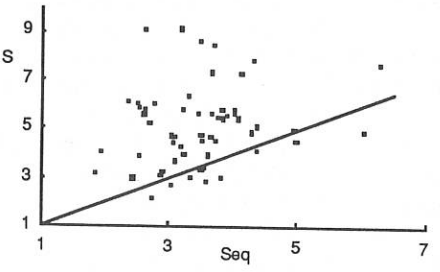

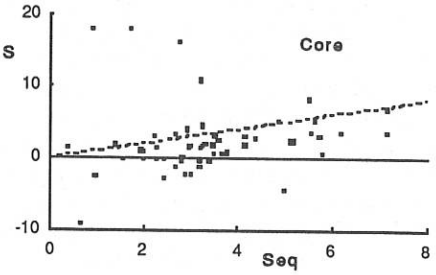

including sawteeth. (These discharges all exhibited sawteeth, but the period was much shorter than the modulation period. The transport coefficients thus include an averaged effect of sawteeth, but specific sawtooth effects, e.g. at low q, were not noted.)

Effects Associated with Density Modulation. The density modulation drives changes in many other plasma parameters, among them electron temperature, edge neutral pressure, and level of internal electrostatic turbulence (measured as high-frequency density fluctuations with a heavy ion beam probe). Special compensation is applied to the vertical field to minimize the plasma motion which would otherwise occur and produce effects itself. The electron temperature is measured by ECE. The fractional modulation in central temperature is approximately the same as that of central density, but it leads the chord-averaged density in phase by ~90°. This implies a significant off-diagonal element in thermal transport, for this is not a consequence of modulation of thermal convection, which would be in phase, or central ohmic power. Neither can it be a consequence of edge effects, for the temperature modulation at larger radii (r>0.5a) is generally smaller than that at the center and shifted by ~180°.

The effects at the edge are equally complex. Neutral pressure modulation (from a fast pressure gauge) at the limiter is not proportional to edge density, as one might expect from recyling, but is significantly smaller in relative amplitude and close in phase to the chord-averaged density. The source (inferred from H_α) is also surprising. Although a view of the modulated gas feed shows strong modulation leading the density in phase, other monitors at the limiter and elsewhere show fractional modulation less than that of edge density and of greatly different phases.

The level of turbulence is modulated throughout the plasma with amplitudes similar to that of the density and linear in the amplitude of density perturbation. The phase lags that of the central density by 90°, but it does not change with radius. The local turbulence does not follow the local phase of density, density gradient, or temperature modulation. (For these experiments, the perturbations to density and density gradient were comparable.)

Thermal Transport. Using analysis similar to that for density perturbations, the sinusoidal temperature variations induced by (square-wave) modulation of centrally deposited ECRH power imply values of thermal diffusivity χ_e, but the results in these experiments are less well determined. A discharge at low density ($< n > = 1.5 \times 10^{19}$ m^{-3}) and low current (q~6) was chosen to provide good ECRH heating without sawteeth. Although ECE data are

generally consistent with Thomson scattering temperature measurements and show no strong non-thermal features, the small phase delay between central and outer channels implies at least transient non-thermal effects and precludes transport analysis. Only the soft x-ray arrays could be used to follow the perturbation. They provide phase data, but not absolute amplitude of the perturbation. Furthermore, the two arrays viewing horizontally and vertically reveal a poloidal asymmetry in the propagation. The perturbation propagates up and down at the same speed, but outwards more slowly, and inwards much more slowly. The absence of amplitude data also introduces more ambiguity in the fits. However, using a ray-tracing calculation of the deposition profile and a radial form for χ like that of the power-balance value, the perturbation analysis is consistent with power-balance, shown as $\chi(r/a)$. The power balance values for the ohmic and heated discharges are shown as solid curves, and the modulation analysis for upward and outward propagation as dashed.

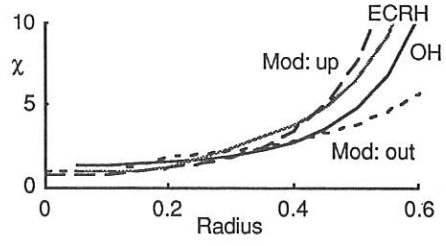

Effects Associated with Temperature Modulation. Like density modulation, temperature modulation affects other quantities, including density and turbulence, and care is required to avoid indirect effects of position modulation. Central heating which induces a 15% temperature modulation causes a weak (1%) density modulation which can only result from a modulation of particle transport coefficients. A variation of at least 15% is required (more if the effect is spatially localized) in either D or V (which are indistinguishable in this context). The increase in D (or decrease in V -- both are implied by transport studies in ECRH plasmas) lags the heating power by 90°, substantially more than the lag in central temperature in this case. The persistence of density changes in the absence of strong heating also casts doubt on the argument that the ECRH effect on particle transport is a direct or local temperature effect.

The effect of ECRH on turbulence in generally similar to that of density modulation. Local turbulence levels are modulated to generally the same degree as the central temperature, but the phase of the turbulence remains approximately constant across the plasma, precluding any association with local temperature.

**Supported by USDOE under grant DE-FG05-88ER-53267.*
†Auburn University, Auburn AL. § Associazione EURATOM/CNR/ENEA, Milano, Italy. ‡ University of California, Los Angeles. ◊ Rensselaer Polytechnic Institute.

1. Gentle, K.W., Physics Fluids **31** (1988), 1105 .

INVESTIGATION OF COUPLED ENERGY AND PARTICLE TRANSPORT

C.M. Bishop, J.W. Connor, M. Cox, N. Deliyanakis, D.C. Robinson

UKAEA/Euratom Fusion Association, Culham Laboratory, Abingdon, Oxon, OX14 3DB, UK.

1 Experimental background

Most theoretical models of coupled transport predict particle and thermal fluxes that are each driven by both density and temperature gradients; one would therefore expect some form of coupling between the energy and particle transport. This contrasts with the assumptions usually made when analysing tokamak thermal transport by equilibrium and dynamical techniques, namely that the thermal flux is driven solely by a temperature gradient and that the thermal diffusivity is a function of radius only. An *effective* thermal diffusivity can be defined for *any* transport model, viz. $\chi_{\rm eff} = -q/nT'$, where q is the total heat flux, but its value will generally depend on the measurement technique. Coupled transport has been invoked as an explanation of the discrepancies between $\chi_{\rm eff}$ values deduced from perturbation and power balance measurements (the former typically being higher than the latter) observed on several tokamaks. The present investigation into coupled transport is motivated by results from the ECRH modulation experiments carried out on the DITE tokamak [1]. Here, in contrast with other experiments, the values of $\chi_{\rm eff}$ inferred from modulation experiments and from power balance and sawtooth heat pulse propagation were all in good agreement, provided that allowance was made for the broadening of the ECRH deposition profile at the higher densities. A small modulation of the line averaged density $\overline{n}_e$ was also observed, being smaller in He than in H/D plasmas; this can arise from three distinct mechanisms. First, off-diagonal terms in the transport equations will lead to a non-linear coupling of the particle and energy balance, possibly different in He and H/D plasmas, which can lead to different values for the thermal diffusivity being inferred from dynamical and equilibrium measurements. Second, the neutral particle density near the edge will be modulated, leading to a corresponding modulation in the edge source, which has been observed in the Hα-radiation signals. Third, the modulation of the plasma pressure will produce a modulated horizontal movement of the flux surfaces, leading to a modulation of the observed line-integrated density (as well as to similar contributions to the vertical SXR and the ECE signals). This paper addresses whether coupled transport can be present even when the various values of χ_{eff} are in agreement, as in the DITE experiments.

2 Analysis

The generalized, non-linear coupled transport equations are:

$$\frac{\partial n_e}{\partial t} = \frac{1}{r}\frac{\partial}{\partial r}\left[rn_e\left(L_{11}\frac{n_e'}{n_e} + L_{12}\frac{T_e'}{T_e} - V_1\right)\right] + S(r,t), \tag{1}$$

$$\frac{3}{2}\frac{\partial(n_eT_e)}{\partial t} = \frac{1}{r}\frac{\partial}{\partial r}\left[rn_eT_e\left(L_{21}\frac{n_e'}{n_e} + L_{22}\frac{T_e'}{T_e} - \frac{3}{2}V_2\right) + \frac{5}{2}rn_eT_e\left(L_{11}\frac{n_e'}{n_e} + L_{12}\frac{T_e'}{T_e} - V_1\right)\right] + Q(r,t). \tag{2}$$

L_{11} and L_{22} correspond, respectively, to the electron thermal (χ_e) and particle (D) diffusivities; the convective contribution of the particle flux to the thermal flux has been

Table 1: Results from analytical investigation of coupled transport systems (relative magnitudes of the steady-state coefficients are shown): density and temperature perturbations, and effective thermal diffusivities, as determined from modulation, sawtooth and power balance measurements.

Model	L_{11}	L_{12}	L_{21}	L_{22}	$\frac{\tilde{n}/n}{\tilde{T}/T}$			$\frac{\chi_{\rm eff}^{HP}}{\chi_{\rm eff}^{PB}}$ $\eta = 1.5$		
					near field		far field	near field		far field
					mod	s/t		mod	s/t	
collisionless neoclassical	1.04	−0.36	−1.40	1.65	0.19	1.04	−1.66	1.59	1.31	2.63
collisional neoclassical	0.33	0.06	−0.27	0.71	−0.08	0.83	0.31	1.43	1.58	1.49
anomalous DTE ($\eta = 1.5$)	2.0	6.0	1.0	15.0	−0.14	0.53	0.47	0.14	12.7	4.56

included explicitly. S is the particle source and Q is the total heating source including ohmic, equipartition, radiation and ECRH terms.

The qualitative effects of coupling have been investigated using an analytical solution of the transport equations, for three transport models, namely the collisionless and collisional neoclassical models, and the anomalous dissipative-trapped-electron (DTE) mode [3]; the latter predicts diffusivities with a cubic dependence on the density gradient. The density and temperature perturbations and effective thermal diffusivities were evaluated for modulated localized heating and sawtooth collapse (assuming density and temperature perturbations of equal scale-lengths). The results, shown in table 1, are broadly consistent with general experimental observations: the *dynamical* values of the effective thermal diffusivity are *higher* than the corresponding *equilibrium* values, and the density perturbations are often smaller in relative amplitude than the temperature perturbations.

The transport parameters are, in general, functions of several plasma variables, and will consequently be modulated. For simplicity, a single radial dependence is assumed here for all the diffusivities, increasing towards the edge for consistency with the results from power balance analysis. The sources will also be modulated, thus producing additional driving or damping terms for the perturbation. The (time-independent) current density profile is determined from neoclassical resistivity; the Ohmic heating term is perturbed via the time-dependent resistivity. The equipartition power density is calculated from the steady-state ion energy density. The power densities of the total and SXR radiation are calculated from the estimated concentration levels of carbon and oxygen impurities. The radial dependence of the modulated ECRH power input was calculated by a ray-tracing code. The particle source and its modulation was not determined directly from these experiments; instead, the effective particle source required to sustain the equilibrium density profile for a given transport model was calculated, and was modulated near the edge using the observed modulation of the Hα emission. An estimate of the modulated, differential shifts of the flux surfaces resulting from the modulation of β_p (but not l_i) is incorporated in the model. Furthermore, a modulated, horizontal shift of the entire plasma column is present, of amplitude comparable to the internal shifts; this response of the plasma column, which depends mainly on the feedback stabilization system, is applied to the outermost flux surface. A transport code has been developed to implement the general model of coupled transport described above, with a view to evaluating a variety of transport models in the presence of modulated heating. Signals of line-integrated soft X-

ray emissivity (for both horizontal and vertical lines of sight), electron cyclotron emission and line-integrated density are generated over the duration of the perturbation. The profiles of modulation amplitude and phase are extracted, for a direct comparison with the corresponding experimental results.

3 Results

The coupled transport model was used to assess the compatibility of coupled transport models with the analysed data from the modulated ECRH experiments on DITE [1]; early results of this investigation were reported in [2]. The equilibrium profiles of density and temperature were established from a combination of experimental observations and calculations of the equilibrium state. The diffusivity matrix of the collisionless neoclassical model (for Z_i=1) was used, with a magnitude and profile chosen for compatibility with power balance observations. Whilst there is no justification in the use of this particular model, since neoclassical theory fails to predict the observed transport, it provides one with a means of testing the basic aspects of coupled transport.

The computed temperature perturbation was broadly similar, in form and magnitude, to that obtained from a simpler diffusive thermal transport analysis. The computed density perturbation was small under some conditions, in particular with off-axis heating; its shorter radial scale lengths also led to a significant cancellation of the modulation amplitude on calculating the line-integrated values. The resulting modulation amplitudes were compatible with the low experimental values. Reasonably good agreement was obtained between the computed and experimental SXR (fig. 1) and ECE (fig. 2) responses, but the fits were less satisfactory than those obtained from a simple uncoupled transport model. The modulated particle source plays an important role in determining the level of the density modulation. As this modulated component of the particle source was included using empirical amplitude levels and phases, this aspect of the model is a significant source of uncertainty. The modulation of the flux surface shifts led to the expected asymmetries, the results being consistent both with the experimental shifts and the modulation data. All the results of the coupled transport model were sensitive to the equilibrium profiles, as well as on the form of the transport model. The effective power balance thermal diffusivity ($0.9\mathrm{m}^2\mathrm{s}^{-1}$ at the radius $a/3$) in the model was in good agreement with the experimental power balance value. Two further transport models have also been assessed: the DTE mode [3], whose diffusion matrix was also used with an empirical radial profile and scaled to give the correct power balance, did not lead to satisfactory agreement with the modulation data because of its sensitive (cubic) dependence on the density gradient; the 'second-order' classical model proposed by Woods [4] was found to reproduce both modulation (fig. 3) and power balance measurements provided that (i) the overall transport was increased by a factor of 3 and (ii) a minimum value of $\chi_{eff} = 0.75m^2s^{-1}$ was imposed near the plasma centre where the Woods model predicts values which tend to zero.

Whilst it has not been possible conclusively to establish the nature of the underlying transport mechanisms, it has been shown that coupling of energy and particle transport is possible in the DITE modulation experiments, although less than one would infer from other tokamak experiments. It has been demonstrated that modulated heating affords one with a powerful technique for assessing transport models.

References

[1] M. Ashraf et al., Proc. 12th IAEA Conf., Nice, Paper A-V-2-1 (1988). See also paper by M Cox et al to be submitted to Nucl. Fusion.
[2] C.M. Bishop et al., Proc. 16th EPS Conf., Venice, **13B** (1989). See also paper by N Deliyanakis to be submitted to Nucl. Fusion.
[3] W. Horton, Phys. Fluids, **19** (1976), 711.

[4] L.C. Woods, *Principles of Magnetoplasma Dynamics*, OUP (1987).

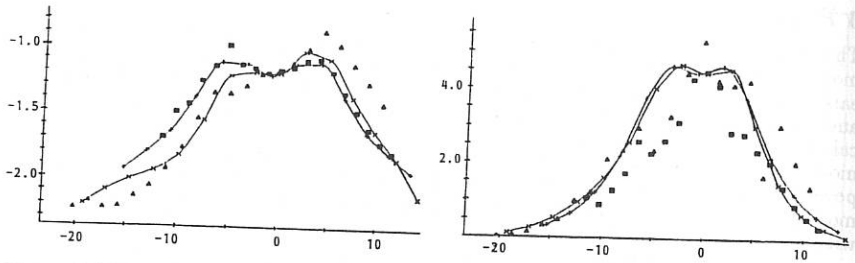

Figure 1: Fits using the collisionless neoclassical matrix to the radial profile of the phase (left) and amplitude (right) of the modulated signal seen by the horizontal (squares) and vertical (triangles) SXR cameras. The abscissa is the chordal radius of line of sight in cm.

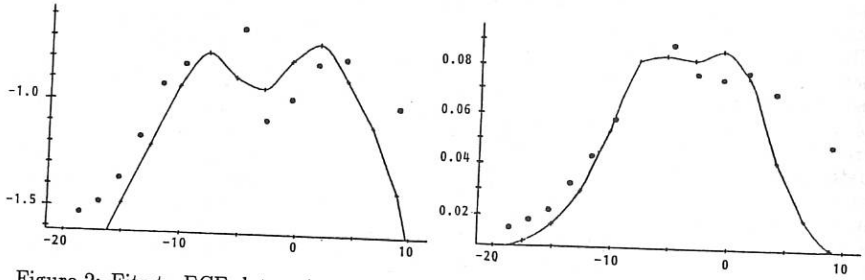

Figure 2: Fits to ECE data using same model as Figure 1.

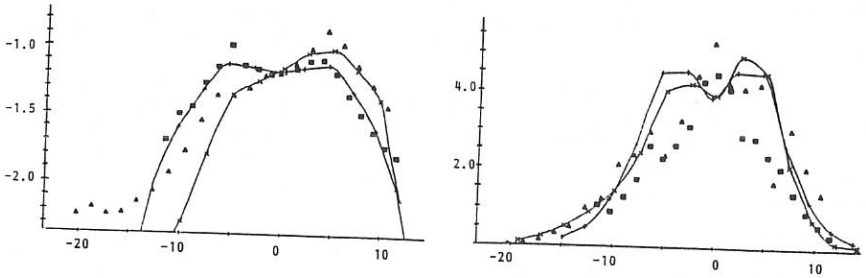

Figure 3: As Figure 1 but for the Woods model.

IS THE ION CONFINEMENT IMPROVING IN ASDEX H-MODE DISCHARGES ?

O. Gruber, A. Kallenbach, E. Simmet, K.-H. Steuer

Max-Planck-Institut für Plasmaphysik, EURATOM Association, D-8046 Garching

There is still uncertainty in the transport channels which actually improve after the L→ H transition. On JET the transport analysis indicates an improvement of the ion transport alone. On ASDEX we have found that it is the electron transport which is reduced. Finally, on DIII-D the H-mode primarily exists at high densities and the close coupling between ions and electrons prevented a clear statement.

In order to explore the changes of electron (χ_e) and ion (χ_i) heat transport from the L- to the H-mode in more detail, a comparative study between auxilliary heated discharges with peaked (L-mode with Ctr-NI) and broad(L-mode with Co-NI, H-mode with Co- and Ctr-NI) density profiles was carried out. Transport analyses of L-mode discharges with TRANSP show that the ion thermal transport and the toroidal momentum diffusivity (χ_φ) - closely connected with it - can be consistently described by a combination of neoclassical and η_i-driven transport improving with peaked density profiles ($\eta = L_n/L_T < 1$), whereas the electron transport remains anomalous.

Enhanced ion energy transport from η_i-modes would, of course, also be expected to persist for the interior regions of H-regime discharges still having $\eta_{e,i} > 1$. And in fact our previous analyses of them have always shown the necessity for an enhancement of χ_i above χ_{CH} in those cases to match the average ion temperature and the magnetically measured plasma energy. But the formally assumption $\chi_i = \alpha\, \chi_{neocl}$ with α = 2-4 yields much more peaked T_i-profiles than given by passive CX measurements. Using $\chi_i = \chi_{CH} + \chi_{\eta i}$ gives again good agreement with the measured profiles, and due to the strong $T_i^{3/2}$ dependence of $\chi_{\eta i}$ even an increase of the ion heat conductivity going from the L- to the H-mode. However, the ion heat conduction losses behave similar with the two χ_i models. The momentum confinement time increases at the L to H transition but χ_φ is not at all reduced. Further analyses of H and H* discharges will be presented, including Z_{eff} measurements to obtain improved ion density profiles.

According to the analysis up to now the confinement improvement at the L to H transition is due to the reduced electron heat transport. Additionally a reduction of convective losses in the ELM-free H*-mode with very broad and even slightly hollow density profiles is observed.

MOMENTUM TRANSPORT STUDIES ON ASDEX

A. Kallenbach, H.M. Mayer, G. Fussmann, O. Gruber, U. Stroth, O. Vollmer

Max-Planck-Institut für Plasmaphysik, EURATOM Association, D-8046 Garching, FRG

1. Introduction

It has been reported from a number of tokamaks, that the global confinement times of energy and angular momentum show similar magnitudes and scalings with plasma conditions. Since the classical perpendicular viscosity is by far too low to explain the observed rotation damping, an anomalous transport mechanism is believed to cause the radial transport of momentum, which is a feature of the ions alone owing to the low mass of the electrons. The correlation of momentum and energy confinement can be taken as a hint for the thermal conduction and momentum diffusion sharing a common transport mechanism. There is also some evidence from theory supporting this assumption: E.g., the ion-temperature-gradient driven class of instabilities produces equal ion heat and momentum diffusivities ($\chi_i = \chi_\phi$) [1]. Therefore, the investigation of momentum transport can be of special interest for the conditions of medium- or high-density discharges, where the ion- and electron heat transport channels often cannot be separated.

We have analyzed rotation velocity profiles during steady-state conditions of about 50 neutral beam heated ASDEX discharges with different experimental parameters. To give an overview to the database, momentum confinement times τ_ϕ are plotted as a function of τ_E in Fig. 1. τ_ϕ and τ_E are equal within a factor of 2 through the whole parameter range with co-injection. There is a slight tendency for τ_ϕ being smaller than τ_E in the lower confinement branch.

During ctr.-NI, the momentum confinement significantly improves over the energy confinement. This improvement has been found to correlate with the peaking of the density profile [2,3]. For H-mode discharges, the improvement of the momentum confinement equals that of the energy confinement, resulting in data points to appear near the diagonal. In the following, we want to discuss the momentum transport for co-NI, L-mode discharges where a sufficient parameter variation for the derivation of scaling laws has been carried out.

2. Experimental results

Toroidal rotation velocities have been measured simultaneously on 5 radial positions in the outer plasma halfplane by means of charge-exchange-recombination spectroscopy [3]. For the further analysis, the corresponding rotation frequencies are extrapolated over the whole plasma volume under the assumption of the constant angular rotation frequency of a flux surface [4]. Fig. 2a shows typical measured data points with the flux surface fit for a discharge with 1.8 MW neutral injection. For comparison, the rotation with 0.3 MW NI under otherwise identical experimental conditions is shown in Fig. 2b. While the profile shape remains the same with

lower NI power, the speed is reduced by a factor which is less than the ratio of the injected powers. The momentum confinement time τ_ϕ improves from 42 to 70 ms, the corresponding energy confinement times $\tau_{E,dia}$ are 43 and 83 ms, respectively. Obviously, the power degradation of confinement behaves similarly for momentum and energy.

In the next step of the analysis, we have calculated $\chi_\phi(r)$-profiles by solving the radial momentum transport equation [3] using the flux surface fit of the measured rotation frequencies. Results for the discharge of Fig. 2 are shown in Fig. 3. Error bars of the momentum diffusivities have been estimated under the assumption of a smooth shape of the rotation profile. This assumption is necessary for the evaluation since the spatial resolution of 5 points does not allow to determine highly resolved profile shapes. In the plasma center, the uncertainty of χ_ϕ increases due to the imperfect resolution of the (small) rotation gradient. Near the edge, the uncertainties of the radial position and the large relative error owing to the small rotation speeds enhance the uncertainty of χ_ϕ. The influx of momentum transport by charge exchange losses has been neglected in the transport analysis and may lead to a slight overestimation of χ_ϕ near the edge. Although the validity of the derived $\chi_\phi(r)$ profile shapes is limited to a radial interval of about $8\ cm < r < 34\ cm$, there is a clear tendency of $\chi_\phi(r)$ to increase from the center to the edge. This finding is in accordance to recent results from TFTR [5], where an increase of momentum- as well as ion and electron thermal diffusivities with radius was observed.

3. Scaling laws

To summarize the results of the experimental parameter variations for co-NI, L-mode discharges, we have derived scaling laws for τ_ϕ, τ_E and a mean $\overline{\chi_\phi}$ which has been derived from the calculated momentum diffusivity profiles by averaging $\chi_\phi(r)$ between r=8 and r=34 cm in order to reduce the uncertainty. About 40 data points of steady state discharge conditions covered the following parameter range:

0.6 MW	$\leq$	P_{abs}	$\leq$	2.3 MW	mean value:	1.45 MW
$1.6 \cdot 10^{19}$ m^{-3}	$\leq$	$\langle n_e \rangle_{line}$	$\leq$	$6.4 \cdot 10^{19}$ m^{-3}		$3.3 \cdot 10^{19}$ m^{-3}
0.25 MA	$\leq$	I_p	$\leq$	0.45 MA		0.38 MA
1.25 amu	$\leq$	A_{eff}	$\leq$	2 amu		1.75 amu
1 amu	$\leq$	A_{beam}	$\leq$	2 amu		1.87 amu

A_{beam} is the atomic mass of the neutral beam particles and A_{eff} is the mean plasma mass per electron charge, which has been estimated from the H/D ratio measured by mass spectrometry and an averaged Z_{eff} under the assumption of a mean impurity charge Z=7.

For simplicity, we used a least squares procedure after a logarithmic transformation to describe

the confinement properties. The regression analysis revealed the following dependencies:

$$\tau_\phi = 30 \cdot P_{abs}^{-0.7} \cdot n_e^{0.45} \cdot I_p^{0.7} \cdot A_{eff}^{1} \cdot A_{beam}^{-.25} \quad \text{[ms, MW, } 10^{19}\ m^{-3}\text{, MA, amu, amu]} \quad (1)$$

$$\tau_E = 36 \cdot P_{abs}^{-0.6} \cdot n_e^{0.4} \cdot I_p^{0.5} \cdot A_{eff}^{0.7} \quad \text{[ms, MW, } 10^{19}\ m^{-3}\text{, MA, amu]} \quad (2)$$

$$\chi_\phi = 1.6 \cdot P_{abs}^{0.65} \cdot n_e^{-0.7} \cdot I_p^{-0.7} \cdot A_{eff}^{-0.8} \quad \text{[m}^2\text{/s, MW, } 10^{19}\ m^{-3}\text{, MA, amu]} \quad (3)$$

Owing to the relatively small database, the τ_E-scaling should only be used as a reference for the τ_ϕ-scaling.

A clear similarity for the scalings of τ_ϕ and τ_E can be seen in (1) and (2). This is especially true for the isotope effect and the current dependence. The more favourable density dependence of $\overline{\chi_\phi}$ in comparison with τ_ϕ (the distinct improvement of $\overline{\chi_\phi}$ with rising density is found throughout the whole density range wich has been investigated) is due to the unfavourable beam deposition effect with increasing density. To illustrate the meaningfulness of the $\overline{\chi_\phi}$-scaling, we have plotted the experimentally determined $\overline{\chi_\phi}$-values versus the prediction of the scaling law (3) in Fig. 4.

It should be noted, that the power degradation of confinement is not very well described by the power law. In fact, the degradation occurs faster at lower and slower at higher power levels. If the discharges with $P_{abs} < 1$ MW are extracted from the database, the power exponents in Eq. (1), (2), and (3) reduce to -0.4, -0.5 and +0.5, respectively.

4. Summary

We have analyzed the transport of angular momentum for a number of different discharge conditions. The similarity of the scaling laws derived for τ_ϕ and τ_E as well as the equal behaviour of both quantities during single parameter variations strongly support the existence of a common transport mechanism for momentum and energy. Under this assumption, the derived χ_ϕ-scaling may be cautiously interpreted as a measure for the anomalous ion thermal conduction.

References

[1] MATTOR, N., DIAMOND, P.H., Phys.Fluids **31** (1988) 1180.

[2] KALLENBACH, A., MAYER, H.M., BRAU, K., et al., in Controlled Fusion and Plasma Physics (Proc. 16th Eur. Conf. Venice, 1989), Vol.13B, Pt. I, European Physical Society (1989) 175.

[3] KALLENBACH, A., MAYER, H.M., FUSSMANN, G., et al., Nuclear Fusion **30** (1990) in press.

[4] BURRELL, K.H., GROEBNER, R.J., St. JOHN, H., SERAYDARIAN,R.P., Nucl. Fusion **28** (1988) 3.

[5] SCOTT, S.D., DIAMOND, P.H., FONCK, R.J., et al., Phys. Rev. Lett. **64** (1990) 531.

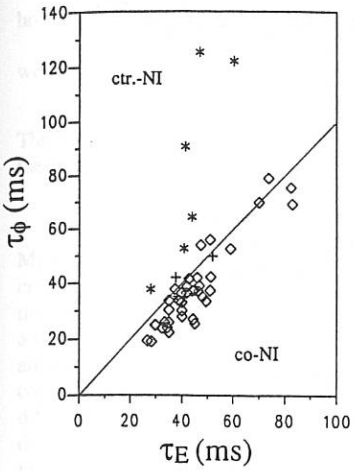

Fig. 1 Momentum confinement time τ_ϕ versus energy confinement time $\tau_{E,dia}$ for various plasma conditions.
◊ co-NI, L-mode; + co-NI, H-mode;
* ctr.-NI;

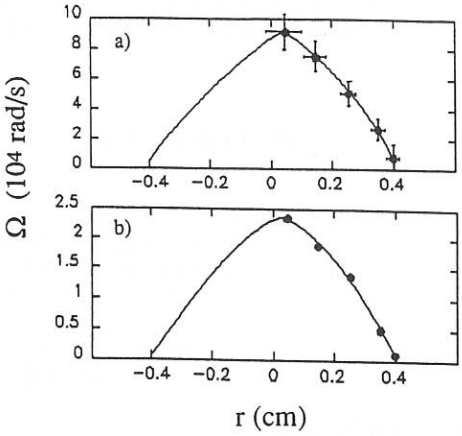

Fig. 2 Angular rotation frequency profiles for a discharge with two different neutral injection powers.
a) P_{NI}=1.8 MW, b) P_{NI}=0.3 MW. $\langle n_e \rangle_{line}=4.6\cdot10^{19}$ m^{-3}, I_p=.42 MA.

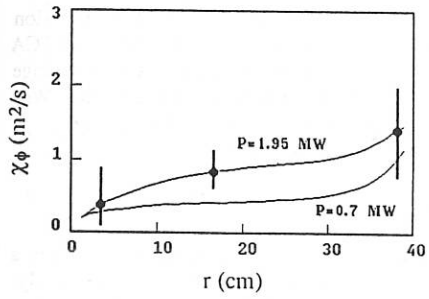

Fig. 3 $\chi_\phi(r)$ - profiles calculated from the rotation frequency fits of Fig. 2 for the two different heating power levels $P=P_{NI}+P_{OH}$.

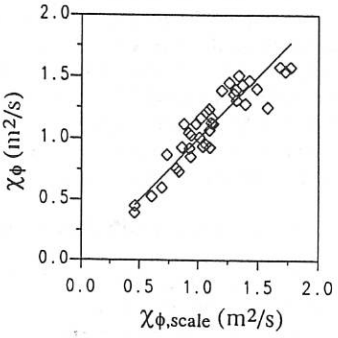

Fig.4 $\overline{\chi_\phi}$ calculated from measurements versus the prediction of the scaling law (3).

DYNAMIC RESPONSE ANALYSIS AS A TOOL FOR INVESTIGATING TRANSPORT MECHANISMS

Th. Dudok de Wit, B. Joye, J.B. Lister, J.-M. Moret*

Centre de Recherches en Physique des Plasmas
Association Euratom-Confédération Suisse
Ecole polytechnique Fédérale de Lausanne
CH-1015 Lausanne, Switzerland

* present address : CEN Cadarache,
13108 St. Paul-lez-Durance, France

I) Introduction

Dynamic response analysis provides an attractive method for studying transport mechanisms in tokamak plasmas. The analysis of the radial response has already been widely used for heat [1,2] and particle transport [3] studies. The frequency dependence of the dynamic response, which is often omitted, reveals further properties of the dominant transport mechanisms. Extended measurements of the soft X-ray emission were carried out on the TCA tokamak in order to determine the underlying transport processes.

II) Dynamic response analysis

The transport processes are investigated by sinusoidally modulating the gas valve opening or the Alfvén RF power amplitude and measuring the subsequent perturbation on the soft X-ray emission. The profiles are obtained from an Abel-inversion of the signals of a 15 channel pinhole camera. The experiments are carried out in the TCA tokamak ($R=0.61$ m, $a=0.18$ m, $I_p \leq 130$ kA, $B_\phi=1.51$ T, $n_e \leq 10^{20}$ m^{-3}) for a frequency range of 30 to 600 Hz, which roughly corresponds to the inverse particle confinement time. We thereafter express the dynamic response of the modulated signals by their relative amplitude and their phase with respect to the external perturbation.

III) Analysis of the soft X-ray emission

Previous results [4] show that both RF power and gas valve modulation lead to a similar response of the soft X-ray emission. Even if a fraction of the RF power is directly thermalised, the large density increase which is simultaneously induced dominates the observed dynamic response. This response is characterised by a discontinuity at mid-radius, fig. 1. A minimum in the phase profile indicates the presence of a local source from which the perturbation emanates. Operation at different plasma currents reveals that this effective source moves with the sawtooth inversion radius. The resulting perturbation displays a fast inward propagation due to sawtooth activity. The outward propagation is

however considerably delayed, which leads to a phase jump, fig. 1.

In order to determine the origin of the observed modulation of the soft X-ray flux, we consider the different parameters which compose it :

$$A = f(Z_{eff})\, n_e^2 T_e^{\alpha} \tag{3.1}$$

The function $f(Z_{eff})$ is roughly proportional to the impurity concentration and $\alpha = 2\text{–}8$ is the temperature exponent. For small perturbations, we obtain :

$$\frac{\tilde{A}}{A} = \frac{\tilde{f}}{f} + 2\frac{\tilde{n}_e}{n_e} + \alpha\frac{\tilde{T}_e}{T_e} \tag{3.2}$$

Measurements of the density profile show that gas valve and RF power modulation create an inward propagating density pulse. Inside the inversion radius, the density and the soft X-ray perturbations are synchronous, fig. 1. Since their relative amplitudes are in a ratio of 1:3, we conclude that a large fraction of the soft X-ray modulation can be attributed to the electron density. Outside the inversion radius however, the picture completely changes, in that both perturbations move in different directions and have a different amplitude ratio. A possible explanation would be that the soft X-ray response is due to either a heat pulse or an impurity flux. Experiments are being carried out in order to determine which effect predominates.

We conclude that the modulation of the soft X-ray emission profile inside the inversion radius can be ascribed to a density modulation, whereas impurity or heat modulation may dominate outside the radius. The perturbation emanating from the inversion radius would be triggered by a change in the density profile gradient.

IV) Transport model

In order to identify the dynamic response analysis to an underlying transport process, we consider two widely used transport models and calculate the resulting dynamic response. The modulated parameter $x(r,t)$ can either be the electron temperature, the density or the impurity concentration since all of these require similar transport equations.

Firstly, convection is taken to be the dominant process, with a spatially constant convective velocity

$$\frac{\partial x}{\partial t} = \frac{1}{r}\frac{\partial}{\partial r}\left(r^2 v \frac{x}{a}\right) + S \tag{4.1}$$

Using the Ansatz

$$x(r,t) = \bar{x}(r) + \tilde{x}(r)\, e^{-j\omega t} \tag{4.2}$$

a solution of the source-free interior of the plasma is obtained

$$\tilde{x}(r) = \frac{\tilde{x}_o}{r^2}\, e^{-\frac{j\omega a \log(r)}{v}} \tag{4.3}$$

The phase can then be expressed as

$$\angle\tilde{x} = \angle\tilde{x}_o - \frac{\omega a \log(r)}{v} \tag{4.4}$$

Such a linear frequency dependence is characteristic of a perturbation which propagates with a pure time delay.

Secondly, we consider a diffusive process

$$\frac{\partial x}{\partial t} = \frac{1}{r}\frac{\partial}{\partial r}\left(rD\frac{\partial x}{\partial r}\right) + S \qquad (4.5)$$

which has the homogeneous solution :

$$\tilde{x}(r) = \tilde{x}_o J_o(kr) \quad \text{with} \quad k = \sqrt{j\omega/D} \qquad (4.6)$$

In general the condition

$$kr >> 1 \qquad (4.7)$$

is satisfied, so that the phase can be approximated by

$$\angle\tilde{x} = \angle\tilde{x}_o + \sqrt{\omega r^2/2D} \qquad (4.8)$$

If a radial variation of the transport coefficients is included, the radial dependence in equations (4.4) and (4.8) changes but the frequency dependence is not affected. Hence a measurement of the phase at different frequencies allows to determine whether convection or diffusion is the dominant transport process. Although the amplitude spectrum can be used in a similar way, we omit it since it requires an absolute calibration.

V) Frequency dependence of the dynamic response

A plot of the soft X-ray emission phase versus the modulation frequency reveals a clear quadratic dependence, fig. 2. This dependence is most evident between 100 and 400 Hz. Below this range, condition (4.7) no more holds. The same dependence reappears when the phase reference is the flux at r=0.088m instead of the RF power. Using equation (4.8), a uniform diffusion coefficient can be obtained inside the inversion radius :

$$D = 1.23 \pm 0.2 \ m^2 s^{-1}$$

This value is about twice the global particle diffusion coefficient. We conclude that the response of the soft X-ray emission to density modulation is dominated by diffusive processes, both inside and outside the inversion radius.

The frequency dependence of the phase profile allows us to further characterise the transport mechanisms. The large phase shift observed just outside the inversion radius was first attributed to a local barrier similar to the thermal insulating layer observed on TFR at the q=1 surface [5]. If this phase shift were due to reduced transport coefficients, it would increase indefinitely with the modulation frequency. Instead, the observed shift saturates at a value below 180°, fig. 2, which is characteristic of a power dipole (source/sink term). This dipole can be explained by local change in the diffusion coefficient at the sawtooth inversion radius as confirmed by a 1-D simulation code. The strong link between this local modulation and the inversion radius suggests that the change in the transport is due to a modification of the sawtooth activity.

VI) Conclusion

Transport mechanisms have been investigated by measuring the dynamic response of tokamak ohmic plasmas to perturbations such as gas valve or RF power modulation. The observed response of the soft X-ray flux can be attributed to a perturbation which starts at the inversion radius and is triggered by a change in the

density profile gradient. Extended measurements of the frequency dependence reveal the dominant nature of diffusive processes and also show a discontinuity in the transport which is due to sawtooth activity.

References

1) Alikaev V. et al., Plasma Physics and Contr. Fusion **29** (1987) 1286.
2) Lebeau D., Koch R. et al., proc. 16th EPS conference, Venice 1989, **III**, 1061.
3) Gentle K.W. et al., Plasma Physics and Contr. Fusion **29** (1987) 1077.
4) Joye B. et al., Plasma Physics and Contr. Fusion **30** (1988) 743.
5) TFR group, Nuclear Fusion **26** (1986) 849.

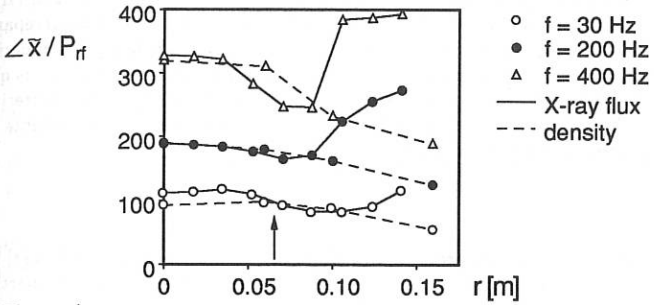

Figure 1
Phase profiles of the perturbed Soft X-ray emission and electron density during RF power modulation, as measured for different modulation frequencies at q(a)=3.1. The arrow indicates the position of the inversion radius. The profiles are symmetric with respect to the centre of the plasma.

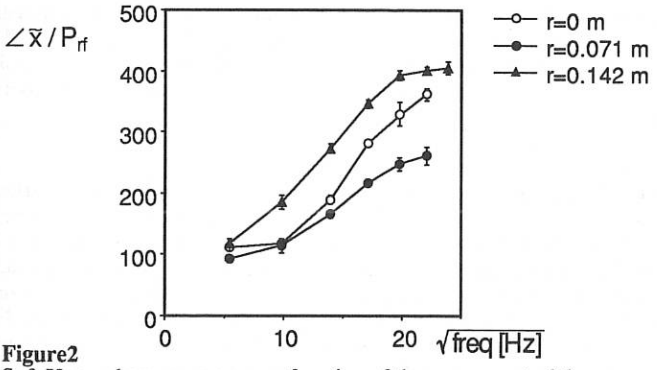

Figure2
Soft X-ray phase response as a function of the square root of the modulation frequency, taken at three radial positions : in the centre, at the inversion radius, and near the plasma edge.

HEAT AND DENSITY PULSE PROPAGATION IN ASDEX

L. Giannone, K. Riedel, U. Stroth, A. Eberhagen, O. Gruber, V. Mertens
and the ASDEX team

Max-Planck-Institut für Plasmaphysik,
EURATOM-IPP Association D-8046 Garching, FRG

1. INTRODUCTION

Experimental measurements of the electron thermal conductivity, derived from the radial propagation of the heat pulse generated by a sawtooth crash, have consistently yielded larger values than those obtained by power balance [1,2]. It has been proposed that this discrepancy could be the result of the coupling of density and temperature perturbations [3]. Numerical modelling of heat and density pulse propagation on ASDEX has been used to address this question. In addition, measurements at various electron densities and in hydrogen and deuterium were undertaken, with the aim of providing a broad base of experimental measurements for testing the various transport models proposed.

2. THEORY

The numerical solution of heat pulse propagation as a forced boundary value problem [4] has been extended to incorporate density and particle flux perturbations. The energy and particle conservation equations [5], with the retention of all terms and including the terms necessary to describe the energy exchange between ions and electrons and Ohmic heating, were linearised. The simplest case of a particle flux in the form :

$$\Gamma = -D\frac{\partial n}{\partial x} - Vn \tag{1}$$

was considered, where D is the particle diffusion coefficient and V is the inwards particle drift velocity. In this case the electron density and temperature perturbations are not coupled by the off-diagonal components of the transport matrix. The equilibrium values of D and V are determined from the zero order particle flux. This flux is calculated from the particle conservation equation :

$$\frac{\partial n}{\partial t} + \nabla \cdot \Gamma = S_e \tag{2}$$

where Γ is the particle flux and S_e is the particle source and sink term due to the ionisation of neutral particles and recombination. The neutral particle density profile needed to determine the ionisation source term is calculated by the AURORA code. Transport modelling on ASDEX shows that $D = 0.2\chi_e^{PB}$ gives good agreement with experimental results [6]. In this way a radial profile of D and V consistent with the zero order particle flux may be calculated. Linearisation of this equation allows the electron density pulse generated by the sawtooth crash to be modelled. Work is in progress to treat the case in which the particle and heat fluxes are functions of both the electron density and temperature gradients.

3. EXPERIMENTAL RESULTS

The local electron temperature is measured at four radial positions outside the mixing radius and sampled at 20 kHz to provide sufficient time resolution of the sawtooth crash. Boxcar averaging of the temperature perturbation generated by the sawtooth crash permits the electron thermal conductivity, χ_e, to be determined by fitting the measured temperature perturbation at each radius to that calculated, with the first channel outside the mixing radius being used as the time dependent boundary condition. Conventional heat pulse analysis uses the radial decay of the heat pulse amplitude and the time of arrival of the peak of the heat pulse at each radius to calculate a value of χ_e.

As a first approximation it is usually assumed that the associated density pulse may be neglected. In this case, analysis of Ohmic discharges with I_p = 320 kA and B_o = 2.17 T (q(a) = 3.3) yields values in deuterium of $\chi_e = 6\pm1\mathrm{m}^2/\mathrm{s}$ at $\bar{n}_e = 1\mathrm{x}10^{19}\mathrm{m}^{-3}$ and $\chi_e = 4\pm1\mathrm{m}^2/\mathrm{s}$ at $\bar{n}_e = 2\mathrm{x}10^{19}\mathrm{m}^{-3}$ (see Fig. 1). The corresponding energy confinement times are 40ms and 69ms respectively. Decreasing sawtooth amplitude with increasing density limits the analysis at higher densities. As in previous experiments, the value of χ_e obtained by heat pulse propagation analysis is consistently a factor of 3 higher than that obtained by power balance.

In hydrogen at $\bar{n}_e = 2\mathrm{x}10^{19}\mathrm{m}^{-3}$ it found that $\chi_e = 4\pm1\mathrm{m}^2/\mathrm{s}$. The limits of experimental accuracy do not allow definite conclusions on the isotope dependence of χ_e at a radial position from 20cm to 30cm (minor radius = 40cm) to be drawn. Given that the energy confinement time in deuterium is about 20 per cent higher than in hydrogen at this density [7], it is clear that an improvement in experimental sensitivity is needed in order that a difference of this order of magnitude in χ_e can be measured.

Experimentally the relative amplitude of the density perturbation in these Ohmic discharges on ASDEX is observed to be considerably smaller than the relative amplitude of the temperature perturbation. However measurements on TEXT at lower q(a) indicate that the density perturbation can be of the same order of magnitude as the temperature perturbation [8]. Furthermore, the diffusion coefficient from density pulse propagation measurements in this experiment was found to be a factor of 3 larger than the value calculated from equilibrium conditions. Even with this assumption and a relative perturbation value of $\delta n/n = 0.2\ \delta T/T$, which is greater than the value experimentally observed for the relevant discharge conditions on ADSEX, it is found that the enhanced heat flux due to a finite density perturbation does not significantly reduce the value of χ_e found by heat pulse propagation analysis. At most this results in a decrease of 20 per cent in the inferred value of χ_e.

The case in which the temperature and density perturbations are coupled by the off-diagonal terms of the transport matrix remains to be investigated. The inclusion of terms describing the plasma parameter dependence of the transport coefficients [1,2,9] is another area that may be studied in detail with numerical modelling. Based on the present results, it would seem that the experimentally observed enhancement of microturbulence during a sawtooth pulse [8] may be directly responsible for the larger values of χ_e and D found in heat and density pulse propagation experiments. A considerable increase in the level of heat transport induced by density perturbations would be necessary, in order that the coupling of temperature and density perturbations alone could be claimed as the reason for the difference between the equilibrium values and those measured using heat and density pulse propagation analysis.

4. CONCLUSION

Numerical solution of the linearised energy and particle conservation equations allow heat and density pulse propagation in ASDEX to be studied. It has been demonstrated that the enhanced values of χ_e found in typical Ohmic conditions on ASDEX are not able to be explained by the contribution of finite density perturbations when the standard description of the particle flux in in terms of a diffusion coefficient and inwards drift velocity is used. A stronger density perturbation than that modelled is necessary to support the contrary theoretical predictions. Should this conclusion also hold after investigation of a coupled density and temperature perturbation, then this would leave the enhancement of χ_e by microturbulent fluctuations as the strongest candidate for explaining the discrepancy between equilibrium values and the values of D and χ_e measured in density and heat pulse experiments.

References

[1] TUBBING, B., LOPES CARDOZO, N., and VAN DER WIEL, M., Nucl. Fusion **27** (1987) 1843.

[2] FREDERICKSON, E. et al., Nucl. Fusion **26** (1986) 849.

[3] BISHOP, C. and CONNOR, J., Heat pulse propagation and the role of density perturbations, Technical Report CLM P873, Culham Laboratory, 1989.

[4] RIEDEL, K. et al., Nucl. Fusion **28** (1988) 1503.

[5] DUCHS, D., 3/2 or 5/2 for convective thermal transport?, Technical Report JET R(89)13, JET Laboratory, 1989.

[6] BECKER, G., Nucl. Fusion **27** (1987) 11.

[7] WAGNER, F. et al., 16th European Conference on Controlled Fusion and Plasma Physics (Venice) **I** (1989) 195.

[8] KIM, S., BROWER, D., PEEBLES, W., and LUHMANN JR., N., Phys. Rev. Lett. **60** (1988) 577.

[9] GENTLE, K. et al., Phys. Fluids **31** (1988) 1105.

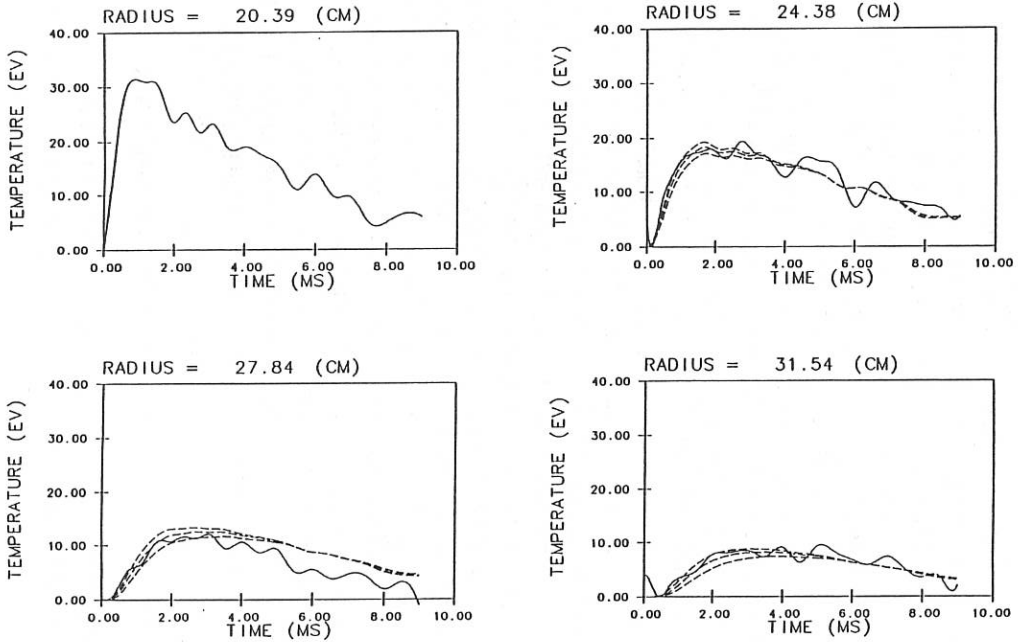

Fig. 1. The ECE measurements of the perturbed electron temperature after a sawtooth crash as a function of radius (solid lines) and the numerical solution of the linearised energy conservation equation (dashed lines) are shown for the Ohmic discharge with $I_p = 320$ kA and $\bar{n}_e = 2 \times 10^{19}$ m^{-3}. A best fit with $\chi_e = 4 +/- 1$ m^2/s is found.

STUDY OF THE ELECTRON HEAT PULSE PROPAGATION FROM ECRH ON T-10

Bagdasarov A.A.,Borshegovskii A.A.,Vasin N.L.,Elisavetin A.A., Neudatchin S.V.,Polevoj A.R.,Roy I.N.,Savrukhin P.V.

I.V.Kurchatov Institute of Atomic Energy ,Moscow,USSR

Introduction

Two reports are united in this paper .The heat pulse propagation (HPP) was studied on T-10 and it had been shown earier in/ 1/ that normal ($\chi_e^{HP} \simeq \chi_e^B$) as well as enhanced ($\chi_e^{HP} >> \chi_e^B$) HPP velocity from ECRH and sawteeth oscillations depending on the regime are observed.It is shown in [2] that under central ECRH in the regimes with high values of $q_1 \simeq 6$ ($\chi_e^{HP} >> \chi_e^B$) in the whole column gradient zone. On the contrary, under central ECRH on the background of the long-time non-central heating the conDuctivity decreases ($\chi_e^{HP} < \chi_e^B$) on the heat wave front. In this case the heat wave sharpens the broad $T_e(r)$ profile created by the non-central ECRH.The influence of the local value $\nabla T_e/T_e$ on the value χ_e^{HP} is observed. The new data on HPP at T-10 are presented below.

STUDY OF HPP FROM ECRH at T-10

HPP under central ECRH at the Ohmic background was studied in two regimes:I_p=200 kA,B_t=3.0 T,$\bar{n}$ =2.0 and $3 \cdot 10^{13} cm^{-3}$,a_L=28 cm, q_L=3.8,P^*_{ECRH}=400 kW The values $\tilde{T}_e^{exp}(r,t)$ measured on the radiation on the second ECR harmonic are shown in Fig.1.($\bar{n}$=3). The curves 1,2,3 -are the experiment under r=14.1,16,19.4cm. The edge of the ECR-power absorbtion zone is located under r=12-13 cm, the resonance under r=2 cm. When the ECRH is switched ON the amplitude as well as the saw-teeth oscillations zone width increase. The method [3] was used to define the value χ_e^{HP}. Let us note, that the basis of this method is the numerical solution of the conductivity equation for $\tilde{T}_e(r,t)$ in the zone $r_1 < r < r_3$ located outside the perturbations source zone.The experimental values $\tilde{T}_e^{exp}(r_1,t))$ were used as boundary conditions and χ_e^{HP} was defined by the choice of value χ_e^{HP} up to the obtaining of the minimal calculation deviation from the experiment in the point

r_2. One can use $r_3=a_L(\tilde{T}_e(a_L,t)=0)$; $r_3=0$ $(\partial\tilde{T}_e(0,t)/\partial r=0)$, or any r_3 $(\tilde{T}_e(r_3,t)=\tilde{T}_e^{exp}(0,t))$ as another boundary condition. The experimental data processing is given in TABLE, where t - time from the ECRH beginning. The results of the regime I_p=200 kA B_t=3.0T, $\bar{n}=2.8\cdot10^{13}cm^{-3}$, a_L=34 cm, q_L=5.8, P^*_{ECRH}=400 kW processing as well as the central ECRH, calculated with due regard to the real experimental density profile are also given in TABLE. It is shown on the TABLE that the value χ_e^{HP} increases significantly under the transfer from the zone r<16(19, a_L=34) to the zone r>16cm(19 for a_L=34) In the zone r<16(19) $\chi_e^{HP}\approx2\cdot\chi_e^{B}$ $_{OH}$ and depends weakly on the value γ($\chi_e^{HP}\sim r^{\gamma}$). In all the calculations the value $\tilde{T}_e^{calc}(r_2,t)$ corresponds to $\tilde{T}_e^{exp}(r_2,t,)$.

comments	$r_{1,2,3}$ cm	$\chi_e^{HP}(r_1)m^2s^{-1}\sim r^{\gamma}$	γ	t ms	χ_e^B
T-10	14.1,16,28	0.38(0.4-0.5)	0	11	0.18
A_L=28 cm		0.4	0	8	
		0.4	1	11	
I_p=200 kA		0.42	2	11	
$\bar{n}$=3	16,19.4,28	1.1	0	11	0.21
		1.3	0	8	
$\bar{n}$=2	14.3,16.3,28	0.5(0.4-0.6)	0	10	0.24
-''-		0.5	0	8	
		.52	1	10	
	16.3,19.7,28	1(0.8-1.3)	0	10	
		1.1	0	8	
$\bar{n}$=2.8	15.3,18.7,34	0.58(0.5-0.7)	0	20	0.17
A_L=34cm		0.68	0	15	
		0.7	1	15	
I_p=200 kA	18.7,22.4,34	1(0.8-1.3)	0	15	0.28
JET, H-mode	$r_{1,2,3}/a$	$\chi_e^{HP}(r_2)$			
P_{NBI}=8 MW	0.42,0.35,0.0	1.7(1.2-2.8)	0	99	.6
$\bar{n}$=5		1.6	0	75	
$T_e(0)=T_i(0)$		1.4	1	99	
		1.2	2	99	
=5 keV	0.49,0.35,0.0	2.8	0	99	.6
		1.7	2	99	
Ref /4/	0.55,0.35,0.0	5(4-6.5)	0	99	.6

The numerical values of $\tilde{T}_e(r_{1,2}$=16,19.4 cm,t) under χ_e^{HP}(14<r<28) =0.5 m^2s^{-1} are shown by the curves 2*,3* in Fig.1. One can see that velocity of HPP at 14<r16 is greater than that in the

experiment. In the zone 16<r<19.4 it is less than that in the experiment.Though the numerical deviation from the experiment is insignificant we obtain the same result in two other regimes.

The inward HPP from the non-central ECRH with $P^* \approx$ 400 kW on the background of the non-central ECRH $P^* \approx$ 400 kW was studied. The inner ECR-power absorption zone edge was placed at r~5 cm, and detail study it is needed for HPP analusis at r>5cm.For the r =2.5cm,0 $\chi^{HP} \approx 0.2\ m^2 s^{-1}$

SIMULATION OF HPP FROM PELLET INJECTION ON JET H-MODE /4/ Curves 1,2,3-the experimental values of $\tilde{T}_e(r_{1,2,3}/a=0.49,0.42,0.35,t)$ are shown in Fig.2.(the experiment under 0.49 and 0.55 factually coincides). The curves 1',2',3'- simulation under 0.49,0.42,0.35,boundary conditions-$\tilde{T}_e^{exp}(0.55a,t)$,$\chi_e^{HP}=5\ m^2 s^{-1}$ $2^*,3^*$-calculation at 0.42,0.35 with boundary at 0.49a, $\chi_e^{HP}=1.7(r/0.35a)^2\ m^2 s^{-1}$ It is seen from the TABLE and Fig.2.that the value χ_e^{HP} depends strongly from r By means of the transport code ASTRA-NB [5] the value $\chi_{eNBI}^{B} \approx 0.6\ m^2 s^{-1}$ was defined.It was shown also,that at t<100ms,r<.49a, $\tilde{Q}_e=Q_e^0((T_e^0/(T_e^0+\tilde{T}_e))^{1.5}-1)$ influence on HPP is insignificant

DISCUSSION AND CONCLUSIONS

a) T-10 In the regimes with central ECRH ,q_L=3.8-5.8 the HPP velocity is enhanced.There is no strong dependence of the value $\chi_e^{HP} - \chi_{e\ OH}^{B}$. on n,and this value tends to be proportional to q_L. A strong dependence of χ_e^{HP} on r seems unclear to us. This may be connected with the fact that the zone 16<r<19cm(18-22,a_L=34)is the end of the gradient zone and the beginning of the periphery one. The q=2 surface is usually located here.The physics as well as the functional dependence χ_e^B in these zones can be different.

b).JET HPP.We cannot agree with the authors [4] who say that the value $\chi_e^{HP}=3\pm0.5\ m^2 s^{-1} \approx \chi_e^B$ .We suppose that χ_e^{HP} changes significantly along the r(1.7 to 4 at r/a=0.35;.49).The value χ_e^B=0.6 (0.4-0.8) ≈const(r)in this regime .Therefore the increased HPP velocity is observed under pellet injection in H-mode

We lack the database from JET and this causes some uncertainties in our understanding of the problem.

FIG 1 Central ECRH, $\bar{n}=3.10^{13}$, I=200 kA, A_L =28 cm
Combined HPP from ECRH and sawteeth on T-10

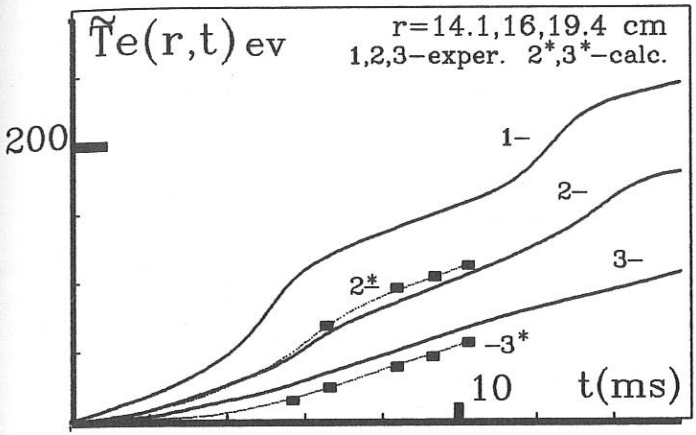

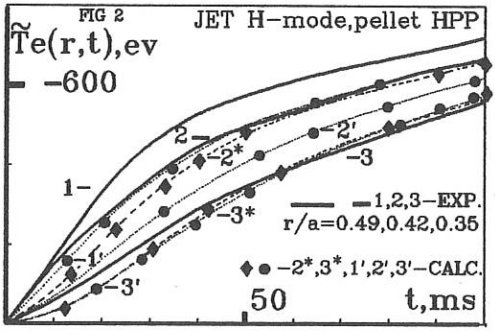

REFERENCES

1 Bagdasarov A.A.,Vasin N.L.,Esipchuk Y.V.,Neudatchin S.V., et. al.,Fizika Plasmy,1987,v.13,p.899

2 Bagdasarov A.A.,Vasin N.L.,Neudatchin S.V.,Savruchin P.V. In:ECE and ECRH Joint Workshop,Hefei,China,1989

3 Neudatchin S. V. In 15th Eur.Conf. on Cont. Fus. and Plasma Heating,1988,Dubrovnik,v.3 ,p.1147

4 Cheetham A.D.,et al.In-12th Int.Conf. on Pl.Ph. and Cont. Nucl. Fus. Res. Nice,1988,IAEA-CN-50/I-2-2

5 Polevoy A.R.,Sharapov S.E. ITER-IL-Ph-6-9-S

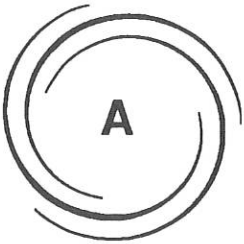

TOKAMAKS

A4 FLUCTUATIONS

DIMENSIONALITY ANALYSIS OF CHAOTIC DENSITY FLUCTUATIONS IN TOKAMAKS

A.M. van den Brink, G.J.J. Remkes, F.C. Schüller and A.C.C. Sips*

FOM-Instituut voor Plasma Fysica Rijnhuizen

Association EURATOM-FOM , P.O. BOX 1207, 3430 BE Nieuwegein, The Netherlands

*Present adress: JET Joint Undertaking, Abingdon, Oxfordshire, United Kingdom

1. Introduction

Anomalous transport in tokamak plasmas is thought to be caused by turbulence. Density fluctuations detected with collective scattering or reflectometry indeed revealed the existence of a broad-band turbulence with $\Delta f/f \approx \Delta k_\perp/k_\perp \approx 1$. The underlying physics mechanisms are difficult to determine because the pertinent equations are highly nonlinear and bound to lead to deterministic chaos as observed. Quasi-linear approximations to the equations yield the limits for the onset of various instability types like drift waves, microtearing, etc, and their typical frequencies and wavelengths at the onset. However, in the experiments the instabilities have grown to a full turbulence at a saturation level which is so high that the various quasi-linear approximations have become invalid. Many plasma quantities in theory assumed to be constant are in reality dragged into fluctuating behaviour, thereby influencing the saturation level, the frequency and wavelength spectra.

Notwithstanding the chaotic nature of the plasma transport one can still try to investigate which plasma quantities are involved in the turbulence, which of those are driving the turbulence and which are damping. The theory of deterministic chaos gives some tools for this. The fractal dimension of the attractor yields the lower bound to the number of fluctuating quantities. The sign of the Lyapunov exponents indicates the driving-damping nature of these quantities, whilst the Kolmogorov entropy being the sum of the positive Lyapunov exponents indicates the strength of the driving terms. In a long term programme one could try to identify which plasma quantities belong to which Lyapunov exponents. In this contribution only the issue of the dimensionality of the attractor will be addressed following the method of Grassberger et al. [1].

2. Previous results

This analysis has been tried before [2,3,4,5], in our view not on the most suitable signals. These authors have analysed the fluctuating poloidal field signals measured by Mirnov coils outside the plasma. However, the sensitivity of the coils falls with $x^{(m-1)}$ in which x is the distance between coil and source and m the polodial mode number. This signal is therefore only relevant for edge turbulence or low m MHD-modes. Low values of the correlation dimension ν were reported (DITE: *2.1* [2]; TOSCA: *2.4* [3]; JET: *2.4-4.* [4]; ASDEX: *2.3-3.7* [5]). In TOSCA edge Langmuir probe signals have been used [4] which is also only relevant for edge turbulence. In ASDEX one has also tried SXR-signals which have the disadvantage of being a signal integrated along the line-of-sight. The author had therefore to report split dimensionalities indicating two independent turbulent phenomena taking place on different plasma radii.

3. Experimental signals

In this paper the analysis of localized density fluctuations will be presented, obtained by two different methods at two totally different tokamaks:

a. Collective scattering of 2 mm waves measured density fluctuations in the small ohmic TORTUR tokamak (R=0.46 m; a=0.08 m; B_T=2.9 T; I_p=40 kA). The measurements analysed were taken at the centre; r/a = 0 and 800<k <1200 m^{-1}.

b. Reflectometer data gave the fluctuating position of six reflecting density surfaces in JET X-point H-mode plasmas at medium (#19662) or high beta (#20877); all positions were in the outer 30% of the minor radius.

All signals indicated a truly chaotic broad-band turbulence with $\Delta f/f \approx 1$ and a positive Kolmogorov entropy. All selected signals were recorded with sampling frequencies at least a factor 10 higher than the frequency with highest amplitude in the spectrum. Normally 8192 samples were used. For the TORTUR data 2048 samples showed a better convergence than 8192 probably because slow relaxation of the plasma profiles occurred during the full 4 ms time window (note that τ_E = 3 ms!). In order to prove that the analysis method gave the same results as the work quoted above, also Mirnov coils signals from TORTUR were analysed. The result ν=3.5 (see Table 1) is indeed in good agreement.

4. Computational techniques

One way of estimating the fractal dimension D is by box counting algorithms (Hausdorff dimension). This involves covering the phase space with a mesh of cells. It turns out that this method is very unsatisfactory whenever D>2. Another possible method has been reported by Grassberger et al. [1]. A phase space is constructed by a set of *d*-dimensional vectors $\{\vec{\xi}_i\}$ with $\vec{\xi}_i = \{x(i), x(i+\tau),.., x(i+(d-1)\tau)\}$ with x(i) the sampled data points and τ a delay time. The embedding *d* is chosen high enough such that the phase space embeds the attractor. The distribution of trajectory points on the attractor can then be characterized by a correlation integral $C^d(r)$, the number of pairs of trajectory points whose Euclidean distance is less than a correlation length r: $C^d(r) = 1/N^2 \, \Sigma_i \Sigma_j \, \Theta \, (r - \| \vec{\xi}_i - \vec{\xi}_j \|)$. Here Θ is the Heaviside function and N the total amount of vectors $\vec{\xi}$. For a variety of attractors the correlation integral $C^d(r)$ displays a power law in the limit for $r \to 0$, $N \to \infty$ and $d \to \infty$: $C^d(r) \propto r^{\nu}.\exp(-K_c.\tau.d)$ and:

$$\mathrm{Ln}[C^d(r)] = \nu \, \mathrm{Ln}[r] - K_c.\tau.d \qquad (1)$$

Here ν is the correlation dimension and K_c the correlation entropy. So, when the number of counted trajectory pointswithin a small correlation length r is large enough, the slope of a curve $\mathrm{Ln}[C^d(r)]$ versus Ln[r] will, with increasing embedding factor *d*, converge to the dimension ν. The mutual spread in the correlation curves will converge to the entropy K_c. In the case of pure white noise, no convergence will appear and the dimension ν will proportionally increase with *d*. Both the Hausdorff dimension D_0 as well as the correlation dimension $\nu=D_2$ are part of a set generalized dimensions $\{D_q\}$ [6] for which one has: $D_0 \geq D_2$. The correlation entropy K_c acts as a lower bound for the Kolmogorov entropy K: $K \geq K_c$. Furthermore, since K>0 is a necessary condition for chaos, K_c>0 is a sufficient condition for chaos.

Assuming that there exists for $C^d(r)$ a power law according to (1), ν and K_c can be extracted at any length r as a function of the embedding *d*, by fitting a short curve $y=\alpha.x+\beta$ onto $Ln[C^d(r)]$ versus Ln[r] at position r. This curve fitting is done with a simple least squares method, in which the number of fit points can be taken arbitrarily. This method will thus yield dimensions $\nu^d(r)$ and entropies $K_c^d(r)$ as a function of embedding *d* and correlation length r. The observed dimension ν is then taken as the *d*-averaged dimensions $\nu^d(r)$ at the smallest convergence length r_c where the variance in the $\nu^d(r)$ values is minimum and, secondly, where the number of counted trajectory points is still above a set value; in this case >100. The entropy K_c is taken as the averaged spread of the correlation curves $K_c = (1/\tau).<Ln[C^d(r)]-Ln[C^{d+1}(r)]>$ at $r=r_c$. For the Lorentz attractor [7] (parameters r=28, σ=10 and b=8/3) which we have simulated with 32000 points, differential step 0.025, a phase space was constructed with delay time τ=1. With this set we obtained $\nu = 2.06 \pm 0.01$ and $K_c = 0.6 \pm 0.2$.

5. Results

In all analyses a delay time τ=1 and embeddings *d* ranging from 13 to 18 are used. The results are given in Table 1 and Figure 1. The following remarks should be made:

1. All locally measured density fluctuations showed a surprisingly high correlation dimension ν indicating that more plasma quantities play a role in the turbulence than often is assumed.
2. There is not much difference in ν between the small TORTUR tokamak and JET, suggesting a universal type of turbulence in tokamaks. The correlation entropy K_c is significantly smaller in the ohmic TORTUR plasma.
3. The convergence is excellent as can be seen from the very low σ_ν values. This suggests that the difference in ν between the various reflectometer signals at different radii is significant.

TABLE 1: *Mean correlation dimension ν and entropy K_c with the standard deviations σ_ν and σ_K in percentage respectively for TORTUR collective scattering, Mirnov coil data and JET H-mode medium and high beta reflectometer data from six reflecting density surfaces ($10^{19}m^{-3}$)*

TORTUR coll.scatt.	ν	σ_ν	K_c (%)	σ_K (%)	TORTUR Mirnov coil	ν	σ_ν (%)	K_c	σ_K (%)
	6.7	1.1	0.4	2.5		3.5	1.2	0.7	15.
JET n_{crit} medium β	ν	σ_ν (%)	K_c	σ_K (%)	JET high β	ν	σ_ν (%)	K_c (%)	σ_K
0.73	7.8*	-	-	-		5.0	1.5	0.8	15.
1.06	6.2	0.9	0.6	13.		6.6	0.8	0.9	15.
1.94	6.5	1.8	0.8	15.		9.3*	-	-	-
2.53	5.8	1.0	0.8	17.		8.6*	-	-	-
3.14	8.3*	-	-	-		5.7	1.2	0.6	23.
4.05	8.2*	-	-	-		5.8	1.4	0.6	23.

* See remark 5.

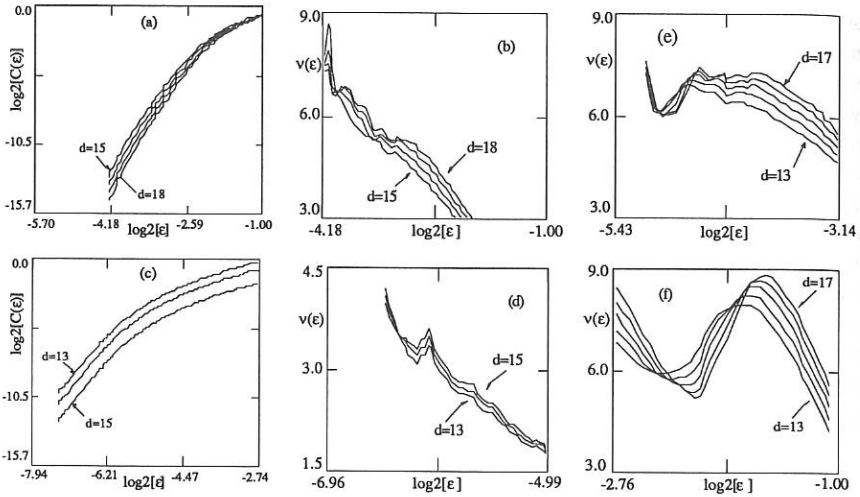

FIGURE 1: *Correlation integrals log2[C(ε)] and correlation dimensions ν(ε) for different embeddings d versus log2[ε] for (a-b) TORTUR collective scattering, (c-d) TORTUR Mirnov coil and (e) JET H-mode and (f) high β reflectometer data at reflecting density surfaces 1.06 and 4.05 10^{19} m^{-3} respectively. Parameter ε represents the correlation length r as a fraction of the maximum signal amplitude r_0: $\varepsilon = r/r_0$.*

4. The influence of high beta on the turbulence is not noticeable notwithstanding the occurrence of a ELM in the middle of the time-window.
5. The lowest trustworthy embedding d should be at least $2\nu+1$; moreover one needs at least 3 embeddings fulfilling this condition, in order to determine ν, σ_ν and K_c. Since CPU limitations prevented $d > 18$, values of $\nu > 7.5$ marked with * in Table 1 could not be regarded as reliable.

6. Acknowledgements

The authors gratefully acknowledge the collaboration with the group of Dr. A. Costley at JET in obtaining the reflectometer data under task agrement between JET and FOM-Rijnhuizen. Furthermore, the suggestions on calculus procedures by Dr. R.W. Leven proved to be of great value [7]. This work was performed under the EURATOM-FOM association agreement with financial support from NWO and EURATOM.

References

[1] P. Grassberger and I. Procaccia, Phys. Rev. Lett. **50**, 346 (1983).
[2] S.J. Gee and J.B. Taylor, 12th Eur. Conf. on Contr. Fusion and Plasma Physics, Budapest, Vol. **2**, 446 (1985).
[3] A. Coté et al., ibid, 450 (1985).
[4] W. Arter and D.N. Edwards, ibid, 442 (1985).
[5] L. Battiston, ASDEX-Team, 13th Eur. Conf. on Contr. Fusion and Plasma Physics, Schliersee, Vol. **1**, 81 (1986).
[6] H.G. Schuster, *Deterministic Chaos*, VCH Verlagsgesellschaft, Weinhein, (1989).
[7] B. Albrecht et al., 19th ICPIG, Belgrade (1989).

DENSITY FLUCTUATION MEASUREMENTS VIA REFLECTOMETRY ON DIII–D DURING L– AND H–MODE OPERATION*

E.J. Doyle, T. Lehecka, N.C. Luhmann, Jr., W.A. Peebles, and R. Philipona

Institute of Plasma and Fusion Research, UCLA, CA 90024, U.S.A.

K.H. Burrell, T.N. Carlstrom, R.J. Groebner, H. Matsumoto,† T.H. Osborne, and the DIII–D Group

General Atomics, San Diego, CA 92138 U.S.A.

The unique ability of reflectometers to provide radial density fluctuation measurements with high spatial resolution (of the order of $\leq$ centimeters, Ref. 1), is ideally suited to the study of the edge plasma modifications associated with H–mode operation. Consequently, attention has been focused on the study of these phenomena since an improved understanding of the physics of H–mode plasmas is essential if a predictive capability for machine performance is to be developed. In addition, DIII–D is ideally suited for such studies since it is a major device noted for its robust H–mode operation and excellent basic plasma profile diagnostic information.

The reflectometer system normally used for fluctuation studies is an O–mode, homodyne, system utilizing 7 discrete channels spanning 15–75 GHz, with corresponding critical densities of 2.8×10^{18} to 7×10^{19} m^{-3}.[2,3,4] The Gunn diode sources in this system are only narrowly tunable in frequency, so the critical densities are essentially fixed. An X–mode system,[5] utilizing a frequency tunable BWO source, has also been used to obtain fluctuation data, and in particular, to "fill in the gaps" between the discrete O–mode channels.

L-H TRANSITION

Several previous scattering experiments in a variety of tokamaks have shown that the relative density fluctuation level decreases during H–mode operation.[6,7,8] However, the improved spatial localization associated with reflectometry can yield significant further information: An invariable observation with the reflectometer system at all L-H transitions is that high frequency ($\geq$50 kHz) density fluctuations are dramatically suppressed in a *localized region* near the edge of the plasma. This region extends from the scrapeoff layer inwards to $\approx$5 cm past the separatrix. In addition, as illustrated in Fig. 1, this suppression typically occurs on a fast timescale of $\approx$100 μs, commencing at a time coincident with the first observable change in the D_α emission. Within the edge suppression zone, the fluctuation changes are observed to occur simultaneously on all channels, to within $\leq$100 μs, though there is some evidence for variation within this timescale. Also, on isolated occasions, for reasons which are not at present understood, the fluctuation suppression has taken as long as $\approx$0.5 ms.

That the suppression zone is localized to the vicinity of the separatrix is demonstrated by the fact that higher density channels, reflecting from deeper into the plasma, show no change at the transition itself. This behaviour is illustrated in Fig. 2,

* This work was sponsored by General Atomics Subcontract SC120536 under U.S. Department of Energy under Contract No. DE-AC03-89ER51114.

† Japan Atomic Energy Research Institute.

which shows the time evolution of the integrated power in a frequency band from 75–400 kHz for several of the reflectometer channels during a discharge with a "dithering" transition, along with a D_α photodiode signal. This form of representation is chosen so as to clearly show the timescale for the suppression of wideband high frequency fluctuations; lower frequencies are excluded as they are not always reduced at the transition, and also because any changes which do occur are constrained to happen on a longer timescale, due to the lower frequencies involved. The suppression of the fluctuations, and the bifurcated nature of the L to H transition, are clearly displayed by the rapid modulation of the fluctuation signal on the lower density channels during the dithers. By contrast, the innermost channel illustrated (2×10^{19} m^{-3}), shows no variation at the transition. The fluctuation level on this channel does decrease later in time as the plasma density rises and the profile evolves, such that this density layer moves outward, towards the fluctuation suppression zone. In Figs. 3a and 3b, the time evolution of the spectra for the 1.3×10^{19} and 2.0×10^{19} m^{-3} density channels, respectively, are plotted for the same discharge as shown in Fig. 2. The very rapid suppression of the fluctuations at the transition is clearly shown on the lower density channel, whereas the later change on the higher density channel can be seen to take significantly longer, $\approx$5 ms. Again, this difference is due to the fact the higher density channel is changing due to the density profile evolution after the transition.

With data such as these, and knowledge of the density profile from the Thomson scattering and broadband reflectometer systems, the depth of the region in which the fluctuations are suppressed has been estimated. The edge fluctuation suppression zone extends in past the separatrix $\approx$5 cm, or $\approx$2–9 poloidal ion gyroradii.[9] Thus, the experimental data are in rough agreement with recent L-H transition theories,[10,11] in both the measured depth of the suppression zone, and the timescale. However, the error bars on the depth estimates are quite large because of the uncertainty associated with the discrete number of reflectometer channels. Recently, the X–mode system has been utilized to improve the accuracy of these estimates by "filling in the gaps" between the narrowband channels, and thus more precisely determine the inner edge of the suppression zone. As the X–mode reflection layer is moved inwards, it is observed to agree in both time evolution and spectral width with successive fixed frequency channels. Data obtained utilizing this technique will be presented at the conference.

ELM ACTIVITY

The behaviour of the density fluctuations during ELM activity presents a considerably more complex picture than that for the L-H transition. This is mainly due to the wide variety encountered in the amplitude, frequency, and type of ELM. However, with all ELMs, the fluctuations are observed to return to L–mode like conditions in amplitude and width in frequency space. Again, this occurs on a fast timescale, typically $\leq$300 μs, supporting the hypothesis that an ELM is a transient reverse bifurcation to L–mode. However, in contradistinction to the L-H mode transition, the fluctuations have frequently been observed to change *before* any observable change in the D_α emission. Also, there have been many occasions when the fluctuations are observed to change on the inner channels first, with the change moving outward towards the separatrix as a function of time.

Such ELM precursors have been observed on both ideal and resistive timescales and are of two distinct types. A "quasi-coherent" mode of $\approx$50 to 120 kHz is sometimes seen before giant ELMs on timescales ranging up to 30 ms before the ELM is triggered. An example of this is shown in Fig. 4, where bursts of a quasi-coherent mode, increasing in amplitude, can be seen to precede a giant ELM. The increase in

the amplitude and width of the broadband turbulence at the ELM itself is also apparent. These fluctuations appear similar in many respects to those reported in Ref. 12, except that on DIII–D they seem to be associated only with giant ELMs, whereas on PDX they were reported as occuring continuously during the H–mode. The other form of precursor activity is a general rise in the overall broadband fluctuation amplitude and spectral width, on timescales of from 100 μs to several milliseconds before the ELM. An example of this is shown in Fig. 5, where an increase in the broadband turbulence level before the ELM can be clearly seen.

SUMMARY

The results presented above for the spatial localization and timescale associated with the L-H transition, as well as ELM precursor activity, confirm the unique capabilities of multichannel reflectometry in providing a spatially localized measurement of internal density fluctuations. In addition, the data adds considerably to the overall understanding of the physics of H–mode operation,[9] and is in qualitative agreement with recent theories. It is intended to further utilize the spatial localization of these reflectometer measurements through the addition of a correlation reflectometer system to directly measure the radial correlation length of the fluctuations. It is hoped to have preliminary data from this system by the time of the EPS conference.

REFERENCES

1. TFR Group, Plasma Physics and Contr. Fusion **27**, (1985), 1299.
2. Peebles, W.A., et al., Proceedings of the Fourth International Symposium on Laser Aided Diagnostics, Fukuoka, Japan, Nov. 1989, pp. 40-67.
3. Lehecka, T., et al., Proceedings of the Sixteenth European Conference on Controlled Fusion and Plasma Physics, Venice, March 1989, Vol. 1, p. 128.
4. Lehecka, T., et al., Rev. Sci. Inst. **59**, (1988) 1620.
5. Doyle, E.J., et al.,"X–Mode Broadband Reflectometric Density Profile Measurements on DIII–D," this conference.
6. Crowley, T., and Mazzucato, E., Nucl. Fusion **25**, (1985) 507.
7. Asdex Team, Nucl. Fusion **29**, (1989) 1959.
8. Philipona, R., et al.,"Microturbulence Studies on DIII–D via Far Infrared Heterodyne Scattering," this conference.
9. Matsumoto, H., et al., "Physics of the L-H Transition in DIII–D," this conference.
10. Shaing, K.C., and Crume, Jr., E.C., Phys. Rev. Lett. **63**, (1989) 2369.
11. Biglari, H., et al., Phys. Fluids **B2**, (1989) 1.
12. Slusher, R.E., et al., Phys. Rev. Lett. **53**, (1984) 667.

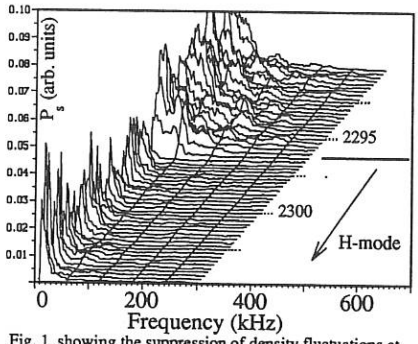

Fig. 1, showing the suppression of density fluctuations at a typical L-H transition. The illustrated power spectrum is that of the channel with a critical density of $1.3 \times 10^{19}\,m^{-3}$ The time interval is from 2290 to 2305 ms.

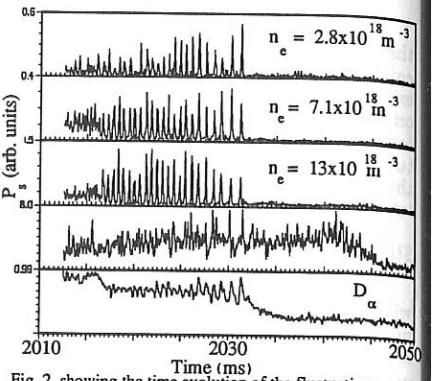

Fig. 2, showing the time evolution of the fluctuations monitored on four reflectometer channels during a dithering transition, as well as a D-alpha photodiode signal.

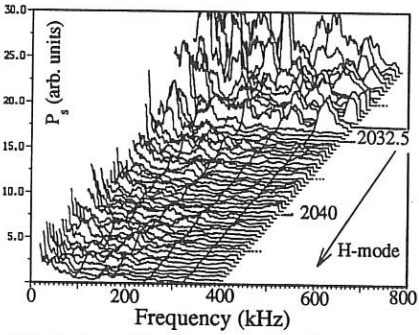

Fig. 3a. Spectrum of the reflectometer channel with a critical density of $1.3 \times 10^{19}\,m^{-3}$ for the same discharge as illustrated in Fig. 2. The time interval is from 2025 to 2047.5 ms.

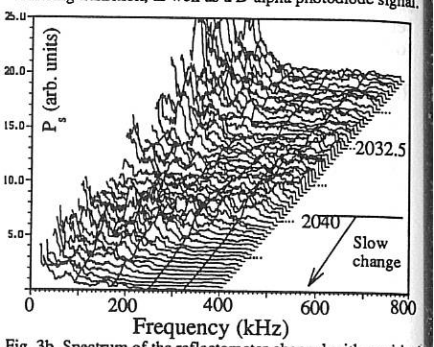

Fig. 3b. Spectrum of the reflectometer channel with a critical density of $2.0 \times 10^{19}\,m^{-3}$ for the same discharge as illustrated in Fig. 2. The time interval is from 2025 to 2047.5 ms.

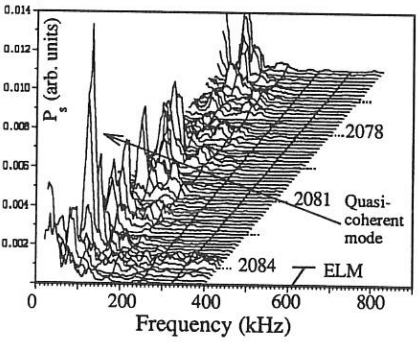

Fig. 4, showing bursts of quasi-coherent fluctuations preceeding an ELM. An increase in the broadband turbulence can be observed at the ELM itself.

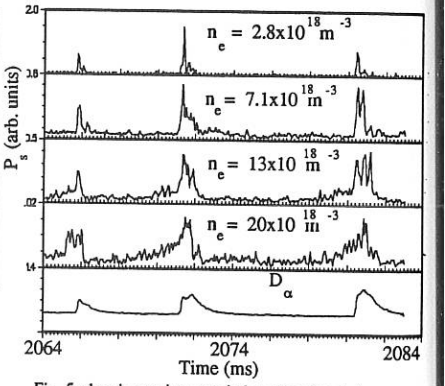

Fig. 5, showing an increase in broadband turbulence on inner reflectometer channels prior to ELMs.

INVESTIGATION OF DENSITY FLUCTUATIONS IN THE ASDEX TOKAMAK VIA COLLECTIVE LASER SCATTERING

G. Dodel, E. Holzhauer, L. Giannone*, H. Niedermeyer*, J. Gernhardt*, and ASDEX Team*.

Institut für Plasmaforschung, Universität Stuttgart, Fed. Rep. of Germany
*MPI für Plasmaphysik, EURATOM Association, Garching, Fed. Rep. of Germany

A 119 µm laser scattering experiment is used on ASDEX to investigate wavenumber and frequency spectra of the density fluctuations occurring in the different operational modes of the machine. The aim of the measurements is to get insight in the physical nature of the fluctuations and their possible role in connection with anomalous transport. Since no complete theory exists, the simple guidelines of gyroradius-scaling and mixinglength level are used in the choice of parameters to be varied. Particular emphasis has been placed on the investigation of the fluctuations in the ohmic phase. Results obtained during neutral injection heating are reported in [1].

Results in ohmic discharges:

A. General features:

Fig. 1 shows a typical k, ω spectrum of the scattered signal power measured in the plateau region of an ohmic hydrogen discharge using the chord 25 cm from the center. The spectrum exhibits the characteristic features observed on many tokamaks: It is broadband in k and ω, the important wavenumber range being below 10 cm^{-1}, the important frequency range below 200 kHz. At frequencies above ≈ 50 kHz the k-spectra show maxima. At low k and ω the scattered signal power increases significantly. This increase could be due to both coherent MHD activity, e.g. tearing modes (above 15 kHz the coherency between the scattering signal and the poloidal magnetic field component measured with a Mirnov coil drops from a value .6 to the noise level) and incoherent density fluctuations in the boundary layer, as observed by Langmuir probes and H_α emission.

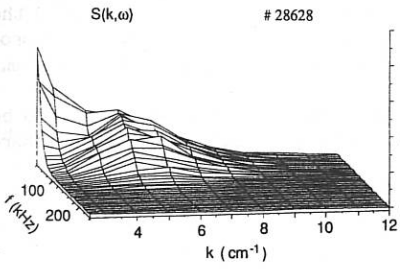

Fig. 1:
Scattered signal power measured as function of wavenumber and frequency in a "cold" ohmic hydrogen discharge. (measuring chord r = 25 cm; n_{eo} = 6 x $10^{13}cm^{-3}$; T_{eo} = 0,5 keV; I_p = 320 kA; B_t = 2.2 T)

B. Parameter variations:
Parameter variations were performed along the following guidelines: If the maxima of the k spectra obeyed a simple ρ_s scaling in the sense that $k^{max} \propto \rho_s^{-1}$ (where $\rho_s = \sqrt{k_B T_e / m_i}/\omega_{ci}$, ω_{ci} - ion cyclotron frequency), these maxima should depend on the ion charge Z, the ion mass m_i, the magnetic field B and the electron temperature T_e as $k^{max} \propto Z \cdot B/\sqrt{m_i \cdot T_e}$. If further the fluctuation level were determined by the mixing length criterion $\tilde{n}_e/n_e \propto (k^{max} \cdot L_n)^{-1}$ ($L_n = (d(\ln n_e)/dr)^{-1}$ = density gradient length) such a scaling would manifest itself also in the relative fluctuation level.

a) Variation of gas filling: "isotope scan".
Fig. 2 shows k spectra measured in hydrogen, deuterium and helium with the laser beam passing through the plasma center, at r = 25 cm (r/a = 0.63) and at the plasma boundary r = 39.5 cm (r/a = 0.99). The mean electron density was kept constant for the discharges. The different peak densities n_{eo} reflect the fact that the density profiles are somewhat different for the isotopes. The different peak electron temperatures are due to the different confinement times τ_E (52 ms in H^+, 80 ms in D^+ and 90 ms in He^{++}).

Hydrogen: The k spectra -frequency integrated in the interval 55-400 kHz - have a maximum in all measuring chords. From Fig. 2a we deduce $0.15 < k_p \rho_s < 0.5$, where k_p denotes the wavenumber of the poloidally propagating fluctuations and the interval reflects the uncertainty due to the spatial variation of ρ_s along the measuring chord. From Figs. 2g), h) i) $0.2 < k_r \rho_s < 0.35$ is inferred, where k_r denotes the wavenumber of the radially propagating fluctuations. Note, however, that the k spectra - frequency integrated in the interval 10-60 kHz - do not exhibit a maximum although their contribution to the total scattered power is substantial or even strongly dominating in the outer vertical chord.

Deuterium: No maximum of the k spectrum in the high frequency interval is observed in the central chord and the total scattered power increases (Fig. 2b). This behaviour is consistent with a ρ_s scaling and the mixing length estimate. A strictly analogous behaviour, however, is not observed in the outer chords (Figs. 2e,h)): at r = 25 cm, e.g., a local maximum of the k spectrum is observed at about the same position as in the case of hydrogen. A substantial difference only occurs at $k < 4\ cm^{-1}$ with a drastic increase of the scattering signal compared to hydrogen. Keeping in mind the finite k resolution of the scattering device ($\pm 1.2\ cm^{-1}$) the dip in the k spectrum on top of Fig. 2e) may in reality be even more pronounced. Again the k spectra in the low frequency range have no maximum.

Helium: The features of the k spectra in He^{++} discharges appear to be somewhat in between those observed in the comparable H^+ and D^+ discharges.

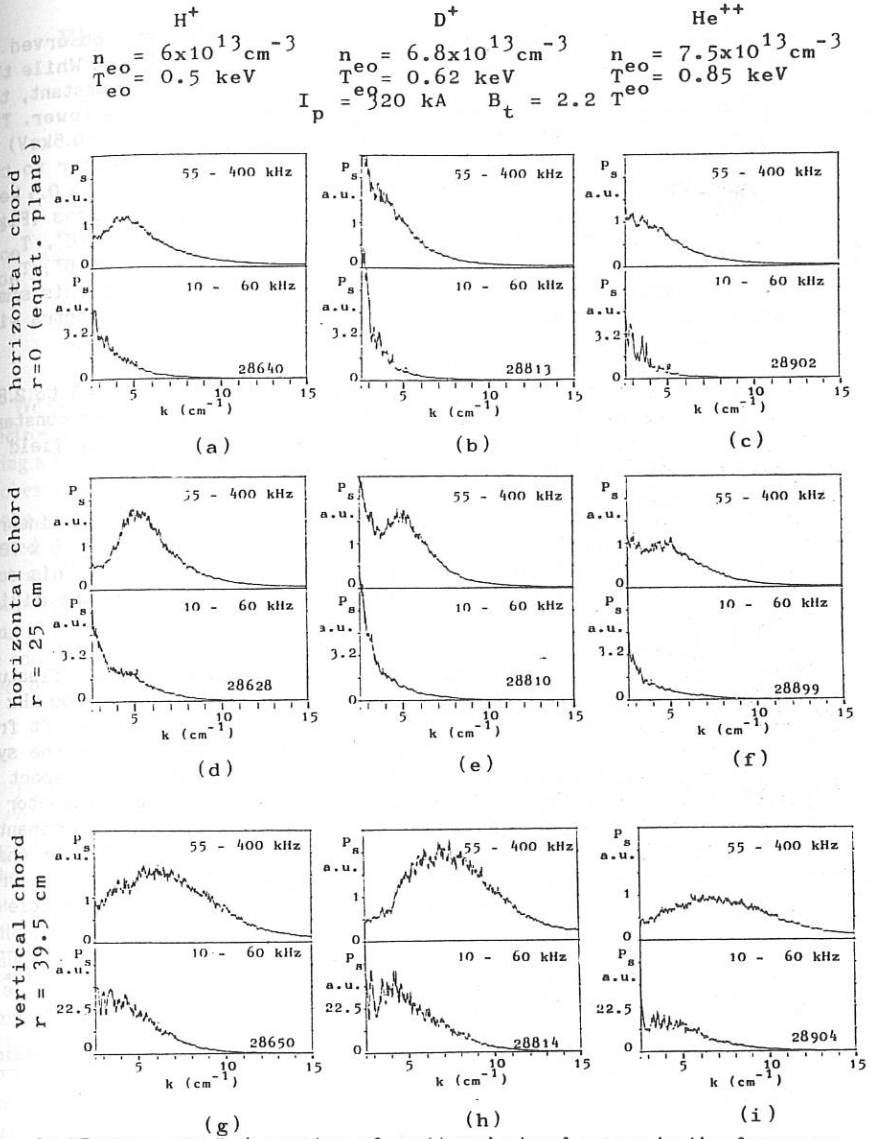

Fig. 2: "Isotope scan": k spectra of scattered signal power in the frequency intervals indicated measured at three different positions with hydrogen, deuterium and helium gas filling. For each row the vertical scales of the plots are comparable. For the columns the vertical scales are not comparable. Different vertical scales for the two frequency channels in particular for the vertical chord r = 39.5 cm.

b) Variation of electron temperature.
Figs. 3a),b) show k spectra - in the interval 55-400 kHz - observed in "cold" and "hot" hydrogen discharges in the chord r = 25 cm. While the discharge current and the toroidal magnetic field were kept constant, the electron densities in the hot discharges are a factor of 4 lower. The change in the shape of the k spectra going from "cold" (T_{eo} =0.5keV) to "hot" (T_{eo} = 1.25 keV) hydrogen plasmas is strikingly similar to the change of the k spectra observed when going from "cold" (T_{eo} = 0.5 keV) hydrogen plasmas to "cold" (T_{eo} = 0.65 keV) deuterium plasmas (Figs. 3 a),c)). This similarity is noteworthy since both changes (H^+, T_{eo} = 0.5 keV) → (H^+, T_{eo} = 1.25 keV) and (H^+, T_{eo} = 0.5 keV) → (D^+, T_{eo} = 0.62 keV) imply about the same change in ρ_s. On the other hand this similarity also shows that no ρ_s scaling of the maxima of the k spectra with T_e can be deduced.

c) Variation of the toroidal magnetic field.
In deuterium the toroidal magnetic field was varied from 1.9 T to 2.8 T while keeping the line electron density and the safety factor constant. A substantial decrease of the fluctuation level with increasing field is observed which is consistent with the mixing length model.

d) Density scaling.
The rms value of the frequency integrated scattered power scales linearly with the mean electron density. This was established for $\bar{n}_e < 5 \times 10^{13}$ cm^{-3} in the important k range and in different spatial chords. This scaling is consistent with a fluctuation level determined by the mixing length criterion.

C. Frequency spectra.
In the central chord which sees primarily poloidally propagating fluctuations a maximum of the scattered power is observed around ~ 100 kHz in the dominant k range. This is on the order of the diamagnetic drift frequency evaluated in the gradient region of the discharge. Using the system in the heterodyne mode the direction of propagation with respect to the laboratory frame can be determined. When the scattering wavevector is oriented poloidally the fluctuations are found to propagate predominantly in the electron-diamagnetic direction for $k \geq 8$ cm^{-1}. In the outer channel close to the separatrix where k is mainly oriented radially narrow frequency spectra centered around zero are observed indicating little or no radial propagation.

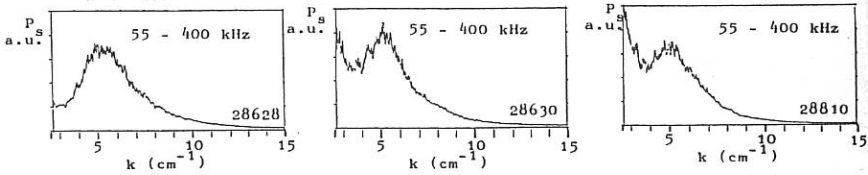

Fig. 3: k spectra in "cold" hydrogen (a), "hot" hydrogen (b) and "cold" deuterium discharges. Note the similarity of the spectra in "hot" hydrogen and "cold" deuterium.

References:

[1] ASDEX-Team, "The H-mode of ASDEX", Nucl. Fus. 29, 1959 (1989)

FLUCTUATIONS AND TRANSPORT IN DITE

G Vayakis and D C Robinson*

AEA Technology Culham Laboratory, Abingdon OX14 3DB, UK
(EURATOM/UKAEA Fusion Association)
*Balliol College, Oxford OX1 3BJ, UK

Introduction

We have investigated the behaviour and effects on plasma transport of edge (r/a>0.9) electrostatic and magnetic fluctuations in the DITE tokamak (R=1.19m, a=0.23m,) using a fast reciprocating array of five 4-pin electrostatic and two-point magnetic ($\dot{B}_r$) probes which extended ≈70° poloidally and was centred on the outside midplane. Each probe had two of the pins aligned in the vertical direction, with two 2.75mm dia. coils placed coaxially 4.0mm behind the pins. The poloidal separation was 4mm. The system was used to produce one-shot radial profiles of mean and fluctuating plasma parameters by acquiring data in short (1ms/2μs) bursts during the stroke or to acquire long (32ms/2μs)streams of data with the probe held at a fixed radius for ≈ 50ms (to be compared with a typical flat-top duration of 300ms.) The results presented here were obtained in helium plasmas (I_p=80-100kA, B_ϕ=1.5-2T.)

Electrostatic fluctuation levels and transport

The simplest of measurements of the electrostatic fluctuation levels assumes that $\tilde{T}_e/T_e \approx 0$. A Langmuir probe held in ion saturation then measures local density fluctuations and if it is left floating it measures plasma potential fluctuations. In tokamaks one finds generally that under this assumption the Boltzmann relation is not satisfied,[1] i.e. $\tilde{n}/n \neq \tilde{V}_p/T_e$, where V_p is the plasma potential and $\tilde{}$ denotes a fluctuating quantity. This has also been found for DITE in hydrogen[2]. In these helium discharges we find that, in the region of the limiter, the Boltzmann relation is approximately satisfied. The presence of temperature fluctuations can affect this simple measurement as well as estimates of particle flux from two-point measurements of V_f. One method that in principle can resolve all the quantities of interest (i.e. $\tilde{n}/n$, $\tilde{E}$, $\tilde{T}/T$ and their cross-correlations has been used successfully on the ZETA device[3] and more recently on the TOSCA[4] and TEXT[5] tokamaks. It involves studying the variation of the current fluctuations to a double probe as a function of applied voltage V_a. If $j = F(x_1 \ldots x_n, V_a)$ then to first order

$$\langle \tilde{j}\tilde{j} \rangle = \sum_{n,m} \frac{\partial F}{\partial x_n} \frac{\partial F}{\partial x_m} \langle \tilde{x}_n \tilde{x}_m \rangle \left(1 - \frac{\delta_{nm}}{2}\right).$$

A linear least-squares fit to the $\langle\tilde{j}\tilde{j}\rangle$ curve may then be used to obtain the time averaged quantities $\langle\tilde{x}\tilde{x}\rangle$. For a double probe aligned in the poloidal direction $x_1 = n$, $x_2 = E_\theta$ and $x_3 = T_e$.

We applied this method to a series of shots during a density scan (Fig.1.) The term $\langle\tilde{n}\tilde{E}\rangle$ is of particular interest in this case as it is proportional to the cross-field particle flux, $\Gamma = \langle\tilde{n}\tilde{E}\rangle/B_0$. Its estimated error (from shot-to-shot scatter and the standard deviation of individual fits) is $\pm 30\%$. In Fig.2 we show the particle confinement time as a function of line average density extrapolated from a measurement 12^o above the midplane. The equivalent confinement time based on limiter probe measurements is also shown for comparison. The corresponding cross-coherence γ_{nE} lies in the region 0.18-0.32, increasing with $\bar{n}_e$, $\tilde{n}/n$ increases with density from ~ 0.2 to ~ 0.4 and $\tilde{E}_\theta$ decreases with density from ~ 4000 to $\sim 2000 V/m$. The fluctuation driven flux as a result has a minimum at $\bar{n}_e \sim 3.5 \times 10^{19} m^{-3}$.

The estimated error on $\tilde{T}/T$ for each $32ms/2\mu s$ acquisition is very large. However by normalising the data to the fitted values of $\tilde{n}/n$, which have small $(2-5\%)$ errors one can obtain from the density scan (16 shots) $\tilde{T}/T_e = \left(0.9^{+0.2}_{-0.4}\right)\tilde{n}/n$, but with no density resolution. Using this formula for $\tilde{T}/T_e$ over the whole dataset we can estimate $\gamma_{TE} = 0.20 \pm 0.15$ and $\gamma_{nT} = 0.15 \pm 0.10$. Here we have assumed that the fluctuation characteristics are insensitive to $\bar{n}_e$. Using the temperature measured at the limiter radius we can obtain a value for the 'convective' heat flux $Q_C = 2 \times \frac{3}{2} T_e \Phi$ where Φ is the total particle outflow and compare it to the total non-radiated power Q_{NR} (Fig.3.) We see that $Q_C < Q_{NR}$ except at the lowest densities. The data on $\langle\tilde{T}\tilde{E}\rangle$ indicate an additional 'conductive' contribution to the heat flow $Q_T = \frac{3}{2} n \langle\tilde{T}\tilde{E}\rangle/B_o = (Q_C \pm 0.75 Q_C)/2$ (electrons only.)

The relation between magnetic and electrostatic fluctuations

We investigate the relation between electrostatic and magnetic fluctuations in three ways: by direct cross-correlation between $\dot{\mathrm{B}}_r$ and the ion saturation current $\tilde{j}$ or the floating potential $\tilde{V}_f$ signals, by comparison of their propagation characteristics and by observing their scalings with varying line average density $\bar{n}_e$. All these methods appear to be dominated by spatial effects, as the $\dot{\mathrm{B}}_r$ coils are sensitive to non-local current perturbations.

Direct correlation measurements on the same probe indicate good correlation amplitude (defined as $\Gamma_{12}(\omega) = \sqrt{(P_{12}(\omega)^2 + Q_{12}(\omega)^2)}/\sqrt{P_{11}(\omega)P_{22}(\omega)}$, where $P(\omega)$ is the power spectrum and $Q(\omega)$ the quadrature spectrum, both averaged over a frequency range $\Delta\omega$) between $\tilde{j}$ and $\tilde{\mathrm{B}}$ in the frequency region of maximum $\tilde{j}$ (at the limiter radius, Fig.4.) A radial scan indicates that this correlation dissappears below that of two uncorrelated noise sources (dashed line) nearer the wall (Fig.5.) The correlation between $\tilde{V}_f$ and $\tilde{\mathrm{B}}$ shows similar behaviour. This is consistent with previous observations on TEXT[6] that showed good correlation only near the limiter radius.

Two-point measurements of $\tilde{V}_f$ and $\tilde{\mathrm{B}}$ provide the mean wavenumber $\bar{k}$ and its standard deviation Δk in the poloidal direction as a function of frequency. In the region of good correlation we find $\bar{k}_m \sim \bar{k}_e/3$, with $\Delta k_{m,e} \sim \bar{k}_{m,e}$, where the subscript

m stands for magnetic and the subscript e for electrostatic. The discrepancy in phase velocity can be explained in terms of spatial filtering which will tend to decrease the signal contributions of high-k_e $\tilde{j}_{||}$ perturbations that do not originate exactly at the probe radius.

As the density increases the peak of the cross-correlation of Fig.4 moves to lower frequencies, following the peak in electrostatic fluctuation spectral power. At the highest densities the cross-correlation dissappears, but this is not surprising as the peak of the electrostatic fluctuation spectrum is now within the dominant core-MHD region ($< 20kHz$.) If we express $\tilde{B}_r/B_0 = G\beta_e\tilde{n}/n$ we find $0.8 < G < 4$, decreasing with increasing $\bar{n}_e$. At the frequency region of good correlation ($\Gamma_{12}/\Gamma_{NOISE} > 2.5$) we find that G it is virtually independent of density at $G = 0.65 \pm 0.05$.

Discussion and Conclusions

The electrostatic fluctuations in DITE are large amplitude and broad-band as in other tokamaks. In general they do not obey the Boltzmann relation $\tilde{n}/n = \tilde{V}_p/T$ although this can be affected by temperature fluctuations. By analysing the double probe mean square current fluctuation characteristic we obtain estimates of density, electric field and temperature fluctuation levels as well as their correlations. The correlation between density and poloidal electric field provides estimates of the fluctuation driven particle flux which are sufficient to account for ohmic and ECRH global particle losses. Temperature fluctuation levels can be relatively high at $(0.9^{+0.2}_{-0.4})\tilde{n}/n$. For $T_i \sim T_e$ the turbulence model of Hahm et al[7] predicts $\tilde{T}/T \sim (L_n/L_T)(m_e/m_i)^{1/6}\tilde{n}/n$ or, for this DITE scan $\tilde{T}/T = (0.1 - 0.4)\tilde{n}/n$, decreasing as $\bar{n}_e$ increases. A possible explanation for the lower densities would be $T_i > T_e$, but not for the higher densities where the discrepancy is largest.

The convected power carried by the electrostatic fluctuations is always significant, although an accurate comparison with the non-radiated power may be affected by possible asymmetries. The temperature fluctuation level alows the possibility of conducted power making up the deficit at high $\bar{n}_e$.

Finally the correlation data between the magnetic and electrostatic aspects of the turbulence suggest that the magnetic fluctuations found at the tokamak edge can be accounted for by the magnetic aspect of the 'electrostatic' turbulence and are not an independent phenomenon. Their levels ($< 0.5G$) are generally too small to cause any significant particle or heat transport in the edge.

References

[1]PC Liewer, *Nuclear Fusion* **25**,543 (1985)

[2]P Mantica et al, *Proc. 16 EPS* **13B**, part 3, p967, Venice (1989)

[3]DC Robinson and MG Rusbridge, *Plasma Physics* **11**, 73 (1969)

[4]AA Howling and DC Robinson in *Plasma Physics and Controlled Fusion* **30** (13), p1863 (1988)

[5]H Lin, RD Bengtson and ChP Ritz, *Phys. Fluids* **B 1**, p2027 (1989)

[6]KW Gentle et al, *Proc.14 EPS*, **11 D**, part 1, Madrid(1987)

[7]TS Hahm et al, *Phys. Fluids* **30**, p1452 (1987)

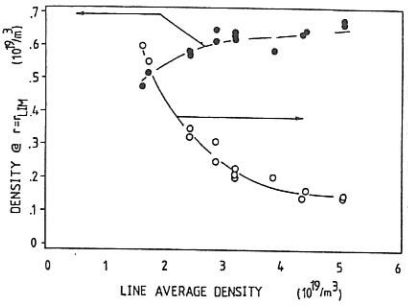

Fig.1: Edge temperature and density at the limiter radius against line average density. He, 80kA, 1.55T.

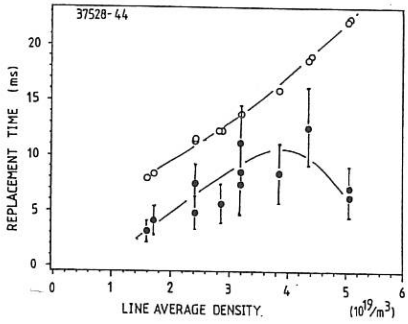

Fig.2: Particle replacement time from the electrostatic fluctuations (•) and limiter probe measurements (o.)

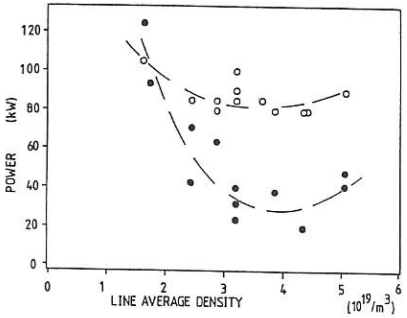

Fig.3: Fluctuation convected power (•) and total non-radiated power (o.)

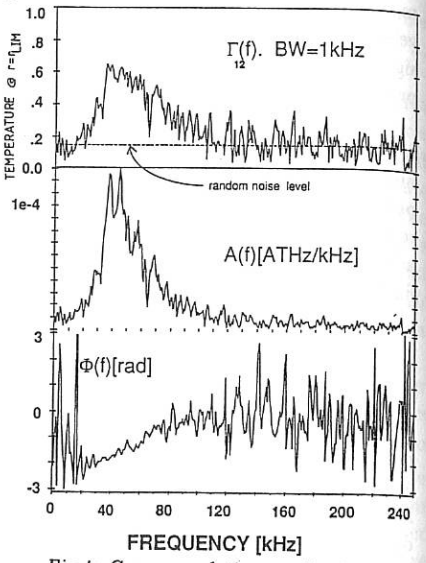

Fig.4: Cross correlation amplitude Γ, cross-spectrum amplitude A and cross-phase Φ between ion current and $\dot{B}_r$ signals on the same probe stalk at the limiter radius. He, 80kA, 1.55T, $2.4 \times 10^{19} m^{-3}$.

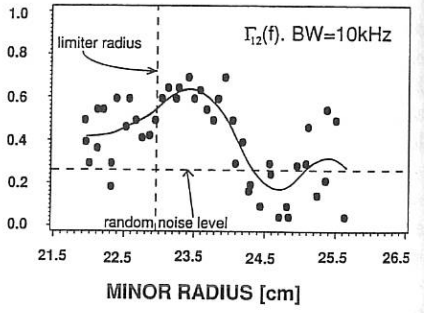

Fig.5: Cross correlation amplitude at the frequency peak of the ion current fluctuations between ion current and $\tilde{B}$ signals on the same stalk, as a function of radius. He, 85kA, 1.62T, $2.55 \times 10^{19} m^{-3}$.

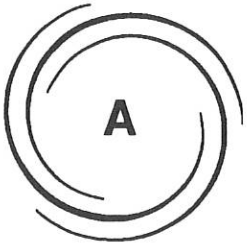

TOKAMAKS

A5 RESULTS PELLET INJECTION

ONLINE DENSITY FEEDBACK ON ASDEX FOR PELLET-REFUELLED DISCHARGES

R. Loch, M. Kaufmann, R. Lang, R. Merkel, V. Mertens, R. Tisma, W. Sandmann

Max-Planck-Institut für Plasmaphysik, EURATOM Association
D-8046 Garching, Fed. Rep. Germany

1) Introduction

During the last few years, injection of frozen H2-D2 pellets into tokamak devices has proved to be a successful tool to refill the plasma and to build up high plasma densities with good confinement properties /1,2/. This is of great importance for the future design of a rector-relevant tokamak machine, where good confinement will be important for ignition /3/.

On ASDEX, where repetitive pellet injection with a centrifuge is possible, the physical properties of pellet-refuelled discharges were intensively studied /2,4,5/.

It was found that the density limit in ohmic as well as in additionally heated discharges can be substantially increased /2/. In ohmic discharges line-averaged densities of $n_e = 1.4 \cdot 10^{20} m^{-3}$ (for q = 2.7) were reached with pellet injection, compared with a maximum of $n_e = 0.6 \cdot 10^{20} m^{-3}$ with gas puff alone.

Parallel to the increase of the density limit, phases with improved particle and energy confinement were found /2,5/. The changes in transport coefficients and the suppression of sawtooth activity triggered by pellet injection lead to enhanced inward drift of particles and correlated peaking of the density profile.

During these sawtooth-free phases in ohmic discharges energy confinement times of up to 170 ms were observed on ASDEX, compared with values of about 85 ms without pellet injection.

It turned out that not every discharge refuelled by pellets shows improved confinement /2,4/. Proper conditioning of pellet and gas puff fuelling is necessary because recycling and the plasma edge density strongly affect the transport properties and confinement. Without the support of additional gas puff and neutral gas flow from recycling, which expands only 1-5 cm into the plasma until it is ionised, most of the ablated pellet mass, which is ablated at about half the minor plasma radius, is lost between two pellets and no density build-up is possible. So careful adjustment of the additional gas puffing rate is necessary to achieve successful density buildup and long-lasting phases of good confinement.

Because of this experience, it was considered useful for further investigations of pellet-refuelled discharges to build up an online feedback system to control simultaneously

- pellet injection by the central density of the plasma
- gas puff by the edge density

by using two channels of the existing 16-channel Thomson-scattering diagnostic in conjunction with a fast microprocessor system.

2) Technical description of the online feedback system

The schematic setup of the feedback system is given in fig. 1. Two channels of the ASDEX Thomson-scattering diagnostic /6/ at the centre (r = 0.1a) and near the edge (r = 0.75a; minor radius a = 40cm) of the plasma were used for the online density measurements. The raw data from the two channels are read out from ADC's by a fast CAMAC microprocessor. The module calculates the temperature and density and creates control signals for the pellet centrifuge and the gas valve within the time interval of two successive laser pulses (17 ms). For development and compilation of the programs the processor module is connected with a medium frame computer (sun workstation).

Pellet injection is coupled to the central density: if the actual density in the plasma centre is greater then the threshold value, an inhibit signal is created. The pellet centrifuge, which is able to inject pellets at minimum intervals of 20 ms, then stops injection until the central density falls below the threshold.

The gas valve is feedback-controlled by the plasma edge density (in this paper "plasma edge" refers to r = 0.75a) measured by the online system and fed into the gas valve control unit. It there replaces the commonly used HCN interferometer signal. To avoid problems in the start phase of the discharges, gas puff control is made with HCN-interferometry until 0.6 s, and then the control is switched to the new online feedback system.

A complete program cycle between laser triggering and response (control signals) takes about 10 ms. The precision of the online measurements is better than 5% in the plasma centre and better than 10% at r = 0.75a.

3) Discharges controlled with the new feedback system

Figure 2 shows an ohmic discharge (B = 2.2 T; I = 380 kA; q = 2.7) where the pellet injection and gas valve are simultaneously controlled by the feedback system. The threshold for pellet injection was $n_e(r = 0.1a) = 7 \cdot 10^{19} m^{-3}$ and the edge density $n_e(r = 0.75a)$ was adjusted to $3 \cdot 10^{19} m^{-3}$. The pellet mass was $4 \cdot 10^{19}$ atoms, the pellet velocity 200 m/s and the repetition rate 30 Hz.

After several injected pellets, when the central density reaches the threshold, the central density still rises because of the anomalous inward drift of the ablated pellet mass. This peaking of the density profile can typically last a few 100 ms. The peaking factor $n_{e0}/ < n_e >$ rises to about 2.6 and the global energy confinement time τ_E increases up to 140 ms. Normally the onset of sawteeth then leads to a sudden drop of the central density resulting in the restart of pellet injection.

Density build-up by pellets, peaking during post-pellet phases and the onset of sawtooth-activity result in a slow oscillation of the central density around the threshold.

The scatter of the online measurement of the plasma edge density leads to fast changes in the gas puffing rate, but the delayed reaction of the plasma averages over a period of about 50 ms so that the edge density remains relatively stable at the adjusted level.

Figure 3 shows a discharge with feedback-controlled pellet injection ($m_p = 1.3 \cdot 10^{20}$ atoms, $v_p = 600 m/s$, threshold $n_e(r = 0.1a) = 1.3 \cdot 10^{20} m^{-3}$) and additional heating

(ICRH 1.6 MW). With high heating power, the particle confinement is rather poor and phases with peaking of density profiles are missing. This results in more rapid oscillations around the threshold of the central density.
In a series of ohmic discharges (B = 2.2 T, I_p = 380 kA, q = 2.7, threshold for pellet injection $n_e(r = 0.1a) = 1 \cdot 10^{20} m^{-3}$), we examined the influence of the edge density for successful density build-up (see fig. 4).
With low edge density ($3.5 \cdot 10^{19} m^{-3}$), corresponding to missing additional gas puff and low recycling, only weak density build-up by pellets can be achieved. Rapid particle loss of the ablated pellet mass due to high density gradients at the plasma edge prevent a substantial increase of the density. With enhanced edge density $n_e(r = 0.75a) = (4 - 5) \cdot 10^{19} m^{-3}$ pellet injection already starts at higher density and the threshold is reached after a few pellets. Higher edge density ($6 \cdot 10^{19} m^{-3}$) leads to even faster density build-up, but results in an early disruption. The observation of enhanced radiation at the plasma edge and in the divertor chamber indicates that the discharge runs into an edge density limit.

4) Conclusions

The new online feedback system has proved to be a promising instrument to optimize density build-up by pellet injection and to stabilize discharges at high densities. Further improvements of the feedback system are planned where additional diagnostics for online recognition of important changes of plasma characteristics can be included. This should allow precautions to be taken to prevent density limit disruptions. Especially close to the density limit, edge radiation cooling and central accumulation of impurities can result in disruptions /2/.

References

/1/ Proc. of "Pellet-Injection and Torroidal Confinement" Workshop
IAEA-TECDOC-534 Gut Ising, FRG (1988)
/2/ M. Kaufmann et al. Nucl. Fus. 28 (1988) 827
/3/ F. Engelhard in /1/ p.89
/4/ G. Vlases et al. Nucl. Fus. 27 (1987) 351
/5/ V. Mertens et al. Proc. 15th Eur. Conf. Plasma Phys. Dubrovnik 1988
/6/ H. Röhr et al. IPP Report III/121B, 1987

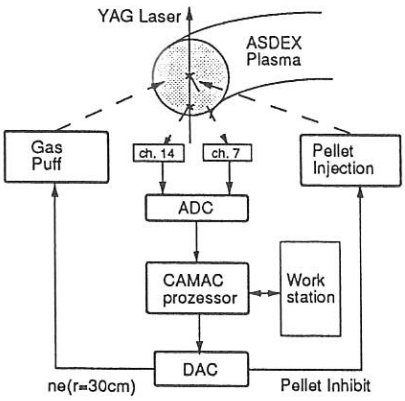

Fig. 1 : Scheme of the online density feedback system

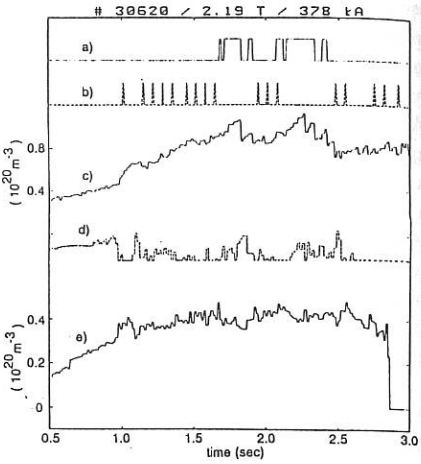

Fig. 2 : Feedback controled discharge with pellet injection
a) pellet inhibit signal
b) injected pellets
c) central density ne(r=0.1a)
d) gas valve
e) edge density ne(r=0.75a)

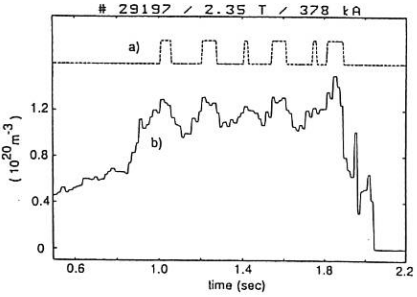

Fig 3 : Discharge with pellet injection and additional heating ICRH 1.6 MW
a) Pellet-inhibit signal
b) ne(r=0.1a)

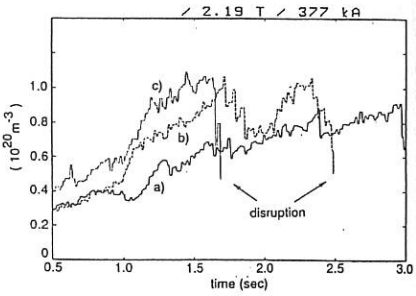

Fig. 4 : Ohmic discharge with pellet injection central density ne(r=0.1a) for
a) ne(r=0.75a) = 3.5 10^{19} m^{-3}
b) 4.5
c) 6.0

SIMULTANEOUS EVOLUTION OF TEMPERATURE AND DENSITY PERTURBATIONS FOLLOWING PELLET INJECTION IN JET.

J.R.Martin-Solis, A.Cheetham[1], K.Erents[2], and A.Gondhalekar.

JET Joint Undertaking, Abingdon, OX14 3EA, UK.
[1]Canberra University, Canberra ACT 2616, Australia.
[2]EURATOM-AEA Association, Culham, OX14 3DB, UK.

INTRODUCTION

Measurement of inward propagation of temperature and density perturbations, produced when a superficially penetrating pellet is injected into JET, have been used previously to determine radial thermal and particle diffusivities in Ohmic and NBI heated H-mode plasmas. These have yielded χ_e, χ_i, D_e and χ_e/D_e simultaneously in the same spatial region in the plasma core[1,2]. Simplifying approximations were made that the evolution of temperature and density could be uncoupled, because T_e was observed to evolve very much faster than n_e. These approximations need to be revised in view of subsequent measurements of the long-time evolution of T_e and n_e into the core and edge plasmas. A coupled model without these approximations reproduces previous results and also describes the new features which are observed experimentally, allowing determination of χ_e and D_e from evolution of $T_e(r,t)$ alone. The coupled model is also used to interpret Langmuir probe measurements of temperature and density perturbations propagating outward to the plasma edge. In this paper we discuss qualitatively the additional features observed experimentally and those obtained in the coupled model simulation. The improved measurement and simulation capability discussed here enlarges the scope of the diagnostic applications of small perturbations produced by pellet injection for transport investigations in JET, yielding simultaneous determinations of radial χ_e and D_e in the core and edge plasmas.

THE MODEL

The equations governing the evolution of electron temperature and electron density profiles are

$$\partial W_e/\partial t + \mathrm{div}\cdot Q_e = -n_e k T_e \cdot \mathrm{div}\cdot V + S_w \qquad \text{eq.1}$$

and

$$\partial n_e/\partial t + \mathrm{div}\cdot \Gamma_e = S_e \qquad \text{eq.2}$$

where

$$W_e = 3/2\cdot n_e(r,t)\cdot k\cdot T_e(r,t)$$
$$Q_e = 3/2\cdot k T_e \Gamma_e - \chi_e \nabla T_e + q_p$$
$$\Gamma_e = -D_e \nabla n_e + \Gamma_p$$

W_e is the electron energy density, Q_e is the electron heat flux, S_w is the thermal heat source. The first term on the right-hand-side of eq.1 is the 'adiabatic source' corresponding to work done by compression due to flow V. Γ_e is the particle flux, and S_e the electron source in eq.2. Q_e is made up of contributions from convection, conduction and a 'thermal pinch' q_p. The particle flux similarly has contributions from diffusion and a 'particle pinch' Γ_p. The use of the 'pinch' terms q_p and Γ_p is suggested by

previous investigations of thermal and density transport in JET[3,4]. The departure from the uncoupled model[1] is the inclusion of convective term in Q_e, the 'adiabatic source', and that eq.1 and eq.2 are integrated simultaneously. The methodology for integrating the continuity equations (1&2) above for electron energy and particle density, and for constructing the initial and boundary conditions has been described before[1].

EVOLUTION OF PERTURBATIONS IN THE CORE PLASMA

Fig.1 illustrates the need for upgrading the model. Fig.1a shows a measurement reported previously[1], shot #12770, for which the plasma parameters are: B_ϕ=2.1T, I_ϕ=3MA, $\bar{n}_e \cong 2\times10^{19}m^{-3}$, $T_e(0)\cong$2.9keV, and $T_i(0)\cong$ 1.5keV with OH alone. The small pellet penetrated to a radius $r_p/a\cong 0.65$, and the sawtooth inversion radius was $r_c/a\cong0.3$. The measured evolution of $T_e(r,t)$ in the region $0.5\leq r/a\leq0.6$ was modelled giving χ_e=2.8±0.3 m^2/s, using the uncoupled model. Similarly for evolution of $n_e(r,t)$, giving D_e=0.4±0.1 m^2/s. However, the uncoupled model is unable to simulate the observed recovery of T_e for long times, and therefore its prediction of T_e evolution deviates from observations such as one shown in fig.1b for #20074. The parameters for #20074 are: B_ϕ=3.2T, I_ϕ=3MA, $\bar{n}_e\cong4\times10^{19}m^{-3}$, $T_e(0)\cong$ 6.7keV, and $T_i(0)\cong$4.2keV with 8MW of ICRF heating. The pellet penetrated to a radius $r_p/a\cong$ 0.47, and the sawtooth inversion radius was $r_c/a\cong0.22$. Pulse #20074 can not be used for simulation of $T_e(r,t)$ evolution because the recorded data is not adequate to construct a reliable initial condition. Therefore #12770 has been modelled for illustration. Fig.2 compares the modelled evolution of $T_e(r,t)$ for #12770 using the model in which the evolution of $T_e(r,t)$ is uncoupled from that of $n_e(r,t)$ by putting $\partial n_e/\partial t=0$, neglecting the convective term in Q_e and the 'adiabatic source' term, with that using the coupled system of eq.1 and eq.2. In both models (S_H - div·q_p) is computed for the equilibrium before the pellet and is kept constant during the subsequent evolution of $T_e(r,t)$. Fig.2 shows that by including the density evolution the long-time behaviour of $T_e(r,t)$ characterized by the minimum in T_e, such as that observed in #20074 shown in fig.1b, can be simulated. Fig.2 also shows that the short-time evolution of $T_e(r,t)$ is not affected by the differences in the two models, and that the same best value of χ_e would be recovered from both. For the simulations of fig.2 typical values $\chi_e=3m^2/s$ and $D_e=0.3m^2/s$, constant between r_p and the measurement points, are used as previously[1]. Fig.3 shows that at fixed χ_e the position of the minimum in the $T_e(r,t)$ evolution is sensitive to the magnitude of D_e. The magnitude of χ_e controls the evolution of $T_e(r,t)$ in the short term, whereas D_e controls its ulterior evolution. Thus D_e may be determined both from evolution of $n_e(r,t)$ as well as from that of $T_e(r,t)$ for the same event. More importantly, both χ_e and D_e can be deduced from measurements of $T_e(r,t)$ alone. This realization is of great value since in JET the measurement of $T_e(r,t)$ is inherently more accurate than that of $n_e(r,t)$. The ability of the coupled model to simulate the minimum in $T_e(r,t)$ is a consequence of allowing evolution of n_e in eq.1, making both T_e and n_e tend to their initial equilibrium. In contrast, in the uncoupled evolution in which n_e was kept constant at its value immediately after pellet injection, T_e evolved to a new equilibrium. Lastly, analysis of the effect of the convective and 'adiabatic source' terms in the coupled model shows that neglecting them does not make a qualitative change to the evolution, but can give inaccuracies in the deduced values of χ_e and D_e.

EVOLUTION OF PERTURBATIONS IN THE EDGE PLASMA

The outward propagation of perturbations has been measured using

Langmuir probes. Fig.4 shows the evolution of T_e and n_e at the plasma edge following injection of a pellet with $r_p/a \cong 0.2$. The plasma parameters for pulse #20936 are: B_ϕ=2.5T, I_ϕ=3MA, $\bar{n}_e \cong 2.3 \times 10^{19} m^{-3}$, $T_e(0) \cong 2$keV, $T_i(0) \cong 1.8$keV, with $r_c/a \cong 0.3$ and with OH alone. The measurements shown in fig.4 indicate that the evolution of T_e and n_e can not be uncoupled and that the perturbations travel to the plasma edge at similar speeds, with $T_e(a)$ reaching a minimum at $\tau_T \cong 100$ms and $n_e(a)$ reaching a maximum at $\tau_n \cong$ 150-200 ms after pellet injection. These measurements have been modelled using the coupled system of eq.1 and eq.2. to yield χ_e, D_e. Fig.5 shows the model prediction for the times τ_T and τ_n, plotted against diffusivities $\overline{\chi}_e$ and $\overline{D}_e$ averaged over the plasma between r_p and the measurement points. Comparison of the measurement and simulation, fig.4 and fig.5, gives $\overline{\chi}_e \cong 2 \pm 0.3$ m^2/s and $\overline{D}_e \cong 0.9 \pm 0.2$ m^2/s, giving $\overline{\chi}_e/\overline{D}_e \cong 2.2 \pm 0.8$. However, in the example used here the pellet penetrates far into the plasma and so in propagating to the edge, the perturbation samples part of the core as well as the edge plasma. Moreover, the perturbation caused in the equilibrium plasma parameters is large. Therefore the results can not be considered to be representative of the plasma in near stationary conditions.

CONCLUSIONS

This paper discusses advances in simultaneous determination of electron thermal and density transport in the plasma core and the plasma edge, using a single pellet induced perturbation event. The realization that accurate measurements of $T_e(r,t)$ alone in the plasma core yield both χ_e and D_e is very valuable. Langmuir probe measurements of perturbations in $T_e(a)$ and $n_e(a)$ permit determination of χ_e and D_e in the plasma edge without recourse to subsidiary assumptions about gas disorption from the walls, as in HPP studies using sawteeth. No general conclusions about the relative behavior of χ_e/D_e in the plasma core and the plasma edge can be made due to weaknesses in available data. The work reported here thus prepares the ground for extensions of ongoing investigations of thermal and density transport in JET, and the relationship between them.

REFERENCES

[1] A.Gondhalekar et at., Plasma Physics and Controlled Fusion, 31(1989)805.

[2] A.D.Cheetham et al., Proc. 12th Int. Conf. on Plasma Physics and Controlled Fusion Research, Nice, 1988. 1(1989)483.

[3] J.D.Callen et al., Nuclear Fusion 27(1987)1857.

[4] A.Gondhalekar et al., Bull. Am. Phys. Soc., 30(1985)1525, and JET Report JET-P(1985)31.

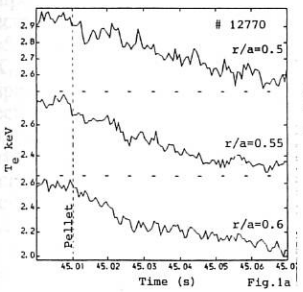

Fig.1a

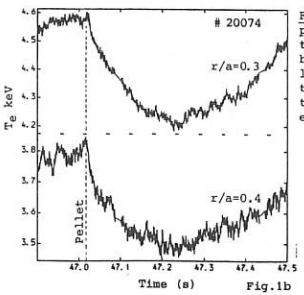

Fig.1b

Fig.1 Evolution of T_e after pellet injection. The short-time evolution is controlled by χ_e (fig.1a) whereas the long-time behaviour, characterized by evolution of T_e through a minimum, is influenced also by D_e, (fig.1b).

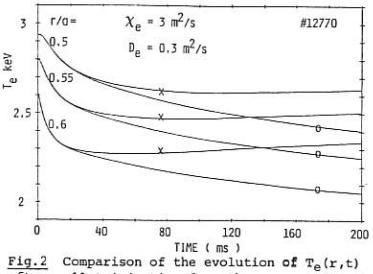

Fig.2 Comparison of the evolution of $T_e(r,t)$ after pellet injection from the uncoupled(⊖) and coupled(⊕) models, for several radii, exhibiting their difference in the long-time evolution.

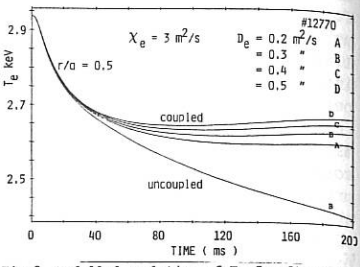

Fig.3 Modelled evolution of T_e for fixed χ_e and different values of D_e from the coupled model. The long-time behaviour is affected by D_e and the minimum in T_e is delayed when D_e becomes smaller. Comparison is also shown with the uncoupled model, which is unable to produce the recovery in T_e.

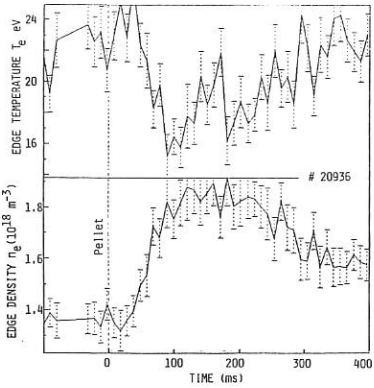

Fig.4 Langmuir probe measurements of edge electron temperature and density evolution following pellet injection.

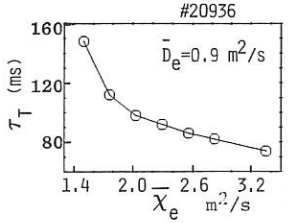

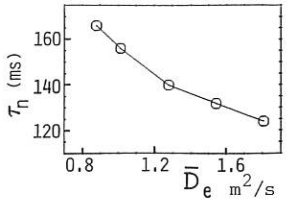

Fig.5 Predicted arrival times in the plasma edge, from the coupled model, of the minimum in T_e (τ_T) and the maximum in n_e (τ_n) after pellet injection as a function of $\bar{\chi}_e$ and $\bar{D}_e$, averaged between r_p and the plasma edge. τ_T is obtained for different $\bar{\chi}_e$ and constant $\bar{D}_e$=0.9 m²/s which corresponds to τ_n=166 ms. In the models the density evolution is independent of T_e, and the coupling only affects the evolution of T_e. Therefore τ_n depends only on $\bar{D}_e$.

IMPURITY BEHAVIOR IN PELLET-FUELLED PLASMA OF JT-60

T.Sugie, H.Kubo, A.Sakasai, H.Yoshida, T.Hirayama, T.Nishitani, K.Nagashima, Y.Kawano, R. Yoshino, Y. Kamada, Y.Koide, N.Nishino*, H.Takeuchi and JT-60 Team

Naka Fusion Research Establishment, Japan Atomic Energy Research Institute, Naka-machi, Naka-gun, Ibaraki-ken, 311-01, Japan

* Energy Research Laboratory, Hitachi, Ltd. 1168 Moriyama-cho, Hitachi-shi, Ibaraki-ken, 316, Japan

Impurity behaviors in pellet fuelled plasmas were investigated in NB heated limiter discharges. The central soft X-ray signals and the intensity of the TiXXI line were decreased just after the pellet injection and after that kept on increasing until large sawtooth oscillation or large m=1 internal mode appeared. The time evolutions of the TiXXI line emission indicated that the density of the titanium ions increased in the central region of plasma.

1. Introduction

In pellet-fuelled JT-60 plasmas, peaked profiles of electron density and sawtooth-free plasmas were obtained, and the fusion product defined by $n_e(0)\tau_E T(0)$ achieved 1.2×10^{20} $m^{-3}\cdot s\cdot keV$ with NB heating [1]. Impurity behaviors of pellet fuelled plasmas were investigated in the hydrogen limiter discharges and the helium limiter discharges with high power (8-20 MW) NB heating. The impurity transport has been analyzed by a one-dimensional and time dependent impurity transport code [2].

2. Experimental observations and results

Time evolutions of the electron temperature and density profiles were measured by a Thomson scattering system in several repeated shots. The Z_{eff} values, impurity lines and soft X-ray emission were measured by visible monochromators, a crystal spectrometer, grazing incidence spectrometers and a PIN photo diode array with 250 μm beryllium windows. The radiation loss was also measured by a bolometer array.

2.1 Hydrogen pellet injection to the hydrogen limiter discharge

The hydrogen pellet injection experiments into the hydrogen limiter discharges were carried out with 8 MW NB heating under the condition of B_T =4.5 T and Ip=2.1 MA. The temporal evolutions of the electron density and temperature profiles are shown in Fig.1. The electron density remained a peaked profile at 200 msec (t=5.6sec) after the pellet injection (t=5.4 sec). Figures 2 (a) and (b) show the time evolutions of the central soft X-ray emission SX_{center} and TiXXI (2.6 Å), TiXX (259.3 Å) and TiXII (460.7 Å) line intensities, respectively. Figures 2 (c), (d), (e) and (f) show the time evolutions of the line integrated electron density n_el (r/a=0.6), NB power P_{NBI}, the central electron temperature Te(0), the central electron density $n_e(0)$, the line averaged visible Z_{eff} (r/a=0.6), and concentrations of carbon and oxygen. In these figures, the central soft X-ray signal and the TiXXI line intensity decreased just after the pellets injection and after that kept on increasing until the sawtooth oscillation appeared. The Z_{eff} values decreased from 2.5 to 1.5 just after the pellets injection and increased to 2.3 after one second. The carbon and oxygen concentrations were estimated by the Z_{eff} values and intensity ratios of CVI (33.7Å) to OVIII (18.97Å) lines [3], as shown in Fig.2(f). In this figure, closed squares and open squares indicate the carbon and oxygen

concentrations respectively. The carbon concentration n_c/n_e decreased from 3.5% of the electron density to 1% just after the pellets injection and the oxygen one n_o/n_e also decreased from 1% to 0.5%. We estimated soft X-ray intensity with using the fraction ratios of carbon and oxygen impurities.

In Fig. 2 (a), the open circles show the time evolution of the central soft X-ray signal which were numerically calculated by assuming dominant light impurities because of little contribution from Ti impurity (~ 0.001%). These values well simulated the measured one by the electron density peaking and the temperature recovering. On the other hand, it is difficult to explain the time evolution of the TiXXI line intensity without the increase of the central titanium ion density. It is roughly estimated that the density of Ti^{20+} ions at 6.2 sec is 1.5 times as high as that at 6.0 sec, because the central electron temperature and the density is almost constant as shown in Fig. 2 (d). This result indicates that the central density of titanium ions apparently increase until the sawtooth oscillation appears. The more detailed analysis has been carried out by the impurity transport code.

2.2 Hydrogen pellet injection to the helium limiter discharge

The hydrogen pellet injection experiments to the helium limiter discharges were carried out with high power (15-20MW) NB heating under the condition of B_T=4.8T and I_p=3.1MA. In these discharges, the large m=1 internal mode appeared. Before the large m=1 internal mode, the peaked electron density profile was kept for about one second after the last pellet injection, as shown in Fig. 3 and Fig. 4 (d). In Fig. 4 (a), the time evolutions of the central soft X-ray signal and the intensity of the TiXXI line decreased just after the pellet injection and after that kept on increasing until the large m=1 internal mode appeared. Since the central electron density and temperature are almost constant from 6.5 sec to 6.8 sec as shown in Fig. 4 (d), the density of the Ti^{20+}ions at 6.8 sec is roughly estimated to be twice as high as that at 6.5 sec. After the large m=1 internal mode appears at 7.05 sec, the density of the Ti^{20+}ions decrease. This means that the density of Ti^{20+} ions, which exist in the central region of plasma, increase until the large m=1 internal mode appears.

3. Summary

Impurity behaviors of pellet fuelled plasmas were investigated. The increase of the titanium ion density in the central region of plasma was observed and quenched, followed by appearing sawtooth oscillation or m=1 internal mode. The analysis by the impurity transport code is in progress.

References

[1] R. Yoshino, Y. Kamada, K. Shimizu, et al., JAERI-M 90-066 (1990).
[2] T. Hirayama, H. Shirai, K. Shimizu, et al., J. Nucl. Materials 145-147 (1987) 854.
[3] H. Kubo, T. Sugie, A. Sakasai, et al., Nucl. Fusion 29 (1989) 571.

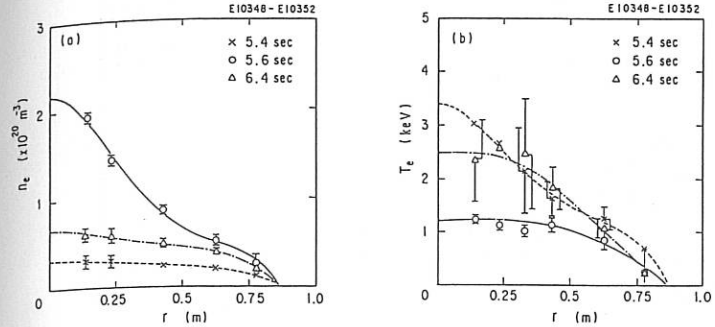

Fig. 1 Radial profiles of the electron density n_e and temperature T_e before the pellet injection (t=5.4 sec), and at 200 msec (t=5.6 sec) and 1.0 sec (t=6.4 sec) after the pellet injection in NB heated hydrogen limiter discharges.

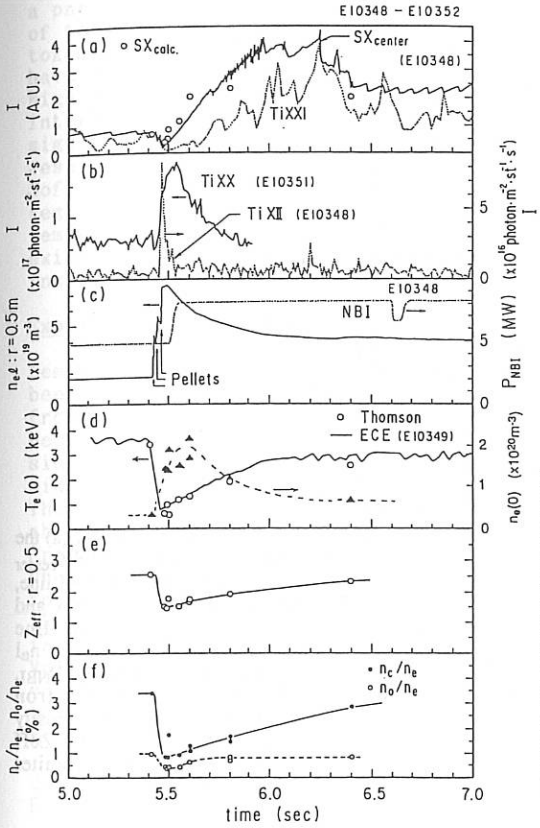

Fig. 2 Time evolutions of (a) the central soft X-ray signal SX_{center} and the intensity of TiXXI line, (b) the intensities of TiXX and TiXII lines, (c) the line integrated electron density n_el (r/a=0.6) and the NB_{power} P_{NBI}, (d) the central electron temperature $T_e(0)$ and density $n_e(0)$, (e) the visible Zeff (r/a=0.6), (f) the carbon concentration n_c/n_e and the oxygen concentration n_o/n_e. (In hydrogen limiter discharges)

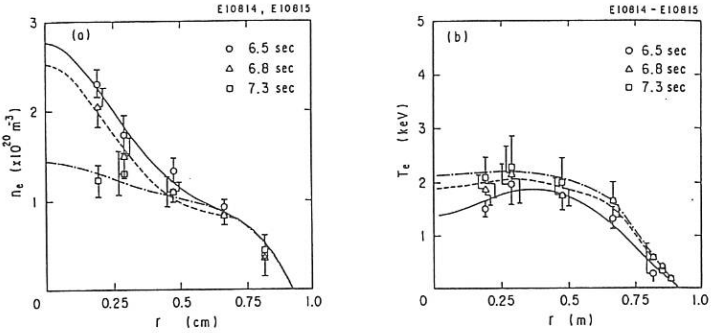

Fig. 3 Radial profiles of the electron density n_e and temperature T_e at 500 msec (t=6.5 sec), at 800 msec (t=6.8 sec) and 1.3 sec (t=7.3 sec) after the pellet injection in NB heated helium limiter discharges.

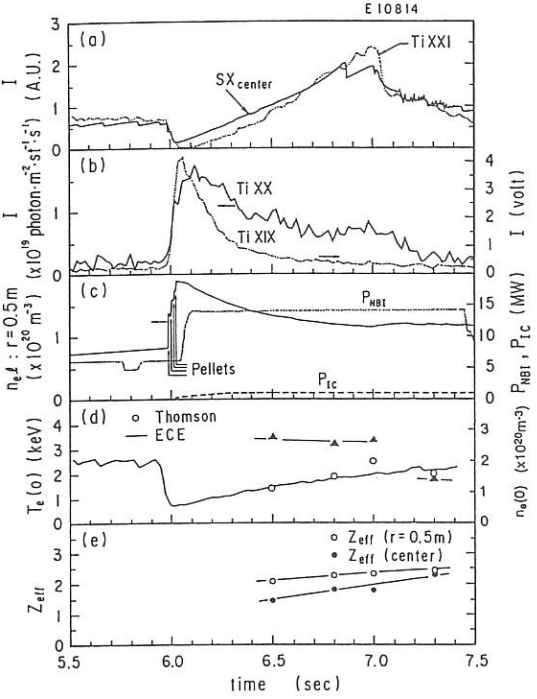

Fig. 4 Time evolutions of (a) the central soft X-ray signal SX_{center} and the intensity of TiXXI line, (b) the intensities of TiXX and TiXIX lines, (c) the line integrated electron density $n_e l$ (r/a=0.6) and the NB_{power} P_{NBI}, (d) the central electron temperature $T_e(0)$ and density $n_e(0)$, (e) the visible Zeff (r/a=0.6). (In helium limiter discharges)

FAST COOLING PHENOMENA WITH ICE PELLET INJECTION IN JIPP T-IIU TOKAMAK

M.Sakamoto, K.N.Sato, Y.Ogawa, K.Kawahata
S.Okajima*), S.Hirokura and JIPP T-IIU Group

National Institute for Fusion Science
Nagoya, 464-01, Japan
*)Department of Applied Physics, Chubu Univ.
Kasugai, 487, Japan

Introduction

Ice pellet injection experiments have been carried out with a pneumatic pellet injector in order to study thermal transport of toroidal plasma just after pellet injection in JIPP T-IIU tokamak. Electron temperature and electron density profiles have been measured by 10 ch. grating polychromator (ECE) with high time resolution (Δt= 2 μsec), and 6 ch. HCN laser interferometer, respectively. The cut-off problem of ECE signals due to density rise has been carefully avoided. The results from the ECE measurements as well as those from the Soft X-ray measurements show fast cooling phenomena inside $q<1$ region. Profile measurements of electron density and temperature just after the pellet injection suggest the existence of anomalously fast thermal conduction of the plasma inside the $q<1$ region.

Experimental Results

Figure 1(a) shows time evolution of the electron temperature at 10 different major radii when an ice pellet has been injected from low-field side into the plasma. Cooling front (the start of temperature decrease at each radius) has been indicated by arrows in the figure. Signals of high-field side decrease almost simultaneously with those of low-field side because of fast thermalization along magnetic field lines. These properties with toroidal symmetry will indicate the absence of cut-off problem of ECE signals due to density rise. Propagation of the cooling front is simply shown in Fig.1(b), where solid line is drawn by least squares method of 4 points for major radius larger than 95 cm. The cooling velocity Vc in the outer region is in the range of about 700m/s~1600m/s, which is comparable or slightly greater than the pellet velocity Vp(400m/s~700m/s). While in the central region, the propagation velocity is significantly greater than the velocity Vp. This behavior has also been observed in the case of soft X-ray signals by 6 ch. detector array(SXR) as shown in Fig.1(b).

In order to examine this fast cooling phenomena at the central region, the density profile is simultaneously measured. Figure 2 shows the electron temperature and density profiles

before and after the pellet injection. The pellet is mainly ablated at about half radius in this case and the density profile becomes a hollow one. The electron temperature in central region decreases quickly and the profile is symmetric with respect to the plasma center. On the other, the central density does not increase so quickly in sharp contrast to the fast decay of the central temperature. These experimental observations suggest that the fast cooling of the central region is attributed to the heat conduction rather than the particle convection.

A drastic change of the velocity Vc seems to occur around the q=1 surface, as shown in Fig.1(b). To examine relation between this position and q=1 surface, pellets have been injected into plasmas with various plasma currents or at the different phase of the sawtooth period. As shown in Fig.3(a), the propagation of ultra-fast cooling front occurs always inside the q=1 surface. On the other hand, when pellet is injected into the plasma with no sawtooth oscillation, cooling front propagates to the plasma center with a constant velocity in the same range with pellet velocity. These experimental observations may indicate the correlation between the q=1 surface and the starting region of propagation of the ultra-fast cooling front. As shown in Fig.3(b), the radius to start propagation normalized by radius of q=1 surface seems to correlate with the phase of sawtooth, where 0% and 100% means just after and just before sawtooth crash, respectively. Although the solid line has an offset, these characteristics might have some relation with sawtooth crash phenomena.

Conclusion

The investigation of ice pellet injection into JIPP T-IIU plasma has been carried out in order to study thermal transport of toroidal plasma.

The experimental results from multi-channel ECE measurements show the significantly fast propagation of cooling front inside the q=1 surface, where the experiments have been done so carefully as to avoid the cut-off problem of ECE signals due to the density rise after the pellet injection. This ultra-fast cooling phenomena has been confirmed also by the measurements of soft X-ray signals. From the simultaneous observations of density and temperature profiles just after the pellet injection, the fast cooling phenomena of the central region of the plasma may be attributed to the heat conduction rather than the particle convection.

In addition, the experiments have been carried out to study the relation of the fast cooling phenomena with the role of q=1 surface. Although the mechanism is not yet clear, the relation between this phenomena and characteristics of sawtooth crash has been suggested.

references

1) K.N.Sato et al.: ICPP '89 (New Delhi,1989) vol.I,p73.
2) TFR Group: Nucl. Fusion 27 (1987) 1975.
3) A.D.Cheetham et al.: 14th Europ. Conf. on Contr. Fusion and Plasma Physics(Madrid,1987) Vol.1, 205.

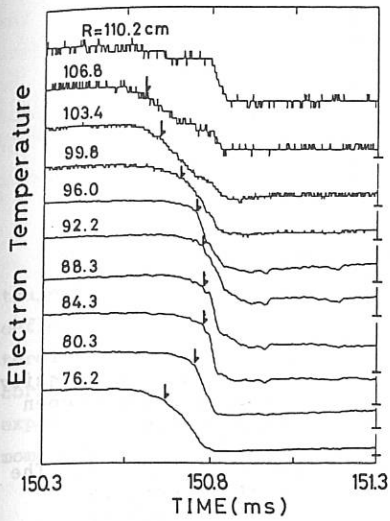

Fig. 1(a) Time evolution of the electron temperature with 10 ch. grating polychromator at different major radius. A pellet is injected from the large major-radius side.

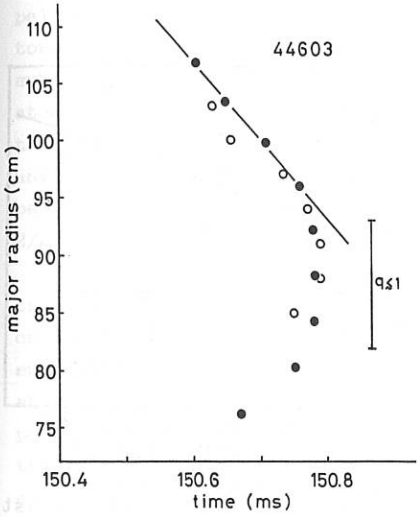

Fig.1 (b) Properties of cooling front measured with ECE (shown by arrows in Fig.1(a); closed circles) and SXR (open ones).

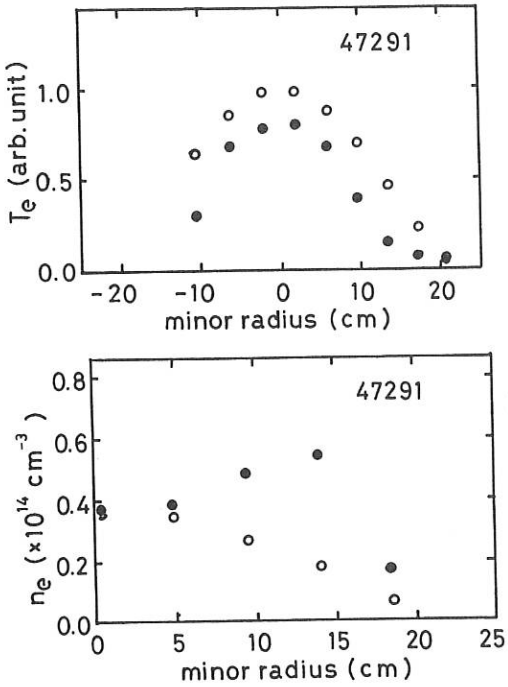

Fig.2 Electron temperature and density profiles before (open circles) and after(closed ones) pellet injection. The electron density profile has been measured with 6 ch. HCN laser interferometer.

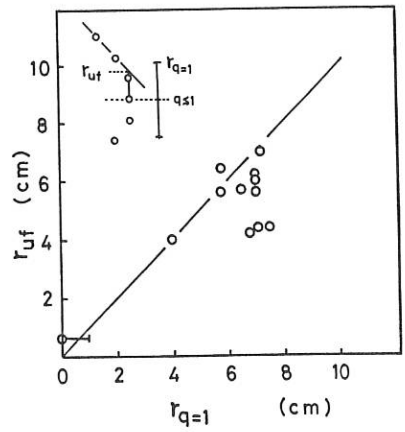

Fig.3(a) Comparison of the radius to start the ultra-fast cooling with that of q=1 surface.

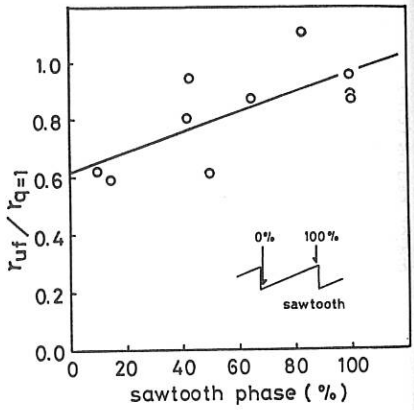

Fig.3(b) Radius to start propagation of the ultra-fast cooling, normalized by that of q=1 surface as a function of sawtooth phase.

THE PELLET TRAJECTORY TOROIDAL DEFLECTION IN T-10

A.A.Bagdasarov*, V.I.Bugarya*, N.L.Vasin*, S.M.Egorov,
B.V.Kuteev, I.V.Miroshnikov, V.Yu.Sergeev, S.N.Ushakov,
V.V.Chistijkov*

Kalinin Polytechnical Institute, Leningrad, USSR

* Kurchatov Institute of Atomic Energy, Moscow, USSR

The runaway electron diagnostics in tokamak using pellet trajectory toroidal deflection was proposed in reference [1]. This deflection is produced by the pressure difference along the toroidal direction during pellet ablation. The simplest situation corresponds to the free-molecular or adiabatic neutral cloud expansion. In this case, following [1] one can obtained the first momentum equation :

$$M_p(t)\frac{d V_{pz}}{d t} = \alpha_s(t) U_s m_c \frac{S_\perp(t)}{\varepsilon}\left[Q_e^-(t) - Q_e^+(t) \right] = \alpha_s U_s \frac{d M_p}{d t} \Psi \quad (1)$$

Here Q_e^+, Q_e^- are co- and counter-current heat fluxes onto the pellet surface; dM_p/dt, M_p, V_{pz} - mass evaporation rate, mass and toroidal velocity of the pellet; m_c, ε = 8.8 eV - atomic mass and sublimation energy of carbon; $U_s = (5kT_s/3m_c)^{1/2}$ - evaporated carbon atom velocity; $S_\perp$ - area of the pellet cross-section perpendicular to the magnetic field line; $\Psi = (Q_e^+ - Q_e^-) / (Q_e^+ + Q_e^-)$ - heat flux asymmetry factor; $\alpha_s = \langle \cos^2\vartheta \rangle$ with ϑ being the angle between the pellet surface normal and magnetic field. The α_s value vary from 2/3 for sphere to 1 for disk pellet form.

There are two circumstances simplifying the analysis of the trajectory deflection for carbon pellet in comparison with hydrogen ones. Firstly, electron heat fluxes incident onto the pellet surface $Q_e^{+,-}$ may be less than their values $Q_{e\infty}^{+,-}$ outside the ablation neutral and plasma clouds. It is known that the hydrogen pellet shielding being significant [2], it is not easy to calculate the shielding factor $\delta^{+,-} = Q_e^{+,-} / Q_{e\infty}^{+,-}$ and asymmetry factor Ψ . The evaporation of carbon pellets in T-10 plasma was described in the terms of the neutral shielding model with $\delta \sim \delta^+ \sim \delta^- \sim 1$ [3,4]. In this case the asymmetry of heat fluxes can be approximated by

undisturbed value $\Psi_o = (Q^+_{eo} - Q^-_{eo})/(Q^+_{eo} + Q^-_{eo})$. Secondly, the evaporation rate $\dot{N}$ being known the carbon pellet surface temperature T_s (5000 °K) and velocity U_s ($2.4 \cdot 10^5$ cm/s) may be calculated [3,4]. In the case of hydrogen pellet ablation the cloud heating by the incident electrons is strong, so the calculation of pressure difference on the pellet surface during evaporation makes a rather complicated hydrodynamics problem.

The values of $M_p(t)$ and dM_p/dt in (1) can be derived using an experimental evaporation rate $\dot{N}(t)$. Thus we calculated asymmetry factor Ψ by means of the pellet toroidal deflection. We also obtained separately Q^+_e and Q^-_e values using the equation for pellet ablation rate

$$\frac{dM_p}{dt} = - m_c \cdot \dot{N} = - m_c \cdot \frac{Q^+_e + Q^-_e}{\varepsilon} \cdot S_\perp \quad (2)$$

Besides we assumed the cross-section area to be

$$S_\perp(t) = \pi r^2_{po} \cdot \left\{ 1 - \left[\frac{1}{2 r_{po} n_c \varepsilon} \cdot \int_o^t [\, Q^+_e(t') + Q^-_e(t') \,]\, dt' \right]^2 \right\}, \quad (3)$$

that can be derived considering that the heat fluxes $Q^{+,-}_e$ onto the pellet surface projection normal to the magnetic field line to be uniform.

Fig.1 presents the scheme of experiment as well as a photograph of carbon pellet moving along the vertical axis of T-10 tokamak. The photograph was taken in the direction perpendicular to pellet trajectory plane in visible spectral range during the whole evaporation time.

In Fig.2 the heat flux $(Q^+_e + Q^-_e)/2$ and asymmetry factor Ψ for shot #47877 with I_p = 306 kA, B_t = 2.76 T, a_l = 32 cm, q_l = 3.2 and $\bar{n}_e = 1.5 \cdot 10^{13}\,cm^{-3}$ are shown. Corresponding evaporation rate curve, the pellet trajectory and the toroidal acceleration are shown as well. Pellet injection was performed during the ECRH pulse. A good agreement between the experimental ablation rate and the calculated ones obtained using the neutral shielding ablation model [3] allows to estimate asymmetry Ψ_o and compare one with Ψ values.

The asymmetry of electron heat and particle fluxes in strongly influenced by the ratio $\gamma = E/E_d$ of electric field E to Driecer field $E_d = 4\pi e^3 n_e \ln\Lambda / T_e$ [5]. Taking into consideration that in fact

$\gamma \sim 0.03 << 1$, we used the classic representation for particle ($j/e = n_e u$) and heat ($q_e = 5n_e T_e u/2 + f(Z_{eff}) n_e T_e u$) fluxes in fully ionized plasma [6]. The weak function $f(Z_{eff})$ is tabulated in [6]: $f(1)= 0.71$; $f(2)= 0.9$; $f(3)= 1.0$. Thus the heat flux asymmetry due to the current density $j(r)$ is

$$\Psi_o(r) = -\frac{q_e}{2\,Q_i} = -\frac{(2.5+ f(Z_{eff}))\cdot j(0)}{\sqrt{8T_e(r)/\pi/m_e}\; n_e(r)\cdot e} \cdot \frac{Z_{eff}(0)}{Z_{eff}(r)} \cdot \left[\frac{T_e(r)}{T_e(0)}\right]^{3/2}, \quad (4)$$

where $Q_i = n_e V_{Te} T_e/2$ is a Maxwellian heat flux. The current density value $j(0)$ in (4) was derived from the total plasma current I_p under the assumption of $Z_{eff} = const(r)$. The absolute value of Z_{eff} in our experiments never exceeded 1.7.

It is evident from Fig.2c that Ψ_o values exceed the experimental ones. This disagreement increases while the pellet penetrates into the plasma. It seems amazing, as one could rather expect the experimental value to be greater due to some other effects (such as runaways) that were not taken into consideration. This kind of mismatch may arise from several reasons. The first one is the influence of $Z_{eff}(r)$, that is hardly known within plasma periphery. However, reasonably changing of Z_{eff} profile can't reduce the current density and Ψ_o values within the evaporation region more than 30-50 %. The second one can be due to the ablation and acceleration models being more sophisticated, so that to reduce Ψ in according to Ψ values.

References.

1. V.Andersen, 12th European conference on Controlled Fusion and Plasma Physics, Budapest, Sept.1985,V.9F, part 2, p.648.
2. P.B.Parks et al., Nuclear Fusion, 1977, V.17, No.5, p.539.
3. B.V.Kuteev et al., Sov.J.Plasma Phys., 1984, V.10, No.6, p.675.
4. P.B.Parks et al., Nuclear Fusion, 1988, V.28, No.3, p.477.
5. A.V.Gurevich et al., Sov.J.Plasma Phys., 1979, V.5, No.4, p.777.
6. S.I.Braginsky, in Rev of Plasma Phys., V.1, Consult.Bureau, N.Y., 1965, p.205.

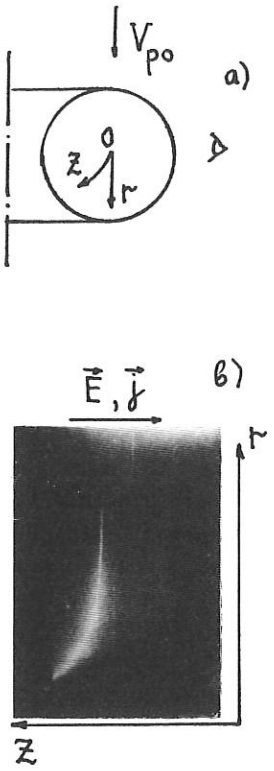

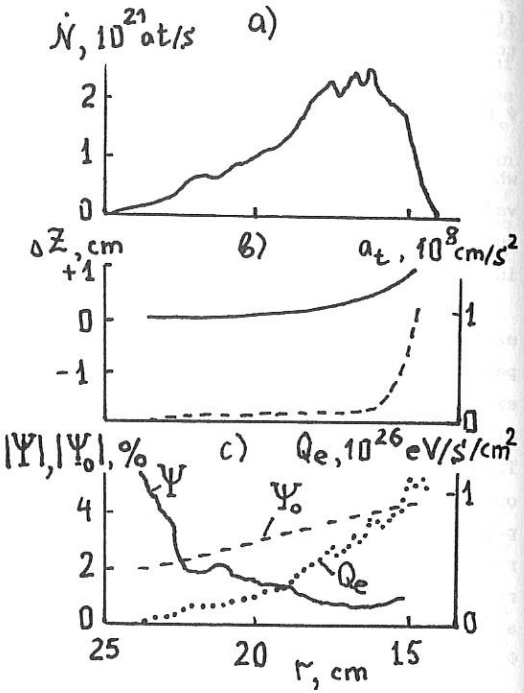

Fig. 1

a) The scheme of experiments on the T-10 tokamak

b) The photograph of carbon pellet trajectory

Fig.2

a) ——— ablation rate

b) ——— experimental pellet trajectory

- - - pellet toroidal acceleration a_t

c) ····· heat flux $Q_e = (Q_e^+ + Q_e^-)/ 2$

——— experimental asymmetry factor Ψ

- - - calculated asymmetry factor Ψ_o

SCALING OF EXPERIMENTALLY DETERMINED PELLET PENETRATION DEPTHS ON ASDEX

R. Loch, W. Sandmann, K. Büchl, R. Lang, V. Mertens

Max-Planck-Institut für Plasmaphysik, EURATOM Association
D-8046 Garching, Fed. Rep. Germany

1) Introduction

During the last decade injection of pellets has been established in a number of laboratories to refill a plasma discharge and improve plasma performances such as the density limit and global confinement times.
The improvement of confinement properties is closely connected with the achievement of peaked density profiles /1/. To establish peaked profiles, it is favourable if the injected pellets penetrate deep enough into the plasma. Especially the scaling to future fusion-relevant tokamaks raises the question of the required pellet velocities for the design of pellet injectors.
Parallel to this, great efforts were made to understand the theory of pellet ablation in a plasma. The commonly used theory for pellet ablation, the Neutral Gas Shielding (NGS) model of Parks et al. and Milora et al. /2,3/, describes the ablation rate as a function of the plasma parameters T_e, n_e, and the pellet mass m_p and velocity v_p. In a later extension of this theory the effect of the shielding due to the ablated cold plasma was included /4/, resulting mainly in a weaker scaling of the penetration depth with the pellet velocity /5/.
In this paper we compare experimentally determined penetration depths on ASDEX with a simple scaling law on the basis of the NGS ablation theory and the additional assumption of linear T_e and n_e profiles, like Büchl et al. /6/.

2) Model of a simple scaling law for pellet penetration depths

If one assumes linear profiles for both the electron temperature and density ($T_e(r) = T_{e0} \cdot (1 - r/a); n_e(r) = n_{e0} \cdot (1 - r/a)$; minor radius a = 40 cm), the integration over the whole ablation process can be solved analytically, if the pellet velocity v_p remains constant. For the penetration depths d one than gets the result /6/

$$d \sim Z^{1/3} \qquad with \qquad Z = \frac{v_p \cdot m_p^{5/9}}{T_{e0}^{5/3} \cdot n_{e0}^{1/3}} \quad ,$$

where T_{e0}, n_{e0} stand for the electron temperature and density in the plasma centre.
The typical temperature profiles for ohmic, NI- and ICRH-heated discharges with q > 2.3 are shown in fig. 1. It can be seen that the assumption fits quite well for ICRH discharges, whereas for ohmic and NI-heated discharges for r < 0.5a the profile begins to flatten.
The assumption of a linear density profile is not critical for the model because the ablation rate is rather insensitive to changes in density compared with changes in temperature. The temperature enters with a higher exponent in the ablation rate than the density.

3) Experimental technique

In ASDEX the pellets were injected with a centrifuge pellet accelerator with a maximum speed of about 700 m/s and a maximum repetition rate of 50 Hz. The actual velocity was measured with a light barrier technique with a precision of better than 1%. The masses of the pellets were varied from 0.1 to 1.5 $\cdot 10^{20}$ atoms and were measured by a microwave detector with an error of about 10%.

The pellet penetration was determined by the H_α radiation which was emitted during the ablation process and measured with fast photodiodes. A typical example of the emitted H_α signal is given in fig. 2. The penetration depth is calculated from the temporal duration of H_α emission and the measured pellet velocity with curvature of the pellet trace in the plasma and changes of the pellet velocity being neglected. Additionally, photos of the pellet ablation trace were taken to identify significant deflection of the pellet.

The plasma temperature and density were measured with the 60 Hz Thomson scattering diagnostic. The accuracy of the data for the central electron temperature and density is about 5%. The range covered by the experimental data varied for the central temperature from 0.5 to 1.5 keV and for the density from 0.3 to $1.5 \cdot 10^{20} m^{-3}$.

4) Results

Several hundred pellets were injected into ohmic and additionally heated discharges (L-mode). The results of the experimentally determined penetration depths plotted versus the logarithmic scaling parameter Z are shown in fig. 3. The error of the penetration depth is about 1 cm if one neglects effects of deflection and deceleration. Comparison with photographic measurements shows significant discrepancies only for high-power NI heating, where interaction with fast ions can result in a change of the transverse velocity of the pellet. The error in Z is about 15% and originates mainly from the pellet mass determination and uncertainties in the plasma temperature.

The data were analysed with the SAS statistic program package /7/. The results of a fit $d \sim Z^\alpha$ are given in table 1. For $q \geq 2.3$, where the temperature profile can be well approximated by a linear profile, the fitted exponents α are in good agreement with our simple model, which gives $\alpha = 1/3$. For low q values of about 2.0 there is a significant change in the temperature profile, which becomes broader (see fig. 1). In this case the assumption of linearity only holds until about r = a/2, whereas towards the centre the temperature profile flattens. Therefore our linear ansatz for these profiles gives too low temperature values for r < 0.5 a. As an approach to the profile effects we included the safety parameter q in our statistical analysis:

$$d \sim Z^\alpha \cdot q^\beta \quad ,$$

which results in a scaling of the penetration depth with $q^{0.5}$.

In a second step we analysed the statistical scaling of the penetration depht with the pellet parameters v_p and m_p. The results are $d \sim v_p^{0.31} \cdot m_p^{0.26}$ for ohmic and $d \sim v_p^{0.35} \cdot m_p^{0.28}$ for NI-heated discharges. This is again in reasonable agreement with the theoretical prediction arising from the NGS theory and our model of linear profiles, which gives $d \sim v_p^{0.33} \cdot m_p^{0.19}$. The slightly higher exponent in the pellet mass may result from the shape of the pellet, which differs from the assumed spherical form.

5) Discussion

For ohmic and NI-heated discharges with $q \geq 2.3$ as well as ICRH-heated discharges, where the assumption of linear temperature profiles holds quite well, the results of our statistical analysis is in good agreement with the scaling law based on our simple model.

In the case of OH- and NI-heated discharges with low q, the temperature profile shows a significant q-dependence and the flattening of the temperature profile towards the plasma centre has to be taken into account especially for low q values. In our simple scaling law this effect was included by the additional factor $q^{1/2}$.

The agreement between the predicted scaling law of our model and the experimental data becomes even better if one corrects the assumed power law $d(r_p)/dt \sim T_e^{5/3}$ in the ablation theory of Parks et al. in the range 100 eV $< T_e <$ 600 eV to $T_e^{1.44}$ according to Chang and Thomson /8/. This leads to a somewhat higher exponent α between 0.33 and 0.37 in the prediction.

References

/1/ M. Kaufmann et al. Nucl. Fus. 28 (1988) 827
/2/ P. Parks et al. Nucl. Fus. 17 (1977) 539
/3/ S. Milora et al. IEEE Trans. Plasma Sci. PS-6 (1978) 578
/4/ W. Houlberg et al. Nucl. Fus. 28 (1988) 595
/5/ W. Houlberg Pellet Workshop in Proc. of "Pellet-Injection and Torroidal Confinement" Workshop IAEA-TECDOC-534 Gut Ising, FRG (1988) 217
/6/ K. Büchl et al. Nucl. Fus. 27 (1987) 1939
/7/ SAS Statistics, SAS Institute Inc., Cary, N. Carolina (1985)
/8/ C. Chang et al. Proc. 12. Europ. Conf. on Plasma Phys. Budapest (1985) 656

	$d \sim Z^\alpha$		$d \sim Z^\alpha\, q^\beta$	
	$q > 2.3$	$q \approx 2.0$		
OH	$\alpha = 0.38(3)$	$\alpha = 0.37(3)$	$\alpha = 0.34(2)$	$\beta = 0.53(4)$
NI	$\alpha = 0.34(2)$	$\alpha = 0.32(2)$	$\alpha = 0.38(2)$	$\beta = 0.54(6)$
ICRH	$\alpha = 0.35(4)$			

table 1 : results of the statistical analysis
the number in parenthesis gives the error in the last figure.

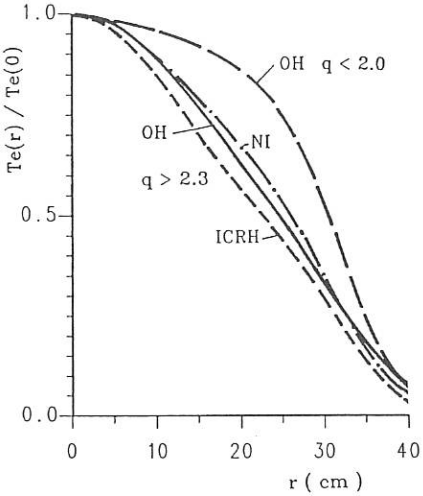

Fig. 1 : measured electron temperature profiles on ASDEX

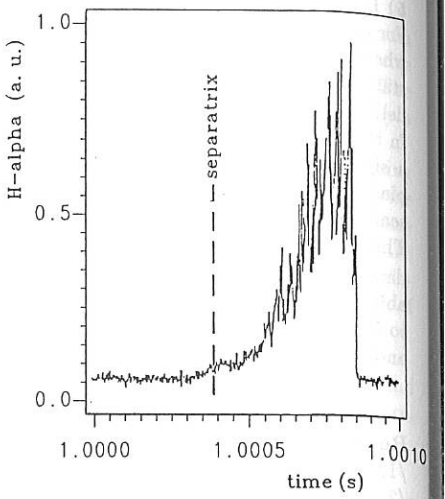

Fig. 2 : H_α signal of a pellet injected into an ohmic discharge

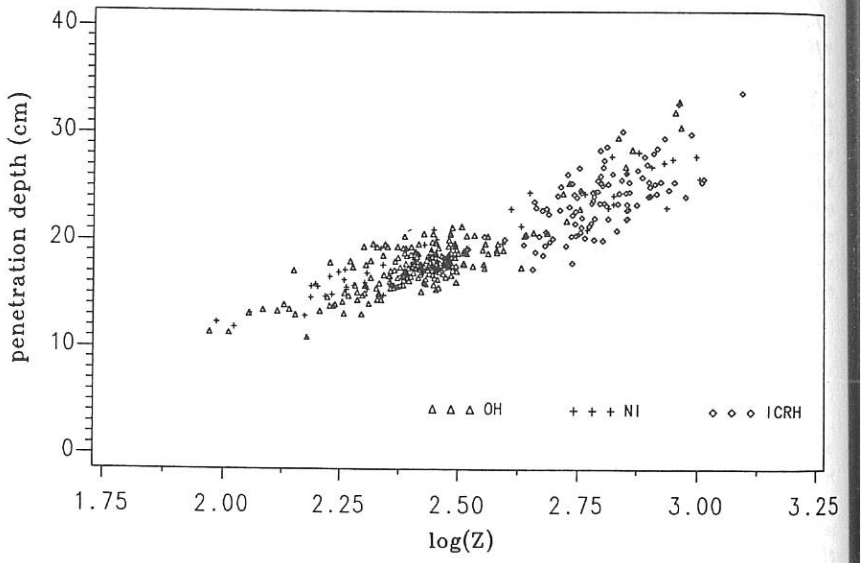

Fig. 3 : Plot of measured pellet penetration depths vs. log(Z)

REPETITIVE PELLET INJECTION COMBINED WITH ION CYCLOTRON RESONANCE HEATING IN ASDEX

J.-M.Noterdaeme, R.Büchse, R.Lang, R.Loch, V.Mertens, F.Ryter, W.Sandmann, F.Wesner, ICRH Team, Pellet Team, ASDEX Team

Max-Planck-Institut für Plasmaphysik
Euratom Association - D 8046 Garching - Fed.Rep.Germany

Introduction Deuterium pellets were injected into ICRF heated discharges (both second harmonic heating and hydrogen minority heating scenarios) with repetition rates between 12 and 30 Hz. The ICRH power deposited in the plasma was increased up to 1.0 MW. Large improvements in the energy content of the plasma could be obtained. In particular with second harmonic heating at P_{tot} = 1 MW and high plasma current (460 kA), confinement times of 100 ms were achieved; this is similar to pellets into an OH plasma, 50 % higher than ohmic and a factor 2 above L-mode. For discharges with successful density and energy content increase a correlation was found at the saturation between the m=1 sawtooth precursor activity at the pellet time point and the energy increase due to the pellet. The machine was boronized.

Second harmonic heating ASDEX discharges (R=1.67m, a=0.4 m, B_t=2.3 T, I_p=380-460 kA) heated with hydrogen second harmonic ICRF (67 MHz) were refuelled with D pellets (up to 20, 5 x 10^{19} atoms, 600 m/s), see also [1]; this is in contrast to injecting the pellets first and then heating the plasma. At low power the density peaks, with a large increase of the stored energy (Fig. 1).

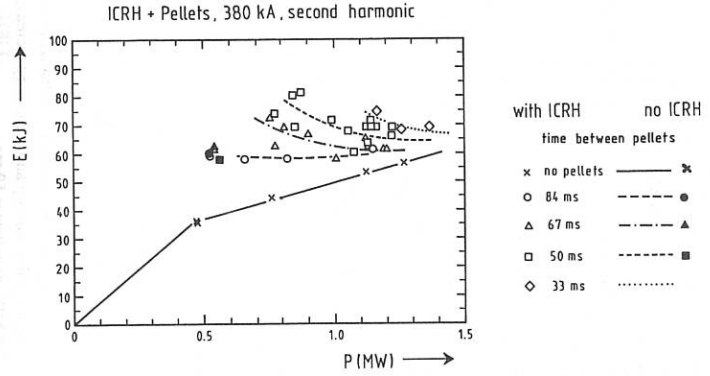

Fig.1. Total stored energy versus total deposited power ($P_{tot} = P_{OH} + 0.6\ P_{ICRH,coupled}$) into the plasma for discharges with 380 kA plasma current and second harmonic heating. The reduction of the energy content at high power can be partially compensated by shortening the time between pellets.

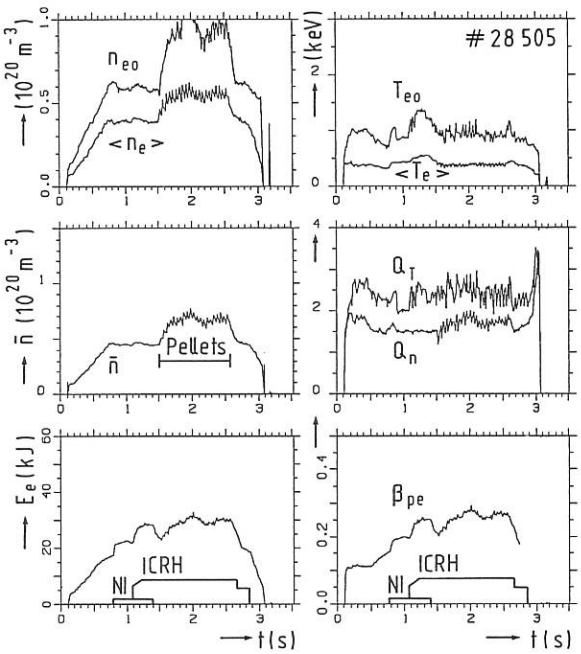

Fig 2a. Time traces for a discharge where the density was successfully built up and the energy increased. Ip=380 kA, Ptot = 1 MW, dt pellets = 50 ms.

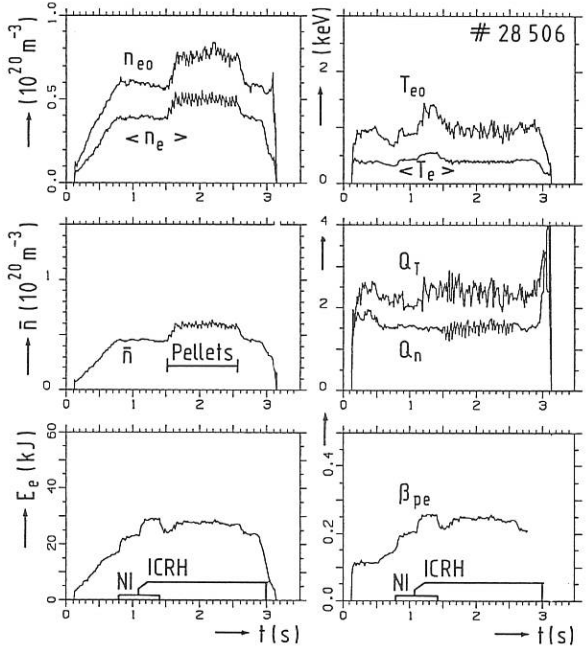

Fig. 2b. Time traces for a discharge where the density could not be markedly improved. All external parameter settings were identical to the discharge of Fig 2a. except for a 1 cm outward shift of the plasma.

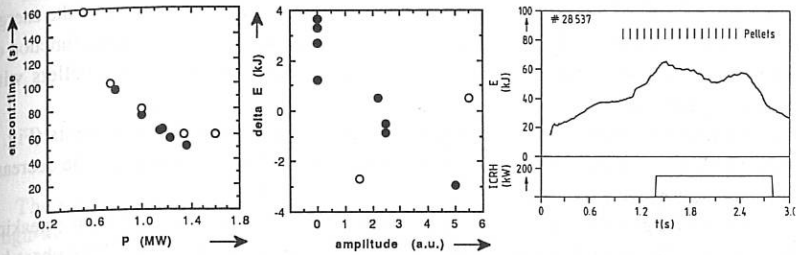

Fig. 3. Confinement time vs power for pellet refuelled discharges. Indicated are (●) ICRH heated discharges at a line averaged density of 0.9×10^{20} m^{-3}, and for comparison, (O) NI heated discharges [2], at 1×10^{20} m^{-3}.

Fig. 4. Change in energy content due to a pellet as a function of the m=1 amplitude

Fig 6. Time traces for a discharge where the pellets were injected first, and the discharge then heated.

At higher power and low repetition rate, the peaking and resulting increase in energy would be gradually lost. It could however be recovered by increasing the repetition rate of the pellets. Penetration depths of the pellets range from 19 to 27 cm (the radius of the q=1 surface for 380 kA is typically 13 cm). The ability to peak the discharge and increase the central density (Fig. 2) seems to be related to a reduction in sawtooth frequency and possibly the ability to deposit the pellet mass closer to the center. The increase in stored energy is directly related to the increase in central density (and the peaking factor). Fig 3. shows the confinement time as a function of power at constant density. The discharges are still sawtoothing and no impurity accumulation is observed.

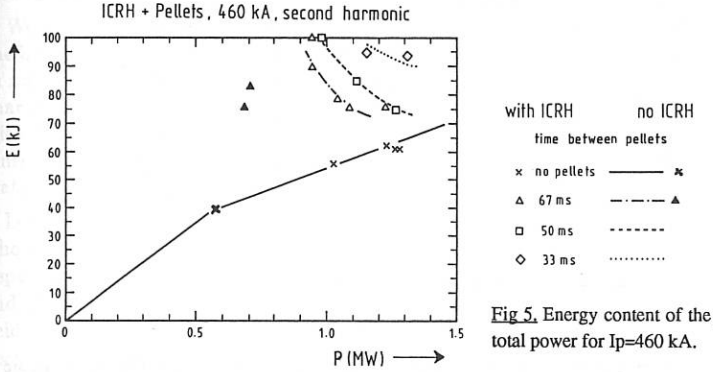

Fig 5. Energy content of the plasma vs total power for Ip=460 kA.

For discharges with successful density increase (Fig. 2a) and improved confinement a strong m=1 activity develops prior to the sawtooth crash. If the pellet comes into the discharge at a time when this strong activity is present, then the pellet often triggers the sawtooth crash, further energy improvement is halted and even reversed (Fig 2a, t=2s). Under some conditions, the phasing of the sawteeth with respect to the pellet time can be such that the sawtooth crash occurs some time prior to the injection of the pellet. At the pellet

time the amplitude of the m=1 oscillation is small or zero and a further increase of the energy is possible (Fig 2a, t>2.2s). Fig 4. shows the energy increase due to a pellet as a function of the m=1 amplitude in which the pellet is injected. The two outliers are pellets with particularly low mass.

The highest values of stored energy were obtained at higher plasma currents (Fig. 5 with values up to 100 kJ, and a confinement time of up to 100 ms, at 460 kA). The decrease with power, however, seems to be steeper.

In a discharge where the pellets were injected first, followed by the ICRH, the peaking obtained with the pellets in the ohmic phase was lost at the beginning of the ICRH phase but started slowly to recover after a while (Fig. 6). Due to pulse length limitations, it is unclear as to whether the discharge would develop fully as in the case where the discharge was first heated and pellets injected into the heated discharge.

Minority heating Deuterium pellets were also combined with H minority heating in He. The improvement with respect to the L-mode is smaller than in the case of second harmonic heating. The peaking factors did not achieve the high values obtained with second harmonic heating. Shown in Fig. 7 is the plasma energy content vs total power for different timing of the pellet injection. Included are also for comparison, points of ICRF heated discharges at constant density, and ICRF heated discharges where a density increase was forced through strong gas puffing. A slight improvement of the energy content is obtained at the higher densities, a further slight improvement can be obtained with the pellets.

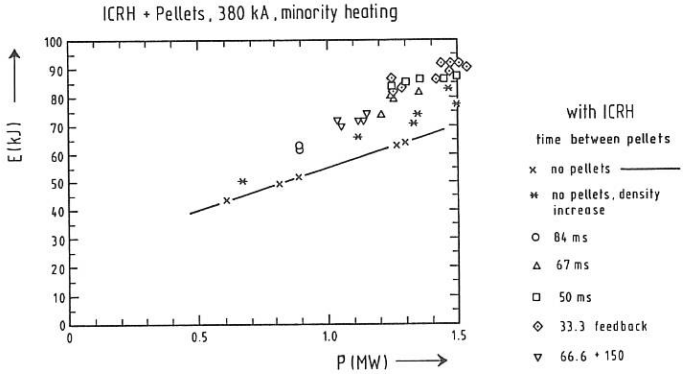

Fig. 7. Energy content of the plasma vs total power, minority heating, Ip= 380 kA. Points are also shown with gas refuelled ICRH discharges at constant density (x) and gas refuelled, forced density increase ICRH discharges (⊛). For the data points (◈), the effective frequency of the pellets was feedback controlled with the central density. At low power it was close to 100 ms, at high power close to 33.3 ms.

References

[1] J.-M.Noterdaeme, F.Ryter et al., Plasma Phys.Contr.Nucl.Fusion, (IAEA Nice 1988), Vol 1 (1988) 583
[2] V.Mertens et al., Europhys. Conf. Abstr.(EPS Dubrovnik 1988), Vol 12B, I (1988) 39

EVOLUTION OF PELLET CLOUDS AND CLOUD STRUCTURES IN MAGNETICALLY CONFINED PLASMAS

L.L. Lengyel and G. Zavala

Max-Planck-Institut für Plasmaphysik, EURATOM Association
D-8046 Garching, Fed. Rep. Germany

The subject of this study is the spatial and time evolution of initially low-temperature high-density particle clouds in magnetically confined hot plasmas, such as those produced by ablating cryogenic hydrogen pellets in fusion machines. Particular attention is given to such physical processes as heating of the cloud by the energy fluxes carried by incident plasma particles (classical flux-limited energy transport by thermal electrons along the magnetic field lines, anomalous heat conduction across them), gasdynamic expansion with $\vec{j} \times \vec{B}$-produced deceleration in the transverse direction, finite-rate ionization and recombination (collisional and radiative) processes, and magnetic field convection and diffusion. The Lagrangian approximation used allows one to take into account all relevant physical processes that affect the radial expansion and deceleration of the cloud particles, including the change of the magnetic field topology [1].

Numerous scenario calculations were made with systematic variation of the four basic input parameters: $\dot{N}_{src}$, n_{e0}, T_{e0}, and B_0 (representing particle source strength, undisturbed plasma parameters, and magnetic field strength, respectively). In each scenario run, the radial distributions of all relevant cloud parameters were computed in a self-consistent way. The cloud characteristics were monitored at the moment of reaching the maximum cloud radius, and at time instants after the quasi-steady state had been reached (i.e. at 10 μs and 20 μs of the cloud expansion time).

We shall give here a brief description of the effects of the major input parameters on the basic cloud characteristics, as seen from the results of calculations. One should bear in mind that the basic cloud parameter that was found to affect all other quasi-steady characteristics is the stopping or confinement radius. The stopping time associated with the radial confinement of the plasmoid ($\tau(R_{cld} = R_{max})$) is closely related to the ionization time of the outer plasmoid layer and is a complex function of various factors (rate of mass deposition, heat input rate, and magnetic field strength).

Let us now consider the effect of the rate of mass release or particle source strength. The results of calculations show that the cloud radius increases as the number of particles deposited. This is so because it takes longer to ionize a larger number of neutral particles and thus the cloud has a longer time to expand before interaction with the magnetic field begins. The bulk (mass-averaged) cloud temperature of the plasmoid notably decreases whereas the average density increases with increasing mass deposition rate, the latter in spite of the larger cloud cross-sections inherent at higher deposition rates. The bulk ionization degree attained at the moment of radial confinement decreases with increasing source strength. It is noteworthy that the radial expansion of the plasmoid comes to a full stop at relatively low average ionization degree values. Of course, the outer plasmoid layer is already ionized at this time. With regard to the effect of the source strength on the diamagnetic state of the cloud, the results show that the average

magnetic field trapped at the moment of radial confinement decreases with increasing source strength. This is a consequence of the larger initial radial momentum gained in the absence of early ionization: after a frozen-in state has been reached at the plasma periphery, the expanding neutral core continues to push this ionized layer outward, thus further reducing the average magnetic field inside the cloud.

With regard to heat flux (background plasma parameters) and magnetic field effects, the time necessary for ionization of the outer plasmoid shells is a function of the balance between the deposition rate of the cold particles and the heat flux available for heating and ionizing these particles. On the other hand, the confinement radius of the plasmoid layers (and thus the value of all quasi-steady plasmoid parameters) is defined by the balance between the pressure build-up (pressure gradients) and the retarding $\vec{j} \times \vec{B}$ forces, both of which are again functions of the energy input rate (the latter through the electrical conductivity value). In addition, the retarding force is also a function of the magnetic field strength and its distribution as well. The results of calculations show that the "quasi-steady" plasmoid properties are complex functions of all these parameters combined. At low and intermediate plasma temperatures ($T_e^{\infty} \simeq 5$ keV for the set of representative pellet and plasma parameters considered), the ionization time and hence the vacuum expansion time preceding the moment of interaction with the magnetic field rapidly decrease with increasing incident heat flux. At the same time, the rate of pressure build-up is not sufficient to balance the $\vec{j} \times \vec{B}$ force (except at rather low magnetic field strengths), and the maximum attainable plasmoid radius continuously decreases with increasing plasma temperature. The stronger the magnetic field, the more pronounced is this effect. At higher energy input rates the pressure build-up is sufficient to prevent further radius reduction or even makes the plasmoid radius grow slightly as the ambient plasma temperature, in spite of the reduced ionization time. The variations of both the maximum attainable and the "quasi-steady" plasmoid radii with the strength of the magnetic field applied are quite pronounced: the stronger the magnetic field the smaller is the stopping radius. The dependence of the average plasmoid density and the bulk plasmoid temperature on the magnetic field strength (i.e. on the magnitude of the stopping radius) is pronounced: the higher the m.f. strength, and thus the smaller the plasmoid radius, the higher is the bulk plasmoid density and the lower is the bulk plasmoid temperature. The plasmoid density, just as the plasmoid radius, is a relatively weak function of the background plasma temperature. More pronounced is the heat flux dependence of the bulk plasmoid temperature. With regard to the diamagnetic state of the plasmoid, the plasmoid becomes pronouncedly diamagnetic when subjected to higher heat fluxes (plasma temperatures), particularly at lower magnetic field strengths. The reason for such behaviour is obvious: higher plasma temperatures means shorter ionization times at the plasma periphery; hence a frozen-in state is reached at an earlier time instant. Furthermore, lower applied magnetic field strengths allow further gasdynamic expansion during the frozen-in state.

The major results of these computations may be summarized as follows (for further details see [1]):

(a) Field-aligned structures

The separation distance between the field-aligned inhomogeneities evolving during the cloud expansion and ionization phases is related to the only characteristic length inherent in this process: the ionization radius. Gaussian (peaked) density profiles and inverted (hollow) temperature profiles result with function value variation of about two orders of magnitude from the plasmoid centre to the plasmoid periphery (see Fig. 1). Also the structure of the field-aligned flutes that develop at the plasmoid boundary coincides, at some time instant, with an $m = 2$ poloidal disturbance pattern, again with the ionization (confinement) radius as characteristic separation length between them. The lifetime of these structures is measured on hydrodynamic and resistive diffusion time scales.

(b) Effect of pellet motion

Since the average expansion velocity of the cloud surrounding the pellet is usually much larger than the pellet flight velocity, a pellet crossing its own ablatant cloud is not likely to affect the cloud structure as long as it is not in direct contact with the high-temperature ionized outer shell. However, during passage through the ionization layer, however short this time period may be, the pellet is exposed to heat fluxes that may be considerably higher than those experienced in the interior of the cloud. Once the pellet is outside the ionization shell, a new low-temperature gas bubble is blown around it and the cloud evolution is expected to repeat itself. Obviously, the ablation rate and the associated cloud expansion dynamics may become strongly modulated by the periodic passages through the high-temperature cloud layers. The alteration of the cloud expansion dynamics and of the ablation rate during the pellet flight across the ionization shell has not yet been quantitatively clarified. Similarly, also the cloud structures associated with pellet velocities comparable to cloud expansion velocities remain to be investigated.

(c) Consequences for pellet ablation models

There are no simple or analytical means of quantitatively predicting the physical properties of shielding clouds surrounding ablating pellets. It is possible, of course, by making rather drastic simplifying assumptions regarding the shielding effect, to derive some scaling laws for the pellet penetration depth, but no reliable predictions can be made on the basis of these laws. It is also possible to set up empirical or semi-empirical relations for the ablation rate and to validate these models (i.e. to select the values of some free parameters entering these relations) on the basis of experimental results. These models cannot, however, be applied, with a sufficent degree of certainty, to predictive calculations either. Experience shows that validating ablation models and fitting calculated pellet penetration depths, density profiles, etc. to measured ones are rather difficult tasks. Uncertainties and/or scattering in some of the crucial experimental data, such as the actual pellet mass interacting with the plasma, the true pellet velocity and its possible temporal variation, the electron temperature profile immediately prior to pellet injection, etc., make validation rather difficult. Ablation rates and pellet penetration depths observed in different tokamaks were reproduced by means of different ablation models, which, however, are not supposed to be machine-specific. The experimental observations of Durst et al. [2] and others, as well as the results of the present and previous calculations, indicate that ablation is an inherently transient process determined on the whole by the evolution of the shielding cloud around it and by the modulation of

the cloud characteristics (in space and time) by the presence of the magnetic field (the magnetic confinement of the ionized fraction of the cloud). Hence an ablation model that is predestined for predictive pellet penetration calculations in fusion-grade plasmas should take these aspects into account. Besides, the development of such a model should be accompanied by experiments with accurate measurements of all essential data concerning not only the pellet-plasma interaction but also the shielding cloud evolution processes. The shielding cloud models, too, need verification or validation.

REFERENCES

[1] L.L. Lengyel, G.G. Zavala, and O. Kardaun, manuscript submitted to Nuclear Fusion.

[2] R.D. Durst, "An Experimental investigation of the Dynamics of Pellet Ablation on the Texas Experimental Tokamak", Ph. D. Thesis, The University of Texas, Austin, Texas, 1988.

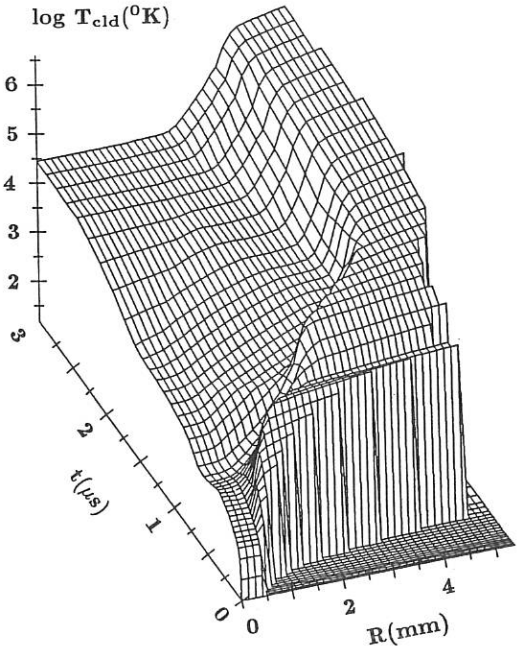

Figure 1: Time evolution of the radial temperature profile in the cloud for a typical particle deposition scenario.

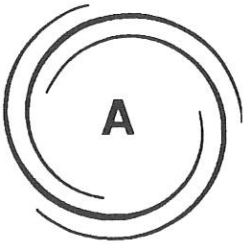

TOKAMAKS

A6 H-MODE

TRANSPORT OF IMPURITIES DURING H-MODE PULSES IN JET

R. Giannella, L. Lauro Taroni# , R. Barnsley+ , N. Gottardi , N.C. Hawkes*,
K. Lawson*, F. Mompean, H. Morsi, D. Pasini, D. Stork

JET Joint Undertaking, Abingdon, Oxon, U.K.
#Imperial College of Science and Technology, London , U.K.
+Leicester University, Leicester, U.K.
*Culham Laboratory, Abingdon, Oxon, U.K.

The transport of impurities during the H-mode is very different from that observed in the other regimes. This is clearly evident in the quiescent discharges where the confinement time of impurities τ_I increases by a much larger factor than the energy confinement time. Large values of τ_I are measured in all the quiescent H-mode discharges in spite of the variety of impurity behaviour observed corresponding to different plasma parameters and operating scenarios. The condition of the machine has an influence on the role played by the various impurities, but this does not seem to affect the flow patterns of these ions substantially. In particular oxygen, which was often detected as the dominant radiator, can be reduced to a negligible fraction by He conditioning of the carbon X-point tiles or limiters or by evaporating beryllium in the vacuum vessel. Nevertheless the behaviour of the residual impurities in otherwise similar discharges remains substantially unchanged.

The transport patterns appear in fact to be affected by the plasma parameters and their profiles. In particular, two extreme transport regimes are presented in the following. These discharges have been modelled with the aid of a recently developed fully time-dependent impurity transport code using heuristic profiles for the impurity diffusion D and the convection velocity v .

High Density H-Mode Discharges. This group is characterised by hollow electron density profiles (fig.1A), whose average value increases with time. Due to the very strong reduction of the oxygen content and the use of strong gas puffing /1/, the duration of the H-mode phase was extended up to 5.4 sec: in such cases the average electron density $< n_e >$ increases during the H-phase from $\sim 2 \cdot 10^{19}\ m^{-3}$ to $\sim 7.5 \cdot 10^{19}\ m^{-3}$.
During the initial 4 sec, most of the radiated power is emitted from an outer layer (indicating accumulation of impurities in that region) and increases linearly with time, i.e. at the same rate as $< n_e >^2$. This behaviour has already been described for oxygen dominated discharges in /2/.
After this time, a new phase develops where $< n_e >^2$ saturates, as well as the radiation from the peripheral layers, and the radiation profile rapidly fills up, indicating a flow of impurities to the plasma centre.
At the transition to L-mode the radiation from the outer plasma abruptly decays and subsequently, while the plasma cools down, the radiation from the centre increases (fig.2) indicating a slow loss of impurities from the central region. This is consistent with a low value of D ($\lesssim 0.05 m^2/s$) in a region around the plasma centre up to $\rho \simeq 0.3$, ρ being the normalized coordinate along the minor radius.
The intensities of all spectral lines emitted inside the separatrix show an increase throughout the H-mode and most of them abruptly fall at the transition to the L-mode, while the lines emitted by Ni-ions whose ionisation potential ranges between $\sim 600eV$ and $\sim 2000eV$ rise strongly after the transition.

Lower Density Discharges. The discharges grouped here display a rather flat n_e profile (particularly for $\rho \lesssim 0.5$) and reach much lower values overall (fig.1B): in a typical discharge $< n_e >$ increases from a value around $1 \cdot 10^{19}$ m^{-3} to about $2.5 \cdot 10^{19}$ m^{-3}.
They present a distinctively different characteristic impurity behaviour: only the K_α line intensity of the most centrally localized ion observed (i.e. NiXXVII) displays a long continuous increase during the H-mode (by a factor $\simeq 5$), while the central electron temperature is decreasing, and decays during the ELM-phase up to the transition to L-mode. The lines from the lowest ionisation stages (NiXVIII,CIII), localized at the very edge, show a sharp decrease at the start, diminish slightly during the H-phase and increase again later. Other spectral lines show an intermediate behaviour between these two: NiXXV, CVI and CV remaining basically constant or slightly decreasing during the H-mode, NiXXVI slightly increasing (by a factor $\simeq 1.5$).
The soft X-ray emissivity (to which only the light impurities contribute significantly) also points to an accumulation of impurities in the internal region ($\rho \simeq 0.25$) and indicates a depletion in the peripheral zone.(fig.3)

Modelling. As pointed out in /2/,the strongly shaped profiles of the radiated power and of the X-ray emissivity require that the convection play a dominant role in the transport of impurities. The v-profiles needed, however, are very different for the two classes of discharges.

The analysis of 1989 high density discharges shows that the transport scheme proposed in /2/ for oxygen is also confirmed for heavier impurities such as chlorine and nickel during the phase when the radiated power increases linearly with time. A strong inward convection ($v \gtrsim 12 m/s$), highly localised in the region close to the separatrix satisfactorily describes the hollowness in the radiative power profile.
Further elements however appear for the case of nickel: on one side the low intensity from the NiXXVII K_α indicates a central concentration of Ni of the order of 10^{-5}, on the other side the high line intensity emitted from the NiXXV ions, whose maximum density lies at about $\rho \simeq 0.8$, implies that at least 30 % of the power radiated from the border of the plasma must be ascribed to the nickel.
Thus, the experimental data suggest that for a period of 3 sec Ni is reduced by more than an order of magnitude between the region of accumulation restricted at the plasma periphery ($\rho \simeq 0.85$) and the internal region extending up to $\rho \simeq 0.6$; such a good screening could be explained in terms either of a $D < 0.05$ m^2/s or a sign reversal of the convection term, i.e. an outward velocity, in the region $\rho \lesssim 0.6$.

The density saturation phase, during which the impurities drift towards the central part of the plasma column in about $500 ms$, needs a substantial reshaping of the velocity pattern; a finite inward velocity is necessary in the central region to obtain the fast "filling up" of the radiative power profile, while a lower value than in the previous phase may be required at the periphery.

Just after the terminal event characterising the transition to L-mode, the central electron temperature T_e falls rapidly from $\simeq 2 keV$ to $\lesssim 1 keV$ while *i)* the central radiated power increases by a factor 3 (fig.2), *ii)* the Ly_α CVI intensity drops, *iii)* the lines intensities from NiXVIII up to NiXXI increase.
All these data imply that the observed radiation cannot be accounted for by a light impurity such as carbon, so heavier impurities need to be invoked. Unfortunately, during this phase only the central electron temperature is available, but simulations carried out with differently shaped, T_e-profiles, show that at the time when the H-mode collapses a Ni axial concentration of the order of $\sim 10^{-3}$ accounts for the increase of the total radiation in the plasma centre.

The experimental evidence for the lower density discharges is that from the onset of the H-mode the influx of impurities is strongly reduced (as indicated by the NiXVII and CIII lines).
The line intensities of ions localised at the plasma periphery and up to $\simeq 20$ *cm* inside the separatrix (NiXXV, CV, CVI) show that the impurity density is reduced in this region, nevertheless the increasing brightness from the NiXXVII, emitting from the very central region, is a clear indication of "accumulation" of impurities toward the centre. So the total impurity content does not vary much during the H-mode, but its distribution inside the plasma is rearranged.
As before, such behaviour cannot be modelled by a purely diffusive mechanism. A velocity profile less pronounced than in the so-called linear phase of the previous case, but localised more deeply into the plasma is required.
In order to reproduce correctly the rate of increase of the NiXXVII line the maximum inward velocity (located at about $\rho \simeq 0.4$) is of order ~ 1 m/s .
The soft X-rays emissivity radial profiles, are mildly hollow, reaching their maxima at $\rho \simeq 0.25$: this feature forces the convection to vanish in the inner core of the plasma.
The simulation of the time evolution of the signal of NiXXVI needs a small or negligible convection velocity for $\rho \gtrsim 0.5$. The resulting v-profile is plotted in fig.4A.
The same velocity pattern cannot be applied to carbon, which has to account for most of the soft X-ray radiation: the convection zone for C has to be extended to the plasma edge (fig.4B).

Conclusions

The convective transport schemes adopted in the simulations of the two types of discharges were inferred from the information gathered in order to draw a consistent picture from all the available experimental data.
The conclusions are of course subject to uncertainty, but still some unequivocal points have emerged.

On the theoretical side, the neoclassical theory /3/, up to now, constitutes the most detailed description against which the experiments should be checked.
According to this theory, the fluxes of impurities are driven by density and temperature gradients, ∇n and ∇T . The two transport regimes described above have been sorted basically by their contrasting densities and density gradients in qualitative agreement with a neoclassical transport mechanism.

The actual possibility of a quantitative comparison is made difficult by problems both with the availability of the experimental data and with the implementation of the theoretical model. Namely:
i) The intrinsic experimental errors of the temperature measurements imply great uncertainties on their gradients
ii) The functional form of the neoclassical coefficients relating the fluxes to the "thermodynamic forces" depend strongly on the collisonality regimes and also on the geometry; their evaluation in /4/ assumes a circular plasma cross section and this must be kept in mind particularly for JET X-point configurations.
With these caveats, simulations adopting the neoclassical coefficients evaluated in /4/ have been carried out. The velocities do show patterns in agreement with the ones inferred: the contrasting order of magnitude and also the different locations in the plasma between the two cases are reproduced satisfactorily. For example, fig.5 shows the heuristic and "neoclassical" v-profiles for NiXXV for the high density discharge #21022.

References
/1/ D.Stork et al.,Bull. Am. Phys. Soc.
34 (9) (1989), 2055
/2/ R.Giannella et al.,Behaviour of Impurities during H-mode in JET, EPS 1989
/3/ S.P.Hirshman and D.J. Sigmar, Nucl.Fus.
21 (1981) 1079
/4/G.Fussmann et al.,Impurity Accumulation in Plasma Regimes with
High Energy Confinement,
J.Nucl.Mat. (1989),14

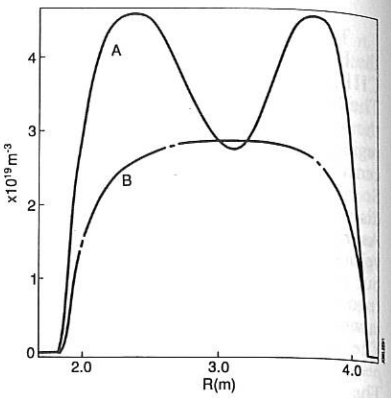

Fig. 1 n_e profiles 0.6 sec into H-mode
A: High Density Discharge #21022
B: Lower Density Discharge #18757

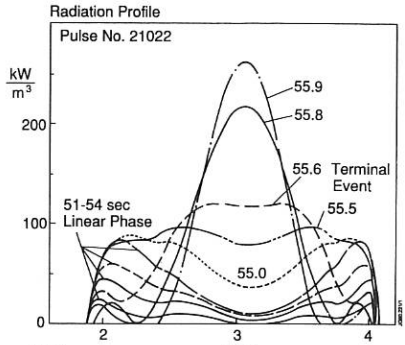

Fig. 2

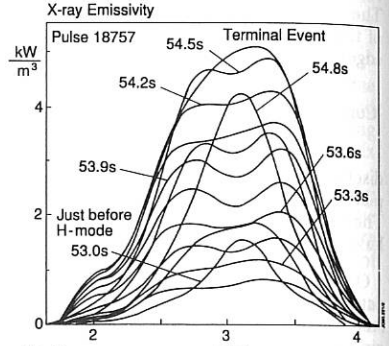

Fig. 3

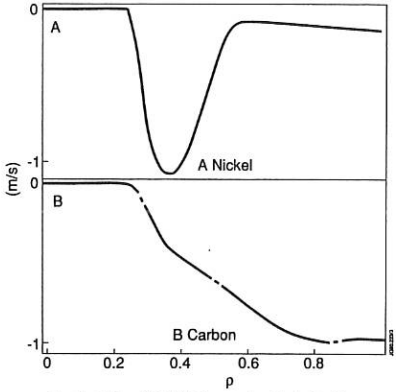

Fig.4 Pulse #18757 Convection Velocity Shapes

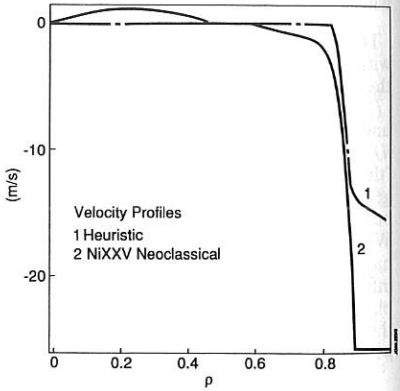

Fig. 5 Pulse #21022 0.6 sec into H-mode

PARTICLE AND HEAT DEPOSITION IN THE X-POINT REGION AT JET

D.P. O'Brien, M.A. Kovanen[1], R. Reichle[2], W. Core, E. Lazzaro, D.D.R. Summers, T. Taylor[3].

JET, Joint Undertaking, Abingdon, Oxon. U.K.
[1] National Research Council for Technology, Lappeenvanta University, Finland.
[2] Euratom Association, Max Planck Institute for Plasmaphysics, Garching, Munich.
[3] General Atomics Incorporated, San Diego, U.S.A.

In several experiments (DIII-D, ASDEX, PBX, JET), the H-mode has been associated with a favourable heat and particle flow pattern at the edge due to the X-point configuration within the tokamak vessel [1,2]. The observations of these flows have been made with CCD cameras and Langmuir Probes and have been interpreted in the conventional way as heat conduction by electrons along the magnetic field lines [3]. This is appropriate for high collisionality plasmas. However in low collisionality plasmas as is the case in many JET discharges heat convection by hot ions is more important. A magnetic separatrix affects dramatically the convected heat flux, because as particles enter a region of vanishing poloidal field the magnetic drift and diamagnetic drift dominate over the parallel flux term. Thus for a given particle energy, the particle drift orbit is further displaced from the magnetic surface on which it started, as B_p decreases. The drift becomes purely vertical for $B_p \cong 0$. The application of the conventional picture has led to some misinterpretation when comparing the plasma strike zones with the location of the magnetic separatrix deduced by the magnetic equilibrium reconstruction code [4]. We consider here a set of discharges where careful CCD camera observations were made and demonstrate how the correct interpretation of the observed heat strike zones on the vessel is obtained by the detailed analysis of loss cone and particle orbit effects near a magnetic stagnation point.

Two CCD Cameras were used to measure the temperature and particle fluxes at the upper X-point region. The field of view is shown in Fig. 1. It shows two of the thirty two bands of tiles which form the target plates for X-point discharges. The infrared images used for the temperature measurements show the strike zones of particles on the target plates as localised bright spots. The maxima of particle flux intensity derived from H_α and carbon line emission coincide with these strike zone positions.

The discrete target tiles are curved in the toroidal direction so that during an Ohmic discharge inner and outer bright spots (called strike zones) appear, each on opposite sides of the apex of the toroidal curvature of the tiles as shown schematically in Fig. 1. The toroidal displacement due to the curvature of the tiles corresponds to flow along the magnetic field lines from different directions.

A first interpretation has been that these strike zones were indeed the footprints of the heat flow along the magnetic separatrix [4]. This interpretation is often at odds with the evidence of magnetic measurements of the separatrix and X-point location: Sometimes the camera sees two hot spots which are well separated radially, when the magnetic X-point is found to be above the tiles. The ohmic phase of discharge 19414 is typical of this type of behaviour (I_p = 3 MA, B_t = 2.8 tesla). In Figure 2a we show the poloidal flux geometry in the vicinity of the target tiles together with the strike zones from the CCD camera, with the X-point position ≈ 4 cm above the target plates.

The magnetic detection of the X-point is obtained from a reconstruction code which solves the full boundary value problem of the Grad-Shrafranov equation using the flux measurements provided by saddle coils and obtaining the best fit to the tangential magnetic field of the pick up coils. The boundary is identified with an accuracy within the standard deviation of the flux measurements (~3%). The reconstruction of numerically generated equilibria is exact. In addition a determination of the X-point involving only a local expansion and using the poloidal magnetic field measurements in the vicinity of the X-point gives similar results as the reconstruction code. The determination of the X-point from both methods indicates the formation of an X-point plasma at the same time. This time coincides with the reduction of H_α emission from the limiter region and the increase of H_α emission in the vicinity of the X-point.

During auxiliary heating with up to 20 MW of neutral beam injection or up to 18 MW of ion cyclotron resonance heating, a third strike zone is observed on the ion drift side of the tile, near the location of the X-point (Fig. 2b). This strike zone has a peak heat flux comparable to or larger than that on the outer strike zone. There is an apparent 200 msec time delay between the rise in the third strike zone and the rise in the heat flux at the outer strike zone, on the electron drift side. The slowing down time for the fast ions for typical edge parameters of T_e = 50 ev, T_i = 1 keV, $n_e \sim 10^{19}/m^3$, is $\tau_s = 10^{-3}$ secs, which is significantly less than the observed delay time. The power deposition at this third zone is consistently located at the X-point position as confirmed by erosion damage to the X-point tiles during the 1989 experimental campaign. The erosion damage during this period is shown in Fig. 3 with a histogram of the location of the X-point. The third strike zone is under the X with the outer strike zone well separated from the separatrix. The third strike zone appears at the X-point location during auxilliary heating, only on the ion drift side of the apex of the tiles. The magnetic determination of the X-point location shows no motion of the X-point from the ohmic to the heated case, and the outer strike zone remains in the same location. A simple fluid model is inadequate to describe this heat flux pattern. The heat flux at the third strike zone and the increase in heat flux at the outer strike zone is likely due to power convected by the ions from the plasma to the tiles.

In order to obtain a better understanding of the particle and power deposition on the X-point target plates, the trajectories of charged particles in the confining magnetic field of JET are considered. The trajectories are calculated

using the HECTOR guiding centre code. The code includes the Coulomb scattering processes of dynamical friction, pitch angle scattering, energy diffusion. It also uses the actual plasma magnetic equilibrium, edge density and edge temperature profiles as input. The strike zones observed with the CCD cameras are compared with the particle deposition obtained by the HECTOR code in Figs 4 and 5. The agreement between the observed and calculated hot spots is seen to be good.

In this model the magnitude of the power flux depends critically on the ion temperature near the plasma boundary. Also the appearance of a strike zone near the X-point depends critically on the X-point location: The X-point must be at or above the surface of the tiles. This restriction is consistent with the location of the X-point during the whole of the 1989 experimental campaign, where most discharges had the X-point outside the tile surface (Fig. 6). Some H-mode discharges were obtained with the X-point well beyond the tile surface (10-15 cm) and could be considered to be limiter H-mode discharges.

The heat flux pattern in JET divertor discharges is explained by including the particle orbit effects. These are of course only important when the poloidal gyroradius is comparable to or larger than the characteristic decay length for the power flow in the edge plasma region and when the collisionality is low. These conditions are readily met in JET heated discharges. The consideration of the particle orbits will play an even more important role in the next phase of JET where the collisionality is expected to be even lower and the ion temperature even higher.

Acknowledgements

We would like to thank M. Keilhacker and G. Cordey for their encouragement during the progress of this work. We would like to thank M. Pick who supplied us with the tile erosion data.

References

[1] F.L. Hinton, M.S. Chu, Nucl. Fusion, 25, Pg. 345, 1985.

[2] A. Tanga, et al., Nucl. Fusion, 27, Pg. 1877, 1987.

[3] B.J. Braams, et al., J. Nucl. Mater, 121, Pg. 75, 1984.

[4] P.J. Harbour, et al., J. Nucl. Mater, 162, - 164, Pg. 236, 1989.

Max-Planck-Institut für Plasmaphysik
8046 Garching bei München

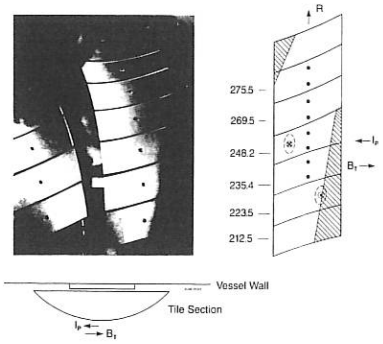

Fig. 1 View of the CCD cameras showning toroidal curvature of the tiles and a poloidal section with the ohmic strike zones shown.

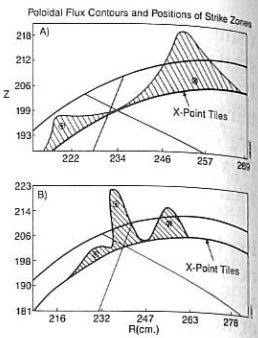

Fig. 2 Separatrix of the JET equilibrium with the heat loading on the tiles during a) ohmic discharge b) Additional heating.

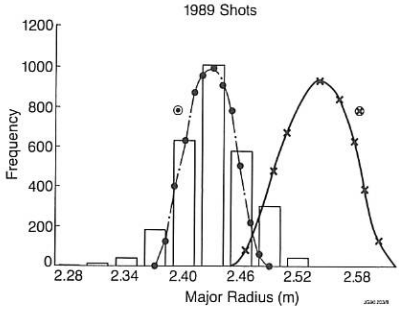

Fig. 3 Frequency of erosion damage on the X-point tiles •, superimposed on a histogram of the X-point position during the 1989 campaign.

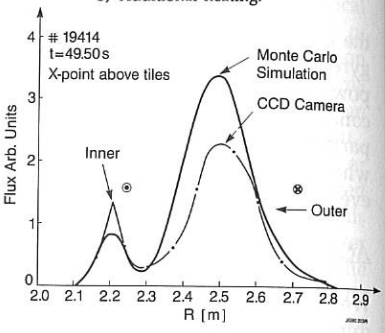

Fig. 4 Comparison of flux intensity from Monte-Carlo simulation with that of the CCD cameras during an ohmic shot.

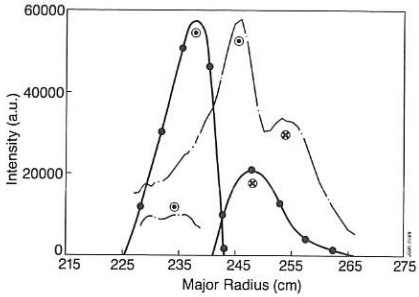

Fig. 5 Comparison of flux intensity from Monte-Carlo simulation with that of the CCD cameras during auxiliary heating.

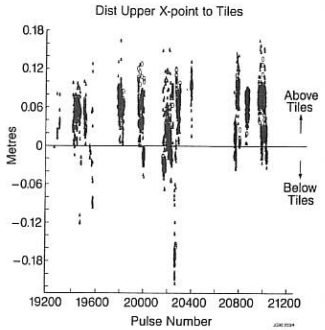

Fig. 6 X-point position relative to target tiles during 1989 campaign. H-mode discharges are indicated by 0.

ICRH PRODUCED H-MODES IN THE JET TOKAMAK

V.P. Bhatnagar, M. Bures, D. Campbell, S. Clement, A.Hatayama*, J. Jacquinot, D.F.H. Start, D. Stork, A. Tanga, F. Tibone, B.J.D. Tubbing

JET JOINT UNDERTAKING
Abingdon, Oxfordshire, OX14 3EA, England.
* Toshiba Corporation
Chome, Chiyoda-Ku, Tokyo 100, Japan.

1. INTRODUCTION. Since the first demonstration of H-mode (high-confinement mode) in 1982 in ASDEX in magnetic divertor configuration using neutral-beam injection (NBI) heating, H-modes are now routinely produced with practically any type (or a combination) of additional heating in most tokamaks that can operate either in closed divertor configuration such as ASDEX, JT-60, or in an open divertor configuration such as JFT2-M, DIII-D, JET etc. (for references see a review paper [1]). In JET, H-modes by ICRH have now been obtained where antennas are located on the low-field side. The early operation carried out with carbon limiters and carbonized nickel antenna screen led to an increased influx of neutral gas and impurities. This tends to impair the edge conditions that are crucial to the production and maintenance of an H-mode. Helium glow-discharge cleaning was also used but, the H-modes with ICRH could only be produced by eliminating specific ICRH impurity effects [2] as follows: (1) Beryllium gettering is applied to the nickel screen and the first-wall of the tokamak, (2) The antenna is used in the dipole $(0, \pi)$ phasing, (3) The antenna screen blades are inclined at 15 deg. (from the toroidal direction) to align them approximately with the total magnetic field. Also, a fast automatic-matching system based on slight frequency changes [3] together with a slower adjustment of mechanical stubs is incorporated to cope with changes of antenna-plasma coupling at the transition and during the H-mode. The observed scaling of impurity release is compatible with a sputtering mechanism due to RF sheath rectification of the applied RF voltage (in combination with the coventional Bohm sheath) which provides a large dc potential drop in which ions accelerate. "Short-length" [4] gap-sheaths (field line crossing between the antenna blades) and the "long-length" [5] front-surface sheaths (between the contact points of the field line on the two sides of the antenna) can be formed. The deleterious effect of the former is eliminated by aligning the screen to the field line and the latter is made ineffective due to the out of phase operation in the dipole mode (net voltage is zero toroidally). In the case of misalignment, the effect of self-sputtering which is the dominant cause of metallic impurity influx is reduced by beryllium coating for which the self-sputtering coefficient is less than unity. Further, there is a strong Be-gettering which reduces oxygen concentration, ($< 0.1\%$) as well as there is a significant reduction of sputtering caused by oxygen ions themselves. Moreover, beryllium environment allows a strong pumping and lowers the influx of neutrals thus reducing recycling. Operation under these conditions allows the production of H-modes with ICRH alone. The duration of H-modes is also longer (in ICRH or other scenarios) as the radiated power is smaller in the Be environment. Though, H-modes have not yet been obtained with monopole operation (which suffers from front-surface sheath effects) of ICRH alone but, the deleterious effects of this phasing do not seem to be dominant in H-modes obtained with combined ICRH + NBI heating taking advantage of better coupling and higher RF power coupled with monopole.

2. EXPERIMENTAL CONDITIONS AND RESULTS. The D-plasma (with H minority-ion) was operated at $B_T = 2.8$ T and $I_p = 3$ MA in the double-null X-point (DNX) configuration and shaped poloidally to match the antenna profile to obtain good

antenna-plasma coupling. Also, the plasma was brought very close to the midplane antenna side-protection tiles (≅1 cm) for better coupling and still produced an H-mode successfully. There are 8 ICRH antennas which are symmetrically distributed around the torus. A JET antenna has essentially two radiating elements that are separated toroidally which can be driven in phase (monopole) or out of phase (dipole). ICRH power is delivered to the plasma by the fast magnetosonic wave which is damped mainly via the minority-ion cyclotron damping in a narrow region (≅30 cm) near the ion-ion hybrid resonance zone.

2.1 Typical ICRH H-Mode Time-Traces. In H-modes produced by ICRH alone, all characteristics typical of H-mode discharges are found (see Fig. 1). At the transition from L to H-phase, one can see a sudden drop in D_α emission, a small decrease and then a gradual increase in the radiated power (P_{rad}) from the plasma, increase in the plasma density and more importantly an increase in the slope of stored energy (W_{DIA}, for example) at a constant power level. Also there is an increase in the ion temperature (T_{i0}) and DD reaction rate (R_{DD}) which eventually decreases due to increase in Z_{eff} or dilution. Further, there is an increase in the edge-density gradient (or a reduction in scrape-off length (SOL), not shown), which results in a decrease of coupling resistance R_c. There is a slight increase in the antenna-plasma distance D_{ap} but this increase is generally not enough to account for the decrease of R_c (see Section 2.4). Generally, P_{RF} reduces after the transition to H-mode due to the decrease of R_c and tripping of some of the generators caused by the voltage-breakdown in the antenna and/or the transmission line. Note that in this shot P_{RF} was reduced in anticipation but the stored energy did not decrease significantly practically until the the H-mode was terminated when P_{RAD} reached the input power level. Sawtooth-free periods (monster sawtooth) created by ICRH are not lost at the transition and their longest duration in ICRH H-modes is 1.3 s. However, even longer sawtooth-free periods are obtained (≅2.5 s) in H-modes with ICRH+NBI heating where monopole can be used which facilitates obtaining the monster sawtooth. For most of the H-phase the D_α signal is ELM free. Also, there is a clear reduction of noise on the coupling resistance trace during H-phase which could be related to the reduced fluctuations on the edge density.

2.2 Energy Confinement. A plot of diamagnetic stored energy vs P_{TOT}- dW/dt is shown in Fig. 2. The data does not distinguish between Be evaporation with C-limiters and Be-limiters. The NBI heated limiter-plasmas agree well with the Goldston L-mode prediction for such plasmas (represented by W_G-line). ICRF heated L-mode DNX-discharges lie between W_G and $1.5W_G$-lines and follow the usual off-set linear behaviour with τ_{inc}≅0.34 s [6] and contain 10-30% fast-ion contribution. The H-mode data obtained by NBI, ICRH and ICRH+NBI is about the same and lie between $1.7\text{-}2.2W_G$.

2.3 Ion and Electron Heating. Central ion temperature T_{i0} (Doppler-broadening of Ni-XXVII line) and electron temperature T_{e0} (ECE) are plotted in Fig. 3-4 as a function of $P_{TOT}/\langle n_e \rangle$ (volume average) for the data set used above. For ICRF heated L and H-modes, the T_{i0} is generally low (4-6 keV) and is a general characteristic of the minority heating. In the case of NBI or ICRH+NBI heating, beam ions relax on plasma ions and heat them preferentially leading to a linear increase of T_{i0} with $P_{TOT}/\langle n_e \rangle$. Since in ICRF heating, a strong minority-ion tail is produced which interacts with electrons, higher T_{e0} values are obtained for ICRH data as shown in Fig. 4. In NBI shots, electron heating is generally poor, but in H-modes with combined heating (P_{RF}/P_{NBI} = 0.4-0.8), ICRH pushes the T_{e0} to highest values. Thus as expected, H-modes with combined heating, allow high values of both T_{e0} and T_{i0}. A TRANSP analysis [7] of an H-mode with ICRH alone has been carried out in which the transport losses are represented by a χ_{eff} where the experimental T_i-profile is not available (except T_{i0}) and $\chi_i = \chi_e$ has been assumed. The discharge simulation shows that χ_{eff} decreases in the outer regions of the plasma. This behavior is similar to that found in H-modes with NBI.

2.4 Antenna Coupling Resistance. The coupling resistance R_c as measured experimentally in JET can be described as the value of antenna resistance seen at a current antinode of the feeder transmission line. The experimentally measured R_c as a function of time for the H-mode shot #20230 is shown in Fig. 5 together with the D_α emission and the mid-plane antenna-plasma distance D_{ap} obtained by IDENTC equilibrium code.

In this and some other shots the transition to H-mode occurs in two steps as evidenced by a double jump in D_α signal. R_c also shows a similar behaviour. After the 2nd transition D_α remains low but R_c decrease slowly together with a small increase in D_{ap}. During the H-phase theoretically calculated [8] values of R_c for dipole are shown with solid circles in Fig. 5 where experimentally measured values of density profiles, SOL, D_{ap}, f, B_T etc are used. The code-calculated radiation resistance R was converted to R_c by multiplying R by the ratio of RF currents flowing in the antenna to that in the transmission line as measured in vacuum in a test-bed. The slow decrease was in agreement with increasing D_{ap} for the measured SOL = 1 cm. But, a large change of R_c from 2.2 to 7 ohms at the transition from H to L or vice-versa can only be modeled if we assume that SOL changes considerably e.g. from values of 6 and 3 cm before 1st and 2nd transition to 1 cm during the H-phase. (see Fig. 5). Estimates from probe measurements made in the X-point region and transformed to mid-plane indicate an increase of SOL by a factor of 2-2.5 atmost. This difference is not well understood and more measurements near the antenna are required.

3. SUMMARY. ICRH produced H-mode discharges in JET are found to have the same characteristics as those produced by NBI or NBI+ICRH and the confinement time approaches two-times Goldston L-mode prediction. For most of their duration they are ELM-free. The monster sawtooth feature of ICRH is maintained during H-modes leading to $T_{e0} = 10$ keV nearly twice the value of T_{i0}. Combined heating H-modes push both T_{e0} and T_{i0} close to 10 keV. ICRH H-modes often occur as a two-step transition and R_c also decreases in two steps. Theoretical values of R_c agree well with experimental values during the H-phase.

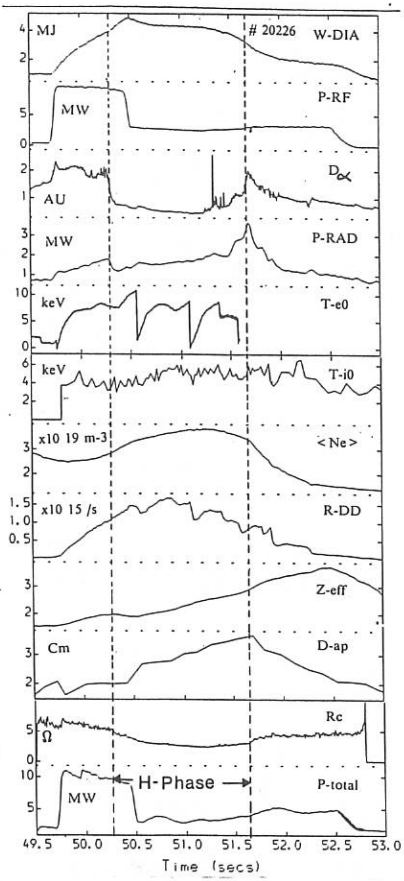

FIG. 1. Time traces for shot # 20226.

Acknowledgement. We wish to thank our colleagues in the JET team, especially the RF plant team, the tokamak operation team and those operating the diagnostics used in the experiments reported in this paper.

REFERENCES.

[1] ASDEX Team, (1989) Nuclear Fusion, 29, 1959.
[2] JACQUINOT J. et al (1989), JET Joint Undertaking, Abingdon, Report JET-P(89)85.
[3] BOSIA, G., et al (1989) Fusion Eng. Design 11, 459.
[4] D'IPPOLITO D.A. et al (1989), Fusion Eng. Design (to be published).
[5] JACQUINOT, J. (1989) Private communication.
[6] BHATNAGAR, V.P. et al (1989) Plasma Phys Contr. Fusion, 31, 333.
[7] BALET, B. et al (1990) these proceedings.
[8] BHATNAGAR, V.P. et al (1982) Nuclear Fusion, 22, 280.

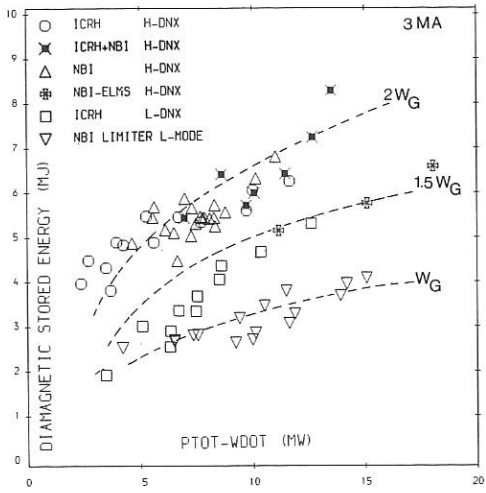

FIG. 2. W_{DIA} vs P_{tot} - dW/dt

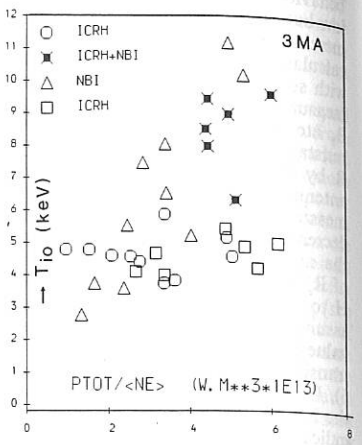

FIG. 3. Central ion temperature T_{i0} vs $P_{tot}/<n_e>$ (volume average).

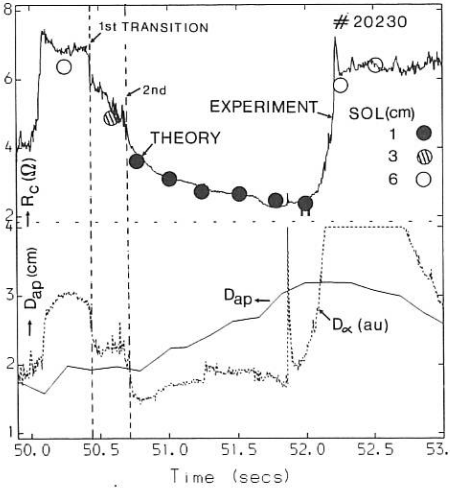

FIG. 5. Coupling resistance R_c, D_α-emission and antenna-plasma distance D_{ap} vs time.

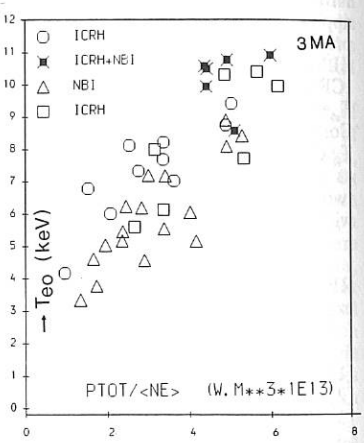

FIG. 4. Central electron temperature T_{e0} vs $P_{tot}/<n_e>$. In combined heating, $P_{RF}/P_{NBI} = 0.4\text{-}0.8$.

The compatibility of the JET H-mode with other regimes of improved performance

A.Tanga, B.Balet, D.V.Bartlett, N.Gottardi, C.Gowers,P.J.Harbour, J.Jaquinot,M.F.Johnson, E.Lazzaro,P.Morgan, F.Porcelli,H.C.Sack,G.Schmidt#,D.Stork,K.Thomsen,B.J.Tubbing, H.Weisen.

JET Joint Undertaking, Abingdon, Oxon OX14 3EA,U.K.

#PPPL,Princeton, New Jersey, USA.

Since the discovery of the H mode in ASDEX, the term has been used to describe plasma regimes characterzed by superior confinement and by specific edge signatures such as reduction of recycling and of high frequency fluctuations. Often H mode discharges, (without ELM's), have shown the undesirable characteristics of impurity accumulation and uncontrolled rise of plasma density. Moreover the H mode tends to produce flat-hollow density profiles and broad temperature profiles. Compatibility of basic H mode characteristics with monster sawtooth, hot-ion mode and pellet peaked density profiles would lead to substantial improvements of plasma performance. In this paper it is shown that the JET H mode can be compatible with these improved regimes. In the new regimes the basic confinement time is little changed from that the basic H mode, whilst the central plasma parameters can be substantially improved.

1) Scaling of plasma electron density and temperature profiles in H mode.

The main features of JET H-mode profiles have been described in reference 1. With NB heating the plasma density profiles are more peaked at lower densities, when central beam fuelling is dominant, and flat to hollow at higer densities. The peaking parameter $n(0)/<n>$, where $<>$ indicates volume average, as measured by LIDAR-Thomson scattering [2] over a large sample number of H modes (with Beryllium gettering) at 3 and 4-4.5 MA can be fitted by

$$n(0)/<n> = 1.3 \times q^{0.25} \times <n>^{-0.3}.$$

where q is the value of the cross section defined cylindrical safety factor, densities are in units 10E19 m^{-3}. Fig 1 shows the plot of n(0) vs. $<n>$.

With NB heating the electron temperature profile during H mode tends to be rather broad and with strong edge gradients (pedestals) [1]. One other characteristic feature is the relatively small sawteeth inversion radius ($r_i/a < 0.4$) probably caused by the effect of bootstrap current in the outer region of the plasma [3].

The electron temperature peaking parameter, $T_e(0)/<T_e>$, as measured by LIDAR-Thomson scattering , ranges between 1.7 and 3.0 and can be fitted by the empirical formula:

$$T_e(0)/<T_e> = 2.1 \times q^{0.35} <n>^{-0.1}$$

The result of this temperature profile fitting is, however, a plot with still appreciable scattering of data, due to weak dependences from other parameters. In the JET H-mode the ion temperature profile is usually very close to the electron temperature profile for $<n> > 2.5 \times 10^{19} m^{-3}$. [1].

2) Sawtooth stabilization during H-mode.

Suppression of sawtooth activity has been observed in JET in in L-mode limiter discharges [4] , q_0 was observed to fall below unity [5] , the stabilization was associated by the fast particles accellerated by the RF fields or injected by neutral beams [6]. In limiter discharges sawtooth activity suppression has also been observed in conditions in which the central value of q has been driven above unity by deep pellet injection [7].

In this section the results of sawtooth stabilization during H-mode, with NB, ICRF and combined NB/ICRF heating, are presented. The time evolution of a series of discharges showing sawtooth suppression during H-mode is presented in fig.2.

With NB heating in excess of 8MW, at least twice the power threshold for H-mode transition, injected in a relatively low density ohmic deuterium target, the H-mode is accompained by a period of sawtooth stabilization of the duration of.6 -.8 s. In this phase a modest enhancement (10-15%) of central ion and electron temperatures is observed.

With ICRF heating during the H-mode [8,9] sawtooth suppression has occurred routinely with ICRF input powers in excess of 7MW. The maximum duration of the monster sowtooth has been 2.5s. The start and end time of sawtooth suppression was not correlated with the H-mode phase, but sometimes the monster crash caused an H to L transition. The temperature peaking factor obtained in sawtooth suppressed H-modes can be compared with the scaling discussed in the previous section, with monster H-modes there is an enhancement of approxomately 50% of the ratio electron $T_e(0)/ < T_e >$ A series of electron temperature profile shapes with sawtooth suppressed H-modes is shown in fig 3. Here the peaking factor ranges between 3 and 4 (with electron pressure peaking factors between 4 and 5) with values of cylindrical q = 3.2 and averages densities in in the range $2 - 4 \times 10^{19} m^{-3}$. It should be noted that in this case the shape of the electron temperature profiles are similar to those obtained in the case of limiter monsters [10] and that the value of the edge plasma temperature is not very high. However, due to the steep edge density gradient the electron pressure profile shows a small edge pedestal $P_{edge}/P(0) = 0.1\text{-}0.2$.

With combined ICRF/NB heating sawtooth suppresion in H-mode has also been achieved, as shown by one of the traces in fig 2. In this pulse, ($P_{RF} = 2$MW and $P_{NB} = 6$MW, $< n > = 2.5$E19m-3), the ICRF had triggered a series of monster sawteeth during the three seconds preceding the H phase and the profiles shown in fig 4. Polarimetric analysis of the safety factor radial profile indicate that the central value of q is driven below unity in a way similar to other monster sawtooth [5] , while estimates of the content of fast particles confirm the agreement with the theoretical expectations of sawtooth stabilization [6] .

3) Effects of pellet injection on H-mode

Pellet injection during an already estabilished H-mode causes a large ELM or precipitates the transition to the L-mode. A series of experiments have been performed aimed at producing pellet peaked plasma density profile just before the application of additional heating. Although the plasma density profile produced by pellet injection was never very peaked, pellet injection was sufficient to suppress sawtooth activity during the wholé duration of the subsequent H-mode phase with a plasma density profile more peaked than the scaling for normal H-mode discussed in the first section In these pellet fuelled discharges the

LIDAR measured density profiles, even toward the end of the H phase, had a bell shaped central region on top of steep edge gradients. Typical parameters were: plasma density peaking factor = 1.6, q = 2.3, $<n> = 4 \times 10^{19} m^{-3}$. Due to the anhancement in the central values of plasma density and temperature some of these pulses have achieved the highest values of the $n\tau T$ product in JET in condition of $T_i \simeq T_e$ ($n_D \tau T_i(0) = 6 \times 10^{20} m^{-3} keV s$)

4) Hot ion H-mode

In limiter discharges at low density with NB heating it is possible to raise the ion temperature well above the value of the electron temperature [11], producing a 'Hot Ion Mode'. In X-point configuration in JET with NB injection on a low density ohmic target it is possible to produce simultaneously $T_i \gg T_e$ and an H-mode [12,13] . The main difference between the short L-phase and the following H phase is the decreasing frequency or disapperance of ELM's activity, which makes the L phase difficult to define. For JET H-modes, $T_i(0) \simeq T_e(0)$, within 30%, for values of $P_{NB}/<n> \lesssim 3.(MW/10^{19} m^{-3})$. For higher values of $P_{NB}/<n>$, $T_i(0) \gg T_e(0)$. Values of the temperature's ratio between 3 and 4 are reached when $P_{NB}/<n> \simeq 10$. Increasing the value of the ratio $P_{NB}/<n>$ the ion temperature profile becomes more peaked: the ratio of central to volume average ion temperature scale approximately as the square root of the central ion temperature, reaching values in excess of 4 for $T_i(0) \gtrsim 20 keV$. Local transport analysis of the Hot-ion H-mode discharges has shown that the high values of the central ion temperature are associated with a further reduction of the ion thermal conduction in the central-half radius region of the plasma [13] where $\chi_i < 1 m^2 s^{-1}$ and $\chi_e/\chi_i \simeq 1 - 3$ In the Hot-ion H-modes the ion transport is dominated by thermal conduction. For the electron channel the equipartition term is comparable to the direct beam electron heating in the outer region of the plasma.

5) Conclusions

The JET H-mode is characterized by an improvement of a factor 2 or 3 in global confinement time over equivalent limiter discharges [1]. The peaking factors of the plasma electron temperature and density profiles fit empirical scalings as a function of the safety factor and average plasma density. The central values of plasma density and electron temperature can be enhanced by 50% in H-modes with pellet injection and sawtooth suppression. With intense NB injection it is possible to produce large values of the central ion temperature in Hot-ion H-mode.

References.. 1) The JET Team (pres.by M.Keilhaker) Proc. 12th Conf.on Pl. Phys. and Cont. Fus. Res. Nice 1988, vol1 p.159.. 2) Salzman, H.M., et al. Inv. at APS topical conf. on plasma diag. Napa Valley,Cal.,USA 1988.. 3) Challis, C.D., et al. Nucl. Fus. vol29 p563-70 (1989).. 4) Campbell, D.J., et al. P.R.L. vol60 p2148 (1988).. 5) Campbell, D.J., et al. ibd 1) vol.1 p378.. 6) Pegoraro,F.,et al. ibd. 1) vol2 p243.. 7) The JET Team (pres. by G. Schmidt) ibd. 1) vol1 p215.. 8) Tubbing, B.J., et al. Nucl. Fus. vol29 p1953 (1989).. 9) Bhatnagar, V.D., et al at this conf.. 10)The JET Team (pres. by J-J Jaquinot) Proc 11th Conf. on Pl. Phys. and Con. Fus. Kyoto 1986 vol1 p449.. 11)Jones,T.T.J., et al. at this Conf.. 12)Balet, B., et al. 'High temperature H and L mode confinement in JET' sub. to Nucl. Fus.. 13)Balet, B., et al. at this conference.

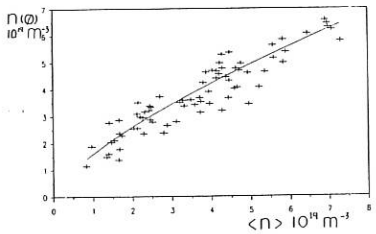

Fig.1 Plot of central values of plasma density versus volume average density, for $<n> > 4 \times 10^{19} m^{-3}$ the density profile is hollow.

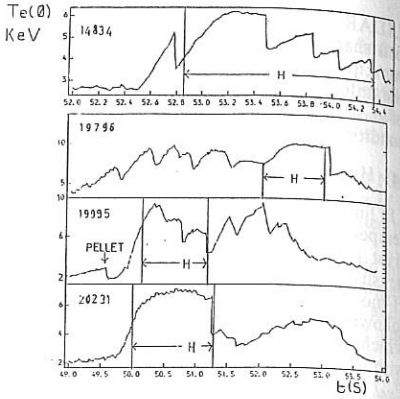

Fig.2 Time evolution of central electron temperature in monster H-modes: #14834 NB alone, #19796 NB/ICRF,#19995 and #20231 H-mode with ICRF alone.

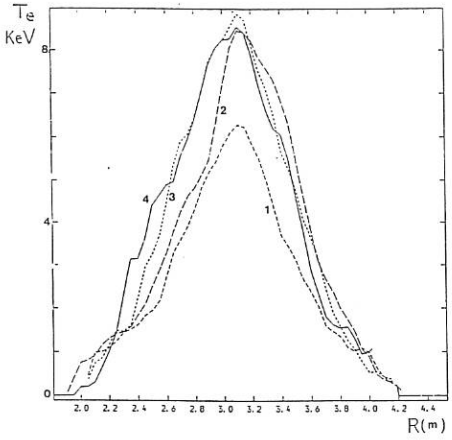

Fig.3 LIDAR electron temperature profiles of Monster H-modes, 1 #20231,3 #19995, 4 #19796, 2 limiter Monster #12924.

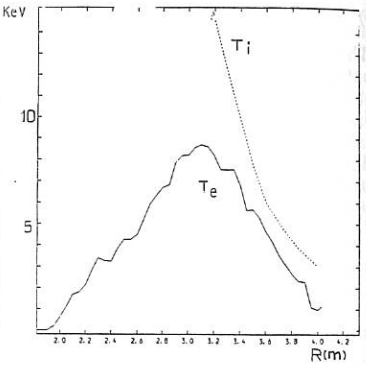

Fig.4 Electron and ion temperature profiles for #19796 at t = 52.5

RADIATION ASYMMETRIES AND H-MODES

N.Gottardi, K.F.Mast[+], P.Thomas, G.Corrigan, R.Giannella and C.Sack

JET Joint Undertaking, Abingdon, Oxon, OX14 3EA, U.K.

(+) Max Planck Institut für Plasma Physik, Garching (FRG).

Abstract: The radiation from JET plasmas, as measured by the bolometer arrays, is characterized by poloidal asymmetries internal and external to the main plasma. This fact limits the capability of producing radiation profiles. Fortunately it has been observed that internal asymmetries are often strongly reduced; this is particularly true for the H-mode plasmas which normally show a high degree of symmetry. We present the analysis of this phenomenon together with our interpretation of the impurity transport mechanisms. The algorithm used, which has been developed as a diagnostic tool to complement the profile reconstruction process, is also presented.

Introduction: Asymmetries of the radiation emitted by the outer plasma region of JET often present an impediment to the profile reconstruction. They are due to contact of the plasma with machine structures (limiter, etc.) or to the shape of the magnetic field (X-point config.) and can be associated with enhanced local recycling and impurity production. To reconstruct the main plasma radiation profile, the sight lines aiming at the localized radiation source are dropped and tomographic programs run with the remaining data. Tomography works in most limiter plasmas, where asymmetries can be defined by the first two terms of a Fourier expansion, but fails in X-point shots because the enhanced radiation from the target plates severely reduces the number of useful channels. In this case the only applicable inversion method would be generalized Abel inversion with the assumption of constant emissivity on the flux surfaces, i.e. no internal asymmetries. Unfortunately, JET plasmas showed from the very beginning of the machine operation, long phases with strong internal asymmetries (Marfes [1], up-down and in-out [2]). Internal asymmetries must be associated with the impurity transport mechanism. In fact, as we will explain later, the radial electric field associated with neoclassical transport can be invoked to explain the asymmetries (not Marfes).

The phenomenon: Symmetric emission is sometimes observed, particularly, during H-modes. The internal asymmetry can diminish or even disappear altogether. This is shown in fig. 1 for the longest H-mode obtained in JET so far. Trace σ is the result of the algorithm to be discussed and can be regarded as a measure of poloidal asymmetry; the other two traces are those of the H-α light and of the line electron density and show the characteristic behaviour of the H-mode. The reduction of the asymmetry was observed in the earliest NBI H-modes in JET (fig. 2) and more recently during ICRH H-modes (fig. 3). Analysis of the behaviour of the asymmetry signal σ for many pulses has brought to further observations: **a)** The amplitude is modulated by oscillations in a frequency range between 7 and 22 Hz. Cross correlation checks show that they do not constitute white noise. Their origin remains unexplained. **b)** The attenuation of σ is often accompanied by a broadening of the density profile (as e.g. at the end of the H-mode). **c)** Sometimes the attenuation corresponds to periods of enhanced confinement (e.g. the ohmic phase between Marfe and the start of NBI in fig 4). **d)** The symmetrisation

of the radiation, however, is not a sufficient indication of enhanced confinement since, it is often observed as a precursor to the change of plasma regime (e.g. fig. 5 shows the traces of the boundary electron temperature and density during a shot with strong gas puff in the X-point. σ decreases during periods of rising boundary electron temperature. **e)** During ICRH H-modes σ is more noisy than during NBI because of impurities coming from the antenna which is at the same poloidal position of the horizontal bolometers. **f)** An inversion can be satisfactorily performed if $\sigma < .03$. **g)** The amplitude of σ is influenced by both temperature and density variation and its trend can be explained by a neoclassical model of impurity transport.

The model: A physical mechanism which can explain the phenomen is based on the friction between impurity and plasma ions [3] with heat conduction and radiation losses accounted for [4]. The results are quite different from those of [3]. A stationary fluid model for the ions and the impurities with electric charge eZ (index I, Z) describes the transport of the impurities on closed flux surfaces. It consists of the momentum equations for the plasma ions and for the impurities with $f_I = 1$ and $f_Z = -1$,

$$-\nabla p_{I,Z} + eZ_{I,Z} n_{I,Z} (E + v_{I,Z} \times B) = \frac{n_z m_I Z^2}{\tau_{jl}} \cdot f[(v_I - v_z) + 2.2\, n_z Z^2 \nabla T_I],$$

the energy equation $5\nabla(nTv) + \nabla q = -\varepsilon(r)$ and the equation of continuity for the impurities in absence of poloidal rotation: $\nabla(n_z v_z) = 0$. The principal physical behaviour is obtained with a test particle approximation ($n_Z Z^2 \ll n_I$) and with the assumption $T_e = T_I = T$, $p = \text{const.}(\psi)$ and concentric circular flux surfaces forming a toroidal coordinate system. A first order solution is given by representing all quantities in a Fourier series of poloidal angle θ and expansion in the inverse aspect ratio r/R_0. The emissivity becomes: $\varepsilon(r,\theta) = \varepsilon^0(r) + \varepsilon^1(r)\sin\theta + \varepsilon^2(r)\cos\theta$ where the second and third terms define an up-down and an in-out asymmetry respectively; their expression is given [with $f_1 = A(r)$ and $f_2 = -B(r)$] by:

$$\varepsilon^{1,2}(r) = \frac{E(r)\, K^0_{\|e}(r)}{R_0^3\, q^2(r)} \frac{2r\, f_{1,2}}{[A^2(r)+B^2(r)]}\, n_z^0(r), \quad (K^0_{\|e} = \text{electr. therm. conduct.}).$$

A(r), B(r) and E(r) are flux surface averaged parameters and depend on n_I^0, n^0, q, T^0 and on the radiation model. For a coronal radiation model the computed normalized $\varepsilon^1(r)$ for carbon and beryllium are shown in fig. 6 with q(a) as a parameter. A pronounced peak of ε^1 for carbon between $T_e = 10$ eV and $T_e = 20$ eV can be deduced from fig. 6 for q(a) ≥ 3. In JET this corresponds to an enhancement of ε at the bottom of the plasma for usual direction of the toroidal field and could trigger a thermal instability (Marfe) near the density limit. With additional heating or at L-H transition the theory predicts a reduction of the rad. asymmetries as reported above.

The algorithm used to produce the asymmetry signal σ is applied before Abel inversion of the bolometer signals. It is based on the transformation of the line integrals which is performed during the generalized Abel inversion procedure used at JET [2]. During this procedure the line integrated measurement I_i collected along the viewing line v_i of each bolometer (which is identified by an angle α_i

and the flux surface ψ_i to which it is tangent) is transformed into two virtual measurements I_i^* and $I_i^{*\prime}$ corresponding to the two projections of v_i into the virtual lines v_i^* and $v_i^{*\prime}$, parallel to the Z torus axis and tangent to the same flux surface ψ_i (fig. 7). If we call a_{ik}, a_{ik}^* and $a_{ik}^{*\prime}$ the paths of the viewing lines inside pixel i, on which the emissivity ε_i is assumed constant, and define $I_i = \Sigma\, a_{ik}\, \varepsilon_i$, $I_i^* = \Sigma\, a_{ik}^*\, \varepsilon_i$, $I_i^{*\prime} = \Sigma\, a_{ik}^{*\prime}\, \varepsilon_i$, $A \equiv [a_{ik}]$, $A^* \equiv [a_{ik}^*]$ and $A^{*\prime} \equiv [a_{ik}^{*\prime}]$, the transformed integrals are given by: $I^* = A^* A^{-1} I$ and $I^{*\prime} = A^{*\prime} A^{-1} I$. The radiation is symmetric if the local separation ΔI^* between any two transformed integrals whose line of sights have the same ψ but different angles is so that $\Delta I^* / \sqrt{\sum_N (\Delta I_i)^2 / N} < 1$, where ΔI_i is the experimental error of detector i. An application of this criterion to the discharge in fig. 2 is shown in fig. 8.a and 8.b for one L and one H mode time slice respectively. The degree of asymmetry, σ, is given by computing the scatter in the transformed line integrals of some central channels (for the X-point discharges: 3 each of the three cameras), the choice of the channels being set by the requirement that any region of external asymmetry (for example the X-point) be avoided. σ is obtained after averaging the normalized square deviation of the transformed integrals from a least square fit parabola drawn through the same points. This is essentially a sort of χ^2 per degree of freedom. The amplitude of the trace depends on the choice of the channels. The same algorithm, applied to outer bolometer channels, could be used for studying the components (up, down, in, out) of the asymmetries.

Acknowledgement: the authors aknowledge useful discussions with P. Cripwell, J. How, E. Lazzaro and D. Stork.

References:

[1] J.Wesson et al.; Nucl. Fusion 29 (1989) 641.
[2] N.Gottardi et al.; Proceed. of the 12th EPS, Budapest (1985) 30.
[3] W.Feneberg et al.;Neocl.Impu.Transp. and Obs. of Pol.Asymm.;JET Rep. R(86)07.
[4] K.F.Mast et al.; Radiation Asymm. and Dens. Limit; (to be published).

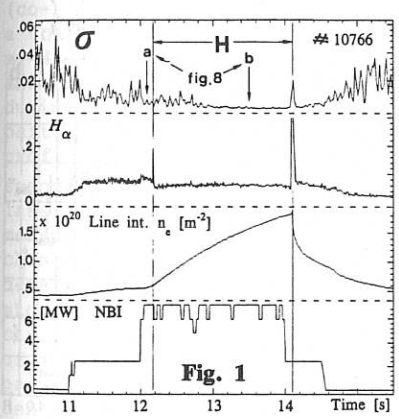

Fig. 1

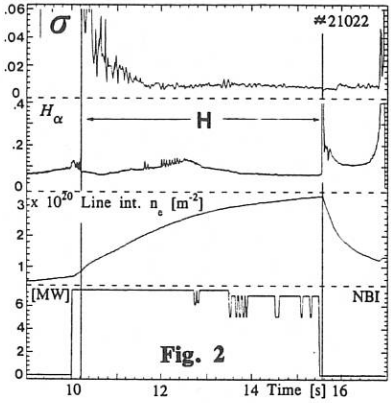

Fig. 2

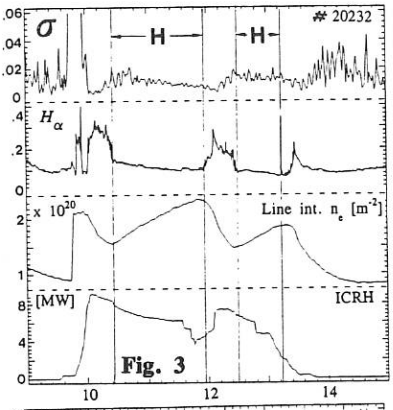

Fig. 3

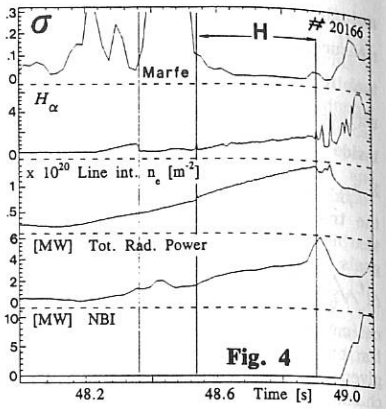

Fig. 4

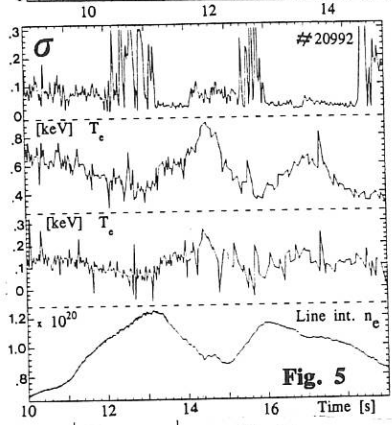

Fig. 5

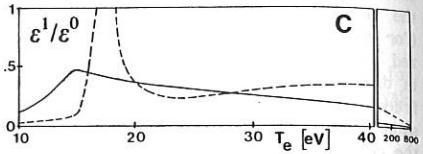

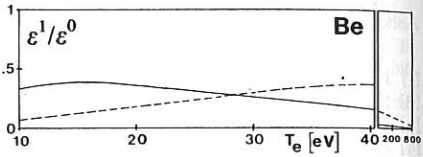

Fig. 6 —— $q_a = 2$, $n_e = 1.\cdot 10^{19}$ [m^{-3}]
---- $q_a = 5$, $n_e = 1.\cdot 10^{19}$ [m^{-3}]

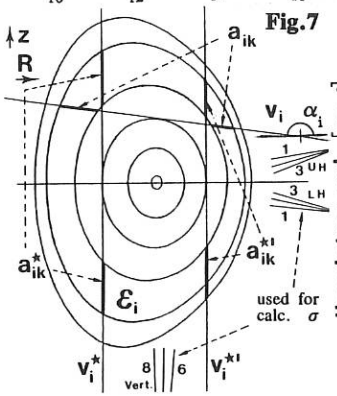

Fig.7

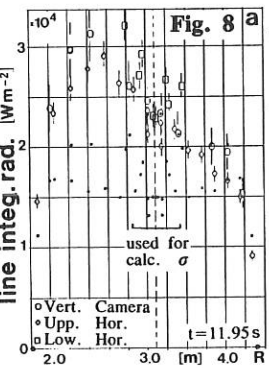

Fig. 8

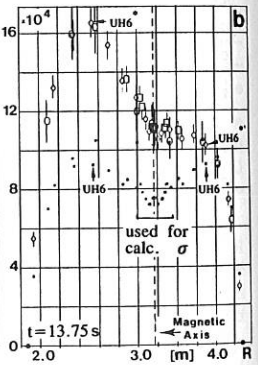

ELECTRIC FIELD PROFILE OF PLASMAS WITH IMPROVED CONFINEMENT IN JFT-2M TOKAMAK

K.Ida, S.-I.Itoh, K.Itoh, S.Hidekuma

National Institute for Fusion Science
Nagoya, 464-01, Japan

Y.Miura, N.Suzuki, M.Mori, T.Matsuda, T.Yamauchi
and JFT-2M Group

Japan Atomic Energy Research Institute
Naka-machi, Naka-gun, Ibaraki, 311-01, Japan

Introduction

The improvement of core confinement has been found in various improved confinement mode such as IOC[1], improved L-mode[2] and plasmas with counter(ctr)- neutral beam(NB) heating[3] and with pellet injection[4]. These plasmas show peaked density profiles and significant inward particle pinch. The inward particle pinch due to the shear of the radial electric field is proposed in the theoretical model[5]. In this paper, the radial electric field and particle flux profiles are presented for the plasma in the JFT-2M tokamak with flat and peaked density profiles.

Temporal evolution and radial electric field

The profile of radial electric field can be controlled somewhat by changing the direction of momentum input, parallel (co-) or anti-parallel (ctr-) to the plasma current[6]. JFT-2M is a tokamak with a major radius R=1.31 m and minor radius a=0.35 m. It has two tangential neutral beams, one is in co-injection and the other in counter injection. We switch the neutral beams during the discharge to study the response of electric field and particle flux. The toroidal rotation and ion temperature profiles are measured with multi-channel charge exchange spectroscopy[7] every 16.6 ms, the line-averaged density with FIR laser interferometer, and total stored energy with diamagnetic measurements. The toroidal rotation velocity and electric field changed within 30 ms after the onset of counter injection, while density peaking parameter, central ion temperature and the total stored energy continue to increase over 100 ms (duration time of ctr injection) as shown in Fig.1 and Fig.2. Since no saturation of density peaking parameter is observed, the scale time of particle pinch estimated with the time evolution of electron density peaking parameter is more than 1 sec, while the scale time of flattening at the onset of co-NBI is 20-30 ms. The scale time of the increase of total stored energy is estimated to be 70 ms, however the estimation of scale time can be 400 ms if we

fit the time evolution of stored energy up to 850 ms with exponential function. The radial electric field profiles are obtained with toroidal rotation velocity and ion temperature profiles and electron density and temperature profiles measured at 690 ms and 890 ms with Thomson scattering using momentum balance equation[8]. As shown in Fig.3 and Fig.4, peaked density profile and large share of electric field are observed in ctr-NBI phase.

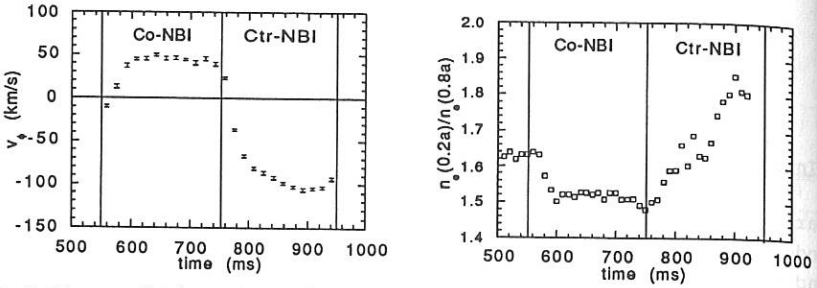

Fig.1 Time evolution of toroidal rotation velocity (v_ϕ) at r=4cm and the ratio of line-averaged electron density measured at r=0.2aand r=0.8a.

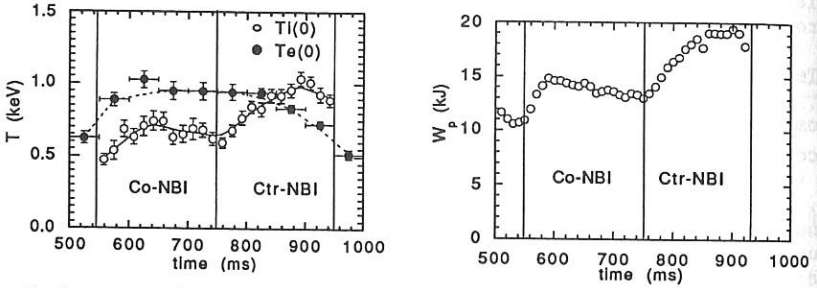

Fig.2 Time evolution of central ion and electron temperature (T_i, T_e) and the total stored energy (W_p).

Particle flux

Since the density peaking is observed in counter phase, inward particle pinch should exists. Particle fluxes are estimated from time evolution of electron density profiles $\partial ne/\partial r(r)$ measured with Thomson scattering and FIR laser interferometer and particle deposition profiles due to neutral beam. Figure 5 shows the particle fluxes, positive is outward and negative is inward, for co- and counter- NBI phase. The particle flux in co-NBI phase is outward and is balanced to particle deposition of NB. The inward particle pinch measured in counter phase is comparable to or greater than outward particle

flux in co-NBI phase.

It is interesting to compare the estimation of particle flux predicted by the inward pinch model[5] using measured density and temperature gradients and radial electric filed profiles. We got the diffusion coefficients D=300 cm^2/s for co-NBI phase and D=130 cm^2/s for ctr-NBI phase to match the experimental values of flux at r=0.15a. The flux is proportional to diffusion coefficients according to the model. Since the profiles of diffusion coefficient in core region is unknown, for these discharges, the comparison with the model is not quantitative. However we have qualitative agreement with measurement of the scale time of 1 sec and the estimation of D. The diffusion coefficient derived from the scale time of density peaking is less than 200 cm^2/s.

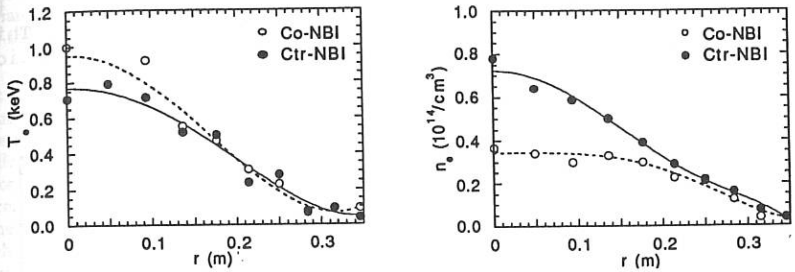

Fig.3 Profiles of electron temperature (T_e) and density (n_e) at t=690 ms (co-NBI) and 890 ms (ctr-NBI).

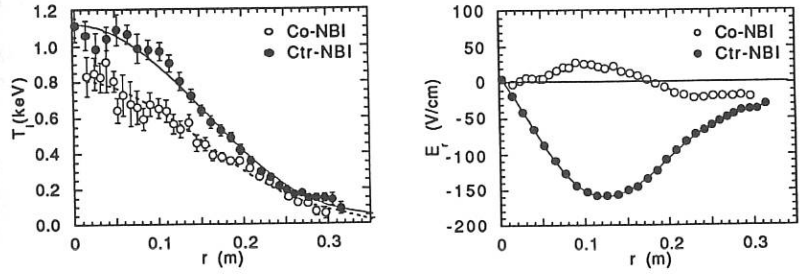

Fig.4 Profiles of ion temperature (T_i) and radial electric field (E_r) at t=690 ms (co-NBI) and 890 ms (ctr-NBI).

Heat flux

Improvement of ion confinement is clear from figure 2, since ion temperature is increased and higher than electron temperature in counter-NBI with the input power similar to that in co-NBI. The energy flow is obtained from beam power deposition and energy transfer from or to electron. The energy

exchange between ions and electrons is reversed in counter-injection phase. The decrease of ion heat flow (q_{co}-q_{ctr}) is larger than the additional inward heat flow (q_{conv}) due to inward particle pinch in counter NBI phase. It is not clear that whether ion conductivity is decreased or additional heat pinch appears in counter-NBI phase.

We introduce effective ion thermal conductivity defined by $q_i/n_i(\partial T_i/\partial r)$ as a measure of improvement of ion energy confinement. The effective ion conductivity at r=0.3a is 2 m^2/s for co-NBI and 0.3 m^2/s for counter-NBI phase, although these increase near the plasma edge. This reduction is consistent with the scale time of the change of energy confinement of > 70 ms. It is open to question whether the improvement of ion confinement is due to the reduction of ion conductivity or heat pinch. However, the inward particle pinch due to the electric field shear associated with the toroidal rotation shear is observed in plasma with counter neutral beam injection. This inward pinch at least qualitatively agrees with the estimation of inward pinch model.

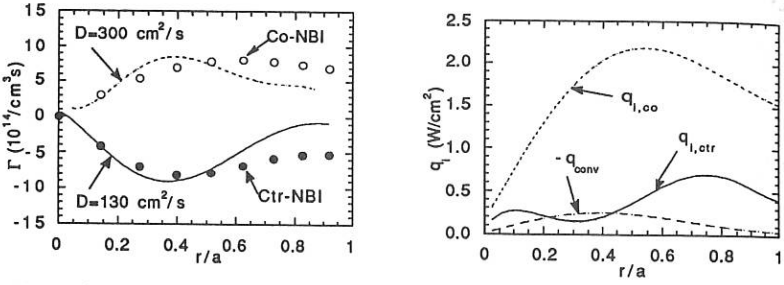

Fig.5 Profiles of particle (Γ) and ion heat flux (q_i) at t=690 ms (co-NBI) and 890 ms (ctr-NBI). In the left figure, open and close circle stand for the measured particle flux, while dash and solid lines are estimation with particle pinch model.

References

1) F.X.Soldner, E.R.Muller, F.Wagner, et al. Phys. Rev. Lett. **61** 1105 (1988).
2) M.Mori, N.Suzuki, et al., Nucl. Fusion. **28** 1891 (1988).
3) O.Gehre, O.Gruber, H.D.Murmann, D.E.Roberts, F.Wagner, et al., Phys. Rev. Lett. **60** 1502 (1988).
4) M.Greenwald, D.Gwinn, S.Milora, J.Paker, R.Parker, S.Wolfe, et al., **53** 352 (1984).
5) S.-I.Itoh NIFS (National Institute for Fusion Science) report #8.
6) G.A.Hallock, J.Mathew, W.C.Jennings, R.L.Hickok, Phys. Rev. Lett. **56** 1248 (1986).
7) K.Ida and S.Hidekuma, Rev. Sci. Instrum. **60** 867 (1989).
8) F.L.Hinton and R.D.Hazeltine Rev.Mod. Phys. **48** 239 (1976).

COMPARISON OF THERMAL AND ANGULAR MOMENTUM TRANSPORT IN NEUTRAL BEAM-HEATED HOT-ION H– AND L–MODE DISCHARGES IN DIII–D*

K.H. Burrell, R.J. Groebner, T.N. Carlstrom, T. Kurki-Suonio,†
J. Lohr, H. Matsumoto,‡ G. Sager, H. St John, R.P. Seraydarian,
D.P. Schissel, and S.M. Wolfe¶

General Atomics, San Diego, California, USA

We have carried out experiments using the hot-ion mode of operation to compare the bulk transport in L–mode and H–mode discharges. These experiments have demonstrated that the confinement improvement in the bulk of the plasma in DIII–D is due to a simultaneous improvement in electron and ion energy transport. In addition, the magnitude of electron and ion thermal diffusivities and angular momentum diffusivity as well as the change in these quantities between L– and H–mode have allowed us to place significant constraints on theories of tokamak transport.

Although the most obvious improvement in confinement at the L to H transition occurs at the plasma edge, there is also a significant improvement in local energy transport throughout the plasma.[1–4] Most of the previous experiments[1–3] in this area made their comparison between L–mode and H–mode plasmas at significantly different densities. This could have affected the results if the local transport depends on density. The work by Jahns, *et al.*[4] was done at the same line-averaged density; they still found a significant improvement in local transport, although they were not able to determine whether the improvement occurred in the electron or ion channel. We have extended the work of Jahns, *et al.* to hot-ion conditions where we can separately study the power flow in the electron and ion channels. We have made detailed comparisons of energy and angular momentum transport between deuterium L– and H–mode plasmas with the same density (3.5×10^{19} m^{-3}), the same current (1 MA), the same toroidal field (2.1 T), the same deuterium neutral beam input power (8.7 MW), and very similar internal flux surface shapes.

HOT-ION MODE OPERATION

In transport analysis, one of the major sources of uncertainty in the inferred thermal diffusivities is the electron-ion energy exchange term. This term is of the form[5]

$$3 \frac{m_e}{m_i} \frac{n_e}{\tau_e} (T_e - T_i)$$

Because this term depends on a temperature difference, the relative error in the exchange term can be significantly bigger than the relative errors in T_e and T_i if T_e and T_i are close to each other. In addition, if the coefficient of the $T_e - T_i$ term is large, then even small relative errors in T_e and T_i can result in large relative errors in the inferred thermal diffusivities.

In order to minimize the errors in the inferred diffusivities, we have chosen to operate in the low density, high temperature regime known as the hot-ion mode. Owing to the

* This work was sponsored by the U.S. Department of Energy under Contract No. DE-AC03-89ER51114.

† University of California at Berkeley.

‡ Japan Atomic Energy Research Institute.

¶ Massachusetts Institute of Technology.

of the energy exchange term. In addition, by operating with deuterium beam injection, the beam energy can be coupled primarily into the ion channel. As can be seen in Fig. 1 this results in $T_i \gg T_e$, which means that the relative error in determining $T_e - T_i$ is almost the same as the relative error in T_i itself. Central T_i of 12 keV has been obtained in the H–mode plasmas used in the present study; other hot-ion H–mode plasmas have had central T_i as high as 17 keV.

Since the density rises after the onset of neutral beam injection in both L–mode and H–mode, accessing the hot-ion mode requires starting with low Ohmic target densities. These low densities are easier to attain at modest plasma currents. For the study reported here, we have utilized operation at 1 MA plasma current. In other work, we have been able to obtain the hot-ion mode at currents as high as 1.5 MA.

The density rise continues in the H–mode shot up until the time of the first ELM; however, the density in the L–mode soon reaches a steady state value. In order to compare the transport in the L–mode and H–mode at the same density, we must analyze the H–mode data during the evolving phase prior to the first ELM. This requires time-dependent transport analysis, which demands a complete time sequence of profile measurements. Although there were sawteeth in these plasmas in the Ohmic phase, they disappeared in the beam-heated phase of both the L–mode and H–mode plasmas. There are no sawteeth during the time interval analyzed.

In order to make the internal flux surface shapes of the plasmas that we are comparing as similar as possible, we have chosen a limiter L–mode and a double-null divertor H–mode plasma. Vertical elongation of the internal flux surfaces is about 1.8 for both. It was necessary to use a limiter discharge for the L–mode case because a divertor discharge with this much input power would have gone into the H–mode so quickly that the L–mode phase could have not been adequately analyzed. Lower power operation would not have been suitable because it would have reduced the difference between T_i and T_e.

TRANSPORT COMPARISON

The differences in the radial profiles of temperature, density and toroidal rotation speed demonstrate that bulk transport of energy and angular momentum is significantly worse in the L–mode plasma than in the H–mode plasma. As shown in Fig. 1, the shapes of the temperature profiles are quite similar, but the central values differ by a factor of about 1.5. A second difference in the profiles is shown in the density profiles in Fig. 2. The H–mode density profile is broad and quite flat in the center, with very steep gradients in the edge. The L–mode density profile is more peaked. These density profile shapes are characteristic of all the L– and H–mode plasmas operated in DIII–D. This broad, flat density profile in the H–mode is very different from the extremely peaked density profiles obtained in TFTR supershots, which also have $T_i \gg T_e$. A third difference between the L–mode and H–mode plasmas is in the magnitude of the toroidal plasma rotation. As is shown in Fig. 3, the angular rotation speed profiles are quite similar in shape, but the magnitudes of the central values differ by a factor of about 1.8.

Transport has been analyzed in detail in these discharges by using the ONETWO transport code.[6] The inferred electron and ion thermal diffusivities χ_e and χ_i and the angular momentum diffusivity χ_ϕ are compared in Figs. 4 and 5 for the H–mode and the L–mode. The most dramatic improvement from L–mode to H–mode is in χ_e, which improves by about a factor of three throughout most of the plasma, with an even larger improvement at near the plasma edge. The improvement in χ_ϕ is similar to that in χ_e. Indeed, outside of $\rho = 0.3$, χ_e and χ_ϕ are basically equal within the error bars in both L–mode and H–mode. The χ_i improves only inside of $\rho = 0.5$; there is no change in χ_i within the error bars in the outer half of the plasma. The χ_i is significantly less than χ_e in the center of both the H–mode and L–mode plasmas. An additional important feature of these inferred diffusivities is that

χ_i inside of $\rho = 0.3$ in the hot-ion H–mode agrees with the predictions of Chang-Hinton neoclassical theory[7] within the error bars.

COMPARISONS WITH THEORY

Although χ_i in the center of the hot-ion H–mode plasmas is comparable to the neoclassical prediction, χ_e and χ_ϕ are much larger everywhere than would be predicted by the neoclassical theory. Accordingly, if we wish to understand the thermal and angular momentum transport, we must consider various fluctuation-based anomalous transport theories. Our experimental observations present a challenge for several of the existing theories of anomalous transport.

Many theories of anomalous electron transport are based on the effects of some form of electron drift wave.[8] However, most of these drift waves are stable in a plasma with a flat electron density profile; accordingly, they would not contribute to transport in our H–mode plasmas. The recently discussed electron drift waves that are driven unstable by electron temperature gradients[9] might be a candidate for explaining electron transport in these plasmas. Since the density gradient is nonzero in the L–mode plasma, electron drift waves might explain the difference between χ_e in L–mode and H–mode.

Drift waves can also be driven unstable by ion temperature gradients in plasmas with flat density gradients[10,11] if the ion temperature gradient scale length L_{T_i} is short enough. These ITG modes would give χ_i about equal to χ_ϕ, which is what is seen in the outer half of our H–mode plasmas. However, they could not explain the results near ρ of 0.3, where χ_i is basically neoclassical but $\chi_\phi \gg \chi_i$.

The usual picture of ITG-driven turbulence is that it is so strong that L_{T_i} drops to the critical value needed for the onset of the turbulence, but is then clamped there by the turbulence. A number of hot-ion H–mode shots in DIII–D with beam powers from 8 to 15 MW and plasma currents from 1.0 to 1.5 MA give a minimum $L_{T_i}/R = 0.08$ to 0.1. As is shown in Fig. 6, the theoretical threshold for L_{T_i}/R for the toroidal ITG mode, including corrections for $T_i \gg T_e$, is in the range of 0.2 to 0.4.[12] Accordingly, either the threshold is incorrectly calculated or the idea that L_{T_i} hovers at the marginal stability threshold is incorrect. An indication that the theory may need refinement is given by the results in Ref. 11, which shows a critical L_{T_i}/R as low as 0.1 when finite Larmor radius and sound wave coupling effects are included in a calculation that assumes $T_i = T_e$. In general, the ITG mode should be more stable when $T_i > T_e$.

REFERENCES

1. Becker, G., *et al.*, Nucl. Fusion **23**, (1983) 1293.
2. Kaye, S.M., *et al.*, J. Nucl. Mater. **121**, (1984) 115.
3. Watkins, M.L., *et al.*, Plasma Physics and Controlled Fusion **31** , (1989) 1713.
4. Jahns, G.L., R.J. Groebner and H. St John, Nucl. Fusion **29**, (1989) 1271.
5. Braginskii, S.I., in Reviews of Plasma Physics (M.A. Leontovitch, Ed., Consultants Bureau, New York,, 1965) Vol. I, p. 205.
6. Pfeiffer, W., *et al.*, Nucl. Fusion **25**, (1985) 655.
7. Chang, C.S., and F.L. Hinton, Phys. Fluids **25**, (1982) 1493.
8. Dominguez, R., and R. Waltz, Nuclear Fusion **27**, (1987) 65.
9. Dominguez, R., General Atomics Report GA-A19531 (May, 1989).
10. Dominguez, R., and R. Waltz, Phys. Fluids **31**, (1988) 3147.
11. Dominguez, R., and M. Rosenbluth, Nucl. Fusion **29**, (1989) 844.
12. Romanelli, F., Phys. Fluids **B 1**, 1018 (1989).

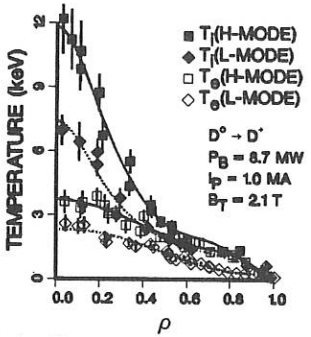

Fig. 1. Electron and ion temperature radial profiles.

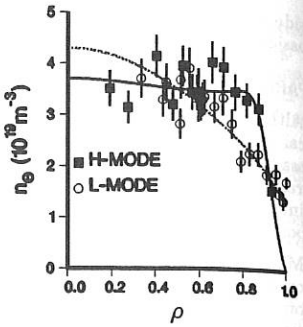

Fig. 2. Density profiles for the hot-ion H–mode and L–mode plasmas.

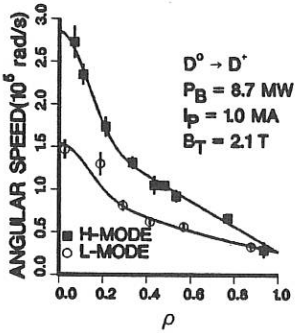

Fig. 3. Angular rotation speed profile for the hot-ion H–mode and L–mode plasma.

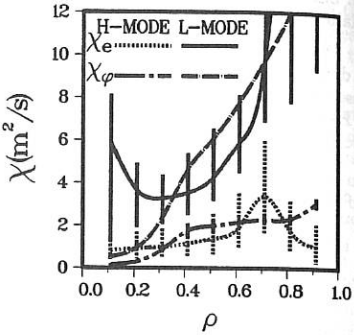

Fig. 4. Electron thermal diffusivity and angular momentum diffusivity as a function of radius in the bulk of the hot-ion L–mode and H–mode plasmas.

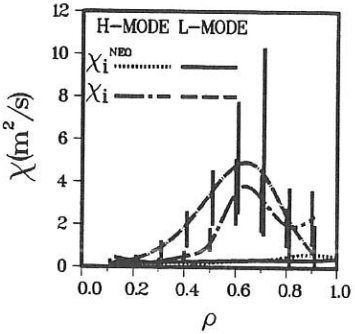

Fig. 5. Inferred and neoclassical ion thermal diffusivities as a function of radius in the bulk of the hot-ion L–mode and H–mode plasmas.

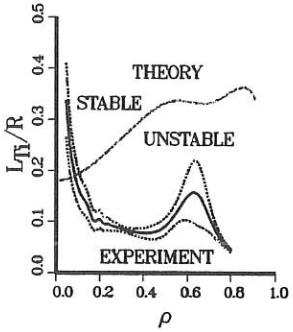

Fig. 6. Comparison of the measured ion temperature gradient scale length L_{Ti} with the theoretical prediction for the critical L_{Ti} at which ion temperature gradient driven turbulence should be excited.[12]

THE EFFECTS OF CARBONIZATION ON THE CONFINEMENT PROPERTIES OF THE DIII–D H–MODE*

D.P. Schissel, J.C. DeBoo, J.R. Ferron, G.L. Jackson, K.H. Burrell, R.J. Groebner, A.G. Kellman, S. Lippmann, T.W. Petrie, E.J. Strait, J. Winter,† and the DIII–D Research Team

General Atomics, San Diego, CA 92138 U.S.A.

Understanding and increasing the energy confinement time ($\tau_E \equiv W_T/P_T$) remains a primary goal of fusion research. A primary technique utilized to increase τ_E within a given machine is to operate at a higher plasma current. Although Z_{eff} in DIII–D is generally ≤ 2, high radiated power ($P_{rad}/P_T \geq 0.6$) and metal accumulation have been observed during high current ($I_p \geq 2$ MA) beam heated $D^\circ \rightarrow D^+$ H–mode discharges. Reduction of metallic impurity influx has been obtained on numerous tokamaks[1] with the introduction of a thin carbon film. This paper reports the successful carbonization[2] of the DIII–D vacuum vessel which allowed for routine high current operation, and it examines the confinement properties of carbonized discharges.

The confinement properties of the DIII–D deuterium H–mode discharges utilizing carbonization have been studied over a wide parameter range. Single– and double–null neutral beam heated divertor discharges have been obtained at 2.1 T with $P_b \leq 18$ MW, $1 \leq I_p(\text{MA}) \leq 3$, and $3 \leq q_{95} \leq 7$. Although no specific L–mode to H–mode transition experiments were performed, the H–mode power threshold for the carbonized plasma was not substantially different from the non–carbonized case. High plasma current operation combined with 18 MW of deuterium neutral beam injection resulted in the largest DIII–D total plasma stored energy presently obtained of 3.6 MJ, and also in the stored energy remaining above 3 MJ for 0.5 seconds. Values of the toroidal beta greater than 5%, at the maximum machine capability for B_T of 2.1 T, were obtained in these same plasmas. Hot ion mode operation with carbonization resulted in higher central ion temperature (15 keV) at the same plasma current, toroidal field and neutral beam power when compared to a non–carbonized plasma. This higher temperature resulted from a lower neutral beam target electron density which was made possible due to a lower locked mode density threshold. This reduction in the locked mode density threshold appears to be related to the smaller concentration of oxygen (factor of ~6) in the carbonized plasmas.

The DIII–D tokamak has 40% of the plasma facing surface protected by graphite and the remaining 60% consists of Inconnel 625. The interior of the DIII–D vacuum vessel was carbonized using a methane glow discharge initially resulting in a 60 nm carbon film, the details of which have been previously reported.[2] The carbonization reduced metallic impurity accumulation during high power H–modes by as much as a factor of 30. Figure 1 compares the temporal evolution of two single–null H–mode discharges at the same power and current but one discharge being representative of before carbonization and the other representative of after carbonization.

A consequence of the smaller metallic impurity concentration was the substantial reduction in P_{rad}/P_T for the carbonized plasmas. The comparison of the time evolution of P_{rad} for the before and after carbonization cases with 6.5 MW of deuterium neutral beam heating is shown in Fig. 1. In the ohmic phase both discharges have low radiated power with the

* This work was supported by the U.S. Department of Energy under Contract No. DE-AC03-89ER51114.

† Institute of Plasmaphysics, KFA.

carbonized discharge having a slightly smaller value. In the beam phase P_{rad} rises dramatically for the non–carbonized case and remains at a high value which was modulated by the giant–ELMs. Non–carbonized discharges with a long enough ELM–free period transitioned back to L–mode due to $P_{rad}/P_T \approx 100\%$. In contrast to the non–carbonized case, the radiated power in the carbonized discharge remains low throughout the entire H–mode phase.

Figure 2 shows the change due to carbonization of the radiated power profile before the first ELM of a 2.0 MA, 6.5 MW H–mode plasma. As is evident from the figure, discharges with carbonization have a dramatically smaller radiation power density in the outer half of the plasma. Furthermore, the profile shape for the carbonized plasma does not change in time whereas the non–carbonized plasma had an increase in central radiation which developed over $\approx$0.75 seconds. The reduction in P_{rad} with carbonization was accompanied by an increase in the heat load to the divertor. This substantial reduction in radiation with carbonization allowed for reliable double–null tokamak operation over a wide range of plasma currents up to and including 3 MA.

The beneficial impurity reduction that resulted from carbonization lasted on the order of 150–250 high power discharges. On a shot to shot basis, the oxygen impurity concentration rose significantly faster than did the nickel concentration. Figure 1 illustrates the change in ELM frequency that was observed between pre– and post–carbonization with the latter case having an increase in ELM frequency. Since carbonization was performed with CD_4, the deposited carbon layer was rich in deuterium which potentially could have been a large fueling source for the main plasma. However, the rate of density increase during the H–mode was not significantly higher than before carbonization most likely due to the 3–5 minutes of helium glow wall conditioning that is performed before every tokamak discharge and a post–carbonization bake to $T_{ave} = 350$ C°. Figure 3 compares the density profiles[2] of a pre– and post–carbonization H–mode discharge created by 6.5 MW of deuterium neutral beam heating. The two profiles in Fig. 3 have similar volume average electron densities with values of 9.0×10^{19} m^{-3} and 9.3×10^{19} m^{-3} for the pre– and post–carbonization discharges respectively. However, as is evident from the figure, the post–carbonization H–mode plasma had a noticeably more peaked density profile with a peak to volume average ratio of ~ 2 compared to a ratio of ~ 1 for the pre–carbonized case. These profiles were measured during the ELMing phase of both H–mode plasmas which would correspond to a time of approximately 2700 ms in Fig. 1. Peaked H–mode density profiles with carbonization were not always obtained and experiments are presently underway to study this phenomenon in greater detail.

Deuterium H–mode energy confinement with carbonization increases with increasing plasma current as was observed before carbonization.[3] The high triangularity of these carbonized plasmas allowed q_{95} to be greater than three for all values of the plasma current which greatly reduced the difficulty of operating at 3 MA. The results of a 9 MW plasma current scan are presented in Fig. 4 where it is evident that the increase of confinement with current ceased near $I_p/B_T = 1$ and $q_{95} = 4$. This result is similar to previous results[4] from DIII–D that indicated that the proper criterion for describing confinement saturation involves I_p/B_T not q. Possible mechanisms for this loss of current scaling that have been rejected are the plasma reaching a β_T limit, a ceiling on confinement imposed by saturated ohmic confinement, and significant coupling of sawtooth and ELM activity. One explanation that is still under consideration is that the confinement saturation at higher current is due to the interaction of an increasing sawtooth mixing radius combined with a broader beam deposition profile. Independently fitting the pre– and post–carbonization confinement data in Fig. 4 yields $\tau_E = 0.84\, I_p^{0.8\pm0.2}$ for both datasets with units of MA and seconds. For the small number of discharges in Fig. 4, the current exponent is unity within the quoted error bars. However, a large volume of non–carbonized D° $\rightarrow$ D$^+$ data gathered over the last year indicates that the dependence of τ_E on plasma current is somewhat weaker than $I_p^{1.0}$.

Deuterium H–mode energy confinement with carbonization decreases with increasing neutral beam power as was observed before carbonization.[3] Figure 5 compares the increase of

W_T with increasing P_T for both discharges with and without carbonization. The carbonized data presented in Fig. 5 is at 2.8 MA but this is in the regime where τ_E no longer depends on I_p. Describing the combined dataset of Fig. 5 with an offset linear representation results in an incremental τ_E of 156 ms and an offset term W_0 of 0.57 MJ.

In summary, carbonization has been utilized on DIII–D which successfully reduced metallic impurity concentrations, reduced P_{rad}/P_T and allowed for routine operation at a plasma current of 3 MA. Although there was no change in energy confinement with carbonization, the higher plasma currents allowed for operation at β_T greater than 5% at 2.1 T. Peaked H–mode density profiles were observed and will continue to be investigated in future experiments. The potential benefit for a reactor like device of a peaked H–mode density profile would be the increase in reactivity resulting in a larger ignition margin for a given value of confinement.

REFERENCES

1. Winter, J., *et al.*, J. Nucl. Mater. **145–147** (1987) 131.
2. Jackson, G.L., *et al.*, "Carbonization of the DIII–D Tokamak," presented at the Ninth International Conference on Plasma Surface Interactions, (Bournemouth, United Kingdom, 1990), to be published in Journal of Nuclear Materials.
3. Schissel, D.P., *et al.*, Controlled Fusion and Plasma Physics **13B**, (1989) 115.
4. Burrell, K.H., *et al.*, Plasma Physics and Controlled Fusion **31**, (1989) 1649.

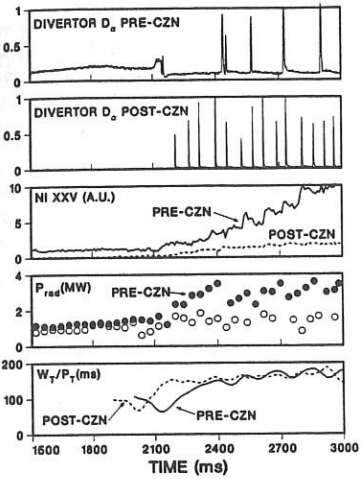

Fig. 1. Various diagnostic signals as a function of time for two typical single-null 2.0 MA H–mode discharges with and without carbonization. The 6.5 MW of deuterium beam heating begins at 2000 ms and 2100 ms for the POST-CZN and PRE-CZN discharges respectively. The radiated power signal was integrated for 20 ms, and the electronic circuitry was unable to handle the spike in radiation flux during a giant-ELM.

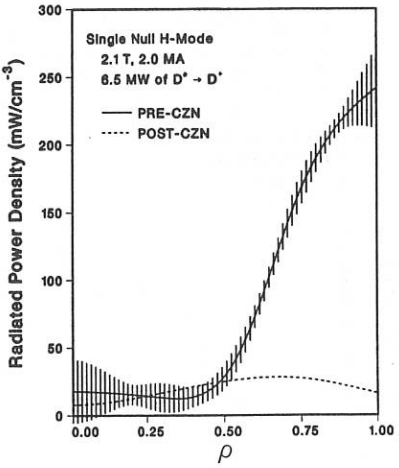

Fig. 2. Radiated power density profiles measured by a 21 channel bolometer diagnostic for two single-null $D^\circ \rightarrow D^+$ H–mode discharges with and without carbonization. The vertical lines represent the typical error band for these profiles.

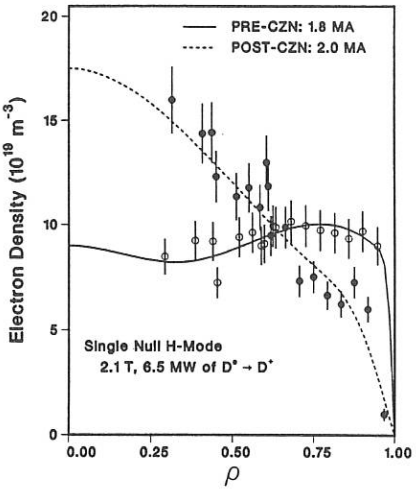

Fig. 3. Electron density profiles measured by Thomson scattering and CO_2 interferometry for two single-null $D^0 \rightarrow D^+$ H–mode discharges with and without carbonization.

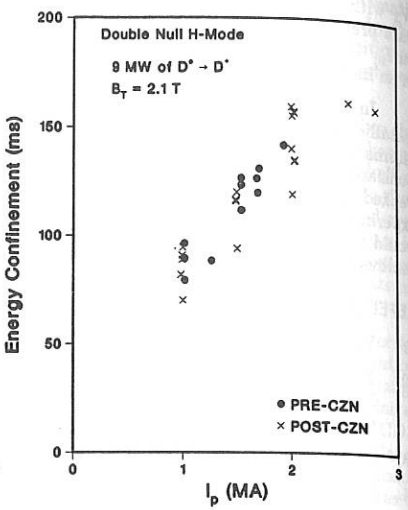

Fig. 4. Divertor $D^0 \rightarrow D^+$ H–mode τ_E versus plasma current for discharges with and without (PRE-CZN) carbonization.

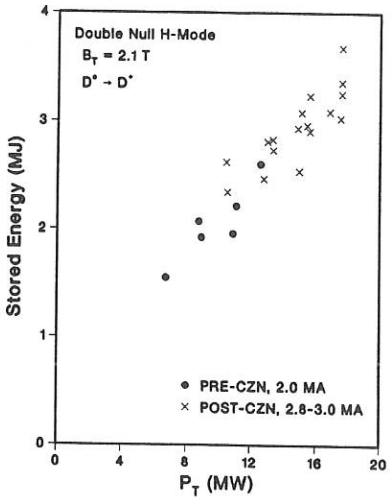

Fig. 5. Divertor $D^0 \rightarrow D^+$ H–mode W_T versus total input power for discharges with and without (PRE-CZN) carbonization.

PHYSICS OF THE L TO H TRANSITION IN DIII–D*

H. MATSUMOTO,† K.H. BURRELL, T.N. CARLSTROM, E.J. DOYLE,‡ P. GOHIL, R.J. GROEBNER, T. LEHECKA,‡ N.C. LUHMANN, JR.,‡ M.A. MAHDAVI, T.H. OSBORNE, W.A. PEEBLES,‡ AND R. PHILIPONA‡

General Atomics, San Diego, California, USA

A decrease in the edge magnetic and density fluctuations is always seen at the L-H transitions in DIII–D. Although H–mode is best known for an increase in energy confinement, in fact, the reduction in the edge fluctuations is one of the most reliable indicators of the L-H transition. In DIII–D, a sudden change of the perpendicular rotation, $V_\perp$ in the edge has been also observed at the transition. Recently, theories that fluctuations are reduced by sheared poloidal flow have been proposed to link these two observations.[1,2] Also, a theory to explain the mechanism responsible for the observed poloidal flow has been proposed.[2] Experimental observations have thus far been consistent with these theories.

EXPERIMENTAL RESULTS

Change in Edge Fluctuations

Mirnov coil measurements show that high frequency magnetic fluctuations ($\geq$10 kHz) are reduced at the L-H transition. Probes close to the plasma surface see the change very clearly. Magnetic fluctuations seen by probes distant from the plasma surface are usually dominated by strong MHD oscillations with low poloidal m numbers. However, background turbulent fluctuation spectra are clearly suppressed at the transition even on these probes. These changes of magnetic fluctuations are seen almost simultaneously on inside and outside probes, to within the instrumental time resolution, $\sim$100 μsec. The use of external magnetic probes makes it difficult to determine the exact spatial location of the observed reduction in magnetic turbulence. However, the suppression is thought to originate from the edge plasma region. Spatially localized measurements [3] of density fluctuations in the edge of DIII–D plasmas are done using "O" and "X"–mode reflectometer systems.[4,5] They clearly see changes in the density fluctuations at the transition localized to a narrow edge plasma region. Figure 1 shows the fluctuation power obtained by digital spectral analysis of the reflectometer signals. The O–mode system consists of 6 channels at 15, 24, 32, 40, 50, 60 GHz, which monitor fluctuations at critical densities 0.28, 0.72, 1.2, 2.0, 3.1, 4.5 $\times$ 10^{19} m^{-3}. In Fig. 1, the channel at 3.1 $\times$ 10^{19} m^{-3} does not the see the change. However, channels at lower densities all see a sudden decrease. Spatial locations of these channel were determined from the density profile just before the transition which is shown in Fig. 2. This density profile is determined from a fitting of Thomson profile and 4 chord interferometer measurements, and the dotted line indicates the statistical error in the measurement. The closed circles show the position of the reflectometer channels for which fluctuation levels are reduced. The open circle indicates the location of the channel which did not see the change. The

* This work was sponsored by the U.S. Department of Energy under Contract No. DE-AC03-89ER51114.

† Japan Atomic Energy Research Institute.

‡ University of California at Los Angeles.

plasma minor radius was 57.4 cm, and we can see that density fluctuations in a narrow edge region 5–10 cm from the separatrix are reduced at the transition. Typical time scale for density fluctuations to decrease at the transition is about 100–300 μsec. All reflectometer channels lying within the region of turbulence suppression are observed to change within 100 μsec of each others.

Change in Poloidal Flow

In DIII–D, a sudden change of poloidal flow in the electron diamagnetic direction was found in the edge region, a few cm inside the separatrix, by spectroscopic measurements of helium lines [6]. Simultaneous measurements of poloidal and toroidal flow allow the change in the rotation perpendicular to the magnetic field to be determined. From this perpendicular flow measurement, radial electric field can be calculated from the following force balance equation, $E_r = \frac{1}{n_i Z_i e} \nabla P_i - (\vec{V}_i \times \vec{B})_r$ where n is ion density, Z is the ion's charge, P is the ion pressure, $\vec{V}$ is the ion fluid's flow velocity, $\vec{B}$ is the total magnetic field. A sudden change of radial electric field at a few centimeters inside the separatrix surface is found. The electric field is inward pointing (negative) prior to the transition, and becomes more so after the transition. The change in the edge radial electric field in the same discharge as of Figs. 1 and 2 is shown in Fig. 3. The time resolution in this rotation measurement was 4 ms, and it is very difficult to determine causality. For example, the data point which showed the sudden decrease of the electric field was measured from 2194 ms to 2198 ms, whereas the L-H transition happened at 2195 ms. However, we have never seen a case where change in poloidal flow takes place after the change in fluctuations. Rather there are some cases where edge rotation starts changing well before the transition. Further inside the plasma, we do not see any significant changes in the $V_\perp$ or radial electric field from charge exchange recombination (CER) measurements. Also, the rotational measurement around the separatrix surface, from the cold component of the He line, gives a small change of the rotation. This suggests the sudden creation of steep shear in the edge radial electric field at the transition. This change in the edge radial electric field is always observed to occur in all kinds of H–mode transitions in DIII–D(neutral beam injected, ECH heated, and ohmic H–mode transitions). The edge CER system has been upgraded recently, and both the spatial and time resolution have been significantly improved, and this should allow the causality and the shear in the radial electric field to be determined.

COMPARISON WITH THEORIES

Biglari et al[1] recently proposed a theory of stabilization of microturbulence by shear in perpendicular flow $V_\perp$. They give the criterion for the stabilization of the turbulence as $\Delta r_t / L_v > \Delta \omega_t / \omega_\theta$, where Δr_t is the radial decorrelation length, L_v is the scale length for shear in v_θ, $\Delta \omega_t$ is the decorrelation rate, and $\omega_\theta = k_y v_\theta$ is the poloidal rotation frequency. If we try a very rough estimate, we can take $v_\theta = 30$ km/s, and $L_v = 2$ cm from CER measurement, Δr_t as a poloidal ion Larmor radius ~ 1 cm, and $\Delta \omega_t = 2\pi \times 100$ kHz $- 2\pi \times 200$ kHz from the reflectometer measurement. This gives a k_y which can be stabilized of $k_y > 0.4$–0.8 cm^{-1}. The observed rotational shear is therefore in the right order of magnitude to reduce the turbulence responsible for the edge transport. Detailed comparison with the theory requires accurate determination of the radial decorrelation length, and the decorrelation time.

Fluctuations at 5–6 cm inside the separatrix are usually quenched at the transition. Therefore, if the theory is correct, shear in the poloidal flow must extend up to that point, or, the poloidal flow must decay further inside thereby producing shear with opposite sign. Biglari et al. predict stabilization with increase in $|dv_\theta/dr|$, and the effect exists with either sign of dv_θ/dr.

Here, we must note that the stabilization condition given by Biglari et al. is the condition that the decorrelation process by rotational shear becomes dominant. It is not a threshold condition. To explain the sudden quenching of the fluctuations, a sudden increase of shear at the transition is required. Shaing's theory[2] suggests that poloidal flow is driven by the ion orbit loss in the layer a few poloidal Larmor radii from the separatrix. He has also demonstrated a bifurcated solution in poloidal flow, thereby allowing a large increase in poloidal flow at the transition to H-mode. Experimentally determined lower bounds for the width of the layer where fluctuations are suppressed are plotted in Fig. 4 against the poloidal ion Larmor radius for that location. Those widths are within 2–9 Larmor radius. In the near future, refined experimental work should allow a more precise comparison with existing theories.

CONCLUSIONS

Edge density fluctuations are found to be reduced in the edge region at the L-H transition. A preliminary estimate of the width of the fluctuation stabilization region ranges between 2 and 9 poloidal gyroradii. Dramatic changes in the edge perpendicular rotation velocity are also observed at all L-H transitions in the DIII–D tokamak. It is quite conceivable that the steep shear in the perpendicular flow is created over the stabilization region and that the turbulence is strongly reduced by this.

1 Biglari, H., Diamond, P.H., and Terry, P.W., Physics of Fluids B2, 1 (1990).

2 Shaing, K.C., and Crume, Jr., E.C., Phys. Rev. Lett. **63**, 2369 (1989).

3 TFR Group, Plasma Physics and Contr. Fusion **27**, 1299 (1985).

4 Lehecka, et al., in Proceedings of the Sixteenth European Conference on Controlled Fusion and Plasma Physics, Venice, 1989, Vol. 13B, p 123.

5 Doyle, E.J., et al., "Density Fluctuation Measurements via Reflectometry on DIII–D during L– and H–mode Operation," this conference.

6 Groebner, R.J., et al., "The Role of Edge Electric Field and Poloidal Rotation in the L-H Transition," submitted to Physical Review Letters.

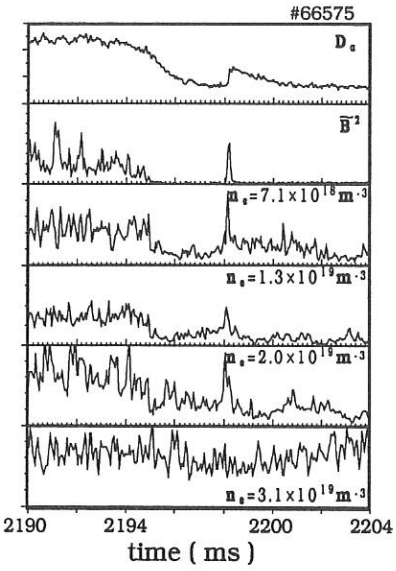

Fig.1

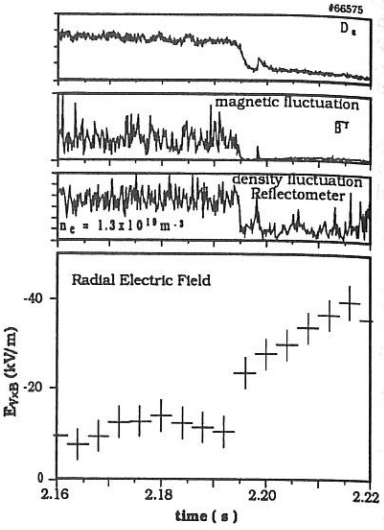

Fig.3

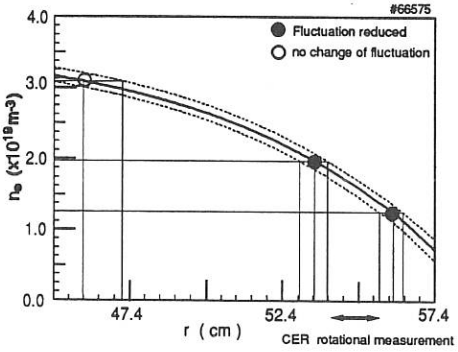

Fig.2

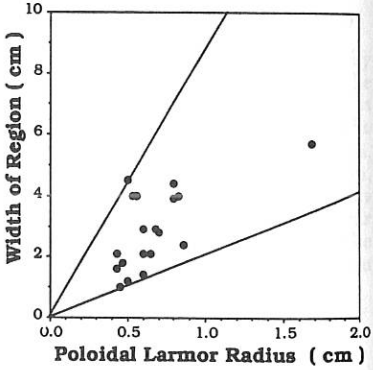

Fig.4

TRANSPORT PROPERTIES OF HIGH β_{pol} PBX-M PLASMAS

B. LeBlanc, S. M. Kaye, N. Asakura, R. Bell, R. Hatcher,
H. Kugel, M. Okabayashi, S. Paul, H. Takahashi
Plasma Physics Laboratory, Princeton University

Princeton, New Jersey 08543, USA

Introduction

One important result from the experimental research on tokamaks is the so called H-mode regime in which the energy confinement time can be a factor of two greater than in the L-mode. The H-mode, first obtained on ASDEX [1], has been observed in many tokamaks. Because this confinement regime could be important in the design of fusion reactors, it has been the object of many different studies. In ASDEX [2], the better confinement of the H-mode regime has been linked to a reduction of the electron thermal diffusivity, χ_e. In JET, a reduction of the ion thermal diffusivity, χ_i, is observed during the H-mode phase [3]. High beta poloidal discharges in PBX-M typically enter the H-mode regime. In what follows, it will be shown that, in PBX-M, the H-mode is characterized by a reduction in χ_i.

The PBX-M tokamak

The objective of the PBX-M project is to understand and improve tokamak plasma stability and confinement to demonstrate access to the second stability regime. Fig. 1 shows a cross-sectional view of the machine. Two unique features of the device, are exhibited, namely: the strong plasma shaping (via a set of shaping coils), and the close-fitting conducting wall for edge MHD stabilization. The indentation coil and its armor plate can be seen at the center-left (1.3 m, 0.m). Up to 6 MW auxiliary heating is achieved by deuterium neutral beam injection into a deuterium target (R_o=1.65 m) plasma. There are four beam injectors; two are at near perpendicular injection angles (R_{TAN}=0.35 m), two at tangential injection angles (R_{TAN}=1.3 m). The beam energy is 40 keV. We will concentrate on high β_{pol} discharges which are produced at a constant plasma current, I_p = 345 kA and a toroidal field, B_t, = 1.35 T during four neutral beam injection of 5.5 MW. The indentation is 15%, the elongation 1.6. and, a, the midplane minor radius ≈ 0.28 m. The Troyon parameter I_p/aB_t [4] is 0.8 with β_{pol} and $\langle\beta_t\rangle/(I_p/aB_t)$ of up to 2.4 and 4.5 respectively. These plasmas typically show an H-mode signature (D_α signal drop followed by increase of the density and stored energy). Later on, the discharge develops with different kinds of MHD

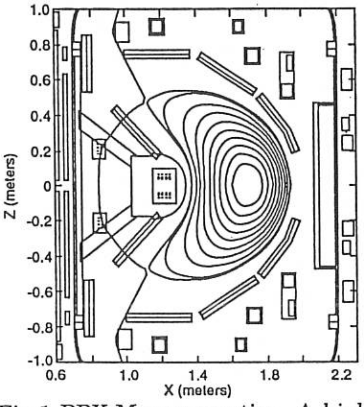

Fig.1 PBX-M cross-section. A high β_{pol} equilibrium is shown along with internal hardware, indentation coil, (center left) and conductive shell

activity. The equilibrium shown in Fig. 1 corresponds to an MHD free H-mode. We can see in Fig.2, the time evolution of some parameters of one discharge. The current (not shown) is maintained constant from 0.3 s on. The neutral beam injector on times are staggered sequentially at 0.05 s intervals from 0.25 s to 0.40 s, with the two tangential beams being injected first. Full beam power is maintained from 0.4 s to 0 55 s. The transition occurs at about 0.375 s as can be seen on the D_α trace. The stored energy reaches maximum value at 0.44 s and, as continuous mode MHD activity develops, it saturates and eventually rolls down. ELMs start at 0.455 s.

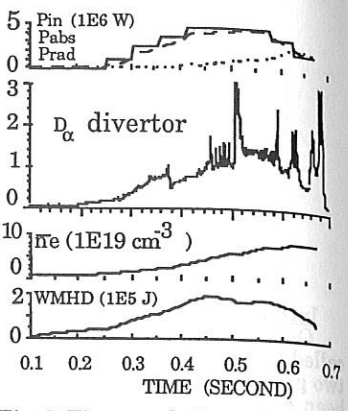

Fig 2 Time evolution of plasma parameters for high β_{pol} discharge in PBX-M

Transport analysis

A documentation of these discharges was made with the PBX-M full array of diagnostics. These include a full profile of the horizontal midplane electron temperature, $T_e(R)$, and density, $n_e(R)$, measured by a 55 channel Thomson scattering diagnostic system. Charge exchange spectroscopy measurement (CHERS system) on one of the heating beams provide the ion temperature and toroidal velocity profiles: $T_i(R)$ and $v_\phi(R)$. This nine channel measurement covers the outer half the plasma except for the last five cm of the edge region. The Z_{eff} profiles are computed from the visible continuum and Thomson scattering data. The radiated power is obtained from an array of 15 tangentially viewing bolometers located at the midplane. Single time point Thomson scattering measurements were concatenated to produce a time evolution of $T_e(R)$ and $n_e(R)$. The conçatenation takes into account the jitter ($\approx$ 0.04 s) of the H-mode transition time which is taken to be at 0.375 s. The end of the MHD free H-mode phase is at 0.46 s, and at 0.49 s the plasma has already experienced MHD activity for about 0.03 s. The Thomson scattering time slices are at : 0.24, 0.27, 0.30, 0.33, 0.40, 0.46 and 0.49 s. Z_{eff} profiles were concatenated similarly. The $T_i(R)$, $v_\phi(R)$ and bolometer data are taken from representative shots. The Ti slices are at every 0.02 s from 0.36 s to 0.46 s plus one slice at 0.49 s. For time points before 0.36 s, TRANSP [5,6] assume the T_i profile to be equal to the one at

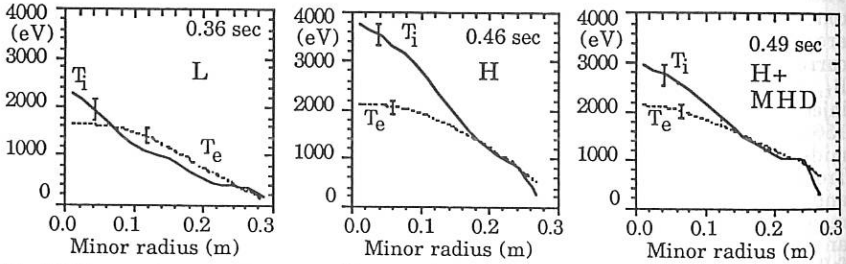

Fig.3 Plasma temperatures profiles at three times of interest: 0.36 s during L-mode, 0.46 s during MHD free H-mode, 0.49 s during H-mode with MHD activity and just prior to and ELM

0.36 s. The plasma boundary was computed by the FQ [7] code at each Thomson scattering time points. All this data was input into the TRANSP code which was run in analysis mode to compute the power fluxes and thermal diffusivities. For this computation, the documentation is interpolated onto a 0.005 s grid. The convection multiplier was set to 3/2. We will concentrate on the time interval 0.35 s to 0.5 s, and we will pay particular attention to three time points namely: 0.36 s (L-mode), 0.46 s (H-mode, no MHD activity) and 0.49 s (H-mode with continuous mode activity, just before ELM onset).
During this time interval, the total stored energy increases from 60 kJ up to 165 kJ at 0.46 s and then remains at at about 160 kJ. Meanwhile the energy stored in the fast ions increases from 35 kJ to 50 kJ. One problem may arise from the fact that in some cases $T_i \approx T_e$ over a substantial portion of the minor radius as can be seen on Fig. 3. This can lead to uncertain separation between the electron and ion channels. Because of the difficulty of evaluating (measuring) small gradients at the plasma center, and because many measurements have larger error bars in the edge region, the region of minimum uncertainty is: $a/3 \leq r \leq 2a/3$. Although no specific study of the error propagation was done for this analysis, past experience indicates the relative error bars to be 50% for $r \approx a/2$. We can see in Fig. 4 a plot of the ion diffusivity, χ_i, and the electron diffusivity, χ_e, as a function of time from 0.33 s to 0.5 s for three values of the midplane minor radius: a/3, a/2 and 2a/3. This choice corresponds to the region of confidence mentioned above. It can be seen that the ion and electron diffusivities differ and that $\chi_i \geq 2\chi_e$. The ion diffusivity falls by a factor of ≈ 3.0 at $r = a/2$, when going from the L-phase to the end of the MHD free H-phase even if one last beam is added at 0.4 s. During the same interval (0.36 s to 0.46 s) the electron diffusivity remains unchanged to within the uncertainty. The time needed for χ_i to drop and achieve its "final" H-mode value is shorter (0.04 s) on the outside then on the inside (0.08 s). We must keep in mind that the time resolution of this analysis is limited by the available experimental profiles to a value between 0.02 s and 0.06 s. Hence the

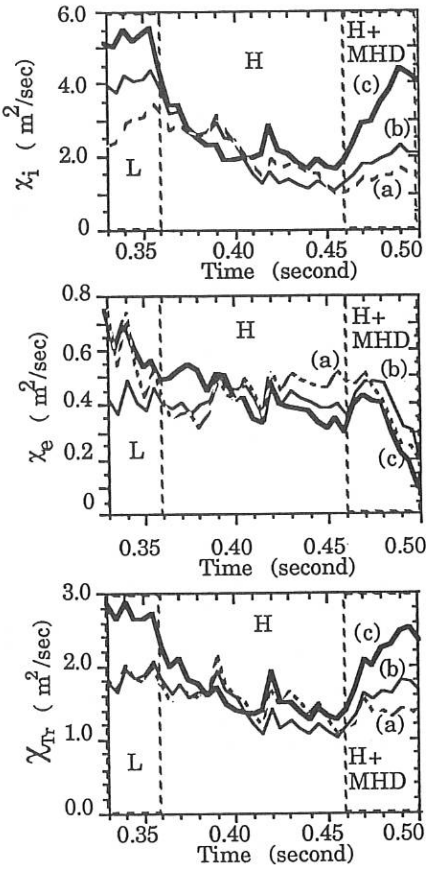

Fig.4 Time evolution of plasma diffusivities for three values of the midplane radius: (a) a/3 , (b) a/2, (c) 2a/3. Values of χ_i and χ_e are computed by TRANSP, see text for definition of the transport diffusivity χ_{Tr}.

two χ_i drop times previously mentioned are upper limits. The "analyzed" transition time of 0.36 s, instead 0.375 s, is acceptable in view of the analysis time resolution. The χ_i profile is inverted (larger value on the outside) during the L-mode, and nearly flat at 0.46 s. The ion diffusivity increases for times > 0.46 s (corresponding to MHD activity) and at 0.49 s, the χ_i profile is inverted again but with smaller values than during the L-mode. The drop in electron diffusivity for t > 0.47 s may be related to an overestimation of the P_{rad} data. As mentioned earlier, the bolometer array is viewing tangentially the machine midplane where most of the plasma interaction with the first wall (indentation coil armor plate, outer limiter and conductive shell) occurs. This radiation which occurs outside the plasma, effectively causes an overestimate of the radiation loss, P_{rad}, inside the plasma. As mentioned previously, there is a problem in estimating the power exchange term, Q_{ie}, between the ions and the electrons when the two temperatures are closer than the size of the error bars. For this analysis (at 0.46 s and r = a/2), Q_{ie} is small (100 kW) compared to ion conduction loss (1 MW), but of the order of half of the electron conduction loss (180 kW). A change within the error bars of the temperatures data can then produced a significant change in χ_e. For the reasons just mentioned, we cannot positively determine the behavior of χ_e across the H-mode transition. On the other hand, χ_i is minimally affected. For completeness, we plot in the last section of Fig. 4 the time evolution of the one fluid transport coefficient defined by:

$$\chi_{Tr}=\frac{P_{Ci}+P_{Vi}+P_{Ce}+P_{Ve}}{(n_e\nabla T_e+n_i\nabla T_i)S}$$

where the $P_{C\alpha}$ and $P_{V\alpha}$ are the volume integrated conduction and convection losses for the ions and the electrons. S is the area of the flux surface. By considering a one fluid plasma the power transfer term between the two species is eliminated. In our case, the evolution of χ_{Tr} follows that of χ_i.

Conclusion

A TRANSP analysis of a PBX-M high β_{pol} documentation was performed to study the transport properties across the L to H-mode transition and the later H-mode deterioration due to MHD activity. It is found that the transition to the H-mode corresponds to a reduction in χ_i by a factor 3.0 at r = a/2 and a flattening of its profile, between a/3 and 2a/3. Considering that a fourth beam was added at 0.4 s, the 3.0 factor is a lower limit. The deterioration of the H-mode during MHD activity is reflected by an increase in the ion conductivity and a return to an inverted χ_i profile but at a level lower than during the L-mode.

References

1-F. Wagner *et al.*,, Phys. Rev. Lett. **49** (1982) 1408
2-M. Keilhacker *et al.*,, Plasma Phys. and Controlled Fusion **26** 1A, (1984)49
3-M.L Watkins *et al.*, JET-P(89)46
4-F.Troyon *et al.*,, Plasma Physics and Controlled Fusion **26** 1A (1984) 209
5-R.J. Hawryluk, in Physics of Plasma Close to Thermonuclear Conditions, International School of Plasma Physics, Varenna,Italy,1979, Vol 1, p.19
6-R.J. Golston *et al.*, J. Comp. Phys. **43** (1981) 61
7-C. Kessel *et al.*, APS 1989, 5Q21

H-MODE BEHAVIOUR INDUCED BY EDGE POLARIZATION IN TEXTOR

R. R. Weynants[1], R.J. Taylor[2], P.E. Vandenplas[1], F. Durodié[1], B. Schweer[3], D. Bora[3], T. Delvigne[1], J. Devos[1], K.H. Dippel[3], M. Gaigneaux[1], B. Giesen[3], Y.T. Lie[3], A. M. Messiaen[1], R. Moyer[2], U. Samm[3], R.P. Schorn[3], C. Stickelmann[3], R. Van Nieuwenhove[1], G. Van Oost[1], G.H. Wolf[3], J.W. Yang[1].

(1) Laboratoire de Physique des Plasmas - Laboratorium voor Plasmafysica
Association "Euratom-Etat belge" - Associatie "Euratom-Belgische Staat"
Ecole Royale Militaire - B 1040 Brussels - Koninklijke Militaire School
(2) Institute for Plasma and Fusion Research, U.C.L.A., Los Angeles, CA 90024
(3) Institut für Plasmaphysik, Forschungszentrum Jülich GmbH, Association
EURATOM-KFA, D-5170 Jülich, FRG.

1. INTRODUCTION.

It was recently reported [1,2] that the setting up of radial electric fields by means of electrodes in the edge of a tokamak plasma could lead to edge rearrangements which are very similar to L-H transitions. In this paper we report on similar experiments in ohmic discharges on TEXTOR. A biasing electrode was introduced up to 6 cm beyond the toroidal belt limiter in full grade TEXTOR plasmas (B_t = 2T, I_p = 175 kA, R = 1.75 m, a = 0.46 m). The probe did not become itself a limiter and was capable of sustaining the heat load from the regular discharge and the extra load connected with the biasing. Clear H-transitions (density rise, profile steepening, D_α drop) are obtained resulting in improvements of about 1.4 in the energy- and 2 to 2.5 in the particle confinement time.

This improvement is achieved using positive, i.e. radially outward pointing fields. Together with the CCT work (negative fields), our experiment then appears to favour such theoretical models in which confinement improvement depends either on the absolute value of the electric field strength or on a gradient in poloidal rotation speed.

2. SYSTEM DESCRIPTION.

The set up used for edge polarisation is shown in Fig. 1. The electrode consists of a canoe-shaped, carbon head with dimensions length =13 cm, width = 3.5 cm and height = 1.5 cm, mounted on a steel shaft housed in an insulating sleeve made of boron nitride. A bias voltage is applied between the electrode and all 8 blades of the toroidal belt limiter ALT2, i.e. the current follows the path: power supply, electrode, ALT2, power supply. It is experimentally found that the probe current I_E is equally distributed over all blades. In the experiments reported here, the probe tip is situated at a plasma radius of 40 cm, a distance L = 6 cm inside the limiter. This zone of width L is henceforth referred to as the electrical layer. Although the bias can in principle have either polarity, it is found that the current that can be drawn from the plasma with negative bias (then limited to the ion saturation current of the electrode) is too small to trigger the H-mode behavior. All results shown

therefore pertain to positive bias, setting up a radial outward pointing electric field in the electric layer.

3. MECHANISM FOR FIELD CREATION AND FOR TRANSITIONS.

Applying a positive bias to the electrode results in the extraction of electrons from the plasma. To prevent an indefinite charge build-up, the plasma reacts by setting-up a radial electric field E_r capable of driving out ions to the wall. In a magnetised plasma this is achieved by the following mechanism: the field provokes an **E x B** poloidal rotation (of speed U_p) which itself yields a radial ion outflow, provided the rotation is hampered by friction (compare with outflow induced by diamagnetic or Pfirsch-Schlüter currents). This outflow will be non-ambipolar if ions and electrons feel a different friction. Such a situation arises e.g. because of parallel viscous stress effects [3] which result in ion poloidal rotation being damped by a force per unit volume of the form $F_p = m\, n\, \nu\, U_p$, where m is the ion mass, n is the ion density and ν is an effective collision frequency [4 -6], and in a radial current density $j_r = - F_p / B_t$, where B_t is the toroidal magnetic field component. From the ion and electron poloidal and radial momentum equations, one then readily obtains the appropriate radial Ohm's law

$$E_r = B_p\, U_t / B_t + \eta\, j_r + \eta_{NC}\, j_r + 1/(en)\ dp_i/dr \quad , \qquad (1)$$

where η is the perpendicular Spitzer resistivity and $\eta_{NC} = B_t^{\,2} / (m\, n\, \nu)$ is the resistivity due to viscosity. It should be noted that η_{NC} is typically 7 orders of magnitude larger than η. In accordance with Refs. [1] and [8], we assume that the contribution of the toroidal velocity U_t to E_r can be neglected. From Eq. (1) an approximate relation can then be derived between the plasma potential at the probe location V_p ($\approx E_r\, L$ [1]) and I_E ($= j_r\, A$, where A is the area of the average magnetic surface in the electrical layer)

$$I_E = - A\, \eta_{NC}^{-1}\, L^{-1} \quad (V_p + \alpha\, T_i / e) \quad , \qquad (2)$$

where T_i is the ion temperature (expressed in eV) at the electrode and α is of order unity.

In Refs. [1,2,4] it is shown that sudden transitions from low to high electric fields can be triggered when (i) ν decreases with increasing U_p [4-6] such that the friction force F_p develops a maximum as a function of U_p, a feature which is experimentally verified in [2] and (ii) an I_E is drawn such that the torque $I_E\, B_t\, L$ exceeds that corresponding to the maximum F_p.

4. EXPERIMENTAL RESULTS.

Figure 2 shows the temporal behaviour of the total stored energy E, the total bolometric radiation loss P_{rad}, the neutron yield Y, the $H\alpha$ radiation at the wall, the line density $\bar{n}_e$, the loop voltage V_l, the central temperature T_{eo}, and the electrode current I_E in response to a trapezoidal electrode voltage V_E. When a critical voltage is reached during the rise and fall, sudden transitions occur in I_E and a concomitant $\bar{n}_e$-, T_{eo}- and E growths and drops are observed. The gas feed rate is constant during the entire time interval. After an initial transient the loop voltage returns to its pre-bias value. The n_e and T_e profiles change as shown in Figs. 3a and 3b. Of particular interest are the profile changes in the edge region. A strong steepening of the density profile results from a decrease at the limiter radius and in the SOL and an increase in the bulk. Further details, obtained from a lithium probing beam, are shown in Fig. 4 for the zone $44 < r[cm] < 50$. The edge T_e profile is essentially unchanged after an initial contraction responsible for the aforementioned V_l-transient.

The energy confinement time τ_E increases, for the discharge of Fig. 2, from 35 ms to 52 ms. As the confinement in ohmic discharges in TEXTOR depends on $\bar{n}_e$, the real gain of τ_E then amounts to about 35 % with respect to non-biased discharges at the same density. In the evaluation of τ_E the biasing power, amounting to about 20 kW after the transition and representing 10 % of the ohmic power, was not included. This power is deposited in the very edge of the plasma and is thought not to contribute directly to the energy increment [7]. One should further note that the confinement improvement is occurring even though the radiation loss (Fig. 2) amounts to practically 100% of the input power.

The gain in the global particle confinement time τ_p, defined as the ratio of the total number of particles found in the discharge to the number of ionisation events inferred from $H\alpha$ measurements, is estimated to reach about 2 to 2.5. $H\alpha$ decreases upon biasing at all 4 monitoring stations around the machine, including at the limiter. The time rate of change of $H\alpha$ is rather slow, as exemplified in Fig. 2. The recycling at the electrode itself has not yet been monitored. However, as I_E decreases at the transition, we expect the particle flux to the electrode to decrease as well.

The setting up of the electrical layer is ascertained from two diagnostics. Preliminary poloidal Doppler shift measurements yield typical field strengths at r = 41 cm of 50 V/cm under conditions where V_E = 420 V. The extent to which the electrode can impose the local plasma potential can also be assessed from the electrode's probe characteristic. The latter indeed imposes , besides Eq. (2), a further relation between I_E and V_p, namely

$$I_E = I_{sat+} - I_{sat-} \exp [(V_E - V_p) / T_e] ,$$

where I_{sat+} and I_{sat-} are the resp. ion and electron saturation currents. It can readily be appreciated that a significant drop of I_E at increasing density and constant temperature presumes a decreasing difference $V_E - V_p$. A quantitative analysis yields the change of V_p *vs* V_E shown in Fig. 5. Applying Eq. (2) allows one to compute $R = L\,\eta_{NC} / A$ and compare η_{NC} with the predictions from theory. This analysis will be published elsewhere.

5. CONCLUSIONS.

We have been able to improve both τ_E and τ_p by setting up outwards pointing fields in the edge of an ohmic plasma. Although the understanding for the improvement awaits further elucidation, our experiment, in combination with the earlier CCT work, should be explained by models in which confinement improvement depends either on the absolute value of the electric field strength or on a gradient in poloidal rotation speed.

References

[1] TAYLOR, R.J., BROWN, M.L., FRIED, B.D., et al., Phys. Rev. Lett. **63** (1989) 2365.
[2] WEYNANTS, R.R. and TAYLOR, R.J., Nucl. Fusion, **30**, May 1990.
[3] CALLEN, J.D., QU W.X., SIEBER, K.D., et al., in Plasma Physics and Controlled Nuclear Fusion Research (Proc. 11th Int. Conf. Kyoto, 1986) IAEA, Vienna, 1987, Vol. 2, p. 157.
[4] STIX, T.H., Phys. Fluids **16** (1973) 1260 .
[5] SHAING, K.C., and CRUME, E.C., Jr., Phys. Rev. Lett. **63**, 2369 (1989).
[6] STRINGER, T.E., J. Plasma Phys. **10** (1973) 433; HIRSHMAN, S.P., Nucl. Fusion **18** (1978) 917.
[7] CALLEN, J.D., CHRISTIANSEN, J.D., CORDEY, J.G., et al., Nucl. Fusion **27** (1987) 1857.
[8] GROEBNER, R.J., BURRELL, K.H., and SERAYDARIAN, R.P., The role of edge electric fields and poloidal rotation in the L-H transition, submitt. to Phys. Rev. Let.

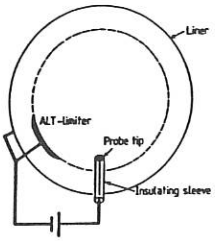

FIG. 1 Experimental set-up.

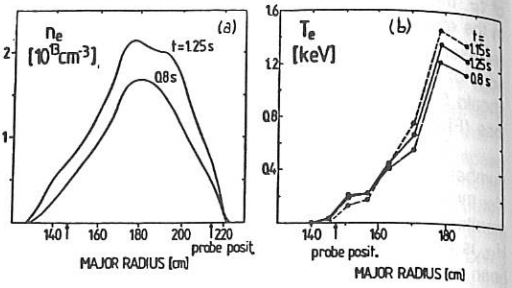

FIG. 3 Electron density (a) and temperature (b) profiles before polarisation (t = 0.8 s) and after transition (t = 1.25 s) for conditions of Fig. 2.

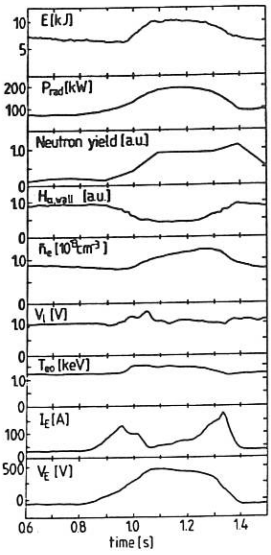

FIG. 2 Temporal evolution of important parameters (both P_{rad} and neutr. yield have 50 ms integration time)

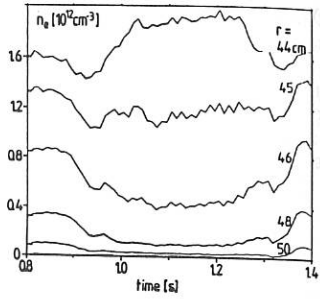

FIG. 4 Edge density as measured by Li-beam for conditions of Fig. 2.

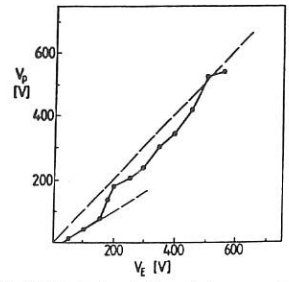

FIG. 5 Computed variation of plasma potential at probe tip location vs probe voltage.

ELMS AS TRIGGERED AND AS TRIGGERING RELAXATION PHENOMENA IN ASDEX

O. Klüber, R. Aratari, R. Büchse, M. Kornherr, H. Zohm
and the ASDEX Team
Max-Planck-Inst. f. Plasmaphysik, D-8046 Garching, FRG, EURATOM-Association

1. Introduction.

In the ASDEX device, the relaxation phenomena known as ELMs /1,2/ are frequently isolated events in that no preceding and no following changes of plasma parameters occur. During the relaxation, a characteristic MHD mode is observed which is no precursor /3,4/. ELMs may be triggered, however, by other MHD phenomena and they are able to trigger the onset of Mirnov oscillations, the transition from L-type confinement behaviour to the H mode and vice versa. This paper summarizes the measurements made in the ASDEX tokamak, in particular those with appropriate temporal resolution, i.e. at a data acquisition rate of typically 200 kHz.

2. Characteristics of ELMs.

ELMs manifest themselves in the signals of practically all diagnostics; the most instructive ones are those of the SX diode cameras, the B_ϑ loops and the emission of H_α / D_α light from the divertor chambers as shown in Fig. 1. The energy loss caused by an ELM leads to a transient decrease of the X ray emission at a time scale of about 0.3 ms. It also shows up in the $\dot{B}_\vartheta$ signal: Due to the decrease of the poloidal beta, the major radius R of the plasma shrinks by an amount which ranges between a few mms and more than a cm causing the negative dip in the $\dot{B}_\vartheta$ signal shown in Fig. 1 (and, accordingly, a positive one in $\dot{B}_\vartheta$ signals arising from Mirnov probes at the high-field side of the torus). For the sake of simplicity, we have selected an example for which the motion of the plasma dominates the amplitude of $\dot{B}_\vartheta$. The superposition of competing MHD activity is discussed in Ref. /4/.

A variation ΔR by 1 cm corresponds to a loss of β_p by about 0.05 (the precise value depending on the initial value of β_p). Changes of R of the order 1 cm are also characteristic for very soft disruptions. In this case, however, ΔR is due to $\Delta\,(\beta_p + l_i/2)$. The loss of internal magnetic field energy then manifests itself in the well-known positive current and negative voltage spikes not observed in ELMs while otherwise well comparable with minor disrutions. We conclude, therefore, that ELMs do not lead to a rearrangement of the current density distribution (say variation of $l_i/2$). This conclusion is important for the interpretation of some of the observations to be presented in the next sections.

The energy lost from the main plasma is at least partially deposited in the divertor chamber which is indicated by the positive spikes in the H_α / D_α emisssion recorded by fotodiodes viewing onto the divertor plates. Signals arising from the upper and the lower divertor at different toroidal positions exhibit no time shift. Hence, an ELM is essentially an $m = 0$, $n = 0$ event.

The statements given above refer primarily to "single" ELMs, i.e. those in which the temporal distance of subsequent ones is large as compared to the duration of the relaxation process of the order 0.1 to 0.3 ms. "Grassy" ELMs having a typical distance of 0.5 ms do not differ in the essential features discussed so far apart from the smaller amplitudes. (The shrinking of the major radius, e.g., is scarcely observable). Due to the large repetition rate, it is practically impossible to identify clear correlations between "grassy" ELMs and other MHD phenomena. For this reason, the following discussion focuses onto "single" ELMs.

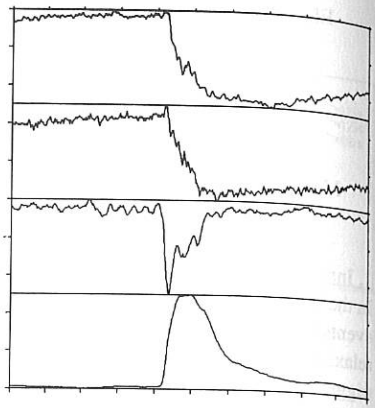

Fig. 1 Signals characterizing an ELM. Time window 2 ms. From top to bottom: SX emission along two chords (radii of tangency being a and a/2 respectively); $\dot{B}_\vartheta$ from a Mirnov probe locacted at the low-field side; H_α / D_α emission from a divertor chamber.

3. ELMs triggered by and triggering MHD activity of a different kind.

The example presented in Fig. 1 was selected such that the relaxation phenomena caused by the ELM are not masked by competing MHD activity neither prior to nor during nor after the relaxation. Hence, it is a typical example for what was called an isolated event in the introduction. ELMs appear to be triggered, however, by the so-called "fishbone-like events" which consist of the increase and decrease of an m = 1 / n = 1 oscillation accompagnied by an n = 1 satellite with large m number. These observations were first reported in ref. /5/. It was also stated there, that fishbone-like events may as well occur without giving rise to ELMs. The increasing part of such oscillations resembles to some extent to the startup phase of a sawtooth relaxation. The oscillation, however, is not restricted to the interior of the q = 1 surface. Rather, it extends over the entire cross section of the plasma column.

An example for an ELM triggered by a fishbone-like event is shown in Fig. 2. This ELM is a particulary violent one which manifests itself in the saturation of the photodiode signal not occuring during the preceding and the subsequent ELM relaxations. In turn, this ELM apparently triggers the onset of an m = 2 / n = 1 mode which finally leads to a disruption.

Usually, H-mode plasmas are free of sawteeth but they may occur at low heating power and are then able to trigger ELMs. This observation supports the interpretation of ELMs as pressure-driven modes: the relaxation leads to a transient increase of the pressure in the near-boundary region. The triggering of ELMs by fishbone-like events, however, cannot be ascribed to such a process.

The m = 2 / n = 1 mode, if occurring during an H phase, is always triggered by an ELM which is also hard to explain since this mode is usually thought to be current-driven. In the preceding section, however, it was pointed out that ELMs do not change the current density distribution. Hence, it must be inferred, that the stability of this mode depends on the pressure profile, too.

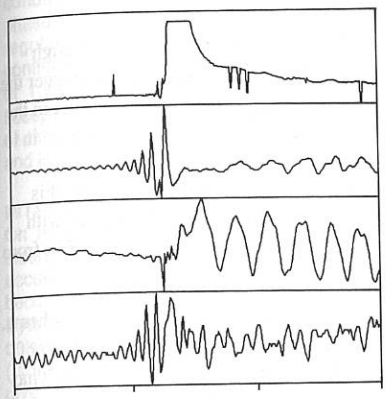

Fig. 2 A fishbone-like event triggers an ELM which, for his part, triggers the onset of an m = 2 / n = 1 mode. Time window 1.5 ms. From top to bottom: H_α / D_α emission from the upper divertor chamber (photodiode signal saturates); $\dot{B}_\vartheta$ signals from Mirnov probes located in the midplane (low-field and at the high-field side, respectively); SX diode signal from a near-centre chord.

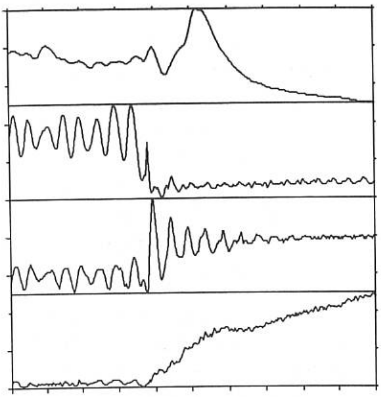

Fig. 3 A sawtooth relaxation triggers an ELM and an L to H transition. Time window 2 ms. From top to bottom: H_α / D_α emission from the upper divertor chamber; SX emission along three chords viewing through the plasma centre and having radii of tangency of a /2 and a, respectively.

4. Triggering of L to H transitions by ELMs.

If an H phase is not finished by a disruption there is always a transition to a second L phase prior to the return to OH confinement bahaviour. It is well known from ASDEX /2/ and, e.g., Doublet III-D /6/ that this H to L transition is commonly initiated by a violent ELM. Apparently, the edge barrier characterizing the H-type confinement cannot be restored in such cases.

Most surprisingly, L to H transitions in ASDEX are usually preceded by ELMs, too. An example is shown in FIg. 3. In this case, the first triggering event is a sawtooth relaxation. The transition manifests itself in the well-known decrease of the H_α / D_α emission in the divertor. Prior to this decrease, however, a peak occurs which exhibits all characteristic signatures of an ELM. The dips in the $\dot{B}_\vartheta$ signals indicating the loss of energy from the main plasma, e.g., can clearly be identified if the amplitude is sufficiently large.

It was reported earlier /2/ that L to H transitions need not be triggered by a sawtooth. At high injection power, only one sawtooth occurs after the onset of the injection and does not trigger the transitons. Also then, at least one ELM appears prior to the decrease of the H_α / D_α signal in the same way as shown in Fig. 3.Regardless on the occurrence or non-occurrence of sawteeth, in lieu of one ELM there might be several ones, typically up to five, with a repetition rate comparable to "grassy" ELMs.It should be pointed out that the observations presented in this section do not refer to rare events. Rather, in the majority of cases (about 90%) recorded with appropriate temporal resolution ELMs are preceding and apparantly triggering the transition from the L-type to the H-type confinement regime.

These experimental findings are hard to reconcile with the widely accepted interpretation scheme. According to this, ELMs are pressure-driven (preferably ballooning) modes and the buildup of steep pressure gradients near the separatrix is a necessary prerequisite. On the other hand, it has to be stated that in the L regime ELMs occur only immediately prior to the H transition and exhibit more resemblance to "grassy" than to "single" ones. Maybe, for beam-heated plasmas, three types of confinement behaviour have to be distinguished, namely L-type, H-type with a few "single" ELMs and an intermediate state characterized by "grassy" ones. Of course, this is steep speculation and should only be considered as a possible useful guideline for further investigations on both the H regime and the occurrence of ELMs.

References:

/ 1/ M. Keilhacker, G. Becker, K. Bernhardi et al., Plasma Phys. Contr. Fusion 26 (1984) 49.

/ 2/ ASDEX Team, Nucl. Fusion 29 (1989) 1959.

/ 3/ K. Toi, J. Gernhardt, O. Klüber, M. Kornherr, Phys. Rev. Lett. 62 (1989) 430.

/ 4/ S. von Goeler, O. Klüber, G. Fussmann, J. Gernhardt, M. Kornherr, Nucl. Fusion 30 (1990) 395.

/ 5/ O. Klüber, J. Gernhardt, K. Grassie, et al., in Controlled Fusion and Plasma Heating (Proc. 13th Eur. Conf. Schliersee 1986) Vol. 10C, Part I, European Phys. Soc. (1986) 136.

/ 6/ N. Ohyabu, K.H. Burrell, T.N. Carestrom, et al., in Controlled Fusion and Plasma Heating (Proc. 15th Eur.Conf. Dubrovnik 1988) Vol. 12B, Part I, European Phys. Soc. (1988) 227.

LONG-PULSE HEATING IN ASDEX L-AND H-MODE DISCHARGES

O. Vollmer, R. Aratari, F.Ryter, K.H.Steuer, F.Wagner,
ASDEX and NI Teams

Max-Planck-Institut für Plasmaphysik, D-8048 Garching,FRG
EURATOM Association

ABSTRACT

The quality of the H-mode benefits from operation with boronized walls and reduced vacuum conductances between divertor and main plasma chamber. In particular quasi-steady H-phases could be maintained up to 2 s (beam pulse limited) by the optimized introduction of regular ELMs (Edge Localized Modes). With an ELM period of typically 4.5 ms, the confinement time was 40 ms for Ip = 0.28 MA (1.9 MW, H -> D) with a Goldston multiplier of 1.7. Compared with the quiescent H-mode, a reduction of 10 - 15% in τ_E has to be accepted in order to establish the quasi-steady state conditions by the ELMs. The distribution of the power load onto the divertor plates indicates the same toroidal asymmetries for L- and H-modes.

INTRODUCTION

On ASDEX quiescent H-phases (H*) with almost no or only a few ELMs are basically non steady-state /1/. The improved confinement properties in the H-phase cause impurities to accumulate in the plasma center and increasing radiation impedes the discharge from becoming stationary (Fig.1). Quiescent H-discharges are analyzed in a companion paper by Ryter /2/. None of the technical means, available on Asdex, has provided steady-state quiescent H-modes. We have tried various divertor configurations, various wall conditions (stainless-steel, carbonization, boronization), pumping (Ti) and non-pumping (Cu) divertor plates and additional Ti-gettering in the divertor chambers. Steady state can, however, be achieved by the introduction of controlled ELM activity. ELMs affect the outer zone of the discharge and the impurity development depends very much on their presence and intensity. This paper describes long quasi-steady state discharges with ELMs (H) in more detail and compares its properties with that of L- and H*-discharges. Quasi steady-state H-modes have also been reported by DIII-D /3/.

QUASI- STATIONARY H-MODE WITH ELMs

Operationally quiescent or ELMy H-phases are produced by careful choice of the plasma position. Basically, the same discharge (I_p = 0.28 MA, q = 3, $\bar{n}_e = 3.1 \times 10^{13}$ cm^{-3}) can reproducibly be developed into an H*- or an H-mode by changing the horizontal position (R_o) by only 1 cm (Fig.1). With the actual neutral beam power (2.2 MW) a single-null divertor configuration is necessary to achieve the H-mode (Δz=1.5 cm). The discharge remains in the L-mode in the double-null configuration (z = 0). During the initial quiescent phases both H-modes show a similar development of the density and radiated power. With the onset of more frequent ELMs, further increase in density and radiated power is prevented and the discharge proceeds in a quasi-steady mode. The level of radiated power, however, is clearly increased in relation to the L-discharge.

Figure 2 illustrates an H-mode discharge with ELMs. The density remains stable in contrast to the H*-mode with its continuous density rise. (The gas valve is closed with the onset of the neutral beams.) The loop voltage drops to 0.3 V and stays low. The confinement time (~ 38 ms) remains constant and recovers to the ohmic level after termination of the

beams. The H-mode lasts for about 50 confinement times and is limited by the pulse length of 2s. The development of the impurities (Fig.3) reflect the stationary behavior of the discharge: The total radiated power P_{RAD} remains constant. The signals from the core of the plasma - soft X-rays (SX(0)) and the emission of copper lines (Cu-XXIV) - slightly decrease during the discharge, probably due to the decrease in beam power. The stationary situation in the plasma center is confirmed by the central Z_{eff}-signal measured by bremsstrahlung, which levels off at about 2.9 and stays constant. An L-mode discharge of similar power has a Z_{eff} of about 1.6. While in H*-modes the profiles, in particular the density profile shows a continuous development throughout the quiescent phase, with ELMs the plasma profiles remain invariant. Altogether, the H-mode with ELMs develops as stationary as long pulse ASDEX L-mode discharges reported earlier /4/.
Reproducible H-discharges with still acceptable confinement require a certain ELM-frequency (125 Hz -250 Hz) which remain to be fairly constant throughout the pulse. The time-expanded H_α-signal measured in the divertor (H_α^{DIV}) in Fig. 2 shows the very regular ELM behavior. During this discharge the ELM-frequency is 230 Hz, the standard deviation from the mean frequency being less than 10% during the H-phase.
Such a stable ELM-behavior has been observed on ASDEX only under special boundary conditions:
1. The divertor chamber has to be as close as possible. Originally, the water cooled divertor for long pulse operation had large by-passes with an overall conductance 2-3 times the neck conductance. The resulting higher gas recycling provided bad H-mode conditions (high power threshold, high ELM-frequency, low confinement).
2. Low-Z wall conditions and removal of oxygen as realized in Asdex with boronization. Thereby, a very stable ELM-behavior can be achieved leading to the favorable H-mode conditions with ELMs reported in this paper.
Under these circumstances recycling control and optimized wall conditions allow sufficient control of the plasma position to avoid degradation in confinement caused by the operationally unstable situation in the sense that a sudden increase in ELM frequency causes a reduction in major radius (from equilibrium) which gives rise to a further increase in the ELM frequency.
The relevance of the H-mode with ELMs depends, of course, on the confinement degradation introduced by ELM activity. Am optimum has to be sought: ELMs have to be frequently enough to prevent impurity accumulation but the energy loss through them has to be minimized. In comparison to quiescent H-modes typically a reduction of 10 -15% in τ_E has to be paid for the quasi-steady state conditions. In the current range .28-.42 MA Goldston multipliers of 1.7 to 1.9 are achieved by ELMy discharges ($P_{NI} \approx$ 2.5MW). For Kaye-Goldston scaling the corresponding multipliers range from 1.9 to 2.2.

POWER LOAD ONTO THE DIVERTOR-PLATES

If one considers the H-mode stabilized by ELMs with this modest confinement reduction as reactor-compatible, the load distribution on the divertor in this discharge is of interest.
On ASDEX time-integrating calorimetric measurements for the toroidal distribution of the thermal load on the divertor panels are available. Figure 4 shows distributions of an ELMy discharge (see Fig. 2) and a single-null L-mode discharge. The two discharges produce very similar toroidal distributions of the deposited power caused by vacuum islands residing at the plasma edge. It is important to note that the power flux across the separatrix via ELMs does not aggravate the problem of asymmetric power distribution.
In contrast to the toroidal distribution, the ratio of the power load to the inner and outer divertor plates is different for the two discharges: The power outflow of the ELMy H-discharge is more symmetric, reducing the inner to outer ratio by a factor of nearly two. Future experiments have to confirm whether this observation is typical.
Furthermore, as the energy lost via ELMs is distributed onto the divertor plates over a larger width the technical problem of handling large power fluxes is further reduced.

CONCLUSION

With boronized walls and reduced gas conductances between the divertor and the main plasma chamber very regular ELMs can be produced in the ASDEX H-mode. They prevent the impurity accumulation usually observed during the quiescent H-mode and allow a quasi-steady discharge for 2 seconds (up to now limited by the pulse length of the neutral beams). The introduction of ELMs under optimized and controlled conditions reduces the confinement time by an acceptable amount of 10 to 15%. An H-discharge with ELMs could therefore be considered as a candidate for reactor application in particular as no additional problems seem to arise from the point of view of power deposition onto the divertor plates.

REFERENCES

/1/ The H-mode of ASDEX, Rep.IPPIII/151, (1989)

/2/ F.Ryter, ELM-free H-mode with Co- and CTR-Neutral Injection on ASDEX, this conference

/3/ K.H. Burrell et al., Plasma Physics and Contr. Fusion, Vol. 31, No 10

/4/ H.Niedermayer et al.,Plasma Physics and Contr. Fusion, Vol. 30, No 11

FIGURE CAPTIONS

FIG.1
Influence of the horizontal (R_o) and vertical (z) plasma position on the development of the discharge (I_p = 0.28 MA; q =3.2, $\bar{n}_e$ = 3.1 x 10^{13} cm^{-3}) during neutral beam heating. A difference of 1 cm in the major radius R_o discriminates between the two H-mode variants.

Fig.2
Time histories of parameters for an H-discharge with ELMs (I_p = 0.28 MA, q = 3.2, ne =3.1E13 1/cm3, τ_E= 38ms, P_{NI} = 2.2 MW). The time expanded insert of H_α-signal shows the very regular ELM-activity (ELM-frequenzy = 230 Hz)

Fig. 3
Impurity development for the H-discharge of Fig.2: Global radiated power P_{RAD} as well as Cu-XXIV line emmision and soft-x radiation (near plasma- center) decrease slightly (probably related to the decreasing neutral beam power). The $Z_{eff}(0)$ stabilizes around 2.9.

Fig.4
Time integrated toroidal power distributions on the inner and outer sectors of the ASDEX divertor for single-null L- and ELMy H-discharges. Both discharges produce very similar toroidal distributions, but the H-mode shows by a factor of two less inner/outer asymmetry.

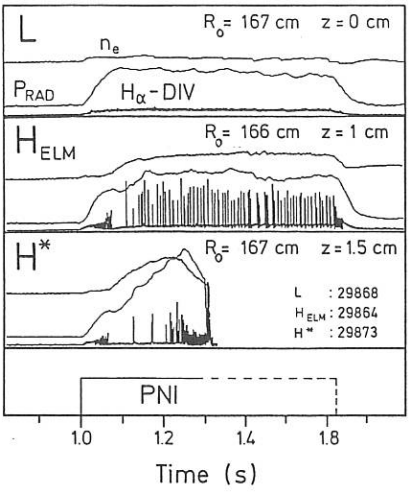

Fig. 1

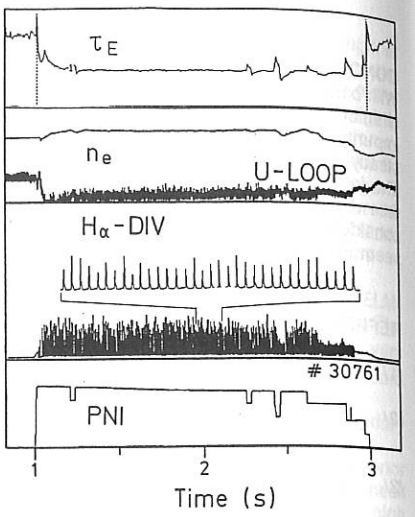

Fig. 2

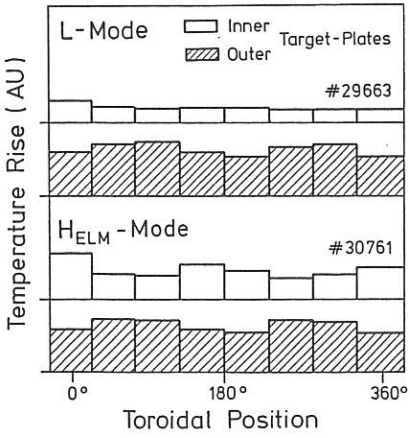

Fig. 4

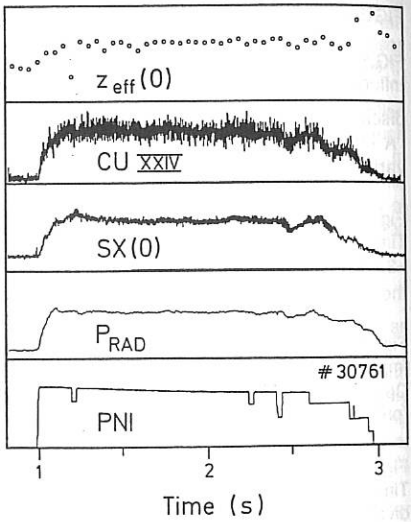

Fig. 3

OHMIC H-MODE IN "TUMAN-3" TOKAMAK

A.I.Arbuzov, L.G.Askinasi, V.I.Afanasiev, V.E.Golant, V.K.Gusev, E.R.Its, A.A.Korotkov, S.V.Krikunov, B.M. Lipin, S.V.Lebedev, K.A.Podushnikova, G.T.Razdobarin, V.V.Rozhdestvenskij, N.V.Sakharov, A.S.Tukachinskij, A.A.Fedorov, S.P.Yaroshevich

A.F.IOFFE PHYSICAL-TECHNICAL INSTITUTE
OF THE USSR ACADEMY OF SCIENCES

The spontaneous transition in the regime of improved confinement has been obtained recently in deuterium plasma in "TUMAN-3" tokamak. Similar H-mode discharges on different tokamaks were observed so far in the experiments with strong auxilliary heating [1-4] and also in ohmic regime on DIII-D in the separatrix configuration [5] . The H-mode-like behavior in "TUMAN-3" took place in ohmically heated discharges where plasma was bound by poloidal limiters. Some features of the appearance of H-mode were observed also in the regime with magnetic compression and second current rise [6].

The distinctive feature of "TUMAN-3" [7] is a small aspect ratio of torus $R/a_l=2.3$ ($R=55$cm, $a_l=24$cm) which allows to obtain a large plasma current I_p in a low toroidal field B_t. In the described experiments the plasma parameters were $I_p=95$kA, $B_t=4.5-6.5$kG, average density $\bar{n}_e=0.5-2\ 10^{13}$cm^{-3}, ohmic power $P_{oh}\gtrsim 200$kW. Under these conditions the corresponding power flux through the plasma surface achived the value $P_{oh}/S = 4$W/cm^2. This magnitude corresponds to the threshold for transition in H-mode on other tokamaks with auxilliary heating [8]. It should be noted that the height of four inconel poloidal limiters inside vacuum vessel was only 1.2cm and probably such limiters did not play an appreciable role for wall protection.

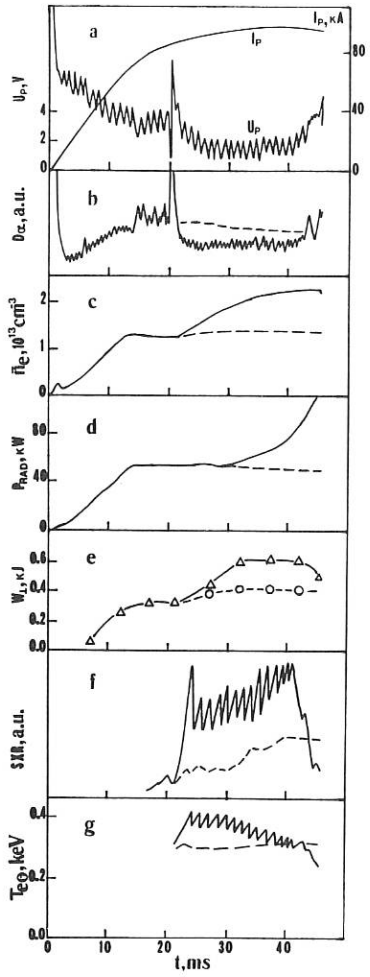

Fig.1. Time evolution of plasma parameters in H-mode discharge . B_t = 6.5kG, q > 3.

The required conditions for obtaining of H-mode were low recycling and small flux of impurities. For the cleaning of inconel vessel the low temperature inductive discharge in O_2 and D_2 was used. As well as in JFT-2M [4] content of impurities and recycling were lower when plasma column had a small shift $\Delta R \sim 2\text{-}3$cm towards the inner wall. After cleaning radiation losses P_{rad} did not exeed $30\%P_{oh}$. Typical value of effective charge was $Z_{eff} \approx 1.5$.

Time evolution of plasma parameters in H-mode discharge (solid lines) and in the discharge without H-mode (dashed lines) is shown on fig.1. The characteristic features of the appearance of H-mode were fast drop in D_α emission and increase in plasma density. In the case of fig.1 (q > 3) the transition occured during the period of plasma current rise at t=20ms when the resonant surface m/n=4 appeared in the vicinity of plasma edge. Apparently the burst of MHD-instabilities at this moment could increase the heat flux to the plasma boundary and thus facilitate the transition. Sometimes a small change of toroidal field $\Delta B_t/B_t \sim 1\%$ was sufficient to diminish the

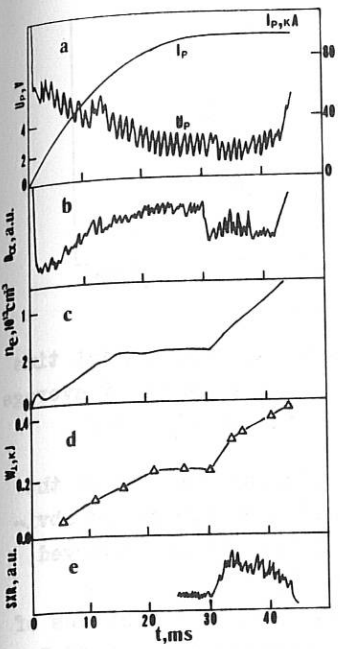

Fig.2.Time evolution of plasma parameters in H-mode discharge. B_t = 4.7kG, $q<3$.

amplitude of MHD-spikes and eliminate the appearance of H-mode.

Fig.2 shows the spontaneous transition in H-mode behavior during the stage of current flat-top. Here the transitions was not connected with any resonant burst of MHD-activity (the value of safety factor q=2.6). In both examples (fig.1 and fig.2) the transition in H-mode was follwed by the increase of plasma energy $W_\perp$ (fig.1e,2d) defined from the measurements of diamagnetic flux, by sharp rise of soft X-ray emission (fig.1f,2e) from plasma center and by the increase of central electron temperature (fig.1g)

The energy confinement time τ_E as a function of average density for two regimes $q>3$ and $q<3$ is plotted on fig.3 and fig.4 respectively. H-mode energy confinement times were a factor of 1.2-1.3 longer than typical values of τ_E in ohmically heated plasmas without H-mode. Similar effect of improvement of energy confinement in ohmic H-mode was observed in DIII-D[5] . In our experiments particle confinement time was increased approximatly 3-6 times after transition.

The distinctive feature of H-mode in "TUMAN-3" was also a significant rise of sawteeth oscillations on the signal of soft X-ray emission (fig.1f,2e). The time evolution of soft X-ray emission in the H-mode regimes indicates the possible formation of peaked current density profile.

The appearance of H-mode caused the rise in radiation

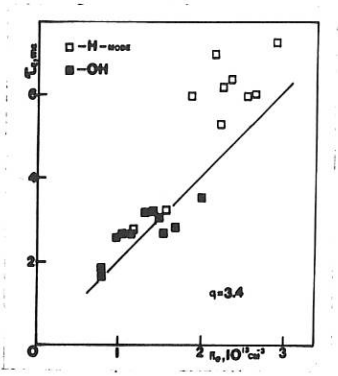

Fig.3. Energy confinement time as a function of average density. B_t=6.5kG

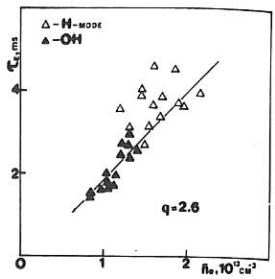

Fig.4. Energy confinement time as a function of average density. B_t=4.7kG

losses (fig.1d), loop voltage U_p (fig.1a,2a) and led to the current disruption. The increase in radiated power was obviously a consequence of accumulation of impurities observed usually in ELM-free H-mode discharges [9].

One should note in conclusion that both observations of H-mode appearance in ohmically heated discharges in DIII-D and in "TUMAN-3" were made in tokamaks with small aspect ratio and in the regimes with low toroidal fields. Ohmic H-mode in "TUMAN-3" was obtained in limiter configuration without magnetic separatrix inside vacuum vessel.

REFERENCES

1.F.Wagner et al., Phys. Rev. Lett., v.49 (1982) 1408
2.K.Steinmetz et al., Phys. Rev. Lett., v.58 (1987) 124
3.J.M.Lohr et al., Phys. Rev. Lett., v.60 (1988) 2630
4.M.Mori et al., Nuclear Fusion, v.27 (1987) 96
5.D.P.Schissel et al., 16th EPS Conf., Venice(1989) I ,115
6.L.G.Askinasi et al., Preprint Phys.Techn.Inst.1425 (1990)
7.G.M.Vorobiev et al., Fizika Plasmy (Sov.)v.13 (1983) 105
8.M.Keilhacker, Plasma Phys. and Contr. Fus.,(1987) 1401v.29
9.E.R.Muller et al., Nuclear Fusion, v.27 (1987) 96

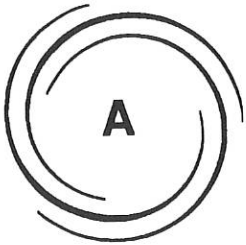

TOKAMAKS

A7

A7 MHD PHENOMENA

RUNAWAY ELECTRON PRODUCTION DURING MAJOR DISRUPTIONS IN TORE-SUPRA

P. JOYER , G. MARTIN

Association EURATOM-CEA sur la fusion / C.E.N. CADARACHE
13108 SAINT-PAUL-LEZ-DURANCE CEDEX / FRANCE

After 18 months of operation at 1.8 Tesla , the toroïdal field of TORE-SUPRA has been increased to 4.5 Teslas , its nominal value . The most unexpected consequence of this field change was the appearance of large amounts of runaway electrons during major disruptions : tens of kA are obtained during the strong disruptions .

These electrons are mostly observed through the photonuclear processes induced when they are lost in the inner wall :
→ Hitting the carbon tiles , they radiate a part of their energy as hard X-rays . The X-ray spectrum ranges from zero up to the initial electron energy .
→ This X-ray beam , going through the vessel materials , can stripe neutrons , protons or alpha particles from the different nuclei . These reactions are observed both by the produced neutrons (photo-neutrons) and the radio-activity of the residual nuclei . Each reaction is possible only if the X-rays have an energy higher than a minimum value , the threshold energy Σ .

Estimations of the electrons individual energy is then performed by an analysis of the radio-isotopes formed , each one corresponding to a given threshold . Its observation indicates that at least some electrons have got an energy higher than the threshold .

Activation of the vessel material (carbon , steel , copper , ...) gives a first set of data . The reaction with the highest threshold clearly seen is : C^{12} (X,nα) Be^{7} -> Σ = 26.3 MeV . With a 54 days half-life , the Be^{7} can be measured during operation shut-down , weeks after disruptions . Its high level observed all around the torus graphite first wall , suggests that runaway electrons have currently reached energy well above 30 MeV .

But no higher threshold can be used with the intrinsic elements of the vessel , the produced radio-nuclei having too short periods to be measured . It is then necessary to place other samples in the hard X-ray beams . The best choice , to obtain high threshold , high cross-sections with appropriate half-lives (a few hours or days) is bismuth . The main reactions , which could be observed , are :

Bi^{209} (X,3n) Bi^{206} : Σ = 22.4 MeV / $T^1/_2$ = 6.2 days
Bi^{209} (X,4n) Bi^{205} : Σ = 29.5 MeV / $T^1/_2$ = 15.3 days
Bi^{209} (X,5n) Bi^{204} : Σ = 37.9 MeV / $T^1/_2$ = 11.2 hours
Bi^{209} (X,6n) Bi^{203} : Σ = 45.1 MeV / $T^1/_2$ = 11.8 hours
Bi^{209} (X,7n) Bi^{202} : Σ = 54.0 MeV / $T^1/_2$ = 1.7 hours

On a bismuth sample , irradiated during one shot , we observed Bi^{204} but no Bi^{203} : electrons have reach an energy about 45 MeV during this disruption . This value will be used in the following .

This 45 MeV value for the electrons energy can be compared to other theoretical estimations :
→ Total integration of the loop-voltage give a maximum value of 80 MeV .
→ The ripple resonant interaction limit the runaway energy at 70 MeV [1] .
→ Confinement by the poloïdal field is not possible , even for 10 MeV electrons : more complex trajectories involving vertical fields must be supposed , and are not yet clearly understood .

The number of electrons produced in one disruption is determined by measurement of the photo-neutron flux (mainly produced by (X,n) reactions on iron) . Estimations of the neutron/electron ratio , obtained from [2] , are of $2\ 10^{-3}$ n/e^- for 50 MeV electrons in a carbon and steel vessel .
Total neutron productions are only known within a factor two , the source geometry being rather different from the one used for calibration of the detectors for fusion neutrons . Two checks of the order of magnitude of the neutron fluxes were obtained : the activation of the copper from the poloidal coils by the capture of the neutrons (after thermalisation) and the level of the Ni^{57} radio-activity in the vessel (Ni^{58} (X,n) Ni^{57}) .

Neutron integrals were currently between 10^{13} and 10^{14} neutrons , with a maximum value of $2.7\ 10^{14}$ on shot TS-2179 . Supposing that all electrons are at 45 MeV , a mean value of $2.5\ 10^{16}$ electrons are accelerated on each disruption . They carry a current of 80 kA , and can deposit almost 180 kJ in the wall where they are lost (the maximum values are 430 kA and 1 MJ respectively) .

72 strong disruptions (dIp/dt > 25 MA/s) have been studied , with plasma current from 0.6 to 1.8 MA , toroidal field from 1.8 to 3.9 T and various electron density and temperature (pellet injection) .
As expected , the number of neutrons increases with the plasma current value , and the steepness of the current fall : they correspond to higher loop-voltage and acceleration time . Typical minimum values to obtain runaways are 0.8 MA before the disruption and 40 MA/s falling rate . Changes in electron density and temperature have a small effect : after pellets injection , where density is doubled and temperature halved , the number of electrons is smaller for the same Ip and dIP/dt .
But , these variations are relatively modest compared with the three orders of magnitude observed in neutron flux evolutions when the toroidal field increases from 1.8 to 3.9 teslas : the hardest disruption under 3. teslas (TS-2397 : 1.5 MA at 100 MA/s) produces less neutrons than lower ones at 3.9 teslas (e.g. 1.2 MA at 50 MA/s) by a factor hundred . A few Typical value have been grouped in table I .

No clear reasons for this evolution has been identified :
→ It does not correspond to a slow evolution of TORE-SUPRA , because disruptions done the same day with variable toroidal field show clearly the phenomenon .
→ Plasma temperature tends to be higher with stronger field : but a simple thermal effect (more electrons close to the critical Dreicer energy) is not coherent with the results obtain with pellet injection .

→ Energy limitations due to ripple interaction [1] is not sufficient to explain such large variations in neutron fluxes .

SHOT	Bt (T)	Ip (MA)	dIp/dt (MA/s)	NEUTRONS
TS-1169	1.84	0.93	53.0	3.10^{8}
TS-1377	1.84	1.13	62.0	2.10^{8}
TS-1202	1.84	1.17	106.0	2.10^{10}
TS-2381	2.62	1.28	31.0	$< 10^{8}$
TS-2386	2.62	1.20	111.0	6.10^{11}
TS-2397	2.93	1.49	105.2	2.10^{10}
TS-2400	3.54	1.07	77.0	2.10^{13}
TS-2286	3.85	0.74	15.0	$< 10^{8}$
TS-2321	3.85	1.28	34.6	4.10^{13}
TS-2156	3.85	0.88	46.0	2.10^{13}
TS-2179	3.85	1.82	72.0	3.10^{14}
TS-2135	3.85	1.28	109.0	3.10^{13}

TABLE I : DISRUPTIONS PARAMETERS

Today , the only explanation seems to be an accumulation of all the previous effects , and other ones , each accounting for an increase of a factor 2 to 4 .

During an opening of the vessel , highly radioactive areas have been observed on the central column , close to the equatorial plane : they are the signature of the electron impacts (photo-nuclear processes) . The toroidal distribution of this activity is represented on figure 1 . The minimum are located under the toroidal coils , and the maximum beetween two adjacent coils . They are slightly displaced from the inter-coil midplane , accordingly with the electron velocity direction .

Two survey have been made : one on the first week of january , after 7 strong disruptions with runaways , and the second in february after 27 other disruptions . The ratio between the 18 peaks (TORE-SUPRA has 18 toroidal coils) was the same , only the absolute value was different from one measurement to the other . This suggests that the electrons impact distribution is the same from one disruption to the other , and the 18 locations between the coils are always struck with the same proportion of the runaways .

A confirmation of this fact has been obtained by an evaluation of the radiological age of the impacts : the ratio beetween short half-life isotopes like Ni^{57} (1.5 day) and long half-life ones like Cr^{51} (27.7 days) or Mn^{54} (310 days) is the same (within 10%) on all location . The first ones have mainly been produced by the last disruptions (4) and the seconds by all disruptions since the toroidal field was increased . Electrons lost during these four last disruptions have then hit the wall with the same spatial distribution as that of all the disruptions before .

The systematic differences from one place to the other must be due to slight mis-alignements of first wall panels respective to the magnetic

lines . The 18 peaks modulation is caused by the magnetic ripple : the distance between the toroidal field line and a circular toroidal line change about 1.1 mm from a under-coil location to an inter-coil one . If this millimeter can explain the factor of ten between the minima and the close maxima , a radial change from one panel to the other of the same order of magnitude can account for the peak difference . A better alignement seems difficult to obtain

Burnt , and even broken , graphite tiles have been discovered , correlated with the highest radioactive spots . If electrons are distributed around the torus proportionaly to the radioactive peaks , an estimated energy from 10 to 100 kJ per disruption is deposited on a few tens of square centimetres . This energy can increase the tile temperature of at least 500°C . Some of them have been broken by the thermal shock

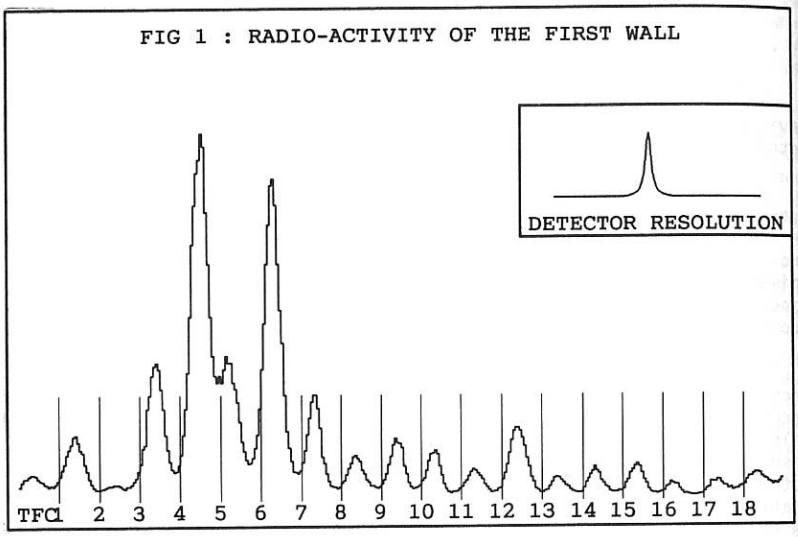

[1] L.LAURENT α J.M.RAX - Europhys. Lett. 11[1990]219
[2] W.C.BARBER α W.D.GEORGE - Phys. Rev. 116[1959]1551

RUNAWAY RELAXATION OSCILLATION ON HL-1 TOKAMAK

Ding Xuantong, Zhang Hongyin, Xu Deming, Zheng Yongzhen
Yan Ying, Zao Janyong

Southwestern Institute of Physics,
Leshan, Sichuan, P.R.China

We have studied the non-thermal radiation in HL-1 tokamak at the frequency 35GHz and 80GHz[1]. In this paper, the experimental results obtained by means of a microwave receiver (the bandwidth of the IF amplifier extends from 20MHz to 100MHz and its gain is 30db. The bandwidth of the video amplifier extends from DC to 100KHz and its gain is about 40db.) at frequency 10GHz will be presented. The microwave radiation with frequency 10GHz in HL-1 device is much stronger than thermal radiation level in lower density. The stationary radiation waveform is similar to the electron cyclotron radiation which has been studied [1], as shown in Fig.1. The feature of the radiation with frequency 10GHz is that a series of sawtooth occurs in certain plasma density range. Fig.2 shows these sawteeth. They only occur in lower plasma density range in which runaway electrons can be developed and the frequency of the radiation satisfies the condition: $\omega < \omega_p < \omega_{ce}$, under which runaway instability may arise, here ω_p and ω_{ce} are plasma frequency and electron cyclotron frequency respectively. The rising time of the sawtooth is in the order of ten s and the falling time is less than 2ms, generally. This period agrees with the experimental result about the runaway relaxation on TFR tokamak[3]. For most conditions, the period of sawtooth is not long. The amplitude and period of sawtooth are in linear relation. Sometimes, when the period of the sawtooth is larger than 1ms, they deviate from linear relation and relate to each other logarithmically. In the following, we will describe some phynomena related to the sawteeth of 10GHz radiation and try to explain them with available theory about runaway instability.

1) Upper and lower limit of plasma density:

The sawteeth of 10GHz radiation occur in low plasma density. Fig.3 shows the relation between the radiation with frequency 10GHz and plasma density. The zig-zag part in the figure represents the sawteeth for the 10GHz radiation. Point a and b denote the begining and end of the sawteeth in time scale, respectively. We found that at point a and b the plasma density is about 0.4×10^{13} /cm^3. At plasma density lower than this value, no sawteeth can be found. We think that this value is a lower limit of plasma density for sawteeth of 10GHz radiation.

According to the relation between the sawteeth of 10GHz radiation and plasma density, it seems that the sawteeth of 10GHz radiation may be caused by magnetic plasma wave, instead of electron cyclotron emission, because frequency of plasma wave, which developes when runaway instability occurs, is equal to $\omega_p k_{//} / k$, and electron cyclotron frequency is only related to toroidal magnetic field B. Since we use a microwave receiver at fixed frequency , the relation $\omega_p \cos\theta < \omega$ is always satisfied when plasma density is low enough. So this wave can not be received at any θ ($\theta = tg^{-1} v_\perp / v_{//}$).

At plasma density higher than $1.8\times10^{13}/cm^3$ the sawteeth disapear in the increase of the plasma density, as shown in Fig.4. So $1.8\times10^{13}/cm^3$ can be regarded as an upper limit of plasma density for sawteeth. The upper limit of density for sawteeth shows that when the runaway electrons are exhausted in higher density range, runaway instability can not develope further.

2) Sawteeth and sudden change of stationary radiation:

In the decrease of plasma density, when plasma density is less than the upper limit, the sawteeth of 10GHz radiation can not always be found. It is possible to find such sawteeth, only after the sudden change of the 80GHz and 35GHz radiation, which have also been studied in reference [1]. After the sudden change of radiation mentioned above, the sawteeth can be found, when plasma density is higher than its lower limit, as shown in Fig.4(A). If plasma density is lower than its lower limit, as shown in Fig.4(B), no sawteeth can be observed. Because the sudden change of the stationary radiation is an important phenomenum that pitch angle of runaway electrons is changed, so the sawteeth of 10GHz radiation is thought to be caused by the same cause.

3) Sawtooth of 10GHz radiation and sawtooth of soft X-ray:

We found that the same sawteeth of the soft X-ray can be observed in the lower density discharge. Both sawteeth have the same period and are in one to one correspondence. However the sawteeth of soft X-ray still exist when the plasma density is lower than $0.4\times10^{13}/ cm^3$.

The sawteeth of soft X-ray in lower density is different from that in higher density, which is thought to be caused by MHD instability. In the case of lower density, inverse sawteeth occur at every radius of cross section. There is no inverse surface at q=1, as shown in Fig.5. The amplitude of the radiation with sawteeth can reach 50 per sent of the total radiations in which there is also stationary radiation. The amplitude of sawteeth in higher density case is about 20 per sent of the total radiation, generally. A possible explanation is that with runaway instability high energy electrons are scattered in the velocity space. Their parallel velocity decreases rapidly and the bremsstrahlung radiation are emitted in soft X-ray range.

Accordion to the phenomena mentioned above, we think that stronger runaway instability is excited in low density discharge of HL-1 device.The sawteeth of 10GHz radiation come from magnetic plasma wave, which may be conversed to magnetoelectric wave because of non-linear wave-wave interaction. Some phenomena related to this instability, for example, periodic bursts of hard X-ray emission and spikes of loop voltage, have not been observed. We think that since the ripple of the toroidal magnetic field of HL-1 tokamak is very small (0.6%), these phenomena is too weak to be observed.

Thanks to Dr. G.C.Guo and Dr. Z.C.Den for the data they provided. Also thanks to all members of the HL-1 tokamak teem for their continuos cooperation in running the device.

References :

[1] Ding Xantong at el. Nuclear Fusion and Plasma Physics in China 9(3) 149(1989).
[2] V.V. Parail at el. Nuclear Fusion 18(3) 303(1978).
[3] P. Brossier at el. Nuclear Fusion 8(8) 1069(1978).

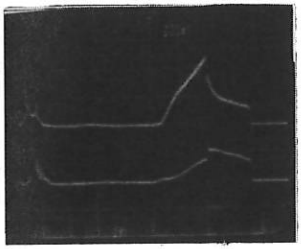

Fig.1 Stationary radiation at frequency 10GHz and 35GHz
a) 35GHz radiation
b) 10GHz radiation

Fig.2 Sawteeth of 10GHz radiation

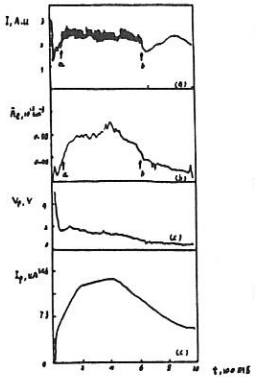

Fig.3 (a) 100Hz radiation (b) density (c) loop voltage (d) plasma current

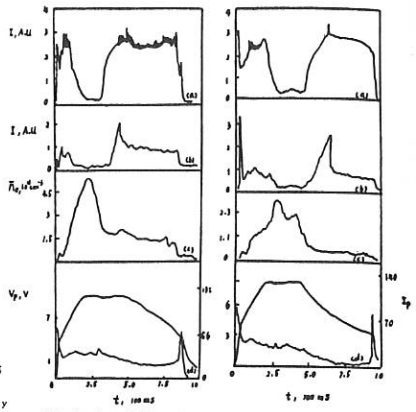

Fig.4 (a) 100Hz radiation (b) 35GHz radiation (c) density (d) loop voltage and plasma current

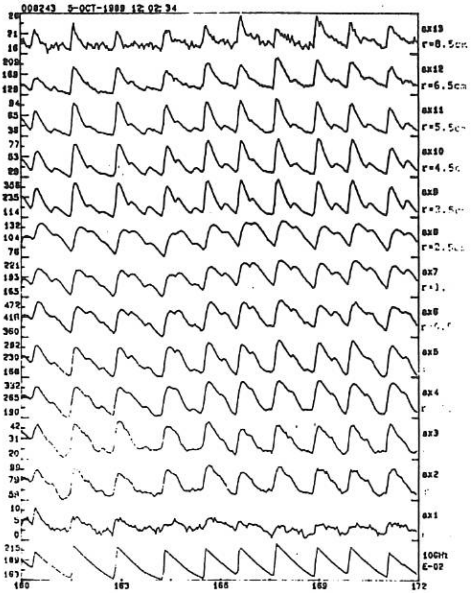

Fig.5 Sawteeth of X-ray and sawteeth of 100Hz radiation 1-13 are sawteeth of soft X-ray at the miner radius r=8.5cm, 6.5cm, 5.5 cm, 4.5cm, 3.5cm, 2.5cm, 1.5cm, 0.5cm, -0.5cm, -1.5cm, -2.5 cm, -3.5cm, -4.5cm. 14 is sawteeth of 100GHz radiation.

ENERGY LOSS IN A MAJOR DISRUPTION AND MHD INSTABILITIES AT LOW q_a IN THE HL-1 TOKAMAK

Qingdi GAO, Yongzhen ZHENG, Gancheng GUO, Libo RAN, Fangzhu LI, Manqiu TAN, Longwen YAN, Huaiguo ZHAO, Keqiang HUANG, Lixin TANG

(Southwestern Institute of Physics, P O Box 15, Leshan, Sichuan, China)

1. Energy loss during a major disruption

During a major disruption, the stored energy is lost in two phases. In the first phase, the plasma loses the major part of its thermal energy in a very short time (50-150 μs) with a large negative spike (300-600v) appearing on the loop voltage signal. In the period of the negative spike there is a short burst of regular oscillation with high frequency ($\sim$100kH,) which disappears as the negative spike ends (Fig.1). The oscillation appears on the signal of the plasma current and the equilibrium magnetic field and is superimposed on the negative spike. The disruption is a loss of confinement due to a fast rearrangement of the magnetic topology which is characterized by a flattening of the current profile. At the begining of a disruption, the plasma current is unchanged and the abrupt reduction of the plasma inductance causes sharp decrease of the loop voltage. In the disruption shown in Fig.1, the width of the negative voltage spike is $\sim$50 μs.During this period the change of the magnetic topology permit the plasma inductance of 1 μh before disruption to be reduced to 0.75 μh according to a reasonable model. The magnitude of the voltage decrease produced by the average changing rate of inductance can be 650v for I_p=130kA. The loss of the thermal energy results in an increase of the plasma resistance as well because of the drop of electron temperature and enhancement of impurities. The increase in resistance corresponds to a voltage change of less than 100v. From the evaluation given above, it is concluded that companying the abrupt release of the thermal energy, a negative voltage spike of several hundred volts can be produced. As is shown in Fig.2, the amplitude of the spike normalized by the plasma current ($\Delta v/I$,) generally decreases as the width of the spike(Δt) increases,which means that the negative voltage spike is related to the changing rate of the plasma inductance. The hard disruption is of the same scenario in the first phase even if it does not terminate the discharge. In this case the external circuit sustains the current and the plasma position unchanged immediately after the energy release, and the temperature profile is recovered. The thick conducting shell in HL-1 can prevent the plasma position from changing too much during a disruptive disturbance, so most of the disruptions are minor disruptions [1]. In a normal termination of discharge the plasma current decreases even quicker than in the disruption case, but there is no large negative spike appearing on the loop voltage signal (Fig.3). This indicates that the magnetic configuration is not destroyed seriously and the quenching of the plasma current is due to the exhaust of volt-seconds and the lost control of the plasma position.

After the first phase, the ensuing increase of the plasma resistance causes the current of the system composed of the plasma and coils coupled together by the

iron core transformer to decrease. The magnetic energy stored in the poloidal field is dissipated into the plasma and lost with the quenching of the plasma current. The waveforms of the current decay in disruptions are rather variable, but the decay rates are much lower compared with other tokamak devices. In a typical disruption case, the current decreases rapidly with $\dot{I}_p \sim -16MA/s$ from the beginning. After a hesitation in the current decay which may be due to the runaway component of current, the original decay rate is recovered. This kind of disruptions are usually low q_a disruptions and they are of a small fraction in the events of disruptive current termination. The majority of major disruptions in HL-1 gave value for $\dot{I}_p$ between limits of $-2MA/s$ and $-8MA/s$, and in some of the cases the current falls quicker at the end of termination. This fast quenching of the plasma current is similar to the normal termination of discharges and is probably a result of lost control of the plasma position.

In an iron core tokamak, the system composed of the primary winding (OH coils) and the plasma can be considered as decoupled from the other coils to a good approximation. The plasma behaves like an independent system with an effective inductance L_{eff} and the time constant of the current decay is L_{eff}/ρ,[2]. L_{eff} can be split into L_i corresponding to the energy stored in the vacuum vevssel (where the loop voltage is measured) and L_e, the external inductance. During the current decay phase, the transient induction in the thick copper shell of HL-1 increases the external inductance, which leads to the low dissipation rate of the magnetic energy. The external inductance under transient condition is determined experimentally, it stays in the range 5-6 μh. The loop voltages measured by flux loops located on the inside and outside surface of the shell are significantly different in the period of disruption, which shows the induced change of the magnetic flux in the shell.

2. MHD activities at low q_a

In the Hugill plot of HL-1 shown in Fig 4, some clear boundaries to operation appear, which correspond to either disruptions or loss of confinement through other ways. Recently the HL-1 tokamak has been operating in ohmic regime with q_a down to 2. This has been achieved in hydrogen and helium discharges, with $B_t \sim 1.8T$ ($I_p \leq 155KA$) and with carbon limiter of 18cm radius. The key point for the low q_a poeration is to overcome the $q=3$ resonance. In the earlier experiments, the low q_a ($q_a<3$) operation regime was prevented by the development of disruptive instabilities and there was a narrow window in the Hugill plot ($0.5<\bar{n}_e \cdot R/B_t<0.65\times 10^{18} m^{-3}T^{-1}$), through which discharges can pass into the low q_a value region. At that time the empirical way to break through $q_a=3$ is to control the ramping rate of current at $0.3<I_p<0.8MA/S$ by making a strong gas puffing just after the start up of the discharge. At prestent both the plasma current and the electron density increase consistantly so as to keep $I_p/\bar{n}_e$ continuously in the range of $(23-40)\times 10^{-20}$ KA $\cdot$ m^3, and in this way the relative amplitude of m=2 mode is suppressed to less than 0.3% during the current ramping phase.

During the quasi-stable phase at $q_a \leq 2.1$ the highest $\bar{n}_e$ achieved is $.5\times 10^{20} m^{-3}$ corresponding to a Murakami parameter of 3 (Fig 4). The sawtooth oscillation has inversion radii between 5 and 8cm, as observed by SXR diodes, with periods from 3 to 10ms and amplitudes $\Delta A/A \sim 20\%$ and $\Delta \bar{n}_e/\bar{n}_e \sim 1\%$ as detected by SXR diodes and HCN

interferometry respectivdy. A low level ($\delta \tilde{B}_\theta / B_{b=a} < 0.3\%$) of MHD activity is detected by magnetic coils when $q_a \leqslant 2.2$. In low q_a discharges two kinds of majar disruptions can occur. The first (Fig 5a) is characterized by the disapparence of sawtooth activity 10-15ms before the slow current decay and it is localized in high $\bar{n}_e$ side of the Hugill plot; the second (Fig 5b) results from an interplay between the m=3 and m=2 modes with the sawtooth activity continuing up to the sudden current termination, and this kind of disruptions are localized in low $\bar{n}_e$ side. In the low q_a disruptive discharges with high $\bar{n}_e$, immediately after the sawtooth disappears a small but clearly detectable inward shift of the plasma column is observed together with an increase in $\bar{n}_e$. The H_α emission and impurity line radiation are enhanced during the same period of time. The soft-X-ray emission profile shows a tendenc to drop in peak value and to become slightly hollow in the centre. A more detailed observation of the MHD activity reveals that after the last detected sawtooth some bursts of m=2 mode with small amplitude show up in the central region of the plasma. In the low q_a diruptive discharges with lower $\bar{n}_e$, however, a quickly oscillating and exponentially growing m=2 and m=3 modes are seen to grow for 2-3ms before the disruption. During the last 0.8ms, the mode oscillation slows down,but apparently not locking.

For a comparison, an improved one-dimensional analysis of the tearing mode instability has been made for j(r)-profile optimization [3]. As q_a is varied in the low q_a regime of HL-1, the caslculation results show that for $q(0) > 1$, stable j(r) - profiles can be found only when $q_a > 2$. But in the case of $0.5 < q(0) < 1$, a j(r)- profile which is stable against all modes except m=1/n=1 exits for $q_a < 2$.

Reference

1. Qingdi, GAO, et al., in Plasma Physics and Controlled Nuclear Fusion Research 1988 (Proc. 12th Int. Conf. Nice, 1988) Vol. 1, IAEA, Vienna, 121
2. TFR Group, Nucl. Fusion, 25 (1985) 919
3. F.Z. Li, et al., SWIP Institute Report, SWIP-R(90-1) (1990)

Figure Captions

Fig.1 The waveforms of V_θ and I_p at the beginning of a disruption.

Fig.2 The amplitude of the negative voltage spikes ($\Delta V/I_p$) Versus their width (Δt)

Fig.3 The evolution of V_θ during normal discharge termination measured with different flux loops

Fig.4 The Hugill plot for HL-1. The shaded area is where disruptions occur.
- low q_a disruptions with sawtooth activity continuing up to the current decay
- low q_a disruptions that follow the disappearance of the sawtooth activity
- disruptions at $q_a=3$

Fig. 5 Evolution of B_θ, SXR emission and I_p for low q_a disruptions: (a) high density, (b) lower density

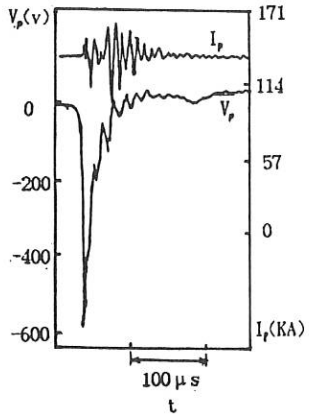

Fig. 1

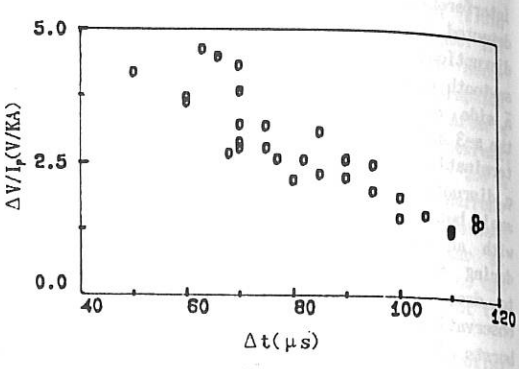

Fig. 2

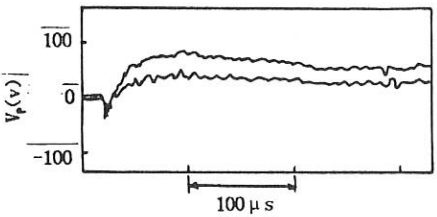

Fig. 3

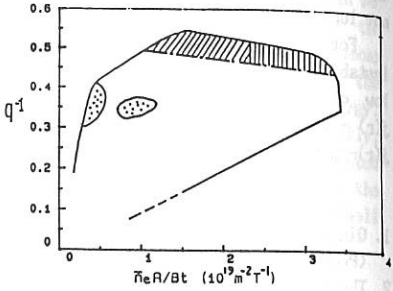

Fig. 4

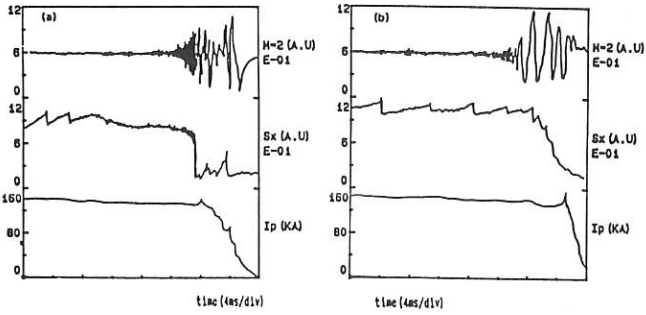

Fig. 5

MHD-PERTURBATIONS IN T-10.

Kislov D.A., Lyadina E.S., Razumova K.A., Savrukhin P.V.

Kurchatov Institute of Atomic Energy, P.O. Box3402, Moscow, USSR

Installation of the soft X-ray imaging system on the T-10 tokamak allows to investigate the internal structure of the plasma perturbations during the three different type of the magnetohydrodynamic instabilities: sawtooth crashes, minor and major disruptions.

As was pointed out before the minor and major disruptions were predominantly characterized by the m/n=2/1 mode which is localized in the outer part of the plasma column [1]. But experiments on JET [2] indicated that the density limit disruptions were proceeded also by the m=1,n=1 "erosion". The T-10 experimental study shows the dominant role of both m=1 and m=2 modes in the processes. (The T-10 imaging system allows to reconstruct the m=2 perturbations, but only in the r/a<0.7 region, so the investigation of the minor and major disruptions was restricted by the high-qL density limit disruptions when the m=2 perturbation was placed well inside this region.)

DIAGNOSTIC AND TOMOGRAPHIC RECONSTRUCTION TECHNIQUE. The T-10 soft X-ray imaging system consists of the 58 silicon surface-barrier diodes arranged in the three arrays (20+19+19) at one toroidal location (poloidal angles to the equatorial plane $\theta = 0°, -30°, +30°$) [3]. The field of view covers the bulk part of the plasma (r/a<0.7) with a spatial resolution up to 2 cm (r/a=0.07). Time resolution of the system is 10 μsec.

The tomographic technique is based on the modified Cormack method and allows to reconstruct the m=0, $\cos\theta$, $\sin\theta$, $\cos2\theta$, $\sin2\theta$, $\cos3\theta$ harmonics of the soft X-ray intensity perturbation in the energy range 2.5-15 keV [4].

MAJOR DISRUPTIONS. The density limit disruption are studied in low Ip discharges (qL=4.5, aL=0.28m) with Ohmic and with the additional Electron Cyclotron heated plasmas.

The key observations of the density limit disruption in Ohmically heated high qL plasma are:

1) A transition from the sawtoothing stage to the "giant" m=1;
2) A growth of the "giant" m=1 mode and its deformation by the m=2 mode;
3) Sharp growth of the m=2 components;
4) Energy quench resulted in the hollow SXR emissivity profiles.

This mechanism is illustrated on Fig.1. representing the temporal evolution of the soft X-ray emissivity integrated along the central "vertical" chord and the sequence of the soft X-ray tomographic images during the precusor m=1 and m=2 oscillations (Fig.1.B.1-7) and after the crash (Fig.1.B.8). Time of the crash is 0.1-0.2 msec.

MINOR AND MAJOR DISRUPTIONS in ECRH PLASMA. "Central" ECRH slows down considerably the stored energy decay rate during the density limit

disruption. Duration of the energy losses phase is 10-20 msec which is in 100-200 time larger than in Ohmic heated plasma. The major collapse was proceeded by a few minor disruptions accompanied by the continuum saturated m=1 sinusoidal oscillations. Such slow energy-degradation indicates the absence of the sudden transformation of the magnetic field configuration.

Fig.2. represented the temporal evolution of the central chord integrated soft X-ray emissivity at sequence of the disruptions during ECRH. The series of the local soft X-ray emissivity tomographic images during the minor disruptions (t= 506 msec) with precusor m=1 oscillations was shown on Fig.2.B. The first minor disruption induced the "giant" m=1 mode extended over r/a<0.4-0.5 region which is up to 2 times widely than the m=1 "sawtooth" mode location. The rotation of the perturbation is seen on the Fig.2.B(1-4). At t=506.04 msec the m=2 deformation appears (Fig.2B.(4,5)). This deformation resulted in the m=1 displacement of the hot core growth (Fig.2.B(6)). After the minor collapse the rotation of the m=1 structure continues and the displacement slightly decreases (Fig.2.B(7,8)).

The internal interaction of the m=1 and m=2 modes at the major disruption in similar to the images shown on Fig.2.B. But at the final stage of the crash the central core eroded totally due to the cold m=2 perturbations invading.

The m=1 "giant" mode can indicate the sharp expansion of the q=1 surface. Such expansion may be explained by the sudden redistribution of the skin current produced during the current contraction at the edge-cooling phase [5].

The prolongation of the energy quench time during the ECRH seems to be connected with the saturation of the m=1 mode. (During the "central" ECRH the position of the EC-resonance zone was maintained in the plasma center R=Ro, but the additional HF power is absorbed not in the central region, but outside the q=1 surface due to the refraction in high density plasma. As was shown before this can produce the stabilization (saturation) of the m=1 mode [6].)

Sometimes the first minor disruptions during ECRH were accompanied by the X-ray emissivity spikes (Fig.2.A(t=493ms)). This spikes seems to be due to the high-energy (E<30keV) radiation delivering in the crash. But the nature of the spikes and their role in disruption are not clear for the moment.

CONCLUSIONS. 1) The density limit disruptions in T-10, as in JET [2], are proceeded by the Te(r) profile contraction at the outer radii. Later phase of the disruption is connected with the m=2 and m=1 modes interaction. Moreover, the "giant" m=1 mode play a key role in the density limit disruption in high-qL (qL=4.5) plasma;

2) The density limit disruption in high-qL ECRH plasma is proceeded by the series of minor disruptions and continuous m=1 mode development. This effect slows down the rate of the energy loses in the disruption (up to 200 times).

REFERENCES.

[1]Kadomtsev B.B. Plasma Phys. Controll. Fusion 26 (1984) 217. [2]-Wesson J.A.,et al.,Nucl.Fus 29(1989)641., [3]-Savrukhin P.V., et al. This Conference.(i.01), [4]-Dnestrovskii Yu.N.,et al. This Conference.(i.05), [5]-Kleva R.G., Drake J.F., UMLPR 89-039,1989. [6]-Bobrovskii G.A.,et al. Fizika Plazmy (1987) 1155.

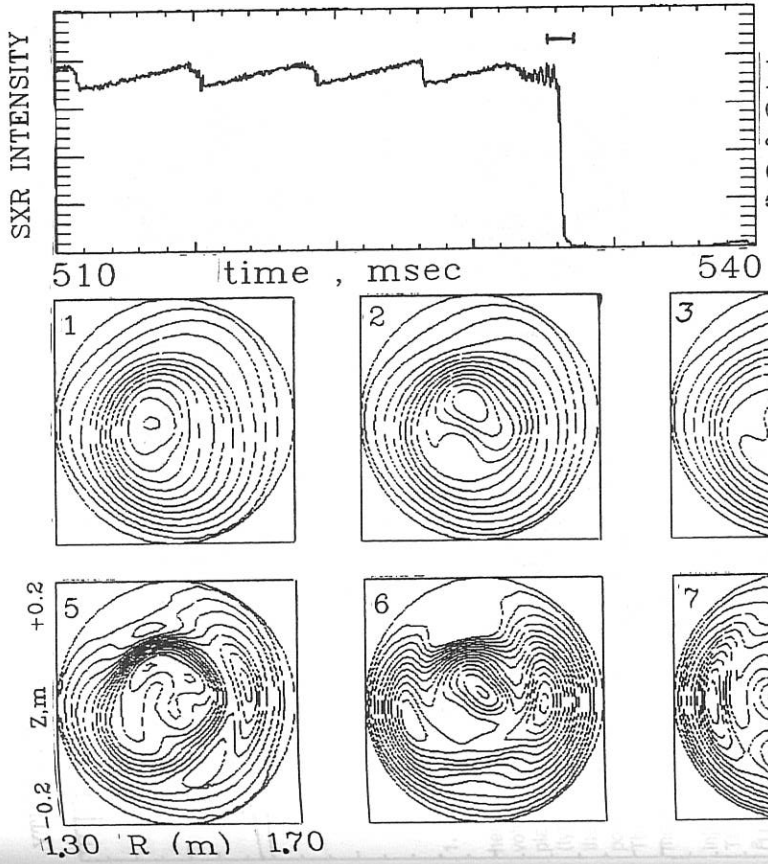

FIG. 1. A) Trace of the X-ray emissivity (central chord) and B) Series of the X-ray images during major disruption in OH plasma [(1)-t=529.95, (2)-530.01, (3)-530.07, (4)-531.41, (5)-531.47, (6)-531.55, (7)-531.61, (8)-531.78 msec).

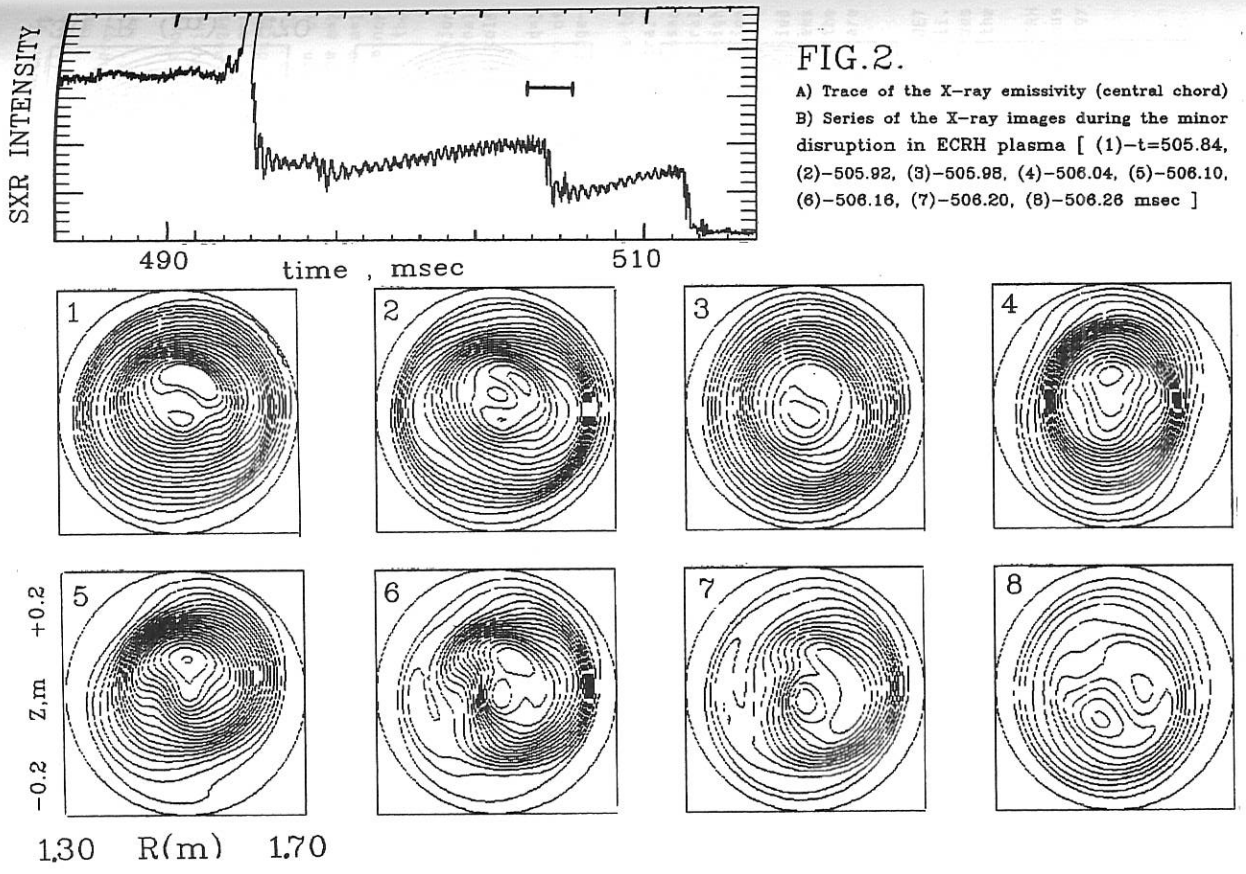

FIG.2.

A) Trace of the X-ray emissivity (central chord)
B) Series of the X-ray images during the minor disruption in ECRH plasma [(1)-t=505.84, (2)-505.92, (3)-505.98, (4)-506.04, (5)-506.10, (6)-506.16, (7)-506.20, (8)-506.26 msec]

SAWTOOTH MODULATED DENSITY FLUCTUATIONS IN THE CENTRAL PLASMA REGION OF NBI-HEATED DISCHARGES IN TEXTOR.

M. Jadoul , G. Waidmann

Laboratoire de Physique des Plasmas - Laboratorium voor Plasmafysica
Association "Euratom-Etat belge" - Associatie "Euratom-Belgische Staat"
Ecole Royale Militaire - B1040 Brussels - Koninklijke Militaire School

Institut für Plasmaphysik, Forschungszentrum Jülich GmbH ,
Association EURATOM-KFA, P.O.B. 1913, D 5170 Jülich, FRG

1. Experimental Conditions.

Local density fluctuations were measured in plasmas with strong neutral beam heating by means of a homodyne 2 mm microwave scattering diagnostic. The scattering volume has a radial half-width of 2 cm and was moved, from shot to shot, in the equatorial plane of the TEXTOR tokamak, from the magnetic axis at the major radius R ≈ 184 cm (typical for NBI) up to R ≈ 205 cm. The selected wavevectors were radial and varied with the position of the scattering volume (k_R [m^{-1}] ≈ 9000 (R[m]-1.75)). The scattered power was analysed with a filter bank covering a frequency band from 200 kHz to 2 MHz. The fluctuation levels $S(k_R,\omega)$ were correlated with the sawtooth evolution observed by means of a 10 channel heterodyne ECE-radiometer diagnostic.

Various plasma densities, currents and neutral beam heating conditions (co-injection, counter, co+counter, co+ICRH, H->D injection, D->D) were investigated. The TEXTOR neutral beams have a Gaussian power density profile of 20 cm half-width aligned to a tangency radius R_t = 165 cm [1].

2. Observations during Co-Injection.

Applying 1.5 MW of co-injection NBH (H->D) induced always observable modifications of the fluctuation levels. When the scattering volume is far from the magnetic axis (R = 200 cm typically), a relatively small increase with respect to the OH phase is observed at all the frequencies (a factor 2 to 4), with weak or no variation during the sawtooth evolution. Moving it to the magnetic axis, where the beam is deposited, drastically changes this picture. Not only the levels can increase by a factor up to 100, but also a strong modulation in some frequency range, correlated with the sawtooth evolution, is observed.

For the cases of low and high current (340 kA and 480 kA), the figures 1a and 1b show the temperature evolution over one sawtooth period observed on 4 neighbouring ECE channels. The bottom curves demonstrate the same for one frequency of the fluctuation spectrum (in the MHz range). This fluctuation level is low just after a sawtooth relaxation, and stays so for typically 12 ms. After that period, there is a big and sudden increase of the fluctuations which is always simultaneous with changes in the detailed temperature profile evolution. At any current, a heat pulse is observed inside the inversion radius (fig. 1aa and 1ba) and outside of it (fig. 1ad and 1bd). In the low current case, the central temperatures will show a large change of slope or even a dip in the intermediate region(fig.1ac), followed by a saturation. Then, depending on the frequency, the fluctuations can decrease or stay up to the next relaxation when it decreases anyway. For the high current case, the slope variation is much smaller, up to the saturation (fig. 1bb and 1bc). At that time a new heat pulse is observed often accompanied by a smooth increase of the fluctuations. The behaviour of the local plasma density was similar to that of the electron temperature.

The modulated behaviour of the fluctuation levels sensitively depends on the plasma density. A small decrease of the density as exemplified in fig. 2 (where $\overline{n}_e$ goes from $3.\times10^{13}$ cm^{-3} to $2.\times10^{13}$ cm^{-3}) can increase very much (by a factor ≈ 10) the modulation of the highest fluctuation frequencies. The fluctuation spectrum during OH and its range of variation during co-injection are shown in fig. 3 for the same discharge as shown in fig. 1b. The strong modulation is clearly located in the high frequency domain. The low frequency fluctuations show only a weak increase and no modulation.

The modulation effect has also a clear spatial location as shown in fig. 4. Here we have normalized it for local density and scattering volume variations. It is usually maximum near the magnetic axis and disappears almost completely at a distance of 10 cm from it.

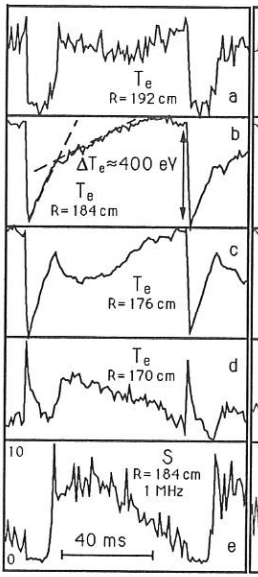

Fig. 1 a

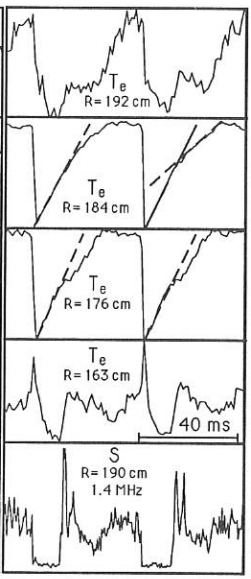

Fig. 1 b

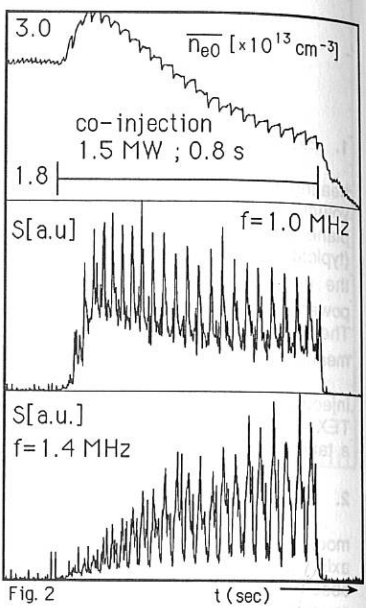

Fig. 2

Fig.1a Sawtooth evolution observed on 4 neighbouring ECE channels and, below, one frequency of the density fluctuation spectrum; Ip=340 kA, $\overline{n}_e \approx 3.2 \times 10^{13}$ cm^{-3}.
Fig.1b The same for a high current discharge. Ip=480 kA, $\overline{n}_e \approx 1.7 \times 10^{13}$ cm^{-3}.

Fig.2 Density dependence of the modulation in the high frequency part of the fluctuation spectrum. The density dropped from $\overline{n}_e \approx 3 \times 10^{13}$ cm^{-3} to $\overline{n}_e \approx 2 \times 10^{13}$ cm^{-3}.

When the density is decreased down to $\overline{n}_e \leq 1.5\times10^{13}$ cm^{-3}, in the low current case, giant sawteeth develop (periods from 300 ms to more than 1 sec). In this case, after a few 100 ms, large repetitive bursts of fluctuations (spaced by ≈ 3 ms) begin to grow, having often a maximum amplitude at the relaxation time (fig. 5). According to the length of the sawtooth, they have been observed during a few tens of millisecond or up to 500 ms. This

effect is again seen for high frequencies in the central plasma region and seems to disappear outside the inversion radius. It recalls somewhat the fishbone phenomena, although no oscillations have been seen on the ECE measurements. For some cases this activity reached a maximum in the middle of the sawtooth period, and a small decrease of the central temperature then was observed.

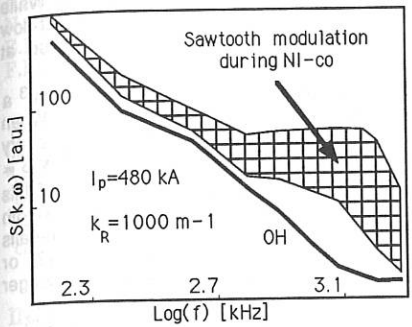

Fig. 3

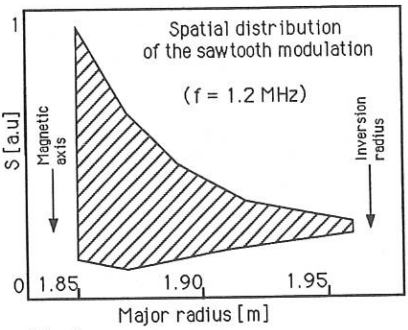

Fig. 4

Fig.3 Fluctuation spectra during the OH and NBI heated phases. The dashed region indicates the range of the sawthooth-correlated fluctuations during NI. The discharge is the same as that shown in fig. 1b. The modulation occurs clearly in the megaherz range.

Fig.4 Spatial dependence of the sawthooth-correlated fluctuations, obtained during a series of high current shots (Ip=480 kA), with a line-averaged density $\overline{n}_e \approx 2.5 \times 10^{13}$ cm^{-3}. The modulation is maximum near the magnetic axis.

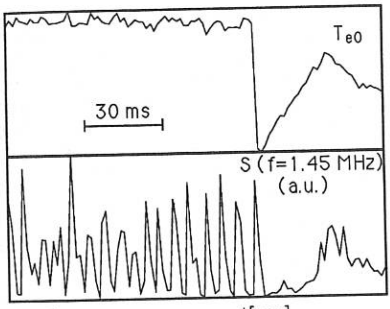

Fig. 5

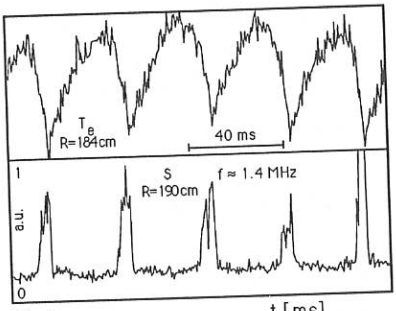

Fig 6

Fig.5 Part of the series of bursts observed during the last 300 milliseconds of a giant sawtooth ($\tau_{st} \approx$ 800 ms). The repetition rate (3ms typically) recalls somehow the fishbone phenomena. $\overline{n}_e \approx 1.3 \times 10^{13}$ cm^{-3} and Ip=340 kA.

Fig.6 Broad fluctuation peaks rising during slow sawtooth relaxations are typical of high density shots heated by counter-injection. Ip=340 kA, $\overline{n}_e \approx 4.1 \times 10^{13}$ cm^{-3}.

3. Observations during Counter-Injection.

In many respects counter-injection behaves differently from co-injection. While co-injection offers large or giant sawteeth with an enlarged inversion radius at low densities, some sawtooth lengthening with counter-injection was easier observed at increased densities and showed a reduced inversion radius.

For a low current of 340 kA, in the density range from $2.\times10^{13}$ to $6.\times10^{13}$ cm^{-3} a big modulation of the fluctuations as described for co-injection was never observed. When the scattering volume is a few centimeters away from the magnetic axis, the stationary fluctuation spectrum is uniformely increased by a factor up to 10. It follows a power law $S \propto f^{-\alpha}$ with $2 \leq \alpha \leq 4$ (Near the axis the fall-off is sharper in the OH phase.). On top of this stationary level, a large peak is growing during up to 5 ms before the end of the sawtooth period (fig 6). During that time the central temperature is relaxing slowly. This recalls previous observations of turbulent sawtooth precursors during OH discharges [2] or specific turbulence associated with sawtooth relaxations [3], but can show a much longer time span.

At high currents (470 to 530 kA) and lower densities (1.4×10^{13} cm^{-3}) a moderate sawthooth lengthening was again observed and the fluctuations showed a modulation similar to those observed with co-injection.

4. Combined Heating.

The addition of either 1.5 MW of counter-injection or ICRH during a co-injection pulse both suppressed the modulation on the high frequency fluctuations, but had opposite effects on the sawtooth period (increasing the period in the case of ICRH). A stationary level approximatively equal to the lowest level of the previous modulation (but higher than in OH) was observed. At the lowest frequencies however an increasing by a factor of 2 was found.

5. Discussion.

We have shown, that co-injection of neutral beams into an Ohmic plasma induces a specific fluctuation phenomenon in the central plasma region. It correlates strongly with the sawtooth evolution. A transport phenomenon is to be associated with these density fluctuations. Possible explanations could involve a direct beam-plasma instability or a plasma profile instability or even a direct effect of fast particles. In all the cases observed, low densities pronounce the effect. Further work will be devoted to this question. A possible link with the mechanism of sawtooth lengthening should also be investigated (could it be fast particles or a profile re-organization). The differences shown for counter-injection might be due to the evolution of the current profile and broader deposition profiles.

Finally let us recall that the interpretation of scattering experiments is complicated by a number of effects like e.g. plasma rotation and by the difficulty to measure the wavevector spectra and the spatial dependence independently.

REFERENCES

[1] R.UHLEMANN, H. EURINGER, M. LOCHTER in FUSION TECHNOLOGY 1988, Elsevier Science Publishers

[2] M.JADOUL, G.WAIDMANN, Proc. 16th EPS Conf. on Controlled Fusion and Plasma Physics (Venice 1989) p.529.

[3] F.GERVAIS, D.GRESILLON,P.HENNEQUIN,A.QUEMENEUR,A.TRUC, idem p.497.

HIGH-BETA REGIMES IN JET

P.Smeulders, J.M.Adams,[1] B.Balet,[2] D.Campbell, A.Cheetham, S.Corti, A.Edwards,[2] N.Gottardi, C.Gowers, T.C.Hender,[3] G.Huysmans,[3] J.Jacquinot, E.Joffrin, O.Kwon,[4] E.Lazzaro, F.B.Marcus, P.Morgan, F.Nave,[4] P.Nielsen, D.O'Brien, J.O'Rourke,[5] F.Porcelli, L.Porte, G.Sadler, G.Sips, D.Start, A.Tanga, D.Ward, H.Weisen.

JET Joint Undertaking, Abingdon, OX14 3EA, UK.
[1]UKAEA/EURATOM Fusion Association,Harwell,Didcot,UK
[2]UKAEA/EURATOM Fusion Association,Culham,Abingdon,UK
[3]FOM-Instituut voor Plasma Fysica,Nieuwegein,NL
[4]Laboratoria Nacional de Engenharia e Tecnologia Industial,Sacavem,Portugal
[5]CRPP-Lausanne,21 Avenue des Bains,Suisse

INTRODUCTION. Previously [1] we studied discharges with very peaked density and pressure profiles and large gradients ($\nabla p > 300$ kPa/m) in the plasma central region. These conditions were obtained in pellet fueled plasmas with Neutral Beam (NB) and Radio Frequency (RF) heating. The value of β saturated at 40% of the Troyon value and started to decline with the appearance of modes with toroidal mode numbers n>1. Calculations showed ideal ballooning unstable regions near the position of the large pressure gradients.
In this paper we study less peaked pressure profiles with broad density profiles in the Double Null (DN) configuration. These, low field, discharges have reached the Troyon limit (2.8 I/Ba [MA,T,m]) [2] during the H-mode phase. The power needed to reach these β values is 10 MW or above, in agreement with calculated values derived from the Goldston scaling [3] and the Troyon limit :

$$P_c = 77\ \kappa\ a^{2.74}\ B^2 / (H^2\ R^{1.5}) \qquad [MW,m,T] \qquad (1)$$

Here κ is the elongation, a the horizontal minor radius, B the toroidal magnetic field, H equal to 1 for L-mode and 2 for H-mode plasmas and R the major radius. In X-point divertor discharges in JET there appears to be a maximum wall loading for the carbon tiles above which increased sputtering of the carbon prevents any further increase of the plasma energy. Beryllium gettering recently installed in JET has increased the plasma purity and decreased the above effect. At low toroidal fields ($B \leq 1.2$ T) the Troyon β limit is reached with additional heating at power levels below which the carbon self-sputtering becomes important.
It has not yet been possible to surpass the Troyon limit as has been done in DIII-D [4], where the ballooning limit can be reached with a marginally stable pressure profile over most of the plasma.
PLASMA PARAMETERS. Fig.1 shows the maximum toroidal beta obtained for all discharges of 1986 till 1989 with a poloidal beta greater than 0.4 as a function of the normalised current (I(MA)/a(m)B(T)). The straight line represents the Troyon-Gruber limit.
A volume-average toroidal β of 5.5% has been reached at this limit in DN H-modes in H plasma with B around 1T. Central electron and ion temperatures of 3.5 and 6 keV have been obtained with 11 MW NB heating in these low q discharges ($q_{95} \simeq 2.2$ or $q_c \simeq 1.6$) with a 2MA plasma current, and a κ of 1.8. Z_{eff} slowly increases in time from 1.3 and levels off at around 2.5.
In these discharges with Be coated walls, β saturation is observed without

disruptions. The saturation is related to MHD-modes, ELM's and n=1 activity. Sawtooth and fishbone events occur and sometimes continuous n=1, 2, or 3 modes appear, which can lead to a β decline.
A peaked and roughly triangular p(r) profile develops from an initially broad profile with the steeper gradient towards the edge. The internal inductance l_i decreases from $\approx$ 1 to 0.7, which indicates a broadening of j(r) towards those profiles used in the β-optimisation by Troyon [2]. The decrease of the inductance is calculated to be due to the bootstrap current, which is approximately 25% of the total current and located in the outer half of the plasma.
BETA SATURATION. The evolution of β for the discharge with the highest β obtained so far is shown in fig.2. Also shown are the periodic changing MHD activity, central ion temperature and volume-averaged density as a function of time. The main β-limiting mechanism in this discharge is the high-β sawtooth. Increased MHD (n=1 and n=3) activity (around t=15 s) leads to a diminished rate of rise in β after the crash and to a decline in the central ion temperature and so contributes to the β saturation.
The high-β sawteeth differ from sawteeth at low β in two ways :
1. The associated heat pulse is very rapid with $\tau_{HP} \approx 100$ μs instead of $\approx$10 ms.
2. Dominant (1,1), (2,1) and higher m pre- and postcursors are seen, similar to fishbones but of twice the amplitude. The modes have a ballooning character near the outer edge with a ratio in amplitude from the low to high B-side of $\approx$10 as seen by the X-rays. Similar to a normal sawtooth, a high-β sawtooth causes a flattening of the pressure profile within the q=1 radius.
The fraction of the losses due to high β sawteeth is 10 to 15% and that due to the intermittently appearing MHD-modes 20 to 30% of the total energy losses. This is sufficient to prevent further β increase since the heating power P is close to the critical power required to reach the Troyon limit. Both the fishbone- and sawtooth events strongly affect the fast particle distribution as measured by the neutron emission. This has important consequences for future α-particle heating, burn control and wall loading.
The central neutron emission drops by 70 % and its total rate by 30 % during a sawtooth. Fishbones are observed which individually cause less than a 10% drop in the global neutron emission. However they occur about 10 times more frequently than sawteeth and may contribute appreciably to the central loss of fast particles and energy.
BETA COLLAPSE. In a few cases in JET high β-collapses occur that are triggered by or preceeded by large n=2 MHD activity with $\delta B_\vartheta \approx 15$ gauss. A typical example is shown in fig.3 where a n=2 mode starts to grow at 11.45 sec after the n=1 modes decrease due to a sawtooth. Then, this n=2 mode locks at 11.9 sec and continues to grow apparently leading to a β-collapse. This collapse differs from the β-saturation in various ways :
- a dominant (3,2) and other coupled n=2 modes are responsible,
- the electron density is mostly affected in contrast to the saturation due to the high β-sawteeth,
- the central ion temperature and the fast ions do not seem to be reduced.

Shortly before the start of the n=2 mode activity there is usually a sawtooth and the (1,1) mode structure observed by the X-ray diagnostic differs from a very similar discharge without a β-collapse. This is an indication for an altered q(r) profile.
PLASMA STABILITY. The stability of the high-β discharges has been examined with the ideal ballooning and low-n free boundary kink stability codes ERATO [5], HBT [6] and BALLOON [7]. The resistive low-n stability is also examined with the fixed boundary FAR code [8]. These stability studies are discussed more fully in [9].

The pressure profiles used for the stability calculations are obtained by normalising the electron LIDAR pressure to the total pressure derived from the plasma diamagnetism. This is corroborated by the similarity of measured electron and ion pressure profiles and the slightly more peaked calculated fast ion profiles. q-profiles are generally obtained from the equilibrium code IDENTC, but have also been deduced from the radial position of the MHD-modes as seen by the X-ray cameras.
It is found that before a high-β sawtooth the central plasma over more than half its radius is close to or even above the marginal ideal ballooning stability threshold. The ideal n=1 internal kink is also found to be strongly unstable for $\beta_N \simeq 1$ when $q_0 \leq 1$. This instability is probably linked to the observed (1,1) instabilities which seem to cause the β-saturation. However before quantitative comparisons with theory can be made fast particle effects must be considered. It is expected that at the β values which have been reached, the stabilizing effects of the fast particles can no longer prevent the excitation of an ideal internal kink mode. In addition, severe fishbone activity is expected in this regime, resulting from the coupling with high energetic beam ions above 40 keV.
It is further found that in the cases where the β-collapse occurs internal modes of either n=2 or n=1 structure, appear to be responsible for the enhanced plasma losses. These modes have been simulated by the FAR code where the q-profile has been tuned to match the measured X-ray fluctuations over the plasma cross-section. In the case where n=1 modes are dominant, the q-profile had to be relatively flat in the centre with $q(0) \simeq 1.1$, supported by Faraday-rotation measurements . The n=2 modes, which generally lead to the β-collapse, also seem to be fitted best by flat q-profiles in the plasma centre, which gives rise to an infernal type mode.
CONCLUSIONS. In low q discharges ($q_{95} \leq 2.2$) at high β, saturation of the plasma energy is observed without disruptions. Global n=1 modes in the form of high-β sawteeth and fishbones are generally responsible for this saturation. β-collapses seem to be related to large n=2 or n=3 MHD modes. Simple triangular temperature profiles exist at the limit. Together with the rather flat density profiles this leads to constant ∇p across the plasma. Such peaked pressure profiles are very favourable for a fusion reactor. Both the fishbone- and sawtooth-events strongly affect the fast particle distribution. This has important consequences for future α-particle heating, burn control and wall loading. The role of the ballooning limit in the inner part of the plasma is not yet clear. Generally good agreement between the theoretically predicted internal modes and the observations at the beta limit, has been obtained. The role of the fast particles on the beta limit needs further studies both theoretically and experimentally.

REFERENCES

[1] G.Huysmans, R.Galvão et al, Plasma Phys.& Controll. Fusion **31**(1989)2101
[2] F.Troyon, R.Gruber et al, Plasma Phys.& Controll. Fusion **26**(1984)209
[3] R.Goldston, Proc.11th Eur.Conf.on Contr.Fusion & Plasma Phys.,Aachen(1984)
[4] T.S.Taylor et al, Proc.16th Eur.Conf.on Contr.Fusion & Plasma Phys., Venice(1989)
[5] R.Gruber et al, Computer Phys. Commun. **21**(1981)323
[6] J.P.Goedbloed,G.M.D.Hogewey et al, Proc.10th Int.Conf.on Plasma Phys.and Contr.Fusion,London 1984,IAEA(1985)165
[7] D.P.O'Brien, C.M.Bishop et al, Proc. 16th Eur.Conf.on Contr.Fusion and Plasma Phys.,Venice(1989)
[8] L.A.Charlton et al, Journal Comp. Phys. **63**,107(1983)
[9] T.C.Hender et al,"Theoretical Analysis of High-β JET Shots", this Conf.

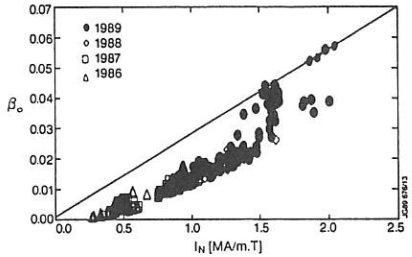

Fig.1 Toroidal beta β_φ versus normalised plasma current $I_N = I/Ba$ for all 1986-1989 discharges with $\beta_\vartheta > 0.4$. The solid line is the Troyon-limit

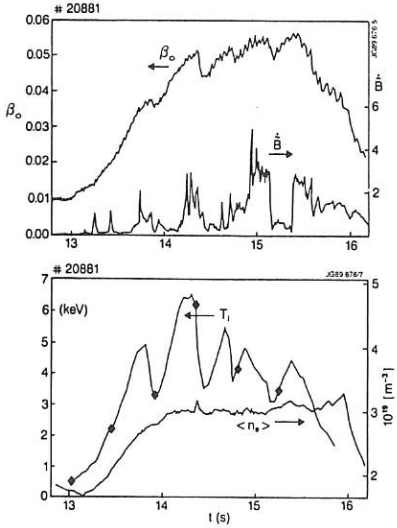

Fig.2 Evolution of β_φ, MHD-mode amplitude $\tilde{B}_\vartheta$, $\hat{T}_i$ and $<n_e>$ for the 5.5 % beta discharge. B_φ is ramped down from 1.2 T at 13 s to 0.9 T at 16 s. P_{NB} is constant from 14 to 15.2 s.

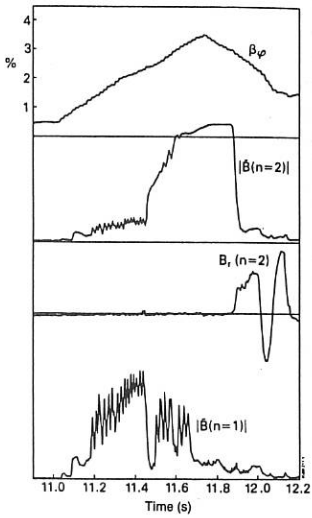

Fig.3 β-collapse due to n=2 modes. A sawtooth at 11.45 s reduces the n=1, the n=2 mode starts to grow and β collapses at 11.7 s with $\tilde{B}(n=2) \approx 6$ G, reaching 15 G at 12.1 s

SAWTOOTH STABILISATION BY FAST IONS: COMPARISON BETWEEN THEORY AND EXPERIMENTS

F. Porcelli, D.J. Campbell, W.D. Diachenko+, L.-G. Eriksson, J. Jacquinot, L.S. Levin+, D.F.H. Start, A. Taroni

JET Joint Undertaking, Abingdon, Oxfordshire, OX14 3EA, U.K.
+Ioffe Physico-Technical Institute, Leningrad, U.S.S.R.

Abstract. Sawteeth in JET have been suppressed [1] for periods of up to 5s during high power auxiliary heating. The value of q on axis is measured to be significantly below unity during the sawtooth-free period. A theoretical model has been developed [2] whereby m = 1 modes are shown to be stabilised in the presence of high energy particles. The aim of the present paper is an assessment of the ability of this model in explaining the experimental observations.

Theoretical considerations. Non-thermal ions having sufficiently high energy can dynamically stabilise collective modes affecting the plasma bulk. The condition on the average fast ion energy, E_h, can be written as $\omega_{Dh} > \omega$, where $\omega_{Dh} = cE_h/(Z_h eBR_o r_s)$ is the bounce-averaged magnetic drift frequency of energetic ions with deeply-trapped orbits (subscript h = hot) and ω is the relevant mode frequency in the plasma rest frame. For the internal kink mode, $\omega \lesssim \max\{\omega_{*i}, \gamma_{mhd}\}$ (provided the fast ion density does not exceed a threshold, see below), where $\omega_{*i} = -(c/eBr_s n)(dp_i/dr)_{r_s}$ is the thermal ion diamagnetic frequency, with $q(r_s) = 1$, and $\gamma_{mhd} \sim \varepsilon_o^2[\beta_p^2(r_s) - \beta_{p,cr}^2]\omega_A$ is the internal kink growth rate in the ideal-MHD limit, with $\varepsilon_o \equiv r_s/R_o$, $\beta_p(r_s) \equiv -[8\pi/B_p^2(r_s)]\int_o^{r_s} dr(r/r_s)^2\, dp/dr$, $\beta_{p,cr} \sim 0.1 - 0.2$, $\omega_A \equiv V_A/\sqrt{3}R_o$ and $V_A \equiv B/(4\pi m_i n_i)^{1/2}$. The condition $\omega_{Dh} > \omega$ is easily satisfied during intense ICRF heating on JET, as in this case $E_h \sim 1$ MeV. Energetic ions and the plasma bulk are no longer decoupled if $\omega_{Dh} \sim \omega$, in which case fishbone oscillations are likely to occur. In addition, resistive effects are important on m = 1 modes. All these effects are described in terms of a single dispersion relation given in Eq. (3) of Ref. 2. This dispersion relation depends on four normalised parameters: (i) $\hat{\gamma}_{mhd} \equiv \gamma_{mhd}/\omega_{Dh}$; (ii) $\hat{\omega}_{*i} \equiv \omega_{*i}/\omega_{Dh}$; (iii) $\hat{\beta}_{ph} \equiv (\omega_A/S_o\omega_{Dh})\,\varepsilon_o^{\alpha}\beta_{ph}$, where $S_o \equiv r_s q'(r_s)$, the index $\alpha = 1$ or $3/2$ for ratios of parallel to perpendicular pressures $p_{\parallel}/p_{\perp h} \lesssim \varepsilon_o$ or ~ 1, respectively, and

$$\beta_{ph}(r_s) \equiv -\left[8\pi/B_p^2(r_s)\right]\int_o^{r_s} dr(r/r_s)^{(3/2)} d\left[(r/r_s)^{(3/2)-\alpha}\, p_{\perp h}\right]\Big/ dr \qquad (1)$$

is a profile dependent poloidal beta of the non-thermal ions; (iv) $\hat{\gamma}_R \equiv \gamma_R/\omega_{Dh}$, with $\gamma_R \equiv \varepsilon_\eta^{1/3}\omega_A$ the growth rate of the resistive internal kink mode and $\varepsilon_\eta \propto \eta$ the inverse magnetic Reynolds number.

Examples of stable regimes are given in Figs. 1 and 2. The stable domain in the $(\hat{\gamma}_{mhd}, \hat{\beta}_{ph})$ plane (Fig. 1) is weakly dependent on $\hat{\omega}_{*i}$ when $\hat{\omega}_{*i} << 1$. The portion of the marginal stability curve at low $\hat{\beta}_{ph}$ depends importantly on $\hat{\gamma}_R$ for $\hat{\omega}_{*i} \sim \hat{\gamma}_R$ (a value of $\hat{\gamma}_R = 2\hat{\omega}_{*i}$ is used in the figure) and approaches the solid-dotted curve for $\hat{\omega}_{*i} >> \hat{\gamma}_R$ ($\eta \to 0$). The stable domain is delimited by resistive internal kinks and low frequency fishbones [2] (with $\omega \sim \omega_{*i}$) at low $\hat{\beta}_{ph}$, by high frequency fishbones [2] (with $\omega \sim \omega_{Dh}$) at high $\hat{\beta}_{ph}$, and by a maximum bulk poloidal beta corresponding to $\hat{\gamma}_{mhd} \sim 0.5$. In Fig. 2 (with $\hat{\gamma}_R = 0$), the stable domain in the $(\hat{\omega}_{*i}, \hat{\beta}_{ph})$ plane becomes narrower as $\hat{\gamma}_{mhd}$ is raised, while the two fishbone regimes merge as $\hat{\omega}_{*i} \sim 1$.

The model assumes that the magnetic shear is finite in the $q \lesssim 1$ region and that the sawtooth crash is initiated by a resistive internal kink mode. The relevant dispersion relation is obtained to leading order in an ε_o-expansion. Resistive effects are treated according to the two-

fluid collisional model. Finally, details of the non-thermal ion distribution function affects the detailed shape of the stability boundary. These restrictions must be kept in mind when comparing the theoretical predictions with the experimental results.

Fig. 1

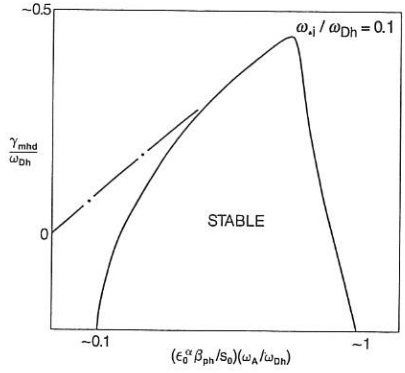

Fig. 2

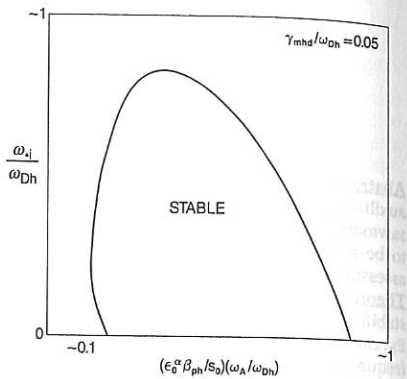

Quantitative comparison. An attempt has been made to evaluate the relevant stability parameters during sawtooth-free periods for comparison with the predicted stable domain. The major difficulty we face is the scarce knowledge of the non-thermal ion profiles, which cannot be measured directly. The available fast ion codes adopt a zero width approximation for the trapped-ion orbit which at high energies fails to give reliable non-thermal ion profiles. While work is in progress to improve the fast ion modelling, in this section we replace the profile-dependent fast-ion parameters with global parameters which are more readily accessible, i.e.: (i) β_{ph} in Eq. (1) is replaced by $<\beta_{ph}> \equiv (8\pi/B_p^2(r_s))(W_{\perp h}/V)$, where $W_{\perp h}$ is the fast ion perpendicular energy content and V the plasma volume; (ii) ω_{Dh} is replaced by $\omega_{Dh}^M \equiv cE_h(0)/(Z_h eBR_o r_s)$, where $E_h(0)$ is the non-thermal ion energy on axis. Clearly, this procedure is valid as long as discharges with similar deposition profiles are selected. Therefore, we restrict ourselves to on-axis ICRF heated discharges. Since $\omega_{*i}/\omega_{Dh} << 1$, the relevant analysis is performed in the (Γ,H) plane, where $\Gamma \equiv \gamma_{mhd}/\omega_{Dh}^M < \hat{\gamma}_{mhd}$ and $H \equiv \varepsilon_o < \beta_{ph} > \omega_A/(S_o\omega_{Dh}^M)$. Results are shown in Fig. 3. Solid circles correspond to discharges in a variety of conditions ($q_\psi = 4 \rightarrow 9$, $P_{RF} = 7 \rightarrow 10$ MW, $<n_e> = 2\text{-}3 \times 10^{13}cm^{-3}$) where sawtooth-free periods are most easily reproduced. To these we have added discharge #19719, marked by ▲, where a sawtooth-free period lasting $\tau_{free} \approx 1.3s$ was produced at the lowest rf power, $P_{RF} \sim 1.2$ MW, in a low-density plasma, $<n_e> \approx 1.3 \times 10^{13}cm^{-3}$, with $q_\psi \approx 4.6$; and discharge #20121, marked by ◊, corresponding to one of the longest sawtooth-free periods, $\tau_{free} \sim 5s$, discussed further in the next section. Error bars in Fig. 3 derive from a presumed 50% uncertainty in the minority concentration. An additional significant source of error is encountered in the evaluation of γ_{mhd}, which, being proportional to the MHD energy functional δW, depends on details of the thermal pressure and q profiles. The predicted stable domain is found to agree with the experimental data within a large uncertainty factor. Clearly, a more firm conclusion on the validity of the fast ion stabilisation model is hindered by sensitivity to parameters that are difficult to measure. An analysis of experimental trends appears more meaningful. This is performed in the next sections.

Dependence on the q = 1 radius. Referring to Fig. 1 and to the definitions of $\hat{\gamma}_{mhd}$ and $\hat{\beta}_{ph}$, the maximum stable poloidal betas are found to scale as $\beta_p^{max} \propto (r_s/a)^{-3/2}$ and $\beta_{ph}^{max} \propto (r_s/a)^{-(1+\alpha)}$.

Fig. 3

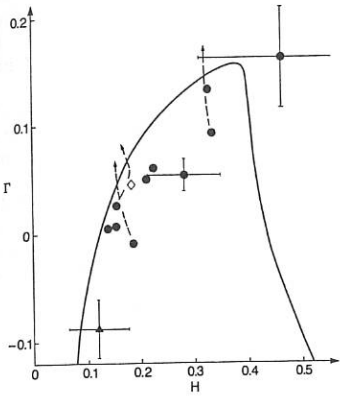

Fig. 4

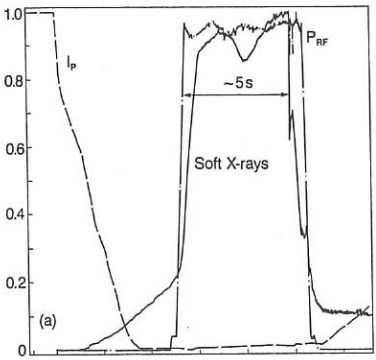

Fig. 5

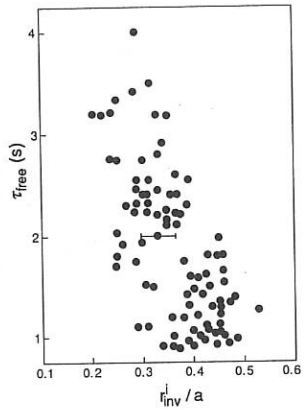

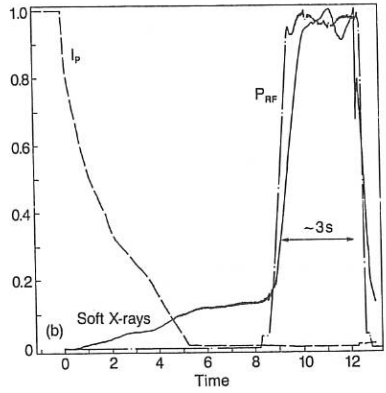

Therefore, a clear prediction of the fast ion stabilisation model is the increasing difficulty in suppressing sawteeth for increasing q = 1 radii. As an example, the three trajectories in Fig. 3 show how stability is lost as the q = 1 radius expands during the sawtooth-free period, from $r_s/a \approx 0.3$ to $r_s/a \approx 0.4$ for the upper trajectory, and from 0.3 - 0.4 to 0.5 for the two lower ones.

Experimentally, the following results are found: (i) so far, the maximum observed inversion radius of the crash terminating the sawtooth-free period is $(r_{inv}^{max}/a) \lesssim 0.6$; (ii) it is more difficult to suppress sawteeth at high currents ($I_p \geq 5$MA, $q_\psi < 4$), unless the rf heating is applied during the current ramp, when r_s/a is still small; in these cases the sawtooth-free period extends into the flat-top and is terminated by a crash with final inversion radius $(r^f_{inv}/a) \sim 0.5$; (iii) fast current ramping at constant plasma volume and early rf switch-on is one recipe to produce long sawtooth-free periods with $\tau_{free} \sim 5$s. An example of this, discharge #20121 in Fig. 4a (with $I_p = 3$ MA, $q_\psi = 4.6$ and $P_{RF} = 7.5$ MW), shows a current ramp with 1 MA/s and an rf switch-on time early on the flat-top, to be compared with a discharge with similar parameters, but with a slower ramp and later rf switch-on time, producing a sawtooth-free period of 3s (Fig. 4b); (iv) considering on-

axis rf heating during the flat top, and sawtooth-free periods terminating while the rf power is still on, the largest values of τ_{free} are obtained for small inversion radii, r^i_{inv}, of the last sawtooth crash before stabilisation, as shown in Fig. 5 for a variety of discharges with $I_p = 2.4 \rightarrow 3$ MA and $P_{RF} = 3 \rightarrow 9$ MW. An additional, roughly linear, dependence of τ_{free} on $W_{\perp h}$ is observed, possibly saturating at higher values of $W_{\perp h}$.

These results suggest that the sawtooth-free period is determined mainly by the time of expansion of the q = 1 radius from $r_s \approx r^i_{inv}$ to $r_s \approx r^f_{inv}$. This time should be a fraction of the resistive diffusion time, determined by the degree of current penetration at the rf switch-on time (which affects r^i_{inv}), and by the thermal and fast-ion energy contents (which affect r^f_{inv}).

ICRH resonance position scan. According to Eq. (1), higher values of β_{ph} are attained when the fast ion pressure is peaked on the magnetic axis. This is the case when rf heating is applied on axis. No sawtooth suppression can be obtained when β_{ph} is negative, i.e. when the rf resonance layer lies outside the q = 1 surface. This prediction has been confirmed in a recent experimental campaign where the position of the rf resonance layer has been scanned. Results are shown in Fig. 6.

Fig. 6

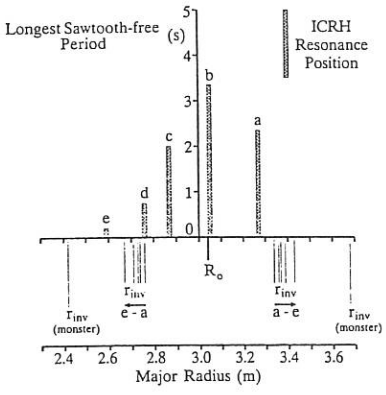

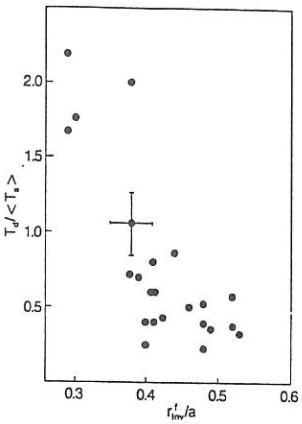

Fig 7

RF switch-off experiments. Possibly the best indication of the role of non-thermal ions in suppressing sawteeth is provided by ICRH switch-off experiments. In these experiments, the stable period is terminated by a sudden interruption of the applied rf field. A time delay, τ_d, is observed between the rf switch-off time and the collapse of the central electron temperature. This delay is comparable with the average fast ion slowing down time within the q = 1 volume, $<\tau_s>$, therefore suggesting that the loss of these ions is the dominant destabilising effect.

Experimental data in the $(\tau_d/<\tau_s>, r^f_{inv})$ plane are plotted in Fig. 7 for a variety of discharges, with $<\tau_s> \sim 0.07 \rightarrow 0.7$ s. Larger values of $\tau_d/<\tau_s>$ are obtained at lower values of r^f_{inv}, possibly indicating that better stability is obtained for lower values of r_s/a.

Neutral beams. Sawteeth in JET are more difficult to suppress with NBI heating alone. Only a limited number of cases have been observed, with a maximum $\tau_{free} \approx 1$ s. On JET, most NBI power is injected at an energy per neutral of 80 keV. The average fast ion energy is around 40 keV. Typically, the ratio of bulk diamagnetic to fast ion precession frequency is $\omega_{*i}/\omega_{Dh} \approx (T_i(r_s)/<E_h>)(R_o/r_p) \sim 1$, with $r_p = |d\ell n p_i/dr|^{-1}_{r_s}$ affected by a large error bar. Therefore one necessary condition for fast ion stabilisation of m = 1 modes may marginally be satisfied (see Fig. 2). An important role played by the beam-driven currents cannot be excluded.

References. [1] D.J. Campbell et al., Phys. Rev. Lett. 60, 2148 (1988). [2] B. Coppi, S. Migliuolo, F. Pegoraro and F. Porcelli, Phys. Rev. Lett. 63, 2733 (1989).

JET NEUTRON EMISSION PROFILES AND FAST ION REDISTRIBUTION FROM SAWTEETH

F B Marcus, J M Adams*, A Cheetham, S Conroy, W G F Core, O N Jarvis, M J Loughlin, M Olsson, G Sadler, P Smeulders, P van Belle, N Watkins*

JET Joint Undertaking, Abingdon, Oxfordshire OX14 3EA, United Kingdom
*AEA Technology, Harwell Laboratory, Didcot, OX11 ORA, United Kingdom

ABSTRACT

Measurements from the JET neutron profile monitor are analysed tomographically to deduce the spatial distribution of emission during NBI heating both before and after sawteeth. The axial neutron emissivity collapses much more than the global emission after a sawtooth. The change is due to fast ion redistribution during beam heating and a decrease in beam-beam emissivity.

INSTRUMENTAL DETAILS AND DATA ANALYSIS METHOD

The neutron emission profile monitor has been described in [1]. The analysis uses 8 vertical channels and 10 horizontal channels. These have a viewing width in the plasma of 0.1 m for the central channels and 0.2 m for the edge channels. The channel to channel systematic error is 10%. The time resolution is limited by the requirement of a few hundred counts in the central channels to obtain better than 10% statistical errors. A global neutron rate of $10^{16} s^{-1}$ requires 10 ms averaging.

To obtain a 2-D emission profile, constrained tomography [2] is used, employing near-elliptic contours described by a 4-term Fourier expansion. The amount of smoothing is chosen so that the deduced emissivity profile gives line-integrals which are within one standard deviation of the channel measurements. The lines-of-sight are assumed to be of zero width. Given these limitations in raw data and analysis, the amount of fine structure detail obtainable is limited. Nevertheless, comparisons with model profiles including 10% random errors show that peaked, flat, hollow, double humped, and outwardly shifted profiles can be distinguished. Global emission is calculated by integrating over the profile and independently measured by absolutely calibrated fission chambers. Absolute yields from the two diagnostics agree within their combined experimental errors of about 20%.

NEUTRON EMISSION REDISTRIBUTION FROM SAWTEETH

To obtain the best time resolution, a sawtooth with a high ($10^{16} s^{-1}$) neutron emission rate is examined in shot 20981 at 10.75 s. The discharge is a double null H-mode plasma with NBI heating by D beams into a D plasma. The global neutron emission measured by fission chambers falls in about 0.4 ms from $9.1 \times 10^{15} s^{-1}$ to $7.5 \times 10^{15} s^{-1}$ (82% of before). The emission recovers to the pre-sawtooth value after 50 ms, and then continues upwards to a peak of $3.5 \times 10^{16} s^{-1}$ at 11.4 s. At 70 ms

before the sawtooth, the electron density and temperature profiles are approximately flat over 1.0 m at the midplane with values of 1.6×10^{19} m^{-3} and 5.0 keV. After the crash, the temperature profile widens and drops slightly and the density remains flat. The soft x-ray emissivity broadens and drops to about 1/2 the peak emissivity.

The line-integral data from the profile monitor shows that the neutron emission redistributes itself within the sampling time of 1 ms. The profiles of line-integral emission in the horizontal and vertical camera channels are strongly peaked axially until the sawtooth occurs. After the crash, the profile is relatively flat with a local peak on the central channel. The profile of neutron emission after the sawtooth evolves slowly for 100-200 ms and becomes clearly peaked again only after about 300 ms. This is a commonly seen feature, where the neutron emission stays broad long after the sawtooth crash.

The neutron emissivity profiles from tomography are shown for shot 20981 in Fig. 1 just before (10.738-10.748 s) and in Fig. 2 just after (10.756-10.766 s) the sawtooth. The neutron emissivity before is highly peaked on axis at 1.9×10^{15} m^{-3} s^{-1}. The emission FWHM is 0.36 m at the midplane. Emission contours are nearly circular on axis and elliptical further out. The profile after the crash is much flatter and broader with a FWHM of 1.2 m, although the global emission has fallen by only 1/5. The poloidally-averaged emissivity inside this region varies within $2\text{-}3 \times 10^{14}$ m^{-3} s^{-1}. This range is less than 1/6 of the pre-sawtooth values. The line-integrals from these profiles are within 5% of measurements for most channels and 12% on the central channel. The profile can be characterized as hollow plus an axial peak. For comparison, a flat emissivity profile requires errors of up to 30% on several channels.

FAST ION AND THERMAL CONTRIBUTIONS TO NEUTRON EMISSION

An improved analytic Fokker-Planck formulation, including the velocity space diffusion effects of finite ion temperature, is used to calculate the expected fraction of beam-beam (bb), beam-plasma (bp) and thermal (t) contributions to axial neutron emissivity, based on measured plasma parameters and calculated beam deposition profiles. The characteristic beam energy is 80 keV. The maximum axial emissivity during shot 20981 at 11.4 s is composed of bb-1/6, bp-1/2, t-1/3, with a beam slowing-down time of 130 ms.

Analysing the data for an interval immediately preceeding the sawtooth at 10.75 s, the slowing down time is 300 ms. The NBI source rate on axis is 10^{20} m^{-3} s^{-1}, injection has lasted only 260 ms, and the deuteron density is about 1.7×10^{19} m^{-3}. The central density is therefore mostly composed of fast ions which have not had time to fully thermalize. The axial neutron emissivity can be accounted for by bb fusion reactions only, using a reaction rate allowing for the beam ions being only partially thermalized. Moving off axis, the fast ion density decreases and the thermal ion fraction increases. The bp reactions dominate over bb, while t reactions are at the 1% level. This general picture is supported by TRANSP simulations [3], where bb dominates on axis, but represents only 1/3 of the global neutron emission.

After the sawtooth, the drop of only 1/5 in the total neutron

emission is consistent with a redistribution of fast ions within the plasma. The bb emission (previously representing 1/3 of the emission) is proportional to the square of the fast ion density and drops with increased volume. The bp emission is approximately unchanged since most fast ions are in a region with similar electron density. Fast ions previously on axis, if mixed with thermal ions, would give additional bp reactions, but with a lower reaction rate.

The remaining neutron emission is therefore mostly bp after the sawtooth, and the profile evolves slowly on the same time scale as beam slowing down. At the same time, newly injected beam ions contribute to the axial neutron emission. Previous JET results on electron temperature sawteeth [4] indicate that a hot core is expelled and expands around a cooler region moved to the center. Observations of redistribution of fast ions during sawteeth have also been obtained [5]. Fast ions conforming to this model would give a neutron emission profile similar to that shown in Fig. 2 with the addition of an axial contribution from ions injected after the sawtooth.

SAWTEETH IN HIGH BETA DISCHARGES

In the 5.5% toroidal beta shot 20881, large sawteeth are observed which occur at the beta limit. The discharge is heated by a deuterium beam into a hydrogen plasma, so the axial neutron emissivity before a sawtooth at 14.36 s is only $5 \times 10^{13} m^{-3} s^{-1}$. The global emission is $5 \times 10^{14} s^{-1}$ which requires an integration time of 100 ms, about equal to the beam slowing-down time of 80 ms. The axial contributions are bb-1/2 and bp-1/2. A ratio of deuteron to electron density of only 1/6 is required for consistency with the total emissivity.

Similarly to shot 20981, the sawtooth results in a fall of the global emission to 2/3 of its previous value. The emissivity profile broadens, with axial emissivity only 1/3 of the pre-crash value. The fall is consistent with a strong drop in the bb component, and an axial increase from newly injected ions.

DISCUSSION

Discharges in JET have varying heating methods, density and temperature profiles, and ratios of bb, bp, and t contributions to neutron emission (with different functional dependences). This results in a wide range of observed ratios of signal amplitudes, before and after sawtooth crashes, due to global neutron emission relative to those from other diagnostics. In discharges dominated by bp emission, large electron sawteeth can be accompanied by almost no change in global neutron emission, but a major change in radial distribution of emissivity. In t-dominated plasmas with sawteeth, as in ohmic or RF heated discharges, quite large sawteeth may be observed in the global neutron emission with even larger falls in central emissivity.

Significant changes in neutron emission profiles can occur in the presence of high density and NBI heating. High density broadens the beam deposition and emission profiles. At the highest densities in H-modes, the emissivity profile shifts outwards in major radius, consistent with injected ions trapped in banana orbits at large major radius [6]. This effect is also observed in pellet fuelled discharges,

where large axial densities suppress beam penetration.

In conclusion, different types of neutron emission source and profile have been observed, which aid in the understanding of: fast ion distributions from beam injection; fast and thermal ion redistribution; ion thermalization profiles due to sawteeth; optimization of neutron yield; and transport analysis with heating from redistributed fast ions.

REFERENCES AND ACKNOWLEDGEMENTS

[1] J M Adams et al, Proc. 16th EPS Conf. Venice, 1989, 13B I, 63.
[2] R S Granetz and P Smeulders, Nuclear Fusion 28 (1988) 457.
[3] B Balet et al, APS Conf. Anaheim 1989, JET Preprint JET-P(89)80.
[4] D J Campbell et al, Plasma Physics and Controlled Nuclear Fusion 1988 (Proc. 12th Int. Conf. Nice), Vol. 1, 377.
[5] G Sadler et al, IAEA Conf. Kiev 1989, JET Preprint JET-P(89)77.
[6] M J Loughlin et al, Proc. 16th EPS Conf. Venice, 1989, 13B I, 83.

We acknowledge and thank D Campbell, R Gill, M F F Nave, P. Stott, and P Stubberfield for data, programs, and useful discussions.

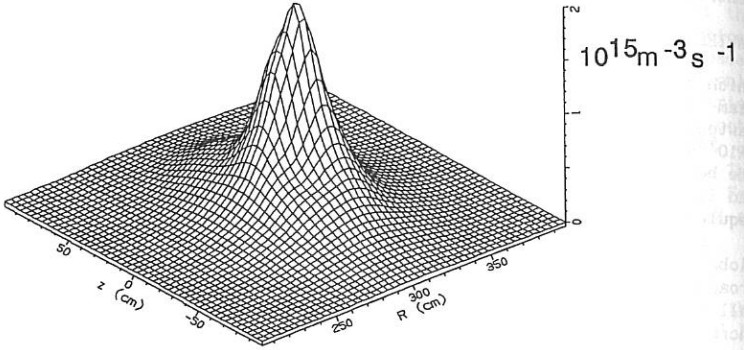

Fig 1 JET Shot 20981 Neutron emissivity before sawtooth, 10.738-10.748 s

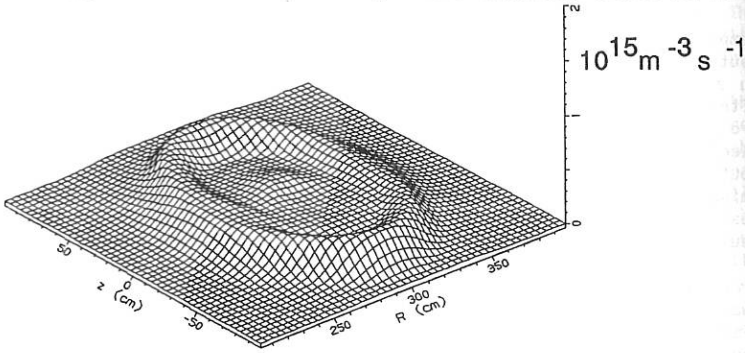

Fig 2 JET Shot 20981 Neutron emissivity after sawtooth, 10.756-10.766 s

THE DETAILED TOPOLOGY OF THE m = 1 INSTABILITY IN THE JET SAWTOOTH COLLAPSE

S W Wolfe, A W Edwards, R D Gill, M F F Nave†, J A Wesson

JET Joint Undertaking, Abingdon, Oxon. OX14 3EA UK.
†Laboratorio Nacional de Engenharia e Tecnologia Industrial, Sacavem, Portugal.

INTRODUCTION - The sawtooth collapse in tokamaks is generally observed to be associated with the growth of an m = 1 instability and a rearrangement of the core plasma. In JET discharges, this occurs very rapidly and often without a growing precursor /1/. Accurate measurements of the details of the rapidly evolving topology during the collapse are necessary to identify the precise mechanism, and tomographic reconstruction of the soft x-ray emissivity profile has been used routinely for this. The profiles observed during the JET sawtooth collapse have been inconsistent with Kadomtsev's theory /2/, prompting much speculation on the correctness of the theory /3,4/ and the reliability of the data analysis /5/. To aid in both questions, the soft x-ray measurements during the collapse have been simulated, using two different theories as guides. In this way, the limitations of the tomographic method were investigated under controlled conditions.

TOPOLOGY - The soft x-ray detector system /6/ consists of 100 surface-barrier diodes arranged in two "pinhole" cameras mounted on horizontal and vertical ports at the same toroidal location. They measure the integrated emission ("brightness") along lines of sight viewing the plasma in two fan-like arrangements. The chords are distributed across the plasma cross-section over a range of radii and angles, but their finite spacing and restricted orientation limits the maximum resolution.

The method used to tomographically reconstruct the two-dimensional emissivity profile from the measured brightness function /7/ involves separating the radial and angular dependence of the emissivity. The angular part is expressed as a sum over Fourier harmonics $\cos(m\theta)$ and $\sin(m\theta)$, and the radial function is expanded as a sum over Zernicke polynomials, a complete orthogonal set. The spatial resolution is determined by the numbers of Fourier and radial harmonics chosen. These numbers in turn are limited by considerations of numerical stability and geometry. For radial resolution, the chord spacing (7 cm on the midplane) sets the optimum number of radial harmonics to be about 12. In poloidal angle, since there are two cameras, only four Fourier harmonics may be found, here chosen to be m = 0, $\cos\theta$, $\sin\theta$, and $\cos(2\theta)$ (but not $\sin(2\theta)$), where θ is measured from the horizontal. This means that in this study, only plasma perturbations with harmonic content no larger than m = 2 may be unambiguously detected.

In the simulation, emissivity profiles are chosen which are consistent with present theories of the sawtooth collapse, and integrals are calculated along detector lines of sight to obtain brightness data. These are then inverted tomographically, and the reconstructed profiles compared with the original. Two models of the sawtooth collapse, Kadomtsev /2/ and quasi-interchange /4/, were used as guides when constructing input profiles. In Kadomtsev's theory, total reconnection of helical flux

and magnetic island growth occur in the vicinity of the q = 1 surface. The plasma core becomes displaced rigidly in the process. This behaviour is modelled simply by shifting the central part of an unperturbed profile (Fig. 1a). The flat region represents the cooler magnetic island. The quasi-interchange theory involves plasma convection, largely confined to the region inside the q = 1 radius. Two convective cells lead to the core being displaced and deformed into a "hot crescent" surrounding a "bubble" of cooler plasma which has moved in to take its place. Figure 1b shows slices through the initial Gaussian profile and a typical displaced one. Both types of profiles conserve plasma energy during the displacement. Note that the models are not rigorous physics simulations, but are adequate representations of predicted plasma behaviour.

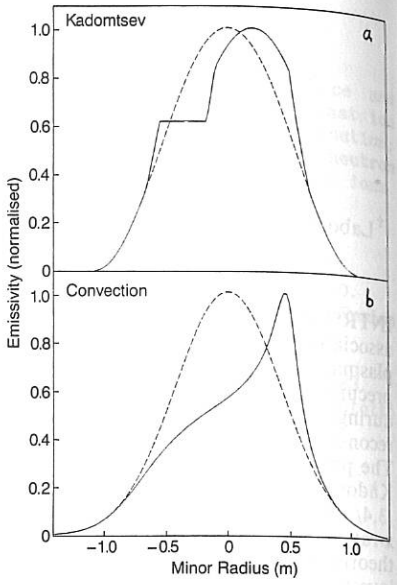

Figure 1. *Typical emissivity profiles along a chord for a) Kadomtsev and b) convection models. The dashed lines are the unperturbed profiles.*

Figure 2 shows the reconstruction of a horizontal perturbation extending to about half the plasma minor radius. This is a typical magnitude observed in sawtooth collapses with additional heating /1/ or after a period of sawtooth stabilisation ("monster" crashes /8/). The contour plots show that the essential features of each case are reproduced faithfully. The sharp features of both cases are smoothed out, as expected, due to the finite radial resolution. But the characteristics which distinguish one profile from the other remain clear.

One may compare these pictures with tomographic reconstructions of JET soft x-ray data. Figure 3 shows a reconstruction done during a monster crash at a time when the core displacement is close to its maximum. Its magnitude is 0.45 m, and the peak emissivity has fallen by <20%, both measured with respect to conditions immediately before the crash. The similarity to Figure 2b is striking. The convection model is clearly a better description of the plasma behaviour in this case.

To investigate the limitations of the tomography more fully, the parameters of the input profile were varied systematically. It was found that the quality of the reconstruction depends sensitively on the angle of the displacement θ_d, the size of the region where the perturbation is confined, and the magnitude of the displacement. Figure 4 shows reconstructions for a case where the displacement is at 45 degrees. (For the Kadomtsev case, the displacement is almost twice as large as that in Figure 2). The image of the rigidly displaced core in the Kadomtsev case becomes "smeared" in angle, and is not readily distinguishable from the convective plasma flow. This loss of angular resolution is not surprising since only the cosine part of the m = 2 harmonic is available. One would expect that as the displacement angle approached values where $\cos(2\theta_d) = 0$, some resolution would be lost and the fitting would deteriorate. The larger displacement is also believed to exacerbate the effect /5/.

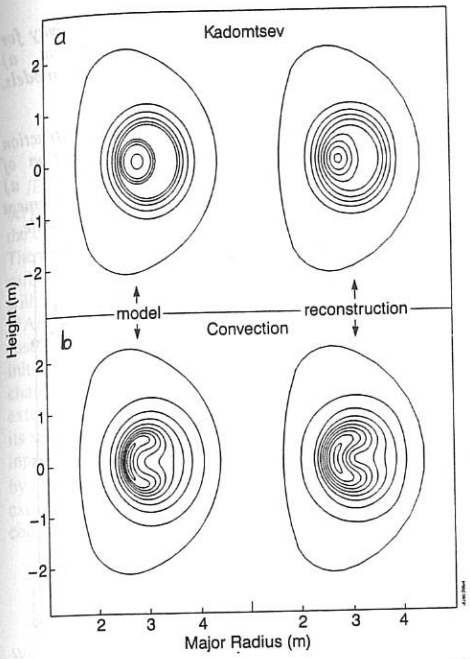

Figure 2. *Contour plots of emissivity for horizontal displacement in a) Kadomtsev and b) convection models. Contour levels are 6% to 97% of maximum.*

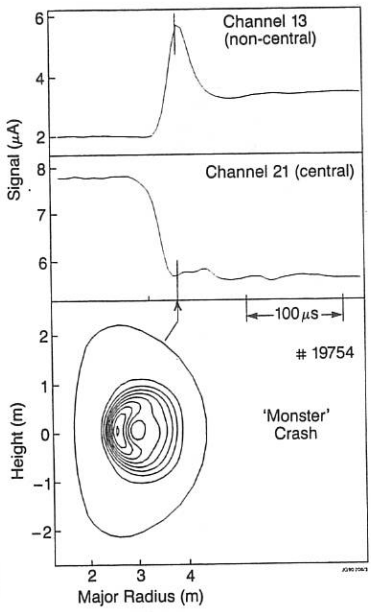

Figure 3. *Time evolution of signals from detectors viewing along chords intersecting the midplane at $R = 3.08$ m (central) and $R = 2.49$ m (non-central); and reconstructed emissivity at the time indicated.*

The global error in the tomographic inversion was evaluated by taking the differences between the reconstructed and input emissivities at each point on a suitable grid. These were squared and averaged to obtain an rms error. For the Kadomtsev case, this quantity is plotted in Figure 5 as a function of displacement angle in the model profile. For a particular size of displacement, relative minima occur for horizontal and vertical angles, where, not surprisingly, $\cos(2\theta_d)$ is a maximum. (There is symmetry with respect to all four quadrants). The largest error does not occur at an angle of 45 degrees, as expected, but at about 60 degrees. This may be related to the plasma elongation (taken to be 1.2 here). Another factor may be the shift (up to 10 degrees) in the angle of the peak in the reconstructed emissivity with respect to that of the input profile (see Fig. 4). The error is in the range of 1% to 10% for reconstructions of both Kadomtsev and convective profiles.

This quantity, being global, does not necessarily give information on those features which distinguish the two profile types. For example, the error decreases with the size of the perturbation, but if this is confined to a region of less than about 25% of the minor radius, both profile types become indistinguishable due to the limited radial resolution and the averaging effect of the measurement.

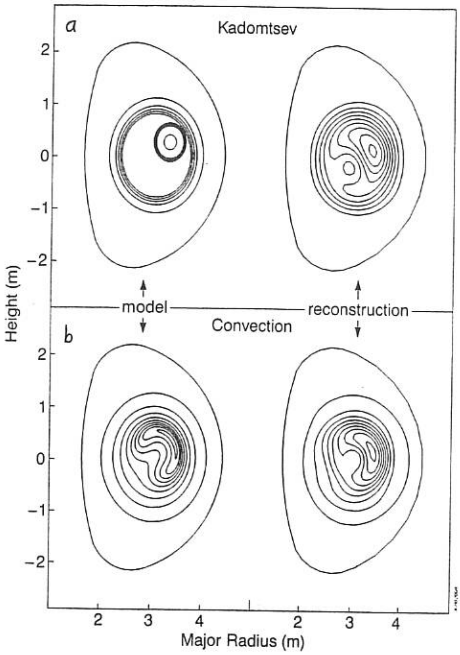

Figure 4. *Contour plots of emissivity for displacement at 45 degrees in a) Kadomtsev and b) convection models. Contour levels as in Fig. 2.*

Figure 5. *rms error in the reconstruction of Kadomtsev profiles as a function of displacement angle and size: a) displacement as in Fig. 4a; b) displacement as in Fig. 2a; and c) unperturbed profile.*

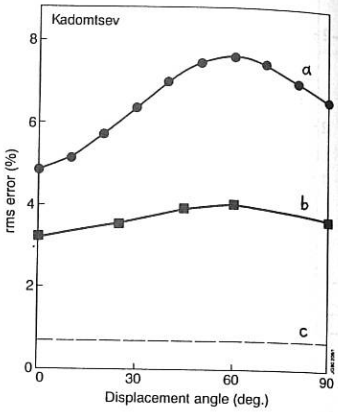

SUMMARY AND CONCLUSION - The topology of the sawtooth collapse in JET plasmas has been investigated in detail by reconstructing the soft x-ray emissivity profile. The tomography algorithm used has been assessed by simulating the brightness measurements from two types of model profiles based on Kadomtsev's theory and plasma convection. Core displacements were varied over a range of sizes and angles.

From this work it can be concluded that sawtooth crashes due to Kadomtsev and convective models can be clearly distinguished when the amplitude of the displacement is greater than about 25% of the plasma minor radius and when it occurs closer than about 20 degrees from the horizontal or vertical planes. This investigation also confirms very strongly that the JET sawtooth collapse follows a convective flow pattern as was reported in analyses of earlier JET data /1,4/.

REFERENCES

/1/ A W Edwards et al, Phys. Rev. Lett. 57 (1986) 210.
/2/ B B Kadomtsev, Sov. J. Plasma Phys. 1 (1975) 389.
/3/ M A Dubois and A Samain, Nucl. Fusion 20 (1980) 1101.
/4/ J A Wesson et al, in Plasma Physics and Controlled Nuclear Fusion Research 1986 (Proc. 11th Int. Conf. Kyoto, 1986), Vol 1, IAEA, Vienna (1987) 3.
/5/ C Janicki, R Decoste, and C Simm, Phys. Rev. Lett. 62 (1989) 3038.
/6/ A W Edwards et al, Rev. Sci. Instrum. 57 (1986) 2142.
/7/ R S Granetz and P Smeulders, Nucl. Fusion 28 (1988) 457.
/8/ D J Campbell et al, in Proc. IAEA Kyoto Conf. (see /4/) p 433.

DENSITY LIMITS IN JET WITH BERYLLIUM

C.G.Lowry , D.J.Campbell, N.Gottardi, K.Lawson, G.Vlases

JET Joint Undertaking, Abingdon, Oxon. OX11 3EA, England

ABSTRACT

JET has now been operated with an evaporated layer of beryllium on carbon and with beryllium as a limiter material. A principal objective of the experiment was to investigate the the effect of beryllium as a first wall material would have on the operational space of JET. The results of this investigation are presented and contrasted with data obtained during the all carbon phase. The gettered phase showed no increase in the gas fuelled density limit except with RF heating. The limit had, however changed in character, with the formation of a MARFE preventing any further increase in density. There was a disruption in only a few cases. In the beryllium limiter phase chlorine was a major contributor to the radiated power, initially radiating 70 % of the total radiated power. In these circumstances the density limit changed little from the gettered phase. However, as the chlorine diminished the limit was extended substantially beyond the level obtained with gettering alone, while still maintaining its soft character. The density at which the soft limit occured is shown to be a function of input power and plasma contamination with a weak dependence on q, and is described well by a scaling law based on a radiation model [1,2] . Helium and pellet fuelled discharges have exceeded the deuterium gas fuelled limits, but we present evidence showing an overall consistency when the edge density is considered.

THE LIMIT CHARACTERISTICS

The density limit in the carbon machine has been described in some detail in a paper by Wesson et al [3]. In the case of the carbon machine with an evaporated layer of beryllium the radiation is dominated by carbon and is similar to the pure carbon case with initially about 30 % of the input power being radiated. As the density is increased the radiation increases in a similar fashion to the all carbon case. Close to the density limit there is a break in the relation between radiation and density (figure 1) which can be identified as the formation of the MARFE. The difference between the carbon and evaporated cases is that in the evaporated case the radiation did not normally symmetrise and persisted at 100 % radiation, usually without disrupting, until the current was ramped down or any additional heating was switched off, which did lead to a disruption. The beryllium belt limiter was different again, although the situation was confused by the presence of chlorine. At moderate densities the radiated fraction was around 20 % and dominated by beryllium. However, as the density was increased the contribution due to chlorine became dominant. The radiation was a smoother function of the density (figure 1) although a break could be seen in some cases. The formation of the MARFE was associated with the break in the radiation but it was not clear which was cause and which was effect. As the radiation reached 100 % the line integrated density began to drop back to the pre-MARFE level. As long as gas was fed into the torus this cycle repeated itself, but as the edge density racheted up the frequency of the instability increased and the drop in radiation was reduced such that the MARFE was not quenched (figure 2). Measurements using Langmuir probes situated on the limiter surface show that the particle flux and electron temperature at the limiter fall dramatically as the MARFE forms [4]. The internal inductance of the plasma during the MARFE generally did not increase, indicating that the plasma was not contracting significantly. This is consistent with the absence of strong MHD fluctuations and disruptions in most cases.

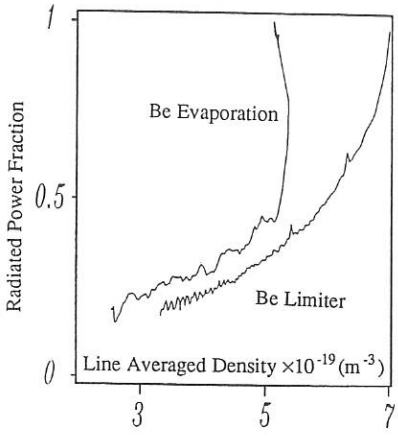

Figure 1. The radiated power fraction as a function of the line averaged density for typical density limit pulses of both beryllium phases.

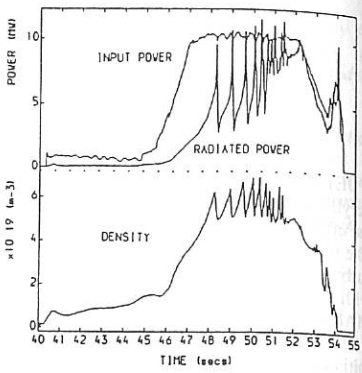

Figure 2. The density and radiated power oscillations during a typical beryllium limiter density limit discharge.

GAS FUELLING VERSUS PELLET FUELLING

To allow comparison with well known parameters of other machines the start of the MARFES have been plotted on a Hugill diagram (figure 3). Several features are apparent. First one can see that the MARFES of the evaporation phase occured at similar densities to disruptions with a purely carbon machine, the one exception being the case with ICRH where in some cases the limit was extended to that with comparable NBI. The second feature is the dramatic increase in the MARFING limit when the beryllium limiters were introduced; the highest densities obtained were over double the density at disruptions in the carbon machine.

As in the carbon phase, the line averaged density could be substantially increased with pellet fuelling in the evaporation phase, providing that the pellet penetrates deeply. The limit for both pellet and gas fuelled discharges can be unified for the evaporation phase (where the impurity specie was always carbon) by considering the edge density and the input power (figure 4). A small q dependance can be seen but the scatter in the data is too great to allow a confident scaling.

SCALING

There are several models for density limits existing in the literature. For the all carbon JET phases, the disruptive density limit was discussed in detail by Wesson et al [3]. We have examined several models, including edge radiation [1,2], edge thermal instability [6,7], shielding of incoming neutrals, and the Greenwald scaling [5]. Of those, the edge radiation model provides the best fit to the entire (Be gettering plus Be limiter) data base. Following a model used earlier for JET [1,2] one assumes that the radiated power is due to a single species, C in the evaporation phase and Cl or Ni in the Be limiter phase, and that the radiation comes from a region between the $q_\psi = 2$ surface and the plasma edge. The density at which the MARFE occurs is then given by

$$n_e = C_z \frac{P_{TOT}^{\frac{1}{2}}}{(Z_{eff}-1)^{\frac{1}{2}}} \left\{ 1-\frac{4}{3q_c} \right\}^{-\frac{1}{4}} \quad \text{where} \quad C_z = \frac{1}{\sqrt{2}\pi} \left\{ \frac{z(z-1)}{L_z} \right\}^{\frac{1}{2}} \frac{1}{(Rab)^{\frac{1}{2}}},$$

n_e is the density within the radiating region and L_z is the cooling rate (taken from a coronal model). Due to a lack of diagnostics in the plasma edge figure 5 shows this function plotted with $C_z = 1$ against the line averaged density, this is appropriate for the flat density profiles of these gas fuelled cases, the fit is quite good for both phases, over a range of Z_{eff} from over 3 to 1.2. When one restricts the scaling to pulses with $Z_{eff}<1.5$, the scaling given by a thermal instability model [6] also fits quite well. The power independant scaling [5] suggested for clean discharges does not fit the data.

CONCLUSIONS

The density limit in the evaporated beryllium and beryllium limiter phases of JET was different in character from that of the carbon phase. Although the limit occured in the same region of the operational space it did not lead to a contraction of the current profile and there was generally no disruption. The limit in both the beryllium evaporation and the beryllium limiter phases was characterised by the appearance of a MARFE. The MARFE either persisted until there was a reduction of the input power or lead to a pump-out returning the discharge to a stable region of the operational space. The density limit was shown to depend on the input power and the impurity concentration much as one would expect from a thermal instability. Since the dominant impurity specie did not change from the carbon to the evaporated phases it was not surprising that the density limit was not increased in this phase, although it does indicate that oxygen was not a significant radiator at high densities in the carbon phase. The situation for the beryllium limiter was confused by high levels of chlorine, but after machine conditioning in which the level of chlorine was reduced the previous density limit was substantially exceeded, although the radiation was still dominated by chlorine. The critical parameters for the formation of a density limit MARFE were shown to be located at the edge. Using both edge density and edge electron temperature it was possible to resolve the differences between gas and pellet fuelled discharges.

REFERENCES

1. Schuller et al, 12th European Conference on Controlled Fusion and Plasma Physics, Budapest 1985, part1 p151.
2. Gibson, NUCLEAR FUSION, Vol 16, No.3 546 (1976).
3. Wesson et al, NUCLEAR FUSION, Vol 29, No.4 (1986).
4. Clement et al, This conference.
5. Greenwald, NUCLEAR FUSION, Vol 28 2199 (1988).
6. K.Borrass, private comunication.
7. Stringer, 12th European Conference on Controlled Fusion and Plasma Physics, Budapest 1985, part1 p86.

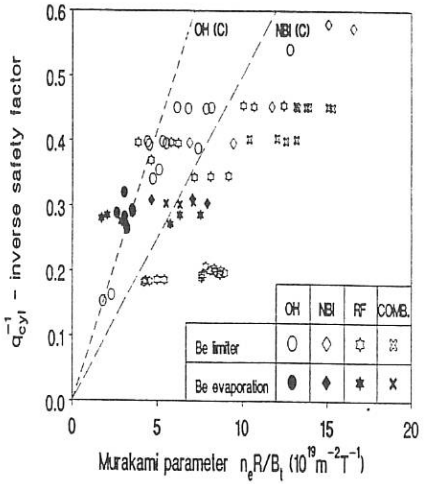

Figure 3. Acomparison of carbon disruptions (lines), Be evaporation (solid) and Be limiter (open) MARFES.

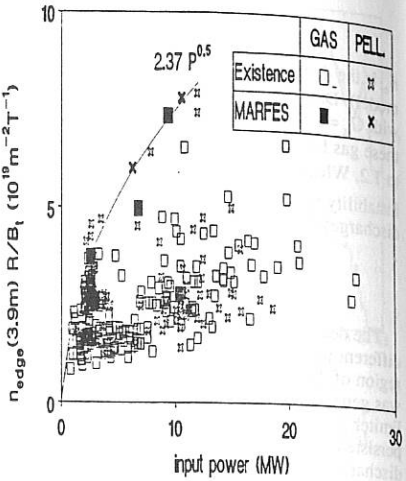

Figure 4. The normalised edge density versus input power showing all MARFES to occur along the edge of a common region of existence.

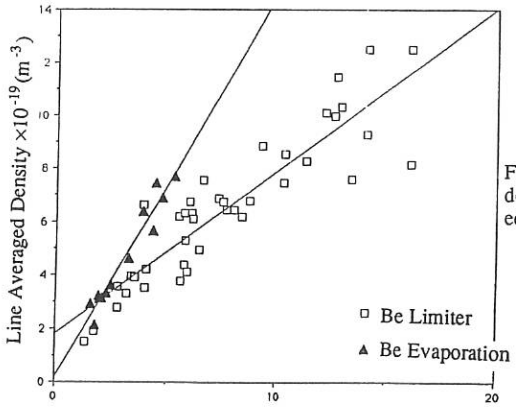

Figure 5. The measured line averaged density plotted versus the scaling of the edge radiation model.

$$\frac{P_{TOT}^{\frac{1}{2}}}{(Z_{eff}-1)^{\frac{1}{2}}}\left\{1-\frac{4}{3q_c}\right\}^{-\frac{1}{2}} \quad (MW)^{1/2}$$

FARADAY ROTATION MEASUREMENTS ON JET, AND THE CHANGE IN THE SAFETY FACTOR PROFILE DURING A SAWTOOTH COLLAPSE

J O'Rourke, E Lazzaro

JET Joint Undertaking, Abingdon OX14 3EA, UK

Introduction

Abel-inversion of Faraday rotation measurements on JET has shown that in the current flat-top of sawtoothing discharges the axial safety factor, q_0, remains significantly below unity (0.75±0.15) throughout the sawtooth period [1]. In this paper we address two limitations of the Abel-inversion technique, namely the dependence of the results on the assumed flux surface geometry (especially the elongation of the flux surfaces near the magnetic axis, κ_0) and their lack of sensitivity to small changes in the poloidal magnetic field. Assumptions about the flux surface geometry have been verified by comparing Faraday rotation measurements along nearly orthogonal chords, and by a self-consistent identification of the plasma equilibrium. The sensitivity to small changes in the poloidal field, such as those which occur during sawtooth instabilities, has been increased by Abel-inverting the changes in the Faraday rotation signals rather than the signals themselves.

Measurements Along a Lateral Chord

Faraday rotation measurements on the 6 vertical chords of the JET polarimeter are affected similarly by variations in the elongation of the flux surfaces, and comparisons between different vertical measurements do not reveal inconsistencies in the assumed elongation. For this reason, a lateral chord of the interferometer, viewing the plasma at 20° to the horizontal, has been commissioned to make polarimetric measurements also. This chord makes use of a mirror mounted on the inner wall of the vacuum vessel, and, in order to preserve the Mach-Zehnder configuration, has entrance and exit windows which are displaced toroidally (symmetrically about the plane which contains the torus axis and the mirror). The linearly polarised radiation propagating along this chord experiences Faraday rotation due to both the toroidal and poloidal magnetic field components. However, because of the 180° phase shift introduced by the reflection at the inner wall, the Faraday rotation due to the toroidal field on the inward path is cancelled by that on the outward path, while the contributions due to the poloidal field add.

To verify whether a given flux surface geometry is consistent with the Faraday rotation measurements, the poloidal magnetic field is computed in this geometry by Abel-inversion of the vertical channels only. The expected Faraday angle for the lateral chord is computed using this field, and compared with the measured angle. If these disagree by more than the error bars of the measurement (5%), the assumed geometry is inconsistent with the Faraday rotation measurements.

In this manner it is found that κ_0 can be constrained to within ±4% and is in agreement with our previous assumptions about the flux surface geometry.

Self-Consistent Equilibrium Identification

In the Abel-inversion procedure, the equilibrium flux surfaces used in the deconvolution of the (chordal) Faraday rotation measurements must be specified a priori. Therefore the poloidal magnetic field distribution which is deduced is not necessarily consistent with the assumed equilibrium. In order to ensure a self-consistent determination of the poloidal magnetic field [2], we seek the plasma equilibrium which best fits:

a) the tangential magnetic field, B_τ, measured by 18 pick-up coils at the vacuum vessel,
b) the Faraday rotation angles, α, along 6 vertical chords, and
c) the line-integrated electron densities, N, along the same chords.

Accordingly, we minimize the functional

$$\phi = \underbrace{\frac{1}{2}\sum_{k=1}^{18}\left(\frac{1}{R}\frac{\partial\psi}{\partial\upsilon}\bigg|_k - B_\tau|_k\right)^2}_{\text{Pick-up coils}} + \underbrace{\frac{1}{2}\sum_{i=1}^{6} W_F\left(C\int_{Li}\frac{n}{R}\frac{\partial\psi}{\partial R}\,d\ell - \alpha_i\right)^2}_{\text{Faraday angles}}$$

$$+\underbrace{\frac{1}{2}\sum_{i=1}^{6} W_n\left(\int_{Li} n\,d\ell - N_i\right)^2}_{\text{Density integrals}} + \underbrace{\frac{1}{2}W_{Rn}\int_0^1\left(\frac{\partial^2 n}{\partial\psi^2}\right)^2 d\rho + \frac{1}{2}W_{RJ}\int_0^1\left(\frac{\partial^2 A}{\partial\psi^2}\right)^2 d\rho}_{\text{Regularising terms}}$$

subject to the constraints of the Grad-Shafranov equation and of fixed total plasma current. Here ψ is the poloidal flux, υ is the normal at the plasma boundary, n is the electron density, and A is related to the toroidal current via

$$J_\phi = \lambda\left(\beta RA + (1-\beta)\frac{A}{R}\right)$$

The weights of W_f and W_n are inversely proportional to the square of the error of the Faraday rotation and electron density measurements. The weights of the regularising terms are chosen so as to allow a fit of the data within their error bars while suppressing artifacts that have an unphysical character (oscillations with a wavelength of the order of the chord spacing, negative densities or current densities, etc). This corresponds to the range of regularising weights within which the normalised χ statistic is approximately equal to 1. The

variation of any equilibrium quantity within this range determines the error introduced by smoothing into the determination of this quantity.

Figure 1 shows the relative errors in the fitting of the magnetic, polarimetric and interferometric data as a function of W_{rj}, in the current flat-top of an ohmic discharge. For values of W_{rj} below 10^{-3}, all the data are fitted within their respective error bars. The corresponding variation in q_o is shown in Figure 2, again confirming the results of the Abel-inversion procedure. We note that the values of κ_o obtained by this self-consistent procedure is in excellent agreement (<3%) with that deduced from SXR tomography.

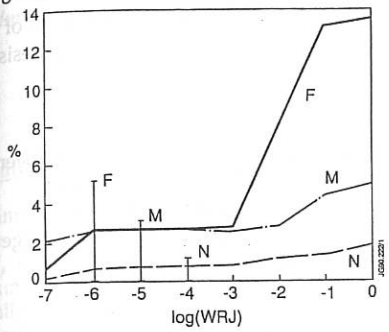

Fig.1 Relative errors in the fitting of the Faraday (F), magnetic (M) and interferometric (N) data as a function of the regularising weight W_{RJ}. (Also shown are typical error bars).

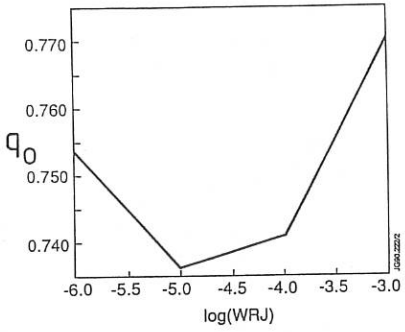

Fig.2 Variation of the axial safety factor with the regularising weight W_{RJ}.

Changes in the Q-Profile at the Sawtooth Collapse

Variations in the safety factor profile, and in particular the change in q_o at a sawtooth collapse, can be studied more sensitively by Abel-inversion of the difference in the polarimetric signals before and after the collapse.

The change in the Faraday rotation angle, $\Delta\theta$, is written as a first order expansion in the parallel magnetic field, $B_{//}$, the electron density, n_e, and the integration path

$$\Delta\theta \sim \Delta\left[\int n_e B_{//}\, d\ell\right] \approx \int (\Delta n_e) B_{//}\, d\ell + \int n_e (\Delta B_{//})\, d\ell + (\Delta \int) n_e B_{//} d\ell$$

where the last term takes into account the change in the Shafranov shift which occurs at the sawtooth collapse. The change in the Faraday angle due to a perturbation of the poloidal field is obtained by subtracting from the total change the contributions from the perturbed density, and the perturbed geometry. The "corrected" angles can then be Abel-inverted for the perturbed poloidal field in the usual manner. Because the sawtooth period in JET is long compared with the integration time of the polarimeter electronics, sawteeth are clearly visible in the raw data and it is not necessary to perform a coherent averaging of many

sawteeth. The fluctuations in the Faraday angle have an amplitude of 0.01-0.05 radians.

Figure 3 shows the change in q_o at a sawtooth collapse as a function of the preceding sawtooth period, for sawteeth in the current flat-top of a number of ohmic and ICRF-heated discharges. Also shown are the lines corresponding to $\Delta q_o/\tau s$ = 0.05, 0.1 and 0.2 sec^{-1}. The most important source of error is the perturbed electron density, which gives rise to a change in the Faraday angle which is of the same order as the change due to the perturbed field.

Field diffusion calculations, assuming neo-classical resistivity and complete reconnection within the q=1 surface, yield typical values for $\Delta q_o/\tau s$ of 0.3-0.5 sec^{-1} in these discharges. Thus our results give support to the hypothesis that complete reconnection does not take place at a sawtooth collapse.

Conclusions

The systematic errors associated with the flux surface geometry have been studied using measurements along orthogonal chords and a self-consistent equilibrium identification algorithm. The results validate our previous inference that q_o remains below 1 throughout the sawtooth period. The change in q_o which takes place at the sawtooth collapse is consistent with this conclusion.

[1] J O'Rourke et al, 15th Euro.Conf. on Contr.Fusion and Plasma Physics, 1988. Europhys.Conf.Abstracts, Vol.12B, part 1, p.155.
[2] J Blum et al, To be published in Nuc.Fusion.

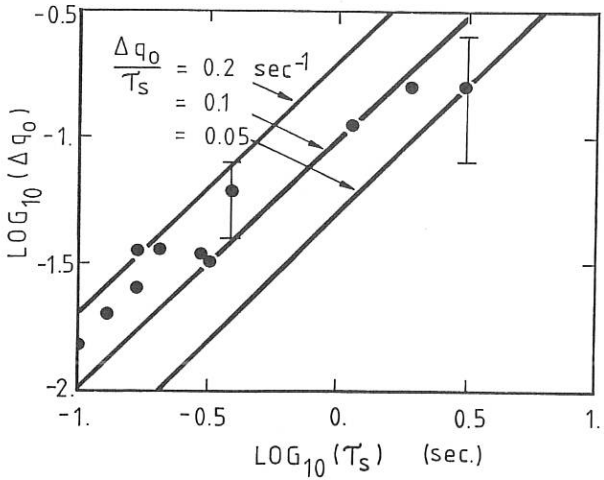

Fig.3 Change in the axial safety factor versus preceding sawtooth period.

SAWTOOTH TRIGGERED DISRUPTIONS AT THE DENSITY LIMIT ON DITE

G.M.Fishpool, A.W.Morris

JET Joint Undertaking, Abingdon, Oxon, OX14 3EA and
Imperial College of Science, Technology and Medicine, University of London, U.K.
·Culham Laboratory, Abingdon, Oxon, OX14 3DB
(Euratom/UKAEA Fusion Association)

Introduction

Magnetic feedback on the DITE machine[1] is successful in reducing the amplitude of the $m = 2, n = 1$ MHD instability. (m = poloidal mode number, n = toroidal mode number. Experiment parameters: R = 1.19m, a = 0.23m, I_p = 70 − 125 kA, B_ϕ = 1.0 − 2.0 T, $\bar{n}_e$ = 3 − 5 × 10^{19}m^{-3}.) The reduction in amplitude of this perturbation, which grows as the precursor to a major disruption, allows operation at densities higher than the previous disruptive limit. A limitation to the success of the experiment is the modulating effect of the internal sawtooth oscillation on the (2,1) perturbation amplitude for discharges with $2.3 \lesssim q_{cyl}(a) \lesssim 4$. This amplitude typically increases by a factor of 3 at a sawtooth crash. One of these increases starts the disruption precursor growth. This behaviour may have some similarities to the 'gong' phenomenon seen on JET[2] and other devices.

This disruption precursor oscillation is clearly visible on all channels of both horizontally and vertically viewing soft x-ray diode arrays. The differences between the forms of the signals is consistent with coupled $m = 1$ and $m = 2$ components of the oscillation.

Sawtooth destabilisation of the (2,1) perturbation

Soft x-ray emission and magnetic pick-up coil data are shown in Figure 1 for a shot close to the density limit with (2,1) magnetic feedback ($q_{cyl}(a) = 2.3$). The soft x-ray emission is from a chord through the plasma with a chordal radius (closest approach to the plasma magnetic axis), r_c = 4cm (inverted sawteeth were seen on x-ray channels with r_c > 9cm). The magnetic pick-up coil signal is obtained from a coil combination detecting mainly (2,1) perturbations. The dominant perturbation component has this (2,1) structure and a frequency of between 8 and 11kHz. This perturbation exists non-disruptively at a level of $\delta B_\theta / B_\theta \sim$ 0.5%, this being reduced by a factor of 5 or more by feedback.

Figure 1 shows the effect of the sawtooth oscillation on the (2,1) perturbation level. A rapid increase in amplitude to a level comparable with δB_θ(without feedback) occurs around the time of the sawtooth crash. This increase occurs in 1 - 2 periods, i.e. probably faster than the $m = 2$ non-linear resistive growth.

Max-Planck-Institut für Plasmaphysik
8046 Garching bei München

The increase in amplitude is followed, in non-disruptive cases, by a slow decrease through the sawtooth cycle. For $q_{cyl}(a) = 2.3$ shots, the variation is small without feedback. The variation is much more obvious for $q_{cyl}(a) \gtrsim 3.0$ even without feedback.

The density limit is reached when the (2,1) mode continues to grow, following the sawtooth, becoming the precursor to a major disruption.

The increase in $m = 2$ activity is apparently triggered by the crash, rather than by, for example, the appearance of the sawtooth precursor oscillation (seen for all DITE sawteeth investigated). The crash takes $\approx$ 100 μs, as measured on the chord integrated x-ray signals. The time, τ, between the crash and the increase in $m = 2$ is $\lesssim$ 100 μs for the majority of cases. In a few cases, $\tau \approx 300$ μs, but chordal integration of the sawtooth precursor $3 \lesssim f \lesssim 6$kHz could contribute to this.

It is to be noted that there are cases when no increase in the $m = 2$ mode is associated with a sawtooth crash. One sample showed that 1 sawtooth in 9 is followed by a lower level of m=2; 1 in 15 exhibit a significant (>10%) reduction.The remainder typically have a factor of 3 increase. This variation may be due to changes in mode coupling.

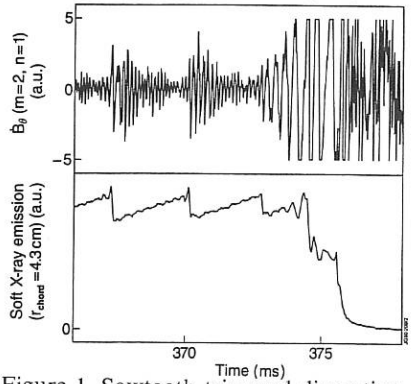

Figure 1. Sawtooth triggered disruption on DITE. Note bursts of (2,1) at each preceeding sawtooth crash.

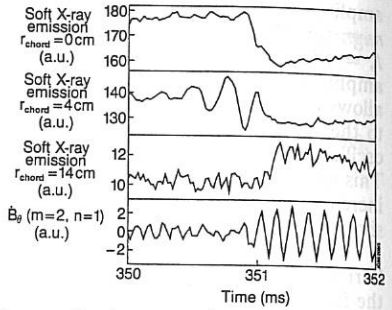

Figure 2. Increase in (2,1) and the sawtooth heat pulse.

Possible mechanisms for $m = 2$ destabilisation

The stability of the (2,1) tearing mode is very sensitive to the current density gradient around the $q = 2$ surface[3]. Thus, a possible mechanism for the observed effect is that changes in the conductivity, and hence $j(r)$, occur close to the $q = 2$ surface following the arrival of the sawtooth heat pulse. Figure 2 shows x-ray signals with chordal radii 0, 4 and 14cm and the $\dot{B}_\theta(2,1)$ signal. $\dot{B}_\theta(2,1)$ is seen to have increased considerably before the heat pulse is seen at 14cm. Since the $q = 2$ surface has a radius of close to 20cm this mechanism is ruled out for this case. In many cases, the $m = 2$ increase occurs before the crash and hence the heat pulse cannot explain the phenomenon.

The $r_{chord} = 4$cm x-ray signal in figure 2 shows the large oscillatory sawtooth precursor which is seen as $m = 1$ in the centre of the plasma, and as $m \approx 3$ (for

$q_{cyl}(a) \approx 3$) on the Mirnov coils. The frequency of this oscillation was close to, but not exactly, half that of the (2,1) mode (except during the disruption precursor when $m = 1$ and $m = 2$ modes appear to be coupled - see next section).

There is a weak correlation between the size of this sawtooth precursor and the post-crash (2,1) activity ($f \approx 10$kHz), although there is usually no strong $m = 1$ successor oscillation.

Disruption Precursor Structure

As the disruption precursor starts to grow, it becomes clearly visible on all channels of the soft x-ray arrays. Comparing the signals from the horizontally and vertically viewing arrays a distinct difference in phase behaviour is observed. The top half of figure 3 shows data from the horizontally viewing array, where the phase of the oscillation changes by only a small angle between each channel. In contrast, the vertically viewing channels, in the lower half of the figure, show two distinct phase inversions (1 channel outside the centre and 7 channels inside). This observation is explicable in terms of $m = 1, n = 1$ and $m = 2, n = 1$ structures locked together, rotating toroidally (poloidal rotation is very small).

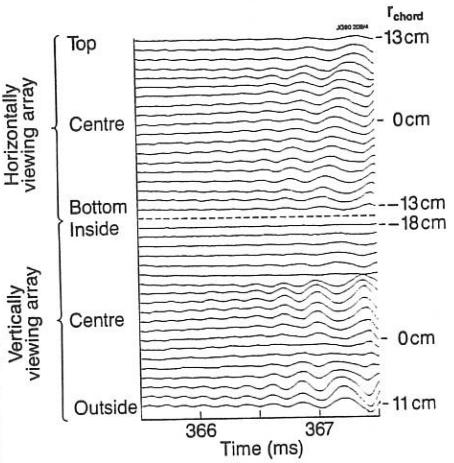

Figure 3. Soft x-ray diode signals from both arrays for a disruption precursor.

The phase variation with chordal radius, r_c, seen on the two cameras is simply explained by considering the geometry of these two modes. Taking emissivities of the form $\varepsilon_m = f_m(r)\cos(m\theta + n\phi - \omega t + \delta_m)$, (where $f_m(r)$ contains the radial dependence of the displacement and the equilibrium emissivity gradient), and performing line integrals for orthogonal viewing directions (the small $\pm 12°$ array fans having little effect), one obtains,

$$I_{\text{total}}(r_c) = C(r_c)\cos(\omega t + \phi(r_c))$$

where I_{total} is the emissivity measured by the diode as a function of the chordal radius (signed). The phase angle, ϕ, is given by

$$\tan\phi(r_c) = \frac{A(r_c)\sin(\theta_0 + \delta_1)}{A(r_c)\cos(\theta_0 + \delta_1) + B(r_c)},$$

where A and B contain the dependence of the line integrated emissivities ($m = 1$ and $m = 2$ respectively) on r_c. Without loss of generality $\delta_2 = 0$, and θ_0 takes the value 0 for the vertical array and $\pi/2$ for the horizontal array. Thus for any functions A, B the vertical array has phase 0 or π since $\sin(\theta_0 + \delta_1) = 0$ whilst the horizontal array phase varies as $\tan^{-1}(A/B)$.

The results in figure 3 have been simulated using this method. The simulation is shown, together with the experimental data, in figure 4. The phase behaviour of the two arrays is relatively insensitive to the radial dependence of the emissivities. This simulation has an $m = 1$ eigenfunction representing a rigid displacement of the core, whilst the $m = 2$ emissivity represents an elliptical distortion which has largest effect on the emissivity at around half the minor radius. The phasing needed to simulate the data indicates that the perturbations align on the outboard midplane (i.e. $\delta_1 = \delta_2 = 0$) consistent with toroidal resistive MHD theory.

Conclusions

Sawtooth activity in DITE strongly affects the amplitude of the $m = 2, n = 1$ perturbation. This results in the triggering of density limit disruptions for discharges with moderate $q_{cyl}(a)$. In most cases the increase of the m = 2 mode appears synchronous with the crash. The destabilising effect occurs on a faster timescale than can be explained by heat pulse propogation. Hence, some other mechanism is required to explain the change of the dominant instability at the crash.

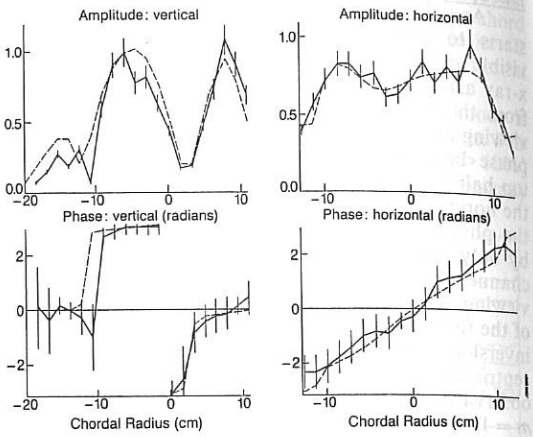

Figure 4. Amplitudes and phases of diode signals at 367ms in figure 3, and simulation (dotted).

On DITE the disruption precursor appears to be a global, $m = 1$ and $m = 2$, $n = 1$ mode.

Acknowledgements

The authors would like to acknowledge the help of W.Millar in the use of the soft x-ray diode arrays and P.C.Johnson, J.Hugill and the DITE operation team for running the machine. This work was carried out as part of Article 14 contract #JE8/9006 for the JET Joint Undertaking under the supervision of P.E.Stott and J.A.Snipes.

References

1. A.W.Morris et al. Physical Review Letters **64**, 1254 (1990).
2. A.Pochelon et al. Proc. 12th Euro. Conf. on Contr. Fus. and Plas. Phys., Budapest, Vol 1 (1985) 126.
3. A.H.Glasser et al. Physical Review Letters **38**, 234 (1977).

ELECTROMAGNETIC INTERACTIONS BETWEEN PLASMAS AND VACUUM VESSEL DURING DISRUPTIONS IN THE HITACHI TOKAMAK HT-2

Mitsushi Abe, Kazuhiro Takeuchi, Hideshi Fukumoto and Michio Otsuka

Energy Research Lab. Hitachi,Ltd., 1168 Moriyama-cho, Hitachi, Ibaraki, Japan

1. Introduction

Disruption is one of the key problems in tokamak device design as it has thermal and mechanical problems. From the viewpoint of mechanical design, predicting the electromagnetic force during disruptions is important[1-3]. Disruptive current decay processes, such as plasma current decay rates and plasma-coil interactions, have been experimentally examined in many tokamaks[4-7]. In this presentation, the toroidal eddy currents and the electromagnetic force due to them are discussed. They are determined by the magnetic fitting technique based on the magnetic data experimentally obtained during the disruptions of ohmically heated plasmas in the Hitachi tokamak HT-2[8]. This presentation focuses on giving a qualitative understanding of tokamak plasma disruptions from an electromagnetic viewpoint. An important point in elucidating the process appears to be the eddy current induced by the plasma movement (shell effect), and this point is intensively examined.

2. Experimental Setup

Experimental device

The experiments are carried out in a small tokamak HT-2[8], with the parameters listed in Table I. The poloidal cross section is given in the Fig.1. The locations of the magnetic sensors are also shown. A feature is a capability to create various cross-sectional plasmas using eight HY coils. B1 and B2 coils are for negative biasing of the iron transformer. ACH coils are for the rapid plasma vertical position Z_P control. Fig.2 shows the plasma cross sectional shapes which are produced in the HT-2 experiments. The vacuum vessel is made of stainless steel 9mm thick. The magnetic penetration time is 1.3ms for the vertical field and 1.5ms for the horizontal field. The one-turn resistance of the vessel is 14m Ω due to the two resistive parts of 8cm width in the toroidal direction. Feedback control of the plasma position is applied in the experiments, but it is not powerful enough to control the position even during the disruption.

Table I Parameters of HT-2 Tokamak

Parameters	Symbol	Values	
Plasma Current	I_P	10-55	kA
Electron Density(line averaged)	n_e	1-3x10^{19}	m^{-3}
Toroidal Field	B_T	1.0	T
Plasma Major Radius	R_P	0.39-0.44	m
Plasma Minor Radius	a_P	0.08-0.12	m
Elongation	K	0.9-1.45	
Iron Core Flux Swing	-	±0.062	Wb

Method to estimate electromagnetic force on vacuum vessel

Eddy currents on the vacuum vessel as well as plasma cross-sectional shapes are determined from the magnetic data measured by magnetic probes and flux loops. The method for magnetic analysis is described in ref.8. A feature is that magnetic probes are placed so as to give pairs of inner (plasma side) and outer (air side) magnetic probes. This placement enables determination of the toroidal eddy current on the vacuum vessel. Magnetic fitting determines magnitudes of seven eddy current Fourier components as well as coil currents on a poloidal cross section. Toroidal eddy current density j_T is calculated by the superposition of the Fourier components and the poloidal field B_P is calculated from the eddy and coil currents. The electromagnetic force f in this study is due to j_T and B_P and is calculated by

$$f = j_T \times B_P \quad (Pa), \qquad (1)$$

The force f is the electromagnetic pressure acting on the vessel. Total force acting on the vacuum vessel is obtained by integrating the pressure f on the vacuum vessel, assuming uniform pressure distribution in the toroidal direction. The estimated error for j_T is around 20% of its maximum value and the error for B_P is less than 5%. The estimated errors for f is less than 25%, against the peak value of the distribution on a poloidal cross section.

3. Electromagnetic Characteristics of Disruptive plasma current decay in HT-2

Plasma current decay date during disruptions

The plasma cross-sectional shapes in these experiments are the same as in Fig.2 and each plasma has different characteristics of the disruptive current decay. A parameter which shows the difference is a time constant of the plasma current decay $\tau_d \{=-I_P/(dI_P/dt)\}$, where I_P is plasma current. The circular plasma has roughly constant dI_P/dt during the current decay and τ_d=0.5ms, while the slightly elongated plasma has τ_d=1.0ms. However the highly elongated plasma has rapid current decay. Examples of the highly elongated plasmas are the plasmas with divertor configuration, which have τ_d=0.25-1.0ms. In the following part, the electromagnetic characteristics of the disruptive plasma current decay are discussed for circular and elongated shaped plasmas, focusing on the characteristics depending on the plasma cross-sectional shape.

Circular plasma disruption

Figure 3(a) shows the time evolution of the plasma current I_P, net vessel toroidal current I_{eo}, total vertical force F_Z and radial force F_R acting on the vacuum vessel, during the I_P decay. The forces are mainly due to the plasma movement (shell effect). This is why the time evolution of the F_R differ from the wave form of I_{eo}. The F_R has a peak just after the current decay starts but the I_{eo} has a peak when the plasma current is decreased to half its initial value. Figure 3(b) shows the magnetic field and electromagnetic force during the disruption, indicating the vessel experiences a counter force (negative radial direction) from the plasma movement. During I_P decay, the circular plasma touches the inner (small major radius side) limiter. The plasma disruption which cause a decrease of plasma thermal energy and force the plasma move inward. This movement squeeze the plasma and the current decay for the circular plasma is rapid. The F_Z equals zero for the circular plasma because it does not moves vertical direction.

Elongated plasma disruption

Figure 4(a) shows the time evolution of the disruption for the slightly elongated plasma. Since the elongated plasma disruptions are accompanied with the vertical instability, F_Z become important. The value n_v $(=-R/B_v \ \partial B_v/\partial R)$ is indicated as a parameter of the elongation, where B_v is the external vertical field. The plasma moved upward and I_P start to decay at 15.6ms. The forces have their peak value just before the start time because of the plasma vertical movement. During the I_P decay, the forces are weak. This is because the eddy current induced by the plasma movement is cancelled by the I_P decay.

Figure 4(b) shows the time evolution of the disruption for the highly elongated plasma. A feature for the highly elongated plasma disruption is that the plasma current decay phase can be divided into two phases. The first is a short period of rapid I_P decay phase which is appeared at 18.4-18.6ms in Fig.4(b). The force F_Z due to the vertical instability increases until 18.4ms which is just before the disruptive I_P decay, but F_Z and F_R are both weak at rapid I_P decay time. The second is a period at which F_Z become large again and is the latter half of the current decay process.

Eddy current distribution helps the understanding of F_Z time evolution.

Figure 5 shows the eddy current distribution along the vacuum vessel wall for the disruption of Fig.4(b). The upper figure is at just before the rapid I_P decay (18.4ms) and the lower figure is at after it (18.8ms). At 18.4ms the eddy current is due to the shell effect for the plasma vertical movement and the vessel experiences the counter force of the shell effect. Most importantly the eddy current near the plasma (at 260deg.) changes its flow direction and the amount of the current (shadowed area in Fig.5) is comparable with the amount of the rapid decay of I_P. A part of the plasma current move to the vessel wall to delete the shell effect and at this time the eddy current and forces are small {at 18.6ms on Fig.4(b)}. This process can be understood as the same mechanism as the slightly elongated case in which the plasma current moved slowly to the vessel wall during all I_P decay phase. After the rapid I_P decay, the shadowed eddy current of I_P direction at 18.8ms, interact with the external poloidal field which caused the Z_P instability before 18.4ms, and after 18.6ms the vessel experiences the vertical force as the plasma experienced before 18.4ms.

The rapid I_P decay is associated with the vertical instability. Figure 6 shows the electromagnetic pressure acting on the vessel wall with the original divertor configuration i.e. with the high elongation. The timing of Fig.6 is just before the rapid I_P decay. The plasma is moving toward bottom. The plasma should experience the upward force of shell effect for the position stability from the eddy current on the vessel and the vessel should experiences the downward vertical force as a counter force. However, the figure shows that the force is mainly directed in the radial direction and the stabilizing effect for the plasma vertical position is small. The reason of such small stabilizing effect is that the poloidal magnetic field on the vessel wall toward which the plasma is moving is small because such point is close to the null point.

4. Conclusion

Electromagnetic interactions between plasmas and the vacuum vessel toroidal eddy current during disruptive I_P decay have been examined experimentally in the Hitachi tokamak HT-2 for three kinds of plasma shapes i.e. circular, slightly elongated and highly elongated. The characteristics of the disruptive I_P decay depend on the plasma cross-sectional shape. The I_P decay rate in the circular plasma is twice as large as that in the slightly elongated plasma. The main cause of the electromagnetic force during the I_P decay is mainly due to the plasma movement (shell effect) for these two kinds of plasma shapes. Very rapid I_P decay is observed in highly elongated plasma. This is associated with the vertical instability. After the rapid I_P decay, eddy current which has a peaked distribution with I_P direction at the point toward which plasma has moved. Such eddy current interact with the magnetic field from poloidal coils and create a large vertical force. The effect of the poloidal vessel current has not yet discussed.

References

[1]FER DESIGN TEAM:JAERI-M 86-134 Japan Atomic Energy Res. Inst. (1986).
[2]T.Kobayashi: Jpn.J.Appl.Phys. 18(1979)2003.
[3]H.Takatsu, et. al.: Nucl. Engrg. Des. 71 (1982)161.
[4]K.McGuire, et. al. : J.Nucl.Mater. 121(1984)329.
[5]S.C.Jardin, et. al.: Nucl. Fusion 27(1987)569.
[6]TFR group: Nucl. Fusion 25(1985)919.
[7]J.A.Wesson, et. al.: Nucl. Fusion 29(1989)641.
[8]M.Abe, et. al.: Kakuyuugou-kenkyu 61(1989)38. and M.Abe, et. al.: Jpn. J. Appl. Phys. 29(1990)395.

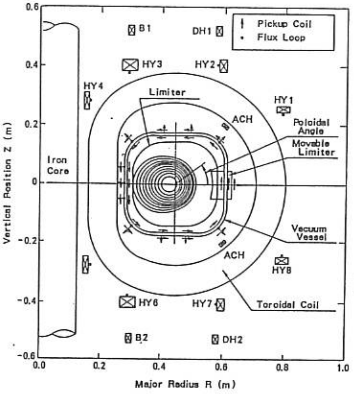

Fig.1.Poloidal cross section of HT-2 tokamak.

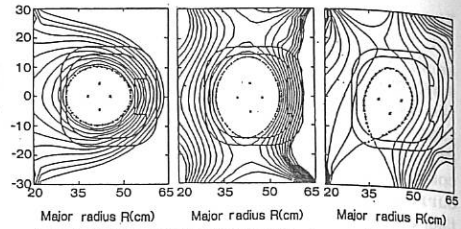

Fig.2.Plasma cross-sectional shapes in the HT-2.

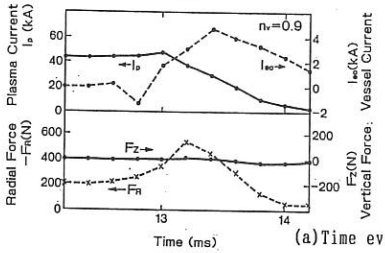

(a)Time evolution

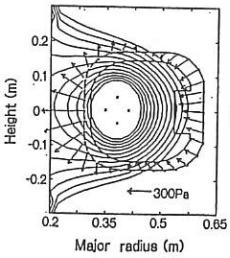

(b)Electromagnetic force

Fig.3.A disruptive plasma current decay with circular shaped plasma.

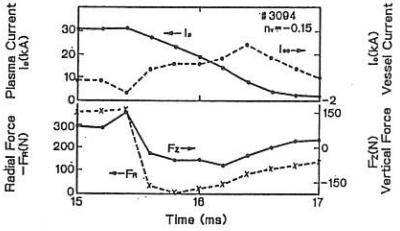

(a)slightly elongated plasma.

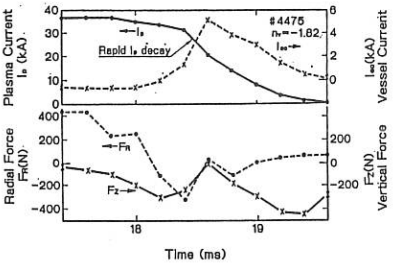

(b)Highly elongated plasma.

Fig.4.Time evolution of disruptive current decay.

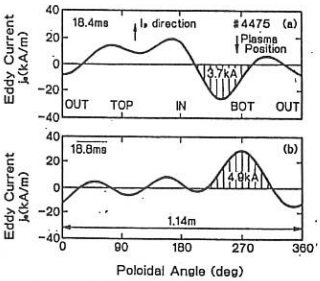

Fig.5.Eddy current distribution

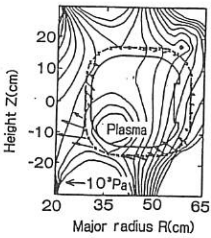

Fig.6. Electromagnetic force during disruptive plasma current decay with high elongation.

ASYMMETRIC EFFECTS OF AN $\ell = 1$ EXTERNAL HELICAL COIL ON THE SAWTOOTH AMPLITUDE ON TOKOLOSHE TOKAMAK.

G. Nothnagel, D. Sherwell, D.E. Roberts, J.D. Fletcher, J.A.M. de Villiers.

Atomic Energy Corp. of South Africa, PO Box 582, Pretoria 0001.

Introduction: Sawtooth theory suggests two q-profiles are of particular interest, namely: (a) a parabolic q-profile with $q_0 < 1$ and (b) a flat central q-profile ($q_0 \gtrsim 1$) for $0 \leq r \leq r_1$ with q parabolically increasing outside r_1, leading to sawtooth crash mechanisms governed by Kadomtsev's total reconnection model [1] and the more recent quasi-interchange model suggested by Wesson [2] respectively. Flat central q-profiles with $q_0 \lesssim 1$ can allow the tearing mode and the quasi-interchange mode to be present simultaneously. An attempt is discussed to distinquish between the profile types (a) and (b) by energising an $\ell = m/n = -1/1$ external helical dipole field winding [3] on Tokoloshe ($R/a = .52m/.24m; I_p = 140kA; B_\phi = .6T$).

Experimental arrangement and results: The helicity of the magnetic field lines in the plasma can be arranged to have a resonant or non-resonant sense relative to the $\ell = -1$ winding by reversing the direction of the plasma current (Fig. 1). Experiments have been performed for both resonant and non-resonant configurations and for both current directions in the helical winding. Two soft X-ray diodes at $\phi = 330^0$ view the plasma at tangent radii 4.5 cm below and above the centre of the radius of inversion ($r_1 = 7.5\,cm$). For a reference shot (i.e. without helical field) the sawtooth amplitudes on the two diodes are similar (Fig. 2(a)). With the winding energised the signals on the two diodes are affected asymmetrically as shown (Figs. 2(b) & 3): For a winding current of $7\,kA$, one diode shows a general decrease in relative sawtooth amplitude ($\triangle A/A$) of $\simeq$ 50 % while a qualitatively different effect is seen on the other diode (figure 3). Starting at a time t_0 during the sawtooth rise phase a hollow in the intensity relative to the other diode signal is seen. The hollow lasts for typically $.6\tau_s$ ($\tau_s \equiv$ sawtooth repetition time) and recovers rapidly over a period of $\simeq .1\tau_s$ just prior to the sawtooth crash. This final spike has an $m = 1$ character. On reversing the I_1 current direction the effects on the diode signals also reverse, indicating the coil-induced nature of the effects (Fig. 3). In the non-resonant configuration similar features are observed. The phase of the asymmetry (i.e. on which diode signal the hollow appears) does not depend on the direction of the plasma current, (resonant or non-resonant) but only on the direction of the I_1 current. Fourier analysis of the measured vacuum helical field reveals a non-resonant ($m/n = 1/1$) component of $\simeq$ 13 % of the size of the resonant ($m/n = -1/1$) component. This could explain the observed non-resonant effects. No statistically detectable change in the sawtooth period is observed as a result of the helical field.

Comparison with numerical calculations: Field line tracing calculations using the q-profiles (a) and (b) and the measured helical field, were performed. For a profile with $q_0 = .7$ (case (a)) and $I_1 = 1\,kA$ a magnetic island is formed relative to the I_1 current direction as shown in figure 4(a). A flat central q-profile (case (b)) with $q_0 = 1.006$ shows no island formation (Fig. 4(b)), but a shift of the hot spot in a direction opposite to that for case (a). The two cases therefore lead to different results with regard to the position of the hotspot relative to the I_1 conductors. The results of the calculations for the non-resonant case show similar effects due to the non-resonant component. Phase agreement, of the hot spot relative to the windings for both I_1 current directions, is found with experiment only for q-profiles with $q_0 < 1$. For $I_1 \geq 4\,kA$ large scale stochasticity is predicted by the field line tracing but is not seen in the experiment where only a small loss in central confinement is observed for $I_1 = 7\,kA$. Field penetration effects may explain this. Figure 4 ($I_1 = 1\,kA$) does however give the correct phasing of the hotspot for each q-profile.

Discussion and conclusions: Comparison of experimental and numerical results suggests that the hollow in the sawtooth amplitude on one diode is due to the appearance of a stationary $m = 1$ island in the field of view of the diode, rather than a shift of the intensity distribution away from it. Further, a shift of the hot spot would be expected to lead to an increase in the one diode signal. What is observed however, apart from the asymmetric appearance of the hollow, is a general decrease in the confinement of the central region. It seems likely therefore that on Tokoloshe, q_0 must be less than one during sawtoothing. The unaltered sawtooth period suggests that the mechanism of the sawtooth crash is not affected by the coil. The final spike (Fig. 3 (a) bottom trace) could be due to the growth of the mode that leads to the crash. There seems to be re-rotation of the mode after a certain amplitude has been reached. Numerical simulations, using an emissivity model with a non-rotating growing island, qualitatively explains the hollow and the final spike. However, the amplitude of the spike cannot be reproduced without assuming rotation.

References:

[1] B B Kadomtsev, Sov. J. Plasma Physics,**1**,389(1975).

[2] J A Wesson, Plasma Phys. Controlled Fusion, **28**,243(1986).

[3] D P Coster et al., 14th Eur. Conf. on Contr. Fusion and Plasma Physics, Madrid,Volume 11 D, part 1, 240(1987).

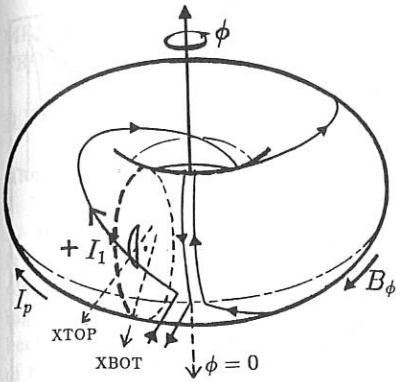

Figure 1: Diagram of the helical dipole winding with the positive I_1 current direction indicated. The plasma current direction for the resonant configuration is shown.

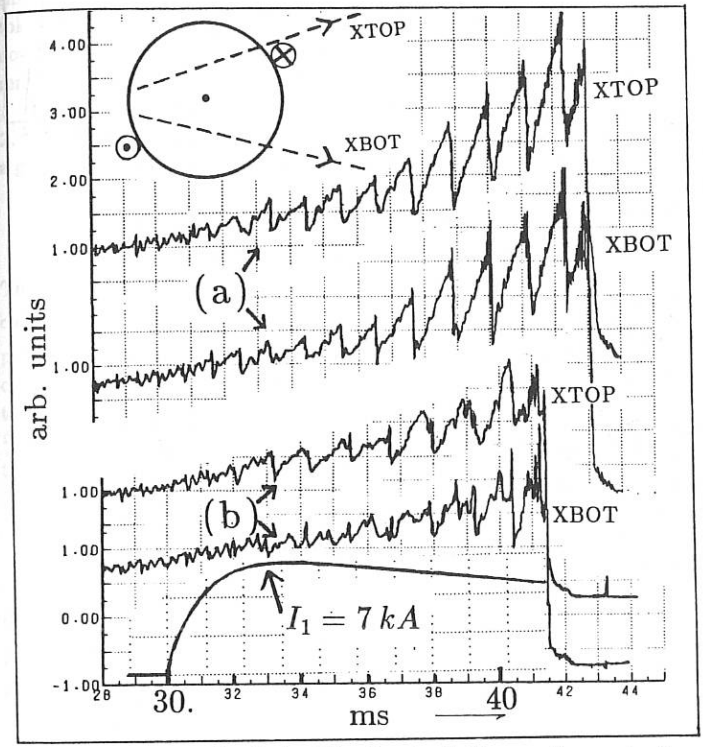

Figure 2: Asymmetric effect of the $\ell = 1$ winding on the sawtooth amplitude. (a) Reference shot (without helical current) and (b) $I_1 = -7\,kA$.

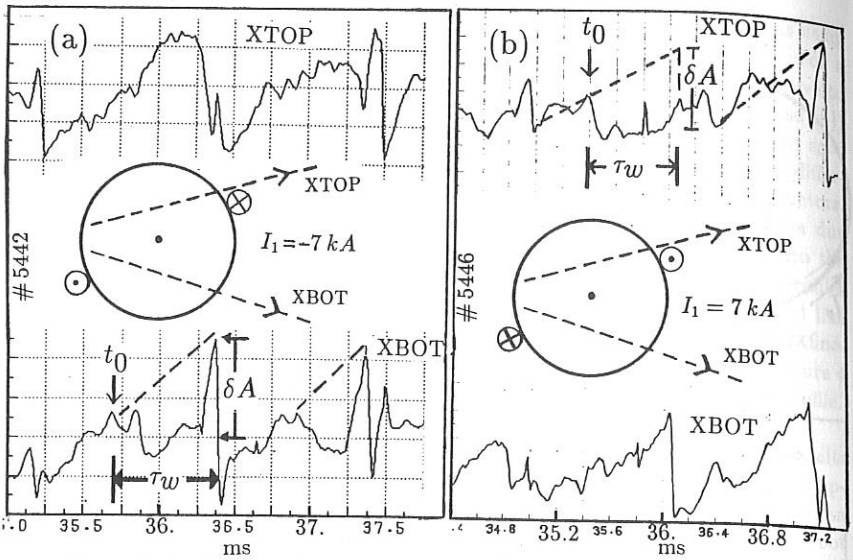

Figure 3: Application of an $m = 1, n = 1$ helical perturbation leads to the appearance of a hollow in the soft X-ray intensity prior to the sawtooth crash. (a) For the negative I_1 current direction (see figure 1) XBOT is affected and (b) for the positive I_1 direction XTOP is affected.

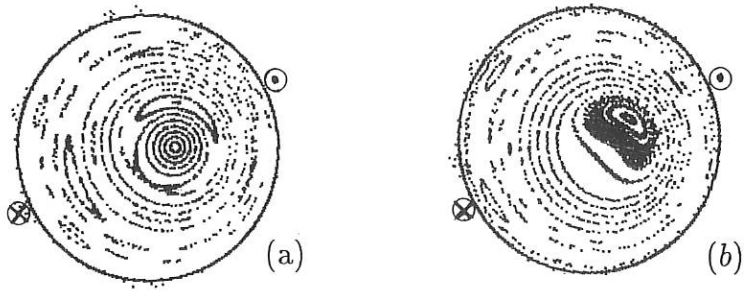

Figure 4: Field line tracing results with a resonant helical $m = 1, n = 1$ perturbation of 1 kA for: (a) a parabolic q-profile with $q_0 < 1$, and (b) a flat central q-profile ($q_0 = 1.006$) with q monotonically increasing outside r_1. For the opposite I_1 current direction the observed features undergo a 180^0 phase shift in θ. The orientation of this phase is independent of plasma current direction.

MEASUREMENT OF OHMIC TOKAMAK MOMENTUM CONFINEMENT TIMES FROM CONTROLLED LOCKING AND UNLOCKING OF TEARING MODES.

D.E. Roberts, J.D. Fletcher, G. Nothnagel, D. Sherwell and J.A.M. de Villiers.

Atomic Energy Corp. of South Africa, P.O. Box 582, Pretoria 0001.

1. Introduction: The global momentum confinement time, τ, of a tokamak plasma is normally estimated from the equation: $\frac{dV}{dt} = L - \frac{V}{\tau}$. In an unbalanced NBI heated plasma with $P_{NBI} \gg P_\Omega$, τ can be estimated both in the steady state, because the driving term L is readily estimated, and from the rate of fall (rise) of momentum following beam switch off (on). Ohmic tokamak plasmas are not so amenable to determination of τ because L is neither easy to estimate nor to control and the rotation velocity, v, is small and difficult to measure accurately. We discuss the measurement of τ for an ohmic tokamak plasma from the rate of increase of its velocity following the controlled slowing down of its rotation. The slowing down is produced by resonant interaction of a current pulse, in an external helical coil, with a large saturated tearing mode in the plasma.

2. Momentum confinement model: We assume toroidal rotation (section 3.) with a global momentum confinement equation:

$$\frac{d\Omega}{dt} = L - \frac{\Omega}{\tau_\phi} - \frac{k_1 I_c \tilde{B}_\theta \sin(\phi - \phi_1)}{\sqrt{1+\Omega^2\tau_w^2}} - \frac{k_2 \tilde{B}_s \tilde{B}_\theta \sin(\phi - \phi_2)}{\sqrt{1+\Omega^2\tau_w^2}} - \frac{k_3 \tilde{B}_\theta^2}{1+\Omega^2\tau_w^2} \qquad (1)$$

The terms in k_1, k_2, k_3 describe, respectively, mode locking due to an external helical coil with current I_c [1], a stray field $\tilde{B}_s$, and eddy currents generated in the wall [2]. The penetration of the tearing mode field $(\tilde{B}_r, \tilde{B}_\theta)$ through the vacuum chamber depends on the factor $(1+\Omega^2\tau_w^2)^{1/2}$, where τ_w is the penetration time of the wall. This means that all three locking terms are highly non-linear in Ω. In the steady state with $I_c = 0$, $\frac{d\Omega}{dt} = 0$ and $\Omega = \Omega_0$ so that L can be obtained from (1). It will be justified *a posteriori* that $k_2 \simeq 0$ so that (1) can then be written as:

$$\frac{d\Omega}{dt} = \frac{\Omega_0}{\tau_\phi} - \frac{\Omega}{\tau_\phi} - \frac{k_1 I_c \tilde{B}_\theta \sin(\phi - \phi_1)}{\sqrt{1+\Omega^2\tau_w^2}} + \frac{k_3 \tilde{B}_\theta^2}{(1+\Omega_0^2\tau_w^2)} - \frac{k_3 \tilde{B}_\theta^2}{1+\Omega^2\tau_w^2} \qquad (2)$$

The external coil can always force locking for sufficiently large I_c. For Tokoloshe $f_0 = 6kHz$ and $\tau_\omega = 0.25ms$, so $\Omega_0\tau_\omega \gg 1$. Thus, re-rotation of the mode ($\frac{d\Omega}{dt} > 0$) after locking ($\Omega = 0$) can only occur, even when $I_c = 0$, if $k_3 \tilde{B}_\theta^2 = \frac{C\Omega_0}{\tau_\phi}$ where $C < 1$. If re-rotation does occur (with $I_c = 0$ and $k_2 = 0$),

$$\begin{aligned} \frac{d\Omega}{dt} &= \frac{\Omega_0}{\tau_\phi} - \frac{\Omega}{\tau_\phi} + \frac{\Omega_0}{\tau_\phi}\frac{C}{1+\Omega_0^2\tau_\omega^2} - \frac{\Omega_0}{\tau_\phi}\frac{C}{1+\Omega^2\tau_\omega^2} \\ &\approx \frac{\Omega_0}{\tau_\phi} - \frac{\Omega}{\tau_\phi} \quad for\ \Omega \geq 0.3\Omega_0\ if\ C = 0.9 \end{aligned}$$

Then $(\Omega_0 - \Omega) = (\Omega_0 - \Omega_1)\exp -\frac{t}{\tau_\phi}$ where $\Omega = \Omega_1$ at $t = 0$. Hence τ_ϕ can be obtained from the slope of $\ln(1 - f/f_0)$ versus t for sufficiently large Ω.

3. Experimental details: We consider an $\approx 10ms$ duration phase of a Tokoloshe plasma during peak I_p ($I_p = 125kA, R = .52m, a = .24m$). In this phase, $q_\psi \simeq 3.3 \pm 0.2$ and two tearing modes are present, an $m = 2\,/\,n = 1$ at $r/a = 0.76$ and an $m = 3\,/\,n = 1$ at $r/a = 0.95$. Due to the low aspect ratio of our machine, we obtain signals on Fourier analysing coils responding to poloidal mode numbers $m = 1, 2, 3, 4$ and 5. These coils all give to within 2% the same Mirnov frequency of $\simeq 6kHz$. Since the toroidal mode number is n=1 and assuming $\omega = \frac{mv_\theta}{r} + \frac{nv_\phi}{R}$ the simplest explanation is that the modes are rotating toroidally with $v_\phi = R\omega_0$. The rotation direction is opposite to that of I_p, while the apparent poloidal rotational frequency of the $m = 2$ mode corresponds in magnitude and direction to the local electron diamagnetic drift frequency. Hard X-ray, Langmuir probe and H_α signals also show the same frequency. Following the onset of sawtooth oscillations, soft X-ray $m = 1$ fluctations centred on the sawtooth inversion radius also show the same frequency as the Fourier coils.

There are four external coils on Tokoloshe, an $\ell = 0$ (purely poloidal) winding and $\ell = 1, 2$ and 3 stellarator type windings. Due to the low aspect ratio, currents in each of the four coils are able to lock the mode structure [3] but with strongly decreasing efficiency as the ℓ-number decreases. During locking with *any* coil all the above mentioned signals slow down in phase (Fig. 1). Thus the plasma appears to rotate essentially as a solid body.

4. Results: Plots of $\ln(1 - f/f_0)$ versus time for seven different shots are shown in Fig.2. These shots cover a range from incomplete locking to a locked phase of $\simeq 7ms$. The linear regions of the plots indicate an increasing momentum confinement time from 0.4 to 0.8ms. The electron energy confinement time $\tau_{Ee} = 1.6 \pm 0.3ms$ at t=5ms so that $\tau_\phi \approx \tau_{Ee}$ as found on NBI heated machines. The decrease of MHD activity at the end of the period studied is due to a narrowing of $j(r)$ which leads to the onset of sawtoothing. The time at which this occurs is progressively delayed as the locked phase becomes longer [Fig. 2] so that the locking itself clearly changes the plasma properties. No significant difference in τ_ϕ is obtained from locking with the $\ell = 2$ or $\ell = 3$ coils though the locking currents are considerably smaller for the $\ell = 3$ (Fig. 1). The relatively undistorted (*sine* like) $\tilde{B}_\theta$ traces after rotation in Fig. 2 (cf Fig. 1) also indicate that stray fields are unimportant during the linear $ln(1 - f/f_0)$ versus time phase of the rotation. The accuracy of the present measurement is limited to $\approx \pm 20\%$ by the fact that there are only a few Mirnov cycles ($\sim$ 3 to 5) in the available range of $\Omega(0.3\Omega \leq \Omega \leq 0.9\Omega_0)$ i.e. $\tau_\phi/T(\text{Mirnov}) \approx 3$ to 5.

5. Conclusions: Measurements of global momentum confinement times of ohmic tokamak plasmas have been made from the acceleration of tearing modes following their controlled slowing down. This method could be useful in probing the regime from ohmic

to weakly (unbalanced) NBI heated plasmas in larger machines. Since τ_ϕ/T(Mirnov) increases rapidly with machine size the measurements could be much more accurate than in the present work while a smaller perturbation of the base frequency Ω_0 could also be used. Clearly a fully toroidal helical coil could not readily be installed on an existing machine. However, a modular coil covering $\leq 1/25$ of the surface of the vacuum chamber should be sufficient to cause an appreciable decrease in v_ϕ on a machine the size of e.g. ASDEX without excessive coil currents ($\leq 10kA$).

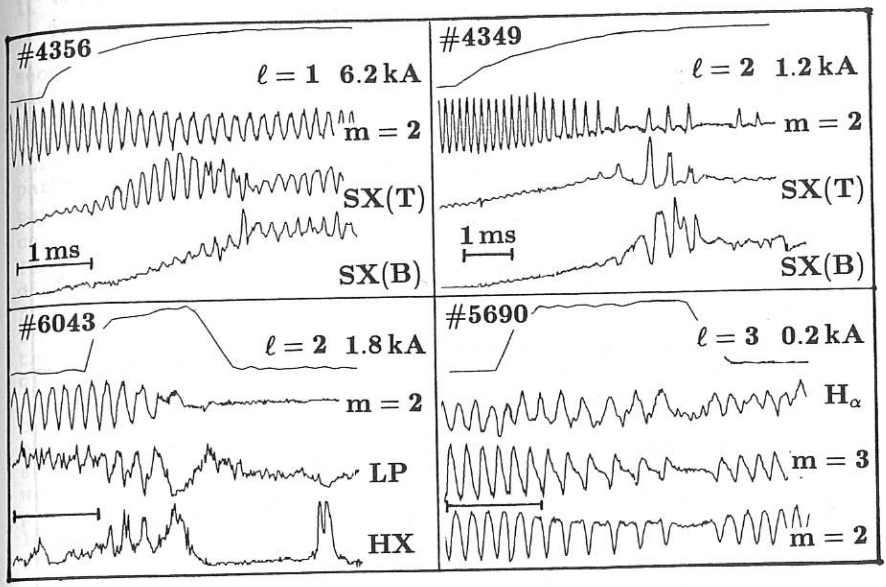

Fig.1 Soft X-ray(SX), Hard X-ray(HX), Mirnov ($m = 2$ and $m = 3$), Langmuir probe(LP) and H_α signals showing slowing down and locking of the rotation frequency due to the $\ell = 1, 2$ and 3 coils (The SX signals are at the sawtooth inversion radius above(T) and below(B) the centre. The LP is biased at $-20V$ and is positioned at $r = 0.23m$)

6. References

[1] T.C. Hender, G.G. Gimblett and D.C. Robinson in Controlled Fusion and Plasma Heating (Proc. 15th Eur. Conf., Dubrovnik, 1988) vol 1, 437

[2] M.F.F. Nave and J.A. Wesson, in Controlled Fusion and Plasma Phys. (Proc. 14th Eur. Conf., Madrid, 1987) Vol.3, 1103

[3] D.E. Roberts, J.D. Fletcher, D. Sherwell, G. Nothnagel, et. al. in Controlled Fusion and Plasma Phys. (Proc. 16th Eur. Conf., Venice, 1989) Vol 13B, II, 493

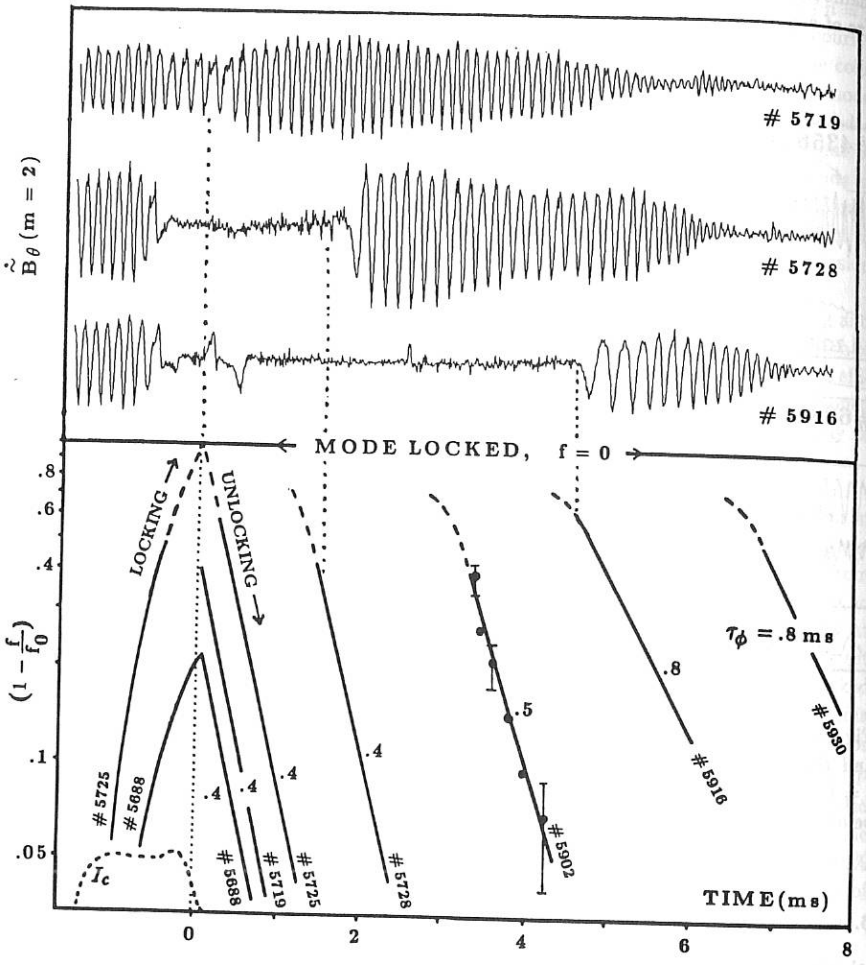

Fig.2 Measured values of $\ln(1 - f/f_0)$ versus time for seven shots showing incomplete locking as well as locked phases of up to $7ms$ duration (i.e.$> 5\tau_{Ee}$). Representative $\tilde{B}_\theta$ $(m = 2)$ traces, with the same time scale, are shown above for three of the shots.

THE CHARACTERISTICS OF LOW-q DISCHARGES ON HT-6B TOKAMAK

Li Guoxiang, Li Linzhong, Xie Jikang, Guo Dequan, Qin Pinjian, Deng Chuanbao, Huang Rong, HT-6B Group

(Institute of Plasma Physics, Academia Sinica, Hefei, P.R.C.)

1. Introduction

HT-6B is a small air core tokamak with circular cross section and without conducting shell and divertor. Its aspact ratio is R/a = 45cm/12.5cm. The operation regime according to the original design was $q(a) \geq 3.0$ ($q(a)$ is the surface safety factor of plasma), and no low-q programm was included[1]. During the initial stage, HT-6B was operated of the following parameters: $q(a)=3.0--6.0$, $n_e=(0.5--2.3)\times10^{13}cm^{-3}$ (in this paper n_e is line averaged electron density) and plasma current I_p =13--35 KA. One year ago, we made the study of the fine structure of discharge region on HT-6B, and five discharge regiones of different characteristics have been found[2]. They are sawtooth region, MHD-oscillation region, transition region,energetic region and runaway region. During that research, the operation regime has been expanded to $q(a) \leq 3.0$.

Recently, by decreasing the impurity level, carefully controlling the plasma current and density rise rates and enhancing equillibrium adjusting ability,HT-6B has been successfully operated in the $1.75 \leq q(a) \leq 3.0$ low-q regime, with special emphasis on the understanding of the confinement property and the low-q disruption. Experiments show that the low-q discharges not only have the same fine structrue of discharge region, but also have special characteristics.

2. Characteristics of Low-q Plasma

The typical plasma parameters of HT-6B operated in low-q are as follows:I_p = 30--50 KA, B_t = 0.4--0.6 T, n_e =(0.4--2.6) $\times10^{13}cm^{-3}$, $<\beta>$ = (0.6--1.3)% and $q(a)$ = 1.75--3.0, and the uncertainty of $q(a)$ is lower than 10%.

2.1. Confinement Property When operated in lower $q(a)$, the circular-cross-section tokamak without a conducting shell usaully has poorer confinement property. On HT-6B, however, stable plasma of well confinement property can be obtained even though $q(a)$ is lowered to 1.75. The comparision between the measured energy confinement time τ_e and the experimental scaling[3]

$$\tau_e\ (ms) = 0.61\times10^{-3}\ T_e^{1.08}\ (ev)\ n_e\ (10^{13}cm^{-3})\ q(a)^{1.17} \qquad (\#)$$

obtained from $1.75 \leq q(a) \leq 3.0$ is given in Fig.1. From scaling (#),one can see that except that τ_e decreases as $q(a)$

is lowered, the energy confinement does not become bad. The τ_e value derived from (#) is similar to that derived from Alcator, Mirnov and DIVA[4] scalings.

2.2. Sawtooth Behavior During low-q discharges, sawtooth activity becomes strong. Sawtooth inversion radius r_s increases as q(a) decreases (Fig.2). The whole plasma is modulated by sawtooth which can be seen even on plasma loop voltage(Vl), Hα emission, diamagnetic signal, hard X-ray (HX) emitted from the limiter and Mirnov signals. The sawtooth magnitude on soft X-ray (SX) signals may reach to (20--30)% in low-q shots, while only (5-15)% in high q(a) shots. The remarkable sequence of strong sawtooth oscillations is that the plasma parameter profiles become broad which is responsible for the growth of some instabilities.

2.3. Broad Profiles "Fat" plasma parameter profiles is the principal characteristic of low-q HT-6B dischardes. In a large central region, the electron temperature and density profiles $T_e(r)$, $n_e(r)$ and SX emission intensity profile $I_{SX}(r)$ are flat. Fig.3 shows the current density profiles estimated from assuming $q(r_s)=1$ and $j(r)=j(0)[1-(r/a)^2]^n$. When $q(a)=1.79$, we have $n=0.99$, and such current profile is unstable to the ideal kink mode[5].

2.4. Low-q Disruption Three kinds of low-q disruptioms, we call them major disruption, soft distuption and sawtooth-like disruption, have been observed[6]. When $q(a)\leq 2.0$, the disruption probability obvisously increases.

3. Low-q Disruption of $q(a)\leq 2.0$ Shots

We specially pay attention to the $q(a) \leq 2.0$ low-q disruption since in plasma there is no q=2 rational surface which is the pre-condition of the growth of m=2/n=1 tearing mode related to most of q(a)>2 disruption. Typical low-q major disruption shot of q(a)=1.8 is shown in Fig.4. The disruption process is similar to that of the q(a)>2 disruption, but the instability related is different.

The growth of m=2/n=1 mode is observed on SX signals and magnetic fluctuation(MF) signals 1~2 ms before the disruption (Fig.4b). The $I_{SX}(r,t)$ profile (Fig.4c) shows that before disruption the central part is flat and a small broad peak appears on the profile near by sawtooth inversion radius r_s (~ 5 cm). Such profile is the result of the strong sawtooth activity. The VUV OVI line measurements show that the total oxygen inpurity does not increased, but the inpurity distribution may change.

It seems that the strong sawtooth activity itself and the special plasma profile caused by it, as mentioned above, play considerable roles in low-q disruption. Fig.5 shows a q(a)=1.91 shot disrupted after some sawtooth collapses which is followed by fast growth of m=2/n=1 mode. Sawtooth is so strong that can be seen on the HX signal, and several positive spikes on Vl also seems to be the sequence of the energetic electron loss caused by the sawtooth crashes. Usually, low-q disruption takes place just after the last sawtooth collapse and, sometimes (Fig.5), the m=2/n=1 mode successively increases

and does not oscillate again, untill disruption occurs.

The growth time τ_g of the m=2/n=1 mode increases as the plasma density n_e increases. When n_e increases from 0.4x $10^{13}cm^{-3}$ to $1.6x10^{13}cm^{-3}$, τ_g is enhanced from 50 us to 400 us. This behavior is very similar to that of the m=2/n=1 kink mode growth time ($\tau_k \sim \rho^{1/2}$, ρ is the plasma mass density) and is different to that of the tearing mode growth time ($\tau_t \sim n_e^{-7/5} \eta^{-9/5}$, η is plasma resistivity). Considering the above results and q(a)<2.0, we believe that the m=2/n=1 mode have ideal kink mode characteristic.

4. Summary

On HT-6B, low-q plasma (q(a)≤2.0) of well confinement property has been obtained. The q(a)<2.0 low-q disruption is the sequence of the strong sawtooth activity and the growth of the edge m=2/n=1 mode which seems to be an ideal kink mode .If we can effectively control the sawtooth oscillation and the plasma profile, it is possible to run tokamak with well confined plasma in lower q(a) and higher $< \beta >$.

References

[1] Zhao Qinchu et al.,IAEA-CN-44/A-V-5 (1984).
[2] Li Linzhong et al.,Chinese Science,3(1990)284 or ASIPP/82
[3] Deng Chuanbao et al.,The Study of Confinement on HT-6B Tokamak,to be published.
[4] DIVA Group,Nuclear Fusion 20(1980)271.
[5] Wesson,J.,Nuclear Fusion 18(1978)87.
[6] Li Guoxiang et al.,The Study of Low-q Disruption on HT-6B ,to be published.

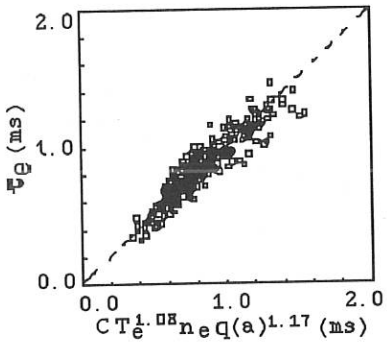

Fig.1 Measured τ_e and the scaling (#).

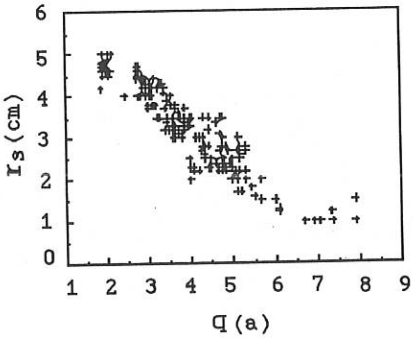

Fig.2 Sawtooth inversion radius as a function of q(a).

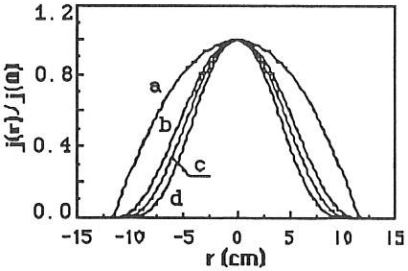

Fig. 3 Current frofiles. q(a)=1.8 2.9, 3.8, 4.8 for a, b, c, d.

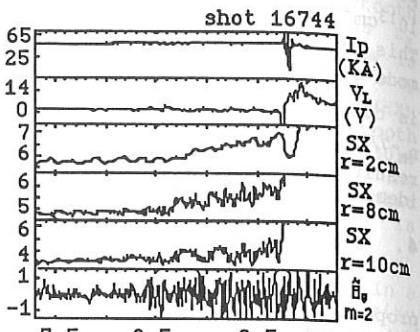

Fig. 4b M=2/n=1 mode grows before low-q disruotion.

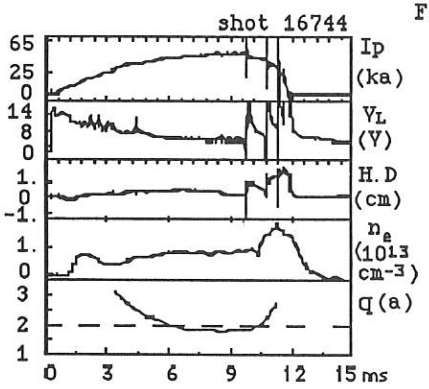

Fig. 4a Low-q disruption. (H.D. is horizontal displacement.)

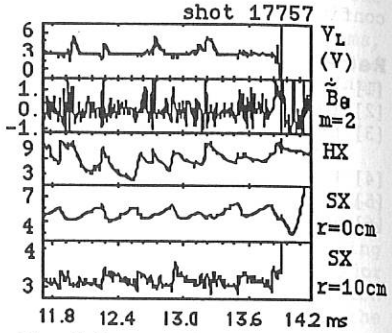

Fig. 5 Low-q disruption and sawtooth activity.

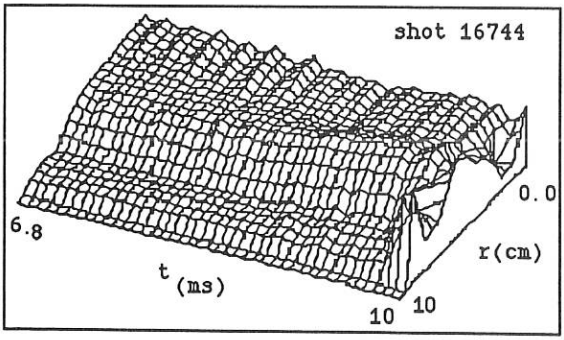

Fig. 4c Soft X-ray intensity profile $I_{SX}(r,t)$.

PROFILES AND MHD ACTIVITIES IN PBX-M TOKAMAK[1]

H. Takahashi, B. LeBlanc, S. Kaye, S. Sesnic, M. Chance,
R. Hatcher, C. Kessel, J. Manickam and M. Okabayashi

Plasma Physics Laboratory, Princeton University, Princeton, NJ 08543, USA

Abstract

An S–α diagram is used to *characterize and catalog* plasma current and pressure profiles modified by tools available to PBX-M. A class of MHD-quiescent plasmas, obtained by skin effect and pellet injection, has broad current and peaked pressure profiles, while a class of MHD-active plasmas, which often leads to a β collapse, has peaked current and broad pressure profiles. The two classes of plasmas trace distinct patterns in the S–α map. The β collapse and ELM events are discussed using the S–α formalism.

The PBX-M tokamak(1) has an array of tools to modify and measure the pressure and current profiles including strong external shaping (bean shape), skin effect (rapid I_p ramp), pellet injection and others. What are stability characteristics of profiles modified by each of these tools? Is it possible to avoid the β collaspe? These are important current topics in the PBX-M project.

Three different operating regimes, produced by different profile modification tools, will be discussed. (1) The first regime, termed 'high β_p', is produced by shaping alone, i.e., a moderate indentation ($\imath \sim 0.15$), ellipticity ($\kappa \sim 1.9$) and triangularity ($\delta \sim 0.5$). This H-mode, steady I_p ($\sim 320kA$) regime is characterized by a high poloidal β value ($\beta_p \sim 2$), but also by active MHD (fishbones, sawteeth, continuous global modes and ELM's) and often a β collapse. (2) The second regime, termed 'high $\langle\beta_t\rangle$', is produced principally by the skin effect resulting from a rapid I_p ramp ($\dot{I}_p \sim 2.5MA/s$) and by strong shaping, i.e., a large indentation ($\imath \sim 0.28$), ellipticity ($\kappa \sim 2.2$) and triangularity ($\delta \sim 0.60$). This L-mode, high I_p ($\sim 570kA$) regime is characterized by a high volume-averaged toroidal β value ($\langle\beta_t\rangle \leq 6.8\%$), Troyon–Sykes parameter ($\beta_{TS} \equiv I_p/(a_{mid}B_{\phi 0}) \sim 2MA/(mT)$) and g-factor ($g \equiv \langle\beta_t\rangle/\beta_{TS} \sim 3.4(\%mT/MA)$), and by a long MHD-quiescent period ($\sim 100ms$) followed by a brief period ($\sim 30ms$) of sawtooth precursor-like MHD activities prior to an unavoidable disruption. (3) The third regime is produced by modifying what would have been a typical high β_p regime discharge by injecting a medium-sized pellet ($D/L \sim 2/3mm$). This L-mode, high density ($n_e(0) \leq 1.5 \cdot 10^{20}/m^3$) regime is characterized by a sustained ($\geq 100ms$) peaked density profile, long MHD-quiescent period ($\geq 80ms$) followed by a brief period ($\sim 20ms$) of MHD activities before a (possibly avoidable)

[1]Supported by U. S. DoE Contract DE-AC02-76-CHO-3073

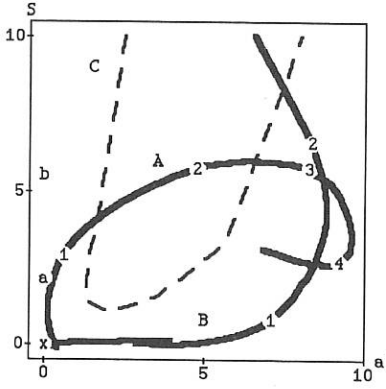

Fig. 1 S–α map formalism: Equilibria of high β_p (A) and high $\langle\beta_t\rangle$ (B) discharges, and a ballooning stability boundary (C).

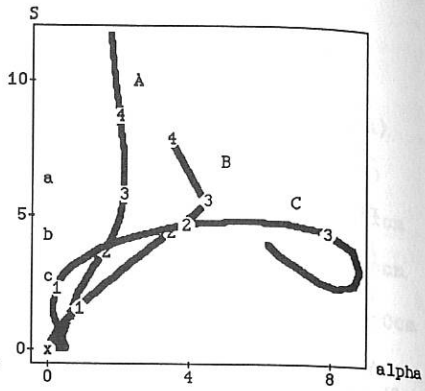

Fig. 2 Equilibria for β collapse sequence: rise phase (A), stauration (B) and just before collapse (C).

disruption, and by an energy confinement time ($\tau_E \sim 45ms$) comparable to that of H-mode discharges.

In this paper the pressure and current profiles are obtained from equilibrium analysis using the measured poloidal flux values, plasma and coil currents, and electron pressure profile as boundary conditions. The total computed pressure is assumed to be proportional to the measured electron pressure. Profile characteristics such as 'peaked' or 'broad', whether expressed qualitatively or in terms of the profile factor (peak-to-average ratio), refer to an integral moment of the profile function. It is, however, the dimensionless pressure and current gradients in relation to each other, which are relevant to stability considerations: speaking of a 'peaked' pressure profile, e.g., is meaningful only in the context of having a particular current profile. A diagram of the shear and pressure gradient parameters, which is commonly used to delineate ballooning mode stability boundaries, is instead used here to *characterize and catalog* pressure and current profiles of experimentally obtained equilibria. The shear parameter in this paper is $S \equiv (2v/q)(dq/d\psi)(d\psi/dv)$, where $v(\psi)$ is the volume within a flux surface given by the poloidal flux function, ψ, and the pressure gradient parameter is $\alpha \equiv (-2\mu_0)(dp/d\psi)(dv/d\psi)\sqrt{(v/(2\pi^2 R))}$, where R is the major radius of the geometrical center of the flux surface. The diagram, here referred to as the S–α map, can be used to describe relationship between the shear and pressure gradient and to make a qualitative assessment of their stability characteristics. The map is used for 'pattern recognition' to *catalog* features of discharges in different regimes. Knowledge of the manner in which each profile modification tool alters the pattern is useful in finding paths to high β states without encountering a β collapse.

In Fig. 1 two equilibria are shown in the S–α map formalism. Each curve is a

parametric representation of $S(\psi)$ and $\alpha(\psi)$ for an equilibrium as the parameter, ψ, is varied from its value on the magnetic axis (x at the origin of the diagram) to the value at the plasma edge (either a or b on the vertical axis). Inbedded numerals mark locations of integer q values. The last segment of each trajectory, representing changes between the last two flux surfaces, is omitted for the clarity of presentation. The curves A and B are typical for high β_p and high $\langle\beta_t\rangle$ regimes, respectively. For localized modes such as ballooning mode, the stability is determined by the locations of these trajectories in relation to stability boundaries. For global modes such as kink mode, the stability depends on the trajectory pattern, in whole or in part, as well as on the wall locations. We will make qualitative observations on these instabilities from the knowledge of their generic characteristics instead of describing details of stability calculations. The *generic shape* of ballooning unstable zone of a flux surface is a 'tongue shaped' region in the diagram extending from the upper right-hand corner toward the origin. The generic shape (but not the size or location) of such a region is indicated by the curve C in Fig. 1. The tongue 'recedes' toward the upper right-hand corner for a series of flux surfaces increasingly farther away from the magnetic axis. Thus, the 'first up, then to the right and finally a downward loop' pattern of the trajectory A is not favorable in avoiding ballooning unstable zones, and also implies expending a limited 'supply' of shear at places where there is no significant pressure gradient. A downward loop of the curve A beyond the $q = 3$ surface means increasing pressure gradient as the shear diminishes and is likely to give unfavorable contributions to the kink stability. In fact, MHD-active, high β_p plasmas in PBX-M are expected from a stability analysis to be external-kink unstable and to have some ballooning unstable interior surfaces. In contrast, the curve B in Fig. 1 is a 'first to the right, and then up' trajectory, and the pressure builds up significantly within the $q = 1$ surface without expending much shear. The trajectory pattern would be helpful in going under the 'tongue', although the trajectory's end near the plasma edge could still run into ballooning unstable zones. Rapidly increasing shear near the edge, as the pressure gradient rises, should also be favorable for the kink stability. Calculations show that MHD-quiescent, high $\langle\beta_t\rangle$ discharges are indeed expected to be stable against ballooning mode, and either stable or marginally stable for $n = 1$–3 kink modes depending upon how the stabilizer plates are modeled.

In Fig. 2 a time sequence of equilibria (from three similar discharges) in the β collapse process[2] is shown: curve A in the β rise phase, B in the saturation and C at the beginning of the collapse phase. In this sequence q_{edge} varies from 6.4 to 4.7 to 4.3 indicating diminishing total available shear as β rises. The curve C shows a characteristic downward loop and a large pressure build-up, without an accompanying increase in the shear, in regions outside the $q = 2$ surface. Following this state β begins to collapse in a series of large ELM events and other global ($n = 1$–3) MHD activities. In Fig. 3 a pair of equilibria (from two consecutive similar discharges) are shown at a moment, just before and after, an ELM event that caused a large ($\sim 10\%$) stored energy loss. A major effect of the ELM on the equilibrium appears in regions outside the $q = 3$ surface: it unravels the downward loop of the trajectory A and flips it upward into a region of higher shear and

[2]discovered in PBX tokamak and reported at EPS (orally) and IAEA (written) meetings(2).

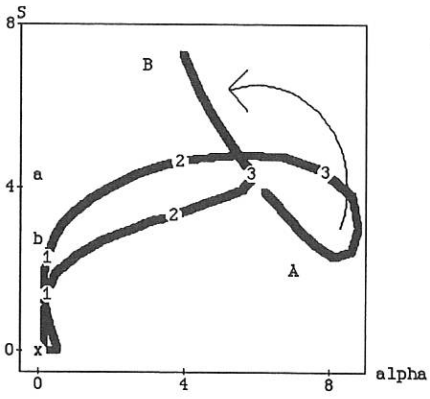

Fig. 3 Equilibria before (A), and after (B), a large ELM event.

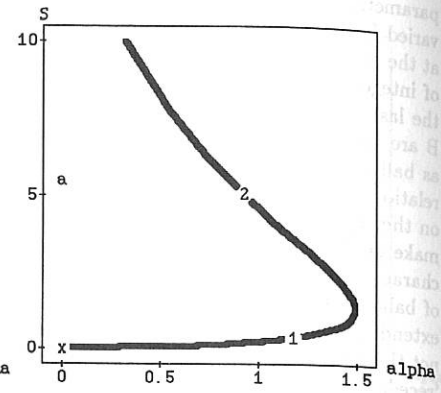

Fig. 4 Equilibrium for a pellet discharge.

reduced pressure gradient. The resultant trajectory B resembles closely the saturation phase trajectory (curve B in Fig. 2). The stored energy often recovers partially untill another ELM occurs. The downward loops appear to be unsustainable and destroyed by ELM's to yield a more stable configuration. Trajectory changes depicted here may suggest that ELM's have features more compatible to kink mode than ballooning mode. A measure of the total available shear, q_{edge}, is unaffected in the ELM event discussed here and therefore the increase in the shear in outer regions would require a compensating decrease elsewhere in core regions.

Qualitative features of the trajectory shown in Fig. 4 representing a pellet fuelled discharge are similar to those of high $\langle\beta_t\rangle$ discharges, i.e., a 'first to the right, and then up' pattern, and a large build-up of the pressure within the $q = 1$ surface. The maximum α value encountered is, however, much smaller as a result of nearly linear $p(\psi)$ function which does not produce a large gradient anywhere. Yet, MHD-quiescent pellet discharges have nearly the same central pressure and stored energy as high β_p discharges, and may represent a way to circumvent the β collapse.

We have shown, using the S–α formalism, that a combination of peaked pressure and broad current profiles of *transient* skin effect discharges has MHD characteristics superior to a combination of broad pressure and peaked current profiles of *steady* high β_p discharges. The strengths of both regimes may be combined possibly by pellet injection and other profile modification tools, especially lower hybrid current drive.

References

(1) K. Bol, et al., PBX-M Project Proposal, Princeton Plasma Physics Lab.(1985)
(2) H. Takahashi, et al., EPS, Budapest(1985); M. Okabayashi, et al. IAEA, Kyoto(1986).

THE BETA LIMIT IN THE DIII–D TOKAMAK*

J.R. Ferron, M.S. Chu, F.J. Helton, W. Howl, A.G. Kellman, L.L. Lao, E.A. Lazarus,† J.K. Lee, T.H. Osborne, R.D. Stambaugh, E.J. Strait, T.S. Taylor, and A.D. Turnbull

General Atomics, San Diego, California, USA

The combination of high power deuterium neutral beam injection and operation with high current double-null divertor discharges has enabled increasingly high values of both toroidal and normalized beta (β_T and β_N respectively) to be obtained in the DIII–D tokamak.[1] The highest achieved values are $\beta_T = 9.3\%$ and $\beta_N = 5\%$-m-T/MA, obtained in different discharges. Here, $\beta_T = (\int PdV/V)/(B^2/2\,\mu_0)$ is the volume average beta and $\beta_N = \beta_T/(I/aB)$ where a is the minor radius of the discharge, B is the vacuum toroidal magnetic field at the geometric center of the discharge, P is the plasma pressure, V is the discharge volume, and I is the plasma current. It is expected that when the beta reaches a threshold value an ideal instability will occur, either the low toroidal mode number (n) ideal kink mode or the high-n, ideal ballooning mode. If all other obstacles to achieving high values of beta are overcome, it is generally postulated that the insurmountable limit to beta will be the stability threshold of one of these modes. According to Troyon-Sykes scaling,[2,3] this limit to β_N is a constant (C_β) with a value which depends on the limiting ideal instability, plasma profiles, and wall stabilization. Previous tokamak experiments[4–7] have found operational limits representing C_β values from 2.8 to 3.5, associated with several types of instabilities. Experimental data is presented in this paper that demonstrates that over a wide range of plasma current, in DIII–D the value of C_β is larger than 3.5. For values of I/aB near 1.1, C_β is demonstrated to be at least 5. Theoretical calculations using measured plasma parameters show that the ideal beta limit is set by the ballooning mode at a value of β_N between 4 and 5, depending on the discharge shape and current.

In practice, the achievable value of beta in any given discharge is not necessarily determined by an ideal beta limit. There are a number of low and high beta phenomena that can limit the confinement time and thus limit the value of β_N that can be obtained with the available heating power. Examples are given here. Discharges in which the value of beta is determined by one of these phenomena should not be interpreted as having reached an ideal beta limit.

The present operating regime for DIII–D is summarized in Fig. 1. Values of β_T near 9.3% have been obtained at the highest values of normalized current, $2.7 \leq I/aB \leq 3.25$. These discharges use the double-null divertor discharge shape heated by up to 20 MW of deuterium neutral beams. The highest value of β_T obtained using the single-null shape is 7.4% (the two shapes are compared in the inset of Fig. 1). Other notable parameter values are (in separate discharges) ion temperature up to 17 keV at $\beta_N = 2.8$ and $\beta_T > 5\%$ at the maximum available toroidal field of 2.1 T.

The data points at the highest values of β_T at each value of I/aB (shown as open circles in Fig. 1) show that the experimentally demonstrated value of the beta limit in DIII–D is at least 3.5 I/aB over the range of current $0.5 \leq I/aB \leq 2.7$. Above this current the data sets a minimum value of the beta limit in the range 2.9 to 3.5 I/aB. The data can only reliably be used to determine a minimum value of the ideal beta limit because the value of β_T in most discharges was limited by confinement, the total heating power, or instabilities other than

* This is a report of work sponsored by the U.S. Department of Energy under Contract No. DE-AC03-89ER51114.

† Oak Ridge National Laboratory.

the ideal kink or ballooning modes. The data with $I/aB \approx 1.1$ demonstrate that the ideal stability limit can be at least as high as $\beta_N = 5$.

In Fig. 2 is shown the time evolution of one of the discharges that reached $\beta_T = 9.3\%$, a high toroidal beta, high normalized current discharge. Figure 3 shows a lower current, high normalized beta discharge with a peak value of $\beta_N = 4.5$. As shown by the divertor D_α signals, both are H–mode discharges with an initial quiescent period followed by a period of continuous edge-localized-modes (ELM). During the D_α quiescent period, the value of β_T increases continuously, reaching a peak value just before the occurrence of the first ELM. In these two cases, the highest values of beta are maintained for 40 to 150 ms, a time period that is short relative to the total length of the discharge but that is long compared to the time scales relevant to the study of ideal stability at high beta. The ideal mode growth time would be expected to be on the order of 10 to 100 poloidal Alfven times (20 to 200 μsec). A non-rotating mode stable in the presence of the conducting vacuum vessel wall but unstable without a wall would be expected to grow on the time scale of the resistive wall skin time, a few milliseconds.

These two discharges have been compared to the stability theory for ideal infinite-n ballooning and low-n kink modes. To do this the measured temperature and density profiles are used with magnetics data to obtain a self-consistent equilibrium that is used as input for stability codes.[8] The ballooning stability calculation finds, at each flux surface, the maximum value of the radial pressure gradient that is ballooning mode stable. In considering stability to ideal kink modes, the analysis has concentrated on external modes, those with a perturbation which is strongly peaked near the edge of the plasma. This is done because $m/n = 1/1$ modes which are typical of an internal kink are not observed to provide an ideal limit to beta in DIII–D and because the present experimental observations of high beta kink-like modes in DIII–D have an external character. The role of the central safety factor q_0 (here taken as 1.05 for stability calculations) and of the fast ion population (here simply added to the thermal ion pressure) are uncertainties which will be the subject of future experiments and calculations.

Figure 4 shows that while the $\beta_T > 9\%$ discharge of Fig. 2 is stable to ballooning modes, the high β_N discharge of Fig. 3 is at the theoretical ballooning mode beta limit. In the case of the higher current discharge [Fig. 4(a)], the regions near the axis and the edge of the discharge are close to the stability limit while in the region in the center of the figure, representing approximately 50% of the plasma volume, the experimental pressure gradient is below the marginally stable gradient. In this case the marginally stable value of β_T is 12%, well above the experimental value of 9.3%. In the case of the high β_N discharge [Fig. 4(b)], the experimental pressure gradient is very close to the marginal ballooning mode gradient at all radii. The marginally stable value of β_T is 6.3% compared to the measured value of 5.9%. Within measurement uncertainty, this discharge is marginally stable to ideal ballooning modes.

Both discharges are calculated to be stable to external kink modes if the effect of a conducting wall at $1.5a$ is included to model the DIII–D vacuum vessel. The high β_N discharge (Fig. 3) is only marginally stable if the conducting wall is not included. A test to determine whether a discharge is close to the kink mode stability limit can be made by checking the stability of equilibria with the same discharge shape and plasma current and similar pressure profile but with higher total pressure. In this manner it was found that neither of the discharges in Figs. 2 and 3 is close to the kink mode stability boundary. In both cases, equilibria with β_N near 5.5 were found to be stable. This is consistent with the results of a numerical study of the kink mode stability boundary as a function of the shapes of the pressure and current profiles. In this study, for a typical DIII–D single-null divertor discharge shape with a conducting wall at $1.5a$, it was shown that with a sufficiently broad pressure profile and sufficiently peaked current profile, the kink mode beta limit could be as high as $\beta_N = 5.8$.

The data points shown as squares in Fig. 1 summarize the calculated stability limits for discharge shapes and profiles measured in several high β_N discharges. In all of these cases, the

calculated kink mode limit is equal to or larger than the ballooning mode beta limit. These calculated stability limits for typical experimental conditions define a curve at $\beta_N \approx 4.5$ to 5 at the lower current and at $\beta_N \approx 4$ at the highest current. Since all DIII–D discharges are located at or below this stability boundary, the experimental data is consistent with these theoretical predictions.

DIII–D discharges are, for the most part, sufficiently below the predicted ideal beta limit that observation of ideal instabilities in high beta discharges would not be expected. There are only two cases of evidence for ideal modes. First, in discharges which are calculated to be near the ballooning stability limit, there have been observations of fluctuations with relatively high frequency ($f \approx 200$ kHz) and toroidal mode number ($n = 5$ to 8) which may indicate the presence of ballooning modes. Second, a small number of discharges with $\beta_N \approx 3$ disrupted at the time of a sawtooth crash after the rapid growth ($\approx$30 μsec) of a non-rotating, $n = 1$ mode which appears to be an ideal, external kink. The ideal nature of the mode is indicated by the short growth time. The external nature is indicated by collapse of soft X–ray emission which occurs first at the plasma edge and by continued rotation of the plasma center after the non-rotating mode has grown to large amplitude. It is believed that these discharges are destabilized by transient pressure or current profiles that are created after a sawtooth crash on a time scale more rapid than heat diffusion times.

Phenomena that can make it more difficult to reach high values of β_N but that do not provide a fundamental upper limit to the value of β_T are distinguished by the ability to increase the value of beta even in their presence. In Fig. 1, the achieved values of β_N for $I/aB > 2.7$ are below the value 3.5 which is typical of lower current operation. This partially reflects the failure of confinement to increase with plasma current that is observed when $q_{95} < 3$. This occurs even at low beta. Sawteeth and ELMs can affect energy confinement, as in the discharge of Fig. 2. The existence of stable equilibria at beta values higher than the steady level during continuous ELMs is demonstrated in the earlier, ELM-free phase of the discharge. Heating and confinement can also be adversely affected by $n = 1$ fishbone modes, and $m/n = 3/2$ and $2/1$ resistive modes, all seen in Fig. 3.

In summary, the highest value of β_T in DIII–D so far is 9.3% and the highest value of β_N is 5, achieved in separate discharges. The discharges with the highest values of β_N give experimental evidence that, at least in a limited range of current, the limit to β_N must be at least as large as 5. These discharges are calculated to be near the theoretical stability limit which is predicted to be set by the ideal ballooning mode at a value of β_N between 4 and 5. The experimental data agree with the calculated stability limit in that all data are at or below the limit and most discharges show little evidence of ideal ballooning or kink mode activity.

REFERENCES

1. Ferron, J.R., *et al.* to be published in Phys. Fluids.
2. Troyon, F., *et al.* Plasma Phys. Contr. Fusion **26**, (1984) 209.
3. Sykes, A., *et al.* in Proceedings of Eleventh European Conference on Controlled Fusion and Plasma Physics, Aachen (EPS, Petit-Lancy, Switzerland, 1983), Vol. 2, p. 363.
4. Stambaugh, R.D., *et al.* Plasma Physics and Cont. Nucl. Fusion Research, (Proceedings of Tenth International Conference, London, 1984), IAEA, Vienna (1985), Vol. I, p. 217.
5. Keilhacker, M., *et al.* ibid, p. 71.
6. McGuire, K., *et al.* Plasma Physics and Cont. Nucl. Fusion Research, (Proceedings of the Eleventh International Conference, Tokyo, 1986), IAEA, Vienna (1987), Vol. I, p. 428.
7. Okabayashi, M., *et al.* ibid, p. 279.
8. Lao, L.L., *et al.* submitted to Nuclear Fusion.

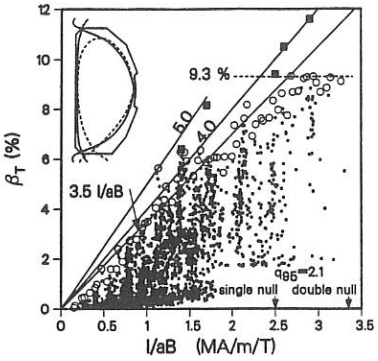

Fig. 1. The database of DIII–D discharges graphed as volume average toroidal beta vs the normalized current. The squares are the calculated, theoretical beta limit for several discharges.

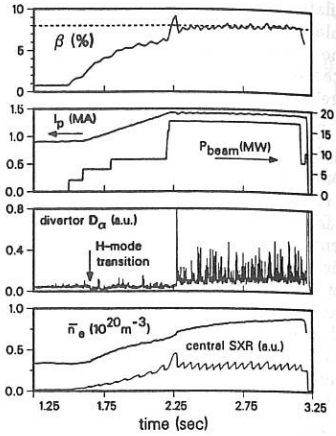

Fig. 2. Time evolution of a high current, high β_T discharge. $B = 0.8$ T, $I/aB = 2.9$, $q_{95} = 2.5$.

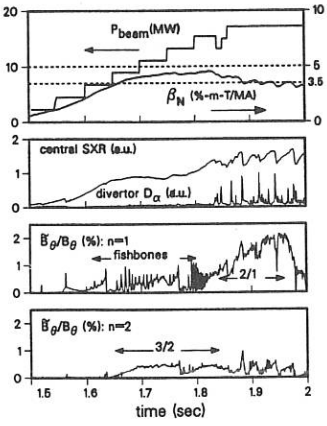

Fig. 3. Time evolution of a discharge with high normalized beta. $B = 0.8$ T, $I = 0.7$ MA, $I/aB = 1.4$, $q_{95} = 4.5$.

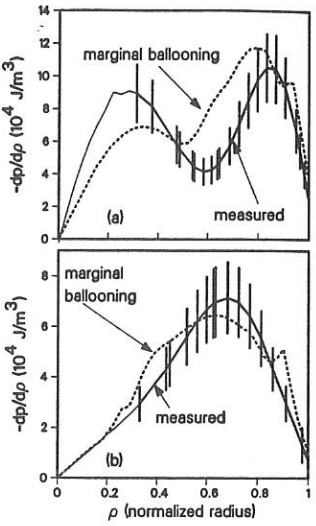

Fig. 4. Radial pressure gradients from the experimental equilibrium fit (solid line) and the calculated ballooning mode stability limit (dashed line). (a) A discharge with peak $\beta_T = 9.3\%$ and (b) a discharge with peak $\beta_N = 4.3$.

MHD CHARACTERISTICS AND EDGE PLASMA STABILITY DURING PERIODS OF ELM ACTIVITY IN PBX-M

S.M. Kaye, J. Manickam, N. Asakura[1], R. Bell, Y.T. Lau[2], B. LeBlanc, F. Levinton[3], C. Kessel, H. Kugel, S. Paul, S. Sesnic, and H. Takahashi

Princeton Plasma Physics Laboratory, Princteon University
Princeton, New Jersey, 08543 U.S.A.

Introduction

A common repetitive feature of H-mode plasmas is the so-called Edge Localized Mode (ELM), which is identified by a rapid increase in the D_α emission, denoting an increase in edge recycling, and is associated with a loss of plasma energy and density. In this sense, the term ELM is a misnomer, as the energy loss can extend into the core of the plasma, and, in some cases, can be coupled to internal activity [1]. The mechanism causing ELMs is still not well understood. It was initially suggested that ELMs in DIII-D could be due to microtearing modes [2], but later stability analysis of detailed profiles near the plasma edge indicated that "giant" ELMs may be triggered by the ideal ballooning instability [3]. In this work, we will show the existence of a high frequency magnetic precursor to ELMs, and we will present the results of stability analyses that indicate the pressure-driven ideal kink to be a likely candidate for driving these oscillations and, therefore, perhaps the ELM itself.

Data

The objective of the PBX-M tokamak is to explore regimes of enhanced plasma stability and confinement. Stability control is effected through the use of a set of close-fitting passive stabilizer plates and through active profile control [4]. Data for this work come from low Troyon parameter (I/aB~0.9 MA/m-T) D^+ plasmas with I_p=330 kA, B_t=1.3 T, n_e=6x10^{13} cm^{-3}, elongation of 1.9, indentation=15%, and 5 MW of D^0 injected power. The magnetic data to be shown come from a poloidal array of 20 Mirnov coils whose distance from the plasma surface is as small as several cm. The data were obtained at a sampling rate of 0.5 MHz.

Figure 1 is an example of a 3 msec period containing a giant ELM in a discharge near the β-limit with β_{pol}=2.0 and $\langle\beta_t\rangle$/(I/aB)=4. Shown in the figure from the top are two chord integrated traces from the horizontally viewing soft X-ray system (one chord viewing near the

[1] University of Tokyo, Tokyo, Japan

[2] University of Maryland, College Park, Md.

[3] JAYCOR Corp., Cal., U.S.A.

top and the other viewing at ≈a/2), raw signals from Mirnov coils situated on the outer midplane, top of the plasma, and on the inside major radius, and the D_α emission on the midplane. In this particular example, the ELM at 497.6 msec occurred during a period of continuous activity consisting of a 13 kHz m=3/n=1 and a 23 kHz m=3/n=2 component. Prior to the rapid rise in D_α that characterizes an ELM is a change in appearance of the Mirnov coil traces. The occurrence, at 497.25 msec, is the high frequency mode that will be shown in more detail. As is seen in the figure, the high frequency burst occurs prior to the drop in any of the SXR signals, also characteristic of ELMs, and thus it is taken to be an ELM precursor.

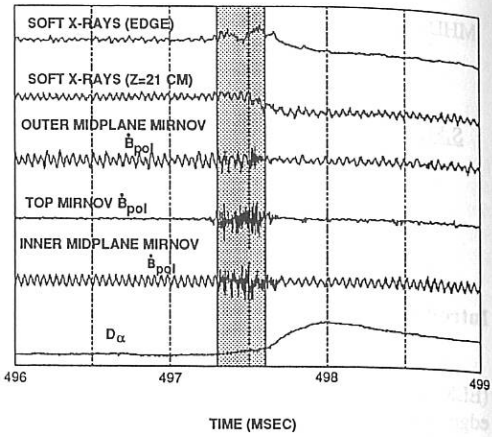

Fig. 1 Overview of ELM event

A 1 msec expanded view of the period that includes the ELM is shown in Fig. 2. The top trace in the figure is the raw Mirnov signal, the middle trace is the D_α signal, and the bottom trace is the Mirnov signal filtered from 200 to 240 kHz. The filtered trace clearly shows the high frequency mode amplitude growing on a time scale of 10 μsec. The burst persists for 350 μsec, and it disappears just prior to the rapid increase in the D_α signal. Spectral analysis of the poloidal and toroidal Mirnov coil arrays indicate the high frequency burst to be incoherent; thus, no poloidal or toroidal mode information could be extracted. One practical difficulty in this identification is the large uncertainty in phase due to the mode frequency being close to the Nyquist frequency (250 kHz) of the time trace. The high frequency precursor is not observed in any of the SXR signals, nor is it associated with any drop in neutron flux (usually associated with instabilities in the plasma core), indicating that the mode is most likely localized, or at the very least more prominent,

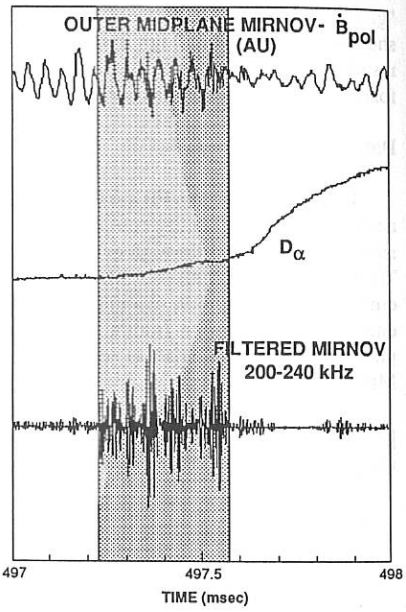

Fig. 2 Expanded time scale of ELM event

at the plasma edge.

To test whether the high frequency precursor is ballooning in character, we have examined the poloidal variation of the mode amplitude. Fig. 3 shows the mode amplitudes as a function of distance of closest approach to the plasma. Encircled in the figure are data from groups of coils on the inner and outer major radius sides. What is clear from the figure is that at comparable distances from the plasma, the inner major radius points exhibit higher amplitudes than those on the outer major radius side. Thus, we conclude that these high frequency ELM precursors are not outward ballooning in character.

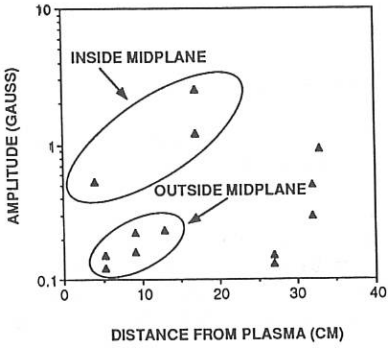

Fig. 3 High frequency mode amplitude as a function of distance between plates and plasma surface

Stability Analysis

In an attempt to determine the source for the high frequency precursor mode, and therefore perhaps the ELM itself, the stability of the edge plasma was studied using kinetic profile data obtained 1 msec prior to an ELM. The data used in the analysis consisted of T_e, n_e, T_i, Z_{eff}, and P_{rad} profiles in addition to a measurement of q(0) (=0.8) by the Motional Stark Effect diagnostic. The data were analyzed using the TRANSP transport code, and the resulting pressure profiles (including beam pressure calculated from a Monte-Carlo algorithm) and current profile (from a self-consistent solution of the Grad-Shafranov equation using the pressure profile and measured q(0) value) were input into the PEST [5] ideal stability code. The data were also analyzed for stability with respect to microtearing modes. The results of these analyses indicated that the edge plasma was stable to microtearing and to ideal ballooning modes (for $n \leq 25$). For $n \geq 25$, a marginal condition with respect to ideal ballooning could be obtained within experimental error; however, it is believed that finite Larmor radius effects would stabilize these high-n ballooning modes. This last result, coupled with the results shown in Fig. 3, make ballooning an unlikely candidate for our case.

The PEST calculations indicate, though, that the n=1 to 3 ideal kink modes are unstable with no conducting wall present. The n=1 mode would be stabilized by a closed, ideal-conducting shell at $r_{wall}/a \approx 1.45$, which is the just inward of the actual position of the plates relative to the plasma in this high-β_{pol} case. For a wall at $r_{wall}/a = 1.55$, the calculations indicate that the n=1 mode consists of many m-components, which would make even toroidal mode identification difficult, with the mode amplitude greatest near the plasma edge. The amplitude on the inner major radius side is expected to be greater than that on the outer major radius side. The growth time of the mode is predicted to be on the time scale of the poloidal Alfven time (μsec), and is consistent with the observed growth times. Furthermore, stability analysis of profiles obtained 2 msec after and ELM indicate the plasma to be more stable to the pressure-driven ideal kink in that this mode is stabilized by a wall farther from the plasma (by a factor of 2) than in the pre-ELM case. Consequently, we suggest the pressure-driven ideal

kink to be a candidate for the high frequency ELM precursor mode, and perhaps the ELM itself.

Conclusions

In summary, we have presented a new observation of a high frequency precursor to an ELM event, and have suggested, based on stability calculations that a likely candidate for this mode, and thus for the ELM, is the pressure-driven ideal kink. This is not meant to dispute the claim by DIII-D that giant ELMs are triggered by ideal ballooning. The ELM, as we characterize it, is a rapid increase in the D_α emission and a loss of plasma energy and density. It is probable that any strong instability localized or prominent near the plasma edge can trigger these effects. It is therefore reasonable to conclude that either or both ballooning and kink modes are possible candidates for driving ELMs.

The PBX-M project is supported by the U.S. Dept. of Energy Contract No. DE-AC02-76-CHO-3073.

References

[1] H. Kugel et al., in Proceedings of the Fourteenth European Conference on Controlled Fusion and Plasma Physics, Vol. 11d, Part I (1987) 185.
[2] N. Ohyabu et al., Nucl. Fusion 29 (1989) 475.
[3] P. Gohil et al., Phys. Rev. Lett. 61 (1988) 1603.
[4] M. Okabayashi et al., in Proceedings of the Twelfth International Conference on Controlled Fusion and Plasma Physics, Nice, IAEA, Vol 1 (1987) 97.
[5] R. Grimm et al., Methods of Comput. Phys. 16 (1976) 253.

RESONANT MAGNETIC PERTURBATIONS AND DISRUPTION STUDIES ON COMPASS-C

A W Morris, R Fitzpatrick, P S Haynes, T C Hender, J Hugill, C Silvester, T N Todd

AEA Technology, Culham Laboratory/Euratom Fusion Association, Abingdon, Oxon, U.K.

Introduction

One of the aims of the COMPASS programme is control of instabilities and disruptions. The first phase of the experiment is conducted with a thin circular vessel with relatively low aspect ratio ($R = 0.56$m, $a_{lim} = 0.2$m, $I_p \lesssim 200$kA, $B_\phi \leq 1.7$T, 0.7mm s/steel vessel), but with the full poloidal field shaping system, allowing, for example, formation of separatrix bounded plasmas with an inboard x-point. Outside the vessel a large number of saddle coils are installed for the production of resonant magnetic perturbations (RMPs), and a flexible high power ECRH system allows good control of the plasma heating profile. In this paper the effect of RMPs (with poloidal and toroidal mode numbers m,n dominantly 2,1; 3,2; 1,1; and 2,1+3,1) on sawteeth, MHD activity and disruptions is investigated. Initial results on sawtooth control with ECRH are presented.

Resonant Magnetic Perturbations

In order to perform controlled studies of applied helical fields, it is necessary that any error fields from the poloidal field coils be nulled. On COMPASS this was achieved by means of 16 high sensitivity pickup coil packages (B_R, B_ϕ, B_z) which allow measurement of low-n perturbations. The poloidal field coils can be shifted, tilted and their ellipticity adjusted *in situ* to minimise error fields, with the result that error fields below 0.5Gauss for $n = 1$ ($\lesssim 5 \times 10^{-4} B_\theta$) with respect to the toroidal magnetic field axis have been achieved. There are 10 toroidal conductors on each quadrant of COMPASS-C (Figure 1), which can be connected in almost any configuration, driven by three independent transistor amplifiers, giving $\lesssim$ 1.2kA in each conductor (only quasi-static perturbations are described in this paper).

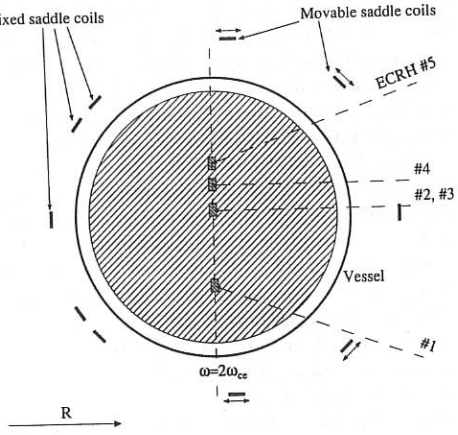

Figure 1 *Cross-section of COMPASS-C showing saddle coils and ECRH injection geometry*

Perturbations with $m,n = 2,1$; 3,2 and 1,1 were applied separately to sawtoothing discharges ($I_p = 100$kA, $B_\phi = 0.6 - 1.0$T, $\bar{n}_e \lesssim 5 \times 10^{19}$m^{-3}) to study the effect on sawteeth and the discharge in general. The field levels were $\sim$ 10Gauss, corresponding to island widths of a few cm (neglecting plasma response) and for $m,n = 1,1$ both resonant and non-resonant helicities were used. There is no substantial change in the sawtooth behaviour : the period, amplitude, precursor activity and heat pulse propagation are all essentially unchanged. Experiments on other devices [1, 2, 3] which have shown some effect have usually used larger perturbations.

For the 3,2 fields, however, the evolution of $\bar{n}_e$ is changed: $d\bar{n}_e/dt$ is reduced with the RMP for the same gas feed programme.

Studies of the density limit have been performed with 1,1; 3,2 and 2,1 perturbations. Only the 2,1 field has a significant effect on the density limit at the levels used (*cf* CLEO where 3,2 fields were best [4]): an increase of up to $\sim$ 15% for $q_\psi(a) \simeq 4.3$ (Figure 2). This is manifest as a delay in the disruption and *increased* rate of rise of $\bar{n}_e$ for the same gas feed rate. There is no obvious change in the H_α or CII radiation from the plasma periphery (3 locations) as the RMP is applied. The $m = 2$ MHD activity is not much affected except just before the disruption (*i.e.* above the normal density limit), but it is to be noted that at this q_ψ disruptions are not stimulated at the maximum saddle current presently available, and $I_{m=2}(\textit{stabilise}) \gtrsim 0.6 I_{m=2}(\textit{disrupt})$ usually (see below). Full mode-locking is not observed, but the distortions that characteristically precede locking are observed when the mode has evolved to large size and low frequency, just before disruption (Figure 2). The final mode growth and deceleration is enhanced with the RMP, when the free energy for the instability is probably larger since the density is higher.

Stabilisation of the 2,1 mode is observed, however, in the low density discharges studied, when there is a 2,1 mode at $\sim$ 15kHz and $\sim 0.1\% B_\theta$. The amplitude decays into the noise for $I_{m=2} \gtrsim 500$A ($B_r(2,1) \sim 0.4\% B_\theta$ at a_{lim}) in a time that can be as small as $\sim$ 2ms from the start of the RMP. The frequency falls by $\lesssim 2 - 3$kHz *i.e.* the mode appears to be stabilised rather than locked. This timescale is similar to that predicted with a Δ' code for poloidally symmetric flattening of $T_e(r)$ and hence $J_\phi(r)$ over a small region near $q = 2$. Velocity gradients near $q = 2$ caused by the mode-locking torque lead to an alternative stabilisation mechanism: the effect is stronger for small islands [5]. The difference from the high $\bar{n}_e$ results where stabilisation is not seen may be due to these discharges being more unstable, *i.e.* requiring more flattening, or to reduced rotation-stabilisation for the larger modes observed.

Disruptions may be stimulated far from the normal operation boundaries if the saddle current is sufficiently high. The disruption occurs when the island almost touches the limiter, supporting the idea that full reconnection occurs just before disruption. In some cases the disruption occurs several ms after I_{saddle} has reached its maximum value. Figure 3 shows a stimulated disruption when a 3,1 field is added to an existing 2,1 RMP (with $I_{m=2} \simeq 0.9 I_{m=2}(\textit{disrupt})$) in a $q_\psi \simeq 3$ low $\bar{n}_e$ discharge. The disappearance of the sawtooth and reduction in central SXR emission suggests that the core confinement is indeed affected just before disruption. In this case, simple island width calculations are consistent with the disruption being related to interaction between the 2,1 and 3,1 islands. Note that the small($\sim$ 10%) toroidal 2,1 sideband of the 3,1 saddle should be added in quadrature as the saddle is displaced 90° toroidally, so the notionally 3,1 RMP should not directly increase the 2,1 island width. These discharges are similar (or even the same) as those where stabilisation is observed. Applying rotation-modified reconnection theory [5] to this data implies that only partial reconnection occurs in the stabilisation process, and that full reconnection only occurs when I_{saddle} exceeds a sharp threshold level.

For all types of disruptions in OH discharges examined to date on COMPASS-C, I_p, falls to zero in $\gtrsim$ 1ms, *i.e.* $dI_p/dt \lesssim 2 \times 10^8$A/s.

ECRH sawtooth stabilisation

Various experiments have shown some effect of ECRH on sawteeth [6], but with different requirements on the ECR location. Initial experiments with ECRH ($P_{inj} \sim 150$kW) have shown *prompt* removal of the sawtooth for the resonance located between $r_{q=2}$ and sawtooth inversion radius rather than at r_{inv}. In these discharges on COMPASS-C there is no lengthening of

the sawtooth period before stabilisation (Figure 4) (the later reappearance of the sawtooth is believed to be due to changes in the power deposition profile as $\bar{n}_e$ evolves in these discharges).

Conclusions

A wide variety of RMP experiments have been performed on COMPASS-C showing that *(i)* the OH density limit may be improved by up to $\sim$ 15% using 2,1 perturbations, but that a 3,2 field has no such beneficial effect; *(ii)* stabilisation (not locking) of $m = 2$ modes is seen and rotation effects may be a possible mechanism without large islands being formed; *(iii)* the influence on the sawtooth of 1,1; 3,2; 2,1 fields is weak in experiments to date, suggesting that large magnetic islands are not be formed; *(iv)* stimulated disruptions may be produced either by a single (2,1) RMP, or by combining 3,1 and 2,1 RMPs, consistent with large driven islands in this case. The sawtooth can be influenced by ECRH, however, with prompt removal occuring when the heating resonance is somewhat outside the sawtooth inversion radius.

Acknowledgements

The authors are grateful for the help of the COMPASS operation team under P C Johnson, and the ECRH team under A C Riviere, and for the support of D C Robinson.

[1] Y Huo et al. *Proc. 12th IAEA conf, Nice*, **1**, 137, 1988.

[2] F Karger et al. *Proc. 6th IAEA conf, Bechtesgaden*, **1**, 274, 1976.

[3] G Nothnagel et al. *Proc 16th European Conf (Venice)*, **2**, 489, 1989.

[4] T N Todd et al. *Proc 14th European Conf (Madrid)*, **1**, 230, 1987.

[5] T C Hender and R Fitzpatrick. *"Interaction of resonant perturbations with rotating plasmas", this conference*

[6] TFR group *Nuclear Fusion*, **28**, 1995, 1988.

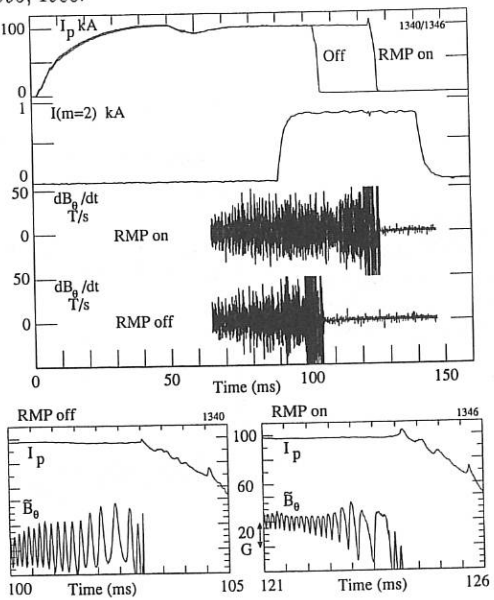

Figure 2 Enhancement of Ohmic density limit by 2,1 helical perturbation. $q_\psi(a) \simeq 4.3$ $\bar{n}_e(max) = 4.4\times10^{19}, 5.2\times10^{19}$ with RMP off and on respectively. The disruption precursors are expanded.

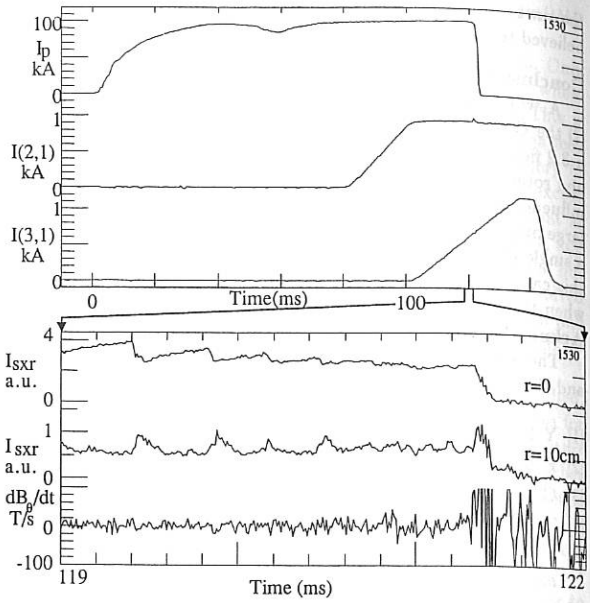

Figure 3 Disruption stimulated by applied $m, n = 2, 1 + 3, 1$ perturbations.

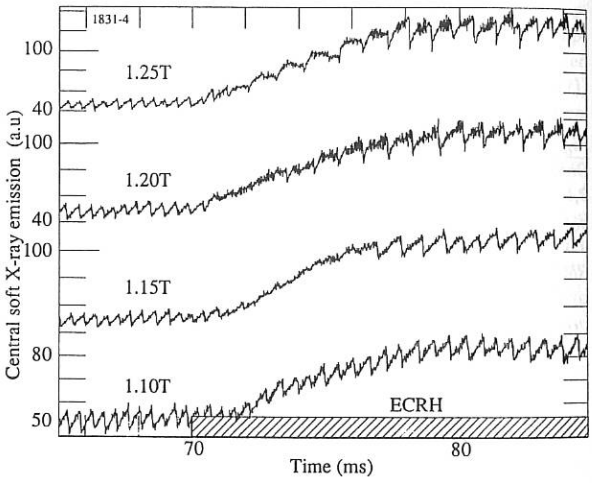

Figure 4 The influence of ECRH (lines #2,#3) on sawtooth activity as the resonance position is scanned. $I_p = 100kA$.

STABILISATION OF SAWTOOTH OSCILLATIONS BY TRAPPED ENERGETIC PARTICLES IN TEXTOR.

J. Ongena, R.R. Weynants, H. Conrads, P. Cornelissen, H. Kever, A.M. Messiaen

Laboratoire de Physique des Plasmas - Laboratorium voor Plasmafysica
Association "Euratom-Etat belge" - Associatie "Euratom-Belgische Staat"
Ecole Royale Militaire - B 1040 Brussels - Koninklijke Militaire School
and
Institut für Plasmaphysik, Forschungszentrum Jülich GmbH, Association EURATOM-KFA,
D-5170 Jülich, FRG.

1. INTRODUCTION.

Sawtooth stabilisation for more than two seconds (corresponding to the maximum heating pulse length) can be achieved in TEXTOR in deuterium discharges by means of neutral beam co-injection. The parameter domain where sawtooth-free operation prevails is larger with D^0 than with H^0 injection. The sawtooth period is found to be much more resistant to changes by counter beams. Although ICRH can stretch the sawtooth period, it never succeeds in full stabilisation. In combination with NI, however, ICRH is capable of extending the operational stabilised domain.

In this paper we present the experimental data, show that q stays below 1 in the sawtooth-free phase and interpret the results in terms of stabilisation of the resistive internal m = 1 mode by trapped energetic ions. The creation of trapped hot-ions populations strongly peaked inside the q = 1 surface is apparently essential for stabilisation. The differences between NI-co, Ni-cou and ICRH can be understood by the differences in power deposition profiles in TEXTOR.

2. EXPERIMENTAL RESULTS.

Neutral beam [1] co-injection proves to be very efficient in stabilising sawteeth in TEXTOR. The co- and cou-beam characteristics are D^0 or H^0 injection in deuterium plasmas at 50-55 kV injection voltage delivering 1.6 to 1.75 MW to the torus. Because of the excellent pumping capabilities of the boronized walls, operation at low density is possible, which turns out to be essential for sawtooth-free conditions.

Figure 1 shows the evolution of the central electron temperature T_{eo} for a sequence of discharges in which identical D^0 beams are injected at t = 0.8 s in discharges of varying density. In some discharges an additional ICRH pulse is applied of power and pulse shape also shown in Fig. 1. From (a) to (d) the line averaged density during the beam phase drops from $\bar{n}_e$ = 3.0 to 2.4, 1.7 and 1.4 x 10^{13} cm^{-3} resp. A progressive stretching of the sawtooth period τ_{st} is seen ending in complete sawtooth stabilisation at densities below $\bar{n}_e$ = 1.55 x 10^{13} cm^{-3}.

Figure 2 shows the evolution of τ_{st} as a function of $\bar{n}_e$ for 5 different conditions: (i) H^0 co-injection at I_p = 340 kA, (ii) D^0 co-injection at I_p = 340 kA, (iii) D^0 cou-injection at I_p = 340 kA, (iv) D^0 injection at I_p = 465 kA, (v) D^0 injection supplemented by 1.4 MW of ICRH at I_p = 340 kA, . In all cases except for counter injection, τ_{st} strongly increases with decreasing $\bar{n}_e$. One notes an isotope (favouring D^0 to H^0) and I_p dependence. Whereas ICRH alone [2] provides some prolongation of τ_{st}, its efficiency in this respect is much lower than that of NI. In combination with NI, however, ICRH is capable of extending the operational stabilised domain.

3. CENTRAL q-VALUES IN STABILISED SAWTEETH.

It is important to establish whether the sawtooth activity ceases as the result of the disappearance of the q =1 surface from the plasma [3], or whether at all times the central q value stays below one [4]. The former situation could arise from a flattening of the current profile brought about by the extra current driven by the beam, whereas the latter asks for a mechanism affecting the m=1 activity which is usually held responsible for the sawtooth relaxation[5]. As no polarimetric data are available for the present shot series, we extract the pertinent information from the experimental data on the evolution of the inversion radius and simulations thereof by means of the TRANSP code. Neo-classical conductivity is assumed to prevail.

The closed symbols in Fig. 3 show the variation of the inversion radius (defined as the radius where the T_e profiles, taken 1 ms before and 1ms after the crash and derived from 9 channels of ECE emission, cross-over) versus the plasma density for cases (i) (triangles) and (ii) (circles) of Fig. 2. It is apparent that for both cases the inversion radius increases with decreasing $\bar{n}_e$. These data then show that during the approach to stabilisation (which is effectively achieved for the lowest densities in the D^o case) the inversion radius r_{inv} is monotonically increasing. The open symbols in Fig. 3 represent simulations by means of TRANSP of the radius at which q equals unity. Except for a constant offset of 2 to 3 cm, this radius is seen to track r_{inv} quite well. The same offset is also found in the ohmic discharges pertaining to this density range, and has been confirmed by polarimetric measurements in ohmic discharges [6].

Since TRANSP is capable of correctly predicting the evolution of the q=1 surface, one can also trust the computed values of q(0). For the conditions of Fig. 3, q(0) slowly changes from about 0.78 at $\bar{n}_e = 4 \times 10^{13}$ cm^{-3} to 0.72 at $\bar{n}_e = 1.4 \times 10^{13}$ cm^{-3}, in agreement with the growth of the q = 1 surface. Sawtooth stabilisation is thus accomplished while q(0) is significantly below unity.

4. COMPARISON WITH THEORIES ON STABILISATION.

A sawtooth cycle usually consists of two stages: a first one during which the current on axis rises on a resistive time scale, and a second , much shorter, phase which begins with the explosive growth of an island leading to reconnection. This large disparity in time scales recently has led to the proposal of a semi-emperical scaling for the sawtooth period [7], purely based on the phenomenology of the first phase. For TEXTOR parameters, this scaling reads τ_{st} [ms] = 28 $T_e^{1.5}$ Z_{eff}^{-1}. The experimentally observed periods of the sawteeth only roughly match the scaling-law prediction of 35 ms at the highest densities. The maximum value predicted at low density amounts to about 55 ms, due to a partial compensation of the temperature increase by a rise in Z_{eff} [8]. We therefore conclude that in the experiment at low density the period is prolonged by a strong reduction in the growth rate of the instability responsible for the sawtooth crash.

Several authors [9-11] have studied the influence of high-energy particle populations on the stability of global modes. In Ref. 11, hot trapped-ions are found to produce a major modification of the MHD theory of the resistive m=1 tearing mode, such that sawtooth stabilisation occurs when the trapped hot-ion poloidal beta β_{ph} at the q = 1 radius ($r=r_o$) exceeds a critical value .

The decisive role of β_{ph} appears to be borne out also in our experiments as can be seen from Fig.4 where the sawtooth period is plotted versus β_{ph} for the data points of Fig. 2, cases (i)-(iv). The definition of the trapped hot-ion β_{ph} used here is that for isotropic hot-ion distributions [12]

$$\beta_{ph} = - \varepsilon_o^{1/2} \; [8\pi/B_p^2(r_o)] \; \int_o^1 \; dr \; r^{3/2} \; d \; (p_{\perp h}) / \; dr, \qquad (1)$$

where $p_{\perp h}(r)$ is the perpendicular component of the hot-ion pressure tensor and is obtained from TRANSP for the pure beam cases; $r \equiv r/ r_o$, where r_o is the experimental inversion radius. The beam injection angle in TEXTOR is such that the actual distribution is characterised by $p_{\| h} \approx 4 \; p_{\perp h}$. We presume that Equ. (1) is a valid first approximation for this relatively weak anisotropic distribution. Each data set exhibits a monotonic increase of τ_{st} with β_{ph} , however at a different rate which presumably depends upon the proximity of the critical beta above which complete stabilisation is achieved. In Ref. 11 e.g., the critical beta is defined as

$$\beta_{ph,c} = | \Lambda_K (0)|^{-1} \; (s_o / \varepsilon_o) \; [\lambda_H + |\varepsilon_\eta \; \omega_A / \; \omega_{di}|^{1/2}]. \qquad (2)$$

and depends on the value at r_o of the shear s_o , the aspect ratio ε_o, the Alfven frequency ω_A , the diamagnetic frequency ω_{di}, the parallel resistivity (through ε_η) and the ideal MHD stability parameter λ_H. The reader is referred to Ref. 11 for further notations. Given the fact that the thermal plasma components are essentially identical [8] in cases (i) and (ii), one expects the pertaining data set indeed to coincide. Changing either the current or the beam direction brings about significant changes in r_o and s_o such that sets (iii) and (iv) should behave quite differently.

Work on more detailed comparisons with theory is in progress. Figure 4 appears, nevertheless, at this stage already to allow the following conclusions:

1. The sawtooth period reacts to the hot particles trapped inside the q = 1 radius.
2. D injection is more efficient because of stronger beam components.
3. The counterbeams produce much smaller β_{ph} . Although significant beam components are produced their spatial distribution is very different from the counter case. This is partly due to the different evolution of the density (more peaked than co) and temperature profiles (broader than co), partly to the differences in the particle orbits. The pertaining $\beta_{ph,c}$ also appears to be higher.

The pure ICRH or combined ICRH-NI operation can not yet be treated by our TRANSP code. Both theory and experiments [13] have shown the RF deposition profiles to be much broader than the co-beam ones. It is further found experimentally [8] that a strong interaction of the ICRH with the beam ions occurs which significantly enhances $p_{\perp h}$ such that in this case a strong stabilising effect should result.

References.

[1] H. Conrads, H. Euringer, F. Hoenen, et al., Proc. 16th Eur. Conf. on Contr. Fus. and Plasma Phys., Venice 1989, Eur. Conf. Abstr. Vol. 13B, part 3, p.1221.
[2] R.R. Weynants, M. Gaigneaux, J-M. Beuken, et al, Proc. 16th Eur. Conf. on Contr. Fus. and Plasma Phys., Venice 1989, Eur. Conf. Abstr. Vol. 13B, part 1, p.7.
[3] F.X. Söldner,K. McCormick, D. Eckhartt, et al, Phys. Rev. Let. **57** (1986)1137.
[4] D.J. Campbell et al, Phys. Rev. Let. **60** (1988) 2148.
[5] J. Wesson, in *Tokamaks*, Oxford Science Publications, Clarendon Press, Oxford, 1987.
[6] H. Soltwisch, private communication.
[7] W. Park and D.A. Monticello, PPPL Report 2601, Princeton Laboratory, 1989.
[8] A.M. Messiaen, et al, invited paper at this conference.
[9] L. Chen, R.B. White, and M.N. Rosenbluth, Phys. Rev. Lett. **52** (1984)1122.
[10] Y.Z. Zhang, H.L. Berk, and S.M.Mahajan, Nucl. Fusion **29** (1989)848.
[11] B. Coppi, P.Detragiache, S. Migliuolo, et al, Phys. Rev. Lett. **63**(1989)2733.
[12] B. Coppi, S. Migliuolo, F. Pegoraro, and F. Porcelli, JET Report P(89)22.
[13] R.R. Weynants, J-M. Beuken. L. De Keyzer, et al, Plasma Phys. and Contr. Fusion Research 1988 (IAEA Vienna), vol. 1,p.571.

FIG. 1 Temporal evolution of T_{e0} for densities decreasing from (a) to (d). When present, the additional ICRH pulse is also indicated.

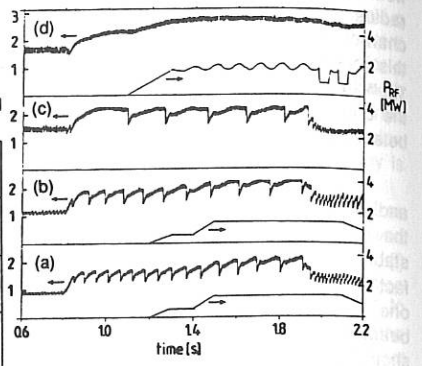

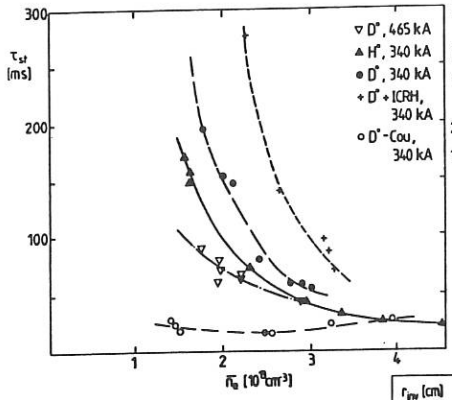

FIG. 2 τ_{st} *vs* $\bar{n}_e$ for 4 conditions with co-injection and one with counter.

FIG. 3

Variation with $\bar{n}_e$ of experimental inversion radius (closed symbols) and computed q = 1 radius (open symbols) for H (triangles) and D (circles) co-inject. at I_p = 340 kA.

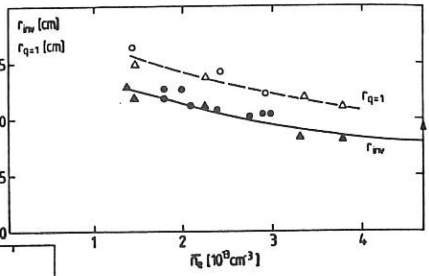

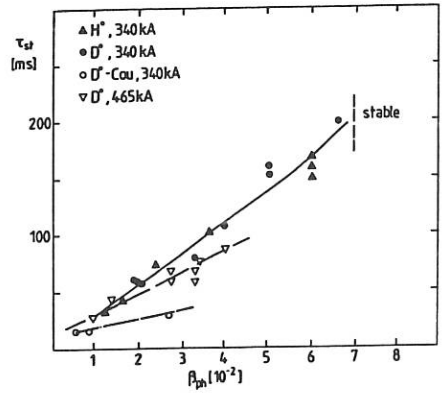

FIG. 4 τ_{st} *vs* β_{ph} for the conditions of Fig. 2.

PRODUCTION OF HIGH POLOIDAL BETA EQUILIBRIA LIMITED BY AN INBOARD SEPARATRIX IN TFTR

S. A. Sabbagh, R. A. Gross, M. E. Mauel, G. A. Navratil
Columbia University, New York, NY U.S.A.

M. Bell, N. Bretz, R. Budny, M. S. Chance, E. Fredrickson, R. J. Hawryluk, A. Janos, S. C. Jardin, D. McCune, K. McGuire, D. Mueller, D. K. Owens, R. Wieland, M.C. Zarnstorff
Plasma Physics Laboratory, Princeton University, Princeton, NJ U.S.A.

J. Kesner, E. Marmar, J. Terry
Plasma Fusion Center, M.I.T., Cambridge, MA U.S.A.

Recent experiments in TFTR have achieved high β_p plasma equilibria that exhibit a natural inboard poloidal field null. Values of $\Lambda \equiv \beta_p + l_i/2 \geq 6$, and $\varepsilon\beta_{p,dia} \equiv 4\varepsilon \int p_\perp dV / \mu_0 R_p I_p^2 \geq 1.3$ were attained, surpassing an apparent limiting value of $\varepsilon\beta_{p,dia} \leq 0.7$ previously observed in TFTR supershots.[1] Here, R_p is defined as the area averaged major radius. These plasmas were achieved up to and perhaps beyond the Troyon limit. While tokamak equilibria of this type have been produced transiently in experiments on the HBT tokamak[2] and values of $\varepsilon\beta_p \sim 1$ without an inboard null have been produced in HBT, DIII-D,[3] and Versator II,[4] these are the first experiments to demonstrate an inboard poloidal field null at high $\varepsilon\beta_p$ sustained for many energy confinement times in a large, neutral beam heated device.

The discharges were formed with $B_t = 4.9$ T, $R_p = 2.45$ m (nominal), at low plasma current (I_p = 280-500 kA) corresponding to cylindrical safety factors between 22 and 12. Neutral beam heating usually began with co-injection only. Subsequently, counter-injected beams were added to provide balanced injection at 18-22 MW during the high $\varepsilon\beta_p$ steady state. Line-averaged target densities were in the range $1\text{-}3 \times 10^{19}$ m^{-3} and typically increased to $3\text{–}4.5 \times 10^{19}$ m^{-3} during the auxiliary heating phase. Two plasma current time histories were employed prior to neutral beam injection: (i) constant current and (ii) current ramp down. In the constant current case shown in Fig. 1a, the ohmic target plasma was formed with $I_p \approx 300$ kA and held for 2 sec prior to neutral beam injection. In the current ramp-down case shown in Fig. 1b, an ohmic plasma was formed with 850 kA and held for about 1 sec. The plasma current was then decreased (I_p ramped down) rapidly (2.5 MA/sec) to a value $I_p \approx 400$ kA and held constant. The highest values of $\varepsilon\beta_p$ were obtained in the ramped down plasmas when neutral beam injection was initiated shortly before or at the time the lower value of current was achieved. In these discharges, the peak ion and electron temperatures were as high as 11 keV and 5 keV, respectively. In the constant I_p discharges, the peak ion and electron temperatures were as high as 5.5 keV and 3 keV.

When the value of Λ exceeded approximately 4.5 during the neutral beam phase, a poloidal field null was observed at the inner wall of the vacuum chamber, causing a transition from a discharge limited on the inside wall, to a naturally diverted discharge, as expected for equilibria with very high values of $\varepsilon\beta_p$. The initially circular ohmic plasma assumed a highly oblate shape with $\kappa \sim 0.7$ at the maximum values of Λ achieved. Separatrix formation was confirmed by the direct measurement of B_p on the inside wall (shown in Fig. 1), an abrupt

drop in the H_α intensity seen from the chord viewing the inside wall on the mid-plane (shown in Fig. 1) followed shortly thereafter by a drop in the H_α intensity seen from the chord viewing just above the mid-plane, a video camera with a tangential view of visible radiation from the plasma, and an MHD model fit to the equilibrium based on external and internal magnetic measurements. Diverted discharges were maintained for up to 0.3 sec, limited by the length of the neutral beam pulse used.

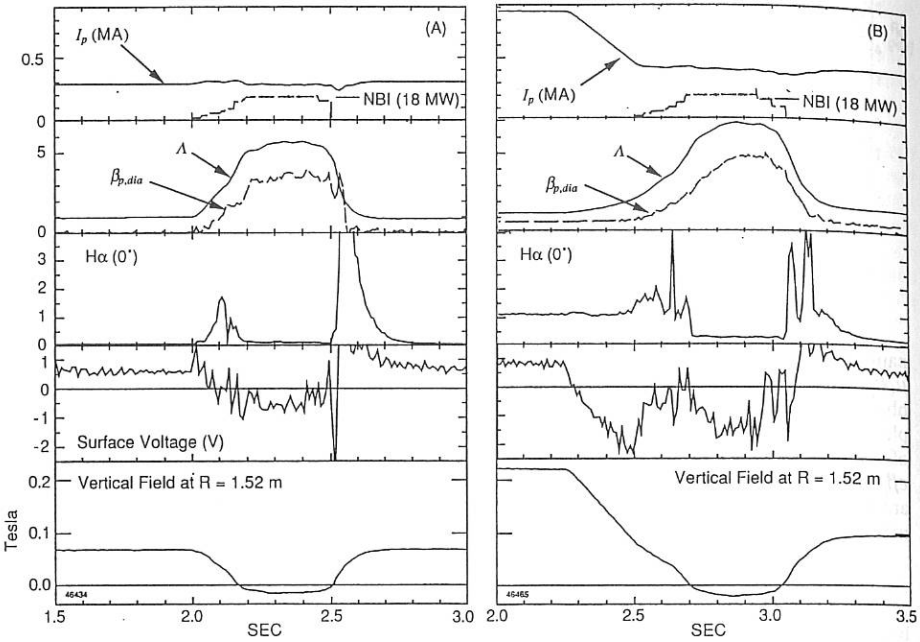

Figure 1. Data illustrating the time evolution of both a constant-I_p discharge (a) and a discharge with a current ramp-down (b). From top to bottom, the signals are (i) the plasma current and neutral beam power, (ii) $\Lambda = \beta_p + l_i/2$ and $\beta_{p,dia}$, (iii) the midplane H_α detector, (iv) the surface voltage, and (v) the inboard vertical field monitor showing reversal as the plasma becomes limited by the separatrix.

Maximum values of Λ and stored energy were achieved in the case of current ramp-down to 400 kA prior to neutral beam injection. In these cases, the energy confinement time is estimated to be about 50 msec. This can be compared with an L-mode[5] value of about 15 msec for these parameters. Estimates of the peak stored energy in the thermal plasma and unthermalized beam ions is estimated to be as large as 1 MJ. No disruptions or large scale MHD activity were observed for the constant current discharges that achieved a value of Λ = 5.5. Soft x-ray measurements showed a very quiescent plasma interior, although some discharges had low-level fluctuations at the edge. However, while these constant I_p discharges had values of $\varepsilon\beta_p > 1.3$, the normalized toroidal beta, $\beta_N = \beta_t aB_t/10^{-8}I_p$ was less than 3. In

current ramp down cases, MHD quiescent plasmas operated with β_N as large as 3.9, but disruptions occurred when β_N reached values near 4.5.

For large values of β_p, large levels of neoclassical bootstrap current[6] are expected if ν^* is less than 1. For equilibria with the largest values of Λ, the plasma was collisionless with central values of $\nu^*_i \sim \nu^*_e \sim 0.1$. Approximately 0.3 V-sec of poloidal flux was removed from the plasma during the ohmic current ramp down from 850 kA to 400 kA. During the neutral beam heated phase, the surface voltage became strongly negative (as shown in Fig. 1b) and the plasma expelled about 0.4 V-sec of poloidal flux while the total plasma current remained approximately constant at 400 kA. For the 300kA constant current discharges that had a smaller, but still significant loop voltage reversal, initial calculations indicate that roughly 25% of the total current is due to the bootstrap effect. Further analysis is needed to quantify all possible contributions to this negative surface voltage before an accurate value for the bootstrap current contribution can be determined. Although balanced co- and counter tangential injection was used, significant beam driven current is expected due to the effects of differential losses and orbit shifts.

A least-squares "best-fit" free-boundary equilibrium representative of the high $\varepsilon\beta_p$ constant current discharges was reconstructed[7] using (i) magnetic field data measured by external flux loops and pickup coils, (ii) the measured values of the plasma and EF coil currents, and (iii) measurements of the internal profile of the poloidal field obtained with a diagnostic using the injection of lithium pellets.[8] Data from 14 similar shots were used to obtain the average and variance of the measurements. The reconstruction consisted of finding the plasma current in terms of polynomial expansions of the gradients of the pressure and toroidal flux that minimize the normalized sum of the squares of the errors between the data and reconstruction. This technique enables the estimation of the $q(\psi)$ and $p(\psi)$ profiles. The model assumes that the pressure was isotropic and that the measured errors were statistically independent. The resulting "best-fit" equilibrium is shown in Fig. 2. The magnetic axis

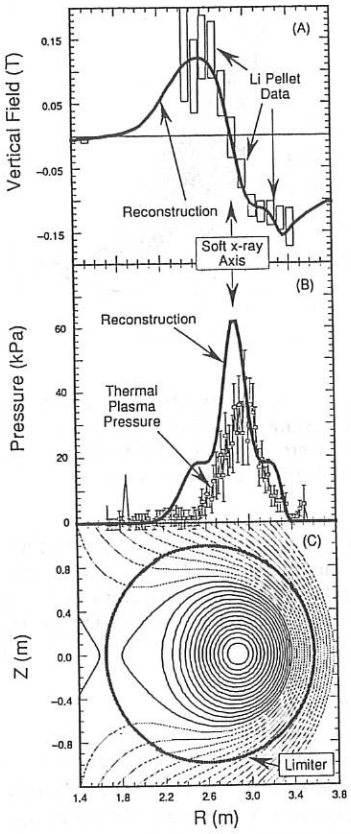

Figure 2. An illustration of the least-squares "best-fit" free-boundary reconstruction of the average of 14 similar constant I_p = 300kA discharges. From top to bottom, (a) the midplane poloidal field as measured from the Li pellet and as reconstructed, (b) the midplane thermal plasma pressure and the reconstructed pressure profile, and (c) the reconstructed poloidal flux, ψ, contours.

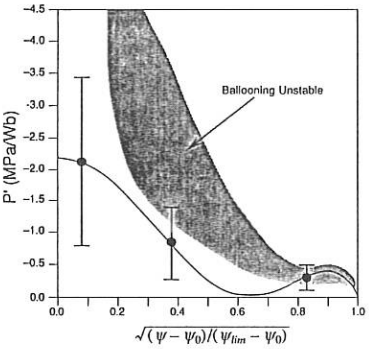

Figure 3. Stability diagram for equilibrium shown in Fig. 2. The error bars were produced from a statistical analysis of the experimental data.

measured by the Li pellet diagnostic agreed with that determined by a multi-chord soft x-ray diagnostic. The reconstructed pressure exceeds the thermal plasma pressure (computed from measurements assuming a carbon impurity with Z_{eff} = 3.5), and this difference probably represents the contribution of the unthermalized beam particles. Other equilibrium parameters for the constant I_p = 300kA discharges are Λ = 5.1 ± 0.33, $\varepsilon\beta_p$ = 1.3 ± 0.12, l_i = 1.2 ± 0.19, and $q(0)$ = 1.6 ± 0.55.

Ideal MHD ballooning stability analysis of the reconstructed, two-dimensional equilibria was performed for the constant current case of Fig. 2. The resulting stability diagram is shown in Fig. 3. Within the error bars of the reconstructed p and q profiles, it is found that the flux surfaces lie primarily in the first stable region. Although the edge flux surfaces are computed to lie in the unstable region, the uncertainty of the equilibrium profile fit near the edge prevents an accurate assessment of their stability. It should be noted that the ideal MHD stability calculation may be pessimistic, since it does not include stabilizing effects of finite Larmor radius that could be large in these relatively low current plasmas. Further equilibrium reconstruction and stability analysis of the constant I_p, and current ramp down cases with larger values of β_N is in progress.

This research is sponsored by the U.S. Department of Energy under contracts DE-FG02-89ER53297, DE-AC02-76-CHO-3073, and DE-FG02-90ER54084.

References

1 McGuire, K., et al., *Plasma Physics and Controlled Fusion* **30** (1988) 1391.
2 Deniz, A. V., Li, X. L., and Marshall, T. C., *Phys. Fluids* **30** (1987) 2527.
3 Simonen, T. C., et al., *Phys. Rev. Lett.* **61** (1988) 1720.
4 Luckhardt, S. C., et al., *Phys. Rev. Lett* **62** (1989) 1508.
5 Goldston, R.J., *Plasma Physics and Controlled Fusion* **26** (1984) 87.
6 Bickerton, R.J., Connor, J. W., Taylor, J. B., *Nature* **229** (1971) 110.
7 Mauel, M.E., et al., in *Plasma Physics and Controlled Nuclear Fusion Research*, **1** (1988) 415.
8 Marmar, E.S., Terry, J.L., Lipshultz, B., Rice, J.E.., *Rev. Sci. Instrum.* **60** (1989) 3739.

SOFT-X-RAY TOMOGRAPHY OF SAWTEETH AND M=1 MODES IN ASDEX

R. Büchse, M. Kornherr and the ASDEX Team

Max-Planck-Institut für Plasmaphysik,
EURATOM-IPP Association D-8046 Garching, FRG

1. Introduction

High resolution tomographic analysis of sawtooth crashs in discharges with neutral beam injection (NBI) and with lower hybrid wave heating (LH) is performed. We find distinctly different temporal developments of precursor oscillations, implying the conclusion that not all crashs may be explainable by the same mechanism. Furthermore, with the injection of neutral beams in counter-direction (ctr-NBI) a compound-like relaxation process is found, which we believe to be due to the presence of two q=1 surfaces.

Stationary (m,n)=(1,1) modes and their impact on plasma heating in discharges with Lower Hybrid Current Drive (LHCD) are also investigated.

2. Soft-X-Ray cameras and the rotation tomography method

Our investigations of central plasma modes are mainly based on measurements of soft X-rays ($0.5keV < E < 20keV$) with 58 Si-diodes arranged in two pinhole cameras.

For the reconstruction of the local emissivity from the line integrated measurements the method of Cormack [1] is used. Because simulations showed that the poloidal resolution attainable with only two cameras is not sufficient to reconstruct details of the mode structure, we make use of the mode rotation on surfaces of constant magnetic flux whenever possible. This allows higher harmonics to be included in the analysis.

3. Sawteeth in NBI-heated plasmas

In this chapter we report on five qualitatively different sawtooth relaxations. An overview of the temporal evolution of SX-intensities during the crashs is given in Fig. 1, for discharge parameters see Table 1. It can already be suspected from the differences in pre- and/or postcursor oscillations that the evolution of flux surfaces may strongly differ from scenario to scenario.

Fig. 2 shows two contour plots of SX-emissivity and cross sections through hot spot and island in the immediate crash phase of sawtooth A. The outward movement of the circular hot plasma core and the decrease in radiation amplitude are clearly visible. This topology is in agreement with models of resistive reconnection [2], whereas the short crash time $\tau_{crash} \approx 200\mu sec$ cannot be explained within this frame [3]. The same result was found for TFTR [4,5].

In plasmas with Ctr-NBI often peaking of n_e [6] and accumulation of impurities is observed, resulting in a flattened current profile and stabilization of sawteeth. Crash B in Fig. 1 is an example of the last crash before stabilization. A common feature is the large (1,1)-successor present for several 10 msec. The tomographic results in Fig. 3 show that the crash phase starts very similar to crash A. But the outward movement (see t=1.25ms) during reconnection is not completed, instead shrinking of the island and a motion of the hot spot back into the core (see t=10.0ms) is observed. The attributed process of shrinking of $r_{q=1}$ at a rate of $\dot{r}_{q=1} \approx 0.5cm/msec$ is seen to last for about 10 msec. Then lowlevel (1,1)-activity may be present for up to 130 msec, which is about 3 sawtooth repetition times. So in these cases sawtooth stabilization does not seem to be due to a vanishing of the q=1-surface, but just to changes in the current profile with $q(0) < 1$. The same may be true for the stabilization of the

Sawtooth	Heating	P[MW]	$\bar{n}_e$ $[10^{19}m^{-2}]$	q_a
A	Co-NBI	2.2	3.6	3.2
B	Ctr-NBI (before accumulation)	1.2	4.8	2.5
C	Ctr-NBI (after accumulation)	1.2	4.8	2.5
D	Ctr-NBI	0.5	4.6	2.5
E	LHCD	0.5	1.4	3.3

Table 1 Plasma parameters for the sawtoothing discharges A-E

m=1: No fast decrease in $r_{q=1}$ is seen, instead the mode vanishes on all channels simultaneously, thus implying that either a q=1-surface remains present or the q-profile inside q=1 is so flat, that the time necessary to raise q(0) above unity by current diffusion is in the order of a very few m=1 rotation cycles ($\approx msec$).

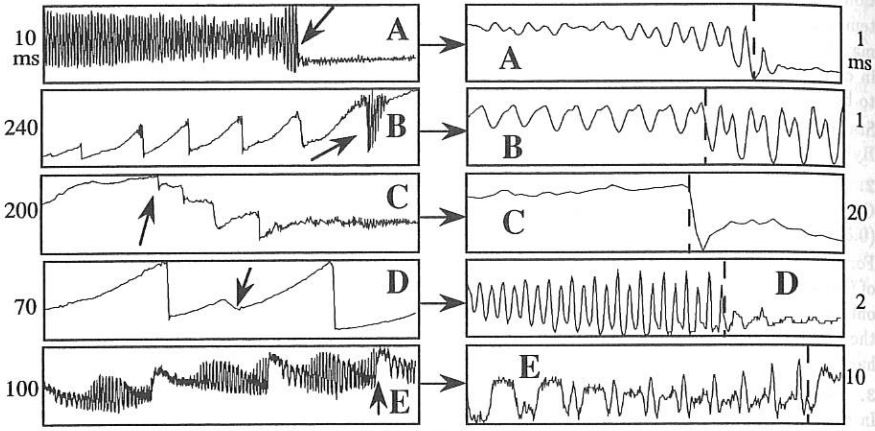

Fig. 1 Soft X-ray signals measured with nearcentral chords during sawtoothing discharges A-E (see Tab 1). The left hand column of plots displays signals for the time intervals given on the outer left, the right hand column shows the same signals with better time resolution around the immediate crash phase. The crashs are marked by arrows and dotted lines.

In the same discharge after a sawtooth-free period of about 200 msec a few T_e- and SX-crashs may occur again. Crashs in this phase of the discharge show an increased inversion radius, very low precursor activity and a comparatively long crash time of $\tau_{crash} \approx 1msec$. Fig. 4 compares the SX-profiles before and after such a crash (C) against the corresponding profiles of an ordinary crash. It is clearly seen that there is only a slight drop in the range $19cm < r < 5cm$, whereas the central value increases by a few percent.

While the results for crash C might be interpreted as a hint to the existence of two $q = 1$-surfaces at $r = 5cm$ and $r = 19cm$, we believe to have better experimental support for the occurrence of such q-profiles for discharge D in Fig. 1. It exhibits compound-like sawteeth [7], but in contrast to such seen in other devices [8], this one shows up in beam heated plasmas and exhibits precursor oscillations different from the common (1,1) precursors. Mode analysis using the data of the two SX-cameras and of a further diode toroidally displaced by 90° yields that there might be two (1,1)-modes present. Tomography supports this structure (Fig. 5). In Fig. 6 the distances of the centres of the two hot areas to the magnetic axis are shown.

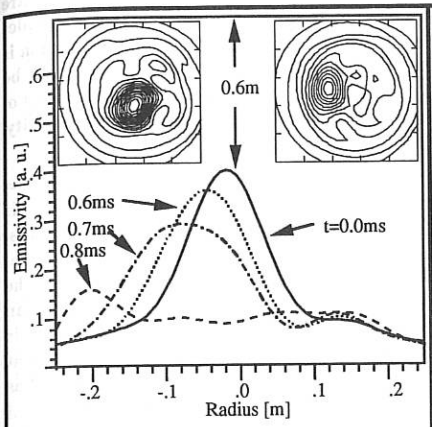

Fig. 2 Development of emissivity profile during crash A

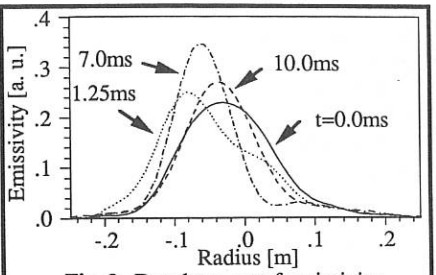

Fig. 3 Development of emissivity profile during and after crash B

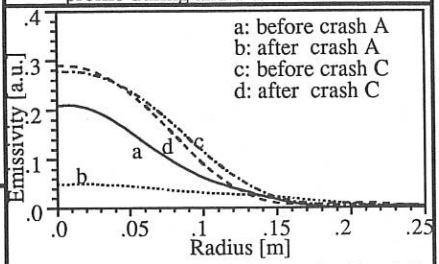

Fig. 4 Profile change during crashs A and C. Note the very unusual behavior of crash C.

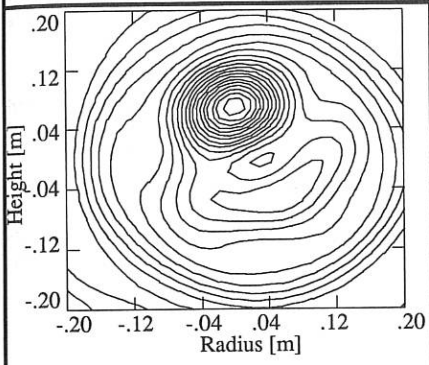

Fig. 5 Contours of constant emissivity during precursor development of Crash D. Two hot spots are seen opposite each other.

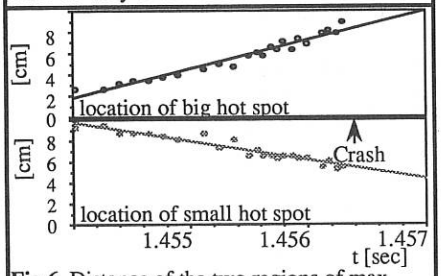

Fig.6 Distance of the two regions of max. emissivity from magnetic axis for discharge D

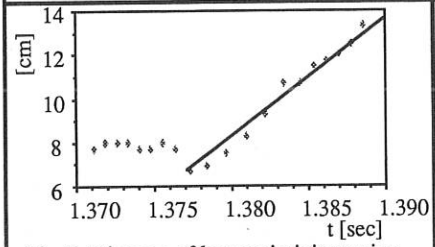

Fig. 7 Distance of low-emissivity region from magnetic axis for crash E. Crash occurs at t=1.390sec.

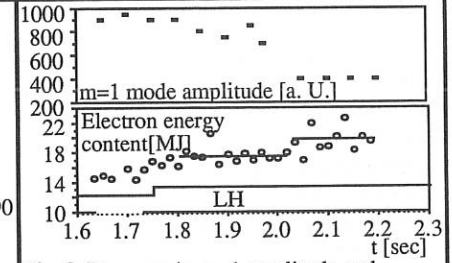

Fig. 8 Decrease in m=1 amplitude and increase in energy content.

The centre of the big inner hot spot is seen to move away from the axis, whereas the centre of the smaller outer one moves towards the axis, so that the distance between the two modes increases. The fast crash may be triggered by a certain critical value [7], but its estimation is beyond the resolution of the measurement. The values plotted in Fig. 6 may actually not be a suitable measure of the exact location of $r_{q=1}$, because for this determination the radius of **vanishing** mode activity might be better suited than the radius of **maximum** mode activity.

4. Sawteeth in LH-heated plasmas

Sawtooth E in Fig. 1 is a typical example of an internal disruption in low-density ($\bar{n}_e = 1.4 \times 10^{19} m^{-3}$) LHCD-discharges. The striking feature of inverted signals in central channels is not just due to a line integration effect or the excitation of certain strong impurity lines, but holds also for the local profile and is not yet understood. The T_e-crash exhibits normal behaviour. Here we want to concentrate on the development of the island as seen from the complicated precursor activity in Fig. 1. Tomography of this phase shows the shrinking of an area of low emissivity, which is the exact opposite to the situation in ordinary crashs. This observation is confirmed by T_e-measurements. Simultaneously the buildup of a strong gradient at the border of the low-emissivity-area is seen. In Fig. 7 the location of this area is plotted as a monitor for island development: From the rather small slope it can be seen that this kind of crash is introduced by changes in mode activity taking place in the 10msec range, whereas for ordinary crashs (e. g. crash A) timescales of 100μsec are commonly seen. A further distinct difference lies in the crash mechanism itself: in the A case the island development and the crash take place on the same time scale, whereas in the LH case the very fast T_e-crash **starts** at the end of the slow island development.

5. Stationary (1,1) modes during Lower Hybrid Current Drive (LHCD)

With LHCD at a power level of $P_{LH} > 0.4MW$ sawteeth are stabilized due to a flattening of the current profile [9]. SX data shows a shrinking of the $q = 1$-surface (typically: $\Delta r_{q=1} = 2cm$) and (1,1)-modes grow to a stationary level, until for $P_{LH} > 0.75MW$ no central modes are seen.

Fig. 8 illustrates the impact of (1,1)-activity on central confinement: When at t=1.99sec the mode amplitude decreases, a rise in electron energy content is seen. Closer investigation shows that the decrease of the line integrated amplitude is accompanied by a further decrease in q=1-radius.

References

[1] CORMACK, A. M., J. Appl. Phys. **35** (1964) 2908.

[2] KADOMTSEV, B. B., Sov. J. Plasma Phys. **1** (1975) 389.

[3] WESSON, J. A., KIRBY, P., and NAVE, M. F., in *Proc. of the* 11^{th} *I.A.E.A. Int. Conf. on Plasma Physics and Contr. Nucl. Fusion Research*, volume 2, page 3, 1986.

[4] MCGUIRE, K., BÜCHSE, R., et al., in *Proc. of the* 16^{th} *Europ. Conf. on Controlled Fusion and Plasma Physics, Venice*, volume 13, page 477, 1989.

[5] BÜCHSE, R., MCGUIRE, K., and NAGAYAMA, Y., to be published .

[6] GEHRE, O. et al., Phys. Rev. Lett. **60** (1988) 1502.

[7] AYDEMIR, A. Y., WILEY, J. C., and ROSS, D. W., Phys. Fluids B **1** (1989) 774.

[8] MCGUIRE, K. et al., in *Proc. of the* 11^{th} *I.A.E.A. Int. Conf. on Plasma Physics and Contr. Nucl. Fusion Research*, page 421, 1986.

[9] SÖLDNER, F. X., MCCORMICK, K., ECKHARTT, D., KORNHERR, M., LEUTERER, F., et al., Phys. Rev. Lett. **57** (1986) 1137.

DENSITY LIMIT IN ASDEX UNDER CLEAN PLASMA CONDITIONS

A. Stäbler, K. McCormick, E. R. Müller, J. Neuhauser, H. Niedermeyer, N. Tsois*
and the ASDEX and NI-Teams

Max-Planck-Institut f. Plasmaphysik, EURATOM Association, D-8046 Garching, FRG
*NRS Demokritos, Attiki, Greece

Introduction

The understanding of the density limit and its parametric dependence is an important prerequisite to determine the operational range of the next step tokamaks presently being designed. The maximum attainable densities on ASDEX and many other tokamaks were found to be strongly dependent on the plasma impurity level. Boronization of the ASDEX vessel resulted in a significant improvement of the plasma purity, especially the oxygen content during a discharge was reduced by about a factor of 5 with Z_{eff} reaching values of 1 - 1.5 at higher densities. Under these well defined conditions the density limit of ASDEX divertor discharges has been investigated over an extended range of q_a for ohmic heating and with additional heating by neutral injection (NI). Special emphasis was put on the documentation of the plasma radiation and the development of the divertor plasma parameters when approaching the density limit.

Experimental Parameters

The density limit in ASDEX is determined in specially dedicated density limit shots where, after a short density plateau, $\bar{n}_e$ is slowly ramped up by feedback controlled gas puffing under otherwise stationary conditions until the plasma disrupts. It has been verified that discharges can be operated at constant densities slightly below ($1\text{-}2\cdot10^{12}$ cm^{-3}) the value of the density limit determined as described above. Under boronized wall conditions and for D^+-plasmas q_a was varied over the range $5.9 \geq q_a \geq 1.9$ (the cylindrical definition of q_a is used throughout this paper) by simultaneously changing I_p and B_t (230 kA $\leq I_p \leq$ 460 kA; 2.8 T $\leq B_t \leq$ 1.8 T) in a series of ohmic discharges and a series of additionally heated discharges with a fixed neutral beam power (P_{NI} = 1.15 MW, H^0-beams, co-injection) applied during the phase of density rise. Less extended q_a-scans were done for ohmic H^+- and He^{++}-plasmas. Comparisons with results just before boronization are available for D^+- (OH and NI) and He^{++}-discharges (OH).

Density Limit Results

Results obtained from the q_a-scan in D^+-plasmas are shown in Fig. 1 where the density limit is presented in form of the Hugill diagram. The overall behaviour agrees with earlier results from ASDEX under clean plasma conditions /1/ (e.g. Ti-evaporation in the divertor region, old divertor configuration): In ohmic discharges the Murakami parameter $\bar{n}_e \cdot R_o/B_t$ increases linearly with $1/q_a$ for $q_a > 2.5$ and a minimum is seen around $q_a = 2.1$. This minimum was observed also in I_p- and B_t-scans and, therefore, is an effect of q_a. Neutral beam heating results in an increase of the maximum attainable density at all q_a-values as is always observed on ASDEX. The minimum around $q_a = 2.1$ is maintained though less pronounced. The linear $1/q_a$-dependence with NI in Fig. 1, however, may be due to the specific choise of I_p and B_t during the q_a-scan, since earlier measurements /2/ have shown that with additional heating the density limit not only depends on q_a but also on B_t (or I_p); the Murakami parameter is generally not a good scaling parameter for the ASDEX density limit with NI.

Independent of the plasma heating method the occurence of marfes is observed for $q_a > 3$ prior to the disruption. They can last for up to 1 s and 0.4 s in OH and NI heated plasmas, respectively. During the marfe the plasma edge density at the outer midplane as determined by a Li-beam stays roughly constant whereas the central density still rises. The maximum $\bar{n}_e$-values used in Fig. 1 are determined omitting

the contribution from the marfe. A profile peaking during marfing is also observed for T_e (from Thomson scattering) and for the current density (from $\beta_p+l_i/2 - \beta_{p,dia}$). A more detailed description of marfes in ASDEX is given in ref. /2/.

The improvement in the maximum attainable density of D^+-plasmas due to boronization is shown in Fig. 2 (OH-plasmas). In the linear range ($q_a > 2.5$) $\bar{n}_e \cdot R_o/B_t$ is increased by a factor of around 1.5; for NI heating the improvement factor due to boronization is around 1.35. At lower q_a-values, however, the shape of the density limit curve is drastically changed. The minimum at $q_a = 2.1$ is not seen for the less clean plasmas. This is also true for NI heated D^+-plasmas without boronization.

Fig. 2 further shows that the density limit under boronized conditions is roughly independent of the discharge gas (H^+, D^+, He^{++}) for all q_a-values. In He^{++}-plasmas, where the density limit without boronization significantly exceeds the one of D^+-plasmas the improvement due to boronization is rather small. Here the minimum at low q_a is already present before boronization presumably due to a reduced low-Z impurity content in He^{++}-plasmas.

Radiation at the Density Limit

It has been reported from other tokamaks (e.g. ref. /3/) that the density limit is reached when the main plasma radiation power equals the input power. Such a behaviour is not found on ASDEX. Fig. 3 shows the total power radiated from the main plasma (P_{rad}) measured during the q_a-scans (D^+-plasmas, OH and NI, boronized walls) as function of the plasma density just prior to the disruption or to the onset of a marfe, respectively (t-Disr). For ohmic discharges measurements taken during the $\bar{n}_e$ plateau phase far away from the density limit are included (t-Plat). P_{rad} in OH plasmas corresponds to 0.3 ($\pm$0.1)$\cdot P_{OH}$ with the pre-disruptive values slightly above the ones far from the density limit. For NI heating the situation is very similar: 30-40% of the total input power is radiated from the main plasma. P_{rad} plus the radiation measured in the two divertors amounts to 60-70% of the input power for all ohmic and NI heated shots and is roughly independent of the time within the discharge. This indicates that still a considerable fraction of power is deposited onto the target plates.

The determination of the main plasma radiation during the occurrence of marfes is difficult due to the poloidal asymmetry of this phenomena but during this phase divertor radiation is still detectable at roughly half the level just prior to the onset of the marfe indicating the existence of a finite power flow into the divertor even during the marfing phase. This is confirmed by probe measurements as will be discussed below. When comparing P_{rad} in ohmic discharges under boronized/non-boronized conditions one finds that boronization reduces plasma radiation by roughly a factor of 2 when plotted against $\bar{n}_e$ at the density limit. Even under these less clean conditions P_{rad} at the density limit is therefore significantly below the input power.

Development of Divertor Parameters

From earlier investigations of the density limit in discharges with peaked density profiles on ASDEX it was concluded that the density limit is a limit to the edge density of the plasma /4/. This may be correlated to the energy balance in the divertor plasma /5, 6/. This section, therefore, deals with the development of divertor parameters, when approaching the density limit. Further informations concerning the plasma edge and scrape-off layer are given in another contribution to this conference /7/.

During the ohmic q_a-scan in D^+-plasmas Langmuir probe measurements of the divertor temperature and density were performed at a fixed probe position close to the maximum of the $n_{e,div}$ and $T_{e,div}$ profiles. During the plasma density ramp-up $n_{e,div}$ rises and $T_{e,div}$ drops. The onset of a marfe is clearly indicated by a sudden reduction in $n_{e,div}$ by about a factor of 2 with only a small increase in $T_{e,div}$. If no marfe occurs the divertor temperature continuously decreases towards values of 4-5 eV whereas the density starts to saturate some 100 ms before the disruption. At the given power flow into the divertor obviously no further increase of the divertor density is possible. For $q_a < 2.5$ the disruption occurs

during the constant rise of $n_{e,div}$ and at $T_{e,div}$ significantly above 5 eV. Data beyond the minimum at q_a = 2.1 are not available.

C III radiation from the divertor plasma is a further signal indicating the divertor temperature. For q_a > 2.5 this signal drops from a constant value during the $\bar{n}_e$-plateau phase to rather low values when approaching the density limit. For lower q_a-values the C III divertor intensity is much higher already during the $\bar{n}_e$-plateau with only a small reduction during the density rise. When q_a is below 2.1, i. e. beyond the minimum in the density limit, the C III intensity decreases again and rather small values are attained at the density limit disruption. This behaviour is linked to the power flow into the same divertor region since the flux of sputtered Cu from the target plate measured by Cu I radiation at the same position is strongly correlated with the C III intensity. Neither the Cu concentration nor the C III line radiation of the main plasma nor the total plasma radiation or Z_{eff} show any correlation with the high divertor radiation.

In order to interpret these observations it is important to know that for q_a below 3 rather strong toroidal asymmetries are seen in the ASDEX divertor loading. Cooling water calorimetry of the different divertor sections reveal differences in excess of a factor of 2. This observation could tentatively be related to the presence of a local m=2 disturbance which could cause a toroidally asymmetric efflux of the power into different divertor sections when the q = 2 surface comes close to the separatrix. The C III and Cu I radiation measurements were performed in a sector which according to the water calorimetry is close to the maximum loading.

If the energy balance in the divertor plasma determines the attainable plasma edge density and therefore the density limit the existence of the minimum in the density limit curve at $q_a = 2.1$ could be tentatively explained by the observed toroidal asymmetry. In divertor regions with minimum power loading the energy balance may be locally violated at a rather low plasma density preventing a further increase of $\bar{n}_e$ and causing the plasma to disrupt.

Conclusions

Boronization of the ASDEX vessel leads to a significant improvement of the density limit. Additional heating by NI further increases this limit at all q_a-values. Plasma radiation under these conditions is, up to the maximum densities, only a small fraction of the input power and, therefore, does not cause the plasma disruption. Lower radiation, of course, increases the power flow into the divertor and may therefore be responsible for the higher density limit. A more detailed investigation of the power depencence of the density limit is planed for the near future. At higher q_a-values the plasma disruption occurs when the divertor temperature reaches values around 5 eV at high divertor densities. The characteristic minimum in the density limit at q_a around 2.1 may be connected with the observed toroidal asymmetries in divertor loading: the maximum attainable density could be determined by the divertor regions with minimum power influx. The operation of future tokamaks at high plasma densities and overall low divertor temperatures in the low q_a-regime, therefore, calls for the achievement of a high toroidal symmetry.

References

/1/ H. Niedermeyer et al., Proc. 11th Int. Conf. Plasma Phys. and Contr. Fus. Research (Kyoto 1966), IAEA, Vol. I (1987), p. 125

/2/ H. Niedermeyer et al., Proc. 12th EPS Conf. Contr. Fus. and Plasma Phys. (Budapest 1985), Vol. I, p. 159

/3/ J. A. Wesson et al., Nuclear Fusion 29 (1989) 641

/4/ A. Stäbler et al., Proc. 16th EPS Conf. Contr. Fus. and Plasma Phys. (Venice 1989), Vol. I, p. 23

/5/ J. Neuhauser et al., Plasma Phys. and Contr. Fus. 31 (1989) 1551

/6/ K. Borrass, NET-Report EUR-FU/80/89-95

/7/ K. McCormick et al., this conference

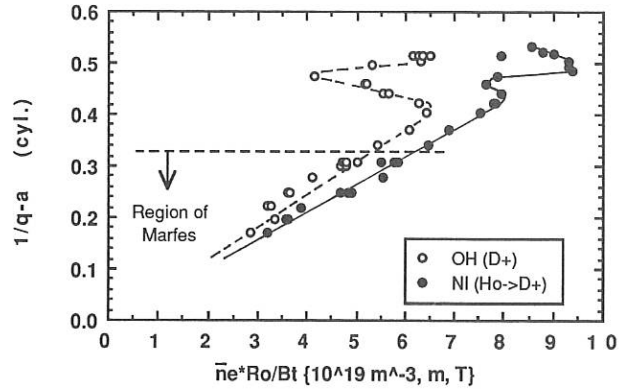

Fig. 1

Hugill plot of density limit, OH and NI (1.15 MW), boronized walls

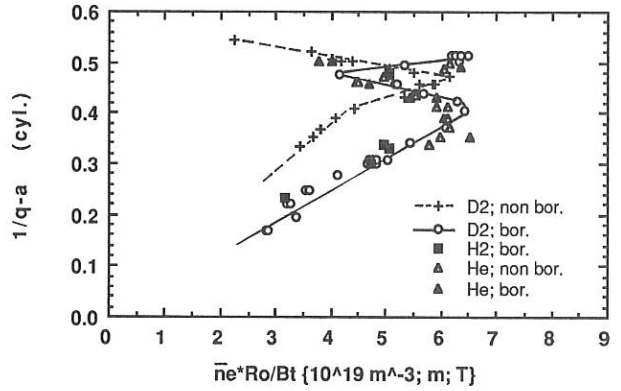

Fig. 2

Hugill plot for OH-discharges in various gases, boronized and non-boronized walls

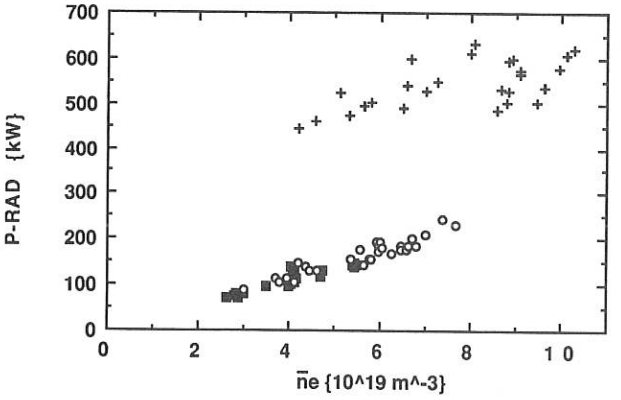

Fig. 3

Radiated power in OH and NI heated plasmas at the density limit or the onset of marfes (t-Disr) and in the n̄e-plateau (t-Plat), boronized walls.

- OH, t-Plat
- OH, t-Disr
- NI, t-Disr

THEORETICAL ANALYSIS OF HIGH–β JET SHOTS

T.C.Hender*, G.T.A.Huysmans+, O.J.Kwon*, J.P.Goedbloed+, E.Lazzaro and D.P.O'Brien.
JET Joint Undertaking, Abingdon, OX143EA, UK.

*UKAEA/EURATOM Fusion Association, Culham Laboratory, Abingdon, UK.
+ EURATOM/FOM Association, FOM Instituut voor Plasmafysica, Nieuwegein, The Netherlands

Introduction

Recent high–β discharges in JET [1] have reached values of β up to the Troyon limit [2] ($\beta_{Troyon} = 2.8I(MA)/B(T)a(m)$). These high–$\beta$ values were reached in double null X-point configurations during the H-mode. To reduce the total heating power needed to obtain these high β's, a low toroidal field ($B_T \sim 1.2-1.5$T) was used. The experimental features are described in more detail in Ref [1]. In this paper we discuss the theoretical ideal and resistive MHD stability properties of these discharges, and comparisons with observed mode structures.

Equilibrium Reconstruction

The equilibria needed for the stability studies are calculated with the IDENT–C code [3] which fits the magnetic measurements and the experimental pressure profile. The pressure profile shape is generally taken from the LIDAR electron pressure measurements and normalised to match the diamagnetic β. This is a good approximation as the electron and ion pressure profiles shapes are generally quite similar in these high–β discharges. It does however mean that the contribution to β from fast particles is included.

For the ideal low-n and ballooning mode calculations the HBT [4], ERATO [5], and BALLOON [6] codes were used, the results being in good agreement. For low-n fixed boundary calculations the resistive MHD code FAR was used [7].

Ballooning Stability

Most high–β discharges develop from a broad pressure profile at low β to a triangular pressure profile shape for $\beta \sim \beta_{Troyon}$ (see Fig 1). The pressure profile here is measured by the LIDAR at a time just before a large sawtooth, corresponding to the maximum β in the shot ($\beta \sim 0.88\beta_{Troyon}$, I_p =2.1MA, B_T=1.2T). The ballooning stability boundary is calculated by increasing the pressure gradient in small steps (keeping the q–profile fixed) until the ballooning limit is reached. This results in marginal stability to ballooning modes, across the entire plasma. In Fig 2 we show the resulting profiles of normalised pressure gradient ($\alpha = 4q_*^2\sqrt{\psi}/(\epsilon B_0^2)dp/d\psi$) versus the square root of the normalised

flux, for both the experimental and marginally stable equilibrium. Comparison of the two, shows the plasma to be marginally stable over more than 50% of the minor radius. Near the magnetic axis the experimental pressure gradient exceeds the ballooning limit. For this case the marginally stable equilibrium has $\beta = 6.3\%$ (which is $4.0I/aB$, the normal limit for ballooning modes).

In a discharge where a pellet is injected coincident with the start of neutral beam heating (14MW), an even larger central pressure gradient occurs. In this case the maximum gradient in the centre seems to exceed the ballooning limit by about a factor of two although experimentally no large degradation in confinement is observed until a large $n = 1$ mode causes a β–collapse (see next section). Within the ideal MHD model a hollow q–profile with negative shear ($q_0 \sim 1.1$, $q_{min} \sim 0.9$) at the position of large pressure gradients can stabilise the ballooning instability, for this pellet case. The hollow current density profile needed for this q–profile, could be produced by the contribution of the bootstrap current.

In a discharge at higher current, $I_p = 3$MA, (and higher startup density) the pressure profile remains broad, with large pressure gradients near the edge, up to a disruption caused by the influx of carbon impurities. The highest β obtained in this case is $0.7\beta_{Troyon}$. These pressure profiles are similar to the broad pressure in the early phases of the discharges mentioned above. The experimental and marginally stable profile of the pressure gradient (α) for this case is shown in Fig 3 (the marginal profile has $\beta \sim 3.4I/aB$). The largest gradients near the edge are close to the ballooning limit, but this is only a region of $\sim$ 15cm.

Low–n Stability

The low–n activity divides into that seen during β–saturation (fishbones, ELM's and sawteeth) and that seen during the β–collapse (large n =1, 2 or 3 activity) [1]. For equilibria reconstructed to fit the β–saturation shots, with $q_0 < 1$, we find that the peaked pressure profiles cause the $n = 1$ internal kink to be strongly unstable. This $n = 1$ instability is probably linked to the fishbone/sawtooth activity, but trapped particle effects must be included before a quantitative comparison can be made.

In the majority of cases in which β–collapses there is large $n = 2$ activity present, however first we discuss a discharge in which a very large $n = 1$ mode ($\tilde{B}_\theta > 25$G) seems to limit the β. This case is the peaked pressure profile pellet case discussed in the ballooning section above. The pellet causes a reduction in l_i of ~ 0.2 and the polarimetry indicates an increase of ~ 0.2 in q_0. Subsequent to the pellet injection, as the β rises to $0.8\beta_{Troyon}$, a large $n = 1$ mode grows to $\tilde{B}_\theta \sim 25$G (by which time it is locked) and a collapse in β follows. This very large $n = 1$ mode is visible on the soft X-ray (SXR) array; a tomographic reconstruction shows a distortion to the core and island–like structures near $q = 2$ (Fig 4a). We have constructed an equilibrium for use in studying the stability of this case by matching the boundary shape, q_ψ and β_p, determined from the magnetics, and have also matched the LIDAR pressure profile and the location of $q = 2$ and 3 surfaces (from SXR's). This leaves the form of the central–q

to be determined. We have tried a flat central–q (with $q_0 \sim 1.0$), a parabolic central–q with ($q_0 \sim 0.9$) and a non-monotone q. From the $n = 1$ eigenfunctions for each class of q–profile, calculated with the linear FAR code, we have reconstructed the flux surface distortions. We find only the flat central–q, with $q_0 \sim 1.1$, gives a good match to the relative phase and amplitude between the core and $q = 2$ distortions in Fig 4(a); the theory result for $q_0 = 1.1$ (flat q) is shown in Fig 4(b). This case is close to the marginal threshold for the $n = 1$ mode; raising q_0 slightly leads to stability.

For the $n = 2$ activity, which generally seems to cause the β–collapse, we have also constructed equilibria by the same technique and considered a range of central q–profiles. For a parabolic central–q with $q_0 \sim 0.9$ the $n = 1$ growth rate exceeds that of the the $n = 2$ mode. However for a flatter central–q, with $q_0 > 0.96$, we find an $n = 2$ 'infernal' type mode [8] which exceeds the $n = 1$ mode growth rate. This $n = 2$ infernal mode has strongly coupled $m = 2$, 3 and 4 components and reconstructions of the line integrated SXR's give a reasonable match to the phase inversions observed experimentally.

Summary

The ballooning studies typically show the plasma pressure to be marginal over the central $\sim 50\%$ of the plasma when $\beta \sim \beta_{Troyon}$, and in many cases the core region is unstable. For a pellet shot, in which an $n = 1$ mode is strongly unstable, stability calculations show that the SXR tomographic results are reproduced best by a flat central–q with $q_0 \sim 1.1$. For $n = 2$ modes which usually cause the β–collapse and seem often to be initiated by a sawtooth [1], flat q–profiles (with $q_0 \sim 0.96$) seem to give the best agreement with SXR's.

Acknowledgement

We are grateful to the JET diagnostic and operating teams for the use of their data, and in particular to the LIDAR group for the pressure profile data.

References

[1] P.Smeulders et al, 'High β regimes in JET', this conf.
[2] F.Troyon et al, Plasma Phys and Contr Fus **26** (1984) 209.
[3] J.Blum et al, report on JET contract JT3/9008 (1985).
[4] J.P.Goedbloed et al, proc 10th IAEA Conf London 1984, IAEA **1** (1985) 165.
[5] R.Gruber et al, Comp Phys Comm **21** (1981) 323.
[6] D.P.O'Brien et al, 16th European Conf on Contr Fus (Venice, 1989).
[7] L.A.Charlton et al, Jrnl Comp Phys **63** (1983) 107.
[8] J.Manickam et al, Nucl Fus **27** (1987) 1461.

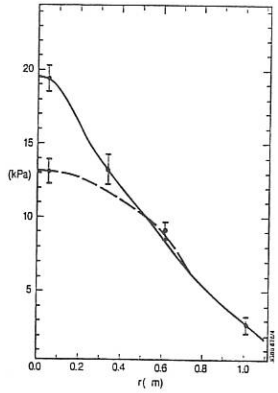

Fig 1 Pressure profile before (solid line, shot 20272) and after (broken line, shot 20274) a β clipping event [1].

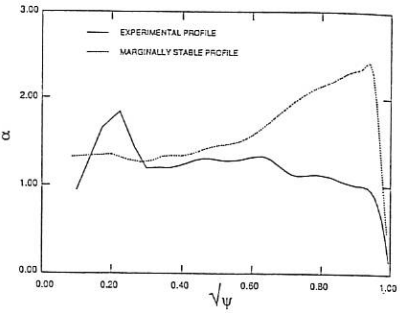

Fig 2 Experimental pressure gradient compared with marginal profile for case shown in Fig 1.

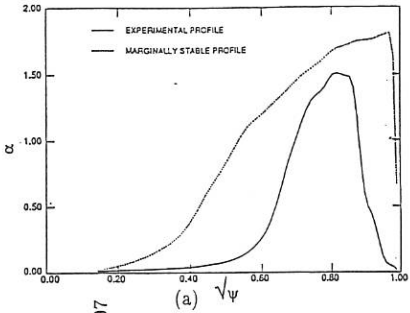

Fig 3 Experimental pressure gradient compared with marginal profile for a broad pressure profile shot (shot 19970).

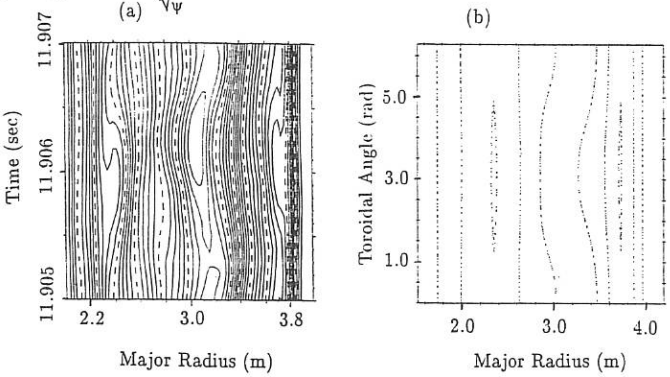

Fig 4 (a) SXR emission contours in the mid-plane during a large $n = 1$ mode; (b) Flux surfaces from an $n = 1$ resistive MHD simulation for this case.

ANALYSIS OF THE ENERGY HEAT QUENCH DURING A DISRUPTION IN TEXTOR

K.H. Finken[1], J.G. Watkins[2], A.J. Russo[2], K.H. Dippel[1], W.Y. Baek[1], D. Gray[3], R.A. Moyer[3]

[1] Institut für Plasmaphysik, Forschungszentrum Jülich, Association EURATOM - KFA, FRG
[2] Sandia National Laboratories, Albuquerque, USA
[3] Institute of Plasma and Fusion Research and Mechanical, Aerospace and Nuclear Engineering Department, University of California, Los Angeles, USA

Introduction

During a disruption, the plasma energy and the electrical current are lost rapidly. The energy decay time is shorter than the current decay time. In JET the time scale for the energy loss of the plasma amounts to about 1 - 2 ms /1/. In TEXTOR the current decay time was measured to be about 10 - 20 ms and the energy decay time determined by ECE to be about 1 ms or slightly shorter /2/. Even shorter than this event is the time scale for the heat quench time measured by heating of the limiter or the wall components. The energy release there can lead to a dangerous overheating and damage of the different materials. Here a technique is described which allows the measurement of this heating over a large area in TEXTOR.

The Experimental Setup

For the observation of the heat flux distribution to the wall, it is desirable to detect the thermal radiation from a large portion of the plasma facing components with high spatial and temporal resolution. The spatial resolution is necessary to discriminate between a very localized heating and a widely distributed one. The high temporal resolution is important because the time scale of the heating burst only is about one-hundred micro-seconds. The simultaneous realization of both requirements leads to an unrealistic amount of diagnostic hardware and memory. An instrument that nevertheless can meet many of these requirements is an IR-scanner. The IR-scanner is widely used for thermography. It operates in the following way: the incoming IR-light is deflected horizontally and vertically by a set of two mirrors and is imaged to an IR-diode (here HgCdTe optimized for radiation of a wavelength of 3 - 6 μm). This instrument produces a TV-picture fulfilling the typical TV standards. We have one camera in NTSC standard and second one in CCIR. In contrast to the CCD cameras the time resolution of the scanner is not limited by the time to complete consecutive frames, each of which has a length of 16.6 ms in the US standard and 20 ms in the European one. The time resolution is very much higher because the diode records the different spatial points consecutively in time. The smallest time interval which is convenient for our analysis is the time duration of one TV line which amounts to about 64 μs for both standards.

In TEXTOR two synchronized IR-scanners are used. One scanner is directed to one of the eight ALT-II toroidal belt limiter blades and sees about two thirds of it, i.e. about 1 m in the toroidal direction; poloidally it covers more than the blade width of 28 cm

so that parts of the wall are also visible. The second scanner is oriented towards the inner bumper limiter looking at an area of about 60 cm in diameter.

Results

Typical heat loads at ALT-II

A typical picture measured with camera 1 during a disruption is shown in fig. 1. This discharge was a high current discharge (I_P = 460 kA) in which 1.2 MW of neutral beam power was switched on at t = 800 ms. At t = 862.6 ms a minor disruption occurred. In this disruption the electrical current was not quenched but the electron temperature in the plasma dropped from about 1450 eV to 1050 eV within roughly a millisecond. The figure is recorded during the time span when the disruption occurred. The top half of the thermographic picture looks rather normal: As already mentioned, the bright part is a section of an ALT-II blade and in the left corner a part of a neighboring blade comes into the line of sight. The temperature distribution along the blade in toroidal direction is rather homogeneous with the exception of the end tiles which receive twice the heat flux as the rest of the blade /3,4/. In the middle of the blade a sudden disturbance in the blade temperature appears and going further down, the blade surface at first is strongly and later moderately heated as compared to the top part. Watching the picture more closely one finds a series of more or less strong disturbances which are indicated by bars at the right edge of the picture.

For a consistent analysis of the photograph we have to make use of the fact that the different local points correspont to different time points as discussed above. The top half of the frame therefore represents the time before the disruption. The disruption itself is a very sudden event. It is structured in time and in this case it consists of six individual sub-events which have different intensities. The thermal quench time of each sub-event is less than or equal to 64 μs corresponding to one TV line. The time duration of the whole disruption agrees fairly well with the decay time of the electron temperature. After the last sub-event the surface temperature decreases within a few milliseconds. During this time the heat wave propagates from the surface into the bulk of the material. The observed time scale is plausible because the surface was exposed to very short heat pulses only.

When first seeing the thermographic pictures of a disruption one may be led to another interpretation than presented here, namely that the heat is deposited only very locally on the limiter blades. The heat would be distributed in a narrow, sharply limited band with a long extension in toroidal direction. When observing different disruptions one finds that the band is not fixed poloidally but covers the blade with the same probability. This strict toroidal orientation of the thermal quench seems very unlikely. The strongest argument against the highly localized structure of the thermal quench, however, comes from a the series of consecutive frames: the frames preceding the disruption normally show a smooth increase of the surface temperature due to the incoming power flux. The frame with the disruption has a clear separation above and below the disruption as already stated, and the frame following the disruption shows again a rather uniform temperature distribution but with a higher temperature than before the disruption. This also means that the cooler area of the blade, which is always above the disruptive pattern, has received heat during the disruption. Therefore the thermal quench is not restricted to a small fraction of the limiter; the heat is distributed rather evenly over at least one blade, possibly it covers the whole toroidal limiter ALT-II. As far as one can judge from the statistical observations of the disruptions one can assume that the relative heat distribution over a blade - i.e. slight

nonuniformities due to the magnetic ripple effect or the higher heat load at the end tile /4/ - is similar in normal discharges and during a disruption. The statement about the relative heat distribution is of course very important for the construction of protective elements in future fusion reactors. To confirm this point it will be necessary to perform simultaneous measurements at different blades.

Simultaneous Observations of ALT-II and the Inner Bumper Limiter

To obtain information about the correlation of the thermal quench at the outer and at the inner limiters, two IR-scanners are used, one looking at an ALT-II blade and the other at the inner bumper limiter. The observations at the bumper limiter are as expected: during the disruptions those parts of the limiter are preferentially heated which normally also see the highest heat flux. The uniformity of the heat transfer, however, is very much poorer than at ALT-II because the flatness of the graphite tiles allows a heating of the edges only. The thermal quench time at the inner bumper limiter is similar to that at ALT-II namely 100 μs or less.

The energy transfer strength at both limiters is not correlated during the disruptions. Under comparable discharge conditions sometimes the outer limiter receives most of the thermal load and in other cases the inner one. If the energy quench of a disruption is detected at both limiters, it is first seen at the outer one and later at the inner one. We have observed a discharge where the plasma first hits the outer limiter weakly, then 30 ms later the inner limiter and another 15 ms later the outer one again. The highest temperature rise of this disruption occured at the end. During our observations this disruption was the only one in which the plasma not only ended at the limiters but also hit the bottom of the vessel. As compared to the heating of the ALT-II limiters the heated spot at the wall was very localized and the spot temperature was higher than normally observed at the limiters. The reason for the strong localization is most likely that the walls are not as smooth as a limiter surface which is designed for a good heat acceptance and distribution.

Conclusions and Summary

The observations with the IR-scanners show that the energy from the plasma boundary is transferred to the wall components in a series of short sub-events. The time duration of these individual events is on the order of a hundred microseconds or less. If the energy quench is deposited on a smooth limiter surface then the energy is distributed over a large area, possibly over the whole limiter. Our observations of the heat quench are not complete enough to construct a firm model of the plasma - wall contact during the disruption. At the moment we tend to the assumption that the plasma looses its axisymmetry and rotates like a snake in the vessel. The areas of contact with the wall are then heated and one can observe the heating several times as long as the plasma winds in the vessel. Another interpretation is that the plasma 'breathes' i.e. it is shifted axisymmetrically several times to the outer vessel. For a detailed understanding, more measurements are necessary.

/1/ J.A. Wesson, R.D. Gill, M. Hugon et al., Nucl. Fusion, **29**, 641 (1989)
/2/ G. Waidmann, Y. Cao and B. Kardon, Plasma Phys. Contr. Fus., **31**, 323 (1989)
/3/ K.H. Finken, J.C. Watkins, W.J. Corbett et al., 15th Conf. Contr. Fus. Plasma Heating, p 663 (1988)
/4/ K.H. Finken, J.C. Watkins, R.T. McGrath et al., J. Nucl. Mat., **162-164**, 655 (1989)

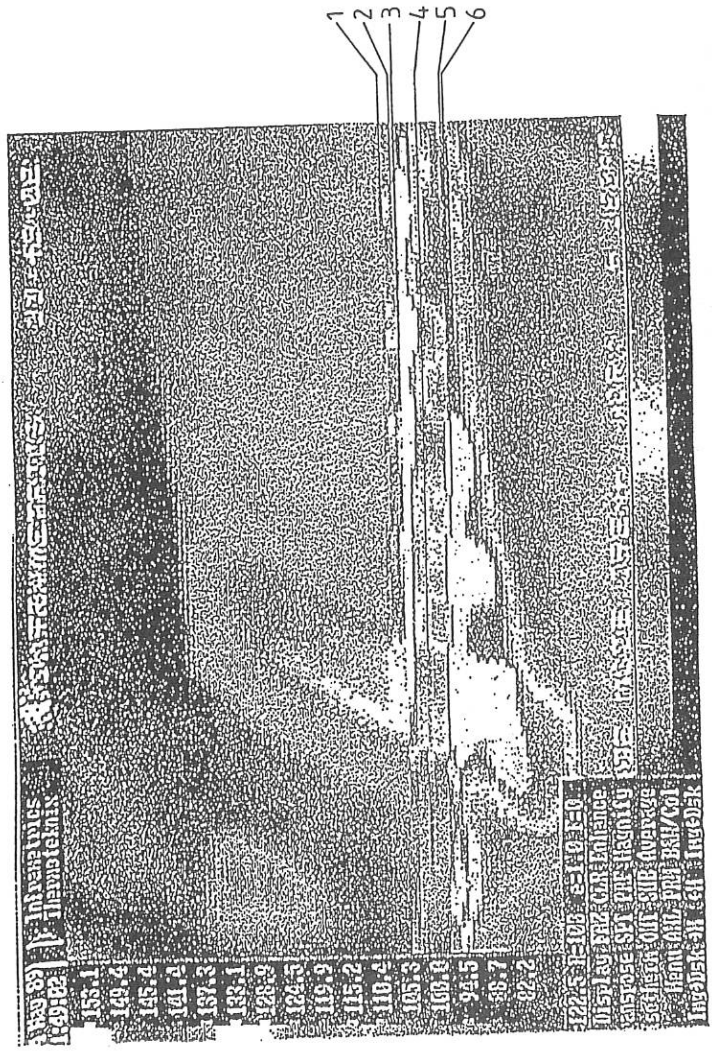

Fig. 1: Photograph of an IR-scanner image of half a blade of the toroidal pump limiter ALT-II. A disruption occured during the recording of this frame. The image elements not only represent different spatial points but are also sequential in time. Therefore the disruption manifests itself as a narrow local disturbance.

ENHANCED TURBULENCE DURING THE ENERGY QUENCH OF DISRUPTIONS

G.J.J. Remkes and F.C. Schüller

FOM-Instituut voor Plasmafysica Rijnhuizen, Associatie EURATOM-FOM, P.O. BOX 1207, 3430 BE Nieuwegein, The Netherlands.

Introduction

One of the real mysteries connected to major disruptions in tokamaks is the sudden disappearance of a major part of the plasma kinetic energy during the energy quench phase. In JET [1], the energy quench phase seems to be divided in a relatively slow phase of typically 1 to 2 ms during which the kinetic energy is redistributed over the cross-section in a toroidally asymmetric (n=1) fashion, followed by a very fast total decay of kinetic energy in less than 100 μs. This last decay means an enhancement above the normal loss rate with a factor 10^4.

The first phase of the energy quench has been explained in the past [2] by the interaction and overlap of tearing mode islands: (n = 1, m = 2), (n = 2, m = 3) and (n = 1, m = 1). The timescale for this $\tau = (\tau_{\theta A}^{2}\ \tau_{\eta}^{3})^{1/5}$, in which τ_η is resistive current penetration time and $\tau_{\theta A}$ the poloidal Alfvén time, gives indeed few ms for large devices as JET. The second phase is unexplained. Suggestions have been made that it could be caused by a massive increase in turbulent heat conduction or by a massive influx of impurities, leading to a radiation loss rate of gigawatts. However, if the latter were true, one would expect a more or less homogeneous heat deposition over the wall, whilst thermographic measurements indicate an inhomogeneous heatload, localized at the same spot where the plasma is normally in contact with the first wall (e.g. limiter, divertor plates, etc.). This suggests a conductive/convective heatloss mechanism.

Collective scattering in the TORTUR tokamak

The TORTUR tokamak (R = 0.46 m; a = 0.08 m; B = 2.9 T, $I_p \approx 40$ kA; $n_e < 10^{20}$ m^{-3} and $V_\Omega = 4 - 5$ V) is rather small for the study of the energy quench. The above mentioned timescale for the first phase of the quench gives 25 μs for TORTUR, i.e. is comparable with the duration of the second phase. A clear distinction between the phases is not really possible. Nevertheless, the observations with a 2 mm collective scattering apparatus are interesing because they reveal an increase in electron thermal diffusivity with 2 orders of magnitude during the quench phase of minor disruptions.

Observations with a 2 mm collective collective scattering set-up have been performed in a wide frequency range from 1 kHz to 100 MHz, for various values of the wave number in the region 400 - 4000 m^{-1}. Scattering volumes have been located in the equatorial plane for various values of the radius, and with k of the density fluctuations oriented in or outwards.

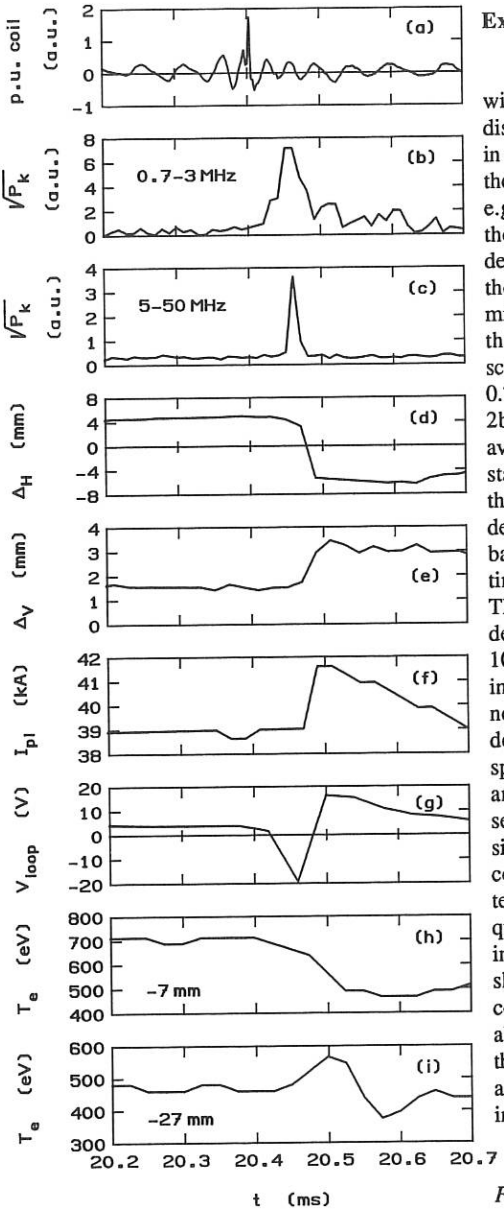

Fig. 1. See the above text

Experimental results.

A number of phenomena associated with minor disruptions in a q(a) = 5 discharge have been observed. The first in the time sequence is a sudden spike on the signals of the magnetic pick-up coils e.g. at 20.4 ms in Fig. 1a. Just before the quench n = 1 and m = 2. Electron density fluctuations strongly increase in the MHz region about one tenth of a millisecond later. This can be seen from the time behaviour of the averaged scattering signals in the frequency bands 0.7 - 3 MHz and 5 - 50 MHz, see Figs 2b and c, resp. The increase of the averaged signal in the 0.7 - 3 MHz band starts somewhat before the increase of the signal in the 5 - 50 MHz band. The density fluctuations in the 0.7 - 3 MHz band relax to the usual level on a timescale longer than their excitation. The duration of the burst of electron density fluctuations is usually about 100 μs. The plasma column shifts inwards (Fig. 2d) and upwards (Fig. 2e) near the ending of the burst of the density fluctuations. Simultaneously, spikes on the plasma current (Fig. 2f) and the loop voltage (Fig. 2g) can be seen. The plasma relaxes to a state similar to the old one on a timescale long compared with the quench phase. The temperature profile broadens during the quench whilst the maximum temperature in the plasma centre decreases. This is shown in Figs 2h and i. In the plasma centre the electron temperature decreases about 100 eV per 0.1 ms starting with the change in MHD activity (Fig. 2h). At about half radius the temperature increases (Fig. 2i).

The time of appearance and the magnitude of the density fluctuations does not depend on radius for r/a ≤ 6/8. However, density fluctuations appear with a delay, are weaker and show a slower relaxtion to normal level fluctuations for r/a > 6/8. This may indicate that an intensive mixing exist in the plasma interior, while, at r/a > 6/8, phenomena follow passively the central events.

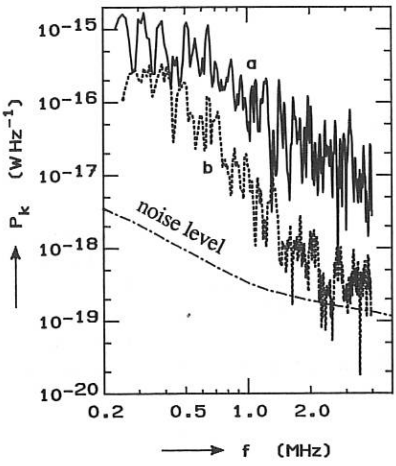

Fig. 2. High-frequency region of spectra obtained at r/a = 0 for k = 18 cm^{-1} during a minor disruption (a) and just before a minor disruption (b).

Changes of a frequency spectrum during a minor disruption can be seen in Fig. 2. The Fourier transforms have been calculated for a time period of 0.1 ms. Two spectra have been obtained just before and during the current spike, curve b and a, respectively. The fluctuation level in the MHz region can be seen to increase by more than an order of magnitude during a minor disruption. Lower frequencies seem to be much less affected. The magnitude of the enhancement of the MHz region is weakly dependent on radius. The enhancement is larger and it extends to higher frequency regions at r/a ≤ 6/8 when compared with observations performed at r/a ≥ 6/8.

The growth rate of unstable modes increases with the increase of the width of the frequency spectrum. The ratio of the growth rate during a minor disruption and during standard plasma conditions can be estimated by $\gamma_{DR}/\gamma \approx 10$ at the plasma interior and by $\gamma_{DR}/\gamma \approx 2$ close to the plasma edge. Apparently the effect of minor disruptions is more pronounced in the plasma interior.

Similar changes in the frequency spectrum during a disruption in TFR were reported by Andreoletti et al. [1].

Poloidal k-spectra have been calculated from the scattered power averaged over 4 ms, see Fig. 3, curve a. It should be noticed that this time interval is much longer than the duration of a minor disruption. The obtained k-spectra are

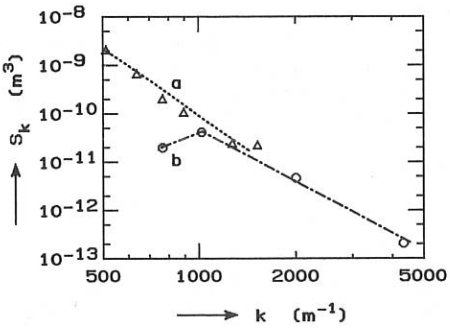

Fig. 3. The observed k-spectra for a plasma with (a) and without (b) minor disruptions, for r/a = 0. S(k) is normalized by the square of the electron density averaged over the scattering volume.

different from those obtained for non-disruptive discharge conditions (curve b) in the following points: 1) no maximum is found and 2) the exponent describing the decay of the spectral density, S(k), is large (- 4.5) compared with the value for a non-disruptive plasma (- 3.5). This implies that the averaged experimental k-value, $\langle k \rangle$, which amounts 1400 m^{-1} for the non-disruptive plasma state, is considerably reduced when disruptions occur. An exact value cannot be calculated, but certainly $\langle k \rangle / \langle k \rangle_{DR} \geq 3$.

Electron thermal transport

Models for the electron thermal conductivity based on $\tilde{E}xB$ transport during drift wave turbulence are employing variants of the mixing-length scaling formula [4]

$$\chi_e \sim \gamma_{max} / \langle k_\perp \rangle^2 \ . \qquad (1)$$

γ_{max} is the maximum value of the growth rate of the unstable mode considered. Numerical values for γ_{max} and $\langle k_\perp \rangle$ have been deduced from the experimental data. The experimentally observed thermal diffusivity, which amounts 0.6 m^2/s, can be retained from the experimental values for γ_{max} and $\langle k_\perp \rangle$ with $\gamma_{max} = 0.5\ \Delta\omega$ and $\langle k_\perp \rangle = 1400\ m^{-1}$ for normal discharges. The value of $(\gamma_{max}/\langle k_\perp \rangle^2)_{DR}$ is at least two orders of magnitude larger. A corresponding increase in heat diffusivity fits well with a temperature redistribution in less than 100 μs compared with the normal confinement time of 3 ms.

Conclusions:

1) During the energy quench phase of minor disruptions enhanced levels of density fluctuations have been observed.
2) Both growth rate and wavelength of these fluctuations increase to such a level, that a corresponding diffusivity would increase with two orders of magnitude. This is in good agreement with the observed temperature redistribution.
3) The frequency of MHz indicates that the energy quench is caused by enhanced turbulence, and not by an explosive growth of a low mode number MHD mode.
4) Further exploration at larger devices is recommendable.

Acknowledgements

This work was performed as part of the research programme of the association agreement of Euratom and the "Stichting voor Fundamenteel Onderzoek der Materie" (FOM) with financial support from the "Nederlandse Organisatie voor Wetenscahppelijk Onderzoek" (NWO) and EURATOM.

References

[1] Wesson J. et al., (1989) Nucl. Fus. **29**, 641.
[2] Callen J. et al., (1978) 7th IAEA Conference on Plasma Physics and Controlled Nuclear Fusion Research, Insbruck, **1**, 415.
[3] Andreoletti J. et al., (1988) EUR-CEA-FC-1336.
[4] Ross D.W. et al., (1987) IPSG panel report, The University of Texas, Austin.

HIGH DENSITY MODE IN "TUMAN-3" TOKAMAK

L.G.Askinasi,T.Yu.Akatova,V.E.Golant,M.P.Gryaznevich,V.K.Gusev,
E.R.Its,S.V.Krikunov,B.M.Lipin,S.V.Lebedev,K.A.Podushnikova,
G.T.Razdobarin,V.V.Rozhdestvensky,N.V.Sakharov,A.S.Tukachinsky,
A.A.Fedorov,F.V.Chernyshev,K.G.Shakhovets,S.P.Yaroshevich

A.F.IOFFE PHYS.-TECHN. INSTITUTE, 194021, Leningrad, USSR

In the experiments on simultaneous magnetic compression and second current ramp up in the "TUMAN-3" [1] the regime with extraordinary high density was found (High Density Mode). The HDM was charachterised with improved confinement properties.

Regimes with high density are of interest due to the importance of the density limit studies [2,3]. It is also interesting to check validity of the "alcator" type scalings ($\tau_E \propto \bar{n}_e$). In [4,5] the significant role of the boundary plasma properties in the density restriction was mentioned. Magnetic compression [6] and fast current ramping [7] allowed to change current density at the periphery and consequently to modify plasma properties in this region.

In the described experimental run the additional gas puffing with simultaneous minor radius magnetic compression and second current ramping was used. Fig.1 shows time evolution of the different plasma parameters in the experiment. Toroidal field was increased two fold during 3.5 ms and then decreased with the time constant 55 ms. Plasma current after the second ramp was 1.4 times higher than the initial one. Current increase time was equal to 4. ms. In the bottom part of Fig.1 dashed line represents the model function of the feedback density control system and solid one corresponds to the density behaviour in the experiment. The density was increased from $1.4 \cdot 10^{13} cm^{-3}$ in the ohmic stage up to highest value $5.2 \cdot 10^{13} cm^{-3}$ in the HDM during 15 ms. Plasma parameters in the HDM and in the initial OH are listed in the Table and presented

	I_p kA	B_T kG	q^{cyl}	$\bar{n}_e$ $10^{13}cm^{-3}$	T_{eO} keV	T_{iO} keV	τ_E ms	τ_p ms	Z_{eff}	β_T^{max} %	$\bar{\beta}_T$ %
OH	94	4,5	2,7	I,4	0,4	0,II	I,5	2,5	2,0	I,9	0,4
HDM	I20	6,7	3,2	5,2	0,5	0,I7	6,5	I5	2,2	3,5	0,9

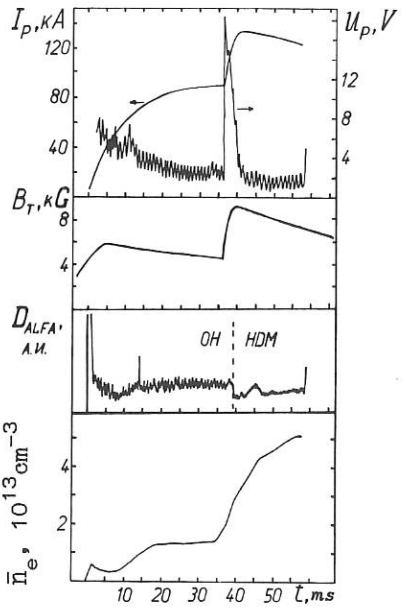

Fig.1. Plasma current, loop voltage, toroidal field, D_α emission and density in the experiment with second current ramp and magnetic compression.

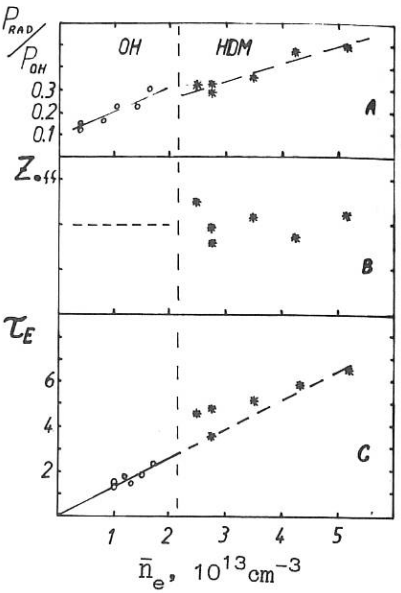

Fig.2. Radiation power to ohmic input ratio (a), Z_{eff} (b) and τ_E (c) dependences on average density in OH and HDM.

in Fig.2. It could be mentioned that attained density was about two times OH limit and corresponded to .85 Greenwald limit [2].

In the HDM an increase of radiation losses was observed. In Fig.2a the ratio of the radiation power to the ohmic input

is shown in the usual OH regimes with $\bar{n}_e = (.4 - 1.6)10^{13}cm^{-3}$ and in the HDM with $\bar{n}_e = (2.5 - 5.2)10^{13}cm^{-3}$. This ratio increased with a density but nevertheless it was far from 100 %. The maximum value of P_{RAD}/P_{OH} was .5. Plasma effective charge didn't decrease with the density. The value of Z_{eff} in the HDM was about 2 and this was close to the ohmic one, Fig.2b. In the OH stage the particle confinement time τ_p was measured using periodic modulation of the neutral influx and was equal to 2.5 ms. An estimation of τ_p value in the HDM was made from the global particle balance equation with the source term derived from D_α emission. Particle confinement time was equal to 15 ms, which corresponded to the time needed for the density to achieve second flattop.

Nonmonotonic evolution of the SXR emission was found in the HDM. As is shown in Fig.3 J_{SXR} rised up to 44 ms and then fell down. Approximately at the same time density increase rate decreased. Our data couldn't clear up what is the reason for the observed restriction of W(0) (energy content at the centre). Perhaps the cause was the peripheral instability or dramatic increase of sawtooth oscillation amplitude due to the approach of $j(0)$ or $\beta(0)$ to a critical value. The deduced from SXR signals $T_e(0)$ drop was confirmed by TS measurements. During 5 ms (from 45 to 50 ms) T_e profile become essentially broader but the whole energy content didn't change significantly. At 45 ms W = 1.13 kJ and at 50 ms W = 1.09 kJ.

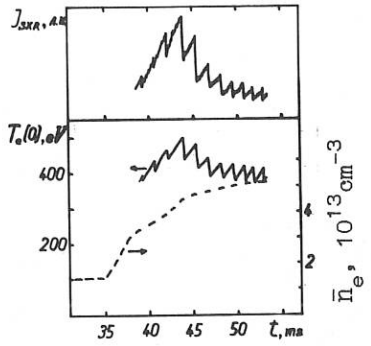

Fig.3. Intensity of SXR emission, deduced from the SXR data $T_e(0)$ and average density evolution in HDM.

Since the HDM discovering allowed to extend $\bar{n}_e$ operational range then it seems to be interesting to compare energy confinement in this new regime with extrapolation of the ordinary OH scaling. Circles on the Fig.2c display τ_E in some OH shots with $q^{cyl}(a)$ close to that one in the HDM. The dashed line is an extrapolation of the linear dependence of $\tau_E(\bar{n}_e)$ in the high density region. This extrapolation is close to Neo-Alcator scaling prediction. The corresponding to the HDM stars lie near or slightly higher than the mentioned line. Taking into account the energy content derivative one can find that experimental τ_E exceeds OH scaling by a factor of 1.2-2.0. This proves an absence of the energy confinement time saturation at high density (saturation of this kind was observed in the experiments on ASDEX [8] and TFTR [9]) and indicates some improvement of τ_E in comparison with OH scaling.

Improvment of the particle and energy confinement in the HDM indicated appearance of H-mode without permanent additional heating. Ohmic H-mode phenomena were observed in the DIII-D experiments [10] and also in our experiments [11]. It should be mentioned that in "TUMAN-3" experiments H-mode were observed in the limiter configuration whereas in DIII-D divertor was used.

REFERENCES

1. Vorobyov G.M. et al, "Fizika Plasmy"(Sov.),1983,9,105.
2. Greenwald M. et al,Nuclear fusion,1988,28,2199.
3. Toi K. et al,Nuclear fusion,1979,19,1643.
4. Stabler A. et al,Proc.16 Eur.Conf. on Contr.Fus. and Plas. Phys., Venice,1989,13B-I,23.
5. Wesson J.A. et al, Nuclear fusion,1989,29,641.
6. Bender S.E.et al,Proc.11 Eur.Conf. on Contr.Fus. and Plas. Phys., Aachen,1983,7D-I,111.
7. Askinasi L.G. et al,"Voprosy Atomnoy Nauki i Techniki", ser. "Termoyaderny Sintez"(Sov.),1988,3,53.
8. Soldner F.X. et al,Phys.Rev.Lett.,1988,61,1105.
9. Efthimion P.C.et al,Proc.14 Eur.Conf.on Contr.Fus.and Plas. Phys., Madrid,1987,11D-I,136.
10. Schissel D.P. et al, Proc. 16 Eur. Conf.on Contr. Fus. and Plas. Phys., Venice,1989,13B-I,115.
11. Arbusov A.N. et al, this conference.

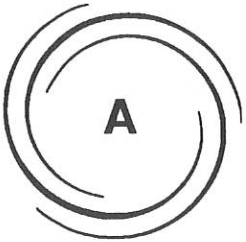

TOKAMAKS

A8 VERTICAL INSTABILITIES

A8

NONLINEAR VERTICAL DISPLACEMENT INSTABILITY OF ELONGATED PLASMA IN TOKAMAK AND ITS STABILIZATION

Yu,G.Y., Du,T.

Institute of Plasma Physics, Academia Sinica (ASIPP)
Hefei, 230031. The People's Republic of China

Abstract Nonlinear vertical displacement instability (nonlinear VDI) for highly elongated plasma with a finite cross-section in tokamak is investigated by solving the equation of plasma motion and Kirchhoff equations of the surrounding conductors. The results show that there are two components of VDI, namely a fast oscillation with a period of few microseconds and a slow shift with a characteristic time comparable to the resistive time of the conductors. The critical elongation for VDI can be explained as that beyond which the fast oscillation can not be suppressed by the passive inductions in the conductors. The active controlling system usually can play almost no role in the elevation of the critical elongation. As an alternative approach, the dynamic stabilization of VDI proposed is shown to be feasible. Its simplicity and wide range of working frequencies indicate that it would be a potentially promising stabilizing method.

I. INTRODUCTION

One of the key problems of the elongated plasma is VDI caused by a negative decay indexn of the equilibrium field B_z applied, defined as

$$n = -\frac{R}{Bz}\frac{\partial Bz}{\partial R} \qquad (1)$$

where R is the coordinate in the major radial direction. For present tokamak experiments, VDI is stabilized by both the passive induction in the surrounding conductors (SCs) and the active feedback system. In case of small displacement VDI and its stabilization can be treated linearly. But for highly elongated case, a finite displacement of plasma leads to that the nonlinear coupling among the various conductors including plasma itself should be taken into account, which is studied in this paper. Since the emphasis is put on how to stabilize VDI in a tokamak, we start from the equation of plasma motion as well as Kirchhoff

equations of SCs.

In sec.II the basic equations are introduced for nonlinear VDI. After the freedback results are shown in sec.III, the dynamic stabilization is studied in sec.IV. Conclusions are given in sec.V.

II. BASIC CONSIDERATION

The vertical motion of plasma can be described by the equation

$$m \frac{d^2 Z}{dt^2} = -2\pi R_p I_p B_R \qquad (2)$$

$$B_R = B_R^{(M)} + B_R^{(S)} + B_R^{(A)} \qquad (3)$$

here Z is the displacement; m, I_p and R_p the mass, current and the major radius of the plasma torus; M, S and A in (3) stand for the equilibrium, the passive-produced and the active-produced fields respectively.

In tokamaks (Fig.1) all of the toroidal currents are coupled with each other, which is governed by Kirchhoff equation

$$\sum_{\beta \neq \alpha} \sum_k \frac{d}{dt} M_{kj}^{(\alpha\beta)} J_k^{(\beta)} + \frac{d}{dt} L_j^{(\alpha)} J_j^{(\alpha)} + R_j^{(\alpha)} J_j^{(\alpha)} + \sum_k \frac{d}{dt} M_{kp}^{(\alpha P)} I_p = V_j^{(\alpha)} \quad \alpha,\beta = S,A \qquad (4)$$

$$V^{(A)} = g R^{(A)} I_p (Z(t) - Z(0)) \qquad (5)$$

where R_j, L_j, J_j, V_j and M_{kj} are the resistance, inductance, current, the applied voltage of the j-th coil, the mutual inductance between k-th and j-th coils, respectively. The subscript p means plasma. V in (5) is for active feedback, with a reference position Z(0) and a gain factorg. We take a finite cross-section of plasma into account and assume that the displacement is rigid. In our case, both R_R's and M_{kj}'s are functions of Z(t) and the problem becomes nonlinear. A fourth-order Runge-Kutta method is used for the numerical solution.

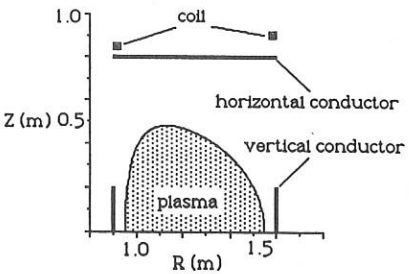

Fig.1 The tokamak model used with parameters of R=1.25m, a=0.3m, Bt=2T, Ip=450KA, e=b/a=1.6 and triangularity=0.4.

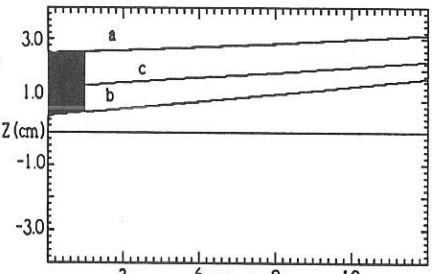

Fig.2 Z(t) of VDI in plasma. 'a','b': the envelopes of the fast oscillation; 'c': the trace of the oscillating center.

III. FEEDBACK STABILIZATION AND CRITICAL ELONGATION

First the passive stabili-

zation is considered only by setting g in (5) to be zero. Figs.2-3 show Z as a function of t. It is seen that VDI can be decomposed into two components, namely a fast oscillation (Fig.3a) with a period of several microseconds and a decaying amplitude (Fig.2), and a slow shift (Fig.3b) with a characteristic time of about several to tens milliseconds depending on the resistive time of SCs. The locus in Fig.3b-3c can be understood as the traces of the oscillating center in Fig.3a. In a stable case, both fast and slow components of Z(t) are decaying with time. If the elongation exceeds a certain value, then the amplitude of the fast oscillation is growing and VDI can't be stabilized no matter how the value of the gain factorg is set, as shown in Fig.4. We believe that this is the reason for the existence of the critical elongation. The closer spacing of the passive conductors w.r.t. plasma can elevate the critical elongation as in Fig.4c.

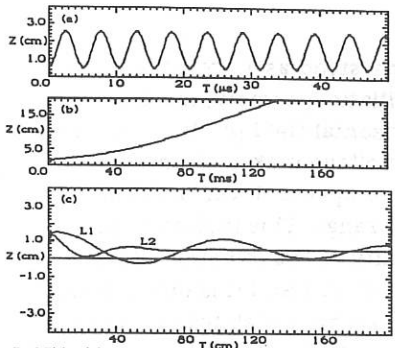

Fig.3 Z(t) in (a) fast oscillation; (b) slow shift without feedback; (c) slow shift with feedback stabilization. L1 : g=80 and Pmax=40KW; L2: g=300 and Pmax=140KW. Pmax is the maximum power required.

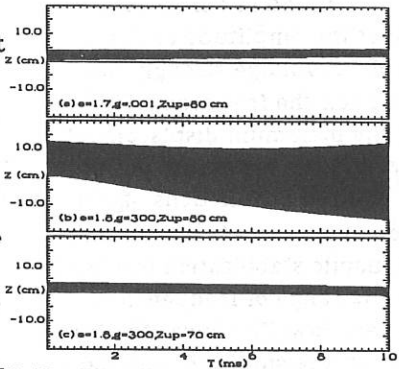

Fig.4 Fast oscillation of VDI with different elongation e, the gain factor g and the height of the passive conductors from the mid-plane Zup. It is seen that the critical elongation for Zup=60 cm is about 1.7.

IV. DYNAMIC STABILIZATION

If we think such a case as stable that the plasma displacement is slowly varying in time but within a certain region, then instead of the feedback control system we apply an a.c. (e.g. cosine) voltage on the active coils by setting

$$V^{(A)} = A\, R^{(A)} I_P \cos(\omega t) \qquad (6)$$

and substitute it into eq.(4). The frequency in (6) is taken to be close to the inverse of the resistive time of SCs. The result shows that for given frequencies a certain range of the amplitude A in (6) can be found to make plasma moving periodically around an equilibrium position, as shown in Fig.5, and hence to make VDI stabilized. Physically it can be

understood as a process of forced oscillation, namely, the periodic horizontal field produced by the a.c.voltage makes plasma torus move up and down within a certain range. This indicates the feasibility of the dynamic stabilization of VDI and it is obvious that the dynamic stabilizing sche-me can make the active controlling system very simple.

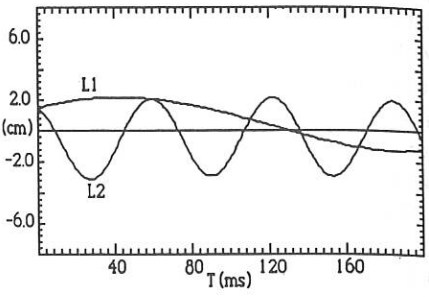

Fig.5 Z(t) in case of dynamic stabilization with Z(0)=0.5cm. L1: ω=15 and Pmax=15KW; L2: ω=100 and Pmax=1100KW.

It is found in our calculation that the amplitude of the applied a.c. voltage strongly depends upon the frequency. Fig.6 gives the maximum displacement Z_{max}, A and the maximum power P_{max} required as functions of ω for a given elongation. It is seen that the dynamic stabilization can work in a wide range of frequencies, even very low. The lower the frequency is, the smaller Z_{max} is and, perhaps more importantly, the less maximum power requirement is.

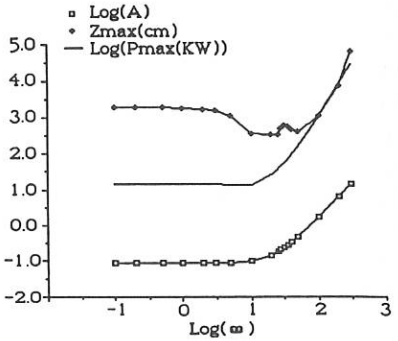

Fig.6 Dependence of Zmax, A and Pmax on ω in case of Z(0)=0.5cm.

V. CONCLUSIONS

1. VDI is composed of a fast oscillation and a slow shift the characteristic times of which are about several microseconds and several to tens milliseconds respectively.

2. The critical elongation can be explained as that beyond which the passive induction can no longer suppress the fast oscillation of VDI. Thus a strong coupling between SCs and plasma is needed to stabilize VDI for highly elongated plasma.

3. Dynamic stabilization is shown to be effective. Its physical feasibility, the technical simplicity, the interesting frequency effect and a low power requirement, make this scheme to be a potentially attractive way in stabilizing VDI.

This work is supported in part by The National Science Foundation of China.

VERTICAL INSTABILITIES IN JET

P.Noll, T.Bonicelli, M.Garribba

JET Joint Undertaking, Abingdon, Oxfordshire, UK

Introduction

The vertical position of the JET plasma is actively stabilised by an externally applied radial magnetic field. Without feedback the vertical position is unstable due to the destabilising effect of the iron magnetic circuit and due to the quadrupolar magnetic field required to obtain the desired elongation b/a = 1.4...1.9 of the plasma cross section. If the stabilisation fails the plasma moves vertically and disrupts causing large vertical and asymmetric radial forces at the vessel which are of concern when operating at high current.

A sudden technical failure of the stabilisation system has been regarded as the most serious fault case and must be considered as possible even though faults of this kind did not occur in JET. The expected effects of a complete stabilisation failure have been studied by deliberately disabling the feedback during the pulse [1,2].

All vertical instabilities observed during normal operation can be ascribed to the existence of a limited stabilisation range and to the effects of large amplitude perturbations leading to saturation and degradation of the stabilisation system.

In the following the electromagnetic aspects of vertical instabilities in JET are examined and the implications for the planned operation with a divertor coil inside the vessel are outlined.

Stabilisation range

The stabilisation of elongated Tokamak plasmas has been widely studied, for example in [3,4,5]. The degree of elongation which can be achieved inside a metallic vessel and with externally applied stabilising fields depends on the plasma/wall gap and on the response time of the stabilisation amplifier. Without stabilisation the instability growth time is roughly proportional to the radial field penetration time Tv of the vessel and it decreases with increasing gap width. For stabilisation the response time Ta of the radial field amplifier must be smaller than the growth time. At some critical gap width an MHD limit is reached where no stabilisation is possible by external means.

In JET quiescent plasmas can be stabilised up to an elongation ratio of about 1.9 (corresponding to a growth time down to about 3 ms). The feedback gain must be set within a window which decreases with increasing elongation. The amplifier response time is Ta $\approx$ 2ms for small amplitudes, but it increases at larger amplitudes. The stabilisation performance degrades therefore if large plasma perturbations are present.

Observations

A frequent cause of vertical instability is a saturation of the amplifier resulting from disruptive plasma behaviour. This is not serious if the instability starts after the beginning of the current quench. However, the saturation and the onset of instability take often place before the current quench, in which case the instability can escalate at high current leading to large vertical forces at the vessel.

An example is the disruption of a 4MA double null magnetic limiter plasma shown in fig.1. Shortly after the energy quench at 12.63 s the feedback control signal (not shown) asks for the maximum possible amplifier voltage (about 4kV). The response is insufficient and the plasma becomes unstable. The vertical displacement δZp reaches about 1m while the current is still large. The original configuration is up/down symmetric. It is therefore apparent that the disruption caused an up/down asymmetric perturbation which exceeded the capability of the stabilising system. The perturbation must have occurred suddenly as can be inferred from the initial plasma displacement of about 3cm within 1ms. From simplified circuit and plasma force balance equations one can interpret this displacement and the associated differential loop voltage $\delta V \approx 150$ V as resulting from a sudden vertical force $Fz \approx -.25$ MN acting on the plasma. The same model indicates that a force of this magnitude drives the amplifier into saturation and causes a vertical instability without possibility of recovery, as observed.

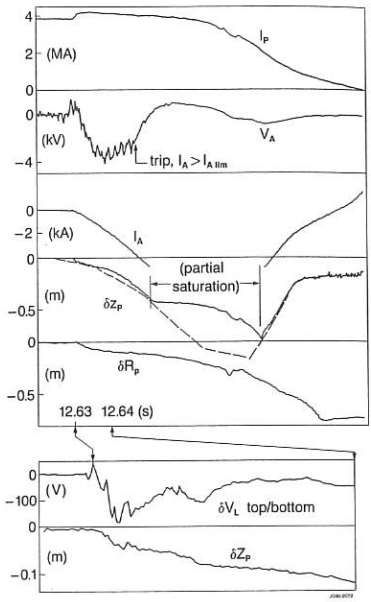

Fig.1 Vertical instability of a 4MA double null plasma (pulse 20802)

The example shown represents the most severe case of a vertical instability observed so far. In most other disruptions of double null plasmas the instability escalated far less dramatically.

There is no significant difference of the disruption and instability behaviour of up/down symmetric plasmas (double null or limiter plasmas) and up/down asymmetric plasmas (single null).

Some vertical instabilities were caused by perturbations which can not be clearly identified. They occurred usually shortly after the removal of neutral beam heating. The instability and the subsequent disruption might have been prevented by a more powerful stabilisation system. In few

cases plasmas became unstable without stimulation during the ramp-up of the destabilising shaping field, starting with growing oscillations as is characteristic when the linear stabilisation range is exceeded.

An important general observation is that the vertical displacement δZp of the plasma reaches some maximum and decreases thereafter. This is not expected from simulations but may be understood in terms of poloidal plasma currents which are branching into the wall.

Forces

During the vertical instability the destabilising force Fd at the plasma must be balanced by stabilising forces. The accountable stabilising forces are -Fr due to the radial field coil current and -Fv due to vessel toroidal currents. One finds that Fv is ignorable around the time when the product $Ip*\delta Zp$ reaches a maximum, and that Fd - Fr > 0. The plasma force balance is only possible by postulating an additional repelling force Fadd = Fd - Fr between the plasma and the vessel. There is evidence from toroidal field measurements inside the vessel that this force arises from poloidal currents circulating in the plasma and the vessel [2].

The maximum vertical force at the vessel is approximately Fvess Fd - Fr. It has been evaluated for a number of instability tests and can be reasonably described by $Fvess \approx f*D$, where f is in the range .25 to .35 MN/(MA^{2}m) depending on the relative magnitude of the shaping field, and D = maximum of $Ip^2*\delta Zp$. D is not predictable, but from a series of vertical disruptions it is found that the equivalent displacement D/Ipo^2 (Ipo = current before the instability) did not exceed 1.07 m. This permits some forecast for operation at higher currents. The vertical force at the vessel supports is measured routinely with strain gauges. One finds $Fsupp/Fvess \approx .6$ (i.e. ≠ 1), probably mainly due to vessel elasticity and inertal effects.

Implications for a divertor operation

The single null plasma of the planned operation with a divertor coil inside the vessel is more unstable than present magnetic limiter plasmas. This requires an enhancement of the stabilisation system. A simplified system analysis indicates that use must be made of the passive stabilising capability of the divertor coil. Simulations with the PROTEUS code give an instability growth time of about 2.2 ms. Therefore a fast radial field amplifier (four quadrant inverter) is foreseen with response time <.5ms. The power rating will be doubled to P = 25 MVA in order to permit a better recovery from perturbations. The fig.2 shows a simulation of the response upon an assumed pulse force Fz = .12 MN applied at a 6MA divertor plasma. The plasma displacement is 4cm and the peak power is 10kV*1.5kA = 15MVA. When fully exploited and optimised it may be possible to obtain recovery from an assumed force of .2 MN which is comparable with the apparent perturbation estimated for the disruption of pulse 20802 shown in fig.1.

Simulations of disruptions and vertical instabilities indicate that the force at vessel supports can reach 6MN which is acceptable. The Fig.3

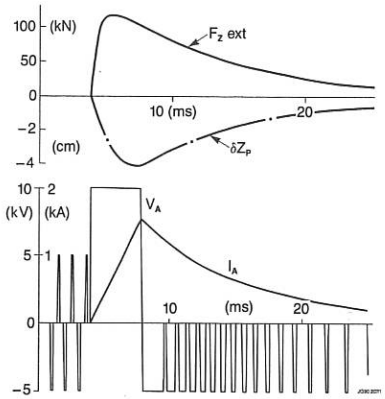

Fig.2 Simulated response of the stabilisation system upon a force perturbation at a 6MA divertor plasma.

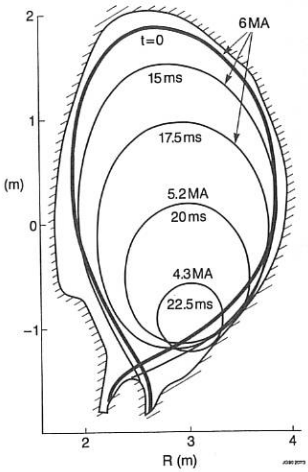

Fig.3 Simulated vertical instability of a 6MA divertor plasma. The current quench is assumed to start with 18 ms delay.

illustrates a downward vertical instability. Poloidal circulating currents are disregarded. This may explain why the simulation shows a monotonous plasma movement contrary to observations in present experiments.

Conclusions

Highly elongated magnetic limiter plasmas have been produced. But the vertical stabilisation has a small margin and larger perturbations such as disruptions can cause saturation and a vertical instability, unexpectedly also in up/down symmetric plasmas. A faster and more powerful amplifier is foreseen for the planned operation with an internal divertor coil. It is expected to improve the robustness of the stabilisation and to reduce the frequency of vertical disruptions.

Acknowledgement

We would like to thank Oreste De Barbieri and Raffaele Albanese who developed the PROTEUS code and gave a tremendeous assistance for its implementation in JET.

References

[1] P Noll et al, Fusion Technology, Vol.15, No 2A (March 1989) 259.
[2] R A Albanese et al, 15th SOFT, Fusion Technology 1988, Vol 1, 694.
[3] M Mori et al, Nucl.Fusion 26 (1987) 725.
[4] N Pomphrey, S C Jardin, D J Ward, Nucl.Fusion 29 (1989) 465.
[5] E A Lazarus, J B Lister, G H Nelson, Nucl.Fusion 30 (1990) 111.

SCALING OF POLOIDAL CURRENTS DURING RAPID VERTICAL DISPLACEMENT EVENTS

G. W. Pacher and H. D. Pacher

The NET Team, c/o Max Planck Institut für Plasmaphysik
Boltzmannstrasse 2, D-8046 Garching, FRG

Abstract:

Currents in the tenuous plasma periphery have been measured in DIII-D[1,6], and their existence had been postulated in JET[2,4], during rapid vertical displacements of the plasma. Since the currents close through the first wall elements, it is necessary either to take into account the electromagnetic forces they produce on the attachments of these components or to insulate the plasma facing components to interrupt the currents. In this paper, we invoke the conservation of toroidal flux to extrapolate these currents to reactor-size tokamaks. The poloidal loop voltage produced by the flux change is so large that insulating gaps between poloidal segments would be short-circuited by plasma.

Introduction:

In order to increase the plasma current at constant safety factor, elongation in reactor-size tokamaks will be high, of the order of two. Such plasmas are unstable vertically, so that their vertical position must be controlled by a rapid feedback system. If this control fails for any reason, the plasma is rapidly displaced vertically, and strikes the bottom (or top) of the containment structure. The vertical displacement is braked by eddy currents induced in the surrounding structures. An electromotive force is produced on the plasma by its motion in the toroidal field. This emf can cause currents to flow in the periphery of the plasma. If the plasma facing components are conductors, which is generally the case, the currents can close through the plasma facing components, thereby exerting localized forces. This paper scales the currents induced in the plasma periphery and closing poloidally through the plasma facing components from present experiments to reactor-sized plasmas under simplifying assumptions discussed in the next section.

Model:

As a model, we take a toroidal plasma moving strictly vertically (i.e. at constant major radius) with a prescribed vertical velocity. During the motion, the shape of the surfaces is assumed not to change. (This corresponds to a plasma moving in a vertical field without curvature, so that in this approach, there is actually no destabilizing force on the plasma. The model is therefore not self-consistent.) As the plasma moves, it touches a horizontal limiting surface, which is assumed to be axisymmetric and which scrapes off the outer layer of plasma. However, there remains a tenuous plasma, the "halo", on the magnetic surfaces intersecting the horizontal limiting surface[6]. This scrape-off layer, a reasonably good conductor, is electrically connected, via the sheath, to the limiting surface. If this surface is also a conductor, we have a circuit whose enclosed area, and therefore enclosed toroidal flux, is decreasing. This induces an electromotive force in the poloidal direction, which can drive a

current through the circuit.

Defining C(b) as the circumference of the surface with vertical half-axis b and assuming constant toroidal field as the plasma moves, we write for the poloidal emf V_{pol}:

$$V_{pol}=\frac{d}{dt}\int B_{tor}\cdot dA=B_{tor}\cdot C\cdot v_{vert}\cdot f(K,\delta)$$

where A is the cross-sectional area and $v_{vert}=db/dt$ is the speed of vertical motion. The function f of elongation K and triangularity δ is a slowly varying geometrical factor in the range of .65 to .9. The emf is applied to a circuit loop containing, in series, the sheath for ion collection, the resistance of the tenuous plasma, the sheath for electron collection, and the resistance of the conducting path in the plasma facing components.

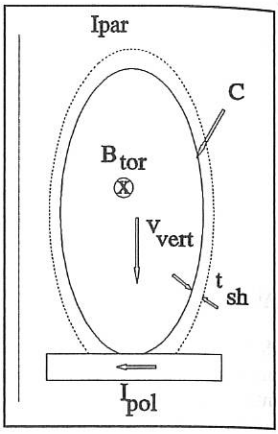

$$V_{pol} = V_{sh} + I_{pol}\cdot R_{pfc} + I_{par}\cdot R_{par}$$

$$R_{par} = L_{par}/(A_{perp}\cdot\sigma) = (C/\sin\beta)/(A_{bdy}\cdot\sin\beta\cdot\sigma)$$

where: I_{pol} - poloidal current in the limiting horizontal conductor, R_{pfc} - resistance of this conductor, I_{par} - current parallel to the magnetic field in the tenuous plasma, emanating from the limiting conductor (note: total parallel current flowing across a vertical cross-section is $I_{par}\cdot q$), R_{par} - resistance of the current path in the plasma (parallel to B), σ - parallel conductivity, A_{bdy} - sheath area, equal to sheath thickness t_{sh} times $2\cdot\pi\cdot R$, β - angle between field line and toroidal direction; for small ß, and small inverse aspect ratio, $\sin\beta \sim \tan\beta \sim C/(2\cdot\pi\cdot R\cdot q)$

Note that, from continuity the poloidal current in the limiting horizontal conductor equals the current in the plasma periphery, i.e. $I_{pol}=I_{par}$, so that

$$I_{pol} = (V_{pol} - V_{sheath})/(R_{par}+R_{pfc})$$

If V_{sheath} and R_{pfc} are small compared to V_{pol} and R_{par} respectively, this simplifies to the expression:

$$I_{pol} = f(K,\delta)\cdot(2\cdot\pi\cdot R)^{-1}\cdot B_{tor}\cdot v_{vert}\cdot t_{sh}\cdot\sigma\cdot(C^2/q^2) \qquad (1)$$

Characteristics of plasma periphery from experiments

The unknown quantities in the expression for I_{pol} are the conditions of the plasma periphery, t_{sh} and σ. However, these are not expected to vary widely. We can substitute the experimental values of B_{tor}, I_{pol}, v_{vert}, C, and q from DIII-D and JET into formula (1) to obtain the product of $t_{sh}\cdot\sigma$ for those experiments.

In JET, the estimate from fig. 5, ref. 4, for shot 15100 at ~50.05 s is: I_{pol}~500 kA, v_{vert}~24m/s. With B_{tor}=1.8T, R=2.96 m, and taking f=0.75, this gives:

$$t_{sh} \cdot \sigma \sim 2.9\text{x}10^5 \cdot (q^2/C^2) \quad \text{ohm}^{-1}\text{m}^{-2}$$

The ratio of (q/C) is estimated from fig.3, ref.3, where q=2.32. We estimate C to be 10 m and assume that the ratio does not change over the next 20 ms, so that

$$t_{sh} \cdot \sigma \sim 1.5\text{x}10^4 \quad \text{ohm}^{-1}\text{m}^{-2} \text{ for this JET shot.}$$

For DIII-D, the estimate is obtained from fig. 12 of ref. 6. At 2684 ms I_{pol}~150 kA, v_{vert}~75 m/s, B_{tor}=2T, R=1.67m. The plasma is not strongly elongated so f~1. This gives:

$$t_{sh} \cdot \sigma \sim 1.05\text{x}10^4 \cdot (q^2/C^2) \quad \text{ohm}^{-1}\text{m}^{-2}$$

To estimate the ratio of (q/C) for this shot at this time, we use the measured total toroidal current in the plasma I_m=0.9MA from fig. 13, ref. 6. For these values of poloidal and measured currents, the contribution ($\sim q \cdot I_{par}$) of I_{pol}(= I_{par}) to the measured toroidal current is significant. A typical value of q is obtained (for a=0.5 m) by taking the enclosed current at a typical point in the plasma periphery, $I_{typ} = I_m - q_{typ} \cdot I_{pol}$. This gives q_{typ}=3, so that (q^2/C^2) ~ 1. Therefore, the estimate becomes:

$$t_{sh} \cdot \sigma \sim 1.\text{x}10^4 \quad \text{ohm}^{-1}\text{m}^{-2} \text{ for this DIII-D shot.}$$

In spite of the approximations and extrapolations, the values obtained are within a factor of two for the two experiments.

Extrapolation to reactor-like machines

For extrapolation to reactor-like machines the value obtained in the preceding section is substituted in equation (1). With $t_{sh} \cdot \sigma = 1.5\text{x}10^4$, R=6 m, C=21 m, B_{tor}=4.85 T, f=0.75:

$$I_{pol} \sim 0.6 \cdot v_{vert} \cdot q^{-2} \quad \text{MA}, \quad V_{pol} \sim 0.08 \cdot v_{vert} \quad \text{KV}$$

Evaluating for v_{vert}=50 m/s, q=3, gives:

$$I_{pol} = 3.5 \text{ MA}, \quad V_{pol} = 4 \text{ kV}, \quad R_{par} \sim 1 \text{ mohm}$$

Voltages between components

In this model, the poloidal voltage is developed by the reduction of enclosed toroidal flux, and is essentially independent of parameters other than the average toroidal field and the time-rate of change of plasma area. Voltage division, however, depends on the characteristics of the circuit. In the preceding section a reasonable speed of displacement of the plasma is shown to produce a poloidal voltage of several kilovolts. For such conditions, and for plasma temperatures typical of the plasma periphery (e.g. 20-30 eV) the sheath voltage will be small compared to the total poloidal emf (justifying a posteriori the neglect of V_{sheath} in the above calculation). The poloidal emf will then be shared between plasma and plasma-facing components in inverse proportion to the resistances R_{par} and R_{pfc}. We have shown that the plasma resistance R_{par} is several milliohms. For the normal case of

conductors (even poor conductors) limiting the plasma, the plasma therefore represents the largest resistance and accounts for the major part of the voltage drop. As a consequence, the toroidal distribution of current would not be expected to be strongly affected by local variations in sheath and boundary conditions.

If the plasma-facing components were insulated, the total poloidal emf developed would remain the same as long as the speed of displacement remains the same. The voltage developed, however, would be concentrated at the insulating gaps. Since emfs of several kilovolts can be developed, the insulating gaps would be short-circuited by the plasma, leading to similar poloidal currents.

In the limiting case in which no current flows to the wall (insulating plasma-facing component tile material), a current could be driven across the magnetic lines of force by the emf in the region where the plasma touches. From MHD considerations, this would be accompanied by a pressure gradient towards the wall, as has been considered in ref. 3 to explain JET observations.

Discussion and Conclusion

For an accurate description, a predictive model is required, which includes MHD effects, sheath resistance, a good description of the plasma halo, and accurate modelling of the passive structures (eddy currents). Such a model is being developed for DIII-D[5].

The scaling presented here can clearly not replace such a model. It assumes purely vertical motion of the plasma without change in shape, which cannot be true in the experiments. The only driving term for the poloidal current considered here results from the reduction of enclosed toroidal flux due to the plasma motion. Depending on the experimental situation, other driving terms, such as the toroidal voltage produced by the plasma current quench (ref. 7) could be of the same order. The vertical speed resulting from the forces due to the poloidal current treated here and other forces such as those arising from eddy currents in passive structures is treated as a known input. In a given experimental situation, however, this force may be a major determining component of the motion. Whenever the velocity is actually measured, it can be inserted into the formula, and, as we have shown, reasonable agreement is found between two experimental situations.

The extrapolation to reactor-size machines gives values of currents in the plasma periphery of several megamperes and poloidal emfs of several kilovolts for vertical speeds in the range of those observed in present-day experiments. Before a complete model is available, these quantities could be predicted more accurately by calculating the plasma motion when vertical position control is disabled, including the effect of passive structures, but ignoring the force resulting from the effect of currents in the periphery. The poloidal currents can then be obtained by a treatment similar to that in this paper, and the resulting force taken into account iteratively.

References

[1] Jensen & Chu, Phys. Fluids B1, 1545 (1989)
[2] P. Noll et al., Proc. 11th Symp. on Fusion Eng., 1985, 1 p.33
[3] R. Albanese et al., Fusion Technology 1988, p. 694 (1988)
[4] P. Noll et al., Fusion Technology 15, p.259, (1989)
[5] T. H. Jensen, D.G. Skinner, "Support of Model for Vertical Displacement Episodes from DIII-D Experimental Results", GA Report GA-A19882, to be published
[6] J. Luxon, T. Taylor, contribution to ITER Phys. R&D, ITER-TN-PH-9-7/PH07-U3
[7] P. Noll, private communication

EXPERIMENTS AT HIGH ELONGATIONS IN DIII–D*

E.A. Lazarus,† A.D. Turnbull, A.G. Kellman, J.R. Ferron, F.J. Helton,
L.L. Lao, J.A. Leuer, E.J. Strait, and T.S. Taylor

General Atomics
San Diego, California 92138, U.S.A.

In this paper we discuss the limitation to elongation observed in D-shaped plasmas in the DIII–D tokamak. We find that as the triangularity is increased and ℓ_i is decreased that the $n = 0$ mode takes on an increasingly non-rigid character. Our analysis shows two aspects of the behavior; first, an increasing variation of the m/n = 1/0 component across flux surfaces and second, an increase in the relative amplitude of a m/n = 3/0 component which couples to the m/n = 1/0 component and further destabilizes the mode.

In previous work[1] we have reported on a study of vertical control and the implementation of those results on DIII–D. In that study we used a single filament, with properties consistent with the radial force balance, to represent the plasma and employed an eigenmode description of the passive shell in order to allow time-ordering of the problem. The most important result of this study was that the active control coil must be positioned in the poloidal plane so as to minimize its interaction with the stabilizing shell currents. As a consequence of plasma toroidicity, these currents flow primarily in the outboard regions of the shell. Thus, control coils on the inboard side of the shell, near the midplane, are required. With such a spatial arrangement we can have radial fields from the active coil penetrating the shell on a time scale faster than the decay of the stabilizing shell currents. In accordance with these model calculations the control system for the DIII–D tokamak has been modified resulting in operation to within a few percent of the ideal MHD limit for axisymmetric stability. In this work we refer to the ideal MHD limit as that of the plasma-shell system. As discussed in Ref. 1, the ideal limit can actually be reduced by a poor choice of the active control coils, however that is not the case for work discussed here.

In Ref. 2 we reported on detailed measurements of the plasma response to that control system and concluded that the model of Ref. 1 is quite accurate and adequate to prescribe the control function. We have also reported in Ref. 2 that the modifications to the control system have enabled us to reach elongation, κ, up to 2.5 transiently and $\kappa > 2.45$ for more than 0.5 second. Also, behavior characteristic of the destabilization of the plasma-shell system by use of control coils on the outboard side of the plasma was experimentally observed. With this improved vertical control, operation of double null divertors with elongations of 2.15 have become routine. Behavior at higher elongations is quite sensitive to the plasma shape and the width of the current profile.

The reader may notice small differences in the stability margins quoted here as compared to those in previous work. The primary reason for differences of several percent is that in previous work we had used the contour of the graphite tiles to define the stabilizing shell. In fact, the conducting shell (vacuum vessel wall) is approximately 5 cm. behind the graphite surface and we have now made this correction. Also, we have refined our calculation of n_c

EXPERIMENTAL RESULTS

We wish to focus on two particular discharges, #60809 and #63422. The equilibrium parameters for these plasmas are given in Figs. 1 and 2. The equilibria are calculated several milliseconds before the vertical instability which results in disruption. The distinction of interest is that the former has a higher ℓ_i and a lower triangularity, δ, than the latter. The motivation for choosing these plasmas is centered about the quantity n/n_c. The decay index n is defined as

$$n \equiv -\frac{R}{B_z}\left.\frac{\partial B_z}{\partial R}\right|_{\substack{R=R_c \\ z=z_c}} ,$$

where R_c ,z_c is the centroid of the plasma current. The critical index, n_c, is

$$n_c \equiv \frac{2\,M_{vp}'^{\,2}\,R_0}{\mu_0\,\Gamma L_v}, \quad \Gamma \equiv \frac{L_{\rm ext}}{\mu_0 R_0} + \frac{\ell_i}{2} + \beta_p + \frac{1}{2} ,$$

* Work sponsored by the U.S. Department of Energy under Contract Nos. DE-AC03-89ER51114 and DE-AC05-84OR21400.

† Fusion Energy Division, Oak Ridge National Laboratory, Oak Ridge, Tennessee 37831, U.S.A.

$L_{ext}/(\mu_0 R_0) \approx \ln(8R_c/\bar{a}) - 2$, $\bar{a}$ is the poloidal contour length over 2π, and $\ell_i \equiv [\oint_S d\ell]^2 \int_V B_p^2 dV / [V \oint_S B_p d\ell]^2$. In Ref. 1 $n/n_c = -1$ was identified as a good approximation for the ideal rigid-body stability limit.

For shot #60809 a value of $n/n_c = -1.04$ was calculated prior to disruption, whereas for #63422 we could only achieve $n/n_c = -0.81$. A multi-filament rigid-body analysis[3] gives similar results, namely values of n/n_c of 0.91 and 0.73 for #60809 and #63422 respectively. This turns out to be typical of the observed behavior, i.e. as ℓ_i is decreased and δ is increased the achievable value of n/n_c also decreases. This behavior is illustrated in Fig. 3 where we plot the achievable n/n_c vs. ℓ_i. In column near each data point are κ, δ, and $Q \equiv [ff']_{\bar{\psi}=.95} f_0/R_0/(\kappa q_0)$, which has been reported[4] as a measure of the departure from rigid-body behavior. In that work Solovev equilibria are used and Q is purely a shape parameter, whereas here Q contains effects of the current profile. A correlation in departure from $n/n_c \sim 1$ is seen with both ℓ_i and with Q. Q shows a local sensitivity to the current profile parameterization which is why we chose to plot the data using ℓ_i, a better-known quantity, as the ordinate. In Ref. 4 departure from rigid-body behavior is seen at $Q < 0$ and Q is bounded by $Q > -.5$, thus we consider the agreement to be quite good.

STABILITY ANALYSIS

In the stability analysis of these plasmas with GATO[5] we use the real wall shape of DIII–D, not a wall conformal to the plasma. This wall has an expansion parameter, which expands the wall in minor radius without changing its shape in the poloidal plane. If, starting with the experimental equilibrium, we find that the expansion parameter must be increased from unity to 1.03 in order to find an instability we shall refer to this as operation at 97% of the ideal limit. For case #60809 the result of this analysis is that we are at 97% of the ideal limit, in good agreement with the rigid-body result of 104%.

For case #63422 the result is 98% of the ideal limit, even though we have only achieved 81% of the rigid-body ($n/n_c = -1$) limit. We will now pursue this discrepancy in a bit more detail. In Fig. 4 we plot the perturbed shape as calculated in GATO and normalized in amplitude so that the perturbed shape of the 95% flux surface just touches the limiting surface of the vessel. The dotted lines are the unperturbed equilibrium. Our control system regulates the vertical position of the current centroid, thus it is of interest to look at this perturbation with the shift in the magnetic axis removed. It can be seen in Fig. 4 that if this axis shift is removed most of the perturbation still remains.

This equilibrium was calculated 2564 ms into the shot. The outer boundary of the plasma at 2566 ms is shown as the broad dashed line in Fig. 4. We see excellent agreement between the calculated and measured deformation of the equilibrium. It is characteristic of vertical disruptions in these D-shaped plasmas that the top of the plasma is moving radially inwards and the bottom radially outwards as the plasma is moving vertically upwards.

As an aid to understanding the perturbation we have spectrally decomposed the results of the GATO calculation. By far the largest component is m = 1, as shown in Fig. 5, The second largest term is m = 3, whereas the m = 2 and m = 4 components are negligibly small except at the very edge where the presence of the divertor increases the breadth of the poloidal spectrum. It should be noted that even the m = 1 mode has a distinctly non-rigid character in the outer region of the plasma. By way of comparison, we show in Fig. 6 the spectral decomposition of case #60809. Here all the components other than m = 1 and m = 3 are negligibly small. Because of the higher ℓ_i the m = 1 amplitude peaks in the central region of the plasma. The m = 3 amplitude is about 19% of the m = 1 as opposed to 33% for #63422. These effects combine to account for the much better agreement with the rigid-shift model.

CONCLUSIONS

We find excellent agreement between the experimentally observed vertical stability limits and ideal MHD stability calculations. Detailed calculation of the perturbed plasma shape done with GATO are in good agreement with experimental observation. The observed behavior is not unexpected. The possibility of an m/n = 3/0 mode was found in the analysis of a square plasma.[6] Departure from a rigid-body stability criterion has been predicted for D-shaped plasmas with high triangularity.[4] Such non-rigid effects have been observed in the PBX tokamak for bean-shaped plasmas.[7]

We find n/n_c an excellent characterization of the rigid-body stability limit and Q is in qualitiative agreement with the observed departure from rigid-body behavior. As can be seen in Fig. 3, axisymmetric instability is seen over a wide range of elongation. It should be noted that reducing triangularity does not allow higher elongation since the additional quadrupole field required would then simply move the MHD and rigid-body limits closer together. For current profiles typical of DIII–D H–mode plasmas the non-rigid effects have limited our maximum elongation to $\kappa = 2.5$.

Over a wide range of plasma conditions we are able to operate to within a few percent of the ideal MHD axisymmetric stability limit. The loss of control is quite abrupt, for instance, we may operate under conditions where $\kappa = 2.33$ is accomplished without difficulty but $\kappa = 2.4$ is impossible. Small changes in ℓ_i become critical in such operation.

It remains unclear as to whether this represents the maximum achievable elongation. Of course, some gain is likely from further broadening of the current profile, but these results indicate that further gains will be modest. It is plausible that one could provide further stabilization of the non-rigid component of the motion with other poloidal coils. Because of the shielding effects of the vessel this could only be accomplished with derivative gain. The reference signal would need to be a measure of the difference between the surface motion and that of the axis. Thus the reference signal would be the derivative of a difference signal which involved many magnetic probes. The control function would need to be done without degradation of the axial control. This idea does not violate the above results since the stability calculations only use the passive shell. However, it remains to be seen whether such control is practically realizable. Note that it is only the completeness of the closely-coupled poloidal coil set of DIII–D which allows consideration of such a control scheme.

1 Lazarus, E.A., Lister, J.B., Nielson, G.H., Nucl. Fusion **30**, (1990) 111.
2 Lister, J.B., Lazarus, E.A., Kellman, A.G., et. al., "Experimental Study of the Vertical Stability of High Decay Index Plasmas in the DIII–D Tokamak," General Atomics report GA-A19843, (April 1990), submitted to Nucl. Fusion.
3 Leuer, J., Fusion Technol. **15**, No. 2 (1989) 489.
4 Bernard, L.C., Berger, D., Gruber, R., Troyon, F., Nucl. Fusion **18**, (1978) 1331.
5 Bernard, L.C., Helton, F.J., Moore, R.W., Comput. Phys. Comm. **24**, (1981) 377.
6 Rosen, M.D., Phys. Fluids **18**, (1975) 482.
7 Jardin, S.C., Delucia, M., Okabayashi, M., Pomphrey, N., Reusch, M., et al., Nucl. Fusion **27**, (1987) 569.

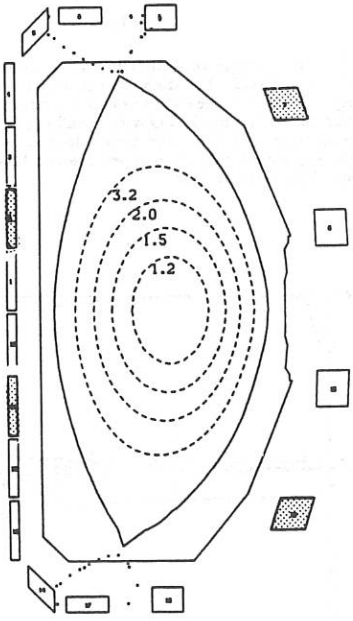

FIG. 1. Shot No. 60809, equilibrium just prior to disruption as calculated from the experimental data. The parameters are $I_p = 1.0$ MA, $B_t = 2.0$ T, $R = 1.69$, $a = 0.59$ m, $q_{95} = 5.7$, $\beta_p = 0.41$, $\ell_i = 1.48$, $\kappa = 2.17$, and $\delta = 0.37$. The coils used for vertical control are shaded.

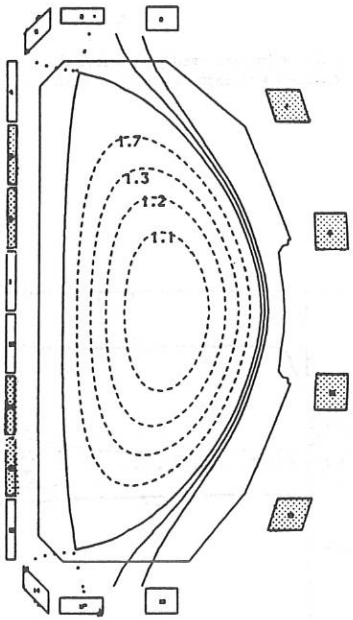

FIG. 2. Shot No. 63422, equilibrium just prior to disruption as calculated from the experimental data. The parameters are $I_p = 1.1$ MA, $B_t = 0.8$ T, $R = 1.69$, $a = 0.54$ m, $q_{95} = 2.7$, $\beta_p = 0.47$, $\ell_i = 0.92$, $\kappa = 2.41$, and $\delta = 0.85$. The coils used for vertical control are shaded.

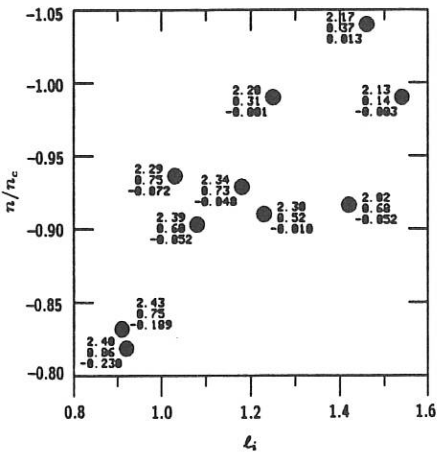

FIG. 3. n/n_c achieved just before disruption *vs.* ℓ_i. Listed at each datum is κ, δ, and Q.

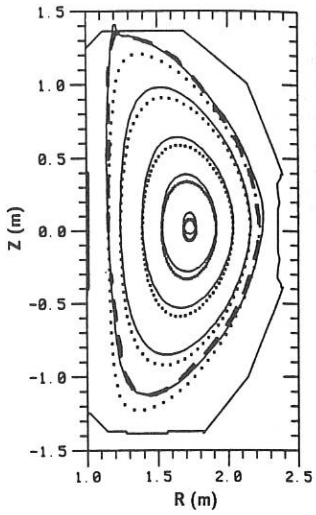

FIG. 4. The perturbation in the equilibrium of case #63422. The dots are the unperturbed equilibrium and the solid lines are the perturbation calculated by GATO with a wall expansion parameter of 1.017. The broad dashed line is the experimentally determined plasma boundary 2 ms later in time.

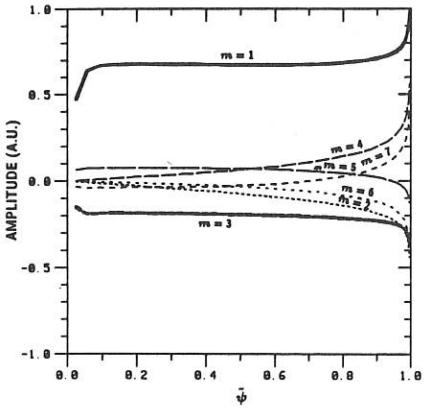

FIG. 5. The poloidal decomposition of the calculated perturbation for case # 63422 normalized to the amplitude of the $m = 1$ component.

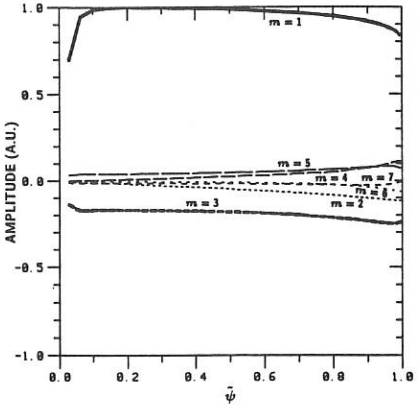

FIG. 6. The poloidal decomposition of the calculated perturbation for case # 60809 normalized to the amplitude of the $m = 1$ component.

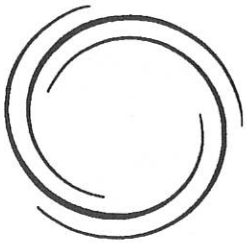

INDEX OF ALL AUTHORS

INDEX

Abe M. I-351
Abramyam L.A. IV-1844
Adams J.M. I-1,323,331
Adati K. I-34
Afanasjev V.I. I-82,299,III-1480
Afshar-rad T. IV-1864
Agarwal A.K. II-966
Agostini E. IV-1701
Aikawa H. III-1452
Airoldi A. II-813,III-1108, IV-1709
Akaoka N. IV-1508
Akatova T.Yu. I-411,III-1125, IV-1684
Akiyama R. I-34
Akulina D.K. II-431
Alava M.J. III-1003
Alcock M.W. III-1283
Alejaldre C. II-489,497,509, III-1255
Alikaev V.V. III-1076,1080, 1084
Alladio F. II-765
Alper B. II-557,565
Alport M.J. IV-1794
Amano T. II-451
Anabitarte E. IV-1492,1572
Andel R. van III-1121
Anderegg F. IV-1811
Anderson W.A. II-931
Anderson D. II-817
Ando A. I-34
Andreeva E.V. II-894
Andryukhina Eh.D. II-463
Angelis R. De III-1435
Aramaki E.A. II-601
Aranchuk L.E. II-651
Aratari R. I-291,295,III-1468
Arbuzov A.I. I-299
Argenti L. III-1112
Arnold R.C. IV-1860
Arsenin V.V. II-589
Arshad S. III-1267,1283
Arutiunov A.B. II-671,777,893
Asakura N. I-283,375
ASDEX-Team I-54,62,70,94,110, 151,207,239,291, 295,391,395,III-1052,1092,1167, 1171,1215,1263, 1287,1291,1323, 1427,1431,1435, 1439,1464,1468, IV-1552,1556,1676
Assis A.S. de II-861,IV-1786
Askinasi L.G. I-299,411
ATF Group II-443
Attenberger S. I-1,5,9
Austin M.E. I-26,150,174, III-1133
Awano M. II-541
Azarenkov N.A. IV-1848
Azevedo C.A. De II-861
Azizov E.A. I-14
Azumi M. III-1011,1307
Baboolal S. IV-1750
Babykin V.M. II-651
Baek W.Y. I-403
Bagdasarov A.A. I-195,231,III-1076, 1080,1084
Bagdoo J. III-1195
Baity F.W. III-1311
Balet B. I-1,5,106,162, 259,323
Bamford R.A. II-553,557
Barbato E. III-1163
Barbian E.P. IV-1528
Barnes C.W. I-114,146
Barnsley R. I-247, III-1365,1413, IV-1608
Barocio-Delgado S. I-30
Barth C.J. IV-1600
Bartiromo R. III-1092,1287, 1291,1323
Bartlett D.V. I-162,259,III-1150, IV-1504,1709
Bastistoni P. II-765
Batani D. IV-1876
Batanov G.M. II-467
Batchelor D.B. III-1311
Bateman G. I-134
Batishchev O.V. IV-1840
Baty H. II-889
Bätzner R. IV-1520
Bayley J. II-663
Becker G. II-826, 833
Beer M. III-1048
Behn R. I-78,IV-1680
Behrisch R. III-1357
Beidler C.D. II-513,517
Belavin M.I. II-593
Belikov V.S. III-1199
Belitz H.-J. IV-1568
Bell G.L. II-439,443,455
Bell J.D. III-1353, IV-1492
Bell M.G. I-114,134,

Bell M.G. 146,387, III-1048,1419
Bell R. I-146,283,375
Belle P. van I-1,331,III-1015,IV-1496
Bengston R.D. III-1456,1460
Berezovskij E.L. I-13, II-785, IV-1488
Berger-By G. III-1231
Bergsaker H. III-1401
Bernabei S. III-1287,1291, 1323
Berni L. II-601
Bertrand P. III-1299
Bessenrodt-Weberpals M. I-58,III-1460
Besshou S. II-459
Besson G. III-1175
Betello G. IV-1717
Beulens J.J. III-983
Bharuthramt R. IV-1750
Bhatnagar V.P. I-255,III-1015, 1019,1150
Bhattacharyya S.N. II-966
Biancalana V. IV-1876
Bianconi F. IV-1876
Bibeau C. IV-1861
Bibet P. III-1231
Bickerton R. I-134
Bieger W. IV-1568
Bigelow T.S. II-443,455
Bishop C.M. I-178
Bitter M. I-114,III-1048
Bittoni E. II-687
Bizarro J.P. III-1231
Blackwell B.D. II-435,521
Blank H.J. de II-919
Blokland A.A.E. van IV-1528
Blum J. II-872
Bobrovskij G.A. IV-1484
Bobylev A.V. II-877
Bogolyubskij S.L. II-609
Boileau A. IV-1664
Boivin R. III-1048
Bomba B. IV-1516,1520
Bombarda F. IV-1713
Bondeson A. II-906,954,962
Bongers W.A. III-1117
Bonicelli T. I-419
Bonoli P.T. III-1100
Bora D. I-287,III-1068
Borg G.G. III-1175,1179
Borie E. IV-1803
Bornatici M. IV-1832
Borozenets A.M. III-1060
Borrass K. III-1393
Borschegovskij A.A. I-195,III-1080,1084
Bosch H.S. II-873,III-1215
Bosch S. IV-1520
Bose M. II-684
Bosman R. III-1117,1121
Boyd D.A. IV-1624,1668
Boyev A.G. IV-1725
Bozin J. III-1405
Braams B.J. III-1417
Bracco G. I-118,IV-1717
Brakel R. II-479
Brambilla M. III-1056
Branas B. IV-1592
Braun F. III-1052,IV-1552
Bretz N.L. I-42,146,387, III-1048,IV-1544
Briguglio S. II-707
Brink A.M. van den I-199
Brower D.L. I-26,150,174, III-1133
Browning B. II-622
Browning P.K. II-577,622
Bruhms H. III-1223
Bruneau J.L. III-1231
Brunsell P. II-573,610
Brusati M. II-719,IV-1709,1713
Bruschi A. I-170,III-1112
Brzosko J.S. IV-1520
Brzozowskij J. II-573,655
Büchl K. I-235
Büchse R. I-66,239,291,391
Bud'ko A.B. II-639
Budny R.V. I-387,III-1419
Bugarya V.I. I-231
Bulyginskij D.G. III-1125,IV-1684
Bunting C. II-553,557,561,565, 573
Buratti P. I-118
Burdakov A.V. II-614
Bures M. I-255,III-1015,1019, 1381
Burhenn R. II-479
Burrell K.H. I-203,271,275,279, IV-1604
Bush C.E. I-114,146,III-1048
Bussac M.N. II-889
Cable M. IV-1861
Cadez V.M. IV-1737
Cai R. III-1341
Cains R.A. III-1035
Caldas I.L. II-675,III-1349
Calker C. van IV-1520
Callen J.D. I-142,II-853

Camargo S.J. II-675
Campbell D.J. I-5,255,323,327,339, III-1015,1019,1150, 1373
Campbell M. IV-1861
Canobbio E. III-1207
Capes H. II-845
Capitain J.J. III-1231
Cardinali A. III-1159,1203
Carlson A. III-1167,1427, 1460,1464,IV-1676
Carlstrom T.N. I-203,271,279
Carolan P.G. II-553,557,561,565, 569,IV-1564
Caron X. IV-1705
Carrao L. II-533,537
Carrera R. II-970
Carreras B.A. II-443,497,509, III-1353
Carter K. III-1353
Cartwright D.C. IV-1875
Castejón F. II-489,III-1255
Castle G. I-174
Cavallo A. I-46,146,III-1048
Cekic M. III-1137
Cenacchi G. II-813
Cercek M. IV-1815
Cesario R. III-1159,1203
Challis C.D. III-1150
Chan V.S. III-1031
Chance M.S. I-367,387
Chang C.S. III-1027
Chang Z. I-142,II-853
Chaniotakis E.A. I-134
Chankin A.V. III-1076,1080
Chaudron G.A. III-1195
Chávez-Alarcón E. I-30
Cheetham A. I-219,323,331,III-1150
Chen J.Y. I-26,III-1133
Chen L. II-707
Cheng C.Z. II-910
Chernenko A.S. II-651
Chernyshev F.V. I-82,411
Chies T. IV-1701
Chistyakov V.V. I-231,III-1076,1080, IV-1536,1616
Chittenden J.P. II-663
Chiu S.C. III-1031
Chodura R. III-1443
Choi D.-I. II-663,752,III-1027
Christiansen J.P. I-5,9, II-797,III-1015
Chu M.S. I-371
Chudin N.V. III-1327
Chudnovski A.N. II-781
Chugunov I.N. IV-1688
Chuvatin A.S. II-651
Cima G. I-174,III-1133
Cirant S. III-1108,1112
Ciric D. III-978
Clement S. I-255,III-1373,1385
Coad J.P. III-1357
Coe S. IV-1864
Cohn D.R. I-134
Colchin R.J. I-439
Coleman L. IV-1861
Colestock P.L. I-134,III-1048
Colunga-Sánchez S. I-30
Compass Group IV-1564
Conn R.W. III-1447
Connor J.W. I-130,178,II-695
Conrads H. I-383
Conroy S. I-98,331
Conway G.D. II-435,521
Cook D.R. III-999
Cooper W.A. II-931
Coppi B. II-793
Coppins M. II-663
Cordey J.G. I-1,106,110,162, II-797,III-1015
Core W.G.F. I-251,331, III-1015,1019
Cornelissen P. I-383
Correll D. IV-1861
Corrigan G. I-263, II-801,805
Corti S. I-323,III-1150
Coster D.P. III-1417
Costley A.E. IV-1500,1504
Cottrell G.A. I-5,9,III-1015,1019
Coulon J.P. III-1365
Cox M. I-130,178, III-1019,1219,1267
Crisanti F. II-765
Croci R. III-1207
Crume E.C. Jr. II-447,455
Cruz Jr. D.F. da III-1121
Culverwell I.D. II-663
Cunningham G. II-622
Cupido L. IV-1560
D'haeseleer W.D. II-748
Dahmani F. IV-1856
Dahyia R.P. III-983
Dam J.W. van II-970
Damstra R.D. III-1117,1121
Dan'ko S.A. II-609
Dangor A.E. II-663
Daniele R. IV-1790
Darrow C. IV-1861
Davis J.I. IV-1861

DeBoo J.C. I-126,275
Décoste R. III-1195
Deha I. IV-1876
Deliyanakis N. I-178,III-1267
Dellis A.N. III-1267
Delvigne T. I-287,III-1040
Demchenko V. IV-1741
Demers Y. III-1195
DeMichelis C. III-1231
Deng C. I-363
Desselberger M. IV-1864
Devos J. I-287
Dewar R.L. II-521
Diachenko W.D. I-327
Dicken D. IV-1680
Diesso M. IV-1548
DIII-D Research Team I-203,275, IV-1596,1604
Ding X. I-307,III-1341
Dippel K.H. I-287,403, III-1447
Dmitrieva M.V. III-1295
Dnestrovskij A.Yu. II-789
Dnestrovskij Yu.N. II-785,894, III-1239 IV-1616,1620
Dodel G. I-207
Dodhy A. II-471,475
Dokuka V.N. I-14
Domier C.W. IV-1798
Domínguez N. II-497,509
Dong J. I-154
Donné A.J.H. IV-1656
Dooling P.J. II-622
Doyle E.J. I-203,279, IV-1596,1604
Drake J.R. II-573
Druetta M. IV-1580
Du T. I-415
Duan X. III-1341
Düchs D.F. II-691, 801
Dudok de Wit Th. I-74,187,III-1476
Dunlap J.L. III-1353,IV-1492
Durodié F. I-287
Durst R.D. IV-1564
Duval B.P. I-74,III-1476, IV-1680
Dyabilin K.S. II-463
Dyer G.R. II-443,III-1353
Dylla H.F. III-1419
Eberhagen A. I-151,III-1263
Eckhartt D. III-1336
ECRH -Team II-471,475, 479,483,484,
ECRH -Team III-1275, IV-1572,1576
Edenstrasser J.W. II-881
Edery D. II-938
Edlington T. III-1267
Edwards A.W. I-5,323,335,III-1150
Efthimion P.C. I-42,50
Egorov S.M. I-231,IV-1536
Ehrenberg J. III-1357
Ehrhardt A.B. III-1417
Ehrlich R. IV-1861
Ejiri A. II-541,549
Elevant T. II-817,IV-1496
Elfimov A.G. III-1064,1141,1315
Elisavetin A.A. I-195
Elizavetin D.Yu. III-1080,1084
Elliott J.A. IV-1778
Ellis J.J. IV-1608
Emmoth B. III-1401
Endler M.A. III-1464
Engelhardt W. I-62
Englade R.C. III-1100
England A.C. II-439,443,455
Erckmann V. III-1271,1275
Erents K. I-219
Erents S.K. III-1373,1381,1385
Eriksson L.-G. I-327,III-1015,1019, 1150
Esch H.P.L. de I-90
Esipchuk Yu.V. III-1080,1084
Est Q.C. van IV-1600
Estrada T. IV-1592
Evdokimov D.B. III-1080,1084
Evrard M.P. III-1019
Fahrbach H.-U. III-1171
Fajemirokun H. IV-1692
Fall T. III-1231,IV-1580
Famà F. IV-1871
Farina D. III-1088
Fasoli A. IV-1807,1811
Federov A.A. I-299,411,III-1480
Federov S.V. III-1295
Fedyanin O.I. II-463
Feix M. III-1299
Feneberg W. II-773,III-1427
Fernández J.C. II-643
Ferrante G. IV-1790
Ferron J.R. I-275,371,427
Fessey J.A. IV-1500
Fidone I. III-1129,1279, IV-1705
Field A.R. IV-1556
Fielding S.J. III-1267,1283,1472
Figueira J.F. IV-1875

Fijalkow E. III-1299
Finken K.H. I-403,III-1447
Fishpool G.M. I-347,III-1283
Fitzpatrick R. I-130,379,II-923
Fletcher J.D. I-355,359
Fonck R.J. I-50
Forrest C. III-1287
Foster M.S. I-150
Fowler R.H. II-439
Frank N.A. II-773
Fredrickson E. I-114,387,III-1048
Fried B.D. I-138
Frieling G.J. IV-1664
Fu B. I-154
Fu G.Y. II-970
Fuchs V. III-1195
Fujii T. III-1007,1011
Fujisawa A. II-541,549
Fujita T. III-1452
Fujiwara M. II-451
Fukumoto H. I-351
Fukuyama A. II-809,III-1011, 1251,1307
Fussmann G. I-62,183,III-1423, 1431,1435,IV-1556
Fyaretdinov A. III-1259
Gabellieri L. III-1335
Gaigneaux M. I-287
Galbiati S. IV-1636
Gandy R.F. I-150,174,III-1133
Gao Q. I-154,311
Garbet X. II-728,736,938, IV-1588
Garcia L. II-493,501
Gardner H.J. II-521
Garina S. III-1064,III-1141
Garribba M. I-419
Gasparino U. III-1271,1275
Gaunt R. IV-1794
Gebhardt U. I-868
Gee S.J. II-622
Gehre O. I-70
Gentille B. de III-1231,1259
Gentle K.W. I-70,174, III-1133,1460
Gernhardt J. I-207,IV-1552
Gervais F. IV-1588
Ghendrih Ph. II-845
Ghizzo A. III-1299
Giannella R. I-9,247,263, III-1365,1413, IV-1608,1713
Giannone L. I-58,151,207, III-1460,1464
Gibson K.J. II-557,561
Giesen B. I-287
Giles P. IV-1584
Gill C. III-1231
Gill R.D. I-335,III-1150
Giruzzi G. III-1129,1259, 1279,IV-1705
Giulietti A. IV-1864,1876
Giulietti D. IV-1876
Gizzi L. IV-1864
Gladush G.G. I-14
Glaude V. III-1195
Glendinning G. IV-1861
Glowienka J.C. II-443,455
Goedbloed J.P. I-399
Gohil P. I-279
Golant V.E. I-82,299,411, III-1480
Golberg S.M. II-659
Goldston R.J. I-134,146
Gondhalekar A. I-219
Goniche M. III-1231
Good T.N. IV-1807,1811
Gordeev E.M. II-609
Gorelenkov N.N. II-914
Gorelov Yu. III-1259
Gorini G. I-170,III-1112, IV-1652
Gossett J.M. II-439
Gott Yu.V. IV-1612
Gottardi N. I-247,259,263,323, 339,III-1019,1150, 1381,1413
Goulding R.H. III-1311
Gowers C.W. I-162,259,323, IV-1504,1692
Graaf M.J. de III-983
Granucci G. III-1112
Grashin S.A. III-1076
Gray D. I-403,III-1447
Greene G.J. III-1048,IV-1540
Grek B. I-42,114,146
Grekov D.L. II-529
Grésillon D. IV-1588,1721
Grimbergen T.W.M. IV-1528
Grisham L.R. I-146
Grishanov N.I. III-1141
Groebner R.J. I-203,271,275,279, IV-1604
Groot B. de III-11121
Gross R.A. I-387
Grua P. II-732
Gruber O. I-94,151,183,182, II-841

Gruber R. II-931
Grunov C. IV-1488
Gryaznevich M.P. I-411,III-1327
Guha S. IV-1758
Guilhem D. III-1231,IV-1580
Guldbakke S. IV-1520
Guo D. I-363
Guo G. I-154,311
Guo Z. II-970
Gurov A.A. III-1080
Gusev V.K. I-299,411
Gyergyek T. IV-1815
Haas F.A. II-942
Haas G. III-1365,1468
Haas J.C.M. de I-158
Hacker H. II-479
Hackmann J. IV-1680
Haegi M. II-687
Haendler B. IV-1861
Haines M.G. II-663
Hale G.M. II-873
Hamada Y. I-34
Hamamatsu K. III-1011,1307
Hamano T. III-1452
Hamberger S.M. II-521
Hammel B. IV-1861
Hammet G.H. I-146,III-1048
Hammett G.W. I-162
Hamnen H. II-817,III-1019
Han S. III-1154
Hanatani K. II-459
Handley M.J. II-773
Hansen P.M. I-166
Hanson G.R. IV-1492
Harada M. II-459
Harbour P.J. I-259,III-1365,1381, 1385
Harmeyer E. II-517
Harris D.B. IV-1875
Harris J.H. III-1353,IV-1492
Harrison M.F.A. III-1397
Hartfuss H.J. IV-1572,1576
Harvey B.M. III-1035
Harvey R.W. III-1259,1323
Hasan Z. IV-1758
Hasegawa K. III-1452
Hastie R.J. I-130
Hatayama A. I-255,III-1211
Hatcher R. I-283,367
Hatcher W. IV-1861
Hattori K. II-545
Hauer A. IV-1875
Hawkes N.C. I-247,III-1365,1413
Hawryluk R.J. I-387,III-1419
Haynes P.S. I-379
Heer F.J. de IV-1664
Heeren R.M.A. III-978
Heikkinen J.A. III-1003
Heindler M. II-638
Hellberg M.A. II-773,IV-1750,1754
Hellblom G. II-573,610
Hellermann M. von I-9,162,III-1150, 1361,1381,1385, IV-1496,1608,1664
Hellsten T. III-1003,1015,1019, 1150
Helton F.J. I-371,427
Hender T.C. I-130,323,379,399, II-923,927,III-1283
Henesian M. IV-1861
Henins I. II-643
Hennequin P. IV-1588
Herrmann W. I-66,III-1171, IV-1672
Hess W. III-1231,IV-1580
Hesse M. IV-1697
Hickok R.L. I-26,38,III-1133
Hidalgo C. III-1353,IV-1492
Hidekuma S. I-34,267
Hill D.N. I-134
Hill K.W. I-42,114,146, III-1048,1419
Hillis D.L. III-1447
Hirano Y. II-545
Hirayama T. I-223
Hiroe S. II-443
Hirokura S. I-34,227
Hirota I. II-545
Hirsch K. IV-1692
Hirshman S.P. II-505
Hively L.M. II-970
Hoang G.T. III-1231
Hoekstra R. IV-1664
Hoenen F. III-1040
Hoffman D.J. III-1048,1311
Hofmann J.V. III-1435,IV-1556
Hofmeister F. III-1052,IV-1552
Hogan J.T. II-825
Hogewey G.M.D. I-158
Hollenstein Ch. III-1476
Holzhauer E. I-207
Honda A. III-1452
Honda R.Y. II-601
Hong B.G. II-711
Honma T. II-585,III-1039
Hoog F.J. de III-983
Hopman H.J. III-978,983
Horton L.D. II-439,447,455

Hosea J. III-1048
Hoshino K. III-1340,1452
Hosokawa M. II-451
Höthker K. IV-1568
Hotston E.S. III-1397
Hou J. I-154
Houlberg W.A. I-134
Houtte D. Van III-1231
Howald A.M. III-1452
Howard J. II-521
Howe H.C. II-443,451
Howell B. I-46
Howl W. I-371
Hsuan H. I-114
HT-6B Group I-363
Huang K. I-311
Huang R. I-363
Hubbard A. III-1195
Hübner K. IV-1516,1520
Hugenholtz C.A.J. III-1121
Hughes T.P. II-553
Hugill J. I-379,III-1267,1283
Hugon M. II-703,962
Hulse R.A. I-46,50
Hutter T. III-1231
Huysmans G.T.A. I-323,399
Hwang A. III-1381
Hyatt A. III-1439
Ichiguchi K. II-459
ICRH-Team I-239,II-479, III-1052
Ida K. I-34,267, II-451, III-1452
Idei H. II-451
Igarashi H. II-585 III-1039
Iguchi H. II-451
Ikeda Y. III-1183
Ikegami H. I-34
Imai T. III-1183
Ingraham J.C. II-581
Ingrosso L. IV-1520
Innocente P. II-533
Irie M. II-626
Ishibori I. III-1452
Isichenko M.B. II-667
Isler R.C. II-439,447,455
Itoh K. I-267,II-740,809, III-1307
Itoh S.I. I-267,II-740,809, III-1307
Itoh T. IV-1508
Its E.R. I-82,299,411
Ivanov A.A. III-1064
Ivanov N.V. III-1080
Izvozchikov A.B. I-82,411,III-1480
Jacchia A. I-166,170
Jackson G.L. I-275
Jacquinot J. I-255,259,323,327, III-1015,1019,1150
Jadoul M. I-319
Jaeckel H.J. III-1365
Jaeger E.F. III-1311
James R.A. III-1259
Jan G.-D. IV-1824
Janeschitz G. III-1365
Janos A. I-146,387,III-1048
Janz S. III-1259
Jardin S.C. I-134,387,III-1191
Jarmén A. II-723
Jarvis O.N. I-1,98,331,III-1015
Jassby D. III-1048
Jelenković B. III-1405
Jelić N. IV-1815
Jernigan T.C. II-443,447,455
JET Team I-110
JFT-2M Group III-1340
Ji H. II-541,549
JIPP T-IIU Group I-227
Jobes F. I-146,III-1048
Joffrin E. I-323
John P.I. IV-1745
Johnson D.W. I-42,46,50,114,146, III-1048
Johnson M.F. I-259
Johnson P.C. III-1267,1283
Johnston T.W. III-1299
Jones T.T.C. I-1,5,9,III-1381
Joye B. I-74,187,III-1179, 1476,IV-1680
Joyer P. I-303,IV-1584
JT-60 Team I-223,III-1183, IV-1508
Kaita R. III-1048
Kajiwara T. II-459
Kakoulidis E. III-1427
Kakurin A.M. III-1080
Kalda J.L. II-667,IV-1820
Kalinin Yu.G. II-609
Kallenbach A. I-58,62,182,183, III-1423
Källne E. II-573,655,IV-1652
Kalyushnij V.N. II-525
Kamada Y. I-223
Kamelander G. II-685
Kamenets F.F. II-639
Kaneko H. II-459
Kaneko O. I-34, II-451

Kania D. IV-1861
Kantor M.Yu. III-1125,IV-1684
Karas' V.I. IV-1840
Kardaun O. I-110, II-797
Karita A. I-34
Karlsson P. II-610
Karney C.F.F. III-1417
Karttunen S.J. III-1303
Karyukin A.V. II-614
Kasai S. III-1452
Kashiwa Y. III-1452
Kasparek W. III-1271
Kauffman R. IV-1861
Kauffmann M. I-215
Kaufman A.N. III-999
Kaw P.K. II-966,IV-1745
Kawahata K. I-34,227
Kawakami T. III-1452
Kawano Y. I-223
Kawashima H. III-1340,1452
Kawasumi Y. I-34
Kayama M.E. II-605
Kaye S.M. I-283,367,375
Kazawa M. III-1452
Keane C. IV-1861
Keilhacker M. III-1369
Kellman A.G. I-275,371,427
Kerdja T. IV-1856
Kernbichler W. II-638
Kesner J. I-387
Kessel C. I-367,375
Kever H. I-383
Khairutdinov R.R. I-14
Khalil Sh.M. IV-1774
Khattak F. IV-1864
Khudoleev A.V. I-82,III-1480
Kiessling M. I-868
Kikuchi K. III-1452
Kilkenny J. IV-1861
Kilpatrick S.J. III-1048,1419
Kim J.Y. II-752,III-1460
Kim S.K. I-150,IV-1656
Kimura H. III-1007,1011
Kingsep A.S. IV-1820
Kiptilyj V.G. I-82,III-1480,IV-1688
Kirov A.G. III-1319
Kislov A.Ya. III-1080,1084
Kislov D.A. I-315,III-1080, IV-1484
Kislyakov A.I. I-82
Kisslinger J. II-517
Kitson D.A. II-577,622
Klein H. IV-1520
Klepper C.C. III-1447,IV-1580
Kleyn A.W. III-978
Klüber O. II-291,837,III-1223
Knight A. I-78
Koch R. III-1044
Kochanov A.E. IV-1733
Kocherga O.D. IV-1819
Kock L. de I-9,III-1357,1373, 1381,1385
Koh W.-H. III-1027
Koidan V.S. II-614
Koide Y. I-223,IV-1508
Kolesnichenko Ya. III-1199
Kolik L.V. II-467
Komori A. II-459
Kondo K. II-459,IV-1524
Koning J.J. III-1121
Konyukhov V.V. II-614
Kooijman W. III-1121
Korelev V.D. II-609
Kornblum H IV-1861
Kornherr M. I-291,391
Korotkov A.A. I-82,299,III-1480
Kostomarov D.P. II-894,III-1239
Kovan I.A. III-991
Kovanen M.A. I-251,III-1019
Kovrov P.E. III-991
Krämer M. III-1167
Krasheninnikov S.I. II-671,777, 789,893
Krieger K. I-66,III-1423,1431, 1435
Krikunov S.V. I-299,411
Kritz A.H. III-1100,1191
Krivenski V. IV-1648
Krivitaky V.S. III-1187
Kruyt O.G. III-1117,1121
Kubo H. I-223,IV-1508
Kubo S. II-451
Kucinski J. IV-1520
Kugel H. I-283,375
Kuhn S. II-715, IV-1782,1786
Kühner G. II-471,475, 484
Kuksov P.V. II-609
Kukushkin A.B. IV-1632
Kumazawa R. I-34
Kunkel W.B. III-979
Kupschus P. I-1,5,9
Kurki-Suonio T. I-271
Kuroda T. I-34
Kurzan B. I-62
Kusama H. II-626
Kusama Y. III-1183
Kuteev B.V. I-231,IV-1536

Kuz'min S.V. II-618
Kuznetsova L.K. III-1247
Kwon M. II-439
Kwon O.J. I-323,399,927
Kyrazis D. IV-1861
Kyriakakis G. III-1427,1439
LH-Team I-70, III-1092, 1171,1215, 1291,1323
Lackner K. II-841
Lallia P. III-1015
Lam N.T. III-1023
Lama F. III-1357
LaMarche P.H. III-1419
Lammeren A.C.A.P. van IV-1600,1656
Lamoureux M. IV-1697
Landen N. IV-1861
Lane S. IV-1861
Lang R. I-215,235, 239,III-1215
Langley R.A. II-455
Lao L.L. I-371,427
Larionov M.M. III-1125
Lasalle J. III-1231, IV-1701
Lashkul S.I. III-1125
Lau Y.T. I-375
Laumann C. IV-1861
Laundy B. I-1
Laurent L. II-728, IV-1693,1721
Laviron C. IV-1588
Lawson J. IV-1861
Lawson K.D. I-247,339, III-1381,1413
Lazaros A. II-479
Lazarus E.A. I-371,427
Lazzaro E. I-251,259, 323,343,399
Lean H. III-1019
Lebeau D. III-1044
Lebedev S.V. I-299,411, II-614
LeBlanc B. I-283,367, 375,III-1048
Lecousty P. III-1231
Lee D.K. II-443
Lee J.K. I-371
Leenstra E.J. IV-1628,1852
Lehecka T. I-203,279, IV-1596
Lehner T. IV-1693,1721
Lehnert B. II-647
Leitao J. IV-1560
Lengyel L.L. I-243
Leonard A.W. III-1452
Leonard M. III-1419
Lerbinger K. II-935
Lerche R. IV-1861
Leuer J.A. I-427
Leung K.N. III-979
Leuterer F. III-1092,1215,1223, 1287,1291,1323, IV-1552
Levin L.S. I-327,III-1125, IV-1684
Levinton F. I-375
Li F. I-311
Li G. I-363
LI J. IV-1836
Li L. I-363
LI W.L. I-150,174,III-1133
Liberman M.A. II-639,659
Lie Y.T. I-287
Lietzke A.F. III-979
Liew S.L. IV-1548
Likin K.M. II-467
Liljeström M. II-756
Lin H. III-1456,1460
Lipin B.M. I-299,411
Lippmann S. I-275
Lisak M. II-817
Lister J.B. I-74,187,III-1175, IV-1680
Litaudon X. III-1231
Litvak A.G. IV-1844
Liu W. III-1154
Lloyd B. III-1267,1283
Loch R. I-215,235,239,III-1215
Lohr J. I-271,III-1259
Lok J. III-1121
Lomas P.J. I-1,5,9,III-1015,1381
Longinov A.V. III-1331
Lontano M. IV-1636,1762
Lopes Cardozo N. I-170,IV-1660
López Fraguas A. II-489,497,501,509
López-Callejas R. I-30
Lorenzen J. II-817
Loughlin M.J. I-1,331
Lowry C.G. I-9,339, III-1015,1381
Lucca F. De I-166,170, III-1112
Luce T.C. III-1259
Luciani J.F. II-889,935
Luckhardt S.C. IV-1624
Luhmann N.C. Jr. I-150,174,203,279,

Luhmann N.C. Jr. III-1133,IV-1596,1604, 1798
Lukash V.E. I-14
Lukin A.A. II-609
Lukinov V.A. III-1331
Lukyanov M.Yu. IV-1725
Lunin N. IV-1762
Lütjens H. II-906
Lyadina E.S. I-315,IV-1484,1616, 1620
Lynch V.E. II-443,497,509
Lyon J.F. II-439,455
Lysenko S.E. II-785
Lysyansky P.B. II-618
Maassberg H. II-484,III-1271,1275
Mace R.L. IV-1750,1754
Machida M. II-601
Maddison G.P. I-130,III-1397
Maeda H. III-1452
Maejima Y. II-545
Magne R. III-1231
Mahdavi M.A. I-279
Mancuso S. II-765
Mandl W. III-1361,IV-1496,1608, 1664
Manhood S.J. III-1267,1283
Manickam J. I-367,375
Manos D.M. III-1417,1419
Mansfield D.K. I-42,50,114,146, III-1048
Manso M.E. II-837,IV-1560
Mantica P. I-166,170,III-1112
Marco F. De III-1159
Marcus F.B. I-1,323,331
Marklin G.J. II-643
Marmar E. I-46,387
Marmillod Ph. III-1175
Martin G. I-303,III-1231,IV-1584
Martin-Solis J.R. I-219
Martinelli A.P. III-1357
Martini S. II-533
Masai K. II-451
Masai M. I-34
Masoud M.M. II-630
Mast K.F. I-263
Mata J. IV-1560
Matias J. II-837,IV-1560
Matjukov A.V. IV-1688
Matsuda K. III-1259
Matsuda T. III-1452
Matsumoto H. I-203,271, 279,IV-1604
Matsuo K. II-459,IV-1524
Matsuoka K. II-451
Matsuura H. II-459
Matthews G.F. III-1283
Mattioli M. III-1231,IV-1580
Mattor N. II-695
Mauel M.E. I-387
Maximov Yu.S. III-1080
Mayanagi K. II-541,549
Mayberry M.J. III-1150,1311
Mayer H.M. I-183
Mayo R.M. II-643
Mazur S. II-573,610
McCool S.C. I-150,174,III-1456
McCormick K. I-58,395,III-1323, 1439
McCracken G.M. I-9,III-1381,1385,1472
McCuire K. I-387,III-1048
McCune D. I-42,387
McDonald T.E. IV-1875
McKenzie J.S. III-1219
Medley S.S. I-134,III-1048
Medvedev A.A. I-13,III-1080,IV-1488
Meigs A.G. I-26
Meisel D. III-1468
Mekler K.I. II-614
Mel'nik V.N. IV-1729
Mélendez-Lugo L. I-30
Mendonça J.T. II-918
II-719, 837
Mennella A. III-1104
Merazzi S. II-931
Merkel R. I-215
Mertens V. I-151,215,235,239, III-1215,1263
Messiaen A.M. I-383,287,III-1040
Messina G. IV-1790
Meyer R.L. IV-1705
Micozzi P. I-122
Migliuolo S. II-898
Miley G.H. II-970
Miller G. II-581
Milligen B.Ph. van III-1121,IV-1660
Minagawa H. II-459
Minardi E. II-857
Minenko V.P. III-1145
Mioduszewski P.K. II-455
Miramar Blásquez J.F. II-488
Mirensky V.Yu. III-1080,1084, IV-1488
Mirnov S.V. I-14
Mironov V.A. IV-1844
Miroshnikov I.V. I-231,IV-1536
Mishin A.S. IV-1688

Mitchell I. II-663
Miura Y. III-1452
Miyamoto K. II-541,549
Mizuuchi T. II-459
Mohamed B.F. IV-1774
Moleti A. IV-1717
Mompean F. I-247,III-1413
Monaco F. III-1287
Monakhov I.A. III-9
Mondt J.P. II-769
Monier P. III-1231
Montalvo E. II-970
Montgomery D. IV-1861
Montvai A. II-691
Morales G.J. I-138,III-995
Moreau D. III-1150,1231
Morera J.P. II-845
Moret J.-M. I-187
Morgan P.D. I-162,259,323, III-1361,1381,IV-1496
Mori M. III-1452
Morita S. II-443,447,451,455
Morotov D.K. II-764
Morotov N.N. II-764
Morris A.W. I-347,379,III-1283
Morris R.N. II-439
Morsi H.W. I-247,IV-1608
Moser F. IV-1803
Moulin B. III-1231,IV-1701
Mourgues F. II-736
Moyer R.A. I-287,403,III-1447
Moyseenko V.E. III-1060
Mu J.-L. II-727,728
Mueller D. I-146,387, III-1048,1419
Müller E.R. I-395,III-1439
Müller G.A. III-1271
Müller R.W. IV-1860
Münich M. III-1287,IV-1552
Munson C.P. II-581
Murakami M. II-443,455
Muraoka K. II-459,IV-1524
Muratov V.I. IV-1880
Murmann H.D. I-54,62,III-1092,1323
Murphy J.A. I-146
Muzzolon A. II-537
Myors D.J. III-974
Nagasaki K. II-809
Nagashima K. I-223
Nagatsu M. I-150,IV-1524
Nagayama Y. I-146,III-1048
Naito O. III-1183
Najdenov V.O. IV-1688
Nakamura Y. II-459
Nakasuga M. III-459
Nardone C. I-166
Narihara K. I-34
Navarro A.P. IV-1572,1592
Nave M.F.F. I-335
Nave F. I-323
Navratil G.A. I-387
Nazikian R. IV-1544
NBI-Team IV-1572,1576
Nefedov V.V. II-894
Neilson G.H. I-134
Nelson B.A. II-605,III-1137
Nemoto M. III-1011,1183
Nemov V.V. II-525
NET-Team III-1397
Neudatchin S.V. I-195
Neuhauser J. I-395,III-1427,1460
Neves J. IV-1560
NI-Team I-54,62,94,295,395, II-479,483,III-1291, 1323,1439,1447
Nicolai A. II-825,III-1409
Niedermeyer H. I-207,395,III-1439, 1460,1464
Nielsen P. I-5,9,162,323, III-1015,IV-1692
Nieswand C. I-78,IV-1680
Nieuwenhove R. Van I-287,III-1068
Nishimura K. II-451
Nishino N. I-223,IV-1508
Nishitani T. I-223
Nocentini A. II-801, 849
Noda N. II-451,459
Noll P. I-419
Nordlund P. II-573,610
Nordman H. II-723
Noterdaeme J.-M. I-239,III-1052,1056, IV-1552
Nothnagel G. I-355,359
Notkin G.E. III-1080,1084
Novokhatskij A.N. III-1480
Nowak S. III-1108,IV-1709
Nunes F. IV-1560
O'Brien D.P. I-251,323,399
O'Brien M.R. III-1019,1219,1267
O'Rourke J. I-5,158,162,323, 343,III-1015,1019, 1150,1381
Obiki T. II-459,IV-1524
Ochirov B.D. II-467
Oda T. II-459
Odajima K. III-1452
Ogawa T. III-1452
Ogawa Y. I-34,227

Oh Y.-H. II-752
Ohdachi S. II-541,549
Ohkubo K. I-34
Ohyabu N. III-1452
Oka Y. I-34
Okabayashi M. I-283,367
Okada T. II-459,IV-1524
Okajima S. I-227,IV-1524
Okamura S. II-451
Okano H. III-1452
Okano K. III-1211
Okretic V.K. IV-1737
Oks E. IV-1644
Olivian J. IV-1588
Olsson M. I-1,331,IV-1496
Ongena J. I-383,III-1040,IV-1532
Oomens A.A.M. III-1121
Oost G. Van I-287,III-1068,IV-1532
Orefice A. IV-1709
Orsitto F. I-118,IV-1640
Ortolani S. II-533
Os C.F.A. van III-979
Osborne T.H. I-203,279,371
Osipenko M.V. III-987
Ostrikov K.N. IV-1848
Otsuka M. I-351
Ott W. II-483
Ottaviani M. II-711
Owens D.K. I-42,387,III-1419
Owens K. III-1048
Oyevaar T. IV-1528
Ozaki T. I-34, II-451
Pacher G.W. I-423
Pacher H.D. I-423,III-1397
Palleschi V. IV-1867,1871
Pan C.-H. IV-1824
Paoletti F. III-1203
Parail V.V. III-1243,1247
Parham B.J. III-1267,IV-1564
Paris P.J. IV-1807,1811
Park C.-H. III-1027
Park H.K. I-42,46,50,114,146, III-1048
Parker R. II-962
Parlange F. III-1231
Partridge J. III-1357
Pasini D. I-5,9,247,III-1361,1381
Patel A. II-557,565,569
Patel T.K. III-1413
Patterson D.M. I-174
Pättikangas T.J.H. III-1003,1303
Paul S. I-283,375
Paume M. IV-1721
Pavlov Yu.D. III-1080
Peacock N.J. III-1413
Pecquet A.L. III-1231
Pedit H. IV-1782
Pedorenko A.V. II-894
Peebles W.A. I-134,150,174, 203,279,III-1133, IV-1596,1604,1798
Pegoraro F. II-793,898,946
Pégourié B. III-1227
Pellet Injection Team I-239, II-479,483, III-1215,1287
Peng Y.-K.M. II-825
Penningsveld F.-P. II-483
Pereira J. IV-1560
Pericoli Ridolfini V. III-1203,1389
Perkins F.W. I-134,III-1031
Persson H. II-817
Pesic S. III-1116
Petravic M. III-1417
Petrie T.W. I-275
Petrov A.Ye. II-467
Petrov S.Ya. I-82
Petrov Yu.V. IV-1684
Petrovic Z. III-1405
Peysson Y. III-1227,1231
Philipona R. I-203,279, IV-1604
Phillion D. IV-1861
Phillips C.K. III-1048
Phillips P.E. I-26,174, III-1133
Pietrzyk Z.A. I-78
Pigarov A.Yu. I-13
Pilipenko V.V. III-1060
Pillon M. I-98
Pimenov A.B. III-1080,1084, IV-1488
Pitcher C.S. III-1381,1417, 1419
Pitts R.A. III-1283,1472
Pivinskij A.A. II-785
Platz P. III-1231, IV-1697,1701
Pochelon A. I-78,IV-1680
Podushnikova K.A. I-299,411, III-1480
Polevoj A.R. I-195
Politzer P. III-1259
Polman R.W. III-1121
Pomphrey N. I-134
Popel S.I. III-1190
Popov A.M. II-894
Porcelli F. I-259,323,

Porcelli F. 327,II-898, 918,946
Porkolab M. I-134,III-1100
Porte L. I-323,IV-1504
Porto P. II-601
Pospieszczyk A III-1447
Postupaev V.V. II-614
Potapenko I.F. II-877, III-1064
Power A. II-663
Pozzoli R. III-1088,1104
Prater R. III-1259
Prentice R. I-5,9,IV-1500
Prokhorov D.Yu. II-777
Pu Z.-Y. II-727,728
Puiatti M.E. II-533,537
Puri S. III-1031,1158, 1315,IV-1770
Qin Pinjian I-363
Qiu X.-M. IV-1824
Quemeneur A. IV-1588
Ramponi G. IV-1709
Ramsey A.T. I-42,46,114, 146,III-1048, 1417,1419
Ran L. I-311
Rasmussen D.A. II-439,443, 455
Rassadin L.A. IV-1688
Rau F. II-517
Rax J.-M. II-938, III-1231, IV-1693
Rayburn T.M. II-439
Razdobarin G.T. I-299,411, III-1125,1480, IV-1684
Razumova K.A. I-315, III-1080,1084
Rebut P.H. II-703
Reichle R. I-251
Reiter D. III-1447
Remkes G.J.J. I-199,407
Renner H. III-1271
Ress D. IV-1861
Rettig C. IV-1604
Rey G. III-1231
Reznichenko P.V. IV-1536
Rhodes T.L. III-1353,1456, 1460
Ribe F.L. II-605, III-1137
Ribeiro C. III-1349
Richards B. I-26,174,
Richards B. III-1133
Riedel K. I-151
Rieser H. II-715
Rij W.I. van II-505
Rimini F. III-1015,1150, IV-1709,1713
Ringler H. II-471,475,484
Ritz Ch.P. I-150,II-581, III-1353,1456,1460
Riviere A.C. III-1267,1283
Roberts D.E. I-355,359
Roberts J. IV-1548
Robinson D.C. I-130,178,s211, III-1267,1283
Robouch B.V. IV-1520
Roccella M. I-122
Rodriguez L. I-22,III-1231
Rodriguez R. III-1259
Rodriguez Yunta A. II-505
Rogdestvensky V.V. I-82
Roger D. III-1456
Röhr H. I-62
Rollet S. IV-1652
Romanelli F. II-707,711
Romannikov A.N. II-914
Romero H. III-995
Ronzio D. III-1104
Roquemore A.L. IV-1548
Rosa M. De IV-1871
Rosenbluth M.N. I-126,II-970
Roubin J.-P. II-728,732
Rowan W.L. I-26,174
Roy A. II-958
Roy I.N. I-195,II-954, III-1080,1084
Rozhansky V. II-744
Rozhdestvensky V.V. I-299,411,III-1480
Ruan L. I-154
Rubel M. III-1401
Rudakov D.L. III-1076
Rudakov L.I. II-609
Rudyj A. III-1460,1464, IV-1676
Rusbridge M.G. II-561,622
Rusbüldt D. III-1472
Russo A.J. I-403
Ryan P.M. III-1311
Rynn N. IV-1811
Ryter F. I-94,239,295, III-1052
Sabbagh S.A. I-387
Sack C. I-263,II-691,801
Sack H.C. I-259
Sadler G. I-1,5,9,98,

Sadler G. 162,323,331, III-1015, IV-1496,1608
Sadowski M. II-634
Sagara A. II-451
Sager G. I-271
Saibene G. III-1357,1373
Saito K. II-545
Saitou N. II-626
Sakamoto M. I-34,227
Sakanaka P.H. II-861
Sakasai A. I-223,IV-1508
Sakharov N.V. I-82,299,III-1480
Salas A. II-501
Salmon N.A. III-1150
Salomaa R.R.E. III-1303
Salvetti A. IV-1871
Salzmann H. IV-1692
Samain A. II-728,736, 845,938
Samm U. I-287,III-1472
Sanchez J. IV-1572,1592
Sandeman J.C. IV-1778
Sandmann W. I-215,235,239
Sano F. II-459
Santi D. I-118
Santiago M.A.M. IV-1786
Sanuki H. II-451
Sapozhnikov A.V. II-467
Sardei F. II-471,475
Sarksyan K.A. II-467
Sartori R. III-1357,1373
Sasao M. I-34
Sato M. II-459
Sato K.N. I-34,227
Sato K. I-34
Savrukhin P.V. I-195,315,III-1080, IV-1484,1620
Saxena Y.C. IV-1749
Sayal V.K. IV-1828
Scarin P. II-533,537
Scharer J.E. III-1023
Scharp L.E. II-521
Scheffel J. II-610,IV-1836
Schep T.J. II-946
Scherbakov A.G. III-1072
Schiffel J. III-1048
Schissel D.P. I-271,275
Schivell J. I-146
Schmidt G.L. I-5,42,46,259, III-1048,1419
Schmidt J.A. I-134
Schneider W. II-841
Schoenberg K.F. II-581
Schooch P.M. I-26,38,174,III-1133
Schoon N. IV-1532
Schorn R.P. I-287
Schram D.C. III-983
Schubert R. IV-1552
Schüller F.C. I-199,407,III-1121
Schüller P.G. III-1271
Schultz G. II-954,III-1133
Schupfer N. IV-1786
Schwartz J. IV-1532
Schweer B.F. I-287
Schwenn U. II-931
Scott S.D. I-50,114,146, III-1419
Seki T. I-34
Sen A. II-966
Sengoku S. III-1452
Seraydarian R.P. I-271
Sergeev V.Yu. I-231,IV-1536
Serra F. II-837,IV-1560
Sesnic S. I-367,375
Sevastyanov A.A. IV-1820
Shakhovets K.G. I-82,411,III-1480
Sharma S.R. IV-1828
Sharma S.K. II-684
Shashkov A.Yu. II-609
Shats M.G. II-467
Shcheglov M.A. II-614
Sheffield J. I-102
Shepard T.D. II-439
Sherwell D. I-355,359
Shibata T. III-1452
Shigueoka H. II-861
Shiina S. II-545
Shiina T. III-1452
Shimada T. II-545
Shimazu Y. II-541,549
Shimpo F. I-34
Shinohara S. II-541,549
Shirai A. II-541,549
Shishkin A.A. II-529
Shishkin A.G. III-1239,1243,1247
Shkarofsky I.P. III-1191,1195
Shoji T. II-451,III-1452
Shoucri M. III-1191,1299
Shukla P.K. II-760,IV-1766
Shuklin A.P. IV-1880
Shurygin R.V. III-987
Shurygin V.A. IV-1612
Shustova N.V. III-1125,IV-1684
Sidle J.B. II-553
Sidorov V.P. III-1145
Siegrist M. IV-1680
Sigmar D.J. I-134
Sigov Yu.S. IV-1840

Silaev I.I. IV-1840
Silari M. III-1112
Silivra O.A. III-1199
Siller G. IV-1560
Silva A. II-837,IV-1560
Silva R.P. Da III-1349
Silvester C. I-379,III-1283
Simmet E. I-182
Simonetto A. III-1112
Simonini R. III-1369
Simpkins J.E. II-455
Simpson J.C.B. III-1357
Simpson P.R. III-1283
Singh A.K. IV-1749
Singh D.C. I-174,III-1133
Singh D.P. IV-1867,1871
Sinman A. II-597
Sinman S. II-597
Sips A.C.C. I-158,199,323, IV-1500
Sitenko A.G. IV-1802
Skiff F. IV-1624,1807,1811
Skovoroda A.A. II-593,III-1072
Smeets P.H.M. III-1121
Smeulders P. I-323,331,III-1150
Smirnov A.I. III-1239,1243,1247, 1480
Smirnova E.A. II-609
Smith B.A. I-150,174
Smith G.R. III-1096
Smith R.J. IV-1628
Smits F.M.A. III-1121
Snider R. III-1259
Sobhanian S. II-451
Solari G. III-1112
Söldner F.X. I-58, II-837, III-1092,1171, 1215,1223,1287, 1291,1323,IV-1560
Soliman H.M. II-630
Soltwisch H. IV-1660
Sosenko P.P. II-686,IV-1802
Soumagne G. IV-1680
Speck R. IV-1861
Spineau F. II-902
Springmann E. II-801
St. John H. I-271
Stäbler A. I-395,III-1439
Stakenborg J. III-1117,1121
Stambaugh R.D. I-134,371
Stamp M.F. I-9,III-1357,1361, 1365,1377,1381, 1385
Stangeby P.C. III-1385,1472
Start D.F.H. I-1,255,323,327, III-1015,1019,1150
Stearns J.W. III-979
Stepanenko M.M. III-1080
Stephan Y. II-872
Stern R. IV-1811
Steuer K.-H. I-62,182,295, III-1052,1423
Stevens J. III-1048
Stickelmann C. I-287
Stojanovic V. III-1405
Stojic A. III-1116
Stokic Z. III-1405
Stork D. I-90,247,255,259
Storm E. IV-1861
Stotland M.A. III-1319
Stotler D.P. I-134,III-1417
Stott P.E. III-1381
Strachan J.D. III-1048,IV-1548
Strait E.J. I-275,371,427
Stratton B.C. I-42,46,50,114, 146,III-1048
Streikov V.S. III-1080
Stringer T.E. II-801,805
Stroth U. I-58,66,151,183
Stubberfield P.M. I-1,5,106,162
Subbotin A.A. III-1327
Sudo S. II-459,IV-1524
Suematsu H. IV-1524
Sugama H. II-459
Sugie T. I-223,IV-1508
Sukachov A.V. III-1319
Summers D.D.R. I-9,251,III-1357, 1377,1381,1385
Summers H.P. III-1361, IV-1496,1664
Sund R.S. III-1023
Sünder D. II-764
Sushkov A.V. III-1076,1080
Suzuki K. III-1452
Suzuki N. III-1452
Suzuki S. III-1452
Synakowski E.J. I-42,46,50,114, 146,III-1048
Szydlowski A. II-634
Tagle J.A. III-1373,1381
Takahashi C. II-451
Takahashi H. I-283,367,375
Takase H. III-1211
Takeiri Y. II-451
Takeuchi H. I-223,III-1183, IV-1508
Takeuchi K. I-351
Takita Y. II-451

Takizuka T. III-1007
Talvard M. III-1231
Tamai H. III-1452
Tamor S. II-970
Tan M. I-311
Tanahashi S. I-34
Tang L. I-311
Tanga A. I-1,255,259,323, III-1015
Taniguchi Y. I-34
Tarasyan K.N. II-785
Taroni A. I-5,327, II-801, II-1365,1369
Taroni L.L. I-247
Tartari U. IV-1636
Taylor G. I-42,46,114,146, III-1048
Taylor R.J. I-138, 287
Taylor T.S. I-251,371,427
TBR-1 Team III-1349
Teichmann J. II-864
Telesca G. IV-1532
Tendler M. II-744
Terry J. I-46,387
Tessema G.Y. IV-1778
TEXTOR Team III-1447
TFTR Group III-1048,IV-1540
Theimer G. III-1464
Thoe R. IV-1861
Thomas C.E. II-439,IV-1492
Thomas D. III-1439
Thomas P.R. I-1,263,III-1015, 1019,1381,1385
Thomsen K. I-110,166,259, II-797,III-1015
Thumm M. III-1271
Thyagaraja A. II-942
Tibone F. I-5,255, II-801,805
Tielemans A.J.H. III-1121
Tilia B. IV-1717
Tisma R. I-215
Titishov K.B. III-1080
Tito C.J. III-1121
TJ-I Team I-18,IV-1512
Tobita K. III-1011,1183
Todd T.N. I-130,379
Toffol Ph. De III-1044
Toi K. I-34
Tokar' M.Z. III-1345,1448
Tokunov A.I. III-1125,IV-1684
Tokutake T. III-1452
Tollivier J.S. II-443
Tonon G. III-1231
TORE SUPRA Team I-86
Towner E.H. I-114
Towner H.H. I-146
Toyama H. II-541,549
Tran M.Q. IV-1807,1811
Trebes J. IV-1861
Tribaldos V. IV-1648
Troyon F. II-954,958
Truc A. IV-1588
Trukhin V. III-1259
Tsai S.-T. II-727,728
Tsois N. I-395,III-1427,1439, 1460
Tsuchimoto M. III-1039
Tsui H.Y.W. II-581
Tsukahara Y. IV-1508
Tsukishima T. IV-1524
Tsunawaki Y. IV-1524
Tsuzuki K. II-451
Tsuzuki T. I-34
Tsypin V.S. III-1145
Tsytovich V.N. III-1190
Tubbing B.J.D. I-1,255,259,III-1015
Tuccillo A.A. III-1287,1335
Tukachinskij A.S. I-299,411,III-1480
Turnbull A.D. I-371,427
Turner M.F. I-130
Turner R. IV-1861
Tutter M. III-1271,IV-1576
Uchino K. II-459
Uckan T. III-1353,IV-1492
Ueda I. II-541
Ueda N. II-809
Ueeda T. III-1251
Uesugi Y. III-1340
Ulrickson M. I-134,III-1417,1419
Uno S. III-1452
Ushakov S.N. I-231,IV-1536
Ushigusa K. III-1183
Vakulenko M.O. II-686
Valencia-Alvarado R. I-30
Valisa M. II-533,537
Vallet J.C. I-86,III-1231
Vallinga P.M. III-983
Vandenplas P.E. I-287
Varela P. IV-1560
Varias A. II-497,509
Vaselli M. IV-1867,1871
Vasin N.L. I-195,231,III-1076,1080,1084, IV-1536
Vayakis G. I-211,III-1283
Vdovin V.L. III-1295
Vega J.A. I-22
Velikovich A.L. II-659

Vergamota S. IV-1560
Verhoeven A.G.A. III-1117,1121
Vershkov V.A. III-1076,1080
Villiers J.A.M. De I-355,359
Vlad G. II-906
Vlad M. II-902
Vladimirov S.V. III-1187
Vlases G. I-339
Vlasov V.P. IV-1488
Voge A. II-950
Volkov V.P. III-1080
Vollmer O. I-94,183,295
VonGoeler S. III-1048
Voropaev S.G. II-614
Voytenko D.A. III-1319
Wade M.R. II-439,443
Wagner F. I-58,94,110,295
Wagner R. IV-1520
Waidmann G. I-319
Wakatani M. II-459
Wallace R. IV-1861
Walsh M.J. II-557,565,569
Waltz R.E. I-126,134
Wan S. III-1154
Wang J.P. II-853
Wang L. III-1149
Ward D. I-323
Warrick C.D. III-1283
Wassenhove G. Van III-1040
Watari T. I-34
Watkins J.G. I-403
Watkins M.L. III-1369
Watkins N. I-331
Weber P.G. II-581
Wegner P. IV-1861
Wégrowe J.-G. III-1235
Weiland J. II-769
Weisen H. I-5,9,90,162,259, 323,III-1361,1385, IV-1496,1608
Weller A. II-479
Wen Y. III-1154
Wenzel K.W. I-150
Wenzel U. IV-1488
Werthmann H. II-715
Wesner F. I-239,III-1052, IV-1552
Wesson J.A. I-335,III-1015
Westerhof E. II-821,III-1121
Weynants R.R. I-383,287,III-1040
Wieland R.M. I-114,146,387
Wienhold P. III-1401
Wilgen J.B. II-443,455,IV-1492
Wilhelmsson H. II-885
Willen U. III-1019
Willi O. IV-1864
Wilson J.R. III-1048
Wing W.R. II-443,455
Winter J. I-275
Wintermeyer G. IV-1794
Winternitz P. II-864
Wira K. III-1263
Wobig H. II-517
Wolf G.H. I-287,III-1447
Wolfe S.M. I-271
Wolfe S.W. I-335
Wolle B. IV-1516
Wong K.L. III-1048,IV-1544
Wootton A.J. I-38,174,III-1133, 1353,1456,1460
WVII-AS Team II-471,475,479,483, 484,517,III-1271, 1275,IV-1572,1576
Wysocki F.J. II-643
Xang X.Z. III-1133
Xiang Z. III-1154
Xie J. I-363
Xu D. I-307
Xu G. I-154
Yagi Y. II-545
Yagura S. III-978
Yakashima T. II-459
Yakovenko Yu.V. II-699
Yamada H. II-451
Yamada M. IV-1811
Yamagishi K. II-541,549
Yamagiwa M. III-1007
Yamamoto T. III-1340,1452
Yamauchi T. III-1452
Yan L. I-311
Yan Y. I-307
Yang J.-G. II-752
Yang J.W. I-287,III-1040
Yang Q. III-1341
Yang S. III-1341
Yang X.Z. I-26
Yaramyshev G.S. III-1080
Yaroshevich S.P. I-82,299,411, III-1480
Yavorsky V.A. II-699
Ye H. III-999
Yin Y. II-679
Yoneta A. III-1039
Yoshida H. I-223
Yoshino R. I-223
Young K.M. I-134
Young P. IV-1861
Yu C. I-150,174,

Yu C.	III-1133,1154
Yu G.Y.	I-415
Yu M.Y.	II-760
Yuan D.	III-1149
Yuan D.C.	IV-1680
Yushmanov P.N.	II-781, 789,III-1080
Zaitsev F.S.	III-1247
Zakharov L.E.	III-1327
Zambotti G.	III-1235
Zamkov V.I.	III-1060
Zang X.Z.	I-38
Zanza V.	IV-1717
Zao J.	I-307
Zarnstorff M.C.	I-42,114,146,387, III-1419
Zastrow K.-D.	II-655,IV-1608
Zavadsky V.M.	IV-1684
Zavala G.	I-243
Zaveri P.	IV-1745
Ze F.	IV-1861
Zebrowski J.	II-634
Zhang D.	III-1149
Zhang H.	I-307
Zhang Z.M.	I-26
Zhao H.	I-311
Zheng S.	III-1149
Zheng Y.	I-154,307,311, III-1341
Zhil'tsov V.A.	II-593,III-1072
Zhong Y.	I-154
Zhu S.	III-1154
Zohm H.	I-54,291,II-837, III-1223
Zolotukhin A.V.	II-529
Zou X.L.	II-736 IV-1693,1721
Zouhar M.	III-1287
Zukakishvili G.G.	III-1060
Zurro B.	I-18,IV-1512
Zushi H.	II-459,IV-1524
Zweben S.	III-1048